

David Izquierdo Villalba

Galactic Bulges, spinning black holes and star forming galaxies in their cosmological context: insights from a semi-analytical perspective

Director/es

Bonoli, Silvia  
Hernández-Monteaudo, Carlos

<http://zaguan.unizar.es/collection/Tesis>

© Universidad de Zaragoza  
Servicio de Publicaciones

ISSN 2254-7606



**Universidad**  
Zaragoza

Tesis Doctoral

**GALACTIC BULGES, SPINNING BLACK HOLES  
AND STAR FORMING GALAXIES IN THEIR  
COSMOLOGICAL CONTEXT: INSIGHTS FROM A  
SEMI-ANALYTICAL PERSPECTIVE**

Autor

**David Izquierdo Villalba**

Director/es

Bonoli, Silvia  
Hernández-Monteagudo, Carlos

**UNIVERSIDAD DE ZARAGOZA**  
**Escuela de Doctorado**

Programa de Doctorado en Física

2020





---

# **GALACTIC BULGES, SPINNING BLACK HOLES AND STAR FORMING GALAXIES IN THEIR COSMOLOGICAL CONTEXT: INSIGHTS FROM A SEMI-ANALYTICAL PERSPECTIVE**

---

DAVID IZQUIERDO-VILLALBA

*A thesis supervised by:*

Dr. Silvia Bonoli

Dr. Carlos Hernández-Monteagudo



**Universidad** Zaragoza



**CENTRO DE ESTUDIOS DE FÍSICA DEL COSMOS DE ARAGÓN  
(CEFCA)**

Cosmology department

**UNIVERSITY OF ZARAGOZA**

Faculty of physics

Theoretical physics department

---

14th September 2020





*“Alguien que hacía cuerdas trenzadas me dijo una vez que las cuerdas representan el mismo flujo del tiempo. Las cuerdas giran... se entrelazan... se desenredan... se rompen... y se vuelven a conectar.”*

Kimi no Na wa.

*“Quando tocchiamo il punto più basso, siamo pronti per i cambiamenti più grandi.”*

The Legend of Korra.

*“Adiós Frodo Bolsón. Te entrego la luz de Earendil, nuestra más preciada estrella. Que ella te ilumine en los lugares oscuros cuando las demás luces se apaguen.”*

El señor de los anillos: La comunidad del anillo.

*“Namárië”*

The Road Goes Ever On, J. R. R. Tolkien.

*“El enemigo únicamente nos triplica en número, alentador para cualquier griego. En este día, liberamos al mundo del misticismo y la tiranía, y damos la bienvenida al futuro más esperanzador que hayamos imaginado.”*

300.

*“Los caracteres de mariposa en japonés son insecto del camino celestial. ¿Por qué?. Rei me explicó que el nombre japonés es de hace mucho tiempo, cuando la gente señalaba a esa criatura mientras se dirigía hacia el sol.”*

March comes in like a lion.

*“Pero acabo de tomar una decisión, voy a viajar por todo el mundo, igual que haces tú. Puede que encuentre muchos peligros por el camino, puede que incluso muera, pero... no me importa. He elegido ya tomar ese camino. Entonces, tal vez algún día podamos encontrarnos de nuevo bajo el firmamento estrellado. Ambos seremos viajeros, Violet Evergarden. Si eso sucediera, ¿podríamos volver a ver juntos las estrellas?, dime, ¿podríamos, Violet Evergarden?.”*

Violet Evergarden.

David Izquierdo Villaba, 2020

Galactic bulges, spinning black holes and star forming galaxies in their cosmological context: Insights from a semi-analytical perspective. Thesis defended: October 2020.

This thesis was carried out at Centro de Estudios de Física del Cosmos de Aragón (CEFCA), Teruel (Spain). The work presented here has been possible thanks to the support of the Spanish Ministerio de Economía, Industria y Competitividad (*AYA2015-66211-C2-2 MINECO/FEDER*), the Aragón Government (*Research Groups E16 17R*) and the grant *Programa Operativo Fondo Social Europeo de Aragón 2014-2020, Construyendo Europa desde Aragón*.

## ACKNOWLEDGEMENTS

*“Se acabo, ¿Se acabo qué? Si doy un paso más sera lo más lejos que he estado de mi hogar en mi vida. Vamos Sam. Recuerda lo que Bilbo solía decir: Es peligroso, Frodo, cruzar tu puerta. Pones tu pie en el camino y si no cuidas tus pasos, nunca sabes a dónde te pueden llevar.”*

*“This is it. This is, what? If I take one more step, I’ll be the farthest away from home I’ve ever been. Come on, Sam. Remember what Bilbo used to say: It’s a dangerous business, Frodo, going out your door. You step onto the road, and if you don’t keep your feet, there’s no knowing where you might be swept off too.”*

El señor de los anillos: La comunidad del anillo.      The Lord of the Rings: The Fellowship of the Ring.

Me gustaría empezar dándole las gracias a mi supervisora Silvia Bonoli, por sus consejos y paciencia. Gracias por haberme apoyado en todo. Tu empatía en momentos difíciles de la tesis siempre me ha servido como empujón en la dirección correcta. También me gustaría agradecer la constante ayuda y consejos de Raúl, Álvaro, Carliños, Carlos, Jesús, Sergio y Yetli. Many thanks also to Volker Springel for hosting me at the Max Planck Institute for a month. They were enriching weeks. Mis compañeros de doctorado han sido una maravilla. Daniele, Giovanni, Gonzalo, Rafa, Siddharta y Matteo. Siempre recordaré las deliciosas cenas de Matteo (que empezaron en Teruel y continúan en San Sebastián), el sarcasmo de Siddharta, la largas charlas en la oficina o en Don Diego con Rafa (cómo olvidar también sus siestas en la oficina), los raros sonidos de Gonzalo y la amabilidad de Giovanni. Por último y no menos importantes, quiero agradecer a Daniele su continua ayuda con el inglés, con los correos, con la física de las galaxias de disco (y física en general) y con mi miedo a volar. Nuestros viajes por toda Europa, Zaragoza y San Sebastián, nuestros desayunos en Granier, nuestras cenas en la Barrica y en Raffaele y las continuas conversaciones de todo y de nada, siempre quedarán en mi memoria. Has sido uno de los mejores compañeros en *este viaje inesperado* que es el doctorado. Mis agradecimientos también incluyen a Gloria Luzón y Theopisti Dafni cuya ayuda y predisposición en todo han hecho mucho más fácil mi relación con la Universidad. Me alegro mucho de haberos escogido como tutoras. Gracias también a toda la gente de CEFCA, en especial a Gema, Juan, Mikel, Alicia, Inés y Maite cuyo trabajo ha sido imprescindible durante mi tesis.

Mis más profundos agradecimientos van a mi familia. A mis padres (Gabriel y María Angeles), hermana (Helena), abuelos (Angelines, Antonio, Milagros y Gabriel) y tíos (Alejandra y Pedro). Vuestro apoyo durante toda mi carrera académica, y de forma general en mi vida, ha sido fundamental. Recuerdo practicar con todos vosotros la charla de mi trabajo de fin de grado. ¡Creo que nunca llegasteis a entender qué diantres era un *muón*!. Gracias a mis abuelas por sus meriendas tras largas horas de estudio (nocilla de tres torretas por parte de Milagros y de jamón por parte de Angelines). Los “no te va a dar tiempo” de mi hermana y los “descansa ya por hoy” de mis padres tampoco se olvidarán nunca. De toda mi familia, y que no se sientan celosos el resto, quiero destacar el esfuerzo de mis padres por darnos unos estudios a mi hermana y a mi. No ha debido de ser fácil.

Gracias María y Marina, que hicisteis los cuatro años de la carrera más llevaderos. Momentos como las inoportunas llamadas de Marina cuando estaba echándome la siesta, nuestras “dificultades” con los

osciloscopios, los continuos calambrazos en técnicas físicas, las acciones más alocadas de María (que han sido unas cuantas) o las interminables horas en la sala de lectura son momentos que nunca olvidaré, ¡siempre seremos ese trío intentando encajar en grupos de dos!. De la gente que conocí en la carrera de física merecen una mención especial Anabel, que ha sido un apoyo incondicional. Tenemos que estar orgullosos de nuestras rarezas y tocs, Anabel. Por cierto, tus momentos de rojez máxima y tus raros gustos de mezclar dos cafés solos de máquina siempre serán famosos. ¡Cómo olvidarme de Nekane! que, a pesar de haber compartido juntos cuatro años en Física, nos conocíamos desde el instituto e incluso desde primaria. Los momentos contigo en la carrera han sido inolvidables, llenos de risas y momentos un tanto peculiares: tus tartas de tres toneladas y media, tus suspiritos, tus arritmias después de beberte de un trago mis *monsters*, tus termos de café en el pabellón de filología, tus “ajustes” de doble exponenciales, tus extrañas compañeras de piso, tus jerbos, tu inexplicable facilidad con la electrónica... Gracias por haber estado ahí y por seguir apoyándome en lo que necesite. Gracias a ti también Alexie y Laura, grandes compañeras de estudios durante un breve año y buenas amigas para el resto de la vida.

Esta tesis también os la agradezco a vosotras Ainhoa, Ana, Cristina, Miriam, Sara y Vanesa, por nuestros más de 16 años de amistad y por los momentos tan buenos que hemos pasado. Risas, cotilleos y excursiones siempre serán nuestra marca de identidad. Cuando salimos de fiesta (aunque yo no lo haga mucho) las risas siempre están ahí: aspiradoras, imitaciones de gente o caídas dentro de la maleta. De todas ellas quiero destacar a Cristina, con la cual he compartido muchos momentos. El destino lo ha querido así. Recuerdo verte a lo lejos por el barrio con tu hermano y de repente, ¡puf! nos hicimos inseparables en el instituto. Gracias por haberme ayudado en tantas cosas, gracias por todo.

Finalmente, quiero darle las gracias a mis compañeras de máster Carmen, Laura, María, Marta, Noe y Sara. Gracias señoras, la vida en Madrid fue mucho más sencilla con vosotras. Doy gracias por el persistente positivismo de Carmen, la dulzura de Laura, los “joe macho” de María, el divertido sarcasmo de Marta, la gran amistad de Noe y el continuo apoyo de Sara. Al principio del máster tenía miedo de no hacer amigos, pero de repente encontré a los mejores. Por cierto, por una vez que nos ponemos de acuerdo para hacer un viaje juntos a Portugal, se nos viene encima esta pandemia. Siempre me acordaré del “yo voy con el coche si hace falta” de Sara. ¿Algún día conseguiremos volver a quedar todos?. De todas formas, y haciendo la analogía a *Casablanca*, ¡siempre nos quedará el antro de pintar tazas!

*Gracias a todos,*

Daijobu uke aimasu,  
大丈夫請け合います



<b>List of Figures</b>	<b>viii</b>
<b>List of Tables</b>	<b>xi</b>
<b>RESUMEN DE LA TESIS</b>	<b>1</b>
<b>ABSTRACT</b>	<b>3</b>
<b>1 INTRODUCTION</b>	<b>5</b>
1.1 The galaxy formation and evolution paradigm . . . . .	5
1.1.1 The cosmological framework: The $\Lambda$ CDM model . . . . .	5
1.1.2 The galaxy formation: how matter transforms into light . . . . .	7
1.1.3 Studying galaxy formation trough computer simulations . . . . .	8
1.1.4 Some open issues in the galaxy formation paradigm . . . . .	11
1.2 Shaping galaxy morphology: A matter of bulge and disk . . . . .	12
1.2.1 A different bulge population: From ellipticals to bulges in late-type galaxies . . . . .	13
1.2.2 The bulge formation scenario . . . . .	14
1.2.3 Simulated bulges in a cosmological context: From semi-analytical models to hydrodynamical simulations . . . . .	17
1.3 Supermassive black holes: A key component of galaxy formation . . . . .	19
1.3.1 Theoretical black holes . . . . .	19
1.3.2 Supermassive black holes: Demography and correlations . . . . .	20
1.3.3 The formation of supermassive black holes . . . . .	23
1.3.4 Supermassive black holes growth through cosmological times . . . . .	23
1.3.5 Supermassive black hole spin: Theory and observations . . . . .	26
1.3.6 Understanding supermassive black holes through simulations . . . . .	31
1.4 The synergy between observations and simulations . . . . .	33
1.4.1 The new challenge for mock lightcones: emission line galaxies as new targets for surveys . . . . .	36
1.5 Objectives and outline of the thesis . . . . .	37
<b>2 L-Galaxies: A MODEL TO STUDY THE GALAXY EVOLUTION</b>	<b>39</b>
2.1 Introduction . . . . .	39
2.2 Dark matter merger trees . . . . .	40
2.2.1 Different subahlos and galaxies: Central and satellite . . . . .	41
2.3 Baryonic physics . . . . .	41
2.3.1 Gas cooling . . . . .	41



2.3.2	Galactic disks: the cold gas and stellar components . . . . .	43
2.3.3	Galactic bulges . . . . .	45
2.3.4	Supermassive black holes and AGN feedback . . . . .	47
2.3.5	Environmental processes . . . . .	48
2.3.6	Stellar population synthesis: The broad band photometry . . . . .	50
2.3.7	Dust model . . . . .	50
2.3.8	Free parameters in L-Galaxies . . . . .	51
<b>3</b>	<b>THE ASSEMBLY OF PSEDOBULGES IN A HIERARCHICAL UNIVERSE</b>	<b>52</b>
3.1	Introduction . . . . .	53
3.2	L-Galaxies semi-analytical model: Understanding the bulge assembly . . . . .	54
3.2.1	The build-up of bulges through mergers . . . . .	55
3.2.2	Disk instabilities: the growth of pseudobulges and classical bulges . . . . .	58
3.3	Results . . . . .	66
3.3.1	Pseudobulges across cosmic time . . . . .	66
3.3.2	Pseudobulges and their hosts in the local universe . . . . .	70
3.4	Summary and conclusions . . . . .	77
<b>4</b>	<b>BARRED GALAXIES IN THE LOCAL UNIVERSE: REVISITING THEIR ANALYTICAL FORMATION FROM A HYDRODYNAMICAL PERSPECTIVE</b>	<b>80</b>
4.1	Introduction . . . . .	81
4.2	Methodology . . . . .	83
4.2.1	The TNG100 simulation . . . . .	83
4.2.2	Bar and unbarred galaxies seen from an hydrodynamical perspective . . . . .	83
4.2.3	Bar and unbarred galaxies seen from an analytical perspective . . . . .	86
4.3	Results . . . . .	87
4.3.1	Differences between BUR and BSR: Distinct analytical results for barred galaxies . . . . .	88
4.3.2	The BSR and UBSR samples: Fake unbarred galaxies in the analytical criterion . . . . .	89
4.3.3	The BUR and UBUR samples: Fake barred galaxies in the analytical criterion . . . . .	90
4.3.4	Reducing the contamination: extra conditions in the analytical criterion . . . . .	91
4.4	Summary and conclusion . . . . .	92
<b>5</b>	<b>SPINNING BLACK HOLES AND WANDERING BLACK HOLES</b>	<b>95</b>
5.1	Introduction . . . . .	96
5.2	Galaxy formation model . . . . .	98
5.3	A comprehensive model of black hole growth . . . . .	99
5.3.1	Black hole seeding and spin initialization . . . . .	99
5.3.2	Black hole gas accretion . . . . .	100
5.3.3	Tracing the BH spin evolution . . . . .	102
5.3.4	Black hole coalescence . . . . .	106
5.3.5	The population of wandering black holes . . . . .	108
5.4	Nuclear black holes . . . . .	113
5.4.1	Black hole mass assembly . . . . .	113
5.4.2	The evolution of bolometric luminosity . . . . .	116
5.4.3	The evolution of black hole spin . . . . .	118
5.5	Wandering black holes . . . . .	120
5.5.1	Wandering black holes across cosmic time . . . . .	120
5.5.2	The environment of wandering black holes in the local universe . . . . .	122
5.6	The imprint of gravitational recoil on the BH global properties . . . . .	122
5.6.1	Black hole occupation fraction . . . . .	123
5.6.2	Effects on the scaling relations . . . . .	125
5.7	Summary and conclusions . . . . .	128

<b>6</b>	<b>MOCK LIGHTCONES FOR PHOTOMETRIC SURVEYS</b>	<b>131</b>
6.1	Introduction . . . . .	132
6.2	Methodology . . . . .	133
6.2.1	Lightcone construction . . . . .	133
6.2.2	Line emission modelling . . . . .	136
6.2.3	Observed magnitudes . . . . .	137
6.3	Validation . . . . .	137
6.3.1	Galaxy number counts . . . . .	137
6.3.2	Emission-line luminosity functions and line dust attenuation . . . . .	139
6.3.3	Clustering of high redshift <i>g</i> -band selected sources . . . . .	142
6.4	J-PLUS mock galaxy catalogues . . . . .	142
6.4.1	Validation of J-PLUS mocks . . . . .	144
6.4.2	Selecting emission-line galaxies . . . . .	145
6.4.3	Understanding the population of interlopers . . . . .	148
6.5	Summary and conclusions . . . . .	149
<b>7</b>	<b>SUMMARY AND CONCLUSIONS</b>	<b>152</b>
<b>8</b>	<b>FUTURE WORK</b>	<b>157</b>
	<b>RESUMEN Y CONCLUSIONES</b>	<b>159</b>
	<b>Bibliography</b>	<b>164</b>
<b>A</b>	<b>The motion of a spinless test body around a black hole: Innermost stable circular orbit</b>	<b>221</b>
<b>B</b>	<b>Feeding constraints on supermassive black hole: The Eddington limit</b>	<b>225</b>
<b>C</b>	<b>Improvements in the bulge size</b>	<b>227</b>
<b>D</b>	<b>The morphology for Millennium and Millennium II: A matter of major, minor mergers and smooth accretion</b>	<b>230</b>
<b>E</b>	<b>Ejections via Gravitational recoil and three body scattering</b>	<b>236</b>
<b>F</b>	<b>X-ray luminosity functions</b>	<b>238</b>
<b>G</b>	<b>Minimum structure repetition in the lightcone construction</b>	<b>241</b>
<b>H</b>	<b>Comparison between observed and predicted luminosity function</b>	<b>242</b>
<b>I</b>	<b>Curriculum vitae</b>	<b>245</b>

## LIST OF FIGURES

1.1	Distribution of dark matter particles in the Millennium II simulation at $z=0$ . . . . .	9
1.2	Gas and stellar surface density of the Milky Way galaxy of the Eris zoom-in simulation	10
1.3	Illustrative scheme of different bulge types . . . . .	14
1.4	Illustrative scheme of the phases of a binary black hole system . . . . .	26
1.5	Illustrative cartoon about the shape that an accretion disk displays around a spinning black hole . . . . .	29
1.6	Comparison between spectroscopy and photometry . . . . .	34
1.7	Comparison between spectroscopy and spectro-photometry survey . . . . .	35
1.8	SED example of an AGN/QSO and starburst galaxy . . . . .	36
3.1	The effect of mergers on the fraction of different morphological types at $z=0$ . . . . .	56
3.2	Number density of major mergers, minor mergers and <i>smooth accretion</i> as a function of redshift . . . . .	57
3.3	The effect of disk instabilities on the fraction of different morphological types at $z=0$ . . . . .	59
3.4	Number of dynamical times between two no consecutive disk instabilities. . . . .	60
3.5	Illustrative scheme of the possible paths of pseudobulge and classical bulge build-up. . . . .	61
3.6	Distribution of $\delta f_M$ and $\delta n^{mM}$ for all galaxies with stable disk that suffered a disk instability after a merger . . . . .	63
3.7	Number density of <i>secular</i> disk instability, <i>merger-induced</i> disk instability, major mergers, minor mergers and <i>smooth accretion</i> . . . . .	64
3.8	Median subhalo mass and stellar mass of galaxies hosting <i>pseudobulges</i> at different redshifts . . . . .	66
3.9	Subhalo - Stellar mass relation for pseudobulges, classical bulges, and all galaxies at $z=0$ and $z=1$ . . . . .	67
3.10	Relative contribution of pseudobulge, classical bulge and elliptical galaxies in the bulge galaxy population $z=0$ and 1 . . . . .	68
3.11	Fraction of pseudobulge galaxies that are centrals of their <i>friend-of-friend</i> halo . . . . .	69
3.12	Bar fraction $f_{\text{bar}}$ in the Millennium and Millennium II . . . . .	70
3.13	Star formation rate (Sfr) - $M_{\text{stellar}}$ plane for $z=0$ pseudobulges and classical bulges galaxies	71
3.14	Stellar population age of $z=0$ pseudobulge and classical bulge galaxies . . . . .	72
3.15	Comparison between the simulated and observed pseudobulges and classical bulges . . . . .	73
3.16	Stellar mass function and redshift of the last interaction (major and minor) for pseudobulge, classical bulge and elliptical galaxies . . . . .	74
3.17	Examples of the Millennium mergers trees for pseudobulge, classical bulge and elliptical galaxies . . . . .	76
3.18	Formation time of pseudobulge and classical bulge structure in pseudobulge galaxies . . . . .	77

4.1	Examples of the face-on surface mass density for a bar and unbarred galaxy . . . . .	85
4.2	Comparison of the bar and unbarred galaxy properties at different times . . . . .	86
4.3	Examples of BSR, BUR, UBSR, UBUR samples . . . . .	87
4.4	Comparison of the BUR and BSR properties at different times . . . . .	88
4.5	Comparison of the BSR and UBSR properties at different times . . . . .	89
4.6	Comparison of the BSR and UBSR stellar and subhalo properties at different times . . . . .	90
4.7	Comparison of the BUR and UBUR properties at different times . . . . .	91
4.8	Comparison of the BUR and UBUR stellar and subhalo properties at different times . . . . .	92
4.9	Plane $\xi$ - $\epsilon$ for BUR, UBUR, BSR and UBSR at different times . . . . .	93
4.10	Ratio of the number of disk instabilities detected with the old and new criterion . . . . .	94
5.1	Distribution of BBH merger delay timescales for different formation redshifts . . . . .	107
5.2	A schematic view of the two pathways that lead to wandering BHs . . . . .	109
5.3	<i>Orphan</i> wBHs orbit extracted from L-Galaxies run on top of MS subhalo merger trees . . . . .	112
5.4	Redshift evolution of the black hole mass function and active BH population . . . . .	114
5.5	Quasar bolometric luminosity functions and quasar luminosity vs black hole mass at different redshifts . . . . .	116
5.6	Black hole spin, $a$ , as a function of black hole mass ( $M_{\text{BH}}$ ) at $z = 0$ . . . . .	118
5.7	Predicted black hole spins, $a$ , as a function of black hole mass ( $M_{\text{BH}}$ ) and at different redshifts and bulge types . . . . .	119
5.8	Redshift evolution of the number density, subhalo mass, stellar mass and position of nuclear and wandering BHs . . . . .	121
5.9	Connection between the wandering black holes and their host subhalos and galaxy stellar mass at $z = 0$ . . . . .	123
5.10	Nuclear black hole occupation fraction as a function of stellar mass, bulge types and redshift . . . . .	124
5.11	Redshift distribution of black hole ejections and reincorporation after a wandering phase . . . . .	125
5.12	Black hole and bulge mass relation for different bulge type with and without wandering phase and recoil velocities . . . . .	126
5.13	Probability of finding a nuclear BH which underwent in a wandering phase . . . . .	127
5.14	Bulge - black hole mass relation for nuclear black holes which underwent a wandering phase . . . . .	128
6.1	The observed colour $g-r$ for galaxies with $M_{\text{stellar}} > 10^{10} M_{\odot}/h$ . . . . .	134
6.2	Spatial distribution of galaxies with $M_{\text{stellar}} > 10^{10} M_{\odot}/h$ inside our mock lightcone . . . . .	135
6.3	Abundance of galaxies as a function of observed magnitude for the 4 different SDSS bands . . . . .	138
6.4	Comparison between the observed and predicted luminosity function of $H\alpha$ , [OII], $H\beta$ , and [OIII] <sub>5007</sub> at different redshifts . . . . .	139
6.5	Redshift dependence of the dust attenuation coefficient . . . . .	140
6.6	Two-point angular correlation function of $g$ -selected galaxies . . . . .	141
6.7	Transmission curves of the J-PLUS system and the wavelength at which the nine different lines included in the mock fall as a function of redshift . . . . .	143
6.8	Predicted flux in the 12 J-PLUS filters for 4 different emission line galaxies in the mock . . . . .	144
6.9	Galaxy number counts in each of the 12 J-PLUS filters . . . . .	145
6.10	Intrinsic $H\alpha$ luminosity function of the local universe . . . . .	146
6.11	Redshift distribution of galaxies selected to have a positive excess in the $J0660$ filter associated to line emission . . . . .	147
6.12	Comparison between the true and inferred values for the continuum density flux . . . . .	148
6.13	Purity as a function of detection threshold of mock J-PLUS galaxies selected to have emission lines . . . . .	149
6.14	Relation between $\Delta m^{\text{cut}}$ and the equivalent width (EW) for three different lines . . . . .	150

A.1	Values of $r_{\text{ISCO}}$ , $r_{\text{ISCO}}$ and $r_{\text{ISCO}}$ as a function of the BH spin parameter in co- and counter- rotating orbit . . . . .	223
C.1	Effective radius of early and late type galaxies at different redshifts after including energy dissipation . . . . .	228
D.1	Number density of major/minor mergers as a function of different merger and binding thresholds . . . . .	231
D.2	Median stellar mass of the merging satellite galaxy . . . . .	232
D.3	Plane binding energy - satellite mass at different redshifts . . . . .	233
D.4	Evolution of the morphological types with different combinations of binding and major/minor merger thresholds . . . . .	234
D.5	Typical merger ratios for minor mergers and <i>smooth accretions</i> at different stellar masses and redshifts . . . . .	235
E.1	Number density of nuclear black holes that are ejected from the nuclear part of the galaxy after a gravitational recoil and after 3-body scattering . . . . .	237
F.1	Hard X-ray luminosity functions at different redshifts . . . . .	239
F.2	Soft X-ray luminosity functions at different redshifts . . . . .	240
G.1	Example of the minimum repetition between Millennium box replications . . . . .	241
H.1	Comparison between the observed and predicted $H\alpha$ luminosity function at seven different redshifts . . . . .	242
H.2	Comparison between the observed and predicted $H\beta$ luminosity function at five different redshifts . . . . .	243
H.3	Comparison between the observed and predicted $[\text{OIII}]_{5007}$ luminosity function at seven different redshifts . . . . .	243
H.4	Comparison between the observed and predicted $[\text{OII}]$ luminosity function at eighteen different redshifts . . . . .	244

LIST OF TABLES

2.1	Values of L-Galaxies free parameters . . . . .	51
4.1	Sample of <i>Weak bars</i> , <i>Strong bars</i> and <i>Unbarred</i> galaxies in TNG100 . . . . .	84

## RESUMEN DE LA TESIS

*“ Cuanto silencio... Es la calma que precede a la tempestad. No quiero luchar en una batalla, pero estar al borde de una de la cual no puedo escapar es aún peor. ¿Hay alguna esperanza, Gandalf, para Frodo y Sam? Nunca ha habido demasiada... tan solo la de un necio.”*

El señor de los anillos: El Retorno del Rey.

*“It’s so quiet... It’s the deep breath before the plunge. I don’ want to be in a battle but waiting on the edge of one I can’t escape, is even worse. Is there any hope, Gandalf, for Frodo and Sam? There never was much hope Just a fool’s hope.”*

The Lord of the Rings: The Return of the King

Durante las últimas décadas, los astrofísicos han desarrollado una teoría sobre cómo se forman y evolucionan las galaxias. A pesar de ser exitosa en muchos aspectos, todavía tiene ciertas limitaciones que trabajos teóricos y observacionales están tratando de resolver. En esta tesis, contribuimos con estos trabajos teóricos abordando tres temas diferentes: bulbos galácticos, agujeros negros supermasivos y el desarrollo de catálogos simulados para la nueva generación de cartografiados de banda estrecha. Hemos abordado todos estos temas utilizando el modelo semianalítico L-Galaxies. A grandes rasgos, los modelos semianalíticos consisten en seguir la evolución de la componente bariónica del Universo utilizando aproximaciones analíticas aplicadas a “árboles” de fusiones de materia oscura. L-Galaxies es uno de los modelos más avanzados de la literatura, cuya capacidad para predecir las propiedades correctas de las galaxias en diferentes tiempos cosmológicos ha sido probada durante la última década en muchos trabajos. Una de las principales ventajas de L-Galaxies es la capacidad de ser ejecutado en los árboles de fusiones de materia oscura extraídos de las simulaciones Millennium cuyas diferencias en tamaños de caja y resolución en masa de materia oscura ofrecen la posibilidad de explorar los procesos físicos experimentados por las galaxias en una amplia variedad de escalas y entornos.

En la primera parte de la tesis, abordamos la formación de bulbos galácticos con especial énfasis en la población de pseudobulbos, cuya evolución en un universo jerárquico no ha sido del todo explorada. Concretamente, estudiamos su proceso de formación y caracterizamos las propiedades de sus galaxias anfitrionas a diferentes tiempos cosmológicos. Dentro del marco que nos proporciona L-Galaxies, las galaxias son capaces de desarrollar un bulbo a través de fusiones con otras galaxias e inestabilidades de disco. Suponiendo que los pseudobulbos solo pueden formarse y crecer a través de una evolución secular, hemos modificado el tratamiento de las inestabilidades del disco de L-Galaxies asumiendo que solo los eventos de inestabilidad desencadenados por procesos seculares conducen a estructuras de barra duraderas que finalmente forman y desarrollan pseudobulbos. Hemos aplicado este escenario en L-Galaxies ejecutado sobre los árboles de fusiones de Millennium y Millennium II. Los resultados del modelo están en concordancia con las observaciones, mostrando que los pseudobulbos en el universo local son estructuras pequeñas ( $\sim 0.5$  kpc) alojadas en galaxias similares a la Vía Láctea. Estos resultados son alentadores y respaldan nuestra principal suposición subyacente de que la estructura de pseudobulbo se forma principalmente a través de una evolución secular. Hemos ampliado nuestro análisis de pseudobulbos estudiando el comportamiento del criterio de inestabilidad de disco utilizada por L-Galaxies cuando es aplicada a una muestra de galaxia con y sin barra extraída de la simulación hidrodinámica cosmológica TNG100, actualmente una de las simulaciones más completas disponible. A

pesar de encontrar una correlación entre las predicciones del criterio analítico y el (no) ensamblaje real de las galaxias con (no) barra, hemos detectado casos en los que el criterio analítico falla, ya sea afirmando estabilidad del disco para galaxias barradas o inestabilidad del disco para las galaxias sin barra. Por ello, hemos propuesto una condición nueva adicional para ser combinada con el criterio de *L-Galaxies*. Esta combinación mejora la detectabilidad de barras y reduce la contaminación de falsas galaxias barradas.

La segunda parte de la tesis explora el ensamblaje en masas y la evolución del espín de los agujeros negros supermasivos a lo largo del tiempo cosmológico. Para ello, hemos actualizado el modelo *L-Galaxies*, incluyendo nuevos procesos físicos. Hemos asumido que el crecimiento de los agujeros negros se desencadena principalmente a través de la acumulación de gas frío después de fusiones de galaxias o inestabilidades de disco. Este crecimiento tiene lugar a través de una etapa de acrecimiento rápido seguida de una lenta. Durante estas fases, la evolución del espín del agujero negro es calculada usando de las propiedades morfológicas del bulbo en el que reside. Las predicciones del modelo muestran una buena compatibilidad con los resultados observacionales como la función de masa de los agujeros negros, la distribución de sus valores de espín, la relación entre la masa del bulbo y la del agujero negro y las funciones de luminosidad. Una de las principales novedades de esta tesis ha sido utilizar el modelo explicado anteriormente para explorar la formación y evolución de la población de agujeros negros errantes, es decir, una población que se encuentra fuera de las galaxias en órbitas cerradas dentro de los subhalos de materia oscura. Hemos descubierto que la formación de este tipo de agujeros negros errantes deja una huella en la co-evolución entre el agujero negro y la galaxia anfitriona, pudiendo ser detectada por los estudios de galaxias actuales y futuros.

Finalmente, la tercera parte de la tesis aborda el desarrollo de catálogos simulados especialmente diseñados para la nueva generación de cartografiados fotométricos de banda estrecha. Con este fin, hemos incluido la construcción de un cono de luz dentro de *L-Galaxies* incorporando en la fotometría de las galaxias simuladas el efecto de líneas de emisión producidas en regiones de formación estelar. Esto último ha asegurado la capacidad de los catálogos para predecir correctamente la fotometría de galaxias en filtros de banda estrecha. Para determinar el flujo exacto en estas líneas hemos utilizado un modelo de emisión nebulosa y de atenuación por el polvo capaz de predecir el flujo emitido por 9 líneas diferentes:  $Ly\alpha$ ,  $H\beta$ ,  $H\alpha$ , [OII], [OIII], [NeIII], [OI], [NII] y [SII]. La validación de nuestro cono de luz se ha realizado comparando con diversas observaciones el número de galaxias detectado en diferentes filtros, la distribución angular de galaxias y las funciones de luminosidad de las líneas  $H\alpha$ ,  $H\beta$ , [OII] y [OIII]<sub>5007</sub>. Hemos utilizado todos estos procedimientos para generar catálogos especialmente diseñados para J-PLUS, un cartografiado fotométrico de galaxias que presenta una gran cantidad de filtros de banda estrecha. Al analizar estos catálogos hemos demostrado la capacidad del cartografiado para identificar correctamente la población de galaxias con líneas de emisión a diferentes tiempos cosmológicos.

Como resumimos anteriormente, en esta tesis hemos abordado varios aspectos relacionados con la formación de galaxias, tratando de unir enfoques teóricos y observacionales. Sin duda alguna, el avance de los modelos teóricos combinado con los datos de experimentos futuros ayudará a construir una imagen más detallada de cómo se forman y evolucionan las estructuras en nuestro Universo.



## ABSTRACT

*“Mi querido Frodo, los hobbits son criaturas sorprendentes. Puedes aprender todas sus costumbres en un mes y después de cien años... aún te sorprenden.”*

*“My dear Frodo. Hobbits really are amazing creatures. You can learn all there is to know about their ways in a month and yet after a hundred years...the can still surprise you.”*

El señor de los anillos: La comunidad del anillo.      The Lord of the Rings: The Fellowship of the Ring.

During the last decades, astrophysicists have developed a theory about how galaxies form and evolve within the  $\Lambda$ CDM cosmological framework. Despite being successful in many aspects, this general picture has still some missing pieces that observational and theoretical works are trying to put all together. In this thesis, we try to answer to some open problems by addressing three different topics: galactic bulges, supermassive black holes and the development of mocks for the new generation of multi-narrow band surveys. We have tackled all these subjects by using the L-Galaxies semi-analytical model (SAM). Roughly, SAMs consist of dark matter merger trees populated with galaxies through analytical recipes. L-Galaxies is one of the state-of-the-art models whose capability to predict the correct galaxy properties at different redshifts has been proven during the last decade in many works. One of the main advantages of L-Galaxies is its flexibility to be run on the dark matter merger trees of the Millennium suite of simulations whose different box sizes and dark matter mass resolution offer the capability to explore different physical processes undergone by galaxies over a wide range of scales and environments.

In the first part of the thesis, we address the cosmological build-up of galactic bulges with special focus on pseudobulges, whose cosmological evolution in a  $\Lambda$ CDM Universe has not been fully explored yet. In particular, we study their formation process and characterize the properties of their host galaxies at different redshifts. Within the L-Galaxies framework, galaxies are allowed to develop a bulge component via mergers and disk instabilities (DIs). Under the hypothesis that pseudobulges can only form and grow via secular evolution, we have modified the treatment of galaxy DIs. In detail, we assumed that only secular DI events lead to the development and growth of pseudobulges through the formation of long-lasting bar structures. We have applied this pseudobulge formation scenario to L-Galaxies, run on top of the Millennium and Millennium II dark matter merger trees. The outcomes of the model are in agreement with observations, showing that  $z = 0$  pseudobulges are small structures ( $\sim 0.5$  kpc) hosted in main-sequence Milky Way-type galaxies. These results give support to our main underlying assumption that pseudobulge structure mainly form via secular evolution. We have extended our analysis of pseudobulge structures studying the performance of the DI criterion used by L-Galaxies when it is applied on a barred and unbarred galaxy sample of the cosmological hydrodynamical simulation TNG100. Despite finding a correlation between the analytical criteria predictions and the actual bar assembly (non-assembly) shown in the barred (unbarred) galaxies, we have detected cases where the analytical criterion fails, either claiming disk stability for barred galaxies or disk instability for the stable unbarred disks. We have proposed a new extra condition whose combination with the L-Galaxies criterion improves the detectability of bar structures and reduces both the contamination of fake barred galaxies and the number of undetected bar formation events.

The second part of the thesis explores the mass assembly and spin evolution of supermassive black holes (BHs) across cosmic time. For this objective, we have updated `L-Galaxies` with new physical prescriptions. We have assumed that BH-mass assembly is mainly triggered by gas accretion after galaxy mergers or disk instabilities, and it takes place through a stage of rapid growth followed by a regime of slow accretion rates. During these phases, the BH spin evolution is followed by linking it with the morphological properties of the hosting bulge. The model predictions display a good consistency with some local observables, such as the black hole mass function, spin values distribution, BH-bulge mass relation and quasar luminosity functions. One of the main novelties of this thesis has been to use the BH model previously explained for exploring the formation and evolution of the wandering black hole population, i.e the population of BH outside of galaxies in bound orbits within the dark matter subhalos. We have found that the formation of these type of wandering black holes leave an imprint in the co-evolution between the black hole and the host galaxy which can be detected by current and future galaxy surveys.

Finally, the third part of the thesis tackles the construction of mocks specially designed for the new generation of narrow-bands surveys. For this, we have inserted the lightcone assembly inside `L-Galaxies`, including in the photometry of the simulated galaxies the effect of emission lines produced in starforming regions. The latter has ensured the mock capability to correctly predict the galaxy photometry in narrow band filters. To determine the exact flux of emission lines we have used a model for the nebular emission in star-forming regions, coupled with a dust attenuation model, able to predict the flux emitted in 9 different lines:  $\text{Ly}\alpha$ ,  $\text{H}\beta$ ,  $\text{H}\alpha$ ,  $[\text{OII}]$ ,  $[\text{OIII}]$ ,  $[\text{NeIII}]$ ,  $[\text{OI}]$ ,  $[\text{NII}]$ , and  $[\text{SII}]$ . The validation of our lightcone has been done by comparing galaxy number counts, angular clustering, and  $\text{H}\alpha$ ,  $\text{H}\beta$ ,  $[\text{OII}]$  and  $[\text{OIII}]_{5007}$  luminosity functions to a compilation of observations. We have applied all these procedures to generate catalogues tailored for J-PLUS, a large optical galaxy survey featuring a large number of narrow band filters. By analysing the J-PLUS mock catalogues, we have proved the ability of the survey to correctly identify a population of emission-line galaxies at various redshifts.

As we summarize above, in this thesis we have tackled several aspects related to the details of galaxy formation, trying to bridge theoretical and observational approaches. The advance of theoretical models combined with the data from future experiments will certainly help to complete a detailed picture of how structures in our Universe form and evolve.

“Esta misión te ha sido encomendada a ti, Frodo de la Comarca y si tu no encuentras la salvación, nadie lo hará.”

El señor de los anillos: El Retorno del Rey.

“This task was appointed to you, Frodo of the Shire. If you do not find a way, no one will.”

The Lord of the Rings: The Return of the King.

## 1.1 The galaxy formation and evolution paradigm

Most of the visible matter in the Universe is condensed in the form of galaxies. How these structures formed and what are the physical processes which have shaped their structure are some of the main questions that astrophysicists try to answer. The set of all theories developed to give such response consolidate the so-called *galaxy formation and evolution paradigm*. In the next sections, we describe key aspects of the current understanding of galaxy formation and evolution, highlighting different computational techniques that have helped shedding light on this knowledge.

### 1.1.1 The cosmological framework: The $\Lambda$ CDM model

To understand how galaxies form and evolve, it is necessary to establish a cosmological framework. Modern cosmology is built on the General relativity theory (GR, [Einstein, 1916](#)) and the *cosmological principle* which states that the Universe is isotropic and homogeneous. Although this assumption might be contradictory with the observations of galaxies and clusters, it still holds when the Universe is averaged over large spatial scales. Joining of the cosmological principle with the Einstein equations of GR leads to the *Friedmann-Lemaître-Robertson-Walker* exact solution or metric which, in brief, describes a homogeneous, isotropic and expanding Universe:

$$ds^2 = -c^2 dt^2 + a^2(t) \left( \frac{dr^2}{1 - \kappa r^2} \pm r^2 d\theta^2 + r^2 \sin^2 \theta d\varphi^2 \right), \quad (1.1)$$

where  $r, \theta, \varphi$  are the spherical spatial coordinates,  $t$  is the time and  $\kappa$  is the curvature of the Universe spanning from 1, 0,  $-1$  for a closed, flat and open Universe, respectively.  $a(t)$  term is the so-called *cosmic scale factor* and describes the expansion of the Universe by encapsulating the change of the Universe scale length with time<sup>1</sup>. By definition, the value of  $a(t_0) = 1$ , where  $t_0$  is an arbitrary time usually chosen to be  $t_0 = t_{\text{today}}$ . Usually, instead of using  $a(t)$ , it is more frequent to describe the expansion of the Universe through the so-called *redshift* parameter,  $z$ , defined as:

$$z = \frac{1 - a(t)}{a(t)}, \quad (1.2)$$

where  $z = 0$  refers to the current time of the Universe. The larger is  $z$ , the smaller is the time passed since the formation of the Universe.

<sup>1</sup>The scale factor it is used to relate the physical or proper coordinates,  $\vec{r}$ , to the comoving ones,  $\vec{x}$ , as:  $\vec{r} = a(t)\vec{x}$ .

By coupling the *Friedmann-Lemaître-Robertson-Walker* metric with the energy-momentum tensor of a perfect fluid with density  $\rho$  and pressure  $P$ , we obtain the *Friedman equations* which, in short, describe how the Universe evolve with time:

$$\left(\frac{\dot{a}(t)}{a(t)}\right)^2 = H^2 = \frac{8\pi G\rho(t)}{3} - \frac{\kappa c^2}{a^2} + \frac{\Lambda}{3}, \quad (1.3)$$

$$\left(\frac{\ddot{a}(t)}{a(t)}\right)^2 = \frac{4\pi G\rho(t)}{3} \left(\rho(t) + \frac{3P}{c^2}\right) + \frac{\Lambda}{3}, \quad (1.4)$$

where  $H$  is the Hubble parameter,  $G$  is the gravitational constant and  $\Lambda$  is the cosmological constant introduced by Einstein in his field equations of GR. Given that the components of the Cosmos can be found in three different flavours: matter (or non relativistic particles, m), radiation (or relativistic particles, r) and vacuum energy (v), it is evident that pressure and density can be rewritten as:

$$\begin{aligned} \rho(t) &= \rho_m(t) + \rho_r(t) + \rho_v(t) \\ P &= P_r + P_v \end{aligned} \quad (1.5)$$

where  $P_m = 0$  since matter has a pressureless nature. The density of each component is not constant with time but it changes as the Universe evolves. While the matter energy density varies as  $\rho_m(t) = \rho_m(t_0) a^{-3}(t)$ , the radiation one does it as  $\rho_r(t) = \rho_r(t_0) a^{-4}(t)$ . Meanwhile, vacuum energy is a constant term with time  $\rho_v(t) = \rho_v$ . The values of  $\rho_m(t_0)$ ,  $\rho_r(t_0)$  and  $\rho_v$  are usually expressed with the *dimensionless density parameters*:

$$\Omega_m = \frac{\rho_m(t_0)}{\rho_{cr}(t_0)}; \quad \Omega_r = \frac{\rho_r(t_0)}{\rho_{cr}(t_0)}; \quad \Omega_v = \frac{\rho_v}{\rho_{cr}(t_0)} = \frac{\Lambda}{2H_0^2} \quad (1.6)$$

where  $\Omega_m + \Omega_r + \Omega_v = 1$ ,  $H_0$  is the Hubble parameter at  $t = t_0$  and  $\rho_{cr}(t_0)$  is called *critical density* of the Universe at  $t = t_0$ , expressed as:

$$\rho_{cr}(t_0) \equiv \frac{3H_0^2}{8\pi G} \quad (1.7)$$

Thanks to many observational works, we know the exact composition of the Universe with high accuracy (see e.g. Colless et al., 2001; Bennett et al., 2013; Planck Collaboration et al., 2014, 2016). Approximately, the values of  $\Omega_m$  and  $\Omega_v$  are 0.3089 and 0.6911, respectively<sup>2</sup>. Commonly, the vacuum energy term,  $\Omega_v$ , is known as *dark energy*. On the other side, the matter component is usually divided between *baryon* and *dark matter*. While the former is composed by protons, neutrons and electrons and consolidate galaxies and stars, the latter does not display electromagnetic radiation, interacts only through gravitational force (collisionless) and dominates the  $\Omega_m$  term ( $\sim 90\%$  of  $\Omega_m$ ). Among all the proposed cosmological models during the last decades, the most popular and used one is the so-called Lambda Cold Dark Matter ( $\Lambda$ CDM or *standard model*) which assumes a flat ( $\kappa = 0$ ) and expanding ( $\Lambda \neq 0$ ) Universe with a cold nature (i.e non-relativistic) for the dark matter particles.

Despite the above cosmological framework is well established and explains the different composition of the Universe, the understanding of how structures formed and grew in our Universe has been one of the most important problems in astrophysics which not all the proposed models have been able to solve. Indeed, very few of them are capable to generate matter distribution compatible with observations. As described above, if the cosmological principle in which is based our modern cosmology would hold perfectly and matter distribution was perfectly isotropic and uniform, no structure formation would be allowed. To overpass this shortcoming some modifications in the cosmological principle were required. The final answer arrived thanks to the temperature map of the cosmic microwave background (CMB). The small temperature fluctuations observed ( $\Delta T/T \sim 10^{-5}$ ) were a proof that the early Universe ( $z \sim 1000$ ) was not purely homogeneous but it contained small inhomogeneities which might have acted

<sup>2</sup>We do not refer to the radiation component given that the today's matter energy density is much larger than the radiation one, dominated by photons of the cosmic background and neutrinos of the early Universe.

as the seeds of the current structures. In theoretical models, these inhomogeneities are parametrized by the *relative density contrast*:

$$\delta(r_i, t) \equiv \frac{\Delta\rho(r_i, t)}{\bar{\rho}(t)} = \frac{\rho(r_i, t) - \bar{\rho}(t)}{\bar{\rho}(t)} \quad (1.8)$$

where the sub-index  $i$  denotes different positions in the Universe,  $\bar{\rho}(t)$  is the mean cosmic matter density of the Universe at time  $t$  and  $\rho(r_i, t)$  the cosmic matter density of the Universe at time  $t$  and position  $r_i$ . Although the small values of  $\Delta T/T$  in the CMB suggest  $|\delta(r_i, t)| \ll 1$ , the regions where  $\delta(r_i, t) > 0$  generated gravitational fields stronger than the average, delaying the expansion of the Universe at that positions and time. As a consequence,  $\delta(r_i, t)$  regions were able to increase with cosmic time causing a stronger and stronger gravitational field, leading regions with larger and larger density contrast in a process known as *gravitational instability*. In some specific cases, these overdense regions were able to collapse by their gravity, reaching a *virial equilibrium* and forming what is known as *virialized structures*. Given that the matter component of the Universe is dominated by dark matter (DM), these virialized mass concentrations are mainly formed by DM and they form the so-called *dark matter halos*. Larger structures will form through the mergers of these dark matter halos leading to the matter distribution that we observe nowadays. Such a model of gravitational instability for the structure formation has been applied to many cosmological models. Interestingly,  $\Lambda$ CDM model has been one of the most successful in reproducing the observed matter distribution of the Universe.

### 1.1.2 The galaxy formation: how matter transforms into light

Our current galaxy formation scenario is based on the [White and Rees \(1978\)](#) paper which proposed that galaxy formation starts as soon as a dark matter halo collapses and virializes. Falling into the potential of the DM halo, part of the baryon component of the Universe collapsed within it. It is established that during the infalling towards the DM halo center, the gas shocks to the halo virial temperature and settles into hydrostatic equilibrium. In massive halos where the virial temperature exceeds  $10^7\text{K}$  the gas would be fully ionized with the only possibility of losing energy, i.e the so-called *cooling process*, through bremsstrahlung emission. In smaller halos with virial temperature  $< 10^6\text{K}$  the cooling process would take place via excitations and de-excitation processes and rotational and vibrational molecular lines ([Dalgarno and McCray, 1972](#); [Abel et al., 1997](#); [Galli and Palla, 1998](#)). During this cooling process, the [White and Rees \(1978\)](#) theory assumes that the gas flows towards the central parts of the dark matter halo forming a rotationally supported gaseous disk. If the amount of gas mass cooled is large enough, its self-gravity dominates over the one exerted by the halo, leading to the collapse of the disk structure and triggering the formation of stars ([Bromm, 2013](#)). If gas cooling is sustained for a long time, the final result is the formation of a large and massive stellar disk. Feedback processes are expected to regulate the star formation in galaxies warming-up and expelling gas from the disk via energy injection. Supernovae and AGN feedback are expected to be the most efficient, involving, respectively, the death of stars and the gas accretion onto the supermassive black holes ([Silk and Rees, 1998](#); [Fabian and Nulsen, 1977](#); [Li et al., 2015](#)). While the former is expected to regulate the star formation in low-mass galaxies, the latter takes place in the most massive ones ([Somerville and Primack, 1999](#); [Croton, 2006](#)). Stellar deaths not only halt star formation, due to feedback on surrounding gas, but also deposit elements heavier than helium/lithium (metals hereafter) in the interstellar medium (ISM). These metals are indeed produced during the evolution of stars through nuclear-fusion reactions. The relative abundance of these metals in the galaxy gas will be reflected in the mass and metallicity of the stars that would be formed in future star formation episodes. The galaxy formation paradigm takes also into account the large scale processes that influence the evolution of galaxies. These processes are galaxy flybys and mergers which in brief provokes changes in the galaxy stellar disk structure (in many cases destroying it) and trigger the formation of a dense and compact stellar structure in the inner region of the galaxy called *bulge* ([Kauffmann et al., 1993a](#); [Mihos and Hernquist, 1996a](#); [Baugh et al., 1999](#)).

### 1.1.3 Studying galaxy formation through computer simulations

Although most of the advances on the galaxy formation and evolution theory have been done thanks to observational studies, numerical simulations have been needed to complement and refine our actual knowledge about galaxies and dark matter halos. In this section we briefly describe the techniques used during the last years devoted to understand the evolution of galaxies through numerical techniques. We refer to [Vogelsberger et al. \(2020\)](#) for a review on this topic.

#### Numerical simulations: From N-body to hydrodynamical simulations

As previously discussed in Section 1.1, the galaxy formation and evolution paradigm establishes that galaxies form at the centers of dark matter overdensities, referred as halos. While dark matter particles are considered to be *collisionless* (i.e. their movement is only influenced by the gravitational force), baryons that constitute galaxies behave as both collisionless (stars) and *collisional* (gas<sup>3</sup>) particles. Simulations which only tackle the description of the DM particles dynamics are usually referred to as *N-body simulations*. This class of simulations solve the *Boltzmann* and *Poisson* equations under the Newtonian formalism because the non-relativistic behaviour of DM particles (i.e. regardless the scale, their speed are always much smaller than the light-speed). The gravitational forces are computed and updated in time-steps, and the particle positions and velocities are tracked accordingly by using numerical integration. During the resolution of Boltzmann equations, non-physical two-body scattering between close particles is avoided by softening the gravitational interactions, causing that particles feel a smoothed density field ([Price and Monaghan, 2007](#)). Finally, at each time of the simulation, dark matter halos are identified through clustering algorithms such as *friend-of-friend* method ([Davis et al., 1985](#)). Among all the N-body simulations performed during the last two decades we can highlight: Millennium ([Springel, 2005](#)), Millennium II ([Boylan-Kolchin et al., 2009](#)), Bolshoi ([Klypin et al., 2011](#)), Millennium XXL ([Angulo et al., 2012](#)), MultiDark ([Prada et al., 2012](#)), Dark Sky ([Skillman et al., 2014](#)),  $v^2$ GC ([Ishiyama et al., 2015](#)) and EuclidFlagship ([Potter et al., 2017](#)).

The analysis of N-body simulations has helped us to understand how DM is distributed in the Universe. The DM large scale structure display a *web-like* distribution consisting of over- and under- dense regions called respectively clusters and voids. As an illustrative example, in Fig. 1.1 we present the large scale structure of the Millennium II simulation. The dark matter distribution at different scales can be quantified by the two-point correlation function method ([Peacock, 1999](#)) which measures the probability excess of finding two halos separated by a given distance. Interestingly, this method shows that DM displays two different behaviours, regardless of redshift. The first one is known as *one halo term* and reflects the correlation of particles in the same halo. The second is the *second halo term* and corresponds to the correlation signal coming from particles of different halos ([Mo and White, 1996](#)). This latter signal traces the large scale structure in which the DM particle is embedded, being larger for the ones hosted in overdense regions. On the small scale side, the dark matter mass distribution within halos has also been studied. It was shown that the DM density profile displays a universal *Navarro-Frenk-White* shape (NFW, [Navarro et al., 1996](#)). However, the specific structure of the inner parts of the halo has been debated during the last years, being proved that baryon effects can modify it. Therefore, some variation of the NFW profile can be found (see eg. [Navarro et al., 2004](#)). Besides, dark matter halos host sub-bound structure called *subhalos* where its specific number increases with halo mass ([Ghigna et al., 1998](#); [Moore et al., 1999](#)).

To study the evolution and assembly of galaxies in numerical simulations we need to introduce baryons in addition to dark matter. The direct simulations that include both components are called *hydrodynamical simulations*. Initially, the baryon component is in the form of gas particles (hydrogen and

<sup>3</sup> The gas component is affected by both gravity and pressure forces



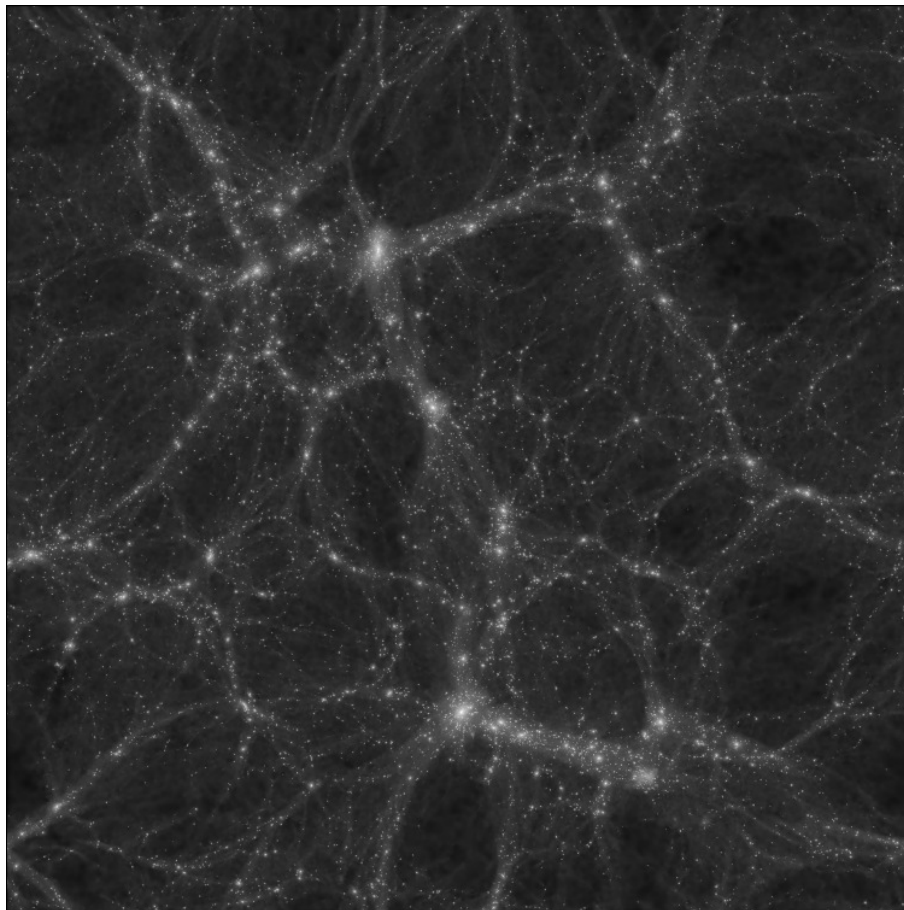


Figure 1.1: Distribution of the dark matter particles in the Millennium II simulation at  $z = 0$ . The size of the picture is  $25 \text{ kpc} \times 25 \text{ kpc}$  with a depth of  $5 \text{ kpc}$ .

helium) which progressively are converted into stars as the proper conditions of star formation get satisfied during the run of the simulation. Gas is described as ideal systems following the *Euler equations* whose solution can be reached by using two different approaches. The first one is the so-called *Eulerian method* which solves the fluid equations on a discrete grid fixed in space. The second method is the *Lagrangian* and, as happened in the N-body simulations, it uses particles to describe the evolution of the gas where the fluid equations are solved at the particle position replacing the true field with a smoothed one estimated averaging the positions of the local particles. In hydrodynamical simulations the Euler equations are complemented by different astrophysical processes such as *gas cooling*, *star formation*, *stellar* and *AGN feedback*, or *magnetic fields*. Given the limited numerical resolution of the simulations, most of these processes are taken into account via sub-resolution or sub-grid models. In short, they are a list empirical and phenomenological recipes that take into account processes occurring below the smallest scale resolved by the simulation (see e.g. [Springel and Hernquist, 2003](#); [Vogelsberger et al., 2013](#); [Weinberger et al., 2017](#)).

Hydrodynamical simulations can be classified in two different classes: cosmological and zoom-in simulations. The former simulates a large volume of the universe ( $\gtrsim 1.23 \times 10^5 \text{ Mpc}^3$ ) and it contains thousands of galaxies with different morphology, kinematics and stellar masses. Among the most famous cosmological simulations we can find *Illustris* ([Vogelsberger et al., 2014b](#)), *Horizon-AGN* ([Dubois et al., 2014a](#)), *EAGLE* ([Schaye et al., 2015](#)), *MassiveBlack-2* ([Khandai et al., 2015](#)), *Bluetides* ([Feng et al., 2016](#)), *IllustrisTNG* ([Springel et al., 2018](#)) and *Simba* ([Davé et al., 2019](#)). Their analysis has helped us to understand how galaxies assemble their stellar mass, shape their morphology and interact with the large scale structure ([Rodriguez-Gomez et al., 2015](#); [Hellwing et al., 2016b](#); [Wilkins et al., 2017](#);

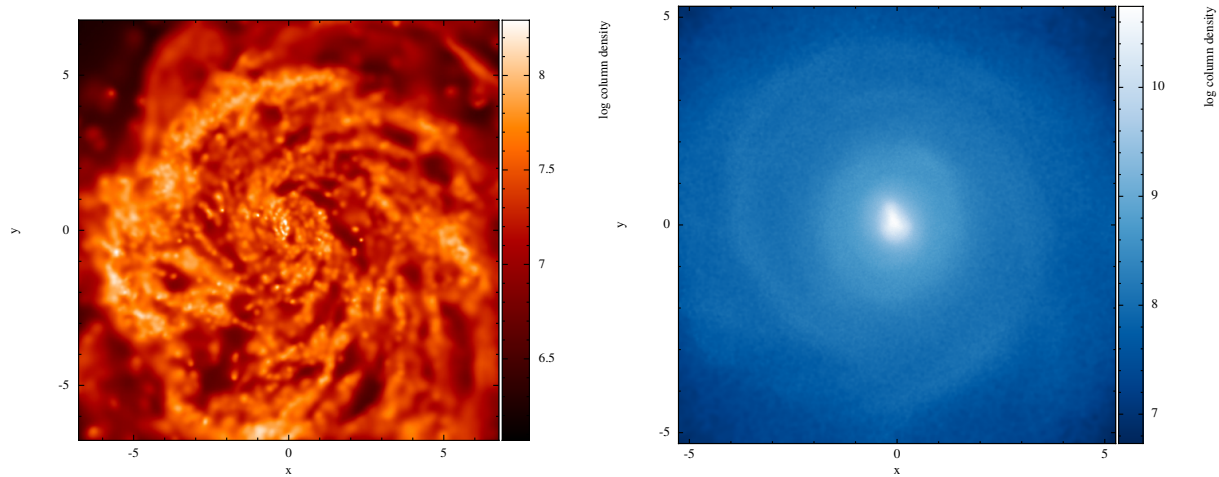


Figure 1.2: Gas (left) and stellar (right) surface density of the Milky Way galaxy of the Eris zoom-in simulation at  $z=1.46$ . The spatial ( $x$ - $y$ ) scale is given in kpc. [Courtesy of Daniele Spinoso from the paper [Spinoso et al. 2017](#)].

[Springel et al., 2018](#); [Dickinson et al., 2018](#); [Yun et al., 2019](#); [Davé et al., 2019](#); [Davies et al., 2020](#)). On the other side, zoom-in simulations are cosmological simulations where a small region (typically the environment of a single galaxy) is re-simulated at a lower resolution. The mass contained in the interest regions is traced back on time and re-initialized at a much higher resolution. Contrary, the surroundings of the regions are sampled at a coarser resolution, providing the necessary tidal field for realistic evolution of the region of interest. This zoom-in technique can also be applied in N-body simulations, see for instance Aquarius ([Springel et al., 2008](#)) Via Lactea II ([Diemand et al., 2008](#)) or COCO ([Hellwing et al., 2016a](#)). Some examples of zoom-in hydrodynamical simulations are Eris ([Guedes et al., 2011](#)), NIHAO ([Wang et al., 2015](#)), AURIGA ([Grand et al., 2017](#)), Cluster-EAGEL ([Barnes et al., 2017](#)) and RomulusC ([Tremmel et al., 2019](#)). As an example, Fig. 1.2 presents the gas and stellar surface density of the Milky Way galaxy of Eris zoom-in simulation. In such simulation, the large scale structure ( $\gtrsim 1\text{Mpc}$ ) is sacrificed to obtain a better mass resolution of the internal parts of a galaxy where a well resolved spiral arms and stellar bulge can be seen.

### Semi-analytical models of galaxy formation

A semi-analytical model (SAM) is a tool that simulates the evolution of galaxy population as a whole in a self-consistent and physically motivated manner. Unlike hydrodynamical simulations, semi-analytical models do not include gas particles and therefore do not solve the Euler equations. Instead, galaxy properties such as star formation rate, stellar mass, luminosity, and magnitudes are a result of a sub-grid model (or empirical recipes) that simultaneously model multiple physical processes, which typically include gas cooling, star formation, AGN and supernova feedback, metal enrichment, black hole growth, and galaxy mergers (see e.g. [Bower et al., 2006](#); [Guo et al., 2011](#); [Lacey et al., 2016](#)). All these processes are implemented through a system of coupled differential equations solved along the mass assembly history of DM objects, given by their respective and so-called *merger tree* (see [Baugh, 2006](#), for a review). In the literature, we can find two different approaches to generate merger trees of DM halos used by the semi-analytical models. The first one, and the most used during the last 10 years, is extracting the dark matter merger history from N-body simulations (see Section 1.1.3 and e.g. [Bower et al. \(2006\)](#); [Guo et al. \(2011\)](#); [Lacey et al. \(2016\)](#) or [Lagos et al. \(2018\)](#)). In short, dark matter halos are identified within the snapshots of the simulation with a friend-of-friend group-finder and then arranged by progenitors and descendent, constructing the merger tree. The second approach, which was more common in the past decades, is using DM merger histories generated from Monte Carlo realizations of the extended *Press & Schechter theory* ([Press and Schechter, 1974](#); [Bower, 1991](#); [Bond et al., 1991](#)). In brief, the theory



assumes that the formation of structures in a hierarchical universe happens in overdense regions of a Gaussian random density field where the number density of halos,  $n$ , in the mass range  $(M, M + dM)$  at redshift  $z$  can be parametrized as:

$$\left(\frac{dn}{dM}\right) = \sqrt{\frac{2}{\pi}} \frac{\rho_0}{M^2} \frac{\delta_c}{\sigma(M)} \left| \frac{d \ln \sigma}{d \ln M} \right| e^{-\frac{\delta_c^2(z)}{2\sigma^2(M)}} \quad (1.9)$$

where  $\delta_c(z)$  is the critical overdensity of a top-hat spherical fluctuation at the collapsing redshift  $z$ ,  $\rho_0$  is the mean density of the Universe and  $\sigma(M)$  is variance of the mass-density field. Based on Eq. 1.9 the extended Press-Schechter theory proposes that an object of mass  $M_2$  at  $z_2$  has a number of progenitors of mass  $M_1$  at  $z_1$  given by (Lacey and Cole, 1993):

$$\left(\frac{dN}{dM_1}\right) = \sqrt{\frac{2}{\pi}} \frac{d \ln \sigma}{d \ln M_1} \frac{M_2 \sigma^2(M_1)}{M_1^2} \left[ \frac{\delta_c(z_1) - \delta_c(z_2)}{(\sigma^2(M_1) - \sigma^2(M_2))^{3/2}} \right] e^{-\frac{(\delta_c(z_1) - \delta_c(z_2))^2}{\sigma^2(M_1) - \sigma^2(M_2)}} \quad (1.10)$$

The main advantage of the Monte Carlo approach over the one of N-body simulations is that the former is able to reach a higher mass resolution in the merger tree given that the whole computer memory is devoted to the history of one single halo. The disadvantage is that the Monte Carlo does not have spatial information of the halos, inability to properly track the connection between galaxy evolution and the large scale structure.

Over the last decades, semi-analytical models have been one of the most used tools to study galaxy formation and evolution, with thousands of articles published based on them. Among many other topics, SAMs have been used to explore the formation of galaxies at high- $z$ , the evolution of galaxy morphology, the growth of black holes, the properties of emission line galaxies, the evolution of the star formation trough redshift and environmental processes (see e.g. Kauffmann, 1996a; Somerville et al., 2001; Croton, 2006; De Lucia et al., 2006; Marulli et al., 2008; Fanidakis et al., 2011; Orsi et al., 2014; Bonoli et al., 2014; Henriques et al., 2015; Valiante et al., 2016; Tonini et al., 2016; Izquierdo-Villalba et al., 2018, 2019, 2020; Marshall et al., 2019b). Among all the SAMs that we can find in the literature, we can highlight: Santa Cruz SAM (Somerville et al., 2001), GALFORM (Lacey et al., 2016), L-Galaxies (Henriques et al., 2017), SAG (Croton et al., 2016), SAGE (Cora et al., 2018), MERAXES (Mutch et al., 2016) and SHARK (Lagos et al., 2018).

### 1.1.4 Some open issues in the galaxy formation paradigm

The galaxy formation and evolution paradigm linked with the  $\Lambda$ CDM cosmological model is a good theory capable to provide a broad understanding of how galaxies behave in a hierarchical universe. However, the theory has still some open issues and there is room for improvements. Among all the limitations of the theory, the ones related to the non-linear processes that take place inside galaxies are the most difficult to solve. For instance, mechanisms halting the star formation (*quenching*) are not well understood yet. Many works have pointed out that the injection of energy in the intergalactic medium through *internal processes* such as supernovae winds or supermassive black holes activity might limit star formation episodes (Heckman et al., 2000; Veilleux et al., 2005; Agertz et al., 2011; Hidalgo et al., 2011; McCarthy et al., 2011; Keller et al., 2016). However, an additional open question arises when trying to disentangle the effects of internal processes in the star formation from the ones produced by *environmental processes*, i.e. those phenomena triggered by the interaction of a galaxy with its surroundings. Among the latter class, usually, ram-pressure stripping and tidal interactions are the most prominent actors. The intricate way in which both internal and environmental processes take place, hinder the possibility of drawing an unique and solid conclusion about the halting of the galaxy star formation.

Other questions that remain still open are related to supermassive black holes. How such massive objects were formed, how they acquired their masses and how they influenced their host-galaxy evolution have been hot topics during the last 15 years (Silk and Rees, 1998; Di Matteo et al., 2005; Fanidakis

et al., 2011; McCarthy et al., 2011). Despite many works have been published regarding all these topics, the formation scenario of supermassive black holes and their main channel of growth are still under debate and many theories have been proposed so far (Volonteri et al., 2003; Di Matteo et al., 2005; Valiante et al., 2016).

How galaxy evolve and their morphology is shaped is another interesting challenge for the galaxy formation paradigm. While the assembly of galactic disks seems to be understood (Navarro and Benz, 1991; Navarro and Steinmetz, 2000), astrophysicists have not reached a consensus about the channels by which galaxies develop and sustain their bulge structure. For instance, while some works point out mergers as main drivers for the bulge formation, others suggest that internal instabilities of galactic disks might play an important role (Kauffmann, 1996b; Navarro and Steinmetz, 2000; Hopkins et al., 2009a; Tonini et al., 2016; Zana et al., 2018a). As we will see in this thesis, the development of a theory capable to explain the whole bulge population is a complex matter considering that fast and secular processes take place in a non-trivial way during the galaxies lifetime.

In the next sections we focus on the current understanding of bulges, supermassive black holes and how numerical simulations try to generate simulated surveys to shed light on the observables that the scientific community should study to fill all the gaps in the galaxy formation and evolution.

## 1.2 Shaping galaxy morphology: A matter of bulge and disk

The primary components of a galaxy are stars and gas. How these stars are distributed between the disk and bulge component leads to many possible galaxy shapes. The first classification of galaxies based the disk and bulge appearance was presented in Hubble (1926). Based on the analysis of 400 photometric galaxy images, Edwin Hubble concluded that most of the observed galaxy shapes fall into a sequence, later on, called *Hubble sequence*. Galaxies with ellipticity  $e \lesssim 0.7$  and luminosity fading from bright nuclei to indefinite edges were called *ellipticals*. Depending on the exact  $e$  value Hubble split this group in 8 different classes: E<sub>0</sub>, E<sub>1</sub>, E<sub>2</sub>, E<sub>3</sub>, E<sub>4</sub>, E<sub>5</sub>, E<sub>6</sub> and E<sub>7</sub>. On the other hand, galaxies with  $e \gtrsim 0.7$  were classified as (*normal*) *spirals* whose subdivision was done based on the relative size of the bulge, the extend of the spiral arms and their degree of resolution. According to these conditions, three spiral groups were differentiated: Sa (early spiral), Sb (intermediate spiral) and Sc (late spiral). In brief, in the Sa type most of the luminosity comes from the bulge, surrounded by coiled and unresolved arms. Sb shows a large bulge with thin and open arms. Finally, Sc displays a small bulge but with a well-resolved arms. Edwin Hubble added an extra branch in the sequence called *barred spirals* (tagged as SB) whose distinctive characteristic was that the spiral arms emerged from the opposite points of a nuclear bar structure with an unwinding trend as they grow. The group SB was also subdivided in *a*, *b* and *c* class. Finally, Hubble (1926) reported a 3% of galaxies with peculiar or irregular morphology. Improvements in the *Hubble sequence* were done by de Vaucouleurs (1974) or van den Bergh (1976) (among many others). For instance, de Vaucouleurs (1974) added a more refined spiral subdivision and included the *T-Types* terminology based on numbers between -6 to 10 to represent the morphological types of the Hubble sequence.

Improvements carried out in observational techniques proved that the Hubble sequence *evolves with redshift*. For instance, Abraham et al. (1996) showed that the number of irregular galaxies at  $0.3 < z < 1$  is larger than the one in the local Universe. Other works such as Fasano et al. (2000) and Smith et al. (2005) found out that the percentage of ellipticals is constant at  $z \lesssim 1$  while the one of spirals decreases. To explain the reason for the Hubble sequence evolution, it is necessary to understand how internal and external processes lead to changes in the structure of the bulge and disk. In the following sections, we explain the current understanding of how galactic bulges form.

### 1.2.1 A different bulge population: From ellipticals to bulges in late-type galaxies

Big advances on the understanding of galactic bulges took place in the 1970s when it became possible to extract accurate stellar kinematics from the observational data. The first galactic bulges being studied were the ones hosted in bright *elliptical* galaxies or *early type galaxies*<sup>4</sup>. Their stellar kinematics was characterized by the analysing of the ratio between the galaxy ordered and random motion ( $V/\sigma$ ) and by the flattening of the bulge ( $\varepsilon$ ). Interestingly, the results showed systems with round shapes ( $\varepsilon \lesssim 0.3$ , Bertola and Capaccioli, 1975; Illingworth, 1977) and small values of  $V/\sigma$  consistent with bulges dominated by random motion. These results were extended to fainter elliptical galaxies. Contrary to what was found in bright systems, faint ellipticals displayed oblate shapes ( $\varepsilon \gtrsim 0.7$ ) with large  $V/\sigma$  values compatible with fast rotators (Davies et al., 1983). With more systematic studies, larger differences in the bulge flattening were found. While slow rotating ellipticals displayed *boxy isophotes* (Davies et al., 1983), fast ones tend to had *disky isophotes* as a consequence of the existence of a smooth and faint disk around the spheroidal component (Rix and White, 1990; Rix et al., 1999). Photometric studies revealed a further deviation between the properties of bright and faint elliptical galaxies. The former showed an old and passive stellar population in accordance with the bulk of the stars formed at  $z \gtrsim 1$  (Bender et al., 1996; Hogg et al., 2002). The latter still displayed starforming regions with blue colors (Kodama et al., 1999; Strateva et al., 2001). Kormendy and Bender (1996) tried to put all these pieces together, writing down the main properties which defined the dichotomy between these two types of elliptical galaxies. According to the Kormendy and Bender (1996) definition, bright ellipticals were boxy and radially anisotropic slow rotators with a break between the outer and inner surface brightness profile with a step cuspy nuclear regions ( $r^{1/4}$  or de Vaucouleurs profile). On the other hand, faint ellipticals were diskly and isotropic fast rotators without a clear break in their surface brightness profile (see further details in Faber et al., 1997; Ravindranath et al., 2001; Cappellari et al., 2007, 2011a,b).

Bulges hosted in *late-type* or *spiral galaxies* were also studied (Kormendy, 1983; Carollo et al., 1997; Gadotti and dos Anjos, 2001). Early results presented bulges with similar surface brightness profiles, red colors and kinematical properties than bright elliptical galaxies, suggesting a common origin. With the improvements in the observations, it was discovered the existence of another type of bulges in spiral galaxies called *pseudobulges*, usually linked with the presence of a bar structure (see Section 1.2.2). These bulges were found to be triaxial and fast rotator systems, being hosted in galaxies with an ongoing star forming activity (Kormendy, 1982, 1983; Gadotti and dos Anjos, 2001). By performing a systematic study of classical and pseudo- bulges, Fisher and Drory (2008a) suggested Sérsic profiles (Sérsic, 1968) as a good analytical expression to fit their light distribution:

$$I(r) = I_0 e^{-\left(\frac{r}{r_0}\right)^{1/n}} \quad (1.11)$$

where  $I_0$  is the surface brightness of the bulge and  $n$  is the Sérsic index. Interestingly, Fisher and Drory (2008a) found that bulges classified as classical bulges had  $n \gtrsim 2$  with a tight correlation with the galaxy bulge-to-total (B/T) mass ratio. Pseudobulges, on the other hand, had  $n \lesssim 2$  and did not show any correlation with B/T value. Drory and Fisher (2007) complemented these results by showing that pseudobulges displayed blue colors similar to the ones characterizing bulgeless galaxies and lower surface density ( $I_0 \sim 20 \text{ mag/arcsec}^2$ ) than classical bulges. Finally, Gadotti (2009) performed an exhaustive analysis of classical and pseudobulges by using the Sloan Digital Survey (SDSS) data of galaxies at  $0.02 \lesssim z \lesssim 0.07$ . He found similar differences between pseudobulges and classical bulges than Drory and Fisher (2007) and Fisher and Drory (2008a). However, Gadotti (2009) results pointed out that classical bulges display an offset with respect to ellipticals in the mass-size plane, indicating that classical bulges are not just elliptical surrounded by disks. In order to guide the reader, in Fig. 1.3 we have presented an illustrative scheme of there different bulge types: (bright) elliptical, classical bulge and pseudobulge/bar.

<sup>4</sup>*Early type galaxies* have been defined in terms of morphology. In short, they are galaxies with a dominant spheroidal component and a smooth or non-existent disk.

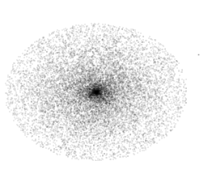
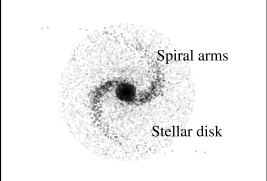
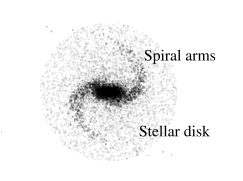
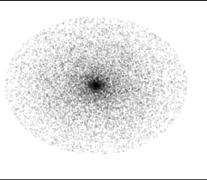
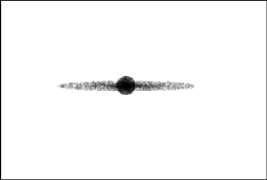

NAME:	Elliptical	Classical bulge	Pseudobulge / Bar
FACE-ON:			
EDGE-ON:			
PROPERTIES:			
*Kinematics	<i>hot</i> ( $V/\sigma < 1$ )	<i>hot</i> ( $V/\sigma < 1$ )	<i>cold</i> ( $V/\sigma > 1$ )
*Profile	Vaucouleurs	Sersic ( $n \sim 0.9 - 2.2$ )	Sersic ( $n \sim 0.4 - 1$ )
*Stellar population	Old	Old	Young

Figure 1.3: Illustrative scheme of the different bulge types. From left to right: Elliptical, classical bulge and pseudobulge/bar. We have listed some of the most representative properties of the population. For the elliptical galaxies, we have selected the properties of the bright population.

## 1.2.2 The bulge formation scenario

As discussed in the previous section, galaxies host a large variety of bulge types. The details on how they were formed and what were the mechanisms which shaped their characteristics are big questions that astrophysicists have been trying to answer for the last 50 years. The development of a theory capable of explaining the whole bulge population is a complex matter considering that both fast and secular processes take place in a non-trivial way during the galaxies lifetime. Differentiating between them and determine which one plays the dominant role in each bulge type is not an easy task. In this section, we describe the main theories developed and tested to understand the different formation pathways of elliptical galaxies and bulges in late-type galaxies.

### The formation scenario of elliptical galaxies

During the 1970s and 1980s, two different theories for the formation of elliptical galaxies were discussed and explored: the *monolithic collapse* and the *merging scenario*.

The monolithic collapse theory (or cold collapse model, [Eggen et al., 1962](#); [van Albada, 1982](#)) assumes that elliptical galaxies were formed at high- $z$  (possibly at  $z > 3$ ) from the collapse of gaseous *protogalaxies*. During this process, the gas was rapidly converted into stars in a single starburst on a time scale shorter than the one required for the gas to be settled into a rotationally supported disk structure. Following the starburst episode, strong supernovae winds expelled the residual gas from the galaxy, inhibiting further star formation episodes ([Matteucci and Tornambe, 1987](#); [Arimoto and Yoshii, 1987](#)). The described picture leads to the outcome of an elliptical galaxy evolution dominated by dissipationless processes (i.e stellar dynamics) where their observed masses and sizes would be only explained if their collapse and formation took place at  $z > 20$ . However, the star formation history reported by many

observational studies suggests this formation time as unrealistic. An additional issue comes from the relaxation process<sup>5</sup> during the dissipationless evolution where both dark matter and stars would mix rapidly, leading to the formation of an elliptical structure with larger dark matter content in the internal parts than the one reported by observations. To address these limitations, many works assumed the possibility that the star formation burst takes a time comparable, or longer, than the one of collapsing. This allows dissipation processes which cause a segregation between the gas (before turning into stars) and dark matter (see [Larson, 1974](#)) whose result is the delay of the elliptical structure assembly and the formation of a galaxy with a dark matter content similar to the observed one. Nevertheless, such dissipative processes are still not able to reconcile the observed formation time of elliptical galaxies with the one predicted by the monolithic collapse. While most of the observational studies point out that the elliptical population was still forming stars or had not yet assembled at  $z \sim 1$  ([Bell et al., 2004](#); [Brown et al., 2007](#); [Taylor et al., 2009](#)) the monolithic scenario linked with dissipative processes suggests an elliptical formation time of  $z \gtrsim 3$  (see the review of [Peebles, 2002](#)).

The merging scenario was proposed as an alternative hypothesis to the monolithic collapse. The theory argues that spiral galaxies were the first ones forming in the Universe and to merge later on, resulting in the formation of elliptical galaxies ([Toomre, 1977](#)). Some pioneering works such as [Farouki and Shapiro \(1982\)](#) or [Negroponte and White \(1983\)](#) tested this theory by performing simulations of merging pairs of galaxies with similar disk-halo ratios. Most of the remnant galaxies of these simulations displayed elliptical features with ellipticity between 0 – 0.7. However, they were rotating too fast with respect to the observed elliptical population as a consequence of the low-mass dark matter halos in which the interacting galaxies were embedded. A few years later, the work of [Barnes \(1988\)](#) showed that extended dark matter halos were very effective in absorbing binding energy and angular momentum from the stellar component, making possible the production of slow rotating elliptical remnants with a surface brightness profiles similar to the de Vacouleurs law. Further studies on this merging scenario were performed by [Hernquist \(1992, 1993\)](#). By using N-body simulations, [Hernquist \(1993\)](#) showed that the remnants of merging spiral galaxies had central mass densities too low when compared with real ellipticals. Based on these results, the authors postulated the so-called *disk-bulge conspiracy* which stated that merger of spiral galaxies would be a viable mechanism for the production of massive elliptical galaxies only if they already contained sufficient mass in a dense spheroidal component. However, later on, works based on hydrodynamical simulations demonstrated that tidal forces during mergers can produce a strong migration of gas towards the center of the remnant galaxy. This gas can be transformed into stars, giving rise to a more concentrated remnant which agrees better with the structure of observed ellipticals (see, e.g. [Mihos and Hernquist, 1996b](#)). A systematic study about the remnant properties based on the mass content of the two interacting galaxies was performed by [Cox et al. \(2006\)](#). The authors found that gas rich mergers, i.e. dissipational systems, could explain the large compactness, the velocity dispersions and the rotation velocities of low-mass elliptical galaxies. However, interactions with a large content of gas had difficulties in producing the low rotation of luminous and massive elliptical galaxies. Indeed, some recent numerical simulations reported in [Khochfar and Burkert \(2005\)](#) and [Naab et al. \(2006\)](#) pointed out that massive ellipticals could be only reproduced through dissipationless processes or gas poor mergers of equal mass elliptical galaxies.

Although the merger theory provided a good scenario to explain the formation of elliptical galaxies, it still needed to be tested in the hierarchical merging scenario of the  $\Lambda$ CDM cosmological model. The first work addressing this was [Kauffmann et al. \(1993a\)](#). By coupling a semi-analytical model where only major mergers lead to the formation of elliptical remnants with the merger trees of dark matter halos extracted from the Press-Schechter theory, [Kauffmann et al. \(1993a\)](#) reported a population of ellipticals in remarkable agreement with observations. Similar results were reported by [Kauffmann \(1996b\)](#) and [Baugh et al. \(1996a\)](#).

---

<sup>5</sup>With relaxation we mean the i) process by which a system approaches equilibrium or ii) by which it returns to equilibrium after a disturbance.



### The formation scenario of bulges in late-type galaxies

Bulges of late-type galaxies can be divided in two categories: *classical bulges* and *pseudobulges*. Based on their characteristics and the different galaxies in which they are hosted, it is expected that they have a different formation pathway. Here we describe the main physical models developed to explain their origin.

(i) *Classical bulges*: Given the similarities of classical bulges with elliptical structures, many studies proposed a formation and assembly scenario related to violent dynamical relaxation after minor mergers. By using numerical simulations, [Mihos and Hernquist \(1994\)](#) explored the possible bulge formation when a galaxy undergoes an interaction with a low-mass dwarf galaxy. These simulations showed that tidal perturbation of the infalling companion was able to generate two spiral features in the central galaxy which drove a large amount of disk gas towards the central region. Despite all the nuclear gas was transformed into stars, the simulations reported that the newly formed stellar population was too compact to contribute to the formation of an extended bulge. Indeed, they showed this population of new stars was deposited in a rotational disk rather than a spherical structure. [Walker et al. \(1996\)](#) went a step further and studied with numerical simulations the characteristics of both disk and bulge of a galaxy after a minor merger. As expected, the minor interaction was not able to destroy the disk of the central galaxy but it contributed to its thickening. Regarding the bulge component, [Walker et al. \(1996\)](#) found out that minor merger caused its growth as a consequence of the  $\sim 45\%$  of the satellite mass reaching the nuclear region ( $\lesssim 2$  kpc). Similar study was done by [Aguerri et al. \(2001\)](#) which reported several simulations of minor interactions between spiral galaxies and dense satellites. By analysing the remnant galaxies, the results pointed out that bulges of the spiral galaxies were able to grow as a consequence of the deposit of most of the satellite mass at the center of the galaxy. A complementary work was done by [Eliche-Moral et al. \(2006a\)](#) which explored with N-body simulations the bulge growth of spiral galaxies after the minor interactions of low-density satellites. Interestingly, the results showed that most of the mass of the satellite galaxy was not settled in the bulge of the spiral galaxy but the tidal interactions before the merger triggered an inward flow of material from the disk to the galaxy nucleus which increased the bulge structure. Besides, the simulations reported that the Sérsic indexes of the bulges increased after the interactions. A systematic study of the bulge formation during merger at different stellar mass ratio was performed by [Bournaud et al. \(2005\)](#). While ratios larger than 3:1 led to the formation of elliptical galaxies, merger ratios with 4.5:1 – 10:1 did not destroy the disk but promoted the formation of a small inner bulge whose kinematics resembled the one of the massive ellipticals.

The alternative *clump-origin bulge* pathway for the classical bulge formation was also proposed. At difference with all previously discussed, this formation scenario is related to secular evolution. [Noguchi \(1998, 1999\)](#) demonstrated with numerical simulations that clumpy structures can form during the first stages of the disk assembly through instabilities of the gaseous component. Via dynamical friction, these clumpy structures can reach the nuclear region of the galaxy and merge in a unique object leading to the formation of a bulge-like structure. However, the outcome of a pseudo or classical bulge structure through this clumpy origin is not fully clear yet. For instance, [Elmegreen et al. \(2008\)](#) showed that the clump-origin bulges should lead to the formation of slow rotation structures with  $r^{1/4}$  density profiles, characteristics of the classical bulge populations. On the observational side, the work of [Sachdeva et al. \(2017\)](#) studied with photometric data the bulge population of  $z \lesssim 1$  bulges, concluding that secular evolution and clump migration alone can not account for the whole bulge growth and minor mergers are required.

(ii) *Pseudobulges*: Current theories suggest that the origin of pseudobulges in late-type galaxies is related to the formation of *bar structures* ([Combes and Sanders, 1981a](#); [Kormendy, 1983](#); [Kuijken and Merrifield, 1995](#); [Bureau and Athanassoula, 2005](#)). In brief, a bar can be described as a non-axisymmetric structure developed by a galaxy as a response to gravitational instabilities taking place in its rotationally supported stellar disk. Although it is well established that bars are structures that grow and form in a

slow and secular process (Debattista et al., 2004, 2006; Méndez-Abreu et al., 2010; Zana et al., 2018a,b) some works have pointed out that flybys or galaxy interactions can also produce them in short time scales (Lang et al., 2014; Zhou et al., 2020). The bar structure has important dynamical consequences since it can redistribute the galaxy angular momentum (Lynden-Bell and Kalnajs, 1972; Tremaine and Weinberg, 1984). This process provokes gas inflows towards the central regions, triggering a central burst of star formation and thus increasing the mass concentration of the galaxy nuclear parts (Kormendy, 1993; van Albada and Roberts, 1981; Schwarz, 1981; Sakamoto et al., 1999; Spinoso et al., 2017). The works of Pfenniger and Norman (1990), Friedli and Benz (1993), Friedli and Pfenniger (1991), Norman et al. (1996) and Valenzuela and Klypin (2003) (among many others) showed using numerical simulations that this increase of concentration is responsible for the disappearance of the orbits sustaining the bar, causing its weakening and eventually its dissolution. As a result of this process, the nuclear parts of the galaxy disk develops a bulge-like structure whose kinematics and profile resembles pseudobulges of late-type galaxies (Kormendy, 1982; O’Neill and Dubinski, 2003).

Other studies proposed an alternative pseudobulge formation scenario starting also from a bar structure. Full three-dimensional numerical simulations have shown that the formation of a bar is accompanied by a secular *bar-bucking instability*, which causes the stars forming the bar to acquire large motions normal to the galactic plane, giving the bar a *boxy* or *peanut shape* (Combes et al., 1990a; Raha et al., 1991; Debattista et al., 2004; Martínez-Valpuesta et al., 2006; Saha et al., 2013; Spinoso et al., 2017). Usually, this morphology gradually appears after the bar has formed and reaches its maximum shape when the bar is in a steady-state (Combes et al., 1990a). Debattista et al. (2004, 2005), by using high-resolution of collisionless N-body simulations, showed that the scaling relations and kinematics of the *boxy-peanut shape* bulge-like structure are similar to the ones observed in pseudobulges.

### 1.2.3 Simulated bulges in a cosmological context: From semi-analytical models to hydrodynamical simulations

All theories previously described to explain bulge formation have been proposed based on N-body simulations of ideal and isolated galaxies detached from the framework of the large scale structure. To check their performance in a cosmological context, many works have included them in semi-analytical models and others have analysed large cosmological hydrodynamical simulations. In this section, we briefly describe the main results of these works.

Given the expensive computational requirements which characterize of cosmological hydrodynamical simulations, semi-analytical models were the pioneers in testing the bulge formation theories. As we discussed previously, Kauffmann et al. (1993a) was the first work in including the merger scenario for the formation of elliptical galaxies in a semi-analytical model based on Monte Carlo dark matter merger trees. Specifically, the model assumed that elliptical galaxies were formed through merger of spiral galaxies whose mass ratio exceed a certain threshold. Kauffmann (1996b) showed that these assumptions led the model to reach a good match in the color-magnitude diagram between predicted and observed elliptical galaxies. Besides, the SAM suggested that most of the mass of elliptical galaxies were already assembled by  $z > 1.9$ . Similar work was done by Baugh et al. (1996a) using a different SAM but applying the same elliptical model of Kauffmann et al. (1993a) and including non-violent mergers (i.e. all those that do not form ellipticals) for the formation of bulges in spiral galaxies. Interestingly, the semi-analytical model pointed out that  $\sim 50\%$  of elliptical and  $\sim 15\%$  of spiral galaxies underwent a major merger at  $z \leq 0.5$ . Further investigations of elliptical galaxies at a different masses and environments were done by De Lucia et al. (2006) with a SAM applied on the merger trees of the Millennium N-body simulation. De Lucia et al. (2006) found out that the merger scenario for elliptical structure formation led to massive elliptical galaxies ( $M_{\text{stellar}} > 10^{11} M_{\odot}$ ) with higher metal abundances, older stellar population and shorter star formation time scales than less massive elliptical systems. Hopkins et al. (2009c) based on the results of Hopkins et al. (2009a) used the Santa Cruz SAM to study the dissipation effects of gas in galaxy mergers. The results showed that gas rich mergers cause a suppression of bulge formation in

low mass galaxies ( $M_{\text{stellar}} < 10^{10} M_{\odot}$ ) since gas dissipation effects reduce the fraction of the disks that get distorted during the merger and cause a rapid disk reassembly.

Semi-analytical models have also studied the formation of bulges via secular evolution. Cole et al. (2000) included the criteria of Efstathiou et al. (1982)<sup>6</sup> to detect instabilities in the stellar disk which lead to the formation of a bar structure and ultimately assembly of a pseudobulge. The assumption used by Cole et al. (2000) was that during a disk instability event the whole galactic disk is destroyed and a spheroidal galaxy is formed (see also Fanidakis et al., 2011; Lacey et al., 2016). Athanassoula (2008) pointed out the procedure of Cole et al. (2000) had shortcomings at the qualitative level since the disk can not disappear without a merger. On the other hand, Croton (2006) included the same criteria of Mo et al. (1998a) in the De Lucia et al. (2006) SAM but assuming that only a fraction of the stellar disk is transferred to the nuclear part during a disk instability. This approach has been included in other semi-analytical models (see eg. Gargiulo et al., 2017; Henriques et al., 2017; Lagos et al., 2018). Despite including the Efstathiou et al. (1982) criterion in many SAMs, it was not until Tonini et al. (2016) when the scientific community started to explore in details the properties of pseudobulges in SAMs. Tonini et al. (2016) showed that  $z=0$  pseudobulge are hosted in intermediate galaxies, especially in the ones with massive stellar disks. Similar results were found in the works of Gargiulo et al. (2017), Izquierdo-Villalba et al. (2019) or Marshall et al. (2019b) based on semi-analytical models. Indeed, the two last works showed a very good agreement between predicted and observed structural properties of pseudobulges and classical bulge structures.

On the side of hydrodynamical simulations, Domínguez-Tenreiro et al. (2004) analysed 4 different cosmological simulations showing that the formation of most of the stars in elliptical systems happened through mergers at low- $z$  and violent multi-clump collapse events at high- $z$ . Domínguez-Tenreiro et al. (2006) extended that work by the analysis of the  $z=0, 1, 1.5$  elliptical galaxies. These results showed that the lower was the redshift, the larger was the mass, radius and velocity dispersion of elliptical systems. Feldmann et al. (2010) focused on the central galaxies of  $10^{13} M_{\odot}$  groups extracted from *zoom-in* cosmological hydrodynamical simulations. They found that at  $z=0$  massive elliptical galaxies with a low amount of gas and low velocity dispersion dominate the center of galaxy groups. By tracing their merger history the authors found that the formation of these structures was caused by continuous major and minor mergers since  $z < 1$ . Naab et al. (2009) reached similar conclusions. The effects of feedback coming from the central supermassive black hole in the formation and evolution of massive elliptical galaxies in cosmological hydrodynamical simulations were studied in Dubois et al. (2013) and Correa et al. (2019). Both works showed an important role of the black hole feedback in quenching the star formation of elliptical galaxies, generating a red and old stellar population and preventing the formation of large and blue disks.

Cosmological studies about bulge formation and evolution in spiral galaxies took longer in arise given the difficulty of hydrodynamical simulations in forming realistic late-type spirals in a  $\Lambda$ CDM universe. Such difficulty was called *angular momentum catastrophe* and it tried to summarize the fact that baryons in hydrodynamical simulations condensed at the center of dark matter halos in a centrifugally-supported disk whose angular momentum was lower than the one observed in real spirals (Navarro and Benz, 1991; Navarro and Steinmetz, 2000). To solve such problem some authors included more realistic sub-grid recipes for supernovae feedback with an improved simulation resolution whose outcome was the production of rotationally-supported disks with exponential scale lengths and angular momentum compatible with the observed ones (see e.g. Governato et al., 2007; Scannapieco et al., 2010; Brooks et al., 2011). After solving the *angular momentum catastrophe* the simulations were ready to study spiral galaxies bulges. Among all the studies addressing this topic, the most popular have been the ones focusing on galaxies hosted in Milky-Way type halos. For instance, Guedes et al. (2011) reported a cosmological *zoom in* simulation in which an analogue of a Milky Way galaxy arose naturally. The

<sup>6</sup>This criterion is based on two-dimensional N-body simulations of purely stellar disks with a fixed subhalo potential.



analysis of the simulation showed that the galaxy displayed a quiet merger history since  $z < 3$  with a bulge surface brightness compatible with a pseudobulge structure. [Bonoli et al. \(2016\)](#) improved the simulation by including a refined model for black hole formation, growth and feedback. Interestingly, the inclusion of these changes modified the structure of both disk and bulge of the simulated galaxy. The disk structure was more prone to disk instabilities which, ultimately, led to the formation of a small pseudobulge embedded inside a strong bar structure (see also [Spinoso et al., 2017](#)). [Rosas-Guevara et al. \(2020\)](#) studied barred galaxies in massive disk galaxies by using the TNG100 cosmological hydrodynamical simulation. The authors found that  $\sim 37\%$  of galaxies with  $M_{\text{stellar}} > 2 \times 10^{10} M_{\odot}$  displayed a bar structure with a faster disk assembly than the one of a disk galaxy control sample. Besides, the barred galaxies had a quiet merger history with few minor mergers and almost null major interactions. Similar work was performed by [Du et al. \(2020\)](#) and [Zhou et al. \(2020\)](#) with analogous results. Further investigations about bulges in galaxies hosted in Milky Way type halos have been performed thanks to the AURIGA *zoom-in* simulations ([Grand et al., 2017](#)). Specifically, AURIGA consists of thirty high resolution cosmological zoom simulations of the galaxy formation in isolated Milky Way halos. [Gargiulo et al. \(2019\)](#) showed that all of the AURIGA bulges display a pseudobulge structure with most of their mass ( $> 75\%$ ) formed *in-situ* the galaxy. [Blázquez-Calero et al. \(2020\)](#) analysed the AURIGA pseudobulges focusing on the galaxies with a bar structure. Interestingly, the authors found 6 barred galaxies with a boxy-peanut structure (or in process of forming) whose sizes were compatible with the observed in real galaxies.

### 1.3 Supermassive black holes: A key component of galaxy formation

Besides bulges, supermassive black holes are another relevant component in galaxies. The full understanding how black holes acquire their mass is crucial since the energy released during their growth has a deep impact on the evolution of galaxy properties, such as morphology and star formation. In this section, we describe the current observational and theoretical knowledge about supermassive black holes, how they correlate with the galaxy properties and we summarize some simulations carried out to understand the specific role played by supermassive black holes in a cosmological context.

#### 1.3.1 Theoretical black holes

Few months after Albert Einstein published the general relativity theory ([Einstein, 1916](#)), the German physicist Karl Schwarzschild obtained, for the first time, the exact solution of the Einstein equations to describe the gravitational field generated by a spherically symmetric and static (i.e no rotating) body ([Schwarzschild, 1916](#)). Such a solution is known as *Schwarzschild metric* and it only holds in vacuum. In time and spherical coordinates  $(t, r, \theta, \varphi)$  the Schwarzschild metric has the form:

$$ds^2 = \left(1 - \frac{2GM}{c^2 r}\right) c^2 dt^2 - \left(1 - \frac{2GM}{c^2 r}\right)^{-1} dr^2 - r^2 d\theta^2 - r^2 \sin^2 \theta d\varphi^2 \quad (1.12)$$

where  $G$  is the gravitational constant,  $c$  is the light speed and  $M$  can be interpreted as the conventional Newtonian mass of the body. For many years, the scientific community put careful attention to the values  $r = 0$  and  $r = 2GM/c^2$  where the metric becomes infinite. After several publications (see eg. [Painleve, 1922](#)), it was proved that  $r = 0$  was a genuine metric singularity. On the contrary, the position  $r = 2GM/c^2$  was a coordinate singularity which could be removed by just applying a coordinates transformation. The position  $r = 2GM/c^2$  was called *Schwarzschild radius* ( $r_{\text{Sch}}$ ) and it delimits the distance ( $r < r_{\text{Sch}}$ ) where proper radial distances and proper time become imaginary. The presence of this radius in the metric implies the existence of a particular object in the Universe called *Schwarzschild black hole* whose mass is concentrated in a radius smaller than  $r_{\text{Sch}}$ .

Fifty years after the publication of the Schwarzschild results, Roy Kerr generalized the Schwarzschild metric to describe the gravitational field of a spherically symmetric and *rotating* body ([Kerr, 1963, 1965](#)).

In the Boyer-Lindquist coordinates (a generalization of the Schwarzschild coordinates) the Kerr metric is given by the expression:

$$ds^2 = -\left(1 - \frac{2Mr}{\Sigma}\right)dt^2 - \frac{4Mar \sin^2 \theta}{\Sigma} dt d\varphi + \Sigma d\theta^2 + \frac{\Sigma}{\Delta} dr^2 + \left(r^2 + a^2 + \frac{2Mr a^2 \sin^2 \theta}{\Sigma}\right) \sin^2 \theta d\varphi \quad (1.13)$$

where  $M$  is the mass of the body,  $a$  is its the specific angular momentum (or spin parameter,  $a = J/M^2$  where  $J$  is the angular momentum of the body),  $\Sigma \equiv r^2 + a^2 \cos^2 \theta$  and  $\Delta \equiv r^2 - 2Mr + a^2$ . As happened with the Schwarzschild metric, the Kerr one has its physical relevant surfaces. One of them is the *Kerr radius*<sup>7</sup> or event horizon,  $r_{\text{Kerr}}$ , whose value can be fully characterized by both  $r_{\text{Sch}}$  and  $a$ :

$$r_{\text{Kerr}} = \left(r_{\text{Sch}} + \sqrt{r_{\text{Sch}}^2 - 4a^2}\right)/2. \quad (1.14)$$

Another important position is the *ergosphere radius*,  $r_{\text{Erg}}$ , which delimits the area in which observers can not remain static, i.e their reference systems are irretrievably dragged by the rotation of space-time caused by the central object. The particular value of the ergosphere radius is:

$$r_{\text{Erg}} = \left(r_{\text{Sch}} + \sqrt{r_{\text{Sch}}^2 - 4a^2 \cos^2 \theta}\right)/2. \quad (1.15)$$

Further generalizations of the Kerr and Schwarzschild metric are allowed. When the charge is included in the Schwarzschild and Kerr metric we have, respectively, the Reissner–Nordström and Kerr–Newman solutions. Nonetheless, as we will see later, astrophysical black holes can be fully characterized by just mass and spin since their charge is quickly neutralized by the accretion of particles oppositely charged. Regarding the mass, astrophysical black holes can be divided into three different classes: stellar-mass ( $\sim 3-10^2 M_{\odot}$ ), intermediate-mass ( $10^2-10^5 M_{\odot}$ ) and supermassive ( $10^5-10^9 M_{\odot}$ ) black holes (Mezcua, 2017). To what concerns to this thesis we will focus on the supermassive black hole (BH) population. Another important theoretical quantity related with black holes is the *innermost stable circular orbit* (ISCO) which corresponds to the smallest stable circular orbit which a particle can establish around a black hole before being accreted into it. As we will see during this thesis (see Chapter 5), this quantity has a large effect on the mass and spin evolution of the black holes. In Appendix A we present a detailed description on how to obtain the position, energy and angular momentum of the ISCO for a Schwarzschild and Kerr black hole.

### 1.3.2 Supermassive black holes: Demography and correlations

Even though the existence of black holes was proposed by Schwarzschild (1916) after solving the Einstein equations, astrophysical black holes were not discovered until many years later. In the 1950s, with the advances in radio astronomy, several scientific works reported a population of compact radio sources whose counterpart in the optical range was absent or, in some cases, only a faint star-like object was detected. Based on their small angular size, the scientific community classified such objects as stars despite they are not expected to be bright in radio frequencies. Interested by their peculiar nature, Maarten Schmidt, by using a spectrograph mounted in a 5 meters telescope, took the spectra of one of these compact radio source (specifically, 3C 273). Expecting a star-like energy distribution, Schmidt reported five broad emission features incompatible with a stellar spectrum. In his work (Schmidt, 1963), he concluded that the most probable nature of this point-like source was a nuclear region of a galaxy with a cosmological redshift of  $\sim 0.158$ . Over the next few years more studies found similar objects (see eg. Matthews and Sandage, 1963; Bolton and Ekers, 1966a,b; Wyndham, 1965; Oke, 1966) gaining more relevance the idea of being cosmological sources. Given their similitude with a star in the optical range, these objects became to be known as quasi-stellar radio sources or just *quasars*.

<sup>7</sup>We called it like that in order do an analogy with the Schwarzschild radius.

The development of the physical understanding of quasars started with [Salpeter \(1964\)](#), [Zel'dovich \(1964\)](#) and [Lynden-Bell \(1969\)](#) which postulated that quasars were powered by supermassive black holes (BHs) ( $> 10^6 M_{\odot}$ ) accreting interstellar gas onto them. A few years later, [Shakura and Sunyaev \(1973\)](#) introduced a theory for the matter accretion onto black holes. To prevent a free fall accretion and allow observational effects, the theory assumed that matter flows towards the BH with considerable angular momentum. During the matter approach to the BH, the balance between centrifugal and gravitational forces allows to the matter rotate in circular orbits, forming a *disk-like* structure, called *accretion disk*. Through particle friction between adjacent layers and radiative viscosity, gas loses gravitational energy and spirals towards the BH until finally reaches the BH gravitational radius where is accreted. Part of this energy loss is turned into thermal energy which is radiated away from the disk surface. The total energy and the spectrum of the outgoing radiation are determined by the BH accretion rate,  $\dot{M}$ , through the equation  $L = \epsilon \dot{M} c^2$  (see [Appendix B](#)) where  $\epsilon$  is a parameter called radiative efficiency and depends on the BH spin. Based on this, one can correlate the amount of matter accreted by the BH and the quasar luminosity. For instance, when  $\dot{M} = 10^{-9} - 3 \times 10^{-8} M_{\odot}/\text{yr}$  the accreting BH is powerful on X-rays wavelengths with  $L \sim 10^{37-38}$  erg/s. On the other hand, at  $\dot{M} > 10^{-9} M_{\odot}/\text{yr}$  the optical luminosity exceeds  $L \sim 10^{33}$  erg/s.

The development of the [Salpeter \(1964\)](#) and [Shakura and Sunyaev \(1973\)](#) theory seeded the idea that the galaxy population reported by [Seyfert \(1943\)](#) several years before [Schmidt \(1963\)](#) could be the same physical objects that quasars but at lower cosmological distances<sup>8</sup>. In particular, Carl Seyfert reported the existence of spiral galaxies whose nuclear spectral energy distribution displayed similar broad emission lines than the ones found by [Schmidt 1963](#). Subsequent studies found many more galaxies displaying similar behaviour in the nearby universe (see [Osterbrock et al., 1976](#); [Wilson and Willis, 1980](#); [Alloin et al., 1985](#)). However, the diversity in the line shapes (broad and narrow), a different type of emission lines and the presence or not of radio emission made it too difficult to conclude that all these objects with peculiar nuclear regions were the manifestation of the same structure, i.e an accreting supermassive BH. During the 90's, it was possible to consolidated the *unification* model ([Lawrence, 1987](#); [Antonucci, 1993](#); [Urry and Padovani, 1995](#)). The theory establishes that all the galaxies containing a nuclear supermassive black hole accreting gas are called *Active galactic nucleus* (AGN) and depending on both the accretion rate onto the black hole and how the matter is distributed between the BH and the observer, the detected characteristics of both radio and line emission are different. Among many others, some AGNs types are Seyfert I and II galaxies, radio galaxies, LINERs or quasars. Based on the idea of BH accretion as the engine of all AGNs, [Soltan \(1982\)](#) constrained for the first time the black hole demography in the nearby universe. By using the available data of quasar bolometric luminosity functions<sup>9</sup> (LFs), the author concluded that the total BH mass density in the local universe would reach up to  $4.7 \times 10^4 M_{\odot}/\text{Mpc}^3$  and, on average, every local giant galaxy should contain a  $10^8 - 10^9 M_{\odot}$  supermassive black hole. However, due to obvious selection bias in the observations and the large errors in the faint end of the luminosity functions, the BH mass density was considered as a lower limit and the presence of BHs in small galaxies could not be constrained. Motivated by these results, more works tried to determine the cosmological evolution of the quasar LFs (see eg. [Schmidt and Green, 1983](#); [Boyle et al., 1988](#); [Hartwick and Schade, 1990](#); [Hewett et al., 1993](#); [Schmidt et al., 1995](#)). Some interesting trends were observed in these studies. For instance, while bright quasars are more numerous at high redshifts, the number density of faint luminosity quasars increases towards low redshifts ([Fan et al., 2001](#); [Hunt et al., 2004](#); [Cirasuolo et al., 2005](#); [Richards et al., 2006](#)). This different redshift evolution of bright and faint quasars were interpreted as a *downsizing* process ([Barger et al., 2005](#); [Hasinger et al., 2005](#)) which implies that BH accretion activity in the low- $z$  universe is dominated by either high-mass BHs accreting at low rates or low-mass BHs growing rapidly.

Direct confirmation of the existence of supermassive black holes hosted in the galactic centres was difficult to obtain. The theoretical models of [Guilbert and Rees \(1988a\)](#) and [Lightman and White \(1988\)](#)

<sup>8</sup>[Morrison \(1969\)](#) suggested that even pulsars could be powered by supermassive black holes.

<sup>9</sup>The quasar luminosity function can be described as the comoving number density of quasars as a function of the luminosity.

established that the accretion disk around the black hole is able to produce the 6.4 keV fluorescent iron line (Fe  $K\alpha$ ) in the X-ray electromagnetic part with a very well defined width of few eV (Guilbert and Rees, 1988a; Lightman and White, 1988; Matt et al., 1997; Holt et al., 1980). Fabian et al. (1989) suggested that the analysis of the Fe  $K\alpha$  line present in the AGNs would be a perfect tracer to detect the presence of supermassive black holes. By performing some Monte-Carlo calculations Fabian et al. (1989) concluded that Doppler and gravitational effects caused by the proximity of the accretion disk to the BH were enough to modify the shape and position of the line. Indeed, the specific changes were traces of the BH spin and the dynamical distribution of matter around the black hole. The first observational work to detect such relativistic effects in the Fe  $K\alpha$  line was Tanaka et al. (1995) in the galaxy MCG-6-30-15. Papers of Mushotzky et al. (1995) and Nandra et al. (1997) reported similar effects in other Seyfert galaxies. Further observational evidences of supermassive black holes were obtained in the optical electromagnetic range by analysing the stellar and gas dynamics in the nucleus of different galaxies (see Kormendy and Richstone 1995). For instance, the sharp rise in the M87 velocity dispersion profile suggested the possible existence of a supermassive black hole of  $\sim 10^9 M_\odot$  (Sargent et al., 1978). The nucleus of the galaxy M31 was extensively studied by Dressler and Richstone (1988) and Kormendy (1988b) which performed a line-of-sight velocity distributions and mass-to-light ratio profiles analysis and concluded that M31 probably contains a BH of  $\sim 3 \times 10^7 M_\odot$ . Further examples of BH masses estimated through stellar dynamics were NGC 3115 ( $\sim 10^9 M_\odot$ , Kormendy and Richstone 1992), M32 ( $\sim 2 \times 10^6 M_\odot$ , Tonry 1984, 1987) and NGC 4594 ( $\sim 5 \times 10^6 M_\odot$ , Kormendy 1988a). Probably, one of the most interesting examples of the BH existence is the one in our galaxy, the Milky Way. The best candidate for being the central BH is the radio source Sgr A\* (Genzel et al., 1994): a very compact object<sup>10</sup> and relatively faint in radio luminosity ( $10^{34}$  erg/s). Genzel and Townes (1987) and Genzel et al. (1994) by analysing the dynamics of the neutral and ionized gas near the Galactic center, reported a mass for Sgr A\* of  $\sim 10^6 M_\odot$ . Other mass estimations were published by Kent (1992) and Evans and de Zeeuw (1994). While the former used a flattened, isotropic Jeans equation model to fit the stellar and gas kinematics in the galactic plane, the latter performed some power-law fits to the inner regions of the Galactic bulge. Both works estimated similar BH masses of  $\sim 2 - 3 \times 10^6 M_\odot$ . The most recent estimates of the black hole mass point to  $\sim 4 \times 10^6 M_\odot$  (Gillessen et al., 2010).

The existence of supermassive black holes in the nucleus of most of the galaxies is now widely accepted and interesting correlations in the local universe between the black hole mass and its hosting bulge were also revealed. The first study reporting a correlation was Kormendy and Richstone (1995), which showed that the BH masses scale linearly with the absolute bulge luminosity of the host galaxy. A few years later, Magorrian et al. (1998) combined both dynamical models and kinematic of 36 nearby galaxies and estimated that the BH mass is connected with the one of the bulge through a  $\sim 0.005$  factor (see similar results of Marconi and Hunt 2003 and Häring and Rix 2004a). Another important correlation was found by Ferrarese and Merritt (2000) which reported that the masses of supermassive black holes tightly correlate with the velocity dispersion ( $\sigma$ ) of their host bulges (approximately as  $M_{\text{BH}} \propto \sigma^4$ ) with a smaller scatter than the one found for the bulge-black hole mass relation. Similar results were published by Gebhardt et al. (2000). In the following years, some other correlations were suggested. For instance, Graham et al. (2001) proposed a relation between black hole mass and the Sérsic index of the galaxy. Although all these previous studies were focused on the nearby universe, other works tried to estimate if the scaling relations still hold at higher redshifts. Treu et al. (2004) used the spectra of 20 Seyfert I galaxies at  $z \sim 0.37$  to estimate a redshift evolution in the  $M_{\text{BH}} - \sigma$  relation, with lower  $\sigma$  at fixed BH mass when the redshift increases (see also Peng et al., 2006; Treu et al., 2007). Merloni et al. (2004) analysing the evolution of the black hole and stellar mass density found similar results, with a moderate redshift evolution with larger black hole masses per stellar mass at higher redshifts (see the compatible results of Hopkins et al. 2006c). Finally, based on analysis of the quasar clustering, Fine et al. (2006) estimated that the black hole mass - dark matter halo relation displays a  $(1+z)^{3.3 \pm 1.3}$  evolution between  $z \sim 0.5 - 2.5$ .

<sup>10</sup>Extending  $\lesssim (1.1 \pm 0.1) \times 10^{-3}$  arcsec (9 AU) at  $\lambda = 1.3$  cm (Lo et al., 1985).



### 1.3.3 The formation of supermassive black holes

As discussed in the previous section, the existence of supermassive black holes in the center of the galaxies has been proved through different observational techniques. However, how such massive objects were formed is still an *open issue*. Different scenarios for BH formation have been proposed so far. One of the most popular theories is the *Pop III scenario* in which the *seeds* of the current supermassive black holes were formed at  $z \sim 15 - 30$  in mini-halos ( $\lesssim 10^6 M_\odot$ ) as remnants of the first generation of stars (Pop III, Yoshida et al., 2008; Agarwal et al., 2012; Valiante et al., 2016). Given that such stars are expected to be formed in metal free gas, their masses can span between  $10^2 - 10^3 M_\odot$  (Abel et al., 2002; Bromm and Larson, 2004), leaving after their death a remnant black hole of  $10 - 10^2 M_\odot$  (Bond, 1984; Heger and Woosley, 2002). Another scenario which leads slightly more massive BH seeds ( $10^3 - 10^4 M_\odot$ ) is the *runaway collapse of nuclear star clusters*. This theory assumes that during the core-collapse of a nuclear stellar cluster, the successive collisions and mergers of stars could lead to a runaway process with ultimately provokes the rapid formation of a very massive object containing the entire mass of the collapsing cluster (Rasio et al., 2004; Devecchi and Volonteri, 2009; Stone et al., 2017). The formation of much more massive black holes ( $10^4 - 10^5 M_\odot$ ) is possible in the *direct collapse* scenario where massive and pristine gas clouds at the center of (proto)galaxies could collapse in a single object without fragmenting into stars. To reach such conditions the model establish certain requisites such as the needed of angular momentum redistribution, the absence of molecular hydrogen ( $H_2$ ) in the gas which acts as main coolant process favouring its transformation into stars and the presence of *Lyman-Werner* photons capable of dissociating  $H_2$  (Haehnelt and Rees, 1993; Haiman et al., 1997; Lodato and Natarajan, 2006; Wise et al., 2008; Johnson et al., 2011). In this scenario, the most difficult step is to get a massive and dense enough central gas cloud. Some works such as Mayer et al. (2007), Bonoli et al. (2014) and Mayer et al. (2015) have proposed that gas rich galaxy mergers at high- $z$  could also lead the formation of such clouds, being an alternative pathway for the birthplace for direct collapse black holes.

Deriving observational constraints on BH formation occurring at very high- $z$  is a challenge and no evidence of any seeding scenario have been reported yet. The best candidate until now is the bright  $Ly_\alpha$  emitter CR7 at  $z \sim 6.6$  (Sobral et al., 2015). The system is formed by three different sources where two of them are thought to host Pop III stars and the other a direct collapse BH. However, its specific nature is still under debate (Bowler et al., 2017; Agarwal et al., 2017). Other recent works have pointed out that maybe dwarf galaxies could be the best places in which seeding theories could be tested. The quiet merger history of dwarf galaxies would have prevented the growth of BH seeds, leaving in the local universe the relics of the black hole formation epoch (van Wassenhove et al., 2010; Mezcua, 2019).

### 1.3.4 Supermassive black holes growth through cosmological times

How supermassive black holes have acquired their mass through the cosmological evolution of the Universe is still under debate. In this section, we present a summary of the main observational findings regarding the triggering mechanisms of the BH accretion phase. Later, we tackle the black hole mass growth through BH-BH coalescences, focusing on the main theories about the binary black hole formation.

#### **Black holes growing through gas accretion: Processes triggering gas inflows**

Even though it is well established that quasars and AGNs are the manifestations of supermassive black holes accreting gas in the center of the galaxies (Salpeter, 1964), it is poorly understood what are the mechanisms driving gas from galactic scales down to subparsec ones, where the supermassive black hole influences the gas dynamics. Theoretical studies have showed that non-axisymmetric disturbances caused by mergers, bars or globally self-gravitating disks can generate strong torques which lead to the rapid inflow of gas into the central  $\lesssim$  kpc of the galaxies (Hernquist, 1989; Barnes and Hernquist, 1991a,

1996; Di Matteo et al., 2005; Li et al., 2007). Once the gas reaches these sub-kpc scales the large-scale torques become inefficient and the transport of gas towards the BH surroundings ( $\lesssim$  pc) happens through local viscous stresses or bar-within-bars structures (Shlosman et al., 1989; Balbus and Hawley, 1998; Thompson et al., 2005). However, the relative importance between torques caused by mergers or by instabilities of self-gravitating disks in the activation of the AGN phase is still not clear. During the last years, a large number of observational studies have investigated if galaxy major mergers are the main mechanisms that constitute the AGN triggering. By using Hubble Space Telescope observations, Bahcall et al. (1997) studied a sample of 20 luminous quasars at  $z < 0.3$  finding that the majority of them were residing in merging galaxies. Similar results were found by Veilleux et al. (2006, 2009). Treister et al. (2012) studied the population of AGNs at higher redshifts ( $z < 3$ ) from multiwavelength surveys. The results pointed out a strong and redshift-independent correlation between the AGN luminosity and the fraction of host galaxies undergoing a major merger. A clear link between AGN activity and galaxy mergers was also seen in the ultraluminous infrared galaxy population (ULIRGs, see Sanders and Mirabel, 1996). Kartaltepe et al. (2012) found that a considerable fraction ( $\sim 70\%$ ) of  $z \sim 2$  ULIRGs showed signs of recent major mergers. Results from radio surveys have also suggested an important role of mergers in the triggering of radio loud AGNs. For instance, Chiaberge et al. (2015) showed that 92% of radio loud AGNs at  $z > 1$  were associated with recent or ongoing merger events. Similar results were found by Ramos Almeida et al. (2012) but with a sample of radio AGNs at much lower redshift ( $z < 0.7$ ).

Despite the results mentioned above, several works suggest that major mergers can not explain the triggering of the whole AGNs population. For instance, after studying asymmetry and concentration indexes of 37 X-ray AGNs, Grogin et al. (2003) concluded that mergers and interactions are not good indicators for AGN activity. Similar results were found by Cisternas et al. (2011) which concluded that the  $\sim 85\%$  of X-ray AGNs at  $0.3 < z < 1$  do not show recent major mergers signatures. Villforth et al. (2014), through the analysis of the morphological properties of AGN host galaxies as a function of the AGN luminosity, showed that  $< 40\%$  of highest luminous AGN display major merger interaction. The triggering mechanism for faint AGNs is also difficult to relate to mergers. For instance, Allevato et al. (2011) analysed the clustering of moderate luminous X-ray AGNs at  $z \lesssim 2.2$  and concluded that major mergers can not reproduce the observed high bias factors. Allevato et al. (2011) suggested the possibility of secular processes such as tidal disruptions or disk instabilities as more plausible AGN triggering mechanisms. On this line, Georgakakis et al. (2009) studied the X-ray luminosity function for AGN at  $z \sim 1$  as a function of morphological type. The authors found that AGNs hosted in disk-dominated galaxies contribute  $\sim 30\%$  of the total AGN, arguing that AGN in disk galaxies are most likely fuelled not by major merger events but by minor interactions or internal instabilities.

Regardless of the process which carried gas in the black hole surroundings, the process of gas accretion releases a large amount of energy in the interstellar medium which has an impact in the star formation of the host galaxy. This effect is known as *AGN feedback*. According to theoretical works, two kinds of feedback are possible: *quasar mode* and *radio mode*. The former was introduced by Silk and Rees (1998) pointing out that BHs consuming gas at high accretion rates are able to generate winds that could sweep up gas into a shell and push it outwards the central parts of the galaxy. If the velocity of the shell is large enough, it will be expelled from the galaxy in form of outflows, reducing the amount of gas in the galaxy and inhibiting further star formation events. Observational evidences of that AGN winds feedback have been reported by many authors (Heckman et al., 2000; Veilleux et al., 2005; Morganti et al., 2005; Holt et al., 2008; Rupke and Veilleux, 2011; Sturm et al., 2011; Nesvadba et al., 2011; Greene et al., 2012). However, disentangle between winds caused by starburst or AGN is not an easy task. On the other hand, the radio mode was introduced to solve the *cooling flow problem* (Cowie and Binney, 1977; Fabian and Nulsen, 1977). The most massive galaxies at the center of groups and clusters are surrounded by gas whose radiative cooling time is short enough to produce cold streams that feed the galaxies with cold gas able the fuel future star formation events. However, observational studies do not see high star formation rates in the central galaxies cluster. The lack of these cooling gas is often

explained by the heating mechanism of the central galaxy AGN, which reduces or stops the cooling rate onto the galaxy (Binney and Tabor, 1995; Churazov et al., 2002; McNamara and Nulsen, 2007).

Galaxy formation simulations have included both models of feedback (Di Matteo et al., 2005; Sijacki et al., 2007; Germain et al., 2009; Dubois et al., 2010; Ostriker et al., 2010; Gaspari et al., 2012; Vazza et al., 2013; Weinberger et al., 2017). Thanks to these processes, all these simulations have been successful in reproducing the black hole and bulge (mass and dispersion velocity) scaling relation.

### Black holes growing through coalescences: The theory of binary black holes

If we connect galaxy mergers with the fact that supermassive black holes are hosted at the center of most galaxies, it can be concluded that the coalescence of  $> 10^6 M_\odot$  black holes are common events in the Universe. Despite this, theoretical studies have demonstrated that the mass accreted by the BHs through coalescence can be neglected with respect to the one accreted via gas consumption (Volonteri and Perna, 2005; Fanidakis et al., 2011). To explain how two BHs end up merging, it is necessary to first understand the processes that reduce their separation and lead to the formation of a binary system. During the last years, the study of how binary black holes (BBHs) form, evolve and coalesce inside galaxies has been an important topic in the astrophysical field (see the review of Colpi, 2014). Most of the studies tackling these topics relay on the pioneering work of Begelman et al. (1980) which described the existence of three main phases in the life of a BBH system: *pairing*, *hardening* and *gravitational wave inspiral* phase. In Fig. 1.4 it is presented an illustrative scheme summarizing all these phases. During the pairing stage, the dynamical friction caused by the galaxy stars acts on the two black holes causing their progressive displacement towards the galactic center. Once reached the galactic center, the two BHs end forming a close Keplerian system as soon as the mass in starts enclosed within their orbits drops below twice the total mass of the binary. To guide the reader, the formation of a Keplerian binary in a singular isothermal sphere happens when the semi-major axis of the orbit,  $r_{\text{BBH}}$ , reaches:

$$r_{\text{BBH}} = \frac{G(M_{\text{BH}_1} + M_{\text{BH}_2})}{\sigma^2} \quad (1.16)$$

where  $\sigma$  is the velocity dispersion of the stellar bulge and  $M_{\text{BH}_1}$  and  $M_{\text{BH}_2}$  are, respectively, the mass of the first and second BH forming the binary. After the formation of the Keplerian system, the BBH enter in the *hardening* and *gravitational wave inspiral* phases where  $r_{\text{BBH}}$  decreases through the energy loss by close encounters with single stars and gravitational wave emissions. According to Sesana and Khan (2015) the change of  $r_{\text{BBH}}$  during hardening and gravitational wave phase can be parameterized as:

$$\frac{dr_{\text{BBH}}}{dt} = \left( \frac{dr_{\text{BBH}}}{dt} \right)_{\text{Hard}} + \left( \frac{dr_{\text{BBH}}}{dt} \right)_{\text{GW}} = - \frac{GH\rho_{\text{inf}}}{\sigma_{\text{inf}}} r_{\text{BBH}}^2 - \frac{64G^3(M_{\text{BH}_1} + M_{\text{BH}_2})^3 F(e)}{5c^5(1+q)^2 r_{\text{BBH}}^3} \quad (1.17)$$

where  $q (\leq 1)$  is the mass ratio of the binary,  $G$  is the gravitational constant,  $c$  is the light speed,  $H$  is a dimensionless hardening rate inferred from three-body scattering experiments (of the order of  $\sim 15 - 20$ , Quinlan, 1996; Sesana et al., 2006),  $\rho_{\text{inf}}$  and  $\sigma_{\text{inf}}$  the density and velocity dispersion of intruding stars at the BBH sphere influence and  $F(e)$  a function which depends on the binary eccentricity ( $e$ , Peters and Mathews, 1963):

$$F(e) = (1 - e)^{-7/2} \left[ 1 + \left( \frac{73}{24} \right) e^2 + \left( \frac{37}{96} \right) e^4 \right] \quad (1.18)$$

Scattering experiments and numerical simulations indicate that the binary eccentricity is not constant during the hardening phase but it increases through stellar encounters (see e.g, Amaro-Seoane et al., 2009, 2010). In particular, the variation of the eccentricity of the BBH can be expressed as:

$$\frac{de}{dt} = r_{\text{BBH}} \frac{G\rho_{\text{inf}}HK}{\sigma_{\text{inf}}} - \frac{304}{15} \frac{G^3 q (M_{\text{BH}_1} + M_{\text{BH}_2})^3}{c^5 (1+q)^2 r_{\text{BBH}}^4 (1-e^2)^{5/2}} \left( e + \frac{121}{304} e^3 \right) \quad (1.19)$$

where  $K$  is the eccentricity growth rate which spans from  $\sim 0 - 0.2$  (Quinlan, 1996; Sesana et al., 2006).

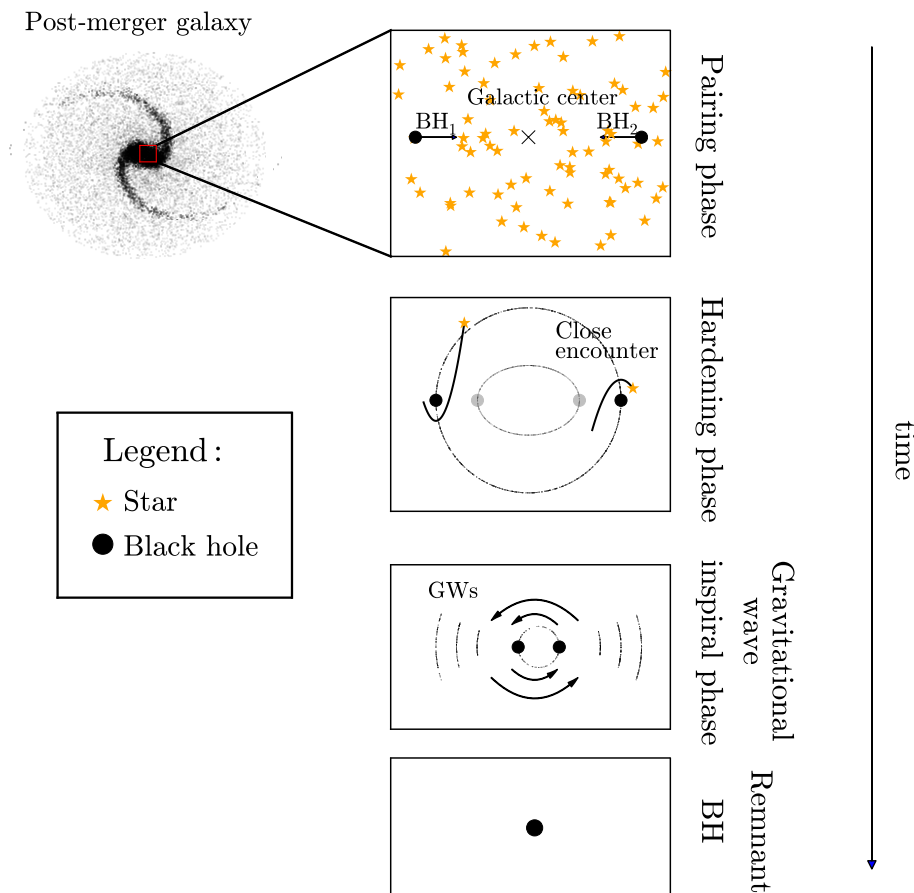


Figure 1.4: Illustrative scheme of the phases of a binary black hole system. From top to bottom: pairing, hardening and gravitational wave inspiralling.

During the process of coalesce, gravitational waves (GW) emitted by the BBH system span for a wide range of frequencies ( $\nu \propto M_{\text{binary}}^{-1}$ ): from the nHz to the mHz (Haehnelt, 1994; Jaffe and Backer, 2003). The range of  $\nu \sim 10^{-5} - 1$  Hz corresponds to the merger phase of BBH system formed by supermassive black holes ( $\sim 10^4 - 10^{10} M_{\odot}$ ) and will be probed by the *Laser Interferometer Space Antenna* (LISA, eLISA Consortium et al., 2013a; Amaro-Seoane et al., 2017a). Specifically, the LISA spacecraft will be the first mission to scan the whole Universe with GWs, allowing the detection of the vast majority of coalescing massive BBHs. LISA is a *L-class mission* consisting of 3 spacecrafts forming a triangular configuration with arm lengths of  $10^6$  km and laser interferometry between *free-falling* test masses. The interferometers are designed to measure the variations in light travel time along the arms due to the deformation of spacetime by gravitational waves. Finally, the GW signal at the frequency range of  $\nu \sim 10^{-9} - 10^{-6}$  Hz is generated by the stochastic GW background produced by the incoherent superposition of radiation from the whole cosmic population of massive BBHs (Sesana et al., 2008; Amaro-Seoane and Santamaría, 2010). This frequency window is accessible by the Pulsar Timing Array (PTA) experiment (Foster and Backer, 1990).

### 1.3.5 Supermassive black hole spin: Theory and observations

Astrophysical supermassive black holes are expected to have angular momentum:

$$J_{\text{BH}} = a \frac{GM_{\text{BH}}^2}{c} \quad (1.20)$$



where  $a$  is the spin parameter  $0 < a < 1$  (Bardeen et al., 1972; Thorne, 1974). The specific value of the BH spin has important relevance in astrophysics. For instance, it is expected to influence on both the formation and direction of radio jets in AGNs (Blandford and Znajek, 1977; MacDonald and Thorne, 1982). Spin could be also a good tracer of the cosmological growth of the BH since its specific value changes through repeated gas accretion events and mergers with other black holes (Volonteri and Perna, 2005; Berti and Volonteri, 2008). In this section, we present the theoretical background to understand how BHs change their spin and the recent observational techniques developed to measure the spin of the local black hole population.

### Modifying the spin of supermassive black holes: Black hole coalescences

The final phase of a BBH system is coalescence. While the first stages of the life of a BBH can be described with the post-Newtonian approximation, the final ones when the two BHs get closer and start rapidly orbiting each other, only numerical simulations provide accurate predictions by solving the full non-linear Einstein equations. The breakthroughs in numerical techniques reached 20 years ago made possible studying systematically the outcomes of binary black hole coalescences. (Pretorius, 2005; Campanelli et al., 2006; Baker et al., 2006b). Early works focused on the mergers of non-spinning binary systems with equal and unequal mass (Campanelli, 2005; Buonanno et al., 2006; Herrmann et al., 2007b,a). Interestingly, all these studies concluded that coalescences of Schwarzschild BHs in realistic astrophysical scenarios would lead to the formation of a Kerr remnant. For instance, Baker et al. (2006a) showed that the merger of two equal mass BHs with  $a = 0$  in a circular orbit results in a Kerr BH with  $a = 0.69$  (see also Hinder et al., 2008). Analytic expressions for the final BH spin were constructed from all these available numerical data. Berti et al. (2007) proposed that the coalescence of two unequal mass Schwarzschild BHs form a remnant whose spin,  $a_f$ , can be approximated to:

$$a_f \simeq 2\sqrt{3}\frac{q}{(1+q)^2} - 2.029\frac{q^2}{(1+q)^4} \quad (1.21)$$

where  $q \leq 1$  is the mass ratio of the two initial BHs. Modelling the final spin of a BBH system formed by two Kerr BHs was more difficult given the 7-dimensional parameter space dependence: mass ratio of the binary ( $q$ ) and the orientation of the two BH spins ( $\vec{a}_1, \vec{a}_2$ ). Thanks to the knowledge gained with the simulations of non-spinning BH coalescences, Campanelli et al. (2007) performed the first simulation of a BBH system formed by unequal mass black holes with misaligned spins. A few years later, Rezzolla et al. (2008b,a) published a general analytic fitting formula for predicting the final spin of any binary configuration of Kerr BHs:

$$\vec{a}_f = \frac{1}{(1+q)^2} (\vec{a}_1 + \vec{a}_2 q^2 + lq) \quad (1.22)$$

where  $l$  denotes the difference between the orbital angular momentum when the binary is widely separated and the angular momentum radiated away in gravitational waves before the merger.

One of the most interesting effects reported by the works which studied Kerr BBH systems was the large recoil velocities undergone by the remnant BH after BH-BH mergers<sup>11</sup> (see e.g. Campanelli et al., 2007). Interestingly, it was proved that these recoils display a dependence with the mass ratio and spins of the progenitor BHs (Lousto and Zlochower, 2011, 2013). One of the major issues to draw solid conclusions about the effects of recoil velocities has been simulating realistic astrophysical environments (Noble et al., 2012; Bode et al., 2012; Bogdanović et al., 2011). Some recent works, performing hydrodynamical simulations have found that BHs surrounded by gas rich environments lead to the spin alignment of the two BHs, disfavouring large kicks (Bogdanović et al., 2007; Dotti et al., 2010).

<sup>11</sup>Recoils appear as a consequence of gravitational waves carrying away linear momentum from the system.

### Modifying the spin of supermassive black holes: Gas accretion

As discussed in Section 1.3.4, the black holes consume gas through transient accretion disks. However, the space-time twist caused by the Kerr black hole induces important changes in the structure of the accretion disk if this one is not settled in the equatorial plane of the BH<sup>12</sup> (Papaloizou and Pringle, 1983; Nelson and Papaloizou, 2000). Bardeen et al. (1972) studied for the first time how the structure of a conventional Shakura and Sunyaev (1973) accretion disk evolves when exists a tilt between disk orbital and BH equatorial plane. Since the angular momentum of the rotating BH pulls the surrounding space into a whirlpool pattern, the disk is promoted to a differential *Lense-Thirring precession* around the rotation axis of the BH (i.e the BH angular momentum direction,  $\vec{J}_{\text{BH}}$ ) with angular velocity (Wilkins, 1972):

$$\omega_{\text{LT}}(r) = \frac{2G|\vec{J}_{\text{BH}}|}{c^2} = \frac{2GaM}{cr^3} \quad (1.23)$$

This differential precession leads to the formation of a *warped accretion disk*. The disk viscosity<sup>13</sup> plays an important role during this twisting process by producing three different torques acting on the disk. The first one, perpendicular to the orbital plane, reduces the angular momentum of the disk and leads to a radial drift. The second one takes place in the disk orbital plane and produces a precession around the symmetry axis of the black hole. Finally, the third one, acts also on the orbital plane by tending to align the angular momentum of the disk with that of the black hole, reducing the inclination angle of the orbital plane. The combination of both Lense-Thirring precession and the internal torques acting on the accretion disk produce the so-called *Bardeen-Petterson effect* whose final outcome is the existence of two disk mid-planes, one aligned in the BH equatorial plane (*warped region*) and the other retaining the initial tilt (Scheuer and Feiler, 1996; Natarajan and Pringle, 1998; Nixon and King, 2012; Lodato and Gerosa, 2013). Consequently, the direction of the angular momentum of the inflowing material changes as it passes through the warped region. The transition radius between these two planes is expected to happen approximately where the rate of disk twisting caused by the differential precession is balanced by the rate at which disk warps are diffused. Besides, the disk can retain a steady warped state since the warp propagates on a time scale much shorter than the local radial viscous time which determines the mass transport (Martin et al., 2007). As an illustrative example, in Fig. 1.5 we present a cartoon about the shape that an accretion disk would display around a spinning BH. As we can see, the outer parts of the accretion disk retain the initial tilt between disk and BH angular momentum ( $\theta$ ). On the contrary, the inner ones lie in the equatorial plane of the black hole. As a consequence, the accretion disk displays a warped shape.

Even though the possibility of a counter-alignment configuration between the warped region and the BH angular momentum during the Bardeen-Petterson process seemed to be ruled out by Scheuer and Feiler (1996), King et al. (2005) revisited this conclusion and proposed that in some cases the counter-alignment is possible. By denoting  $\vec{J}_{\text{d}}$  as the angular momentum of the disk, the total angular momentum of the BH-accretion disk system,  $\vec{J}_{\text{T}}$ , can be defined as:

$$\vec{J}_{\text{T}} = \vec{J}_{\text{BH}} + \vec{J}_{\text{d}} \quad (1.24)$$

which is a constant vector since during an accretion event both the orientation and magnitude of the spin are fixed. By using the cosine theorem, the magnitude of  $\vec{J}_{\text{T}}$  can be expressed as:

$$J_{\text{T}}^2 = J_{\text{BH}}^2 + J_{\text{d}}^2 + 2J_{\text{BH}}J_{\text{d}} \cos \theta \quad (1.25)$$

where  $\theta$  ( $0 < \theta < \pi$ ) denotes the angle formed between the BH and disk angular momentum, i.e the mis-alignment angle. Note that  $\theta = 0$  will correspond to full alignment while  $\theta = \pi$  will characterize a full

<sup>12</sup>In case the disk is settled in the equatorial plane of a Kerr BH without any tilt, the gas is dumped directly down the hole from the ISCO.

<sup>13</sup>The viscosity of an accretion disk have two different contributions. One of them ( $\mu_1$ ) corresponds to the azimuthal shear. The second one ( $\mu_2$ ) represents the vertical shear.

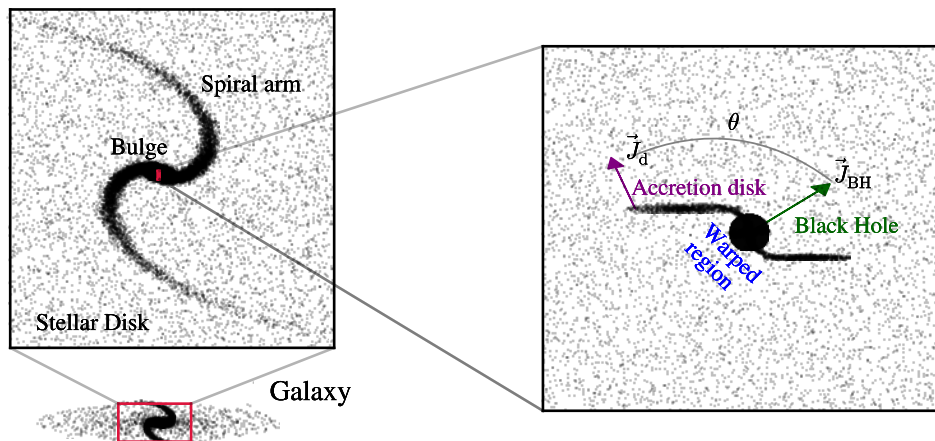


Figure 1.5: Illustrative cartoon about the shape that an accretion disk displays around a spinning black hole. The variable  $\theta$  corresponds to the angle formed between the black hole and accretion disk momentum ( $\vec{J}_{\text{BH}}$  and  $\vec{J}_{\text{d}}$ , respectively).

antialignment. According to Eq. (1.25), King et al. (2005) conclude that a counteralignment in the accretion happens when  $J_{\text{BH}}^2 > J_{\text{T}}^2$ , which requires:

$$\cos \theta < -\frac{J_{\text{d}}}{2J_{\text{BH}}} \quad (1.26)$$

Both alignment and counter-alignment have an important effect on the final angular momentum of the BH (and therefore in its spin) after an accretion event. According to Eq. (1.25) counter-alignments will reduce  $J_{\text{T}}$ , spinning-down the BH. On the contrary, alignments will increase  $J_{\text{T}}$ , producing a spinning-up of the BH. Thus, the specific way in which the gas is accreted onto the BH will completely determine the final spin value. Several accretion scenarios have been proposed so far. For instance, Volonteri et al. (2005) comparing the alignment time of the warped disk with the timescale for the mass of the BH to increase via accretion, concluded that the BH will align with the outer disk before it accretes much mass. This led to the conclusion that most of the mass accreted by the BH happens in a continuous prolonged or *coherent* way, spinning up the BH until  $a \sim 1$ . On the other side, the picture of spin evolution via prolonged accretion was questioned by King et al. (2005), King and Pringle (2007) and King et al. (2008) which suggested that, as a consequence of self-gravity, the gas consumption onto the BH always takes place via low-mass accretion disc episodes, all chaotically oriented with respect to one another. As a consequence of that *chaotic accretion*, the BH can rapidly decrease its spin down to a value of  $\sim 0.2$ .

### Observing black holes spin

Advances on both observational techniques and theoretical modellings of accretion disks have allowed to give constraints on the spin of a handful of supermassive black holes (Brenneman and Reynolds, 2006; de La Calle Pérez et al., 2010; Patrick et al., 2011b; Gallo et al., 2011). In the literature we can find 5 different methods to constrain the BH spin from observational data (see Brenneman, 2013). All of them, listed below, rely on two assumptions: general relativity provides a correct description of the space-time around a BH and it exists a monotonic correlation between the ISCO radius and the spin (see Appendix A).

- i) *Inner disk reflection modelling*: Gas consumption by a black hole releases a large amount of energy throughout the whole electromagnetic spectrum. The X-ray emission ( $> 2 \text{ keV}$ ) is dominated

by UV photons comptonized<sup>14</sup> by the hot electrons plasma which surrounds the disk. While part of these photons are radiated away by the system, a small fraction is *reflected* towards the accretion disk surface causing the excitation of the Fe K $_{\alpha}$  line at 6.4 keV in rest-frame (Guilbert and Rees, 1988b; Lightman and White, 1988). The *inner disk reflection modelling* technique is based on the analysis of this iron line. Doppler and relativistic effects close to the BH causes a broadening and skewness in the Fe K $_{\alpha}$  profile, far from its near delta behaviour. Specifically, the red wing of the Fe K $_{\alpha}$  line profile relates directly with the location of the ISCO radius and thus with the BH spin (Reynolds and Nowak, 2003; Brenneman and Reynolds, 2006). The advantage of this methodology is that it does not require a priori knowledge of both mass and distance to the BH. However, the disadvantage arises when gas along the line of sight provokes complex absorption features making it a challenging to determine the red wing of the Fe K $_{\alpha}$  line.

- ii) *Thermal continuum fitting*: The basis of this technique is treating the inner parts of the accretion disk as a modified black body of temperature  $T$  whose value can be related to the ISCO radius ( $r_{\text{ISCO}}$ ) through the equation (Zhang et al., 1997):

$$r_{\text{ISCO}} \propto \sqrt{F \cos(i)} d T^2, \quad (1.27)$$

where  $F$  is the flux of the accretion disk,  $d$  is the distance between the observer and the source and  $i$  is the inclination angle relative to the BH spin axis. Based on  $r_{\text{ISCO}}$ , the spin of the BH is estimated from Eq. A.22. This technique has some limitations when measuring the spin of supermassive black holes<sup>15</sup> (see McClintock et al., 2014). Particularly, since the temperature of the accretion disk correlates with mass as  $\propto M^{-1/4}$ , the black body for a quasar/AGN peaks in the UV wavelengths. The presence of the absorption features in this range can present serious complications to accurately measure the flux ( $F$ ) of the AGN accretion disk.

- iii) *High frequency quasi-periodic oscillations*: This technique is based on the fact that the X-ray emission from the inner accretion disk displays some variability at certain frequencies. Despite the physical mechanism generating such phenomena is still not well understood, the frequencies where this variability happens are related with the ISCO radius. This method has been mainly used in the studying of stellar-mass black holes (Morgan et al., 1997; Homan et al., 2001), being reported such quasi-periodic oscillations by just one AGN (Gierliński et al., 2008).
- iv) *X-ray polarimetry*: The reflected emission coming from the inner accretion disk of a BH is expected to be polarized (Laor et al., 1990; Matt et al., 1993). The degree and angle of polarization with respect to the energy distribution displays a characteristic shape with depends on the BH spin and the ISCO position (Stark and Connors, 1977; Connors et al., 1980; Schnittman and Krolik, 2009).
- v) *Imaging the event horizon shadow*: Sub-mm Very Long Baseline Interferometry (VLBI) is used to obtain images of the innermost accretion disk surrounding a BH. The BH spin can be constrained by comparing these images with models of disk inner parts appearance. Given that this technique needs a very good spatial resolution ( $\sim 10 \mu\text{acsec}$ ), the sample of BHs in which this method can be used is limited to SgrA\* and the BH of M87 (Doeleman et al., 2008; Event Horizon Telescope Collaboration et al., 2019).

Even though all these techniques had shed light on the spin values of some local supermassive black holes, their values are still controversial. Several free parameters entering in all these five methodologies create severe degeneracy problems. For instance, several works obtained different estimation for the spin of the supermassive black hole hosted in the MCG-6-30-15 galaxy:  $a > 0.98$  (Brenneman and Reynolds, 2006),  $a = 0.86 \pm 0.01$  (de La Calle Pérez et al., 2010), and  $a = 0.49 \pm 0.20$  (Patrick et al., 2011b). Even more dramatic is the case of the galaxy NGC 3783, for which some works pointed out a spin value of  $a > 0.88$  (Brenneman et al., 2011) while others  $a < 0.32$  (Patrick et al., 2011a).

<sup>14</sup>Comptonization means that the photons have lost of energy via Compton scattering

<sup>15</sup>This technique is mainly used to compute the spin of stellar mass BHs given the good accuracy in measuring the distance to the source and the inclination of the accretion disk

### 1.3.6 Understanding supermassive black holes through simulations

To understand the complete black hole formation and evolution scenario, it had been important to complement observational studies with the ones done by using semi-analytical models and hydrodynamical simulations. One of the first works addressing the evolution of BHs in a cosmological framework was performed by [Kauffmann and Haehnelt \(2000\)](#) (see also [Cattaneo 2001](#)). In that work, the authors included the growth of BHs inside a cosmological context by using a semi-analytical model based on the extended Press-Schechter theory to generate Monte Carlo realizations of the merging paths of dark matter halos. Motivated by the reported scaling relation between BHs and elliptical galaxies, [Kauffmann and Haehnelt \(2000\)](#) assumed that the main mechanism by which the BHs can grow is via gas accretion after galaxy major mergers ([Haehnelt et al., 1998](#)). This simple assumption leads to the SAM the capability of reproducing the observed trends of the B-band luminosity function of  $z < 2$  quasars, reinforcing the theory of mergers as important drivers of BH growth. In the same year, [Haehnelt and Kauffmann \(2000\)](#) explored the BH scaling relations using the same SAM of [Kauffmann and Haehnelt \(2000\)](#). As in observations, the predictions reported a tighter correlation between  $M_{\text{BH}}$  and  $\sigma$  than with  $M_{\text{Bulge}}$ . This difference was attributed to the fact that the bulge mass showed a strong redshift dependence while velocity dispersion did not. [Volonteri et al. \(2003\)](#) used a similar approach than [Kauffmann and Haehnelt \(2000\)](#) to study the evolution of supermassive black holes. By coupling a simple model where quasar activity is driven by major mergers with a Monte Carlo algorithm to trace the halo merger history, the authors generated a reliable BH population. Including a model for the BBH hardening and gravitational wave inspiral phase, [Volonteri et al. \(2003\)](#) concluded that up to 10% of the nearby galaxies might host a nuclear BBH system. Besides, this model reported a large level of triple BH interactions at high- $z$  which ultimately led to the expulsion of one of the three BHs from the host galaxy. The expelled BHs constitute a population of wandering black holes orbiting within dark matter halos without a host galaxy. A few years later, using the same SAM, [Volonteri et al. \(2005\)](#) studied for the first time the cosmological evolution of supermassive black hole spins. By including BH-BH coalescence and gas accretion events as mechanisms leading to spin changes, the authors ascertained the latter process as the dominant one for the formation of rapidly spinning BHs.

Theoretical studies to understand the evolution of the quasar luminosity function were also performed within a semi-analytical framework. [Marulli et al. \(2008\)](#) and [Bonoli et al. \(2009\)](#) included in the L-Galaxies SAM ([Guo et al., 2011](#)), run on top of the Millennium merger trees ([Springel, 2005](#)), a refined prescription to describe the BH luminosity during each gas accretion phase after a *major* and *minor* galaxy merger. In their implementation, BHs do not accrete mass instantaneously. Instead, the accretion is coupled to a light curve model consisting of two different phases. One in which the BH growth is Eddington limited, while the other is a quiescent regimen in which the BH grows at low Eddington rates. These two-phases model showed a good performance to reproduce the evolution of the faint end of quasar bolometric luminosity and the clustering of  $z < 3$  quasars. However, the model displayed a limitation when reproducing the number of bright quasars at  $z \geq 3$ , suggesting that high- $z$  BHs might accrete gas through other physical processes. [Hirschmann et al. \(2012\)](#) performed a very similar work than [Marulli et al. \(2008\)](#) but including disk instabilities, i.e torques caused by self-gravitating disks, as an extra mechanism to trigger AGN/quasar phase. The inclusion of these extra process allowed the model to achieve a good agreement in the X-rays and bolometric luminosity functions of  $z \leq 5$  quasars. However, [Hirschmann et al. \(2012\)](#) included *ad hoc* the assumption that disk instabilities only trigger very sub-Eddington BH accretion rates, losing the possibility of concluding if disk instabilities can be more important than mergers during BH growth. [Fanidakis et al. \(2011, 2012\)](#) shed more light on this topic. By including in GALFORM SAM ([Lacey et al., 2016](#)) a comprehensive modelling of BH growth where gas accretion during mergers and disk instabilities are coupled with spin evolution, [Fanidakis et al. \(2012\)](#) concluded that disk instabilities play an important role in the mass evolution of supermassive black holes. The model predicted that, regardless of redshift, BHs consume typically  $\sim 2$  dex more gas through disk instabilities than via major and minor mergers. In addition, [Fanidakis et al. \(2011\)](#) tested in GALFORM two different BH models of spin evolution during gas accretion: coherent and chaotic



(see Section 1.3.5). While the former gives a population of low spinning black holes ( $a \sim 0.2$ ), the latter predicts highly spinning black holes ( $a \sim 1$ ). By comparing model predictions with the observed bolometric and radio luminosity functions of quasars, Fanidakis et al. (2011) concluded that the low spinning BH population provide a better agreement with observations. Menci et al. (2014) was also one of the pioneering works investigating the role of disk instabilities in the growth of supermassive black holes. Unlike other models, Menci et al. (2014) included in a SAM a sophisticated prescription for the gas mass inflow after disk perturbations based on the physical description of the Hopkins and Quataert (2011) numerical simulations. The work showed that while the bright end of the AGN luminosity in the B-band at  $z < 4.5$  can only explained thanks to disk instabilities, at  $z > 4.5$  the abundance of bright quasars is underestimated if disk instabilities are the only mechanisms of BH feeding.

In addition to the pioneering works of Volonteri et al. (2005) and Fanidakis et al. (2011), further investigations about the cosmological evolution of supermassive black hole spin were performed by Volonteri et al. (2013). For such purpose, the authors included in a SAM a model of black hole growth similar to the one presented by Marulli et al. (2008) but tracking the change of the BH spin through a chaotic and coherent scenario during gas-poor and gas-rich galaxy mergers, respectively. Under these assumptions, the outcomes of the model pointed towards a drastic decrease in the number of highly spinning BHs with cosmic time as a consequence of an increased incidence of chaotic accretion processes. Similar trend was reported by Barausse (2012) who concluded that  $z > 3$  black holes are maximally spinning while  $z < 2$  BHs are characterized by low spin values ( $a \lesssim 0.2$ ). Sesana et al. (2014) revisited the work of Barausse (2012) including a novel spin model where the properties of the accretion flow onto BHs are linked to the morphological characteristics of the host galaxies. On the contrary to what was reported by previous works, the results showed a population of supermassive black holes with moderate spin ( $a \sim 0.4$ ) regardless of the redshift.

More recent works about supermassive black holes have focused on the black hole formation problem. For instance, Valiante et al. (2016) included in GAMETE SAM both PopIII and direct collapse scenarios of the formation of supermassive black holes. The model predictions suggested that direct collapse BHs were the most plausible progenitors of  $> 10^8 M_{\odot}$  black holes at  $z > 6$ . However, the interplay between chemical, radiative and mechanical feedback effects included in the model did not make possible draw conclusive results. On the other hand, Ricarte and Natarajan (2018) tried to disentangle signatures of the BH seeding process by using a SAM based on Press-Schechter merger trees. Interestingly, the black hole occupation fraction or the bright end of the high- $z$  quasar LF could retain some memory about the BH seeding mechanism.

In addition to semi-analytical models, a large number of works have studied the evolution of supermassive black holes by using hydrodynamical simulations. One of the first studies was the one of Di Matteo et al. (2005) (see also Springel et al., 2005), which presented detailed numerical simulations of isolated galaxy mergers. The results showed that the collision of galaxies causes a strong nuclear inflow that can feed with gas the supermassive black holes and power the quasar phase. In a more cosmological context we can find the work of Di Matteo et al. (2012) which using the MassiveBlack simulation of  $0.75 \text{ Gpc}^3$  studied the growth of supermassive black holes at  $z > 7$ . The results showed that steady high density cold gas flows could lead to the rapid growth of supermassive black holes in the early Universe. Hirschmann et al. (2014) explored the evolution of the quasar bolometric luminosity functions at  $z < 5$  inside two cosmological simulations of  $\sim 68 \text{ Mpc}$  and  $\sim 500 \text{ Mpc}$  of box length. Interestingly, as found in observations, the simulations corroborated the idea of BH downsizing. Sijacki et al. (2015) performed a similar study but using the Illustris-100 simulation. In addition to finding a good agreement with both the bolometric and X-ray quasar LFs, Sijacki et al. (2015) reported that the correlation between BH and host galaxy was blurred in low and star-forming galaxies (see also Weinberger et al. 2018). Regarding the BH activity through cosmological time, Rosas-Guevara et al. (2016a) explored the population of inactive BHs in the EAGLE simulation ( $\sim 10^6 \text{ Mpc}^3$ ). While at high- $z$  most of BHs are in an active phase,

at  $z \sim 0$  they were inactive or growing at very low Eddington ratios.

To date, very few works have addressed the evolution of BH spin in hydrodynamical simulations. [Dubois et al. \(2014b\)](#) was one of the first works by including a similar semi-analytical approach to the one of [Fanidakis et al. \(2011\)](#) to track the spin evolution in the outputs of a 50 Mpc box side hydrodynamical simulation. The outcomes displayed that coherent gas accretion is the main driver of growth for BHs of  $10^6 < M_{\text{BH}} < 10^8 M_{\odot}$ , leading a final spin value close to  $a \sim 1$ . At larger masses, the contribution from binary coalescence to the final BH spin becomes significant. [Fiacconi et al. \(2018\)](#) went a big step further, including in the moving-mesh code AREPO ([Springel, 2010](#)) a model to track the BH spin evolution during gas accretion events. Even though [Fiacconi et al. \(2018\)](#) only tested the code in idealized systems of BH and accretion disk, they find interesting results. For instance, the simulations displayed that BHs with mass  $\lesssim 10^7 M_{\odot}$  experienced quick alignment with the accretion disk, favouring prolonged phases of spin-up.

Finally, a significant effort has been devoted to the black hole formation by using numerical simulations. While some works have focused on the direct collapse black holes ([Habouzit et al., 2016](#); [Agarwal et al., 2017](#); [Maio et al., 2019](#)), some others have studied on the Pop III scenario ([Whalen et al., 2013](#); [Smith et al., 2018](#)). The final findings of all these works can be summarized by the conclusions that both the amount of metals in the pristine gas and the number of photons that can dissociate molecular hydrogen play an important role in the formation of a black hole.

## 1.4 The synergy between observations and simulations

Galaxies are bound systems of gas and stars releasing radiation through the whole electromagnetic spectrum, from ultraviolet to infrared. Determining what is the energy emitted by a galaxy per surface area at any wavelength or frequency, hereafter just flux density, consolidates the so-called *spectral energy distribution* (SED). Although the processes shaping the radiation produced by a galaxy can be extremely complex, SEDs are relatively simple displaying only two different components. The first one is known as *galaxy continuum* and is formed by the superposition of the spectra of all the individual stars that consolidate the galaxy. The second part is the *line* component and corresponds to an excess (*emission line*) or defect (*absorption line*) over the continuum caused by bound-bound transitions with atoms, ions and molecules produced in the stellar photosphere and/or in the intergalactic gas. The different contribution of these two components in the SED gives an incredible amount of information about the physical processes that have and are taking place in the cosmological evolution of the galaxy. For instance, the younger is the stellar population, the larger is galaxy continuum at small wavelengths. On the contrary, the older is the population the larger is the continuum flux at large wavelengths. Emission lines give also very valuable information on the star formation process, black hole activity, the abundance of different elements (such as hydrogen, helium or oxygen) or the temperature and ionization state of the interstellar gas.

Two different techniques have been developed to determine the flux density emitted by a galaxy: *spectroscopy* and *photometry*. The former provides the exact flux density received from a galaxy over a wide portion of the electromagnetic spectrum. The latter measures the median flux of an object in a certain wavelength band, constrained by a *filter* which only allows the light to pass with particular transmission. Typically, if the wavelength range covered by the filter (hereafter filter width) is larger than  $\sim 1000 \text{ \AA}$  we speak about broad band filters. On contrary, if the width is smaller we have narrow bands. In [Figure 1.6](#) we present an example of the density flux as a function of wavelength measured from a galaxy at  $z \sim 0.7$  by using the two different techniques. As we can see, spectroscopy provides a much better wavelength resolution than photometry where the flux is averaged over the wavelength range determined by the filter, in this case  $5200 \sim 7000 \text{ \AA}$ . Although spectroscopy appears to be the best technique to extract information about continuum and lines, it still has its limitations. For instance, it

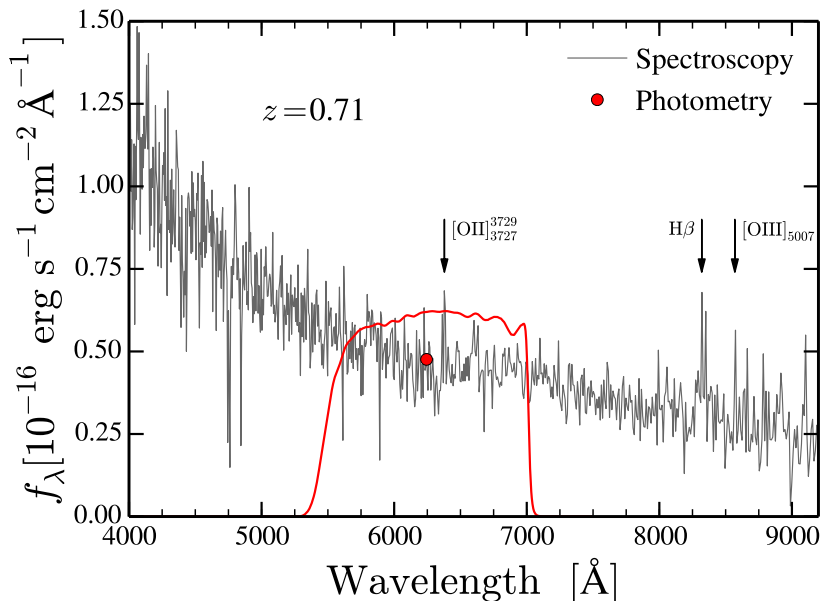


Figure 1.6: Comparison between the data obtained from spectroscopy (grey line) and photometry (red dot) by using a  $z \sim 0.7$  galaxy as an example. As we can see, spectroscopy provides a well sampled galaxy SED where continuum and emission lines ([OII], [OIII] and  $H\beta$ , highlighted with arrows) are more than evident. On the other hand, the photometry is represented by one single dot since the flux is averaged over the wide wavelength range determined by the filter (red line). The spectroscopy data has been extracted from the SDSS survey database and the photometry is obtained by convolving the SDSS spectra with the transmission curve of the SDSS  $r$ -band (red lines).

is time-consuming since requires pointing object by object for the SED extraction. Besides, the target sample needs to be pre-selected, leading to problems of biases and selection functions. The photometric technique, on the other hand, does not have these biases given that one filter pointing obtains photometry data of all the objects within the field of view without previous selection. To overcome the poor wavelength resolution and achieve the large electromagnetic spectrum coverage of spectroscopy, some photometric works have sampled the galaxy SED with many filters. The combination of a large number of narrow and broad filters to trace both continuum and emission lines is a method which can obtain very similar SEDs to those of spectroscopy. This approach is commonly called spectro-photometry and it has been used since the beginnings of 2000 in surveys such as COMBO-17 (Wolf et al., 2003), ALHAMBRA (Moles et al., 2008), MUSYC Cardamone et al. (2010), CLASH (Postman et al., 2012), SHARDS (Pérez-González et al., 2013), J-PAS (Benitez et al., 2014), J-PLUS (Cenarro et al., 2019) or PAU (Párida et al., 2019). As an illustrative example, in Figure 1.7 we present the SED of the same galaxy of Figure 1.6 but traced by the survey J-PAS (synthetic photometry) which consists in a filter system composed by 3 broad bands and 56 narrow bands. As we can see, the spectro-photometry technique retrieves a very similar SED than spectroscopy. Thus, this example can be considered as a visual prove that galaxy continuum and emission features can be perfectly traced by the combination of many filters placed at different wavelengths.

Although the spectro-photometry technique is a potentially powerful approach to obtain similar basic information about galaxies as spectroscopy, developing a methodology to extract such details from the data is not a trivial matter. Indeed, reaching accurate results free of both measurement biases and selection effects requires a detailed understanding of how to handle the data. Simulations can help the scientific community by providing simulated spectro-photometry data to learn how to optimally extract the desired information from multi-bands photometric surveys. Indeed, it was already in the early 2000s



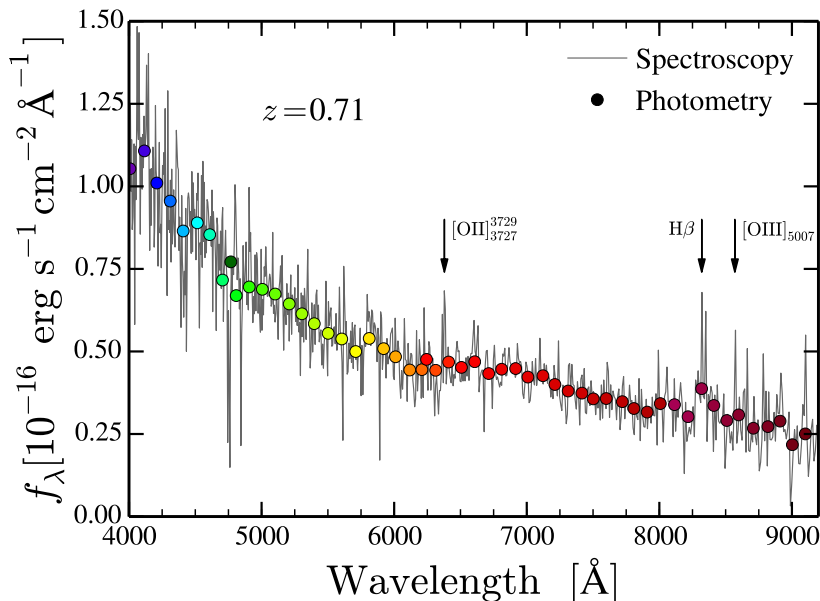


Figure 1.7: Comparison between the density flux,  $f_\lambda$ , obtained from SDSS spectroscopy (grey line) and the J-PAS spectro-photometry (colored dots) by using a  $z \sim 0.7$  galaxy as an example. The J-PAS photometry has been obtained by convolving the SDSS spectroscopic data with the filter transmission curves of J-PAS. As we can see the spectro-photometry provides a SED as good as photometry where the continuum and emission lines can be distinguished. The spectroscopy data has been extracted from the SDSS survey database and the photometry is obtained by convolving the SDSS spectra with the transmission curve of the 59 J-PAS bands.

when the increase in the number of broad bands photometric surveys pushed the scientific community to start integrating into the survey development the construction of simulated catalogues for helping in the data interpretation. These catalogues, called mocks, are not easy to produce as they should include realistic galaxy properties at any redshifts and reproduce the observed galaxy distribution. To fulfil all these requirements, the first mocks of broad bands photometric surveys were made by using semi-analytical models based on merger trees extracted from N-body simulations. To construct artificial observations from the simulated universe of the SAMs, it was necessary to position a virtual observer at  $z = 0$  in one of the box corners and finding those galaxies which lie on the backward lightcone, defined as the space-time region satisfying the condition that light emitted from every point is received by the observer now. However, during the early 2000s the box side-length of the dark matter simulation used by the SAMs were too small to rarely overpass a redshift depth of  $z \sim 0.2$ . This was imposing a strong limit in the cosmological volume that mocks could encompass. To overpass such limitations the works of [Blaizot et al. \(2005\)](#), [Kitzbichler and White \(2007a\)](#) and [Merson et al. \(2013\)](#) developed different techniques to convert the outputs of semi-analytical models into deep lightcones. In short, their methodology consisted in i) replicating the box taking advantage of its periodic nature, ii) interpolating the positions, velocities and physical properties of the galaxies between two discrete snapshots of the SAM and iii) avoiding structure repetitions through a smart definition of the lightcone line-of-sight.

Thanks to the previously mentioned works, SAMs could overpass the box limitations and the discreteness effects due to the limited number of snapshots of the dark matter merger trees. Indeed, nowadays SAMs are still one of the best tool to build mock galaxy lightcones for photometric surveys. However, as we will describe in the next section, they still need to deal with the inclusion of emission lines in the final galaxy photometry, a task which has been addressed by very few works ([Stothen et al., 2018](#); [Izquierdo-Villalba et al., 2019](#)). Finally, because of the large advances in the computational techniques undertaken during the last 5 years, many works have started to deal with the lightcone con-

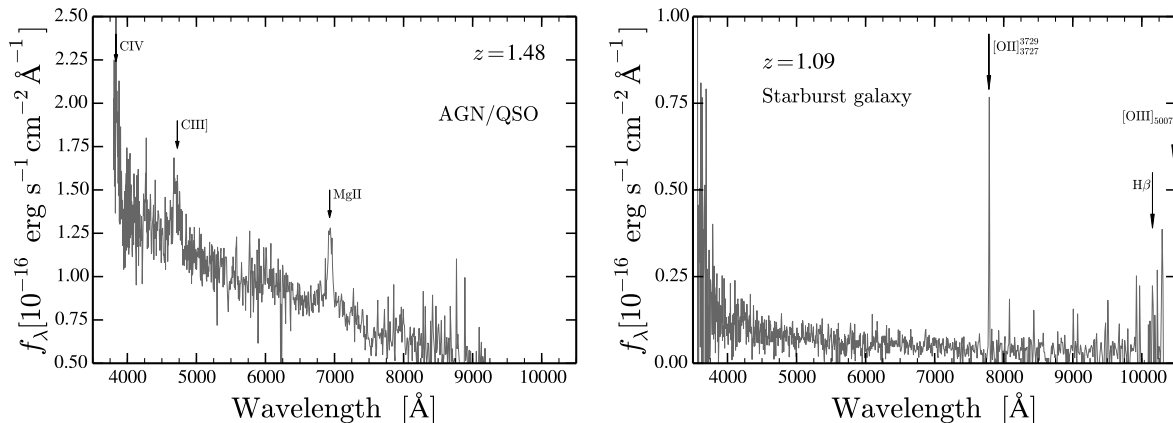


Figure 1.8: **Left panel:** SED of an AGN/QSO at  $z \sim 1.5$ . It has been highlighted the position of CIV, CIII] and MgII lines. **Right panel:** SED of a starburst emission line galaxy at  $z \sim 1$ . It has been highlighted the position of [OII], H $\beta$  and [OIII]<sub>5007</sub> lines. The spectroscopy data of both panels have been extracted from the SDSS survey database.

struction in hydrodynamical simulations. As an illustrative example we can find the Horizon lightcone (see Hatfield et al., 2019).

#### 1.4.1 The new challenge for mock lightcones: emission line galaxies as new targets for surveys

As we discussed before, the presence of emission lines in the galaxy SED is a valuable source of information regarding the fundamental processes taking place within the galaxy. Galaxies exhibiting these emission features are usually called *emission line galaxies* (ELGs) and they are commonly divided into two different types. The first one is formed by the AGNs. As we extensively discussed in Section 1.3.2, AGNs are related to matter accretion onto supermassive black holes. During this process, the accretion disk emit high energy photons able to ionize the surrounding gas, producing excitations and de-excitations of atoms whose outcome is the presence of *broad* and/or *narrow* emission lines in the SED of the galaxy hosting the AGN. Among all the lines we can find in AGNs, the most relevant ones are SiIV (1397Å), CIV (1549Å), CIII] (1908Å) and MgII (2799Å) (see e.g. Chaves-Montero et al., 2017; Spinoso et al., 2020). The other type of ELGs is the one formed by *star forming galaxies* or *starburst galaxies* whose lines are produced through star formation processes. As happens with AGNs, the process of forming new stars generate high energy photons capable to ionize the HII regions around stellar birthplaces, yielding to *narrow* collisional excited lines (Dopita et al., 2003; Peimbert et al., 2017). Of course, the production of these excitation lines depends on many galaxy conditions such as the number of ionization photons (*ionization parameter*) or the amount of metals and dust present in molecular clouds. The most relevant emission lines that we can find in *starburst galaxies* are [OII] (3727Å, 3729Å), H $\beta$  (4861Å), [OIII] (4959Å, 5007Å) and H $\alpha$  (6563Å). As an illustrative example, in Figure 1.8 it is presented the SED of an AGN/QSO and starburst galaxy. As we can see, both of them present strong emission lines along the whole optical range.

Star forming emission line galaxies have sparked the interest of the scientific community for the past 10 years. Despite being less numerous than red and dead galaxies, the position of their emission lines offers an incredible opportunity to determine with high accuracy their redshift distribution and, thus, perform a detailed analysis of the large scale structure of the Universe at different cosmological times (Gunawardhana et al., 2013; Sobral et al., 2009, 2013, 2015; Comparat et al., 2016; Hayashi et al., 2018; Spinoso et al., 2020). For this reason many *next generation surveys* have been developed specifically to detect emission line galaxies. Among these surveys, we can find EUCLID (Laureijs et al., 2011),

WFIRST (Dressler et al., 2012), J-PAS (Benitez et al., 2014; Bonoli et al., 2020) or PAU (Padilla et al., 2019). While the two formers are principally spectroscopic surveys with a special focus on starburst galaxies at  $1 \lesssim z \lesssim 2$ , the two latter are spectro-photometric with a particular interest in both AGNs and star forming galaxies at  $z \lesssim 3$ . To assess the capability of these surveys in detecting starburst ELGs, few mocks have been developed by applying in different SAMs the lightcone construction previously described. Even though SAMs describe pretty well the galaxy continuum, they have a lack of emission line modelling during star formation events. For that reason, the creation of realistic mocks for emission line surveys had pushed SAMs to include some modelling for treating the line production. The most extended methodology has been the one relating the line flux production with the galaxy metallicity, ionization parameter and the star formation rate. By using this approach, Merson et al. (2018) and Zhai et al. (2019) computed the number density of galaxies detected by EUCLID and WFIRST with  $[\text{OIII}]_{5007}$  and  $\text{H}\alpha$  emission features. Interestingly, they reported that the expected number of sources would be large enough to ensure that both surveys could carry out cosmological studies. On the other hand, the works of Stothert et al. (2018) and Izquierdo-Villalba et al. (2019) performed mocks about the effect of the emission lines in the final photometry of the narrow and broad band photometric surveys. Among all the interesting results, we can highlight that Izquierdo-Villalba et al. (2019) showed that extracting unbiased flux measurements from the narrow band galaxy photometry is not an easy task where many effects, such as the continuum shape, have to be taken into account. The works of Merson et al. (2018); Stothert et al. (2018); Izquierdo-Villalba et al. (2019) and Zhai et al. (2019) have opened the path for the development of more sophisticated works and techniques about mocks for emission line surveys.

## 1.5 Objectives and outline of the thesis

As discussed in the introduction, developing an ideal methodology for the construction of mocks for emission line surveys, understanding the formation of different bulge types and exploring the cosmological evolution of the supermassive black hole population are currently hot topics which are going to be addressed in this work. The thesis can be outlined in three main objectives tackled through the usage of a semi-analytical model (SAM). The first objective address the formation and evolution of galactic bulges. In particular, we focus on the pseudobulge population whose cosmological evolution in a  $\Lambda$ CDM Universe has not been fully explored yet. Questions about their formation time, the merger history of their host galaxy or the possible existence of composite bulges are the ones that we want to answer in this thesis. The second objective consists in including in a SAM an advanced model on the spin evolution and the growth of supermassive black holes, able to give useful predictions about the properties of supermassive black holes at different cosmological times. These predictions would be fundamental for the next generation of gravitational wave detectors such as *LISA*. We also study the population of wandering black holes, an elusive type of supermassive black holes whose nature is not well understood yet as a consequence of the challenges in their detection. Finally, the last objective lies in presenting a new technique for the assembly of mock lightcones for the next generation of multi-narrow and -broad band photometric surveys.

The thesis is divided as follows:

- **Chapter 2: L-Galaxies: A model to study galaxy evolution**

In this chapter we describe the semi-analytical model (L-Galaxies) used in this thesis. We briefly describe the dark matter simulation from where the merger trees are extracted and we summarize the main physical processes included in the SAM to deal with the galaxy formation and evolution paradigm.

- **Chapter 3: The assembly of pseudobulges in a hierarchical Universe**

In this chapter we study the cosmological build-up of pseudobulges using the L-Galaxies SAM with a new approach for following separately the assembly of classical bulges and pseudobulges.

We analyse the evolution of the pseudobulge population through cosmological time and we compare their properties with the ones displayed by classical bulges.

- **Chapter 4: Barred galaxies in the local Universe: Revisiting their analytical formation from a hydrodynamical perspective**

In this chapter we study by employing cosmological hydrodynamical simulations the performance of the analytical criterion for bar formation used in *L-Galaxies*. We explore the limitations of the preconception to properly trace the onset and assembly of bar structures.

- **Chapter 5: Spinning black holes and wandering black holes**

In this chapter we study the mass assembly and spin evolution of supermassive black holes (BHs) across cosmic time as well as the impact of gravitational recoil on the population of nuclear and wandering black holes (wBHs) by using *L-Galaxies*. Besides, we study the spins and masses of the population of nuclear black holes hosted by different galactic bulges: ellipticals, classical bulges and pseudobulges.

- **Chapter 6: Mock lightcones for photometric surveys**

In this chapter we present a procedure to generate a synthetic galaxy lightcone especially designed for narrow-band optical photometric surveys. We apply this procedure to a specific survey (J-PLUS) and we study its ability to correctly identify a population of emission line galaxies at various redshifts.

- **Chapter 7: Conclusions**

In this chapter we summarize the main findings of this thesis.

- **Chapter 8: Future work**

In this chapter we give a brief outlook to future work.

## CHAPTER 2

### L-GALAXIES : A MODEL TO STUDY THE GALAXY EVOLUTION

*“Eso desean quienes viven estos tiempos.  
Pero no les toca a ellos decidir. Lo único  
que podemos decidir es qué hacer con el tiempo  
que se nos ha dado. Hay otras fuerzas en este  
mundo, Frodo, además de la voluntad del mal.  
Bilbo estaba destinado a encontrar el Anillo y  
como consecuencia tú estabas destinado a tenerlo.  
Y ese es un pensamiento alentador.”*

El señor de los anillos: La comunidad del anillo.

*“So do all who live to see such times.  
But that is not for them to decide.  
All we have to decide is what to do with  
the time that is given to us. There are other  
forces at work in this world Frodo, besides the  
will of evil. Bilbo was meant to find the Ring.  
In which case, you were also meant to have it.  
And that is an encouraging thought.”*

The Lord of the Rings: The Fellowship of the Ring.

## 2.1 Introduction

In this thesis we make use of L-Galaxies semi-analytical model (SAM) to study the assembly of galactic bulges, the growth of supermassive black holes and the build-up of mock galaxy lightcones for the new generation of narrow band photometric surveys. While for the two former scientific cases we use L-Galaxies in the version of [Henriques et al. \(2015\)](#)<sup>1</sup>, for the latter we use the [Guo et al. \(2011\)](#) one. The aim of the SAM is to simulate the evolution of the galaxy population as a whole in a self-consistent and physically-motivated manner. For this, L-Galaxies includes different physical ingredients such as gas cooling, star formation, AGN/SuperNovae feedback, metal enrichment, black hole growth or galaxy mergers. All these processes are implemented through a system of coupled differential equations solved along the mass assembly history of dark matter objects, given by their respective merger tree.

L-Galaxies SAM is based on the early work of [White and Rees \(1978\)](#) who developed a semiquantitative model to study how galaxies evolve in a hierarchical universe. The basis of the model was that galaxies were formed by the cooling and fragmentation of pristine gas within the potential wells of collapsed dark matter halos whose specific abundance at each redshift was derived from the Press-Schechter formalism ([Press and Schechter, 1974](#)). Galaxies were evolved assuming that all the gas able to cool in less than one halo dynamical time was converted into stars with an efficiency regulated by supernovae feedback. Besides, after one dynamical time, the haloes were assumed to merge while galaxies survive intact. With these assumptions, the semiquantitative model of [White and Rees \(1978\)](#) was able to derive galaxy luminosity functions in agreement with observations. One decade later, [White and Frenk \(1991\)](#) updated this model for the specific case of  $\Lambda$ CDM cosmology by incorporating an extension of the Press-Schechter theory for better treatment of merging haloes in a statistical point of view ([Bower, 1991](#); [Bond et al., 1991](#)). On the baryonic side, refinements in the gas cooling, star formation and stellar feedback and the inclusion of chemical enrichment and the stellar population model of [Bruzual A. \(1983\)](#) were fundamental to improve the predictions. A step further was performed by [Kauffmann et al. \(1993a\)](#), who aiming to study in more details merging galaxies, included in the [White and Frenk \(1991\)](#) semi-analytical model a new Monte Carlo technique of generating merging histories trees for dark matter halos. In such

<sup>1</sup><http://galformod.mpa-garching.mpg.de/public/LGalaxies/>

a way, the model was able to trace the ancestry of an halo structure through all the progenitor halos from which it formed. The inclusion of that technique gave for the first time to the model the capability of providing explanations of galaxy colours and morphologies. Even though the Monte Carlo approach of [Kauffmann et al. \(1993a\)](#) was one of the biggest improvements added in the semi-analytical model, it had the limitation of lacking information about the spatial distribution of galaxies. To overpass this shortcoming, [Kauffmann et al. \(1999a\)](#) grafted in the SAM the merger trees of high-resolution N-body DM simulations. In subsequent papers, the authors used this methodology to make predictions about the evolution of clustering to high redshift ([Kauffmann et al., 1999b](#)), construct realistically mocks for surveys ([Diaferio et al., 1999](#)), study the evolution of the quasar number density trough redshift ([Kauffmann and Haehnelt, 2000](#)) and explore both spatial and kinematic distributions of galaxies within clusters ([Diaferio et al., 2001](#)).

After [Kauffmann et al. \(1999a\)](#) the SAM was always used with the merger trees of DM simulations (see e.g [Springel et al., 2001](#)) with the main objective of refining the treatment of the baryonic physics. In particular, there are five main papers which contributed significantly to the model improvements: [De Lucia et al. \(2004\)](#), [Croton \(2006\)](#), [De Lucia and Blaizot \(2007\)](#), [Guo et al. \(2011\)](#) and [Henriques et al. \(2015\)](#). In [De Lucia et al. \(2004\)](#) it was introduced a model for the transport of metals between the stars, cold gas in galaxies, hot gas in dark matter haloes, and intracluster gas outside virialized haloes. [Croton \(2006\)](#) grafted for the first time the merger trees of Millennium simulation ([Springel, 2005](#)) and extended the black hole growth of [Kauffmann and Haehnelt \(2000\)](#) in order to link the black hole activity with the halt of star formation in massive galaxies. [De Lucia and Blaizot \(2007\)](#) improved the grafting of the Millennium merger trees and performed a new formalism for dust attenuation. [Guo et al. \(2011\)](#) revisited the gas cooling in the SAM, added a model for the computation of galaxy radii, included different environmental processes acting in galaxies, introduced the concept of *orphan* galaxies and grafted the merger trees of Millennium II ([Boylan-Kolchin et al., 2009](#)). Finally, [Henriques et al. \(2015\)](#) revisited both environmental processes and reincorporation times of gas ejected of [Guo et al. \(2011\)](#) and introduced the possibility of calibrating all the SAM free parameters with a Monte Carlo Markov Chain (MCMC) methodology (see [Henriques et al., 2009](#), for more details).

In the following sections we summarize the main assumptions and equations implemented in [Guo et al. \(2011\)](#) and [Henriques et al. \(2015\)](#) versions of L-Galaxies to property follow the formation and evolution of galaxies through cosmological time. In Section 2.2 we present the main properties of the dark matter simulations used by the SAM. In Section 2.3 we briefly describe the whole physical ingredients include in L-Galaxies to properly follow the evolution of the galaxy baryonic content.

## 2.2 Dark matter merger trees

The backbone of L-Galaxies semi-analytical model are the subhalo merger-trees catalogues obtained by the Millennium (hereafter MS, [Springel, 2005](#)) and Millennium II (MSII, [Boylan-Kolchin et al., 2009](#)) N-body simulations. The first one follows the cosmological evolution of  $2160^3$  dark matter (DM) particles with mass  $8.6 \times 10^8 M_\odot/h$  inside a periodic box of  $500 \text{ Mpc}/h$  on a side, from  $z = 127$  to the present. The latter follows the same number of particles but with a 125 times higher particle mass resolution ( $6.885 \times 10^6 M_\odot/h$ ) in a box of  $100 \text{ Mpc}/h$  on a side. Both simulations were run with GADGET code ([Springel et al., 2001](#); [Springel, 2005](#)) by using WMAP1 & 2dFGRS concordance cosmology:  $\Omega_m = 0.25$ ,  $\Omega_b = 0.045$ ,  $\Omega_\Lambda = 0.75$ ,  $h = 0.73 \text{ km s}^{-1} \text{ Mpc}^{-1}$ ,  $n = 1$ ,  $\sigma_8 = 0.9$  ([Colless et al., 2001](#)). Particle data information from the MS and MSII simulations was stored, respectively, at 63 and 68 epochs or *snapshots*. The first 58 and 65 snapshots of MS and MSII were temporally spaced according to:

$$\log_{10}(1 + z_n) = \frac{n(n+35)}{4200} \begin{cases} \text{where } 0 \leq n \leq 58 & \text{for Millennium} \\ \text{where } 0 \leq n \leq 64 & \text{for Millennium II} \end{cases} \quad (2.1)$$

while the four and three remaining MS and MSII snapshots were manually added at  $z = 30, 50, 80, 127$



and  $z = 40, 80, 127$ , respectively.

While dark matter *halos* were found within snapshots by using a friend-of-friend (FOF) group-finder, *subhalos* structures, i.e locally overdense, self-bound particle groups formed inside the DM halos, were identified with SUBFIND algorithm (Springel et al., 2001). Since the latter only considers as subhalos to those substructures with at least 20 self-bound particles, MS and MSII catalogues contain a minimum subhalo mass of  $M_{\text{halo}}^{\text{min}} = 1.72 \times 10^{10} M_{\odot}/h$  and  $M_{\text{halo}}^{\text{min}} = 1.38 \times 10^8 M_{\odot}/h$ , respectively. By using L-HALOTREE code (Springel, 2005) all halos and subhalos were arranged in merger trees structures, allowing to follow the evolutionary path of any DM (sub)halo in the simulations. We highlight that L-Galaxies is based on the subhalo population instead of the halo one. This enables L-Galaxies to build-up a more realistic galaxy population, making more reasonable predictions for galaxy merger rates and clustering. Even though the DM merger trees are the skeleton of L-Galaxies, the finite number of outputs of the DM simulations causes that the time resolution they offer is not enough to properly trace the baryonic physics. Thus, to accurately follow the galaxy evolution between two consecutive DM snapshots, the SAM does an internal time discretization between them with approximately  $\delta t \sim 5\text{--}20$  Myr of time resolution. These extra  $\delta t$  temporal subdivisions used by the SAM are called *sub-steps*.

Finally, the latest L-Galaxies version was tuned on a re-scaled versions of MS and MSII simulations (Henriques et al., 2015). The re-scaling procedure (presented in Angulo and White, 2010) allows the two simulations to match the cosmological parameters provided by Planck first-year data (Planck Collaboration et al., 2014):  $\Omega_{\text{m}} = 0.315$ ,  $\Omega_{\Lambda} = 0.685$ ,  $\Omega_{\text{b}} = 0.0487$ ,  $\sigma_8 = 0.829$  and  $h = 0.673 \text{ km s}^{-1} \text{ Mpc}^{-1}$ . After re-scaling, the particle mass corresponds to  $1.43 \times 10^9 M_{\odot}/h$  and  $7.68 \times 10^6 M_{\odot}/h$  for MS and MSII respectively.

### 2.2.1 Different subhalos and galaxies: Central and satellite

SUBFIND algorithm classifies subhalos in two different categories. While the most massive subhalo in each FOF is referred as *main subhalo*, the rest ones are tagged as *satellites*. This distinction is used by L-Galaxies to do its own galaxy classification. A *central galaxy* (or *type 0*) is referred to the galaxy who sits in the potential minima of a main subhalo. On the other hand, galaxies hosted in *satellite subhalos* are tagged as *satellite galaxies* (or *type 1*). Additionally, L-Galaxies follows satellite galaxies which do no longer correspond to a resolved subhalo (i.e they have already lost their host subhalo) but are not merged with its central galaxy. This type of satellites are called *orphan galaxies* (or *type 2*).

## 2.3 Baryonic physics

L-Galaxies code tracks the time evolution of gas, stars and supermassive black holes (BHs) within their host DM subhalos through a series of differential equations and analytic prescriptions. In the following sections we briefly describe the main equations implemented in the SAM.

### 2.3.1 Gas cooling

In the current understanding of how cosmological structures form, it is accepted that the initial density fluctuations of the early universe act as the birthplaces of dark matter (sub)halos (Press and Schechter, 1974). As soon as gravitational instability triggers the collapse of these density fluctuations, part of the diffuse baryonic matter present in the Universe is attracted and collapsed within them. Following this scenario, the starting point of the galaxy evolution model is the association of a baryonic matter to each new collapsed DM subhalo (i.e, newly-resolved subhalo in the DM N-body simulation). This process is

modelled by assigning an amount of baryons,  $M_{\text{bar}}$ , to each subhalo (see [White and Frenk, 1991](#)):

$$M_{\text{bar}} = f_{\text{bar}} \cdot M_{\text{halo}}. \quad (2.2)$$

where  $M_{\text{halo}}$  is the subhalo virial mass and  $f_{\text{bar}}$  is a value given by the cosmic baryon fraction, determined by the  $\Omega_{\text{b}}/\Omega_{\text{m}}$  ratio. However, this simple scenario needs to be modified since the photo-heating caused by the ultraviolet (UV) background (produced by stars and AGNs) plays an important role in reducing the infalling of baryons onto the dark matter structures ([Doroshkevich et al., 1967](#); [Couchman and Rees, 1986](#)). As pointed out by [Efstathiou \(1992\)](#) this effect is particularly important in low mass halos where the UV background raises enough the thermal energy of the pregalactic gas to make difficult the condensation of gas inside shallow potential wells. To take into account this process, the SAM includes the approach presented in [Gnedin \(2000\)](#) assuming that  $f_{\text{bar}}$  displays a dependence with redshift and subhalo mass:

$$f_{\text{bar}}(z, M_{\text{halo}}) = \frac{\Omega_{\text{b}}/\Omega_{\text{m}}}{\left[1 + (2^{\alpha_{\text{bar}}/3} - 1) \left(\frac{M_{\text{F}}(z)}{M_{\text{halo}}}\right)^{\alpha_{\text{bar}}}\right]}, \quad (2.3)$$

where  $M_{\text{F}}(z)$  is the filtering DM mass below which the baryonic infalling is effectively suppressed. The exact values of  $\alpha_{\text{bar}}$  and  $M_{\text{F}}(z)$  were obtained from the high-resolution cosmological hydrodynamical of [Okamoto et al. \(2008\)](#). While the former is a fix value set to 2, the latter depends on redshift according to tabulated values provided by [Okamoto et al. \(2008\)](#). For instance,  $M_{\text{F}}(z)$  varies from  $6.5 \times 10^9 M_{\odot}$  at  $z \sim 0$  up to  $\sim 10^7 M_{\odot}$  at  $z \sim 8$ .

The baryonic mass after collapsing within the DM subhalo is assumed to form a diffuse, spherical and quasi-static atmosphere of pristine<sup>2</sup> hot gas, with mass  $M_{\text{hot}}$  and radius equal to the subhalo virial radius,  $R_{200}$  ([White and Rees, 1978](#); [Blumenthal et al., 1984](#)). A fraction of this atmosphere is allowed to cool i.e, gradually reduce energy and migrate towards the center of the DM subhalo. Following [White and Rees \(1978\)](#), the gas cooling rate,  $\dot{M}_{\text{cool}}$ , is determined by the amount of hot gas enclosed within the subhalo cooling radius,  $r_{\text{cool}}$ , defined as the radius at which the subhalo dynamical time,  $t_{\text{dyn,h}}$ , equals the cooling time,  $t_{\text{cool}}(r)$  ([De Lucia et al., 2004](#)). The former is defined as  $R_{200}/V_{200} = 0.1H(z)^{-1}$ , where  $V_{200}$  is the subhalo virial velocity. The latter is given by the ratio between the specific thermal energy of the gas and its cooling rate per unit volume ([Springel et al., 2001](#)):

$$t_{\text{cool}} = \frac{3}{2} \frac{\bar{\mu} m_H \kappa T_{200}}{\rho_{\text{hot}}(r) \Lambda(T, Z)}, \quad (2.4)$$

where  $\bar{\mu} m_H$  is the mean particle mass,  $\kappa$  is the Boltzmann constant,  $T_{200} = 35.9 (V_{200}/\text{km s}^{-1})\text{K}$  is the virial temperature of the halo,  $\Lambda(T, Z)$  is the cooling functions ([Sutherland and Dopita, 1993](#)) and  $\rho_{\text{hot}}(r)$  is the hot gas density at a radius  $r$ , assumed to display a simple isothermal model:

$$\rho_{\text{hot}}(r) = \frac{M_{\text{hot}}}{4\pi R_{200}^2 r^2}. \quad (2.5)$$

The exact value of  $r_{\text{cool}}$  implies the presence of two different cooling regimes in the SAM: the *rapid infall* ( $r_{\text{cool}} > R_{200}$ ) which leads to the fast condensation of the whole hot atmosphere:

$$\dot{M}_{\text{cool}} = \frac{M_{\text{hot}}}{t_{\text{dyn,h}}}, \quad (2.6)$$

and the slower *hot phase* ( $r_{\text{cool}} < R_{200}$ ), in which only a fraction of the hot gas is allowed to cool down ([Guo et al., 2011](#)):

$$\dot{M}_{\text{cool}} = \frac{M_{\text{hot}} r_{\text{cool}}}{t_{\text{dyn,h}} R_{200}}. \quad (2.7)$$

---

<sup>2</sup>Meaning with pristine a zero-metallicity gas.



### 2.3.2 Galactic disks: the cold gas and stellar components

After the cooling event, the gas settles into a disk-like structure by inheriting the specific angular momentum of its host DM subhalo (Guo et al., 2011). If the mass of the cold gas disk,  $M_{\text{cold}}$ , is large enough, star formation (SF) episodes are prompted leading to the build up of the stellar disk component,  $M_{\text{disk}}$ . The SAM assumes that at each *sub-step* the star formation rate (SFR or  $\dot{M}_{\text{star}}$ ) in the galactic disk is given by:

$$\dot{M}_{\text{star}} = \alpha_{\text{SF}} \frac{(M_{\text{cold}} - M_{\text{crit}})}{t_{\text{dyn}}^{\text{gas,disk}}}, \quad (2.8)$$

where  $t_{\text{dyn}}^{\text{gas,disk}} = R_{\text{gas}}^{sl} / V_{\text{max}}$  is the cold gas disk dynamical time with  $V_{\text{max}}$  and  $R_{\text{gas}}^{sl}$  the maximum circular velocity of the DM subhalo and the scale length of the cold gas disk (for more details of  $R_{\text{gas}}^{sl}$  see Section 2.3.2). While the parameter  $\alpha_{\text{SF}}$  controls the efficiency of cold gas being transformed into stars,  $M_{\text{crit}}$  imposes a gas mass threshold below which the disk can not trigger the formation of new stars. According to Kauffmann (1996a) and Croton (2006) the value of  $M_{\text{crit}}$  can be approximated as:

$$M_{\text{crit}} = M_{\text{crit},0} \left( \frac{V_{200}}{200 \text{ km/s}} \right) \left( \frac{R_{\text{gas}}^{sl}}{10 \text{ kpc}} \right), \quad (2.9)$$

with  $M_{\text{crit},0}$  a free parameter which controls the normalization of  $M_{\text{crit}}$ .

### Supernovae feedback

From all the stellar mass formed in a given star formation episode,  $\Delta M_{\text{Stars}}$ , the SAM assumes that a fraction of it (set to  $R_{\text{ret}} = 0.43$  according to the initial mass function of Chabrier, 2003) corresponds to massive and short lived stars which explode as supernovae (SNe) immediately after the SF event. This explosions enrich the environment with newly formed heavy elements and inject energy in the cold gas disk able to reheat a fraction of it. This is the so-called *supernovae feedback*. Following the observational results of Martin (1999), the SAM estimates that after the SNe explosions the amount of reheated cold gas and, thus, moved into the hot halo atmosphere is:

$$\Delta M_{\text{reheat}} = \epsilon_{\text{reheat}} \Delta M_{\text{Stars}}, \quad (2.10)$$

where  $\epsilon_{\text{reheat}}$  is approximated to:

$$\epsilon_{\text{reheat}} = \epsilon_1 \left[ 0.5 + \left( \frac{V_{\text{max}}}{V_{\text{reheat}}} \right)^{-\beta_1} \right], \quad (2.11)$$

where  $\epsilon_1$ ,  $V_{\text{reheat}}$  and  $\beta_1$  are three free parameters which describe the efficiency of the SNe and its dependence with the subhalo maximum circular velocity,  $V_{\text{max}}$ . That expression of  $\epsilon_{\text{reheat}}$  was introduced by Guo et al. (2011) with the objective of reproducing the slope of the stellar mass function at low masses.

Besides cold gas reheating, if the energy injected by SNe is large enough, part of the hot gas atmosphere can be expelled from the subhalo in form of *outflows* or *super-winds* and being deposit in the intracluster medium (ICM, see eg. Shapley et al., 2003; Rupke et al., 2005; Martin et al., 2012). The amount of gas ejected is estimated as:

$$\Delta M_{\text{ejected}} = \frac{\Delta E_{\text{SN}} - \frac{1}{2} \Delta M_{\text{reheat}} V_{200}^2}{\frac{1}{2} V_{200}^2}, \quad (2.12)$$

where  $0.5 V_{\text{SN}}^2$  is the mean kinetic energy injected per unit mass of newly formed stars (fixed to 630 km/s as in Croton, 2006) and  $\Delta E_{\text{SN}}$  the total amount of energy injected by the SNe explosion (Croton, 2006):

$$\Delta E_{\text{SN}} = \frac{1}{2} \eta_{\text{halo}} \Delta M_{\text{Stars}} V_{\text{SN}}^2, \quad (2.13)$$

where  $\eta_{\text{halo}}$  has the dependence:

$$\eta_{\text{halo}} = \eta_1 \left[ 0.5 + \left( \frac{V_{\text{max}}}{V_{\text{eject}}} \right)^{-\beta_2} \right], \quad (2.14)$$

where  $\eta_1$ ,  $V_{\text{eject}}$  and  $\beta_2$  are three free parameters. As in the case of  $\epsilon_{\text{reheat}}$ , the parametric form of  $\eta_{\text{halo}}$  displays a dependence with the maximum circular velocity of the halo to reproduce both the low-mass end of the stellar mass function and the galaxy gas-stellar ratio (we refer to Guo et al., 2011, for further discussion). The total hot gas mass expelled during the SNe events,  $M_{\text{ejected}}$ , is stored in a reservoir around the subhalo. This mass is allowed to be reincorporated at latter times into the hot gas atmosphere and being available again for cooling onto the galactic disk. The SAM estimates that the rate of reincorporation,  $\dot{M}_{\text{ejected}}$ , is:

$$\dot{M}_{\text{ejected}} = \frac{M_{\text{ejected}}}{t_{\text{reinc}}}, \quad (2.15)$$

where  $t_{\text{reinc}}$  is the reincorporation time scale. L-Galaxies assumes that  $t_{\text{reinc}}$  scales directly with the host halo mass and does not depend on redshift:

$$t_{\text{reinc}} = -\gamma_r \left( \frac{M_{\text{halo}}}{10^{10} M_{\odot}} \right)^{-1}, \quad (2.16)$$

where  $\gamma_r$  is a free parameter. This dependence is supported by the cosmological hydrodynamical simulations of Oppenheimer and Davé (2008) and Oppenheimer et al. (2010) which pointed out that the recycling time of ejected material is shorter in higher-mass systems. This mass dependence is able to solve the SAM issue of forming too early ( $z > 2$ ) low-mass galaxies ( $10^8 \leq M_{\text{Stellar}} < 10^{9.5}$ ) and hence being too passive at later times (see Henriques et al., 2013)

## Metal enrichment

Stars produce heavy elements (or just *metals*) through nuclear fusion process. After their death, these elements are released in the interstellar medium. L-Galaxies follows this scenario assuming that after supernovae explosions all the metals produced in the stars are mixed instantaneously into the cold gas disk of the galaxy. Particularly, the metal enrichment model of L-Galaxies assumes a 100 per cent mixing efficiency and a mass  $y$  (free value) of heavy elements produced by each solar mass exploded. Although metals are deposited in the cold gas disk, they can be exchanged between the different gas components of the galaxy as a consequence of the supernovae feedback. For instance, during the re-heating process, some part of the metals are added in the galaxy hot gas atmosphere. A similar process can take place during the gas ejection, where part of metals can be expelled from the subhalo. We highlight that during the cooling process, a fraction of the metals in the hot gas atmosphere is also settled onto the galaxy cold disk. For further details, we refer the reader to De Lucia et al. (2004).

## Disk size

L-Galaxies includes a realistic disk model which distinguishes between cold gas and stellar disk radii. In particular, the model assumes that both disks are in centrifugal equilibrium with an exponential surface mass density profile:

$$\Sigma^{\text{gas}}(R) = \Sigma_0^{\text{gas}} e^{-R/R_{\text{gas}}^{\text{sl}}}, \quad (2.17)$$

$$\Sigma^{\text{disk},\star}(R) = \Sigma_0^{\text{disk},\star} e^{-R/R_{\star}^{\text{sl}}}, \quad (2.18)$$

where the variables  $R_{\star}^{\text{sl}}$  and  $R_{\text{gas}}^{\text{sl}}$  are the scale lengths of the stellar and gas disks and  $\Sigma_0^{\text{star}} = M_{\text{disk}}/2\pi R_{\text{star}}^{\text{sl}}$ ,  $\Sigma_0^{\text{gas}} = M_{\text{cold}}/2\pi R_{\text{gas}}^{\text{sl}}$  their central surface densities. By assuming a flat circular velocity curve, the disk scale lengths are determined by L-Galaxies as:

$$R_{\text{gas}}^{\text{sl}} = \frac{|J_{\text{gas}}^{\text{Total}}|/M_{\text{cold}}}{2V_{\text{max}}}, \quad (2.19)$$

$$R_{\star}^{sl} = \frac{|J_{\star}^{\text{Total}}|/M_{\text{disk}}}{2V_{\text{max}}}, \quad (2.20)$$

where  $J_{\text{gas}}^{\text{Total}}$  and  $J_{\text{star}}^{\text{Total}}$  are respectively the stellar and cold gas angular momentum. Given that galaxies are not static objects, both internal and external processes taking place in the galaxy evolution induce modifications on the  $J_{\text{gas}}^{\text{Total}}$  and  $J_{\text{star}}^{\text{Total}}$  values, leading to the change of the galactic disks.

As presented in Guo et al. (2011), the variation of  $J_{\text{gas}}^{\text{Total}}$  can be written as:

$$\delta J_{\text{gas}}^{\text{Total}} = \delta J_{\text{gas,cooling}} + \delta J_{\text{gas,SF}} + \delta J_{\text{gas,merger}}, \quad (2.21)$$

where the three components on the right-hand side are the *variation* of the cold gas disk angular momentum induced by gas cooling ( $\delta J_{\text{gas,cooling}}$ ), star formation ( $\delta J_{\text{gas,SF}}$ ) and galaxy mergers ( $\delta J_{\text{gas,merger}}$ ). Presuming that the newly cooled gas carries the same specific angular momentum of the hosting subhalo ( $J_{\text{DM}}/M_{\text{halo}}$ ), the change due to cooling can be parametrized as:

$$\delta J_{\text{gas,cooling}} = \dot{M}_{\text{cool}} \frac{J_{\text{DM}}}{M_{\text{halo}}} \delta t, \quad (2.22)$$

where  $\dot{M}_{\text{cool}}$  is the cooling rate and  $\delta t$  is the time of the *sub-step* in which the gas is cooled. Regarding the merger events, the model assumes that the cold gas of the satellite galaxy ( $M_{\text{cold}}^{\text{sat}}$ ) is settled into the disk of the central one carrying the same specific angular momentum of the hosting subhalo. Thus, the corresponding change is:

$$\delta J_{\text{gas,merger}} = M_{\text{cold}}^{\text{sat}} \frac{J_{\text{DM}}}{M_{\text{halo}}}, \quad (2.23)$$

During star formation episodes, the cold disk angular momentum undergoes modifications a consequence of gas being transformed into long lived stars ( $(1 - R_{\text{ret}}) \dot{M}_{\text{star}}$ ) and being reheated/ejected through supernovae feedback ( $\Delta M_{\text{reheat}}$ ):

$$\delta J_{\text{gas,SF}} = - \frac{J_{\text{gas}}}{M_{\text{cold}}} \left[ (1 - R_{\text{ret}}) \dot{M}_{\text{star}} \delta t + \Delta M_{\text{reheat}} \right], \quad (2.24)$$

where it has been assumed that the newly formed stars carry the same specific angular momentum of the gas ( $J_{\text{gas}}/M_{\text{cold}}$ ).

Finally, an analogous relation can be written for the variation of the *stellar* disk angular momentum but with the simplified assumption that star formation events are the only ones able to modify  $J_{\text{star}}^{\text{Total}}$ :

$$\delta J_{\text{star}}^{\text{Total}} = \delta J_{\text{star,SF}} = \dot{M}_{\text{star}} \frac{J_{\text{gas}}}{M_{\text{cold}}} \delta t. \quad (2.25)$$

### 2.3.3 Galactic bulges

Regarding the bulge component, galaxies are allowed to develop/grow a dense pack of stars in the nuclear region via mergers and disk instabilities (DI). While the former is a natural consequence of the hierarchical growth of the DM subhalos, the latter plays a crucial role in galaxies in isolation and closely related to star formation. Here we briefly describe the main aspects that L-Galaxies includes to build-up bulges. In Chapter 3 we will investigate in more detail how these two processes ultimately lead to the formation of different types of galactic bulges.

In the hierarchical model of structure formation, dark matter subhalos grow through DM accretion (such as dark matter stripping of satellite subhalos) and repeated mergers with other subhalos (Salvador-Solé et al., 1998; Kauffmann et al., 1999a; Stewart et al., 2009; Genel et al., 2010). This growth of DM structures causes that galaxies also merge and interact. In L-Galaxies, galaxy encounters follow the

merger of the two parent subhalos on a time-scale,  $t_{\text{friction}}$ , given by the dynamical friction presented in [Binney and Tremaine \(1987\)](#):

$$t_{\text{friction}} = \alpha_{\text{fric}} \frac{V_{200} r_{\text{sat}}^2}{GM_{\text{sat}} \ln \Lambda}, \quad (2.26)$$

where  $\alpha_{\text{fric}}$  is free parameter introduced by [De Lucia and Blaizot \(2007\)](#) in order to reproduce the bright end of the  $z=0$  luminosity functions.  $M_{\text{sat}}$  is the total mass of the satellite galaxy (dark matter and baryonic),  $\ln \Lambda = \ln(1 + M_{200}/M_{\text{sat}})$  the Coulomb logarithm and  $r_{\text{sat}}$  is the separation between the central and satellite galaxy at the moment when the latter loses its host subhalo. According to the baryonic (gas and stars) mass ratio,  $m_{\text{R}}$ , of the two involved galaxies the model distinguish between two types of galaxy interactions: *major* and *minor*. When  $m_{\text{R}} > m_{\text{R}}^{\text{th}}$  a major merger takes place, otherwise is a minor. After a major merger the disks of both galaxies are completely destroyed and the remnant galaxy is a pure spheroidal. In minor merger, instead, the remnant retains the stellar disk of the large progenitor and its bulge gains only the stars from the smaller progenitor. In both mergers types, the descendant galaxy undergoes a star formation process, know as *collisional starburst*, which lead the formation of an amount of new stars given by ([Somerville et al., 2001](#)):

$$M_{\text{star}}^{\text{burst}} = \alpha_{\text{SF}}^{\text{burst}} m_{\text{R}}^{\beta_{\text{SF}}^{\text{burst}}} M_{\text{cold}}, \quad (2.27)$$

where  $\alpha_{\text{SF}}^{\text{burst}}$  and  $\beta_{\text{SF}}^{\text{burst}}$  are two free parameters. The supernova process during the collisional starbursts is the same as the secular star formation.

Concerning the galaxy secular evolution, the code takes into account the disk instabilities (DIs) to lead the formation of galactic bulges. In this context, DIs refers to the process by which the stellar disk becomes massive enough to be prone to non-axisymmetric instabilities which ultimately lead to the formation of a central ellipsoidal component ([Combes and Sanders, 1981b](#); [Pfenniger and Norman, 1990](#); [Athanassoula, 2005](#)). The criterion used for modelling the disk instabilities is an analytic stability test based on [Efstathiou et al. \(1982\)](#):

$$\frac{V_{\text{max}}}{(GM_{\text{disk}}/R_{\star}^{\text{sl}})^{1/2}} \leq \epsilon^{\text{DI}}, \quad (2.28)$$

where  $R_{\star}^{\text{sl}}$  and  $M_{\text{disk}}$  are the scale-length and the mass of the stellar disk and  $\epsilon^{\text{DI}}$  is the parameter which measures the self-gravity of the disk. When the instability criterion is met, the code transfers the sufficient stellar mass from the disk,  $\Delta M_{\text{stars}}^{\text{DI}}$ , to the bulge to make the disk marginally stable again:

$$\Delta M_{\text{stars}}^{\text{DI}} = M_{\text{disk}} - \left( \frac{V_{\text{max}}^2 R_{\star}^{\text{sl}}}{G \epsilon_{\text{DI}}^2} \right). \quad (2.29)$$

### Bulge size after a merger

As we have discussed previously, during both major and minor mergers the bulge component of the remnant galaxy grows in mass and changes its size. In order to determine the latter, L-Galaxies assumes energy conservation:

$$E_{\text{f}} = E_{\text{ini}}, \quad (2.30)$$

where  $E_{\text{f}}$  and  $E_{\text{ini}}$  are the final and initial energy of the system, respectively. Following [Covington et al. \(2008\)](#),  $E_{\text{f}}$  is assumed to be the gravitational self-binding energy of the remnant bulge, defined as:

$$E_{\text{f}} = C \frac{GM_{\text{rem}}^2}{R_{\text{rem}}}, \quad (2.31)$$

where  $G$  is the gravitational constant,  $C$  is a structural parameter with takes into account details of how matter is distributed inside the system and  $M_{\text{rem}}$  and  $R_{\text{rem}}$  are the total mass and half-mass radius of the remnant bulge, respectively. As pointed out by [Guo et al. \(2011\)](#) the value of  $C$  varies from 0.49 in an

exponential disk to 0.45 in a  $r^{1/4}$  bulge profile. For simplicity the SAM assumes  $C = 0.5$ .

On the other hand, the initial energy is determined by the sum of the self-binding energy of the two initial systems ( $E_0^i$  with  $i = 1, 2$ ) and the orbital energy at merger ( $E_{\text{orbital}}$ ):

$$E_{\text{ini}} = C \sum_{i=1}^{i=2} E_0^i + E_{\text{orbital}} = C \sum_{i=1}^{i=2} \frac{GM_{P_i}^2}{R_{P_i}} + f_{\text{orb}} \frac{G M_{P_1} M_{P_2}}{R_{P_1} + R_{P_2}}, \quad (2.32)$$

where  $f_{\text{orb}}$  is a coefficient which quantify the interaction energy deposited in the bulge and  $M_{P_i}$  and  $R_{P_i}$  the mass and the half mass radius of the  $i$  progenitor involved in the bulge formation. Guo et al. (2011) set  $f_{\text{orb}} = 0.5$  motivated by the recent results of Boylan-Kolchin et al. (2005). In the case of *major* mergers, the values of  $M_{P_1}$  and  $M_{P_2}$  are the sum of stars and cold gas converted into stars during the collisional starburst (see Eq 2.27) of the two merging galaxies.  $R_{P_1}$  and  $R_{P_2}$  correspond to their respective half mass radii. For *minor* mergers,  $M_{P_1}$  and  $R_{P_1}$  are the mass and half-mas radii of the central galaxy bulge, and  $M_{P_2}$  and  $R_{P_2}$  are the satellite total stellar mass (bulge and disk) and its half-mass radii.

### Bulge size after a DI

The change of bulge size during disk instability events is also modelled by L-Galaxies. As discussed in Section 2.3.3, when a DI episode takes places at  $t^{\text{DI}}$ , an amount of disk mass  $\Delta M_{\text{stars}}^{\text{DI}}$  is transferred to the bulge. In the case in which the galaxy does not host any bulge before the DI episode, the half mass radius of the newly formed bulge,  $R_{\text{rem}}$ , is determined after solving:

$$\Delta M_{\text{stars}}^{\text{DI}} = 2\pi \Sigma_0^{\text{star}} R_{\star}^{\text{sl}} \left[ R_{\star}^{\text{sl}} - (R_{\text{rem}} + R_{\star}^{\text{sl}}) e^{-R_{\text{rem}}/R_{\star}^{\text{sl}}} \right], \quad (2.33)$$

where  $\Sigma_0^{\text{star}}$  is the galaxy stellar disk surface density (see Eq.2.18) and  $R_{\star}^{\text{sl}}$  its scale length (see Eq.2.19). In the case of a pre-existing bulge (with mass  $M_{\text{Bulge}}(t_{\text{DI}})$  and half mass radius  $R_{\text{Bulge}}(t_{\text{DI}})$ ) the model assumes that the instability generates a new bulge with half mass radius  $R_{\text{bulge}}^{\text{DI}}$  (given by Eq. 2.33) which instantaneously coalesces with the pre-existing one in the same way as explained during galaxy mergers. In this particular case in the values are  $M_{P_1} = M_{\text{Bulge}}(t_{\text{DI}})$ ,  $R_{P_1} = R_{\text{Bulge}}(t_{\text{DI}})$ ,  $M_{P_2} = \Delta M_{\text{stars}}^{\text{DI}}$ ,  $R_{P_2} = R_{\text{bulge}}^{\text{DI}}$ ,  $C = 0.5$  and  $f_{\text{orb}} = 2^3$ .

### 2.3.4 Supermassive black holes and AGN feedback

During the last decades, observational works have confirmed the existence of supermassive black holes (BHs) at the center of most massive galaxies (Soltan, 1982; Haehnelt and Rees, 1993; Faber, 1999; Häring and Rix, 2004b; Kormendy and Ho, 2013; Savorgnan et al., 2016). Following these works, L-Galaxies includes in the centre of *all* galaxies a BH with an initial mass of  $10^{-7} M_{\odot}/h$ . This seed BH is allowed to grow in mass through two different channels: coalescences with other BHs right after a galaxy merger and gas accretion. Regarding the latter, the model divides the BH growth into two different modes. The first one is called *quasar* mode and it is related with the consumption of cold gas from the galactic disk right after a galaxy-galaxy encounter. The second one is referred to as *radio* mode and is linked with the hot gas accretion onto the central black hole.

#### Quasar mode

Simulations have shown that gravitational torques during galaxy mergers are able to drive cold gas towards the galaxy inner regions, triggering the black hole accretion (Di Matteo et al., 2005; Springel,

<sup>3</sup>The value of  $f_{\text{orb}}$  is set to 2 in order to account for the fact that the inner disk and the initial bulge are concentric without relative motion, see Guo et al. (2011).

2005; Hopkins et al., 2009a). Following these results, the model assumes that whenever two galaxies in the SAM merge, a fraction of the galaxy cold gas,  $\Delta M_{\text{BH}}^{\text{gas}}$ , is accreted onto the central BH (Kauffmann and Haehnelt, 2000; Croton, 2006):

$$\Delta M_{\text{BH}}^{\text{gas}} = f_{\text{BH}} \frac{m_{\text{R}}}{1 + (V_{\text{BH}}/V_{200c})^2} M_{\text{gas}}, \quad (2.34)$$

where  $m_{\text{R}} < 1$  is the galaxy baryonic merger ratio,  $V_{200c}$  is the virial velocity of the host DM halo, and  $V_{\text{BH}}$  and  $f_{\text{BH}}^{\text{merger}}$  two free parameters. During this quasar mode, the BH consumes instantaneously the whole  $\Delta M_{\text{BH}}^{\text{gas}}$  mass.

### Radio mode

The radio mode is the result of hot gas accretion onto the central supermassive black hole from the diffuse hot gas atmosphere that surrounds its host galaxy (see Section 2.3.1). Following Henriques et al. (2015) (see also Croton 2006) the BH mass accretion rate during this phase is:

$$\dot{M}_{\text{BH}} = k_{\text{AGN}} \left( \frac{M_{\text{hot}}}{10^{11} M_{\odot}} \right) \left( \frac{M_{\text{BH}}}{10^8 M_{\odot}} \right), \quad (2.35)$$

where  $M_{\text{hot}}$  is the total mass of galaxy hot gas atmosphere,  $M_{\text{BH}}$  is the mass of the central supermassive black hole and  $k_{\text{AGN}}$  is a free parameter tuned to reproduce the turnover at the bright end of the galaxy luminosity function. To regulate the increase of the stellar component in massive galaxies, the SAM relates the growth of the BH during the radio mode with the halting of the galaxy star formation. This is the so-called *AGN radio mode feedback*. The approach implemented in L-Galaxies to include the AGN feedback is modifying the galaxy cooling rate according to (see Croton, 2006):

$$\dot{M}_{\text{cool}} = \dot{M}_{\text{cool}} - 2 \frac{L_{\text{radio}}}{V_{200}^2} \quad (2.36)$$

where  $L_{\text{radio}}$  is the mechanical heating generated by the black hole accretion:

$$L_{\text{radio}} = \epsilon \dot{M}_{\text{BH}} c^2, \quad (2.37)$$

where  $\epsilon$  is the BH radiative efficiency, (for simplicity taken to be 0.1),  $c$  the speed of light and  $\dot{M}_{\text{BH}}$  the accretion onto the BH due to radio mode.

### 2.3.5 Environmental processes

When satellite galaxies orbit within dark matter halos, they are promoted to undergo both tidal and hydrodynamical forces generated by other galaxies and the hot gas through which they move. The effects of such forces are known as *environmental processes*. The role played by these processes in the galaxy evolution has been extensively studied during the last three decades. For instance, Dressler (1980) found out a correlation between the galaxy morphology and the local density in which the galaxy resides. Bernardi et al. (1998) showed that field elliptical galaxies display a younger stellar population than those in clusters. Similar results were found by the more recent paper of Cooper et al. (2010) which concluded that at fixed stellar mass, galaxies in higher density regions were formed earlier. Other correlations between environment and galaxy colour, morphology and star formation rate can be found in the works of Postman and Geller (1984), Skibba and Sheth (2009), Grützbauch et al. (2011) and Davidzon et al. (2016) (among many others). Regarding the importance of environmental processes in the evolution of galaxies, L-Galaxies includes both *ram pressure* and *galaxy tidal disruption*.



### Stripping the hot gas

When a subhalo falls into a large system, its mass growth is halt since *tidal forces* start to remove dark matter particles<sup>4</sup>. Following the assumption that the distribution of hot gas in a subhalo follows perfectly the one of the dark matter, L-Galaxies presumes that the tidal interaction acts identically on both hot gas and dark matter component at each position. In this way, the hot gas mass content inside the subhalo is reduced proportionally to the dark matter lose<sup>5</sup>:

$$\frac{M_{\text{hot}}}{M_{\text{hot,infall}}} = \frac{M_{\text{halo}}}{M_{\text{halo,infall}}}, \quad (2.38)$$

where  $M_{\text{hot,infall}}$  and  $M_{\text{DM,infall}}$  are the hot gas and subhalo mass just prior to the infall i.e, the last moment when the associated central galaxy was a type 0. On the other hand,  $M_{\text{hot}}$  and  $M_{\text{halo}}$  are the current masses of these two components. After each tidal interaction, the new radius of the hot gas atmosphere,  $R_{\text{hot}}$ , is recomputed by using the relation:

$$R_{\text{hot}} = \left( \frac{M_{\text{halo}}}{M_{\text{halo,infall}}} \right) R_{200}^{\text{infall}}, \quad (2.39)$$

where  $R_{200}^{\text{infall}}$  is the virial radius of the subhalo just before it became satellite. Notice that, by construction, the tidal stripping in L-Galaxies removes all the hot gas once the galaxy becomes a type 2, i.e its associated DM subhalo is not resolved any more by the underlying DM merger tree.

In addition to tidal forces, the hot gas surrounding the satellite galaxy can be also stripped away by *ram pressure forces* as a consequence of the satellite motion through the intracluster medium. This effect is only considered by L-Galaxies when the satellite subhalo falls within the  $R_{200}$  of its main subhalo. The distance  $R_{\text{press}}^{\text{ram}}$  from the central galaxy *below* which the hot gas of the satellite galaxy is completely stripped away is determined by solving the balance relation between galaxy self-gravity and ram pressure:

$$\rho_{\text{satellite}}(R_{\text{press}}^{\text{ram}}) V_{\text{sat}}^2 = \rho_{\text{par}}(R) V_{\text{orbit}}^2, \quad (2.40)$$

where  $\rho_{\text{satellite}}(R_{\text{press}}^{\text{ram}})$  and  $\rho_{\text{par}}(R)$  are, respectively, the hot gas density of the satellite subhalo at a radius  $R_{\text{press}}^{\text{ram}}$  and the hot gas density of the parent dark matter halo at a distance  $R$  from the centre of its potential wells. The densities are estimated assuming a simple isothermal profile. Regarding the velocities,  $V_{\text{sat}}$  is the  $V_{200}$  of the satellite subhalo at the moment of the infall and  $V_{\text{orbit}}$  the orbital velocity of the satellite, taken to be the virial circular velocity of the main subhalo. Finally, to obtain a good match between SAM predictions and the observed fraction of quenched satellite galaxies, the model includes the free parameter,  $M_{\text{halo,ram}}^{\text{th}}$ , which sets a minimum subhalo mass below which no ram pressure stripping is considered.

### Galaxy tidal disruption

L-Galaxies includes the stripping of stellar and cold gas via *tidal disruption*. In this case, since both components are more concentrated than the dark matter halos, the SAM only considers disruptions events when galaxies have already lost their dark matter halos and hot gas component, i.e they have become a type 2. The code determines that a galaxy undergoes a disruption process when the baryonic density within the half mass radii of the satellite galaxy,  $\rho_{\text{satellite}}(R_{\text{satellite,half}})$ , is smaller than the dark matter density of the host halo at the pericenter of the satellite orbit,  $\rho_{\text{halo}}(R_{\text{peri}})$ :

$$\rho_{\text{halo}}(R_{\text{peri}}) \equiv \frac{M_{\text{halo}}(R_{\text{peri}})}{R_{\text{peri}}^3} > \frac{M_{\text{satellite}}}{R_{\text{satellite,half}}^3} \equiv \rho_{\text{satellite}}, \quad (2.41)$$

where  $R_{\text{satellite,half}}^{\text{half}}$  is the satellite galaxy half mass radii,  $M_{\text{satellite}}$  is the total satellite baryonic mass,  $R_{\text{peri}}$  is the pericenter of the satellite galaxy orbit and  $M_{\text{halo}}(R_{\text{peri}})$  the total dark matter mass of the host dark

<sup>4</sup>In L-Galaxies this means that the subhalo changes from main to satellite subhalo (see Section 2.2.1)

<sup>5</sup>This dark matter lose is followed by the original dark matter simulation.

matter halo inside  $R_{\text{peri}}$ . The value of  $R_{\text{peri}}$  is computed assuming both conservation of energy and angular momentum and a singular isothermal profile for the orbit <sup>6</sup>:

$$\left(\frac{R}{R_{\text{peri}}}\right)^2 = \frac{\ln(R/R_{\text{peri}}) + 0.5(V/V_{200})^2}{0.5(V_t/V_{200})^2}, \quad (2.42)$$

where  $V$  and  $V_t$  is the total and tangential velocity of the satellite with respect to the halo center. As soon as the satellite galaxy is disrupted, its star component is added to the intracluster medium of the hosting subhalo. On the other hand, the cold gas is included in the hot gas atmosphere of the central galaxy.

### 2.3.6 Stellar population synthesis: The broad band photometry

Besides stellar mass, gas content or metallicity, L-Galaxies computes broad band photometry which can be more directly compared with observations. For that, the SAM uses stellar population synthesis models combined with a dust-reddening. In short, stellar population synthesis models predict the luminosity emitted by a single star formation event (usually called *Simple Stellar Population* or SSP) of a given metallicity and initial mass function (IMF). L-Galaxies employs these models to produce tabulated grids of the observed luminosity in a given filter system generated by a SSP of fixed mass as a function of the stellar age and metallicity. During each episode of star formation, L-Galaxies saves the mass of the newly formed stars, their formation time and metallicity, being this latter the same as the cold gas disk metallicity. In case various star formation events take place at the same time, L-Galaxies recomputes the mass and metallicity saved at that moment by performing a mass-weighted average between the previous and current star formation episode. The galaxy photometry at each snapshot of DM simulation is calculated by using the tabulated grids of L-Galaxies which determines the exact observed luminosity of each star formation event performing a linear interpolation in stellar age and metallicity. The age of a given star formation episode is computed as the difference between their formation time and the current age of the galaxy in the snapshot. We highlight that before producing the photometry, L-Galaxies reprocess the luminosity of the stellar emission through a dust model (see Section 2.3.7) to take into account dust-reddening. Concerning this thesis, Guo et al. (2011) model uses the Bruzual and Charlot (2003) synthesis model with the Chabrier (2003) initial mass function (IMF). On the other hand, Henriques et al. (2015) model uses the Maraston (2005) synthesis model with the Chabrier (2003) IMF.

### 2.3.7 Dust model

The luminosity generated by each star formation event is modified according to the dust content of the galaxy. The modelling of dust attenuation was introduced in L-Galaxies by De Lucia and Blaizot (2007). It assumes that the dust extinction is caused by the *molecular clouds* (BC) where the stars are formed and the diffuse *interstellar medium* (ISM). The value of the optical depth in the ISM,  $\tau_{\lambda}^{\text{ISM}}$ , is assumed to vary as

$$\tau_{\lambda}^{\text{ISM}} = (1+z)^{-1} \left(\frac{A_{\lambda}}{A_V}\right)_{Z_{\odot}} \left(\frac{Z_{\text{gas}}}{Z_{\odot}}\right)^s \left(\frac{\langle N_{\text{H}} \rangle}{2.1 \times 10^{21} \text{ atoms/cm}^2}\right), \quad (2.43)$$

where  $s = 1.35$  for  $\lambda < 2000 \text{ \AA}$ ,  $s = 1.6$  for  $\lambda > 2000 \text{ \AA}$  and  $\langle N_{\text{H}} \rangle$  is the mean column density of hydrogen, computed as:

$$\langle N_{\text{H}} \rangle = \frac{M_{\text{cold}}}{1.4 m_{\text{p}} \pi (a R_{\text{gas}}^{\text{sl}})^2} \text{ atoms/cm}^2, \quad (2.44)$$

where 1.4 accounts for the helium presence,  $R_{\text{gas}}^{\text{sl}}$  is the cold gas disk scale length and  $a$  is set to 1.6 in order to make  $\langle N_{\text{H}} \rangle$  represent the mass-weighted average column density of an exponential disk.

---

<sup>6</sup> $\Phi(R) = V_{200}^2 \ln(R)$



On the other hand, the value of the optical depth in the molecular birth clouds,  $\tau_\lambda^{\text{BC}}$ , is assumed to follow the expression:

$$\tau_\lambda^{\text{BC}} = \tau_\lambda^{\text{ISM}} \left( \frac{1}{\mu} - 1 \right) \left( \frac{\lambda}{5500\text{\AA}} \right)^{-0.7}, \quad (2.45)$$

where  $\mu$  is drawn randomly from a Gaussian distribution with mean 0.3 and standard deviation 0.2, truncated at values 0.1 and 1.

Finally, the total absorption coefficient is given by:

$$A_\lambda = -2.5 \log_{10} \left( \frac{1 - e^{-\tau_\lambda^{\text{ISM}} \sec \theta}}{\tau_\lambda^{\text{ISM}} \sec \theta} \right) - 2.5 \log_{10} (e^{-\tau_\lambda^{\text{BC}}}), \quad (2.46)$$

where  $\theta$  is the angle of inclination of the galaxy relative to light-of-sight.

### 2.3.8 Free parameters in L-Galaxies

In this section we present the Table 2.1 where we list the values of the free parameters used by L-Galaxies in the Guo et al. (2011) and Henriques et al. (2015) version.

Parameter	Equation	Model version		Units
		Guo et al. (2011)	Henriques et al. (2015)	
$\alpha_{\text{SF}}$	2.8	0.02	0.025	-
$M_{\text{crit},0}$	2.9	$3.8 \times 10^9$	$2.4 \times 10^9$	$M_\odot/h$
$\epsilon_1$	2.11	6.5	2.6	-
$V_{\text{reheat}}$	2.11	70	480	km/s
$\beta_1$	2.11	3.5	0.72	-
$\eta_1$	2.14	0.32	0.62	-
$V_{\text{eject}}$	2.14	70	100	km/s
$\beta_2$	2.14	3.5	0.80	-
$\gamma_{\text{r}}$	2.16	-	$3 \times 10^{10}$	yr
$\alpha_{\text{firc}}$	2.26	2.34	2.5	-
$\alpha_{\text{SF}}^{\text{burst}}$	2.27	0.56	0.60	-
$\beta_{\text{SF}}^{\text{burst}}$	2.27	0.7	1.9	-
$\epsilon_{\text{DI}}$	2.28	1.0	1.0	-
$f_{\text{BH}}$	2.34	0.03	0.041	-
$V_{\text{BH}}$	2.34	280	750	km/s
$k_{\text{AGN}}$	2.35	-	$5.3 \times 10^{-3}$	$M_\odot/\text{yr}$
$m_{\text{R}}^{\text{th}}$	-	0.3	0.1	-
$M_{\text{halo,ram}}^{\text{th}}$	-	-	$1.2 \times 10^{14}$	$M_\odot/h$
$y$	-	0.03	0.046	-

Table 2.1: Values of L-Galaxies free parameters for the model of Guo et al. (2011) and Henriques et al. (2015).

## CHAPTER 3

# THE ASSEMBLY OF PSEUDOBULGES IN A HIERARCHICAL UNIVERSE

*“La furtiva sombra que aviesa tiñe el este, adquiere forma. Sauron no sufrirá rival alguno. Desde la cúspide de Barad-dûr, su Ojo vigila sin tregua, pero no es tan poderoso, aún no es inmune al miedo [...]. Contra todas sus argucias nos resta una ventaja. El anillo sigue oculto, y que no cejemos en destruirlo no ha sido concebido ni en sus más oscuros sueños.”*

El señor de los anillos: Las dos torres.

*“The veiling shadow that glowers in the East takes shape. Sauron will suffer no rival. From the summit of Barad-Dûr his Eye watches ceaselessly. But he is not so mighty yet that he is above fear [...]. But for all their cunning, we have one advantage. The Ring remains hidden, and that we should seek to destroy it has not yet entered their darkest dreams.”*

The Lord of the Rings: The Two Towers.

This Chapter is based on the paper: *The build-up of pseudo-bulges in a hierarchical universe*. David Izquierdo-Villalba; Silvia Bonoli; Daniele Spinoso; Yetli Rosas-Guevara; Bruno M. B. Henriques; Carlos Hernández-Monteagudo *Monthly Notices of the Royal Astronomical Society, Volume 488, Issue 1, pp.609-632 (2019)*

## ABSTRACT

In this chapter we study the cosmological build-up of pseudobulges using the `L-Galaxies` semi-analytical model for galaxy formation with a new approach for following separately the assembly of classical bulges and pseudobulges. Classical bulges are assumed to be the result of violent processes (i.e., mergers and starbursts), while the formation of pseudobulges is connected to the secular growth of disks. We apply the model to both the `Millennium` and the `Millennium II` simulations, in order to study our results across a wide range of stellar masses ( $10^7 - 10^{11.5} M_{\odot}$ ). We find that  $z=0$  pseudobulges mainly reside in galaxies of  $M_{\text{stellar}} \sim 10^{10} - 10^{10.5} M_{\odot}$  ( $M_{\text{halo}} \sim 10^{11.5} - 10^{12} M_{\odot}$ ) and we recover structural properties of these objects (e.g., sizes and bulge-to-total ratios) that are in good agreement with observational results. Tracing their formation history, we find that pseudobulges assembled in galaxies with a very quiet merger history, as opposed to the host galaxies of classical bulges. Regarding the bulge structure, we find that  $\sim 30\%$  of the galaxies with a predominant pseudobulge feature a composite structure, hosting both a pseudo and a classical bulge component. The classical component typically constitutes  $\sim 10\%$  of the total bulge galaxy mass. When looking at the properties of the host galaxies, we find that  $z=0$  pseudobulges are hosted by main sequence galaxies, characterized by a stellar population which is generally younger compared to the one of the hosts of classical bulges.

### 3.1 Introduction

According to the current picture of galaxy formation and evolution, the collapse of primordial and diffuse gas into condensed structures follows the aggregation of dark matter halos (White and Rees, 1978; Forcada-Miro and White, 1997; White and Frenk, 1991; Birnboim and Dekel, 2003). During this process, the hot gas cools down and settles into rotationally-supported disks which act as birthplaces for galaxies. At later times, protogalaxies grow and evolve via a combination of *ex-situ* and *in-situ* processes which gradually shape their morphology, giving rise to the diverse population of galaxies in the mature universe, characterized by different proportions of bulge and disk components and complex features such as spiral arms and bar structures. While *ex-situ* mechanisms can be dynamically fast and violent phenomena which take place, for instance, during galaxy mergers, the *in-situ* processes comprise phenomena such as cooling of gas, internal star formation activity and instabilities in the galactic structure (see Kormendy and Kennicutt, 2004a; Kormendy and Ho, 2013). These processes can be long compared to the dynamical time of the galaxy, in which case they are referred to with the term *secular*.

It is broadly accepted that elliptical galaxies and classical bulges are formed via galaxy encounters during their hierarchical growth (Kauffmann et al., 1993b; Baugh et al., 1996b; van Dokkum, 2005; Benson et al., 2002; Menci et al., 2004; Moorthy and Holtzman, 2006; Eliche-Moral et al., 2006b; Ryan et al., 2008; Carpineti et al., 2012; Kormendy and Ho, 2013). Despite sharing common properties, a slightly different formation scenario has been proposed for each of them. Elliptical structures are expected to be the result of collisions between galaxies with similar baryonic mass, during which any memory of previous structural features, such as bulge morphology or disk component, is lost and the final galaxy is transformed in a pure-bulge (Eliche-Moral et al., 2006b; Côté et al., 1998; Barnes, 1999). Classical bulges, on the other hand, are formed in galaxy encounters with small satellites where the nuclear region of the central galaxy experiences a significant growth as a consequence of the satellite mass incorporation (Doyon et al., 1994; Aguerri et al., 2001; Tacconi et al., 2002; van Dokkum, 2005; Hammer et al., 2005; Bournaud et al., 2005; Dasyra et al., 2006, 2007; Hopkins et al., 2009c; Rahimi et al., 2010). This seems to be a simplified scenario, as pointed out by e.g. Hopkins et al. (2009b); Ueda et al. (2014), who found that some remnants of a equal-mass galaxy merger can still host a small disk component.

On the other hand, bulge structures developed in isolated galaxies are thought to follow a different formation pathway than ellipticals and classical bulges (see e.g. Kormendy and Kennicutt, 2004a; Athanassoula, 2005). Within this evolutionary channel, morphological modifications are mostly governed by the self-gravity of the galactic disk: spatially extended and massive disks are susceptible to undergo a wide range of dynamical instabilities, characterized by the formation of non-axisymmetric and/or spiral structures usually referred to as *bars* or *spiral arms*, respectively (Kalnajs, 1972; Ostriker and Peebles, 1973; Combes and Sanders, 1981b; Toomre, 1981; Efstathiou et al., 1982; Pfenniger and Norman, 1990; Mo et al., 1998a; Athanassoula, 2005; Sellwood, 2016). In particular, bar instabilities can have an important role in shaping galaxy morphology by acting on the disk via angular momentum redistribution and gravitational torques (Athanassoula, 2012). One of the net effects of these complex dynamical processes is the formation of a nuclear structure known as *pseudobulge* shortly after bar formation, as consequence for instance of the buckling of the nuclear stellar orbits (Pfenniger and Norman, 1990; Bureau and Freeman, 1999; Combes, 2009; Athanassoula, 2012; Kormendy and Ho, 2013).

The basic elements of this picture are supported by several studies based on observational data. Doyon et al. (1994); Papovich et al. (2005); Tamburri et al. (2014), for instance, showed that classical bulges are usually characterized by *elliptical-like* properties, such as high Sersic indexes ( $n > 2$ ), old stellar populations, lack of star-forming activity and stellar kinematics dominated by velocity dispersion. On the other hand, pseudobulges display properties more related to disk-like structures, such as lower Sersic indexes ( $n < 2$ ) or ongoing star formation (see e.g. Drory and Fisher, 2007; Fisher and Drory, 2008b; Fisher et al., 2009). Nevertheless, deviations from this *archetypal* behaviour for pseudobulges/classical bulges have been found, for instance, by Ribeiro et al. (2016). To complicate this picture further, some works have argued that bulge formation could not be a consequence of just mergers and bar instabilities

(Noguchi, 1998, 1999; Obreja et al., 2013; Laurikainen and Salo, 2016). In order to shed light on the possible formation mechanisms of pseudobulges, classical bulges and ellipticals new efforts have been pursued from an observational perspective by, e.g., Gadotti (2009). This work supported the idea of classical bulges and pseudobulges being formed via different evolutionary pathways, which would leave their respective imprint in the bulge structural properties. According to this work, Sersic indexes and *bulge-to-total* ratios in classical bulges follow an elliptical-like correlation, suggesting a structural similarity between these two classes of objects. However, at the same time, classical bulges appear to be offset in the mass-to-size relation, as to confirm that classical bulges are not just ellipticals surrounded by disks. Finally, Gadotti (2009) showed that classical- and pseudo-bulges overlap when their host structural parameters (such as bulge or disk scale lengths) are taken into account. These findings suggest that bulge formation is an extremely complex phenomenon, which might be shaped by both mergers and secular processes during the complex cosmological evolution of galaxies (see e.g. Bournaud and Combes, 2002; Obreja et al., 2013; Erwin et al., 2015; Laurikainen and Salo, 2016).

Bulge formation has been extensively studied also via numerical approaches. Noguchi (1998, 1999), for instance, used simulations of isolated galaxies to introduce the *clumpy-origin* bulge formation mechanism. This scenario is based on the radial migration and aggregation of several stellar clumpy structures during the high-redshift assembly of galaxy disks. Similar results have been obtained by Dekel et al. (2009) in a theoretical work. Spinoso et al. (2017) analyzed the bar-induced formation of a pseudobulge structure within a Milky Way-like galaxy produced by the ErisBH cosmological zoom-in simulation (Bonoli et al., 2016). According to their analysis, a combination of the central black hole feedback at high redshift and the galaxy quiet merger history at lower one could have delayed the growth of the galaxy bulge, producing a disk more prone to bar instabilities at  $z < 0.5$ . Nevertheless, all these numerical works could only focus on the analysis of few specific objects, suffering low statistics issues. Semi-analytical models (SAMs) have shown to be an useful tool to shed light to this complicated bulge formation paradigm under a statistical point of view (see e.g. Gargiulo et al., 2015; Guo et al., 2011; Lacey et al., 2016; Lagos et al., 2018; Marshall et al., 2019b), despite some intrinsic limitations in modelling galaxy evolution processes. For instance, by using the L-Galaxies SAM, Shankar et al. (2012) could reproduce some observed properties of early type galaxies, such as effective radii or black hole-bulge mass relation. Other recent works used a simple approach to model the bulge growth and were able to *naturally* obtain the observed fraction of bulge galaxies and the galaxy size - stellar mass relation (Tonini et al., 2016; Lagos et al., 2018).

In this chapter we use an updated version of the L-Galaxies semi-analytical model (Henriques et al., 2015) to study the evolution of bulges, following separately classical and pseudo-bulge components. The code is run on both the Millennium and Millennium II merger trees (Springel, 2005; Boylan-Kolchin et al., 2009), enabling us to study a wide range in stellar mass ( $10^7 - 10^{11.5} M_{\odot}$ ). The main novelty of our approach is that we differentiate between *merger-driven* and *secularly-driven* disk instabilities, linking the former to the growth of classical bulges, and the latter to the formation of bars and pseudobulges. The outline of this work is as follow: In Section 3.2 we present updates in the L-Galaxies SAM that lead to a better description of galaxy morphology, and our approach in following the formation and evolution of bulge structures. In Section 3.3 we present our results, focusing on the properties of galaxies that host pseudobulges across cosmic time and on the structural properties of the simulated pseudobulges. Finally, in Section 3.4 we summarize our main findings. A lambda cold dark matter ( $\Lambda$ CDM) cosmology with parameters  $\Omega_m = 0.315$ ,  $\Omega_{\Lambda} = 0.685$ ,  $\Omega_b = 0.045$ ,  $\sigma_8 = 0.9$  and  $H_0 = 67.3 \text{ km s}^{-1} \text{ Mpc}^{-1}$  is adopted throughout the chapter (Planck Collaboration et al., 2014).

## 3.2 L-Galaxies semi-analytical model: Understanding the bulge assembly

In this section we focus on the modification introduced in L-Galaxies semi-analytical model (Henriques et al., 2015) to better describe galaxy morphology and the pseudobulges build-up. We refer the

reader to Chapter 2 for a detailed description of the whole baryonic physics included in the SAM. We have explored the model predictions for both Millennium (MS) and Millennium II (MSII) merger trees. We *stress* that the accuracy of the results presented in this work at  $M_{\text{stellar}} < 10^9 M_{\odot}$  for MS are limited by subhalo mass resolution issues. In these cases, we will rely in the MSII predictions whose limitation is at  $M_{\text{stellar}} \sim 10^8 M_{\odot}$ .

### 3.2.1 The build-up of bulges through mergers

Galaxy morphology in L-Galaxies is mainly driven by mergers and disk instabilities. Here we describe how the model treats these processes and the modifications we introduced to better describe the abundance of the different morphological types across a wide range of stellar masses and to follow secular-evolution processes. Besides, in Appendix C we present the modifications introduced in the bulge size computation of L-Galaxies (see Chapter 2, Section 2.3.3) to properly reproduce the observed trends.

#### Smooth accretion: a new recipe for extreme minor mergers

Galactic encounters are driven by the merger of the parent dark matter subhaloes. The time-scale of these processes is given by the dynamical friction experienced by the merging galaxies, as presented in Guo et al. (2011). In the standard picture of L-Galaxies, the ratio  $m_R = (M_{\text{cold},1} + M_{\text{stellar},1}) / (M_{\text{cold},2} + M_{\text{stellar},2})$  between the baryonic masses of the two galaxies is used to differentiate between *major* ( $m_R > m_R^{\text{th}}$ ) and *minor* ( $m_R < m_R^{\text{th}}$ ) interactions. In the *standard* version of the model,  $m_R^{\text{th}}$  is set to 0.1. Major mergers are assumed to be able to completely destroy the disks of the two interacting galaxies, leading to a pure spheroidal remnant which suffers a *collisional starburst*. In minor mergers, instead, the disk of the larger galaxy survives and experiences a burst of star formation, while its bulge incorporates the entire stellar mass of the satellite that survived stripping (as modelled by Guo et al. (2011)).

In Fig 3.1 we show how the standard L-Galaxies model recovers the morphological distribution of galaxies, as a functions of stellar mass, for both the MS (left) and MSII (right) runs. Lines refer to ellipticals (red), spirals (green) and extreme late types (blue), while coloured dots represent a collection of observational data, as in Conselice (2006)<sup>1</sup>. Morphological types definition is somewhat arbitrary (see Lagos et al., 2008; Guo et al., 2011; Gargiulo et al., 2015); in what follows we define extreme late types, spirals and ellipticals as galaxies with *bulge-to-total* ratios (hereafter B/T) of, respectively,  $B/T < 0.01$ ,  $0.01 < B/T < 0.7$  and  $B/T > 0.7$ . As we can see, Fig 3.1 in dash-dotted lines shows that the Henriques et al. (2015) standard version of L-Galaxies ( $m_R^{\text{th}} = 0.1$ ,  $f_{\text{binding}} = \text{None}$  and  $\epsilon^{\text{DI}} = 1.0$ ) reproduces the general trend presented in Conselice (2006) on both MS and MSII. Nevertheless, in both cases the population of (extreme late-type) spiral and elliptical galaxies is (over-) under-predicted in the range  $10^{10} - 10^{11} M_{\odot}$  (blue, green and red solid lines, respectively). Besides, the MSII does not converge with the MS, showing a large excess with respect to observations in the spiral population at low stellar masses  $< 10^{9.5} M_{\odot}$ .

After a detailed analysis of the impact that the current treatment of merger events has in the definition of galaxy morphology and its dependence on the resolution of the DM simulation used, we found that an improvement in the morphological distribution of galaxies and a reasonable convergence between MS and MSII can be reached when including the following two modifications: (i) set the threshold between major and minor mergers to the value  $m_R^{\text{th}} = 0.2$  and (ii) introduce a new approach in the treatment of extreme minor-mergers. The first modification leads to a better convergence between the MS and the MSII in terms of the number density of major merger events (see the details in Appendix D), and helps increasing the fraction of spirals in galaxies below  $\sim 10^{11} M_{\odot}$ , as can be seen in Fig 3.1 (dashed lines).

<sup>1</sup>Conselice (2006) defined ellipticals as galaxies with a morphological type T within  $-4 < T < -3$ , which would corresponds to bulge-to-total ratios of about  $[0.6 - 0.7]$  (see Mo et al., 2010; Simien and de Vaucouleurs, 1986, for more details)



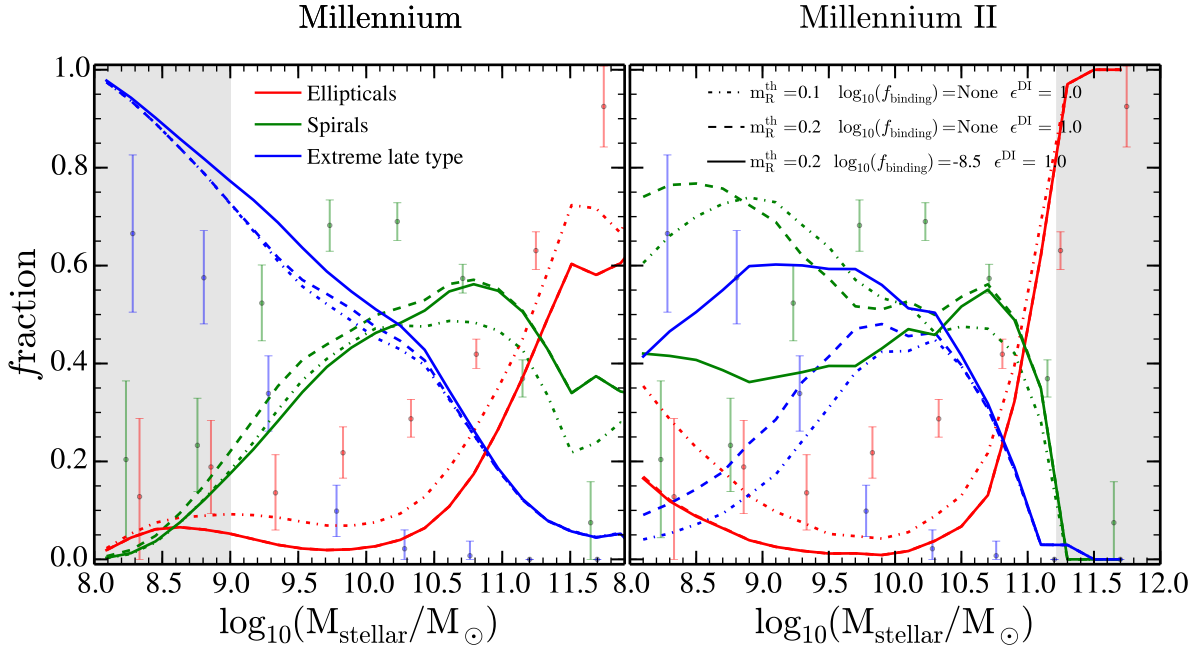


Figure 3.1: Fraction of different morphological types as a function of stellar mass for the MS (left panel) and MSII (right panel) at  $z=0$ . The DI stability parameter is set to  $\epsilon_{\text{DI}} = 1.0$  (see Section 3.2.2). Following Henriques et al. (2015) we define as early type (red curves), spiral (green curves) and extremely late-type (blue curves) galaxies with respectively bulge-to-total ratio  $B/T > 0.7$ ,  $0.01 < B/T < 0.7$  and  $B/T < 0.01$ . The points of corresponding colours represents the observational constrains presented in Conselice (2006). Line styles are associated to different set of the parameters  $m_{\text{R}}^{\text{th}}$  and  $f_{\text{binding}}^{\text{th}}$ . Shaded areas in the left and right plots marks the range where our results might be compromised by respectively the Millennium coarse mass resolution and low subhalo statistics of Millennium II (i.e less than 20 objects).

The second change has a very strong effect on both the convergence of the number density of minor merger events and on the morphological distribution of small galaxies (i.e,  $M_{\text{stellar}} < 10^{9.5} M_{\odot}$ ). In this mass range star formation in the disk can stall, as the cold-gas content of these low-mass galaxies is typically too low to an important trigger star formation event<sup>2</sup>. Therefore, the only events leading to morphological changes for galaxies with  $M_{\text{stellar}} < 10^{9.5} M_{\odot}$  are mergers. In the MSII, in particular, these small galaxies experience a significant number of extreme minor mergers, as the simulation is able to resolve much smaller structures compared to the MS (the most extreme and numerous encounters are with satellite galaxies of the order of  $M_{\text{stellar}} \sim 10^5 M_{\odot}$ ). If such extreme interactions are treated as *normal* minor mergers the bulges of these small galaxies grow by incorporating the stellar mass of the satellites, while their disks are unable to increase in mass, as star formation is stalled (and merger-induced bursts are negligible as less than 0.2% of the cold gas mass is transformed into stars). This leads to the large fraction of spirals (and lack of extreme disk), as shown in Fig 3.1 with dash and dotted lines. We thus update the model, introducing a new set of prescriptions to treat these extreme minor mergers, to which we refer with the term *smooth accretions* (see e.g. Abadi et al., 2003; Peñarrubia et al., 2006; Sales et al., 2007; Kazantzidis et al., 2008). In those extreme minor mergers, one might expect that the stellar satellite mass might not be able to reach the bulge of the central galaxies, but gets disrupted by the disk of the central galaxy and get incorporated by it.

<sup>2</sup>in L-Galaxies the threshold for star formation is  $M_{\text{crit}}^0 = 2.4 \times 10^9 M_{\odot}$  (see Eq.S14 of Henriques et al. (2015)). Note that a more accurate description of star formation might come by linking this process with the molecular gas component instead of the total cold gas (see Lagos et al. (2011)), as also discussed in Henriques et al. (2015)

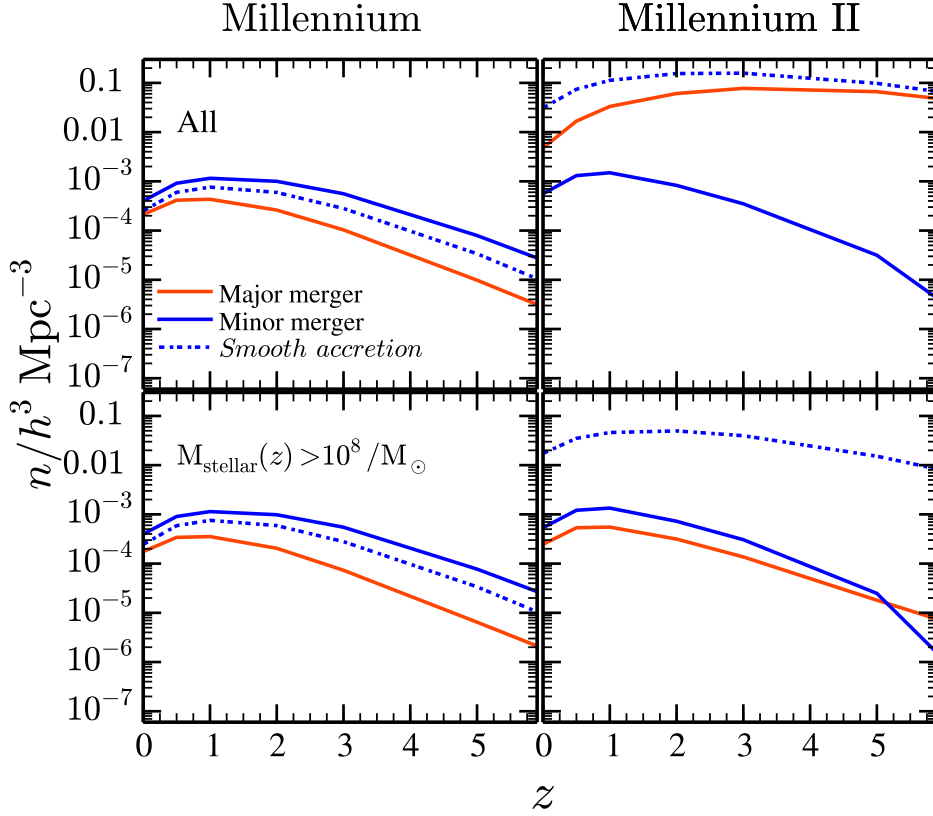


Figure 3.2: Number density of major mergers (red solid line), minor mergers (solid blue line) and *smooth accretion* (dashed blue line) as a function of redshift. The left and right columns display the results for the Millennium and Millennium II simulation, respectively. In the first row we present the results for *all* galaxies in the simulation. The second one represents the same but for galaxies with  $M_{\text{stellar}} > 10^8 M_{\odot}$  at a given redshift.

We make use of the ratio  $f_{\text{binding}}$  between the binding energies of the merging structures to disentangle between *normal* minor mergers and *smooth accretion* episodes. We assume that the interacting (sub-)systems are i) the whole stellar satellite galaxy and ii) the central galaxy stellar disk (gas+stars), we compute the satellite  $f_{\text{binding}}$  by considering the entire satellite stellar mass, and only the disk mass (gas+stars) for the central galaxy, respectively:

$$f_{\text{binding}} = \frac{E_{\text{binding}}^{\text{Satellite}}}{E_{\text{binding}}^{\text{Central}}} = \frac{M_{\text{Sat,Stellar}}^2 R_{\text{disk}}^{\text{Central}}}{M_{\text{Cent,disk}}^2 R_{\text{Stellar}}^{\text{Sat}}}, \quad (3.1)$$

where  $R_{\text{Stellar}}^{\text{Sat}}$  is the mass-weighted average half-mass radii of the satellite bulge and disk, while  $R_{\text{disk}}^{\text{Central}}$  is the same quantity for the disk of the central galaxy (as it is composed by both gas and stars). The larger the value of  $f_{\text{binding}}$ , the closer are the binding energies of the merging galaxies, so the remnant of the satellite galaxy might survive the interaction with the central disk and reach the centre of its massive companion (*usual* minor merger). On the opposite case, we assume that the central galaxy can easily unbind the satellite stellar system, which will be incorporated in the central galaxy disk (*smooth accretion*). Following this approach, the best agreement with observational data is obtained by imposing  $f_{\text{binding}}^{\text{th}} = 10^{-8.5}$  as a threshold value to discriminate between the two scenarios. This low value of  $f_{\text{binding}}^{\text{th}}$  corresponds more or less to a cut in satellite stellar mass  $\sim 10^7 M_{\odot}$ , as it is shown in Fig D.3 of Appendix D. As can be seen in Fig 3.2, by imposing  $f_{\text{binding}}^{\text{th}} = 10^{-8.5}$  we obtain a remarkable agreement in the minor merger predictions for both MS and MSII merger trees (see blue solid lines). Concerning the *smooth accretion* events (blue dotted lines), MSII and MS merger trees display different predictions.



In the former, the *smooth accretion* has 1 dex larger number density than in the latter, being the dominant type of interaction at any redshift.

To summarize:

$$\begin{cases} \text{minor merger} & f_{\text{binding}} > f_{\text{binding}}^{\text{th}} \ \& \ m_{\text{R}} < m_{\text{R}}^{\text{th}} \\ \text{smooth accretion} & f_{\text{binding}} < f_{\text{binding}}^{\text{th}} \ \& \ m_{\text{R}} < m_{\text{R}}^{\text{th}} \end{cases}$$

with  $f_{\text{binding}}^{\text{th}} = 10^{-8.5}$  and  $m_{\text{R}}^{\text{th}} = 0.2$ . The results obtained with this new recipe for both MS and MSII are shown with solid lines in Fig 3.1. Our new prescription leaves the morphology distributions almost unchanged in the case of the MS, while it improves them for the MSII, providing a better agreement between data and model predictions. A detailed analysis showing the morphology evolution with respect to  $m_{\text{R}}^{\text{th}}$  and  $f_{\text{binding}}^{\text{th}}$  parameters can be found in Fig D.4 of Appendix D. Besides, we have checked that the mass injected in the disk by *smooth accretion* accounts for less than the 5% of the total stellar disk, with a decreasing trend with stellar mass. For instance, in Milky Way-like galaxies the *smooth accretion* contributes with less than 0.5%. Note that our approach of *smooth accretion* in the stellar disk is not the only possibility. For instance, during such events the satellite stellar mass could be added in the stellar subhalo or ICM (see eg. Brook et al., 2004, 2012).

Finally, as we can see in Fig 3.1, in spite of the morphological improvements achieved at low stellar masses by changing the merger recipe of L-Galaxies, we can not find a significant improvement in the intermediate population  $10^{10} - 10^{11} M_{\odot}$ . From this, we can draw a simple conclusion: mergers do not have the dominant role in this range of masses. In the next section we will explore the effects of the other bulge formation channel (disk instabilities) in the galaxy morphology.

### 3.2.2 Disk instabilities: the growth of pseudobulges and classical bulges

In addition to mergers, the *disk instabilities* (DI) channel is an important pathway for bulge growth in L-Galaxies. Within the context of this work, DI refers to the process by which the stellar disk becomes massive enough to be prone to non-axisymmetric instabilities which ultimately lead to the formation of a central ellipsoidal component via the buckling of nuclear stellar orbits (see references in Mo et al., 2010). During this process, a possible result is the formation of a *bar structure* (Kalnajs, 1972; Ostriker and Peebles, 1973; Combes and Sanders, 1981b; Efstathiou et al., 1982; Pfenniger and Norman, 1990; Mo et al., 1998a; Athanassoula, 2005; Sellwood, 2016). Galactic bars have a deep impact the morphology of the nuclear parts. On one hand, they can efficiently modify the gas disk structure via gravitational torques able to produce strong nuclear gas inflows which can be transformed into stars inducing the formation of disc-like pseudobulge structure. On the other, shortly after the bar formation the structure can experience a bending mode that thickens it and forms a boxy/peanut pseudobulge (see e.g. Pfenniger and Norman, 1990; Kormendy and Kennicutt, 2004b; Saha, 2015; Spinoso et al., 2017). As we discussed in Chapter 2, the L-Galaxies model accounts for galactic DI with a simple analytic stability criterion, based on the Efstathiou et al. (1982) and Mo et al. (1998a) 2d simulations:

$$\frac{V_{\text{max}}}{(GM_{\star,d}/R_{\star}^{\text{sl}})^{1/2}} \leq \epsilon_{\text{DI}}, \quad (3.2)$$

where  $V_{\text{max}}$  is the maximum circular velocity of the host dark matter subhalo<sup>3</sup>,  $R_{\star}^{\text{sl}}$  and  $M_{\star,d}$  are the exponential scale-length and stellar mass of the stellar disc respectively and  $\epsilon_{\text{DI}}$  a parameter which determines the importance of the disk self-gravity (set to 1.0 in the standard version of L-Galaxies). If this stability criterion is met, an amount

$$\Delta M_{\star}^{\text{DI}} = M_{\text{disk}} - M_{\text{crit}}^{\text{DI}} = M_{\text{disk}} - \frac{V_{\text{max}}^2 R_{\star}^{\text{sl}}}{G \epsilon_{\text{DI}}^2}, \quad (3.3)$$

<sup>3</sup>We found no significant differences in our results when using the *disk* circular velocity  $V_c(r=2.2R^{\text{d}}) = \sqrt{GM_{\text{DM}}(r)/r + GM_{\text{bulge}}(r)/r + V_{\text{disk}}^2(r)}$ . This definition is obtained by assuming an Hernquist (Hernquist, 1990) and NFW (Navarro et al., 1996) profile for the bulge and DM subhalo, respectively.

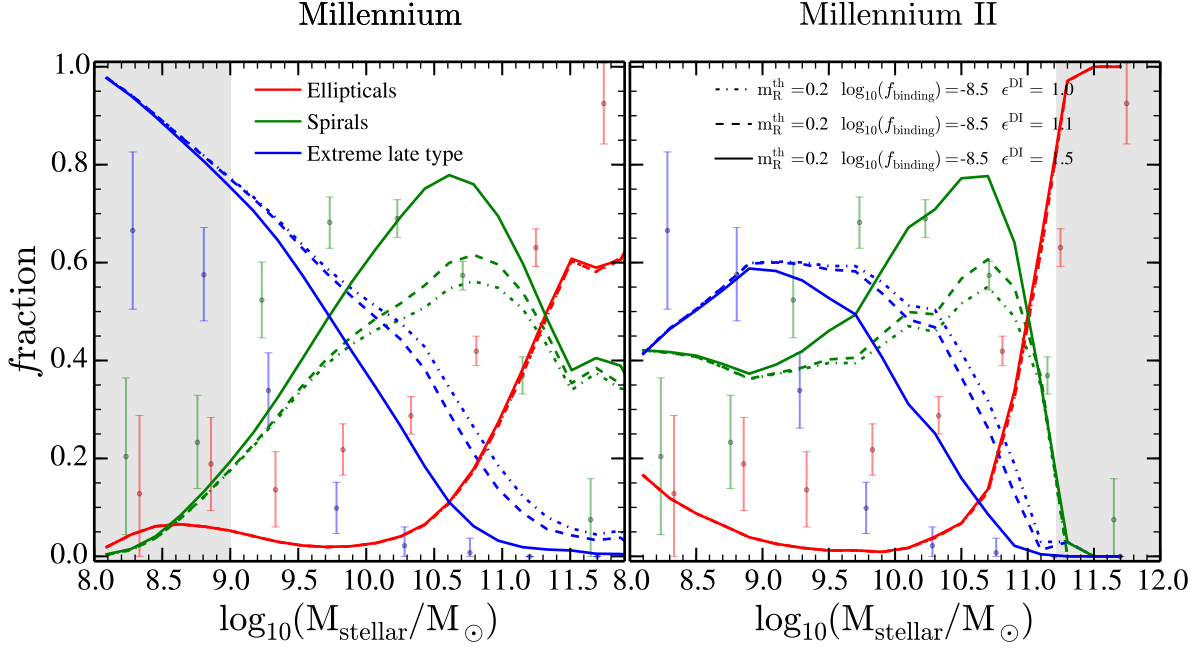


Figure 3.3: Same as Fig 3.1 but assuming a fixed values of  $m_R^{\text{th}} = 0.2$  and  $\log_{10}(f_{\text{binding}}^{\text{th}}) = -8.5$  and varying  $\epsilon_{\text{DI}}$ .

of the disk stellar mass is transferred to the bulge in order to restore the disk (marginal) stability. Despite the limitations of Eq.(3.2) (see Athanassoula, 2008), this criterion to follow disc stability has the advantage of being simple and to depend only on global galaxy properties, accessible by the model.

According to Efstathiou et al. (1982); Mo et al. (1998a)  $\epsilon_{\text{DI}} \approx 1.1$  for a family of exponential-profile stellar disk models. Nevertheless, in order to improve the morphology at intermediate stellar masses and following the approach of other SAMs (Hirschmann et al., 2012; Menci et al., 2014; Lacey et al., 2016; Lagos et al., 2018) we have tested the model with different values of DI stability parameter,  $\epsilon_{\text{DI}}$ . The results are presented in Fig 3.3. As we can see, we found that a slightly higher value (namely  $\epsilon_{\text{DI}} = 1.5$ ) provides a better agreement with observations in the mass range  $10^9 < M_{\text{stellar}} M_{\odot} < 10^{11}$ . The change of parameter value causes galaxies to be more easily prone to instabilities, thus a larger fraction of stars is transferred from the disk to the bulge component, increasing the fraction of spirals and reducing the one of extreme late types in this mass range. Notice that the change of  $\epsilon_{\text{DI}}$  does not have any impact in the elliptical population. In a recent paper, Irodou et al. (2018) achieved a better improvement of the spiral and elliptical population in L-Galaxies by imposing angular momentum losses during the gas cooling and allowing DI in the galaxy gaseous disk. Nevertheless, the results were not checked in MSII. Here we decide no to use that approach and keep our independent merger/disk instability analysis which lets us reach the convergence between MS and MSII and update/ improve the L-Galaxies standard merger recipe. Besides, we have checked that the increase of the stability parameter has a similar effect in the spiral galaxy population that the one achieved by adding angular momentum losses during the gas cooling.

### A discretization effect: Linking different DI events as a single episode

The adopted approach to treat DIs in L-Galaxies (see Section 3.2.2), is such that galaxy equilibrium is restored by transferring the minimum amount of mass from the disk to the bulge. This means that the disk easily becomes unstable again in the one (or more) of the subsequent *sub-step*. This generates a series of disk instabilities in a galaxy which are, effectively, all connected. This is especially true in

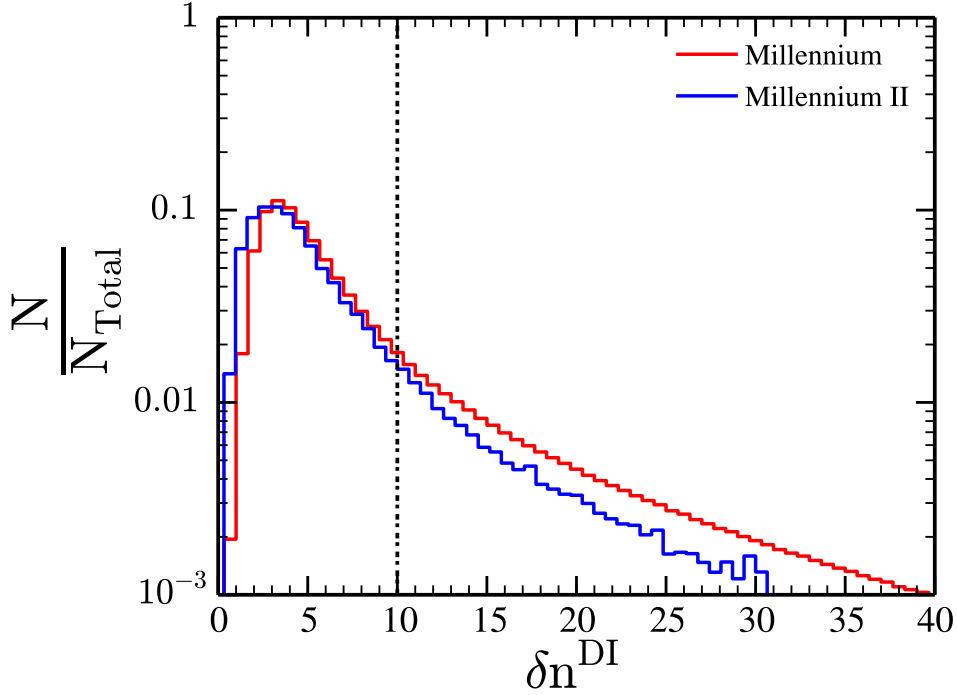


Figure 3.4: Number of dynamical times ( $\delta n^{\text{DI}}$ ) that a galaxy experiences between two no consecutive disk instabilities. Red histogram represents the results for MS while in blue the ones for MSII. Dotted vertical line represents our threshold to consider two no consecutive DIs as the same episode.

systems in which the cooling rate is high enough to quickly replenish the stellar disk (Porter et al., 2014). While two consecutive disk instability events (in two subsequent *sub-steps*) can be easily assumed to be part of the same event, connecting events which are more spread in time is less straightforward. In order to join separate DI events, thus erasing the discretization effects of the time resolution of the simulation, we start by studying the typical time difference between two no-consecutive DIs in the same galaxy. For this, we define the quantity  $\delta n^{\text{DI}}$ , defined as the time-difference between two events and normalized by the dynamical time of the galaxy:

$$\delta n^{\text{DI}} = \frac{t^{\text{Last DI}} - t^{\text{Current DI}}}{t_{\text{dyn}}^{\star, \text{disk}}|_{\text{Last DI}}}, \quad (3.4)$$

where  $t^{\text{Current DI}}$  is the lookback time of the current DI,  $t^{\text{Last DI}}$  is the lookback time in which the galaxy experienced the last disk instability and  $t_{\text{dyn}}^{\star, \text{disk}}|_{\text{Last DI}}$  is the dynamical time of the stellar disk at the epoch of the last DI. The distributions of  $\delta n^{\text{DI}}$  for MS (red) and MSII (blue) are presented in Fig 3.4. As we can see, both distributions present a clear peak at values of  $\delta n^{\text{DI}} \sim 5$ , indicating that a large fraction of DI events are separated by few dynamical times, and are likely causally connected. We then assume that DI events which are separated by less than  $\delta n_{\text{th}}^{\text{DI}} \times t_{\text{dyn}}^{\star, \text{disk}}|_{\text{Last DI}}$  are causally connected. In what follows, we will assume a threshold value of  $\delta n_{\text{th}}^{\text{DI}} = 10$ . We have checked that the results presented in this chapter have a very weak dependence on the exact value of the threshold for  $\delta n^{\text{DI}}$ , as long as the peak of the distribution is included in the sample.

### From disk instabilities to bulges: *merger-induced* vs. *secular* processes

Disk instabilities presented in L-Galaxies have been already used to study spheroidal components (see Shankar et al., 2012, 2013). In the model presented here, we re-visit the way DI are treated, by linking DI to the formation of both classical bulges and pseudobulges. Following the history and the physical

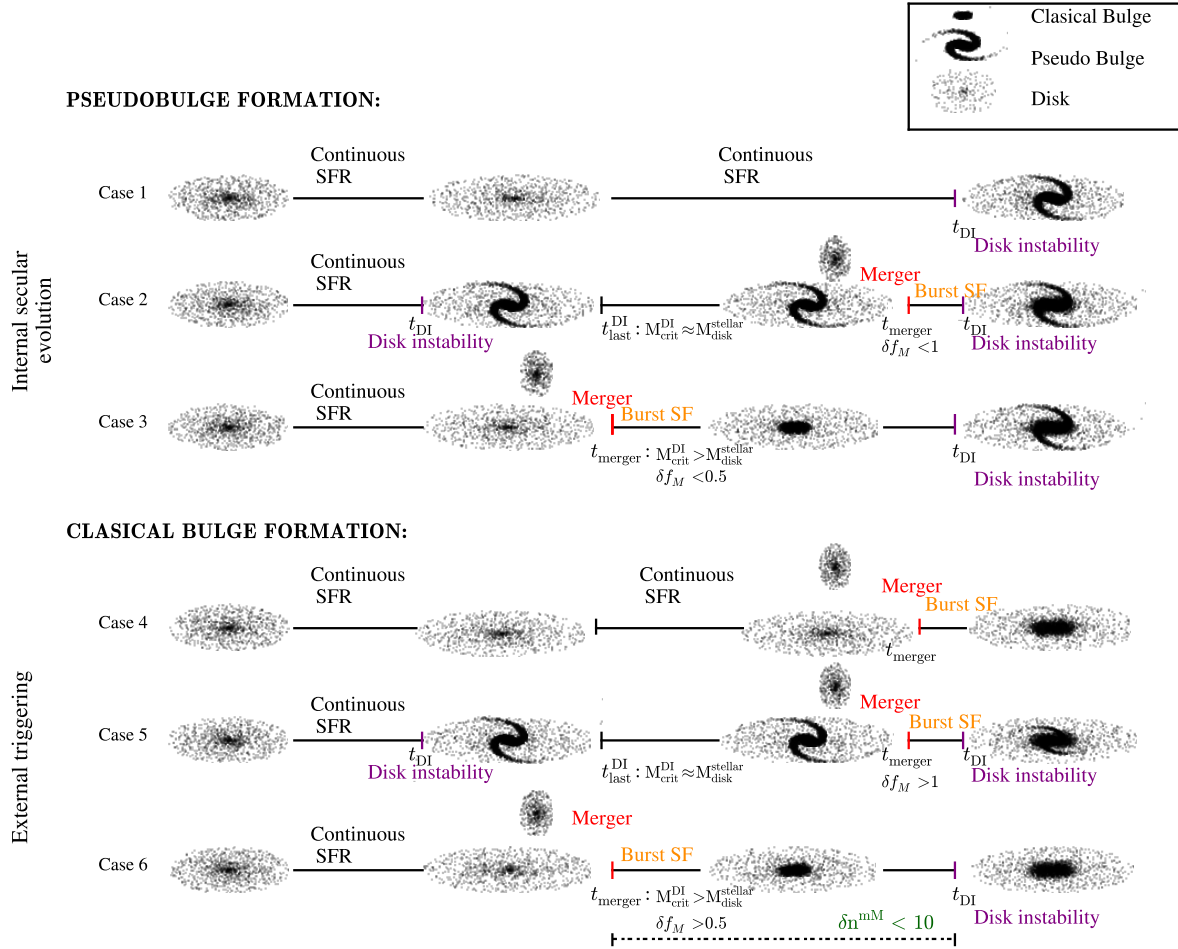


Figure 3.5: Possible paths of pseudobulge and classical bulge build-up. Following [Kormendy and Kenicutt \(2004a\)](#) we have assumed that the build-up of pseudobulges is triggered by internal evolution (Case 1, 2 and 3). In the case of classical bulges, we have assumed an external mechanism of formation (Case 4, 5 and 6).

conditions of the galaxy in which a DI takes place, we are able to distinguish between instabilities that are *merger-induced* and the ones that are a consequence of the slow, *secular* evolution of galaxies. Here we describe the details of how to discriminate between different instability events, and how these events lead to the build up of classical bulges and pseudobulges.

On one hand, *merger-induced* DIs are produced as a consequence of the fast increase of stellar disk mass after the collisional starburst or *smooth* satellite galaxy accretion. On the other hand, *secular* DIs result from the slow, but continuous, mass growth of the disk, playing an important role in galaxies evolving in isolation. Under the assumption that bars are a consequence of the secular evolution of galaxies ([Debattista et al. \(2004, 2006\)](#); [Méndez-Abreu et al. \(2010\)](#); [Kormendy and Ho \(2013\)](#); [Kim et al. \(2016\)](#); [Moetazedian et al. \(2017\)](#); [Zana et al. \(2018a,b\)](#)) and that bars lead to the formation of pseudobulges<sup>4</sup>, we link *secular* DIs to the formation of galactic bars and pseudobulges. Therefore, we assume that the mass removed to the disk during the DI phase (according to Equation 3.3), is transferred to the pseudobulge, which we treat as a new component of the galaxy. On the other side, *merger-induced* DI, closely associated with injection of external stars or/and SF burst triggered during the interaction, are

<sup>4</sup>Numerical simulations have shown that shortly after the bar formation the structure suffers a bending mode that thickens it and forms the boxy/peanut pseudobulge shape (see [Combes et al., 1990b](#); [Méndez-Abreu et al., 2019](#)). Also galactic bars can produce, via gravitational torques, strong nuclear gas inflows which can be transformed into stars inducing the formation of disc-like pseudobulge structure.

assumed to be the ones that lead to the formation of a classical bulge structure. In Fig 3.5 we present an illustrative scheme of the scenarios that lead to the growth of both the pseudobulge and classical bulge component of the galaxy. Case 1 and Case 6 are the two simplest scenarios, as described above. In the first case, the galaxy experiences continuous star formation until the disk becomes unstable, forms a bar and the stellar component removed from the disk is transferred to the pseudobulge. In Case 6, the galaxy, starting from a stable configuration, experiences a merger (either a minor merger or a *smooth accretion* as described in Section 3.2.1), which triggers a burst of SF that causes the disk to become unstable, and the stellar component removed from the disk to restore stability is effectively transferred to the classical bulge component.

However, the life of a galaxy can be rather complicated, with continuous mergers and episodes of star formation, that make it more difficult to discriminate between the two scenarios. Naively we could think that a DI which takes place right after a merger is a consequence of it. Nevertheless, this is not necessarily true. In order to quantify the importance of a minor merger or a *smooth accretion* in triggering a DI event, we are going to study how efficient is the interaction in injecting new stars in a stable (or marginally stable) disk. To check that, we introduce the quantity  $\delta f_M$ , defined as follows:

$$\delta f_M = \begin{cases} \frac{\Delta M_{\text{stars}}^{\text{Burst}} + \left[ M_{\text{stellar}}^{\text{Satellite}} H(f_{\text{binding}}) \right]}{(M_{\text{crit}}^{\text{DI}} - M_{\text{disk}})} & \text{for } M_{\text{crit}}^{\text{DI}} > M_{\text{disk}} \text{ at } t = t_{\text{merger}} \\ \frac{\text{SFR}_{\text{isnt}}^{\text{merger}}}{\text{SFR}_{\text{isnt}}^{\text{sec}}} & \text{for } M_{\text{crit}}^{\text{DI}} \approx M_{\text{disk}} \text{ at } t = t_{\text{merger}}, \end{cases} \quad (3.5)$$

where  $H(f_{\text{binding}})$  is a unit step function, whose value depend on the type of interaction:  $H = 0$  for minor mergers ( $f_{\text{binding}} > f_{\text{binding}}^{\text{th}}$ ) and  $H = 1$  for *smooth accretion* events ( $f_{\text{binding}} < f_{\text{binding}}^{\text{th}}$ ), as explained in Section 3.2.1. The first condition refers to events in which the disk is stable ( $M_{\text{crit}}^{\text{DI}} > M_{\text{disk}}$ ) at the time the merger takes place ( $t = t_{\text{merger}}$ ). In this case,  $\delta f_M$  indicates how much the stellar disk grows with respect to how stable the disk is ( $M_{\text{crit}}^{\text{DI}} - M_{\text{disk}}$ ). If the interaction is a minor merger the entire stellar component of the satellite is transferred to the bulge of the central, and the only new contribution to the disk is given by the burst of SF,  $\Delta M_{\text{stars}}^{\text{Burst}}$ . In the case of *smooth accretion*, the stellar disk of the central galaxy increases its mass not only through the SF burst, but also by incorporating the stellar component of the satellite, as described in Section 3.2.1.

The larger is the  $\delta f_M$ , the stronger the impact of the merger on the next DI event. In the upper panels of Fig 3.6 we present the distribution of  $\delta f_M$  for the MS (left panels) and MSII (right panels) for all the events which satisfy the first case of Eq.(3.5). The values of  $\delta f_M$  are shown separately for *smooth accretion* (blue) and minor merger events (red). The differences in the relative abundance between minor mergers and *smooth accretion* in MS and MSII is just a consequence of resolution, as already discussed in Section 3.2.1. Except for the differences due to resolution effects, distributions of  $\delta f_M$  for both minor merger and *smooth accretion* peak at low values ( $\sim 0.001 - 0.01$ ) for both simulations. This points to the conclusion that most of the interactions have a minimum contribution in the DIs happening after mergers. The small fraction of events characterized by high  $\delta f_M$  values, however, can have a considerable impact on a subsequent disk instability. To differentiate between interactions that are responsible to a DI and the ones that do not, we set the limit to  $\delta f_M = 0.5$ : only the minor mergers/*smooth accretions* that reduce the galaxy disk stability  $\sim 50\%$  are assumed to be responsible for the following DIs.

In addition to the  $\delta f_M$  condition, we have also imposed that the mergers/*smooth accretions* have to be causally connected to the subsequent DI, by imposing a maximum time scale that can pass between the two events, defined to be a multiple of the dynamical time of the galaxy stellar disk at the moment of the interaction. To set this value, we analyze the quantity  $\delta n^{\text{mM}}$ , defined as:

$$\delta n^{\text{mM}} = \frac{t_{\text{minor Merger}}^{\text{Last}} - t_{\text{DI}}^{\text{First}}}{t_{\text{dyn}}^{\star, \text{disk}} |_{\text{minor Merger time}}}, \quad (3.6)$$

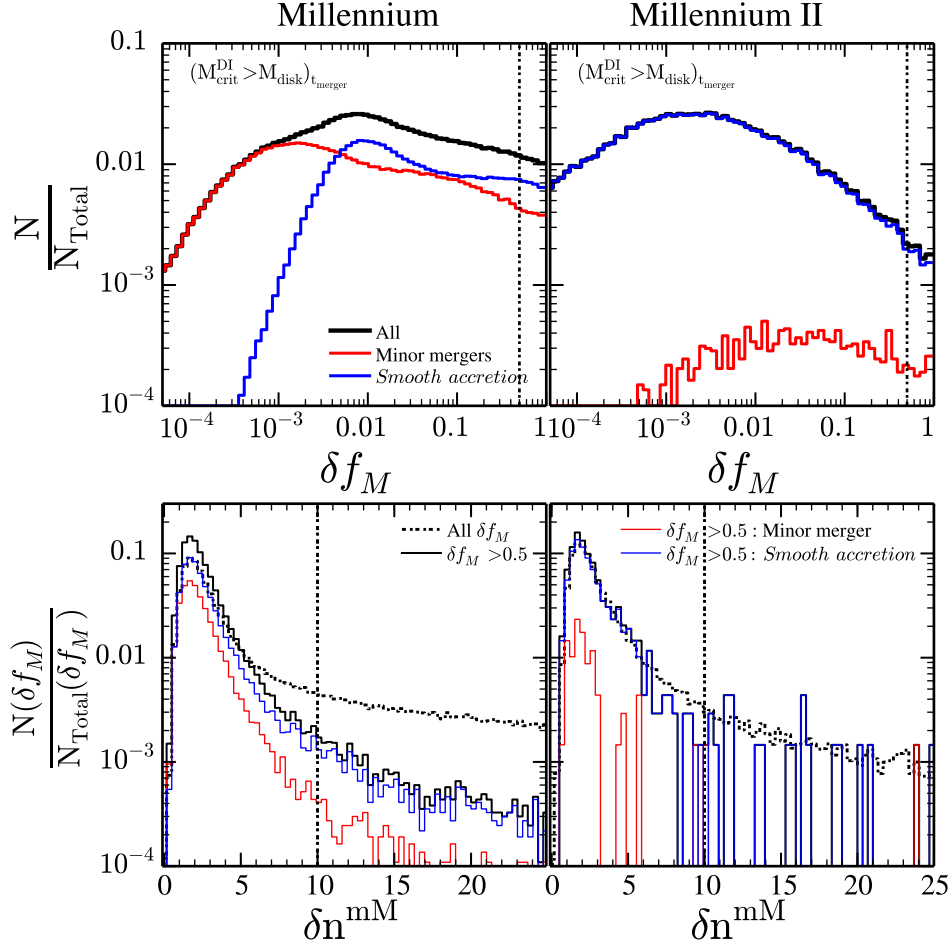


Figure 3.6: **Upper panels:** Distribution of  $\delta f_M$  for all galaxies that suffered a DI after a merger in which the disk was stable, i.e  $M_{\text{crit}}^{\text{DI}} > M_{\text{disk}}$  at  $t = t_{\text{merger}}$ . Black line represents all the events while red and blue only the ones after a minor merger and *smooth accretion*, respectively. **Bottom panels:** In dotted lines the  $\delta n^{\text{mM}}$  distribution of all the events which satisfy Eq.(3.5). Solid lines represent the same but imposing the extra condition of  $\delta f_M > 0.5$ : in red minor mergers and in blue *smooth accretion*. In all the panels, left and right columns display, respectively, the results for MS and MSII.

where  $t_{\text{merger}}^{\text{Last}}$  is the lookback time of the last minor merger or *smooth accretion*,  $t_{\text{DI}}^{\text{First}}$  is the lookback time of the first DI after the galaxy interaction and  $t_{\text{dyn}}^{\text{disk}}|_{\text{minor Merger time}}$  is the dynamical time of the galaxy stellar disk at the moment of the interaction. The distribution of  $\delta n^{\text{mM}}$  for both the MS and the MSII are shown in the lower panels of Fig 3.6. As we can see, the distribution of  $\delta n^{\text{mM}}$  is more concentrated towards lower values when we consider only events with  $\delta f_M > 0.5$  (solid black lines). Interestingly, the distribution of  $\delta n^{\text{mM}}$  peaks close to few number of dynamical times ( $\delta n^{\text{mM}} \sim 2 - 5$ ) with a very sharp decrease at large  $\delta n^{\text{mM}}$ . This is a clear signal that the *smooth accretion* and minor merger are responsible for the triggering of a subsequent instability. Moreover, when we distinguish between minor merger and *smooth accretion* (red and blue lines respectively), we find that the distribution of  $\delta n^{\text{mM}}$  for minor mergers is more concentrated towards lower values than the one for *smooth accretion* events. This suggests that minor mergers are typically able to destabilize the galaxy disk in shorter times scales than *smooth accretion*.

Based on these results, we set that all instabilities happening within 10 dynamical times from the interaction ( $\delta n^{\text{mM}} = 10$ ), and for which  $\delta f_M > 0.5$ , are *merger-induced*. These events thus lead to the growth of the classical bulge component (Case 6 in Fig 3.5). On contrary, all DI events for which  $\delta f_M < 0.5$  or  $\delta f_M > 0.5$  and  $\delta n^{\text{mM}} > 10$  are assumed to be secular processes which contribute to the



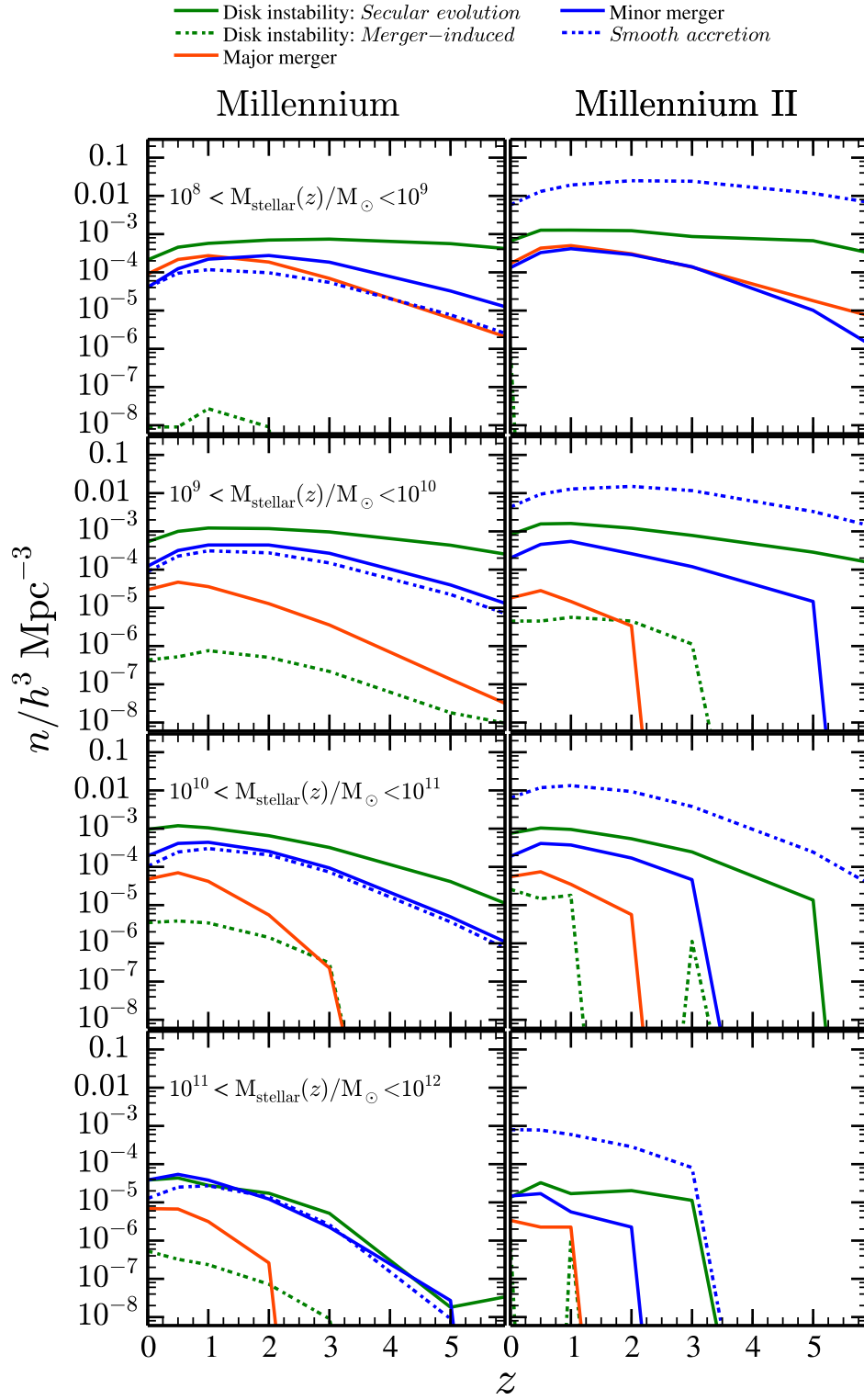


Figure 3.7: Number density of 5 different type of events: *secular* disk instability (solid green line), *merger-induced* disk instability (dashed green line), major mergers (red solid line), minor mergers (solid blue line) and *smooth accretion* (dashed blue line). The left and right columns display the results for the MS and MSII simulations, respectively. The different rows represent the number density for different stellar mass bins at a given redshift.

formation of a bar and a pseudobulge (Case 3 in Fig 3.5).

Finally, the second case in Eq.(3.5) addresses the peculiar case in which a merger event happens in a galaxy characterized by a marginally stable disk after a DI, i.e  $M_{\text{crit}}^{\text{DI}} \approx M_{\text{disk}}$  (with  $M_{\text{crit}}^{\text{DI}} \gtrsim M_{\text{disk}}$ ). In this cases the DI is induced immediately ( $\delta n^{\text{mM}} = 0$ ). However, it is difficult to say if the merger was a necessary phenomena to trigger a DI in the galaxy given that any event producing stars (either internal SF or merger burst) would rise the disk stellar mass over the critical threshold. Despite this cases are not as common as the ones described by the first case in Eq.(3.5) (less than the 10% of the whole DI *merger-induced*) we still take into account them by studying the relative importance of the interaction with respect to the continuous star formation happening in the disk in the triggering of the subsequent DI. When  $\text{SFR}_{\text{isnt}}^{\text{merger}} > \text{SFR}_{\text{isnt}}^{\text{sec}}$ , i.e  $\delta f_M > 1$ , we assume that the minor merger/*smooth accretion* dominates the disk growth and the subsequent DI is *merger-induced* (Case 5 in Fig 3.5). Otherwise we assume the DI to be of *secular* origin (Case 2 in Fig 3.5).

In Fig 3.7 we present the predicted number density of *secular* and *merger-induced* DIs<sup>5</sup>(solid and dashed green lines, respectively) for different stellar mass ranges. Left and right panels are, respectively, the L-Galaxies predictions run on top of MS and MSII merger trees. For completeness, we have added the predictions of major/minor mergers and *smooth accretion*. As we can see, *secular* DIs evolution dominates the DI number density, being *merger-induced* DIs  $\sim 3$  dex less abundant. Even though Fig 3.7 shows that DI *secular* events dominate over mergers in all mass bins, this does not mean that the importance of such events is the same. For instance, galaxies with stellar mass in the range  $10^8 - 10^9 M_{\odot}$  *secular* DI contributes with  $10^5 - 10^6 M_{\odot}$  to the bulge per event while galaxies with  $10^{10} - 10^{11} M_{\odot}$  the DI *secular* events are characterized by  $10^8 - 10^{10} M_{\odot}$  of mass transferred (these numbers corresponds to DI events defined as in Section 3.2.2).

About the redshift distribution, *secular* evolution DIs take place at any redshift and they are the main mechanisms of bulge formation/growth at high- $z$ . On contrary, *merger-induced* DIs occur at  $z \sim 1$  with a sharp cut-off towards higher redshifts. Even more, they are rare events at  $z > 3$ . Besides, we can see that *merger-induced* DIs can not compete at any redshift with mergers (major/minor) in the classical bulge formation/growth given that their number density is a factor 100 smaller and the amount of mass transferred per event is less than the  $\sim 0.1\%$  of the whole galaxy stellar mass. Nevertheless, these events can complement classical bulge build-up at low redshifts. As can be seen, both MS and MSII predicts similar redshift distributions for the *merger-induced* DIs and *secular* DIs, and similar values of number densities, even though the MSII predicts slightly larger number densities of *merger-induced* DIs, as the number of *smooth accretion* is much larger than in the MS.

We want to highlight that, in a hierarchical universe, each case presented in Fig 3.5 does not live in isolation. Due to the complex merger history that a galaxy can experience, the final bulge can be the result of a multiple physical processes, being a composite structure formed by both classical and pseudobulge component (see, Erwin et al., 2015; Di Matteo et al., 2015; Fragkoudi et al., 2017; Blańa Díaz et al., 2018). For simplicity, we are going to use the following criteria to define galaxy bulge morphology:

- **Pseudobulge:** We assume that a galaxy hosts a pseudobulge when the fraction of bulge formed via *secular induced* DI is at least  $2/3$ . This cut allows us to be confident about the fact that the pseudobulge is the dominant structure in the bulge. Galaxies hosting this type of structures are going to be tagged as *pseudobulge galaxies*.
- **Classical bulge:** The fraction of bulge formed via *secular induced* disk instabilities is smaller than  $2/3$  of the total bulge mass and its *bulge-to-total* is  $0.01 < B/T < 0.7$ . Galaxies with  $B/T < 0.01$  are considered bulgeless galaxies. Galaxies hosting this type of bulges are going to be called *classical*

<sup>5</sup>In both types of DIs, we correct for time-discretization effects using the procedure presented in Section 3.2.2

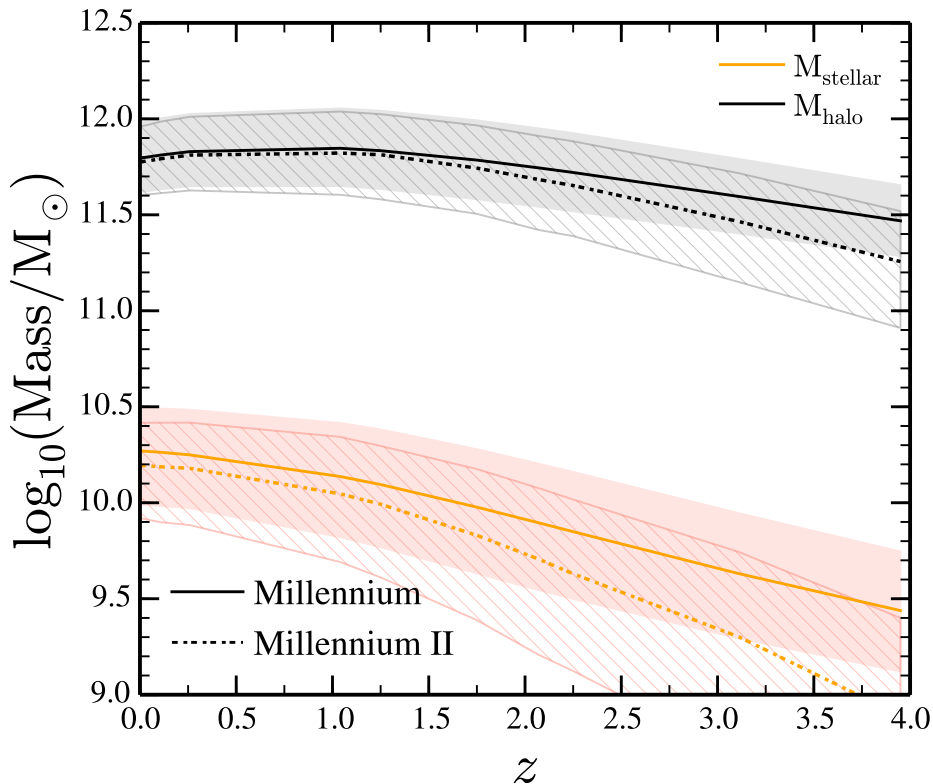


Figure 3.8: Median subhalo mass ( $M_{\text{halo}}$ , black) and stellar mass ( $M_{\text{stellar}}$ , orange) of galaxies classified as *pseudobulge galaxies* at different redshift. The selection of this population at any redshift were done following the definition presented in Section 3.2.2. The solid line and shadow region represents the median and  $1\sigma$  values for MS. The dashed line and the lined area with lines symbolizes the same but for MSII.

*bulge galaxies.*

- **Ellipticals:** The fraction of bulge formed via *secular induced* disk instabilities is smaller than  $2/3$  of the total bulge mass the *bulge-to-total* ratio is  $B/T > 0.7$ . Galaxies hosting this type of bulges are *elliptical galaxies*.

### 3.3 Results

In this section we present the main findings of this chapter. We first focus on characterizing the properties of pseudobulges and host galaxies at different cosmic times. We then explore the structural properties of pseudobulges predicted for the local universe and compare with available data.

#### 3.3.1 Pseudobulges across cosmic time

In Fig 3.7 we have shown that *secular* DIs are quite frequent at all cosmic times and for a broad range of stellar masses, although we discussed that the amount of mass transferred to the pseudobulge component is very modest for galaxies with  $M_{\text{stellar}} < 10^9 M_{\odot}$ . We thus do not expect a significant pseudobulge component in small galaxies. Using the criteria described at the end of the last section to select pseudobulges, we study the properties of their hosts across cosmic time.

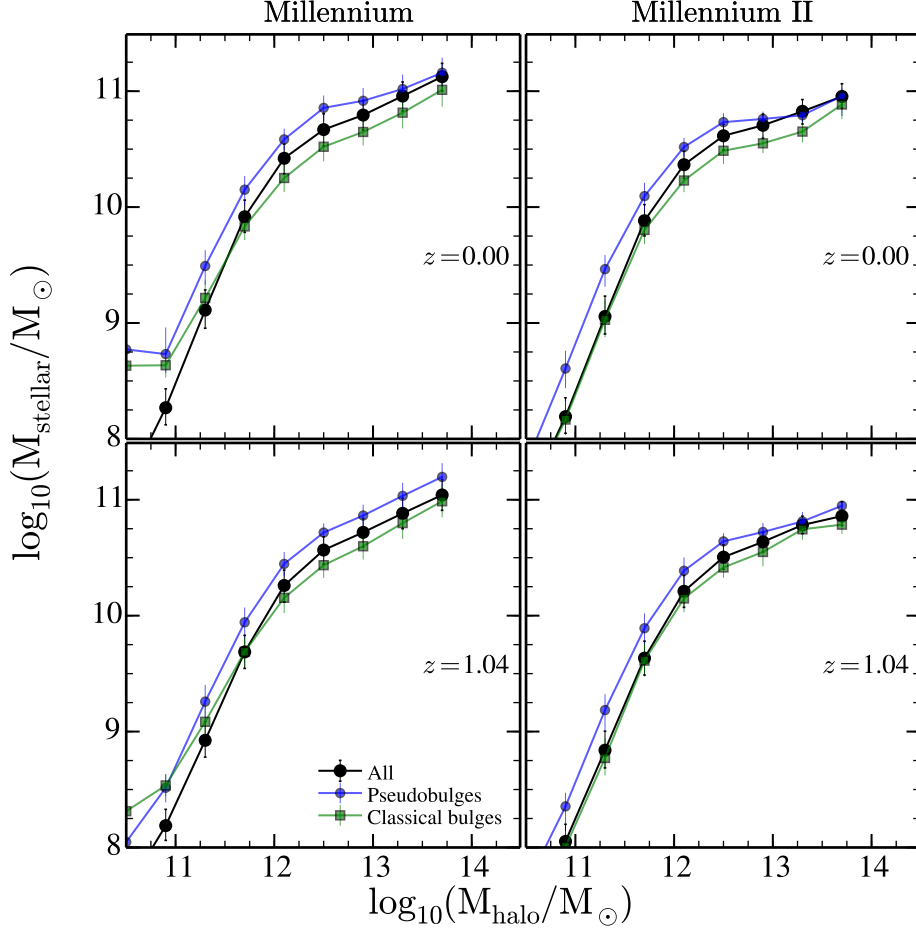


Figure 3.9: Subhalo - Stellar mass relation for pseudobulges (blue) classical bulge (green) and all (black) galaxies in MS (left) and MSII (right) at different redshifts ( $z=0$  (top),  $z=1$  (bottom)). The error bar represents the  $1\sigma$  dispersion. Here we present the relation for central and satellite galaxies. By dividing the galaxies in central and satellites we find the same trend.

In Fig 3.8 we present the typical subhalo and stellar masses of galaxies hosting pseudobulges at different redshifts, for both MS (solid line) and MSII (dashed line). As expected, galaxies hosting pseudobulges are typically more massive than  $M_{\text{stellar}} \sim 10^9 M_{\odot}$ . In particular, we find that pseudobulges tend to be hosted by galaxies in a relatively small range of stellar masses, with values mildly evolving with time. In the MS the typical host stellar mass grows from  $M_{\text{stellar}} \sim 10^{9.5} M_{\odot}$  at  $z > 2.5$  to  $M_{\text{stellar}} \sim 10^{10.3} M_{\odot}$  at  $z=0$ . A similar trend is shown also by MSII, even though smaller masses are reached at higher redshifts. Despite this little difference, the MS and MSII simulations agree within  $1\sigma$  confidence level at any redshift. On the subhalo mass side, pseudobulges are hosted in Milky Way-like subhalos (i.e.  $\sim 10^{11.8} M_{\odot}$ ) at  $z=0$  in both MS and MSII. Moreover, the typical subhalo mass evolution seems to be truncated at  $z \sim 1.25$ , where the increasing trend exhibited from  $M_{\text{halo}} \sim 10^{11.4} M_{\odot}$  at  $z=4$  up to  $\sim 10^{11.9} M_{\odot}$  at  $z=1.5$ , changes into a decreasing tendency. We interpret this as a consequence of the hierarchical growth of structures: pseudobulge galaxies are less likely to be hosted by very massive subhalos at low- $z$ , as these subhalos are closely related to major mergers events who deeply impact the host galaxy structure erasing any secular evolution characteristic.

To understand if pseudobulge are hosted in peculiar type of galaxies with respect to the standard population, in Fig 3.9 we show the  $M_{\text{halo}} - M_{\text{stellar}}$  plane at different redshifts for MS and MSII (right and left

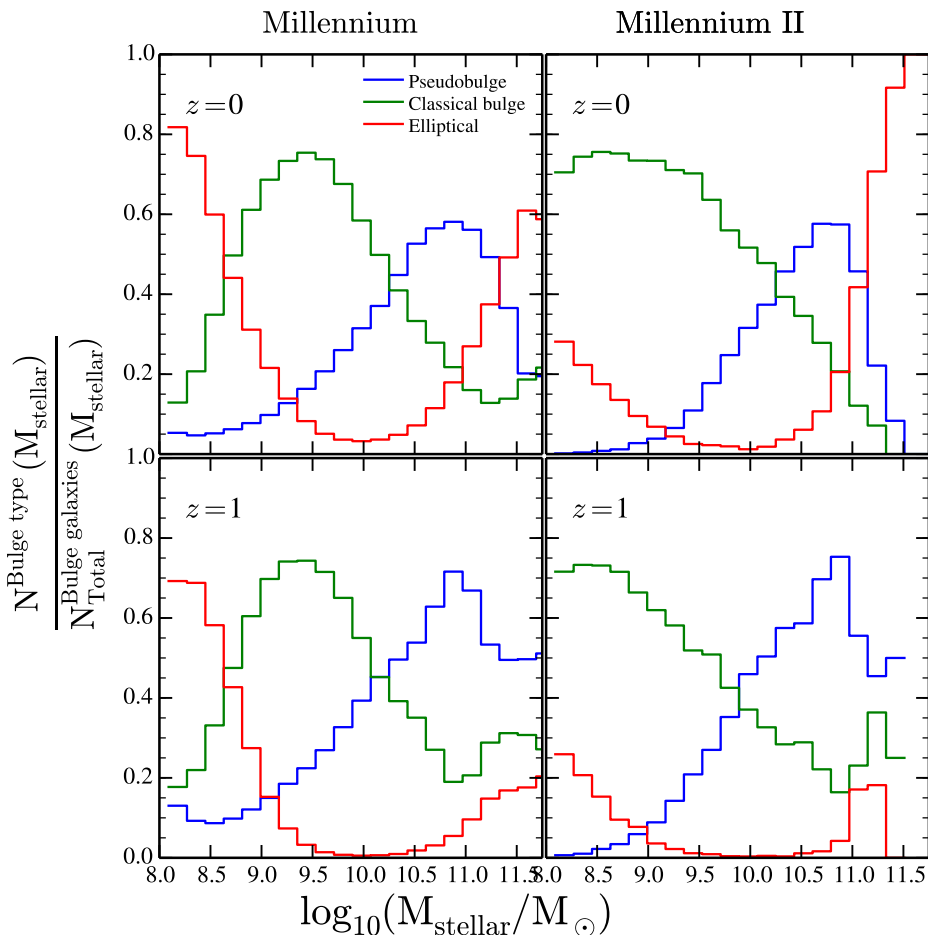


Figure 3.10: Relative contribution of pseudobulge (blue), classical bulge (green) and elliptical (red) galaxies in the bulge galaxy population. Upper and lower rows represent the results at  $z = 0$  and  $1$ , respectively. In the left the results for MS and in the right for MSII.

respectively)<sup>6</sup>. As can be seen in the relation, galaxies which display a dominant pseudobulge structure (blue dots) are systematically above the galaxy median relation (black dots) at any redshift, i.e., at fixed subhalo mass, pseudobulge structures are hosted by galaxies more massive than the median population. On the contrary, when we place the classical bulge galaxies (green dots) on the plane, it is evident that they populate a different region. While for  $M_{\text{halo}} < 10^{12} M_{\odot}$  classical bulges lie on the median relation, in the most massive subhalos ( $M_{\text{halo}} > 10^{12} M_{\odot}$ ) their host galaxies are characterized by systematically smaller stellar masses (notice that the results for the range  $M_{\text{halo}} < 10^{11} M_{\odot}$  suffer of low-resolution statistics in the case of the MS). As we will see later in Section 3.3.2, pseudobulges are typically hosted by star-forming galaxies, while classical bulges tend to live in more quenched systems, explaining why pseudobulges tend to have higher stellar content than classical bulges, at a fixed subhalo mass.

To see the relative importance of different classes of galaxies, in Fig 3.10 we show the relative contribution of pseudobulges (blue), classical bulges (green) and elliptical (red) galaxies to the total population of galaxies with a bulge (i.e.  $B/T > 0.01$ ), at different stellar masses. Results at  $z = 0$  and  $z = 1$  are shown respectively in first and second row. At  $z = 1$  both MS and MSII show that pseudobulges are the main type of galaxies at large stellar masses (i.e.  $M_{\text{stellar}} > 10^{10.5} M_{\odot}$ ) while classical bulges and ellipticals are the main ones for  $M_{\text{stellar}} < 10^{10.5} M_{\odot}$ . While at low masses there is little evolution between  $z = 1$  and  $z = 0$ , at high masses we find that, by  $z = 0$ , ellipticals dominate the galaxy population. As previously discussed, this is a result of the hierarchical growth of structures: pseudobulges hosted in the most massive

<sup>6</sup>We have done the same plot dividing between central and satellite galaxies. No difference with the Fig 3.9 has been found.

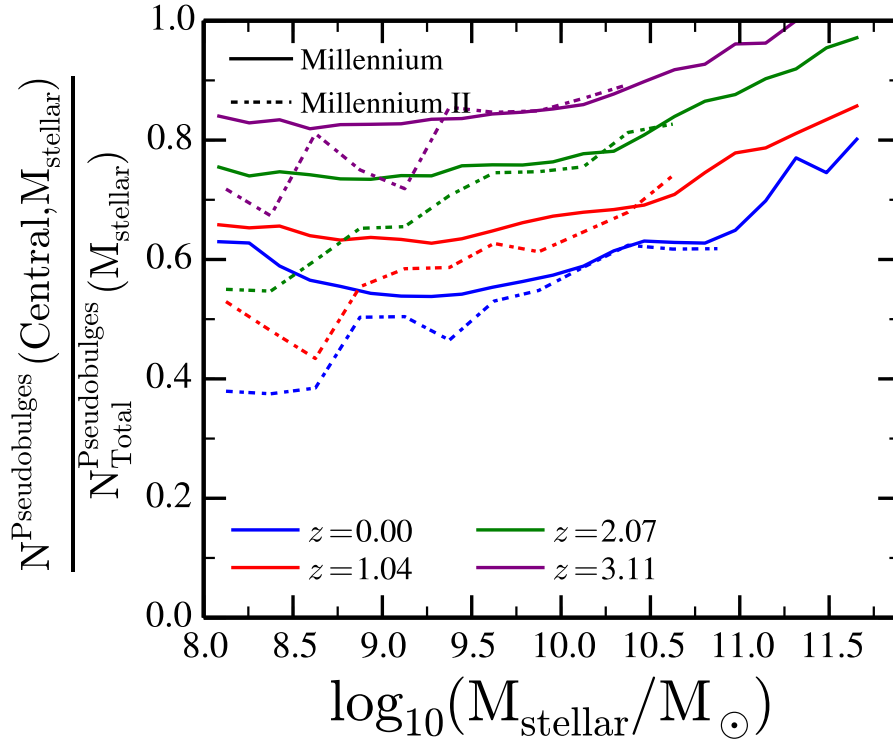


Figure 3.11: Fraction of pseudobulge galaxies that are centrals of their *friend-of-friend* halo. Solid and dashed lines represent the results for MS and MSII, respectively. Pseudobulge galaxies at different redshift were selected following the definition presented in Section 3.2.2. For MSII it is plotted until the stellar masses in which the simulation predicts, at that redshift, a total number of objects larger than 10.

galaxies at high- $z$  are subsequently destroyed by major mergers which turn galaxies into pure bulges (see example  $f$  of Fig 3.17). Additional support to this picture can be gained by studying the fraction of pseudobulge galaxies who are *centrals* of their FoF group, as a function of redshift. Fig 3.11 shows that  $\sim 80\%$  of pseudobulges at  $z = 3$  were centrals (with larger fractions reached for more massive galaxies stellar mass), and the percentage drops to  $\sim 60\%$  at  $z = 0$ . This points out that pseudobulge galaxies are less likely to be hosted in the central subhalo of their FOF at low  $z$ , independently of their stellar mass. This trend is well followed by both MS and MSII at high stellar masses, while at small ones MSII predicts slightly larger fractions of satellite pseudobulges. Note that this difference is consequence of the MS subhalo mass resolution issues at  $M_{\text{stellar}} < 10^9 M_{\odot}$ . Therefore, we rely in the MSII predictions whose limitation is at  $M_{\text{stellar}} \sim 10^8 M_{\odot}$ .

Finally, in Fig 3.12 we present the bar fraction  $f_{\text{bar}}$  as a function of redshift and stellar mass for the two simulations. We have defined  $f_{\text{bar}}$  as the number of galaxies hosting a pseudobulge over the total number of spiral galaxies ( $B/T < 0.7$ ) in a given bin of mass and redshift. The fraction of pseudobulge in spiral galaxies has a peak at  $M_{\text{stellar}} \sim 10^{10.5} M_{\odot}$  with a sharp cut-off towards low stellar masses. This trend is broadly in agreement with the observational results of Cervantes Sodi et al. (2015) and Gavazzi et al. (2015). The fact that our predictions lie above is reassuring, as we regard our fraction as upper limits, given that a fraction of galaxies that we tag as pseudobulges might not have a clear detectable bar.



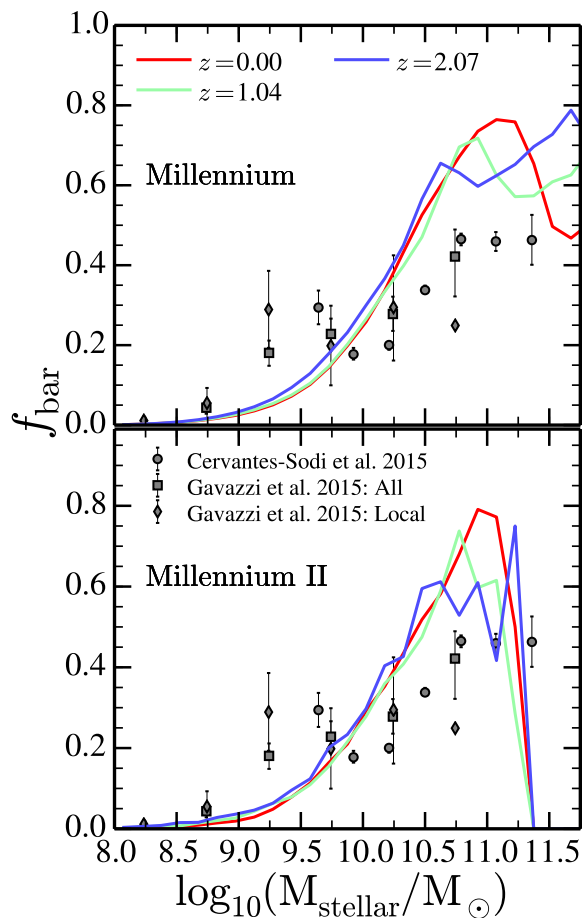


Figure 3.12: Bar fraction  $f_{\text{bar}}$  in the MS (top) and MSII (bottom). We define  $f_{\text{bar}}$  as the number of galaxies hosting a pseudobulge (bar, boxy/peanut or disc-like structure) over the total spiral galaxies population ( $B/T < 0.7$ ) in a given mass bin and redshift. Colors encode different redshifts. We compare this with recent observation by [Cervantes Sodi et al. \(2015\)](#) and [Gavazzi et al. \(2015\)](#).

### 3.3.2 Pseudobulges and their hosts in the local universe

In this last part we analyze the properties of  $z = 0$  *pseudobulge galaxies* such as star formation and stellar age (Section 3.3.2), structural properties (Section 3.3.2), redshift of the last major/minor interaction and pseudobulge structure formation (Section 3.3.2).

#### Star formation in pseudobulge galaxies

In the previous section we have seen that, at fixed host subhalo mass, pseudobulges tend to live in galaxies more massive than what predicted by the median  $M_{\text{halo}}-M_{\text{stellar}}$  relation. Pseudobulge galaxies thus seem to not suffer from the same quenching mechanisms that other galaxies experience (e.g., AGN feedback) and that cause massive galaxies to be inefficient star forming engines. When looking at the star formation properties of local pseudobulges predicted by the model, we find indeed that galaxies hosting a pseudobulge are efficient in producing stars. We show this in Fig 3.13, where pseudobulges and classical bulges predicted by the MS are shown in the  $\text{Sfr}-M_{\text{stellar}}$  plane. To guide the reader we have added in dashed black line the *main sequence*<sup>7</sup> of star formation from [Cano-Díaz et al. \(2016\)](#). At  $M_{\text{stellar}} < 10^{9.5} M_{\odot}$  the hosts of both classical and pseudobulges follow the main sequence. At higher stellar masses, however

<sup>7</sup>The main sequence is defined as the relation of actively star-forming galaxies which relates their star formation rate and their stellar mass ([Brinchmann et al., 2004](#); [Noeske et al., 2007](#); [Cano-Díaz et al., 2016](#))

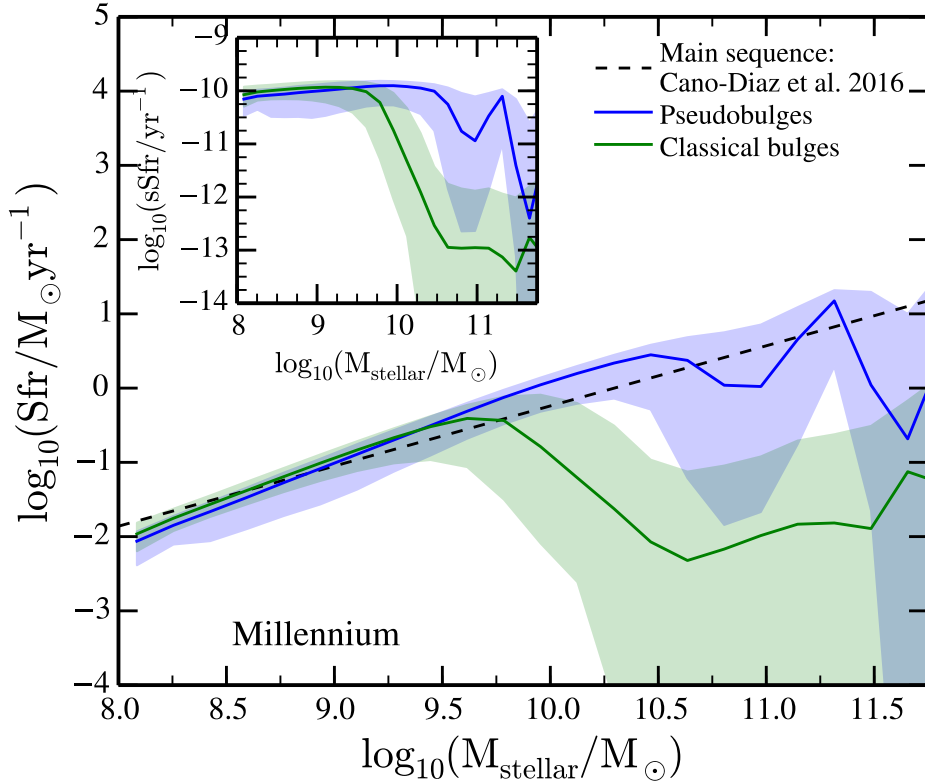


Figure 3.13: Star formation rate (Sfr) -  $M_{\text{stellar}}$  plane for  $z=0$  pseudobulges (blue) and classical bulges (green) galaxies predicted by MS. The solid lines represent the median of the distribution while the shaded area represents the  $1\sigma$  dispersion. Black dashed line is the main sequence fit of [Cano-Díaz et al. \(2016\)](#). The inset plot represents the same but for the plane specific star formation rate (sSfr) -  $M_{\text{stellar}}$ .

( $M_{\text{stellar}} > 10^{9.5}M_{\odot}$ ), pseudobulges and classical bulges follow two different trends. While the former population remains on the main sequence and only starts deviating for very massive systems, classical bulges present a clear shift in their relation, falling in the *red sequence* region with  $\sim 2$  dex of lower star formation than pseudobulges. In the inset of Fig 3.13 we show the plane specific star formation rate (sSFR) -  $M_{\text{stellar}}$ . As we can see, the trend is similar to the Sfr -  $M_{\text{stellar}}$  one.

Fig 3.14 shows instead the mass-weighted age of the stellar population in pseudobulge and classical bulge galaxies. While the typical age of stars in pseudobulge galaxies seems shows a very weak dependence with stellar mass, classical bulges hosted in massive galaxies  $M_{\text{stellar}} > 10^{10.5}M_{\odot}$  are significantly older. At low masses (i.e.  $M_{\text{stellar}} < 10^{9.5}M_{\odot}$ ), instead, classical bulges are hosted by galaxies with slightly younger average stellar populations. This is due to the different merger history of classical bulges and pseudobulges as we will show in Fig 3.16. In this mass range, in fact, almost all the classical bulges experienced at least one minor (major) mergers at  $z \sim 0.5$  which rejuvenated the galaxy population via SF burst. On contrary, pseudobulges did not suffered any (major) minor merger and their stellar population only grew via internal star formation. We remark here that also classical bulges in massive galaxies experience mergers at recent times, but, as discussed above, star formation in these galaxies is quenched by AGN feedback and the cold gas fraction in these massive systems is lower. The MSII gives very similar results, do not shown here to avoid redundancy.

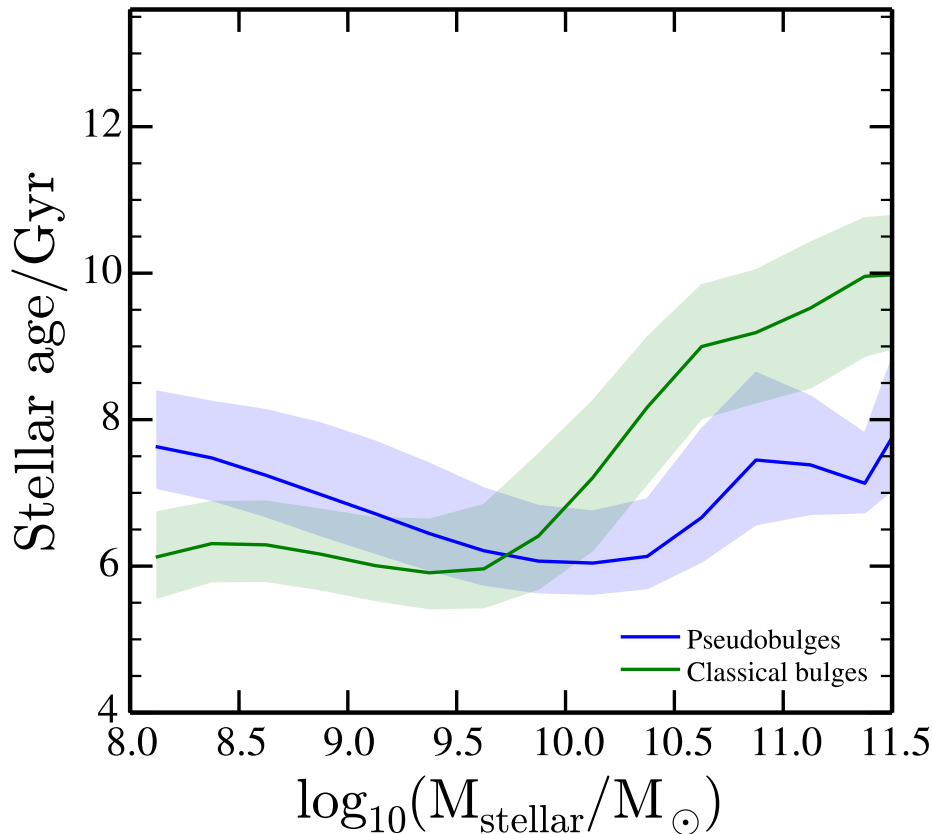


Figure 3.14: Stellar population age (mass weighted age) of  $z = 0$  pseudobulge (blue) and classical bulge (green) galaxies predicted by MS simulation (MSII display similar behavior). The solid lines represent the median of the distribution while the shaded area represents the  $1\sigma$  dispersion.

### Structural properties of pseudobulge galaxies

We now move to the analysis of the structural properties of the pseudobulges that our model predicts and compare our predictions with the observational results of [Gadotti \(2009\)](#). In that work Gadotti studied bulge properties, such as B/T ratios, bulge masses and scale length parameters, for a sample of 963 galaxies with masses  $10^{10} \lesssim M_{\text{stellar}} \lesssim 10^{11.5} M_{\odot}$  and redshift range  $0.02 \leq z \leq 0.07$ . The sample was divided in disk galaxies and ellipticals. The former ones were further sub-divided in galaxies hosting a pseudobulge, classical bulge or bulgeless. To compare with the observations, we generated a galaxy sample using the MS which reproduces the exact stellar mass selection of [Gadotti \(2009\)](#), but with a much larger number of galaxies (about a factor of ten). We could not do the same exercise with the MSII, as the smaller box does not allow to properly sample the most massive galaxies. The definition of pseudobulges, classical bulges and ellipticals is the one used in this work, as presented at the end of subsection [3.2.2](#).

Results for pseudobulge, classical bulge and elliptical galaxies in MS are presented in [Fig 3.15](#). We show the distribution of disk scale length ( $h$ ) as a function of the stellar mass (top left), the distribution of the bulge effective radius ( $R_e$ ) versus stellar mass (top right), the B/T distribution and the effective bulge radius as a function of the bulge mass (bottom left and right, respectively). Overall, the structural parameters  $h$  and  $R_e$  for pseudobulges, classical bulges and elliptical galaxies are reasonably well reproduced by the model. Nevertheless, classical bulges show  $h$  values which are slightly offset, i.e. disks are larger than the observed one, and the number of massive disks is also larger than observed. Regarding bulge to total ratios, pseudobulges broadly follow the distribution found by [Gadotti \(2009\)](#), even though we seem to lack pseudobulges with very small B/T ratios. Other studies, however, found

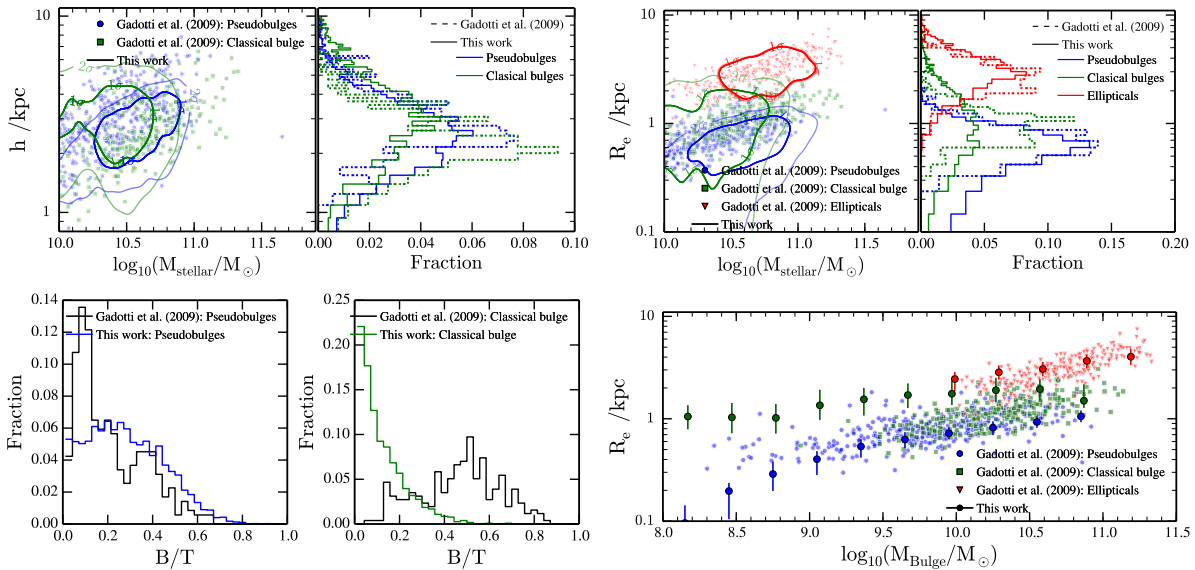


Figure 3.15: **Upper left:** In the left panel the distribution of disk scale length ( $h$ ) as a function of the stellar mass ( $M_{\text{stellar}}$ ) for pseudobulges (blue points) and classical bulges (green squares) galaxies. The contours represent the  $1$  and  $2\sigma$  dispersion of the relation  $h - M_{\text{stellar}}$  predicted in this work in the MS simulation. In the right panel we represent the  $h$  distribution for pseudobulges (blue) and classical bulges (green) galaxies. Dashed and solid histogram display respectively the observed and predicted distribution. **Upper right:** In the left, the distribution of bulge effective radius ( $R_e$ ) as a function of the stellar mass for pseudobulges (blue points), classical bulges (green squares) and ellipticals (red triangles) galaxies. The contours represent the  $1$  and  $2\sigma$  dispersion of the relation  $R_e - M_{\text{stellar}}$  predicted in this work. In the right, the  $h$  distribution for pseudobulges (blue), classical bulges (green) and ellipticals (red) galaxies. Dashed histogram display the observed distribution while the solid one the predicted. **Lower left:** In the left and right, the distribution of *bulge-to-total* ratio  $B/T$  for pseudobulges and classical bulges galaxies. In black the observed distribution and in blue and green the predicted one for pseudobulges (blue) and classical bulges (green) galaxies. **Lower right:** Relation of bulge mass ( $M_{\text{bulge}}$ ) vs effective radius of the bulge ( $R_e$ ) for pseudobulges (blue), classical bulges (green) and ellipticals (red) galaxies. The points represent the median of each sample while the error bars the  $1\sigma$  dispersion.

that most pseudobulges are hosted by galaxies with  $B/T > 0.2$  (see Fisher and Drory, 2008a, 2010), which is consistent with our results. On the other hand, the  $B/T$  distribution for hosts of classical bulges peaks at  $\sim 0.1$  with a fast decrease towards large  $B/T$  values. Once again, this points towards typically too-massive stellar disks being hosted by galaxies with classical bulges in our model. A population of overly-large disks was already present in the Henriques et al. (2015) version of the model. This could be due to the delayed growth of black holes hosted in classical bulges: as these objects accreted most of their mass at low redshift, their associated AGN feedback has been very modest at high- $z$ , allowing for a significant and prolonged growth of the stellar disc. An improved version of the black hole growth model and its impact on galaxy morphology is going to be presented in a following paper (Izquierdo-Villalba et al., 2020). Finally, the model reproduces well the typical values of  $R_e$  found by Gadotti (2009) as a function of bulge mass for pseudobulges, classical bulges and ellipticals, even though classical bulges lie slightly above the observations. Despite this, we can confirm the Gadotti (2009) findings: classical bulges appear to be offset in the mass-to-size relation with respect to ellipticals, pointing out to fundamental structural differences, and that they are not simply ellipticals surrounded by disks. Indeed, bulge formation is an extremely complex phenomenon, which is shaped by both mergers and secular processes. As we explore in the next section, while in pseudobulge galaxies the process that dominates galaxy evolution is *secular* DI and in classical bulges is minor mergers, both population experience the two bulge formation mechanisms during their complex cosmological growth.

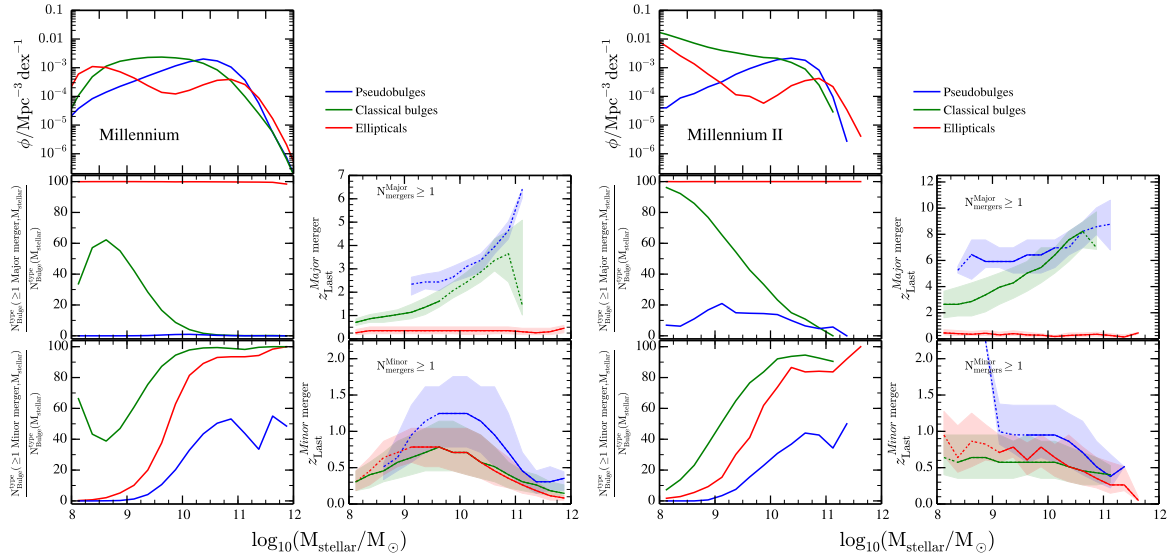


Figure 3.16: **Left panels:** *First row:* Stellar mass function of pseudobulges (blue), classical bulges (green) and ellipticals (red) galaxies at  $z=0$  in the MS simulation. *Second row:* Percentage of  $z=0$  pseudobulges, classical bulges and ellipticals galaxies that experience at least one major merger (left). From those ones we have presented the redshift in which the last one took place (right). *Third row:* Percentage of  $z=0$  pseudobulges, classical bulges and ellipticals galaxies that experience at least one minor merger (left). From those ones we have presented the redshift in which the last one took place. **Right panels:** The same as the left ones but for the MSII simulation. In all the plots, the shaded area represents the  $1\sigma$  dispersion of the distribution and dotted lines represents the regions in which the percentage of having suffered a minor/major merger is less than 10%.

### Merger history of galaxies

The main assumptions of our model for bar and pseudobulge formation, is that those are linked to the secular growth of disks, while violent events, such as mergers and their consequent starbursts are responsible for the growth of classical bulges. We expect the merger history of galaxies hosting pseudobulges to be different from the one of elliptical and classical bulge hosts. In the remaining of this section we explore the (major/minor) merger history of  $z=0$  pseudobulge, classical bulges and ellipticals galaxies and we present some archetypal examples of their merger trees. Finally, we explore the imprints that the galaxy interaction history leaves in the pseudobulge structure.

In the second row of Fig 3.16 it is presented, per stellar mass bin, the percentage of  $z=0$  pseudobulges (blue), classical bulges (green) and ellipticals (red) galaxies that experience at least one major merger (left plot) and from those ones the redshift in which the last major merger took place (right plot). The third row shows the same but for minor mergers. The left panels show the results for the MS and the right ones for the MSII. To guide the reader we have added the  $z=0$  stellar mass function of pseudobulges, classical bulges and ellipticals. As we can see, all elliptical galaxies experienced at least one major merger, being the last one at  $z < 0.5$ . On contrary, pseudobulges display a much more quiet major merger history. Only 0.5% of them experienced one and only at very high redshift, being this higher for more massive galaxies: from  $z \sim 2$  at  $M_{\text{stellar}} = 10^9 M_{\odot}$  up to  $z \sim 6$  at  $10^{11} M_{\odot}$ . The MSII pseudobulges present a similar behaviour: for this simulation, the percentage of pseudobulges which underwent a merger is larger ( $\sim 10\%$ ), because of the larger number of small galaxies resolved, and most of these mergers took place at very high redshifts. Regarding classical bulges, we can see that the ones hosted by galaxies with  $M_{\text{stellar}} > 10^{10} M_{\odot}$  follow a similar trend that pseudobulges, i.e a quiet merger history. On the other hand, at  $M_{\text{stellar}} < 10^{10} M_{\odot}$  the majority of classical bulge galaxies suffered a recent major merger

at  $z \lesssim 2$ . Notice that the drop in percentage presented in MS at  $M_{\text{stellar}} < 10^{8.5} M_{\odot}$  is mainly due to resolution. Actually, MSII predicts that the  $\sim 100\%$  of those galaxies experienced at least one major merger.

Regarding minor mergers, all classes of bulges display a similar trend: the fraction of galaxies that experienced at least one minor merger increases with stellar mass, although this fraction is never above 50% for pseudobulges. Also, for both the MS and the MSII the typical redshift of the last minor interaction decreases with increasing stellar mass. For classical bulges and ellipticals, however, the typical redshift of the last minor merger is lower than for the pseudobulge population. However, the agreement of classical bulges and ellipticals between MS and MSII decreases when we study galaxies at  $M_{\text{stellar}} < 10^9 M_{\odot}$ . While MS predicts a decreasing trend in the redshift distribution, MSII finds a flattening at  $z \sim 0.5$ . Again, this is due to resolution effects which affect the MS in that stellar mass range.

In order to illustrate the different build-up of pseudobulges, in Fig 3.17 *a* and *b* we present two typical examples of  $z = 0$  pseudobulges mergers trees in the Millennium simulation. Examples of classical bulges and ellipticals can be seen in *c-d* and *e-f*, respectively. We have selected galaxies with  $z = 0$  stellar mass  $\sim 10^{10.5} M_{\odot}$ , i.e the peak of  $z = 0$  pseudobulges stellar mass function (see Fig 3.16). In the plot we represent the stellar and bulge components (empty and filled circles respectively). The size of the circles is proportional to mass. The color of the symbols represents the fraction of bulge mass coming from DI *secular evolution*. In each merging branch we have added the mass ratio of the merger. Ticks with  $m_R$  corresponds to major/minor merger while ticks with  $m_R^{\text{sth}}$  refers to *smooth accretion*. Merging branch without any  $m_R$  value means that the galaxy was disrupted by environmental processes before the merger, and its mass added in the *Intra-Cluster Medium* (most of these galaxies are close to  $M_{\text{stellar}} \sim 10^7 M_{\odot}$ ).

As it was discussed above, pseudobulges have a very *quiet* merger history. For instance, the first pseudobulge merger tree (*example a*) just displays one *smooth accretion* at  $z \sim 0.9$  with  $m_R = 6 \times 10^{-3}$ . No other interaction takes place in its cosmological evolution. The pseudobulge structure appears after the *smooth accretion* as a consequence of a DI *secular evolution* causally disconnected from the satellite interaction. Therefore, the pseudobulge evolved through *internal secular evolution* represented by Case 1 and Case 2 in Fig 3.5. In the case of the second pseudobulge galaxy (*example b*), its bulge formation history is slightly more complicated, resulting from a combination of Case 4 and Case 1 from in Fig 3.5. The galaxy developed a small bulge component as a consequence of a minor merger with  $m_R = 3.4 \times 10^{-2}$ . After  $\sim 1$  Gyr from the merger (at  $z \sim 0.7$ ), an important disk instability took place, blurring the classical bulge structure and resulting in the birth of a prominent pseudobulge.

Regarding classical bulges and ellipticals galaxies, we can see that all the merger trees (*example c,d,e,f*) are much more complicated than in the previous two cases. For instance, in the *example c* it is presented an archetype of classical bulge build-up (Case 4 Fig 3.5): the bulge structure was generated by a minor merger at  $z \sim 0.7$  and strengthened by a more recent minor merger ( $z \sim 0.3$ ). No signatures or secular evolution in the bulge can be seen. *Example d* represents another type of classical bulge galaxy evolution. In this case, the bulge structure was not completely build-up by mergers but by a combination of DI and minor mergers. The bulge was born via DI *secular evolution* at  $z \sim 2$  but at  $z \sim 1.5$  a DI *merger-induced* (Case 5 in Fig 3.5), consequence of a *smooth accretion*, triggered the birth of a classical bulge component. The galaxy started to evolve and via secular DIs made the pseudobulge structure grow again. Nevertheless, the constant minor mergers interactions that the galaxy experienced at  $z = 0.4, 0.3$  and  $0.2$  led to the growth of a prominent classical bulge, where the pseudobulge component is negligible ( $< 4\%$  of  $M_{\text{Bulge}}$  at  $z = 0$ ). Finally, *examples e* and *f* display some pathways of elliptical galaxy formation. In *example e* the galaxy started as a classical bulge galaxy, with the bulge component being due to several minor mergers, while in *example e* the galaxy hosted a prominent pseudobulge at high  $z$ . In both cases, however, a major merger took place at  $z \sim 0.5$ , which erased the previous galaxy morphology and formed a pure elliptical galaxy.

Finally, despite having quiet merger history, pseudobulge galaxies still have some minor/major mer-



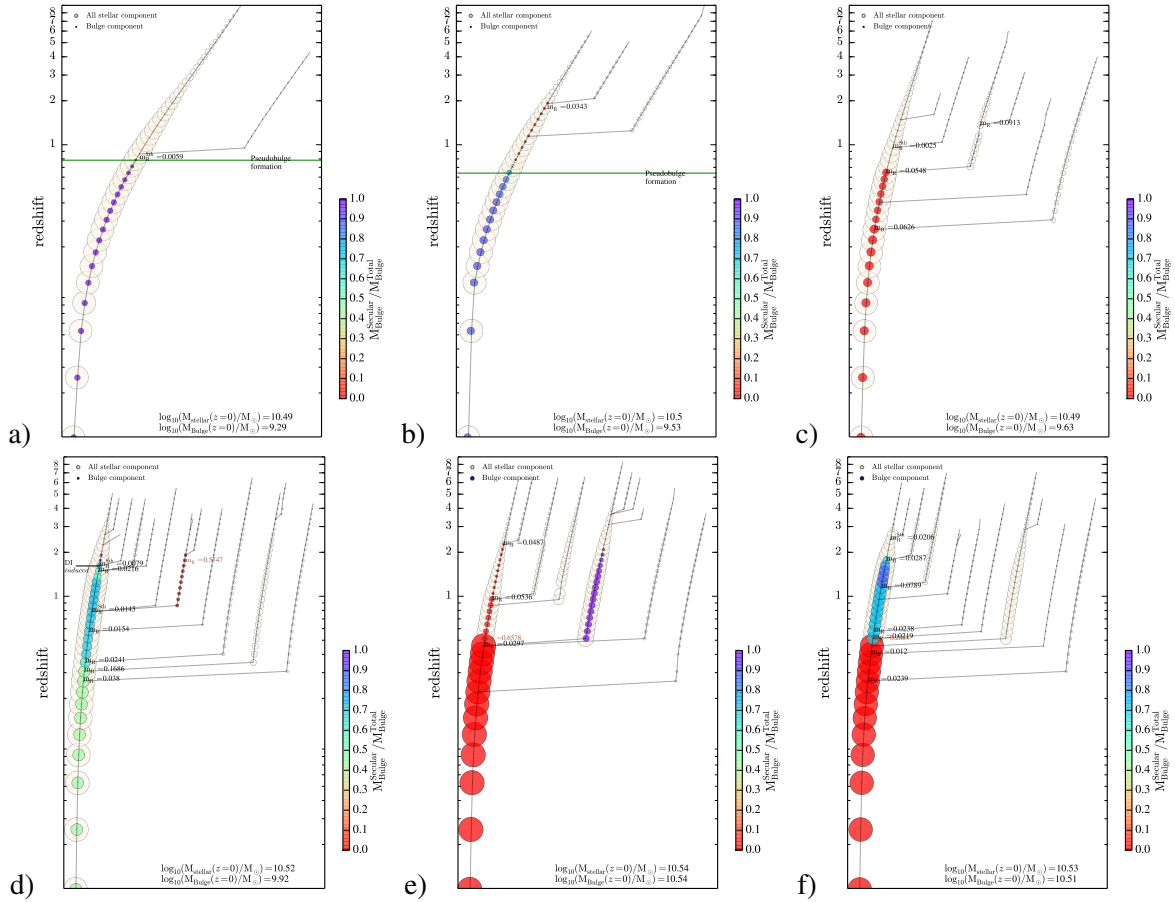


Figure 3.17: Examples of the MS mergers trees for pseudobulges (examples *a* and *b*), classical bulges (examples *c* and *d*) and ellipticals (examples *e* and *f*). We have selected the galaxies with  $M_{\text{stellar}} \sim 10^{10.5} M_{\odot}$ . In the plot we represent the stellar and bulge components (empty and filled circles respectively). The size of the circles is proportional to its respective mass. The bulge color represents the fraction of bulge mass coming from *DI secular evolution*. In each merging branch we have added the merger ratio. Ticks with  $m_R$  corresponds to major/minor merger while ticks with  $m_R^{\text{Sth}}$  refers to *smooth accretion*. Merging branch without any  $m_R$  value means that the galaxy was disrupted by environmental processes before the merger. Most of those galaxies are the ones close to  $M_{\text{stellar}} \sim 10^7 M_{\odot}$ . In this cases, the satellite stellar mass was added in the *Intra-Cluster Medium (ICM)*.

ger interactions which can provide a classical component to the final bulge. In particular, the 31% and 32.4% of MS and MSII pseudobulge galaxies host a classical component, contributing typically with the  $\sim 7\%$  of the whole bulge mass. To support the idea of last minor mergers being the main responsible for the strengthening of the classical bulge structure in pseudobulge galaxies at  $z = 0$ , we define the formation redshift of the classical component (i.e.  $z_{\text{formation}}^{\text{Cb structure}}$ ) as the moment in which it reached the 70%<sup>8</sup> of its final mass at  $z = 0$ . As shown in the lower panel of Fig 3.18, the formation time of this component follows the same trend of  $z_{\text{Last merger}}^{\text{Minor}}$  presented in Fig 3.16. The last merger is thus responsible for the building (or strengthening) of the classical bulge structure in  $z = 0$  pseudobulge galaxies. We highlight that, in the  $10^9 - 10^{10} M_{\odot}$  mass range, MSII predicts slightly lower time-formation values than MS. This is because MSII galaxies within this specific mass range are affected 5 times more frequently by *merger-induced DIs* than MS (taking place at  $z \sim 1$ , see Fig 3.7).

Regarding the pseudobulge structure, in Fig 3.18 we present the distribution of formation times,  $z_{\text{formation}}^{\text{Pb structure}}$ , as a function of stellar mass. This value has been defined as the moment in which the pseudob-

<sup>8</sup>We have checked that the results do not suffer significant changes when we assume a value between 50% - 90%

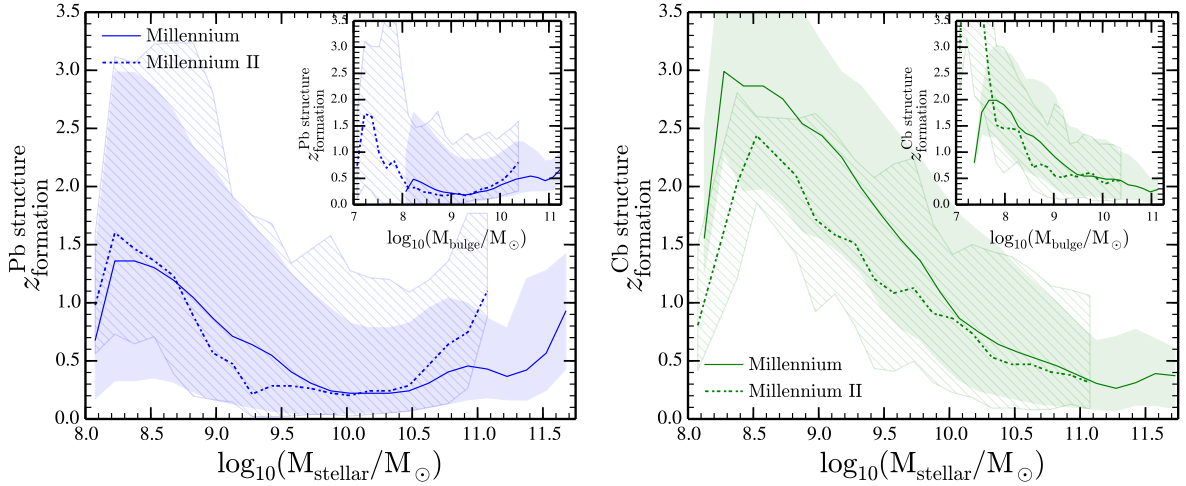


Figure 3.18: **Upper panel:** Formation time of pseudobulge structure as a function of stellar mass ( $M_{\text{stellar}}$ ) in pseudobulge galaxies. Solid and dashed line represent respectively the median relation for MS and MSII. The shaded and lined areas represent the  $1\sigma$  dispersion value. In the insert plot we present the same but as a function of the bulge mass ( $M_{\text{bulge}}$ ) **Lower panel:** Formation time of the classical component as a function of stellar mass ( $M_{\text{stellar}}$ ) for pseudobulge galaxies. In the insert plot we present the same but as a function of the bulge mass ( $M_{\text{bulge}}$ ). Line styles represent the same as the upper plot.

ulge component reached the  $2/3$ <sup>9</sup> of its  $z=0$  total bulge mass. As we can see, while pseudobulge galaxies with  $M_{\text{stellar}} < 10^9 M_{\odot}$  formed their pseudobulge structure mainly at  $z \sim 1.5$ , more massive galaxies (i.e.,  $M_{\text{stellar}} > 10^9 M_{\odot}$ ) formed it in the low- $z$  universe, although the scatter is larger. Interestingly, this trend is broken for most massive pseudobulge galaxies ( $M_{\text{stellar}} > 10^{10.5} M_{\odot}$ ) where the  $z_{\text{formation}}^{\text{Pb structure}}$  rises again up to  $z \sim 0.5-1.0$ . We interpret this turn-over as an effect of the star-formation rate damping induced by AGN feedback in these galaxies. As a consequence of feedback, the DIs frequency is severely decreased and pseudobulge formation is suppressed in many massive galaxies at low- $z$ . The sSfr distribution (Fig 3.13) supported this scenario, by showing a clear drop at  $M_{\text{stellar}} > 10^{10.5} M_{\odot}$ . The insert plot in Fig 3.18 shows the same distribution but for fixed bulge mass. As we can see, the fixed-bulge trend is similar to the previous one: small-bulge galaxies formed their pseudobulge component at higher redshifts with respect to more massive-bulge ones. Our findings of pseudobulge formation at intermediate redshifts are supported by a recent work of Gadotti et al. (2015) who found that the bar in the Virgo galaxy NGC 4371 formed a pseudobulge at  $z \sim 1.8$  (with an uncertainty of  $\sim 1$  Gyr).

### 3.4 Summary and conclusions

In this chapter we have studied the cosmological build-up of pseudobulges using the last public version of the L-Galaxies semi-analytical model (SAM, Henriques et al., 2015). Taking advantage that L-Galaxies can be run on top the merger trees of both the Millennium and the Millennium II N-body simulations, we have been able to study the formation of pseudobulge structures and properties of their hosts across a wide range of stellar masses ( $10^8 - 10^{11.5} M_{\odot}$ ). In order to reach a reasonable convergence between the MS and MSII in terms of distribution of galaxy morphology and number density of merger events across cosmic time, we first had to introduce some small modifications to the parameters that distinguish between major and minor mergers and that set the conditions for disk instability events. Moreover, to improve the predictions of the MSII for the morphological distribution of low stellar mass systems ( $M_{\text{stellar}} < 10^{9.5} M_{\odot}$ ), we introduced a new prescription for the interactions in which the binding energy of the satellite galaxy is very small compared to the one of the central galaxy. For these events,

<sup>9</sup>i.e, the moment in which, independently of redshift, the galaxy would be always selected as a pseudobulge galaxy

which we refer to with the term *smooth accretion*, we assume that the stellar core of the satellite gets incorporated by the disk of the central galaxy, being unable to reach its nucleus before being disrupted.

Assuming that pseudobulges can only form and grow via secular evolution (e.g., [Kormendy and Ho, 2013](#)), we have modified the treatment of galaxy disk instabilities (DI), distinguishing between two kinds of events: DI *secular-induced*, which is a consequence of the slow and continuous mass-growth of galaxies, and DI *merger-induced*, linked to the fast growth of disks during galaxy interactions. The former are the events which we assume to lead to long-lasting bar structures and the formation/growth of pseudobulges, while *merger-induced* instabilities contribute, together with mergers, to the growth of classical bulges. Our SAM predicts that merger-induced instabilities have a number density  $\sim 2 - 3$  dex smaller than the DI *secular evolution* at all cosmic epochs, and that it is a secondary channel in the growth of classical bulges, being classical-bulge growth during the merger event the primary channel at all redshifts. On the other hand, *secular-induced* DIs are the most abundant events at any redshift and stellar masses. However, while in galaxies with  $M_{\text{stellar}} = 10^9 - 10^{10} M_{\odot}$  these events are able to substantially contribute to the growth of the bulge, by transferring up  $\sim 10\%$  of the total stellar content to the pseudobulge, in galaxies with  $M_{\text{stellar}} = 10^8 - 10^9 M_{\odot}$  DIs can only lead to a small (sub-percent) transfer of mass from the disk to the pseudobulge. As a consequence, predominant pseudobulge structures are typically present in galaxies in the range  $10^{9.5} < M_{\text{stellar}} < 10^{10} M_{\odot}$ , at high- $z$ , moving to slightly higher values at more recent cosmic times. At  $z = 0$ , in particular, pseudobulges are hosted by galaxies in a very narrow stellar and subhalo mass window,  $10^{10} < M_{\text{stellar}} < 10^{10.5} M_{\odot}$  and  $10^{11.5} < M_{\text{halo}} < 10^{12} M_{\odot}$ , i.e Milky-Way type galaxies. Moreover, while at high- $z$  pseudobulges are the dominant bulge structures in massive galaxies ( $M_{\text{stellar}} > 10^{11} M_{\odot}$ ), they get systematically *depleted* in such massive systems with decreasing redshift. We interpret this as a consequence of the hierarchical growth of galaxies: pseudobulges are less likely to be hosted by very massive systems at late cosmic times, as the assembly of these galaxies is closely linked to numerous merger events which dramatically modify the dynamics of the galaxy, leading to deep morphological transformations.

When looking at the properties of the hosts, we find that pseudobulges are hosted by actively star forming galaxies (in the main sequence of star formation), and with a relatively young stellar population (mass weighted age  $\sim 6 - 8$  Gyr, independently on the host stellar mass). Classical bulges, instead, reside in star forming galaxies only if the host mass is below  $\sim 10^{9.5} M_{\odot}$ , while more massive systems are quenched, or in the process of quenching, and are characterized by an older stellar population.

Tracing the history of galaxies hosting pseudobulges at  $z = 0$ , we found that they are characterized by an extremely-quiet merger history. The Millennium and Millennium II simulations predict, respectively, that only 0.5% and 11% of galaxies with a pseudobulge at  $z = 0$  experienced a major merger, and this took place at very high redshifts  $2 < z < 7$ . Also minor mergers are rare in the history of today's pseudobulge galaxies, with less than 30% of pseudobulges hosts having experienced a minor merger. Because of the minor mergers, however, these galaxies also contain a small classical bulge component ( $\sim 7\%$  of the total bulge mass). The two structures are characterized by different formation times: while the pseudobulge was formed at  $z \lesssim 0.75$ , the classical one did it at  $z \lesssim 1.5$ , the time in which the last minor merger took place.

Finally, we have created mock samples of local pseudobulges and classical bulges, to compare with the observational results of [Gadotti \(2009\)](#), who analyzed the properties of pseudobulges in galaxies above  $\sim 10^{10} M_{\odot}$ . We found that the pseudobulge structural properties predicted by the model are broadly consistent with observations. In particular, we find a good agreement in the effective radii distribution of different classes of bulges. The distribution of *bulge-to-total ratios* for pseudobulges is also consistent with the results of [Gadotti \(2009\)](#), while classical bulges are predicted to be in galaxies with disks larger than observed. These results are quite encouraging and give support to our main underlying assumption that pseudobulge structure can form mainly via secular evolution.

Despite the promising results, more investigation is needed to understand bar and pseudobulge formation in a broad cosmological context. Our simple approach is highly complementary to more sophisticated simulations which try to study the complex dynamical evolution of disk galaxies. More synergy among different theoretical approaches and observations are certainly needed to reach a more clear picture on the different mechanisms that lead to formation of different bulge classes.

## CHAPTER 4

# BARRED GALAXIES IN THE LOCAL UNIVERSE: REVISITING THEIR ANALYTICAL FORMATION FROM A HYDRODYNAMICAL PERSPECTIVE

*“Veo la Comarca, el río Brandivino... Bolsón Cerrado... los cohetes de Gandalf... las luces de la fiesta del árbol. Rosita Coto, bailando. Llevaba cintas en el pelo. Si me hubiera podido casar, habría sido con ella. Sólo con ella. Me alegro de estar contigo, Samsagaz Gamji. Aquí, al final de todas las cosas...”*

El señor de los anillos: El Retorno del Rey.

*“I can see the Shire... the Brandywine River... Bag End... Gandalf's fireworks.. the lights in the Party Tree. Rosie Cotton dancing. She had ribbons in her hair. If ever I was to marry someone, it would've been her. It would've been her. I'm glad to be with you, Samwise Gamgee, here at the end of all things.”*

The Lord of the Rings: The Return of the King.

This Chapter is based on the paper **in preparation**: *Barred galaxies in the local universe: revisiting their analytical formation from a hydrodynamical perspective*. (David Izquierdo-Villalba; Silvia Bonoli; Volker Springel, Yetli Rosas-Guevara; Daniele Spinoso; et al.)

## ABSTRACT

In this chapter we study the performance of the [Efstathiou et al. \(1982\)](#) analytical description of disk instabilities to bar-modes. We made use of a barred and an unbarred galaxy samples extracted from the TNG100 cosmological hydrodynamical simulation. We have found a correlation between the analytical criterion predictions and the actual bar assembly (non-assembly) shown in the TNG100 for the barred (unbarred) galaxies. However, in both samples, we have detected cases where the [Efstathiou et al. \(1982\)](#) criterion of disk instability fails, either claiming disk stability for barred galaxies or disk instability for unbarred (hence stable) disks. We have explored the galaxy and subhalo properties of these events. The main differences between barred and unbarred galaxies in which the analytical prescription claims disk stability reside in the subhalo circular velocity and the stellar-to-halo mass ratio within the disk scale length, being these two quantities larger in the barred sample. On the contrary, the differences between barred and unbarred samples identified as unstable by the criterion reside in a larger subhalo circular velocity and stellar disk spin displayed by barred galaxies. Regarding these results, we propose an extra criterion based on the subhalo circular velocity, stellar disk spin and stellar-to-halo ratio to be applied on top of the [Efstathiou et al. \(1982\)](#) one. We have shown that the combination of the old and new criterion improves the detectability of bar structures and reduces both the contamination of fake barred galaxies and the number of undetected bar formation events.

## 4.1 Introduction

Nowadays we know that bars are a common structure of galaxies in the local Universe where nearly 60% of the disk dominated galaxies host one (Knapen, 1999; Eskridge et al., 2000; Grosbøl et al., 2004; Menéndez-Delmestre et al., 2007; Barazza et al., 2008a). However, the number of barred galaxies is not constant with time but seems to decrease towards higher redshifts (Jogee et al., 2004; Elmegreen et al., 2004; Marinova and Jogee, 2007; Sheth et al., 2008). Bars are believed to be important structures concerning the galaxy secular evolution. Their capability of redistributing the galaxy angular momentum leads to gas inflows towards the galaxy nuclear parts, triggering star formation episodes which ultimately prompt the formation of a pseudobulge (Lynden-Bell and Kalnajs, 1972; Tremaine and Weinberg, 1984; Kormendy, 1993; van Albada and Roberts, 1981; Schwarzschild, 1981; Sakamoto et al., 1999). Besides, it has been shown that bar evolution is accompanied by a secular *buckling instability*, causing the bar to acquire large motions normal to the galactic plane, giving the bar a *boxy shape* (Combes et al., 1990a; Raha et al., 1991; Debattista et al., 2004; Martinez-Valpuesta et al., 2006; Saha et al., 2013) whose kinematics and structural properties place them among the pseudobulge class (Debattista et al., 2004, 2005).

Current simulations are able to track the evolution of stellar disks (Navarro and Benz, 1991; Navarro and Steinmetz, 2000), but it remains unclear why certain galaxies end up developing a bar structure and some others, apparently similar, do not. One of the pioneer works addressing the complex matter of bar formation was Efstathiou et al. (1982) which explored the global stability of cold stellar disks (i.e. when most of the kinetic energy of the disk is in rotational motion) by performing a set of 2D N-body simulations. Interestingly, the authors found a simple analytical prescription to determine the stability against bar formation:

$$\epsilon = \frac{V_{\max}}{(GM_{\text{disk}}/R_{\star}^{sl})^{1/2}} \quad (4.1)$$

where  $G$  is the gravitational constant,  $V_{\max}$  is the maximum rotational velocity,  $R_{\star}^{sl}$  is the scale length of disk and  $M_{\text{disk}}$  its total mass. The simulations showed that the onset of the bar instability requires a threshold,  $\epsilon_{\text{DI}}$ , equal to 1.1. In this way, at  $\epsilon \leq \epsilon_{\text{DI}}$  stellar disks become bar unstable, while at  $\epsilon > \epsilon_{\text{DI}}$  they are stable against bar formation. The performance of this criterion was shown to be independent of the mass-concentration of the halo and bulge component, independent to a considerable increase of random motions in the central part of the disk and unaffected by changes in the adopted rotational curves. Further studies on Efstathiou et al. (1982) criterion were performed by Mo et al. (1998b) who explored the dependences with the disk mass and angular momentum. Other N-body simulations addressing the bar formation were performed by Athanassoula and Sellwood (1986) which showed that the disk velocity dispersion has an important influence on the bar stability, which in turns depends on both disk random motion and halo masses. The subsequent studies about bar formation focused on the disk-halo interaction. Traditionally, as in Efstathiou et al. 1982, the dark matter halo was assumed as a rigid component, which does not respond to the stellar disk dynamics. However, many works showed that when both stellar and halo components are allowed to interact, the angular momentum exchange between them enhance the growth of bars. This effect was found to be a consequence of the halo transporting outwards disk angular momentum via resonant interactions (Debattista and Sellwood, 1998; Holley-Bockelmann et al., 2005; Weinberg and Katz, 2007a,b; Romano-Díaz et al., 2008; Dubinski et al., 2009; Saha and Gerhard, 2012). Regarding the halo properties, Athanassoula and Misiriotis (2002a) explored the effect of halo concentration on the bar formation. By comparing two numerical simulations with the same disk-halo ratio but different halo concentrations Athanassoula and Misiriotis (2002a) showed that the one with larger concentration developed a much stronger, larger and thinner bar than the simulation with the less concentrated halo. Similar results were reported by Debattista and Sellwood (1998, 2000) and Athanassoula (2003), who found differences in the bar pattern speed and bar strength at different halo concentration. Besides, Athanassoula (2003) explored the effect of the halo mass on the bar formation. The simulation showed that while the most massive halos had the strongest bar, the less massive ones displayed weaker bars. The halo spin seems to play also an important role in the stability of stellar disk



against bar modes. Non-rotating dark matter halos are able to stabilize the disk against bar formation (Ostriker and Peebles, 1973). On the contrary, it has been suggested that rotating ones can enhance the growth of a bar (Weinberg, 1985). For instance, Saha and Naab (2013) demonstrated that dark matter halos with a spin parameter between 0 and 0.07 in co-rotation with the stellar disk are able to prompt the formation of bars and boxy bulges. Finally, Athanassoula et al. (2013) showed that the halo shape might play a relevant role in the bar formation. By performing N-body simulations, the authors showed that halo triaxiality has an impact on the bar formation, being galaxies hosted in halos with larger triaxiality the ones that develop earlier their bar structure.

Although most of the studies have focused on the effect of the halo properties on bars, there are some works addressing the effect of bulges in the bar assembly and evolution. Since bulges are a high-mass concentration at the center of the galaxies, they can have a deep impact on the radial forces acting in the disk. Kataria and Das (2018) used N-body simulations of bar formation in isolated galaxies to study the effect of a bulge mass and concentration on the bar assembly. Interestingly, the results suggested a delay in the bar formation as a function of the galaxy bulge-to-disk ratio (B/D). Particularly, they reported a B/D upper cut off above which the development of a bar is suppressed. While in dense bulges such cut was at  $B/D \sim 0.2$ , in the less dense ones was a  $\sim 0.5$  (see also the paper of Kataria et al. 2020). Similar bulge dependence could be hinted when comparing the zoom-in hydrodynamical simulations Eris and ErisBH (Guedes et al., 2011; Bonoli et al., 2016). While the bulge of ErisBH was smaller than the one of Eris, the former displayed a bar structure and the latter not (Spinoso et al., 2017). Some observational studies have also shown such correspondence between the presence of bulges and bars. For instance, the results of Barazza et al. (2008b) and Aguerri et al. (2009) point out that the bar fraction decreases with increasing bulge luminosity.

In order to describe the complex processes of bar formation listed above with a single analytical prescription, most of the semi-analytical models (SAMs) in the literature have relied on the 40-years-old Efstathiou et al. (1982) criterion (see e.g. Guo et al., 2011; Barausse, 2012; Croton et al., 2016; Lacey et al., 2016; Cora et al., 2018; Marshall et al., 2019b). These models have shown that disk instabilities caused by such prescription are one of the main mechanisms of the bulge growth, leading to pseudobulge/bar structures mainly hosted in Milky-Way type galaxies (Tonini et al., 2016; Izquierdo-Villalba et al., 2019; Marshall et al., 2019b). Despite SAMs provided results in broad agreement with observations (Izquierdo-Villalba et al., 2019), the Efstathiou et al. (1982) criterion can not fully describe the multi-dependent and non-linear nature of bar formation processes (see Athanassoula, 2008). Therefore, to refine SAM predictions, further studies are required to develop a criterion able to broadly capture the whole physics and dependences involved on the bar onset in a wide cosmological context (Algorry et al., 2017; Valencia-Enrquez et al., 2019). These studies are now possible thanks to the enormous advance of cosmological hydrodynamical simulations, which can follow the physical assembly of galaxies down to relatively small scales in large cosmological volumes (see e.g. Dubois et al., 2014b; Schaye et al., 2015; Nelson et al., 2018; Dav et al., 2019).

In this chapter we present an ongoing work whose aim is testing the Efstathiou et al. (1982) analytical criterion of bar formation with a sample of  $z = 0$  barred and unbarred galaxy extracted from the TNG100 hydrodynamical simulation (Nelson et al., 2018; Pillepich et al., 2018a). By studying the properties of the barred and unbarred galaxies in which the criterion fails, we propose an additional condition applied on top of Efstathiou et al. (1982) analytical criterion to improve its performance. The outline of this work is as follows: In Section 4.2 we describe the main characteristics of the TNG100 simulations and the bar/unbarred galaxy sample. We apply the Efstathiou et al. (1982) analytical criterion to these two samples. In Section 4.3 we analyse the properties of the galaxies in which the analytical criterion for bar formation fails and we explore a new condition applied on top of the Efstathiou et al. (1982) to improve its performance. Finally, in Section 4.4 we summarize our main findings. A Lambda Cold Dark Matter ( $\Lambda$ CDM) cosmology with parameters  $\Omega_m = 0.309$ ,  $\Omega_\Lambda = 0.691$ ,  $\Omega_b = 0.047$ ,  $\sigma_8 = 0.816$  and

$H_0 = 67.74 \text{ km s}^{-1} \text{ Mpc}^{-1}$  is adopted throughout the chapter (Planck Collaboration et al., 2016).

## 4.2 Methodology

Our purpose is checking the performance of Efstathiou et al. (1982) analytical prescription for bar formation with galaxies extracted from cosmological hydrodynamical simulations. Specifically, we test this criterion in two different disk-dominated galaxy samples: one composed by galaxies hosting bar structures and the other containing unbarred galaxies. We expect the Efstathiou et al. (1982) criterion to be able to find a larger number of disk instability events in barred galaxies, close to their bar formation time. On the contrary, we expect a few of these events (or none) in the unbarred sample. In this work, we focus on  $z = 0$  galaxies, making use of the bar and unbarred galaxy sample of Rosas-Guevara et al. (2020) extracted from the TNG100 simulation. In the following sections, we briefly describe the main characteristics of the hydrodynamical simulation, the procedure employed to detect barred and unbarred galaxies and their stability against bar formation reported by the Efstathiou et al. (1982) analytical criterion.

### 4.2.1 The TNG100 simulation

*The Next Generation Illustris Simulations*<sup>1</sup> (IllustrisTNG or just TNG) are a set of gravo-magneto-hydrodynamical simulations of large cosmological volumes run with the moving-mesh code AREPO (Springel, 2010). To follow the evolution of galaxies and subhalos, AREPO solves the coupled equations of ideal magneto-hydrodynamics and self-gravity and includes an updated version of the Illustris<sup>2</sup> *subgrid* galaxy formation physics (Vogelsberger et al., 2014a,b). Among many others, the *subgrid* model includes prescriptions for radiative gas cooling, stellar evolution, AGN/supernovae feedback, chemical enrichment, gas recycling, black hole seeding, black hole growth and metal loading of outflows (Vogelsberger et al., 2014b). Regarding the updates with respect to Illustris, the underlying TNG *subgrid* includes a new radio mode AGN feedback (Weinberger et al., 2017), updates the supernova wind model (Pillepich et al., 2018a), refines the chemical evolution (Naiman et al., 2018) and introduces magneto-hydrodynamics effects (Pakmor et al., 2011; Pakmor and Springel, 2013; Pakmor et al., 2014; Pillepich et al., 2018a,b).

The TNG project includes three different simulations: TNG300, TNG100 and TNG50 (Nelson et al., 2018; Pillepich et al., 2018a; Springel et al., 2018; Nelson et al., 2019; Pillepich et al., 2019). In this work we make use of the TNG100 which follows the evolution of  $2 \times 1820^3$  particles (gas and dark matter) in a box of  $75 \text{ Mpc}/h$  which translates into a baryon and DM mass resolution of  $9.5 \times 10^5 \text{ M}_\odot/h$  and  $5 \times 10^6 \text{ M}_\odot/h$ , respectively. The collisionless and gas softening lengths at  $z = 0$  are  $0.5 \text{ kpc}/h$  and  $125 \text{ pc}/h$ . The TNG100 simulation was started at  $z = 127$  with initial conditions set by the Zeldovich approximation and cosmological parameters consistent with Planck Collaboration et al. (2016):  $\Omega_m = 0.3089$ ,  $\Omega_\Lambda = 0.6911$ ,  $\Omega_b = 0.0486$ ,  $\sigma_8 = 0.8159$ ,  $n_s = 0.9667$  and  $h = 0.6774 \text{ km s}^{-1} \text{ Mpc}^{-1}$ . Particle data was stored at 100 different snapshots from  $z \sim 20$  to  $z = 0$ . Dark matter subhalos and galaxies were identified within these snapshots by using a friend-of-fiend group finder (Davis et al., 1985) and SUBFIND algorithm (Springel et al., 2001). Finally, by applying L-HALOTREE and SUBLINK algorithms (Springel, 2005; Rodriguez-Gomez et al., 2015) all DM subhalos and galaxies were arranged in merger trees structures.

### 4.2.2 Bar and unbarred galaxies seen from an hydrodynamical perspective

In this work we use the  $z = 0$  TNG100 barred and unbarred galaxy sample of Rosas-Guevara et al. (2020). In the following paragraphs, we briefly describe the procedure employed to identify them.

<sup>1</sup><https://www.tng-project.org/>

<sup>2</sup><https://www.illustris-project.org/>

Sample	Number	$M_{\text{stellar}} [M_{\odot}]$
<i>Weak bars</i>	48	$10^{10.4} < M_{\text{stellar}} < 10^{11}$
<i>Strong bars</i>	59	$10^{10.4} < M_{\text{stellar}} < 10^{11}$
<i>Unbarred</i>	131	$10^{10.4} < M_{\text{stellar}} < 10^{11}$

Table 4.1: Number of objects and stellar mass range of *weak bars*, *strong bars* and *unbarred* galaxies in TNG100 simulation.

Based on the Genel et al. (2015) kinematic bulge-to-disk decomposition of TNG100 galaxies, Rosas-Guevara et al. (2020) selected a galaxy sample at  $z=0$  with *disk-to-total* ratio  $> 0.7$ , guaranteeing a galaxy morphology fully dominated by the disk structure. To ensure a well-resolved disk, the extra condition of more than  $10^4$  stellar particles within the galaxy half mass radius ( $R_{\text{half}}$ ) was also imposed. Such particle limit set a low stellar mass cut of  $10^{10.4} M_{\odot}$ . From this disk-dominated galaxy sample, the authors identified stellar bars by performing a Fourier decomposition of the face-on stellar surface density ( $\Sigma_{\text{stars}}$ , Athanassoula and Misiriotis, 2002a; Valenzuela and Klypin, 2003). Specifically, they determined the strength of a non-axisymmetric nuclear component ( $A_2$ ) by computing the ratio between the second and zero terms of the Fourier expansion:

$$A_2(r) = \frac{|\sum_j M_j e^{2i\theta_j}|}{\sum_j M_j}, \quad (4.2)$$

where  $M_j$ ,  $\theta_j$ , and  $r$  are, respectively, the mass, angular position in the galactic plane ( $x, y$ ) and radial distance from the galactic center of the  $j$  stellar particle. The sums of Eq.4.2 were performed over all particles within cylindrical shells of 0.12 kpc with and 2 kpc high. In short,  $A_2(r)$  displays an increasing trend up to a distance  $r_{\text{max}}$  where the strength of the *non-axisymmetric structure exhibits a maximum* ( $A_2^{\text{max}}$ ). After  $r_{\text{max}}$ , the values of  $A_2(r)$  gradually decrease to zero. The position  $r_{\text{max}}$  were used as an estimate of the bar length ( $r_{\text{bar}}$ ). Finally, to avoid confusion between bars and other non-axisymmetric structures such as spiral arms (or spurious detection), the authors imposed that the phase of the second Fourier mode:

$$\varphi(r) = \frac{1}{2} \arctan \left[ \frac{\sum_j M_j \sin(2\theta_j)}{\sum_j M_j \cos(2\theta_j)} \right] \quad (4.3)$$

has to be constant<sup>3</sup> within the bar length. This Fourier decomposition allowed Rosas-Guevara et al. (2020) to divide the disk dominated galaxy sample in three different groups: *unbarred sample* ( $A_2^{\text{max}} < 0.2$ ), *weak bar sample* ( $0.2 < A_2^{\text{max}} < 0.3$ ) and *strong bar sample* ( $A_2^{\text{max}} > 0.3$ ). In Table 4.1 we summarize the number of objects in each sample and the stellar mass range. In what follows, we only study the unbarred sample and strong bars (hereafter *barred sample*). We highlight that instead of using the values of  $A_2^{\text{max}}$  get from the  $A_2(r)$  profiles, we use the ones obtained from the cumulative ones,  $A_2(<r)$ <sup>4</sup>. Notice that the values of  $A_2^{\text{max}}(<r)$  are *smaller* than  $A_2^{\text{max}}$  (see Figure 2 of Rosas-Guevara et al., 2020).

Similar as in Rosas-Guevara et al. (2020), we define the bar formation time,  $t_f^{\text{bar}}$ , as the moment in which the  $A_2^{\text{max}}(<r, t_{\text{lookback}})$  is for the first time always large than 0.15. For the unbarred sample we define the formation time as the median value of  $t_f^{\text{bar}}$  of the strong barred galaxy sample. To properly compare the bar evolution of the whole galaxy sample we will use the *normalised time since the bar formation*,  $\delta t$ , defined as:

$$\delta t = \frac{t_f^{\text{bar}} - t_{\text{snp}}}{t_f^{\text{bar}}} \quad (4.4)$$

<sup>3</sup>The term constant refers to a median value of  $\varphi(r) - \tilde{\varphi}(r)$  at  $r < r_{\text{bar}}$  smaller than  $5^\circ$ . The value of  $\tilde{\varphi}(r)$  is the median of  $\varphi(r)$  at  $r < r_{\text{bar}}$ .

<sup>4</sup>The difference between  $A_2(r)$  and  $A_2(<r)$  is that the in the latter the summation is carried over all particles enclosed within a cylinder of radius  $r$ .

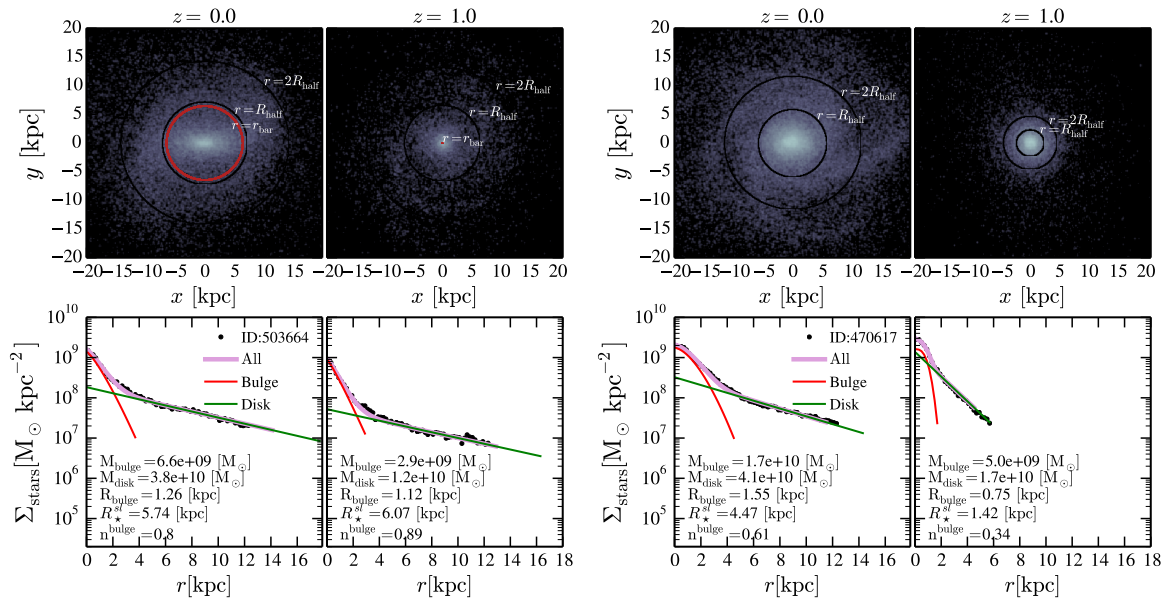


Figure 4.1: **Left panels:** Evolution of a barred galaxy at  $z=0$  and  $z=1$ . The upper panels display the galaxy face-on surface mass density. While the red circle highlights the bar length ( $r_{\text{bar}}$ ), the black ones represents the one and two half-mass-radius ( $R_{\text{half}}$ ). The lower panels display the galaxy face-on surface mass profile: pink, red and green represent the fit for the all galaxy, the bulge and the disk component, respectively. **Right panels:** The same as the left panels but for an unbarred galaxy.

where  $t_{\text{snap}}$  corresponds to the lookback time of the simulation snapshot. To guide the reader,  $\delta t = 0$  represents the bar formation time while  $\delta t > 0$  ( $\delta t < 0$ ) corresponds to times after (before) the bar formation.

Given that the [Efstathiou et al. \(1982\)](#) disk instability criterion depends on the stellar disk mass and its scale length (see Eq.4.1), we need to extract these quantities from our sample of disk-dominated galaxies. For that we compute for each galaxy its face-on surface mass profile<sup>5</sup>,  $\Sigma_{\text{stars}}(r)$ , and we fit it to a sum of a Sérsic model ([Sersic, 1968](#)) and an exponential profile:

$$\Sigma_{\text{stars}}(r) = \Sigma_{\text{b}} e^{-b_n \left[ \left( \frac{r}{R_{\text{b}}} \right)^{\frac{1}{n}} - 1 \right]} + \Sigma_0^{\text{disk}, \star} e^{-\frac{r}{R_{\star}^{\text{sl}}}}, \quad (4.5)$$

where the first and second term represent the bulge and disk component, respectively.  $\Sigma_{\text{b}}$ ,  $R_{\text{b}}$  and  $n$  represent the central surface mass density, effective radius and Sérsic index of the bulge component. On the other hand,  $\Sigma_0^{\text{disk}, \star}$  and  $R_{\star}^{\text{sl}}$  are, respectively, the central surface mass density and the scale length of the galaxy stellar disk. The  $b_n$  value is such as  $\Gamma(2n) = 2\gamma(2n, b_n)$  where  $\Gamma$  and  $\gamma$  are, respectively, the *complete* and *incomplete* gamma function. The fits have been done by finding first the optimal parameters of the exponential disk profile and afterwards modelling with the Sérsic profile the central residual excess, i.e bulge (see [Scannapieco et al., 2011](#); [Marinacci et al., 2014](#)). We have used the kinematic bulge-to-disk decomposition of [Genel et al. \(2015\)](#) as an initial guess for the break at which the change between the exponential and the Sersic law happens. These fits have been done up to  $2R_{\text{half}}$  and throughout the whole cosmological evolution of the galaxy. As an example of the fit performance, in Fig. 4.1 we present the face-on stellar surface density profile and its disk-bulge decomposition for an unbarred and a barred galaxy at  $z=0$  and  $z=1$ . As we can see, in both galaxies and redshifts the structural decomposition finds a well behave exponential declining trend corresponding to the galactic disk structure.

<sup>5</sup>The surface mass profile is computed in concentric annulus of 0.2 kpc wide centred in the position of the most bound particle of the galaxy.

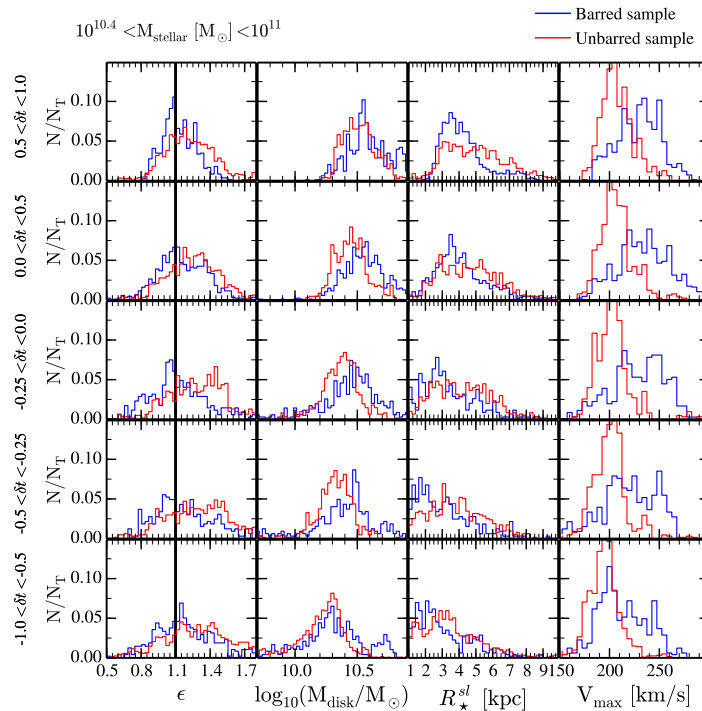


Figure 4.2: Distribution of  $\epsilon$ ,  $M_{\text{disk}}$ ,  $R_{\star}^{sl}$  and  $V_{\text{max}}$  for bar (blue) and unbar (red) sample at different bar times ( $\delta t$ , see Eq.4.4). Positive (negative) values of  $\delta t$  represent galaxy moments after (before) the bar formation. The solid vertical line in the first column highlights the value of  $\epsilon_{\text{DI}}$ .

### 4.2.3 Bar and unbarred galaxies seen from an analytical perspective

In this section we apply the disk instability criterion of [Efstathiou et al. \(1982\)](#) to the barred and unbarred sample. We explore if the criterion is able to capture the formation/assembly of the TNG100 bar structure and capable to explain its absence in the unbarred sample. Hereafter, and following the approach of many semi-analytical models, the value of  $V_{\text{max}}$  in the Eq.4.1 is going to be assumed the maximum circular velocity of the subhalo (see e.g [Guo et al., 2011](#); [Tonini et al., 2016](#); [Gargiulo et al., 2017](#); [Izquierdo-Villalba et al., 2019](#)).

In Fig. 4.2 we present at different  $\delta t$  the distribution of  $M_{\text{disk}}$  and  $R_{\star}^{sl}$  for the barred and unbarred sample. As shown, the former displays slightly more massive stellar disks than the latter. The largest difference is reached at  $-0.5 < \delta t < 0.5$ . By looking at the disk scale length, we can see that regardless time the  $R_{\star}^{sl}$  distribution of the bar sample generally peaks at lower values ( $\lesssim 3$  kpc) than the unbarred one ( $\gtrsim 3$  kpc). These results point out that unbarred sample have more extended and diffuse stellar disks than the barred one. We have also explored the distribution of the subhalo maximum circular velocity,  $V_{\text{max}}$ . Interestingly, at any  $\delta t$ , galaxies displaying bar features are systematically hosted in subhalos with larger  $V_{\text{max}}$  than unbarred galaxies.

In the left panels of Fig. 4.2 we present the evolution of the  $\epsilon$  distribution. Concerning the barred sample, we can see a correlation between  $\epsilon$  and the bar formation and assembly. While at  $\delta t < -0.25$  the distribution peaks at  $\epsilon > \epsilon_{\text{DI}}$ , when approaching to  $\delta t = 0$  it moves towards low values, concentrating at  $0.9 < \epsilon_{\text{DI}} < 1.3$ . Once  $\delta t > 0$  is reached, the peak of the  $\epsilon$  distribution is systematically found at the unstable region of the [Efstathiou et al. \(1982\)](#) criterion. For the unbarred galaxies, we see the opposite trend, being  $\epsilon$  systematically larger than  $\epsilon_{\text{DI}}$  at any  $\delta t$ . Despite in both samples the  $\epsilon$  distribution displays a correlation with the (no) bar assembly, there are cases where the [Efstathiou et al. \(1982\)](#) criterion does not capture the (in)stability of the stellar disk. For instance, in the bar sample we have cases in which



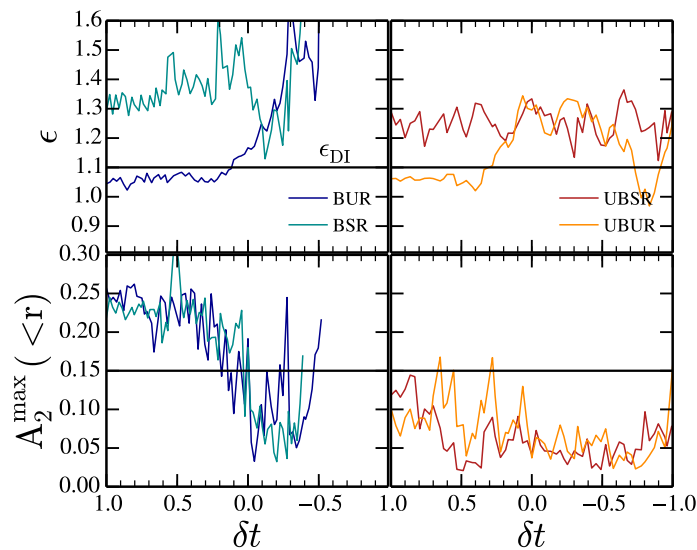


Figure 4.3: Examples of *barred in the unstable region* (BUR, cyan lines), *barred in the stable region* (BSR, purple lines), *barred in the unstable region* (UBUR, magenta lines) and *unbarred in the stable region* (UBSR, green lines). The upper panels display the values of  $\epsilon(\delta t)$  while the lower ones the  $A_2^{\max}(<r, \delta t)$ . The horizontal black line represents the value of  $\epsilon_{\text{DI}}$ .

close to the bar formation  $\epsilon > \epsilon_{\text{DI}}$ . On the other hand, for the unbarred galaxies we find examples where  $\epsilon < \epsilon_{\text{DI}}$  but the TNG100 galaxy did not develop a bar structure.

In order to draw a more robust conclusion and avoid confusion with transient bars or bar dissolution events, we have selected a sub-sample of strong bars whose value of  $A_2^{\max}(<r)$  is always  $\lesssim 0.15$  and, at a certain time close to  $\delta t \sim 0$ , it starts to monotonically increase as a consequence of the bar assembly. In this sub-sample, we have differentiated between two groups. The first one is formed by galaxies satisfying the [Efstathiou et al. \(1982\)](#) criterion, i.e  $\epsilon$  decreases down to values smaller than  $\epsilon_{\text{DI}}$  at  $\delta t \sim 0$  at the same time that  $A_2^{\max}(<r)$  grows because of bar formation. Hereafter such group is going to be called *barred in the unstable region* or just BUR. The other group consists of barred galaxies whose value of  $\epsilon$  is systematically larger than  $\epsilon_{\text{DI}}$  before and after the bar formation and assembly. This group has been tagged as *barred in the stable region* or BSR. We have done a similar procedure for the unbarred galaxies, selecting a sub-sample of galaxies whose  $A_2^{\max}(<r)$  is smaller than 0.15 at any time. We differentiated between galaxies where  $\epsilon < \epsilon_{\text{DI}}$  and galaxies where  $\epsilon > \epsilon_{\text{DI}}$ . Analogously to what we did with the sub-sample of barred galaxies, the former group is called *unbarred in the unstable region* (or just UBUR) and the latter *unbarred in the stable region* (or just UBSR). In Fig. 4.3 we present an example of the galaxy types BUR, BSR, UBUR and UBSR, showing the  $\epsilon$  and  $A_2^{\max}(<r)$  evolution as a function of the normalized time since the bar formation. As we can see, while the  $A_2^{\max}(<r)$  evolution in BUR and UBUR samples is very similar, their  $\epsilon$  values are completely different. One is systematically in the stable region while the other is in the unstable one. Similar trend is shown in the UBSR and UBUR examples, being the former classified as barred galaxy by the [Efstathiou et al. \(1982\)](#) criterion.

### 4.3 Results

In this section we explore the performance [Efstathiou et al. \(1982\)](#) analytical prescription for the BUR, BSR, UBUR, UBSR sub-samples, whose bar/no-bar evolution is well defined. The aim of this section is understanding the limitations of the [Efstathiou et al. \(1982\)](#) criterion.



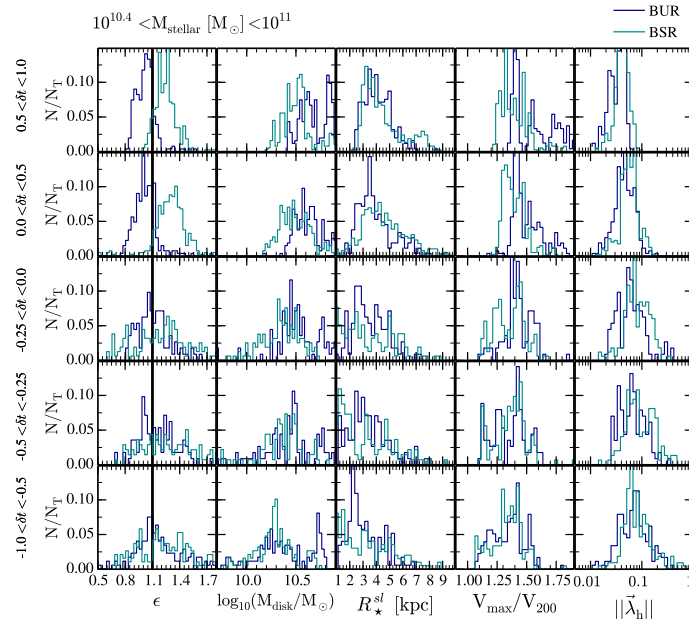


Figure 4.4: Distribution of  $\epsilon$ ,  $M_{\text{disk}}$ ,  $R_{\star}^{\text{sl}}$ ,  $V_{\text{max}}/V_{200}$  and  $\|\vec{\lambda}_{\text{h}}\|$  for BUR (dark blue) and BSR (cyan) sample at different bar times ( $\delta t$ , see Eq.4.4). The solid vertical line in the first column highlights the value of  $\epsilon_{\text{DI}}$ .

### 4.3.1 Differences between BUR and BSR: Distinct analytical results for barred galaxies

In Fig. 4.4 we present the comparison between the BUR and BSR samples. As we expected, the BUR displays a nice correlation between  $\epsilon$  and the bar formation. On the contrary, BSR has systematically  $\epsilon > \epsilon_{\text{DI}}$ , especially at  $\delta t > 0$ . Interestingly, while the two samples have a similar radius, BSR displays smaller disk masses. These results suggest that while Efstathiou et al. (1982) criterion can capture, at a fixed stellar mass, the disk instabilities leading to the bar formation in relatively compact disk, in less compact ones is not able to properly determine the onset of disk instabilities. We have checked that the differences shown in  $\epsilon$  do not come from the values of  $V_{\text{max}}$  given that both distributions are really similar. We have further explored the properties of the subhalos hosting the BUR and BSR samples. Some theoretical works have pointed out that large subhalo concentration and spins can lead to a faster bar growth and formation (Athanasoula and Misiriotis, 2002b; Saha and Naab, 2013). In Fig. 4.4 we present the evolution of  $V_{\text{max}}/V_{200}$ , where  $V_{200}$  is the subhalo virial velocity. This quantity is an approximation of the subhalo concentration and it is widely used in many works (see e.g. Gao and White, 2007)<sup>6</sup>. As shown, both samples display very similar distribution and evolution of  $V_{\text{max}}/V_{200}$ , peaking typically at  $\sim 1.4$ . In the same figure we show the modulus of the subhalo spin ( $\|\vec{\lambda}_{\text{h}}\|$ ), obtained following Bullock et al. (2001):

$$\vec{\lambda}_{\text{h}} = \frac{1}{\sqrt{2}} \frac{\sum_j M_j \vec{r}_j \times \vec{v}_j}{M_{\text{halo}} V_{200} R_{200}} \quad (4.6)$$

where  $M_j$ ,  $\vec{r}_j$  and  $\vec{v}_j$  are the mass, radius and velocity of the  $j$  dark matter particle.  $M_{\text{halo}}$  and  $R_{200}$  represent the virial mass and radius the subhalo. As happened with the subhalo concentration, no evident differences are seen in the values of  $\|\vec{\lambda}_{\text{h}}\|$  for BUR and BSR. According to these results, we can conclude that the main differences between the two sub-sample of barred galaxies reside in the properties of their stellar disk rather than the ones of their hosting subhalos.

<sup>6</sup> The advantage of this concentration definition is that it is not required any model to fit the simulation data.

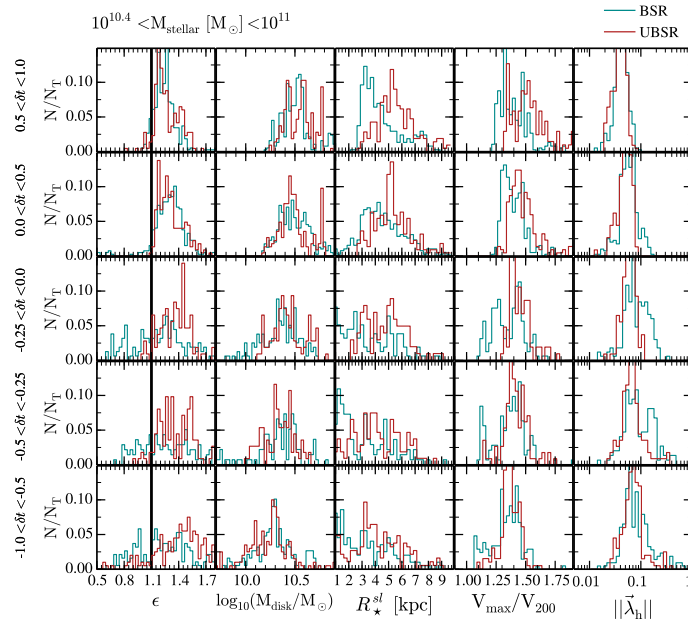


Figure 4.5: Distribution of  $\epsilon$ ,  $M_{\text{disk}}$ ,  $R_{\star}^{\text{sl}}$ ,  $V_{\text{max}}/V_{200}$  and  $\|\vec{\lambda}_{\text{h}}\|$  for BSR (cyan) and UBSR (dark red) sample at 5 different bins of bar times ( $\delta t$ , see Eq.4.4). The solid vertical line in the first column highlights the value of  $\epsilon_{\text{D1}}$ .

### 4.3.2 The BSR and UBSR samples: Fake unbarred galaxies in the analytical criterion

As we showed in Section 4.2.3 there are galaxies in the barred sample in which the analytical prescription for bar formation is not able to capture the disk instability events which ultimately lead to the growth of a bar structure. In order to understand what are the discrepancies between the outcome of the hydrodynamical simulation and the analytical criterion, in this section we compare the BSR sample with the UBSR one. This comparison will help to understand what are the differences between *false* stable disks in the Efstathiou et al. (1982) criterion and the *true* ones.

In Fig. 4.5 we present the distribution of  $\epsilon$  for BSR and UBSR. As expected, both samples are systematically in the disk stable region. Regarding the stellar disk properties, we can see that BSR and UBSR are very similar type of galaxies, showing comparable evolution in their disk stellar masses and scale lengths. However, at  $\delta t > 0.5$  we find significant differences in  $R_{\star}^{\text{sl}}$ . While BSR typically hosts disks with  $R_{\star}^{\text{sl}} \sim 3$  kpc, UBSR has  $R_{\star}^{\text{sl}} \sim 4.5$  kpc. Similar behaviour is found in the subhalo concentration, where at  $\delta t > 0.5$  UBSR are hosted in subhalos slightly more concentrated than BSR (1.5 against 1.35, respectively). Concerning the subhalo spin, we do not find relevant differences at any  $\delta t$ . In Fig. 4.6 we have explored the differences in the modulus of the stellar disk spin, defined as (Springel and White, 1999):

$$\|\vec{\lambda}_{\text{disk}}\| = \frac{j_{\text{disk}}}{m_{\text{disk}}} \|\vec{\lambda}_{\text{h}}\| \quad (4.7)$$

where  $m_{\text{disk}}$  is the ratio of the stellar disk mass over the subhalo one ( $M_{\text{disk}}/M_{\text{halo}}$ ) and  $j_{\text{disk}}$  is the ratio between the disk and subhalo angular momentum ( $\|\vec{J}_{\text{disk}}\|/\|\vec{J}_{\text{halo}}\|$ ). As happened with the subhalo spin parameter, both distributions of  $\|\vec{\lambda}_{\text{disk}}\|$  for BSR and UBSR display similar trends, spanning from 0.01 up to 0.5. The main differences are seen in  $V_{\text{max}}$  and the ratio between the total stellar and subhalo mass within the disk scale length,  $m_s(< R_{\star}^{\text{sl}})$ . As we can see, the BSR have larger velocities ( $V_{\text{max}} \gtrsim 220$  km/s) than the UBSR ( $V_{\text{max}} \lesssim 220$  km/s). On the other hand, regardless of time,  $m_s(< R_{\star}^{\text{sl}})$  in the UBSR has a clear cut off at  $\sim 0.8$ . On the contrary, the BSR sample has a distribution clearly peaked at  $m_s(< R_{\star}^{\text{sl}}) \sim 1$ , which becomes more and more concentrated at  $\delta t > -0.25$ . To further explore the differences between BSR and UBSR, in the right panel of Fig. 4.6 we present the plane  $(\|\vec{\lambda}_{\text{disk}}\|, m_s(< R_{\star}^{\text{sl}}))$ , where the color

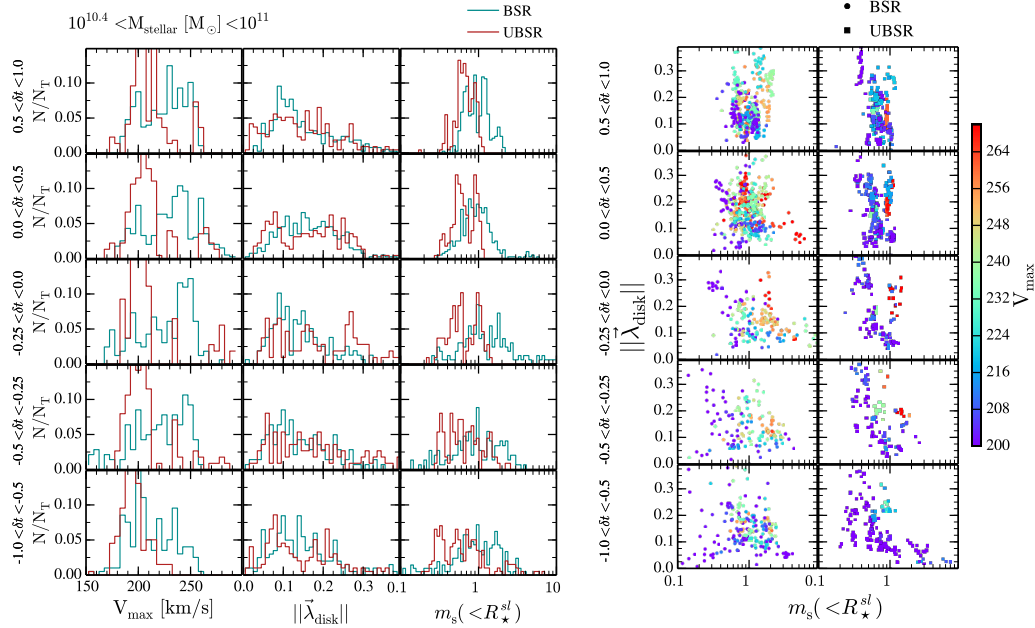


Figure 4.6: **Left panels:** Distribution of  $V_{\max}$ ,  $\|\vec{\lambda}_{\text{disk}}\|$  and  $m_s(<R_{\star}^{sl})$  at 5 different  $\delta t$  intervals. Cyan and dark red lines represent the BRS and UBSR samples, respectively. **Right panels:** Plane  $(\|\vec{\lambda}_{\text{disk}}\|, m_s(<R_{\star}^{sl}))$  for BSR (circles) and UBSR (squares). The color encodes the maximum circular velocity of the hosting dark matter subhalo ( $V_{\max}$ ).

encodes the value of  $V_{\max}$ . As shown, there is a correlation between  $m_s(<R_{\star}^{sl})$  and  $V_{\max}$ : at larger values of  $m_s(<R_{\star}^{sl})$ , the larger is  $V_{\max}$ .

### 4.3.3 The BUR and UBUR samples: Fake barred galaxies in the analytical criterion

Similar to what we did in the previous section, here we compare the BUR sample with the UBUR one. This comparison will shed light in the differences between *false* unstable disks in the [Efstathiou et al. \(1982\)](#) criterion and the *true* ones. As shown in Fig. 4.7, the criterion claims disk instability against bar formation ( $\epsilon < \epsilon_{\text{DI}}$ ) in BUR and UBUR. However, these samples have different stellar disk mass and radius evolution. While BUR sample has stellar disk of  $M_{\text{disk}} \gtrsim 10^{10.5}$  with  $R_{\star}^{sl} \sim 3$  kpc, UBUR displays less massive and more extended ones ( $M_{\text{disk}} \lesssim 10^{10.5}$  and  $R_{\star}^{sl} \sim 2$  kpc). On the subhalo side, we do not find significant differences in the concentration ( $\sim 1.5$ ) and spin ( $\sim 0.07$ ).

Regarding the subhalo maximum circular velocity, in Fig. 4.8 we show their distributions at different  $\delta t$ . As happened with the barred galaxies in the stable region, BUR displays systematically larger  $V_{\max}$  than UBUR, which has a sharp cut off at  $\sim 220$  km/s. Interestingly, on contrary to what happened with the galaxies in the stable region, the main difference between BUR and UBUR is found in  $\|\vec{\lambda}_{\text{disk}}\|$  and not in  $m_s(<R_{\star}^{sl})$  where both samples have  $m_s(<R_{\star}^{sl}) > 1$ . As we can see, the distributions of  $\|\vec{\lambda}_{\text{disk}}\|$  for UBUR is concentrated at  $\sim 0.05$  with very few cases larger than 0.1. On the other hand, BUR has larger disk spin values, peaking typically at  $\sim 0.175$ . In order to find correlations between  $\|\vec{\lambda}_{\text{disk}}\|$ ,  $m_s(<R_{\star}^{sl})$  and  $V_{\max}$ , in the right panels of Fig. 4.7 we display the plane  $(\|\vec{\lambda}_{\text{disk}}\|, m_s(<R_{\star}^{sl}))$  where the color represents the  $V_{\max}$ . Interestingly, for the BUR at  $m_s(<R_{\star}^{sl}) \sim 0.2$  we find the galaxies with the largest  $V_{\max}$  ( $\gtrsim 240$  km/s). Apart from that, we do not see further correlations.

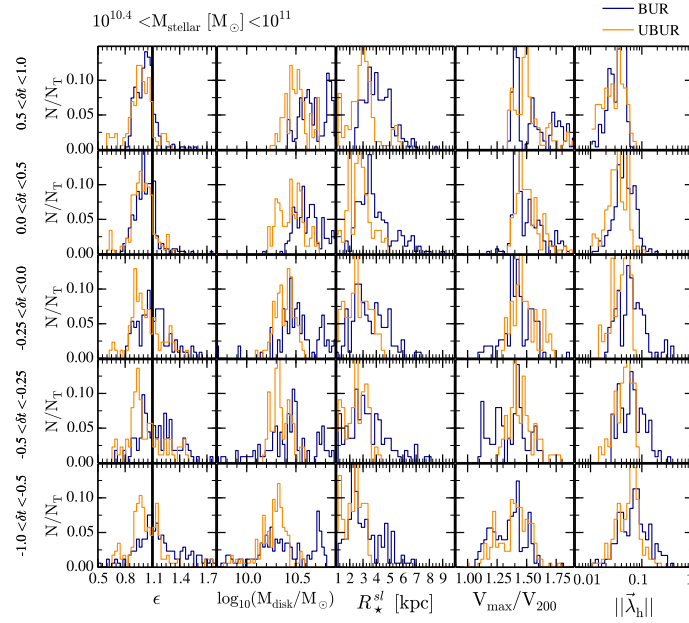


Figure 4.7: Distribution of  $\epsilon$ ,  $M_{\text{disk}}$ ,  $R_{\star}^{\text{sl}}$ ,  $V_{\text{max}}/V_{200}$  and  $\|\vec{\lambda}_h\|$  for BUR (orange) and UBUR (dark blue) sample at 5 different bins of bar times ( $\delta t$ , see Eq. 4.4). The solid vertical line in the first column highlights the value of  $\epsilon_{\text{DI}}$ .

#### 4.3.4 Reducing the contamination: extra conditions in the analytical criterion

As we have shown in Section 4.3.2 and 4.3.3, there are cases in which the Efstathiou et al. (1982) analytical criterion for the bar formation is not able to properly capture the stability/instability of the galactic disk. Regarding the differences between BSR/UBSR (see Fig. 4.6) and BUR/UBUR (see Fig. 4.8), we explore an extra condition applied on top of the Efstathiou et al. (1982) to determine if the disk is truly stable or unstable. Such criterion is going to be parametrized as:

$$\xi = m_s(< R_{\star}^{\text{sl}}) \left( \frac{V_{\text{max}}}{220} \right) \left( \frac{\|\vec{\lambda}_{\text{disk}}\|}{0.15} \right) \quad (4.8)$$

where the normalization factors in  $V_{\text{max}}$  and  $\|\vec{\lambda}_{\text{disk}}\|$  have been obtained according to the peaks in the distribution of BSR/UBSR and BUR/UBUR, shown in Fig. 4.6 and Fig. 4.8. In order to explore the performance of the new parameter  $\xi$ , in Fig. 4.9 we present the plane  $(\epsilon, \xi)$  for the BSR/UBSR and BUR/UBUR samples at different  $\delta t$ . As show,  $\xi$  is systematically larger in both barred samples than in the unbarred ones. While the former samples have  $\xi \gtrsim 1.0$ , the latter ones display  $\xi \lesssim 1.0$ . Regarding these results, we suggest that the analytical stability/instability of a stellar disk should be determined as:

$$\left\{ \begin{array}{ll} \text{Disk is unstable against bar formation} & \text{when } \epsilon \leq \epsilon_{\text{DI}} \ \& \ \xi \geq \xi_{\text{DI}} \\ \text{Disk is unstable against bar formation} & \text{when } \epsilon > \epsilon_{\text{DI}} \ \& \ \xi \geq \xi_{\text{DI}} \\ \text{Disk is stable against bar formation} & \text{when } \epsilon > \epsilon_{\text{DI}} \ \& \ \xi < \xi_{\text{DI}} \\ \text{Disk is stable against bar formation} & \text{when } \epsilon < \epsilon_{\text{DI}} \ \& \ \xi < \xi_{\text{DI}} \end{array} \right.$$

where, according to Fig. 4.9, we set the value of  $\xi_{\text{DI}}$  to 1.1. In Fig. 4.10 we present for the whole bar unbarred sample the ratio between the number of disk instabilities detected when the new criterion is applied and when it is not. As we can see, the number of detected disk instabilities in the barred sample when the new extra condition is applied is larger or equal than when only the Efstathiou et al. (1982) criterion is applied. On the contrary, for the unbarred galaxy sample we can reduce more than the half of the events considered as a disk instabilities.

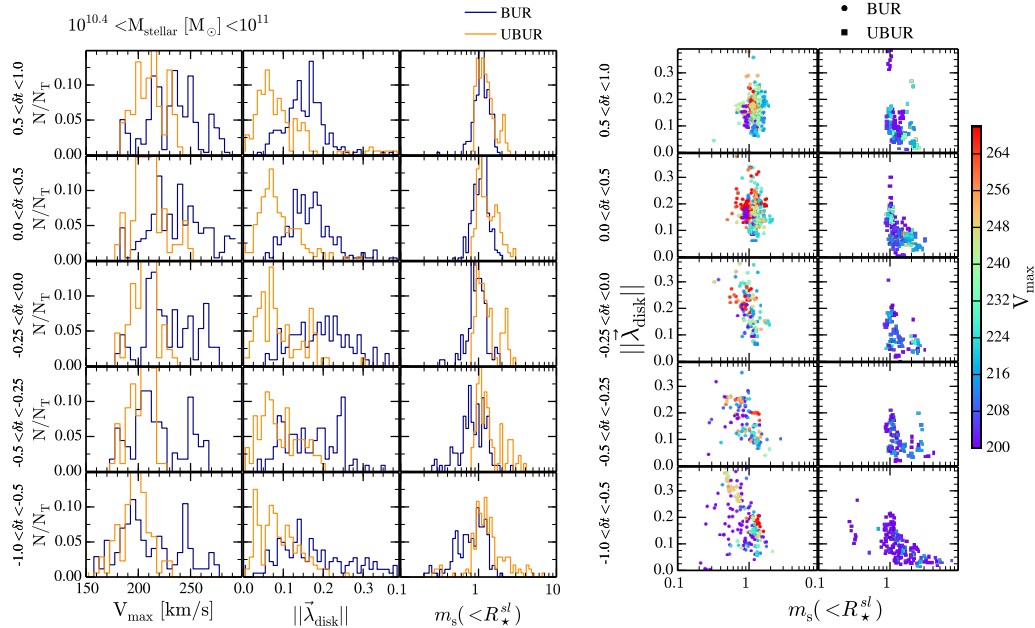


Figure 4.8: **Left panel:** Distribution of  $V_{\max}$ ,  $\|\vec{\lambda}_{\text{disk}}\|$  and  $m_s(<R_{\star}^{sl})$  at 5 different  $\delta t$  intervals. Dark blue and orange lines represent the BUR and UBUR samples, respectively. **Right panel:** Plane  $(\|\vec{\lambda}_{\text{disk}}\|, m_s(<R_{\star}^{sl}))$  for BUR (circles) and UBUR (squares). The color encodes the maximum circular velocity of the hosting dark matter subhalo ( $V_{\max}$ ).

#### 4.4 Summary and conclusion

In this chapter we have presented an ongoing work whose aim is studying the performance of [Efstathiou et al. \(1982\)](#) analytical prescription for bar formation. For that, we have made use of the strong bar and unbarred galaxy samples of [Rosas-Guevara et al. \(2020\)](#) extracted from the TNG100 cosmological hydrodynamical simulation. Specifically, they are formed by galaxies with disk-dominated morphologies (disk-to-total ratio  $> 0.7$ ) in the  $10^{10.4} - 10^{11} M_{\odot}$  range of stellar mass. Given that the [Efstathiou et al. \(1982\)](#) criterion requires the mass ( $M_{\text{disk}}$ ) and scale length ( $R_{\star}^{sl}$ ) of the galaxy disk, we have fitted for all galaxies in our samples their face-on stellar surface density to a sum of a Sérsic and an exponential disk model. These fits have been done throughout the whole cosmological evolution of the galaxies. When applying the [Efstathiou et al. \(1982\)](#) prescription we have found a correlation between the analytical criterion predictions and the actual bar assembly (non-assembly) shown in the TNG100 barred (unbarred) galaxies. While close to the onset of the bar most of the galaxies in the barred sample display unstable stellar disks against bar formation, galaxies in the unbarred sample are in the disk stable region. Despite this, we have detected cases where the [Efstathiou et al. \(1982\)](#) criterion does not capture the onset of the bar. For instance, while for some barred galaxies we have cases in which close to the bar formation the criterion claims disk stability, for some unbarred galaxies it asserts disk instability when the TNG100 galaxies do not develop a bar structure.

In order to have a better understanding of the limitations of [Efstathiou et al. \(1982\)](#) criterion, we have only analysed a sub-sample of barred and unbarred galaxies with a smooth bar (non-) assembly evolution. This concerns to galaxies in the unbarred sample which never developed a non-axisymmetric structure during its cosmological evolution. For the barred sample we refer to galaxies with a monotonic and well behaved bar formation and assembly. With these samples we have been able to obtain robust results about secular bar formation, avoiding confusions with transient or non-permanent non-axisymmetric structures caused, for instance, by fast interactions as fly-bys. These sub-samples have been divided into two different groups. The former is formed by galaxies which are systematically in the stable region (SR)



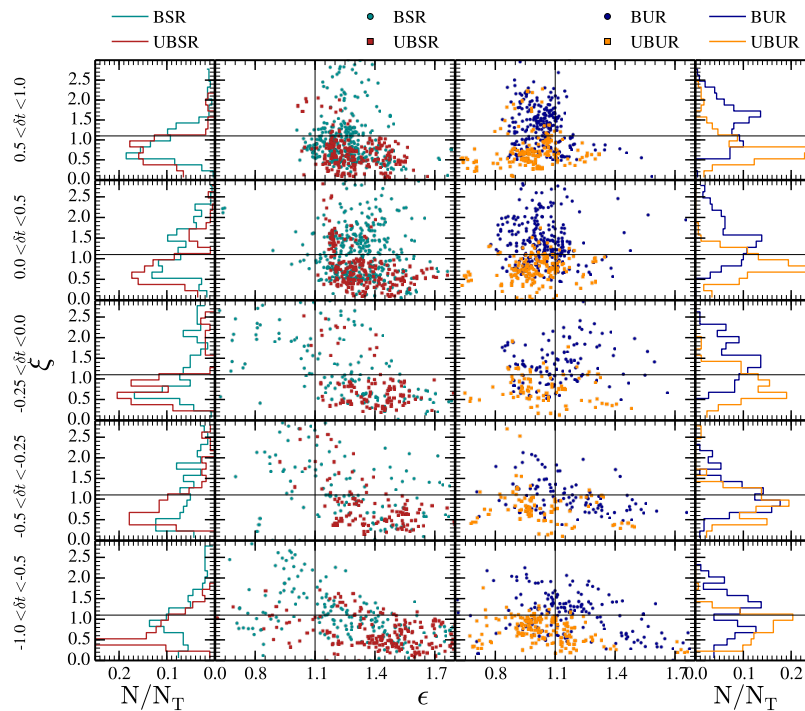


Figure 4.9: The central panels represent the  $(\epsilon, \xi)$  plane at different  $\delta t$  for the BSR (cyan circles) UBSR (dark red squares), BUR (dark blue) and UBUR (orange). While the horizontal line highlights the value  $\epsilon_{\text{DI}}$ , the vertical one highlights  $\xi_{\text{DI}}$ . Left and right panels with histograms represent the distribution of  $\xi$  parameter.

of the [Efstathiou et al. \(1982\)](#) criterion: BSR and UBSR for the group of barred and unbarred galaxies, respectively. On the contrary, the second is composed by galaxies displaying regularly disks in the unstable region (USR) of the [Efstathiou et al. \(1982\)](#) criterion: BUR and UBUR for the group of barred and unbarred galaxies, respectively. By analysing the properties of BSR and UBUR samples we have been able to understand the properties fake negative and fake positive barred galaxies on the [Efstathiou et al. \(1982\)](#) criterion.

Regarding the cases of *false* stable disks in the [Efstathiou et al. \(1982\)](#) criterion, we have compared the BSR sample with the UBSR one. Interestingly, before the bar formation no significant distinctions in the stellar disk mass, disk scale length, subhalo concentration and subhalo spin are displayed. The differences are seen in the maximum circular velocity of the subhalo ( $V_{\text{max}}$ ) and in the stellar-to-halo ratio within the disk scale length ( $m_s(<R_{\star}^{\text{sl}})$ ), being these quantities larger for the barred sub-sample. On the other hand, the cases of *false* unstable disks have been analysed by comparing the BUR and UBUR sample. Unlike the previous cases, BUR and UBUR samples have different stellar disk mass and radius evolution before and after the bar formation, being these properties larger in the BUR. While BUR sample has stellar disk of  $M_{\text{disk}} \gtrsim 10^{10.5}$  with  $R_{\star}^{\text{sl}} \sim 3\text{kpc}$ , UBUR displays less massive and more extended disks ( $M_{\text{disk}} \lesssim 10^{10.5}$  and  $R_{\star}^{\text{sl}} \sim 2\text{kpc}$ ). However, the main differences are shown in the  $V_{\text{max}}$  and the stellar spin ( $\|\vec{\lambda}_{\text{disk}}\|$ ) where the latter quantity is  $\sim 2$  times larger in the barred sub-sample before and after the onset of the bar structure.

After investigating the properties of *false* stable/unstable disks according to [Efstathiou et al. \(1982\)](#), we are planning to propose an extra condition applied on top of the [Efstathiou et al. \(1982\)](#) criterion to determine if the disk is truly stable or unstable. Such condition correlates with  $V_{\text{max}}$ ,  $\|\vec{\lambda}_{\text{disk}}\|$  and  $m_s(<R_{\star}^{\text{sl}})$ . Interestingly, after applying the new condition, the number of bar formation events in the barred sample



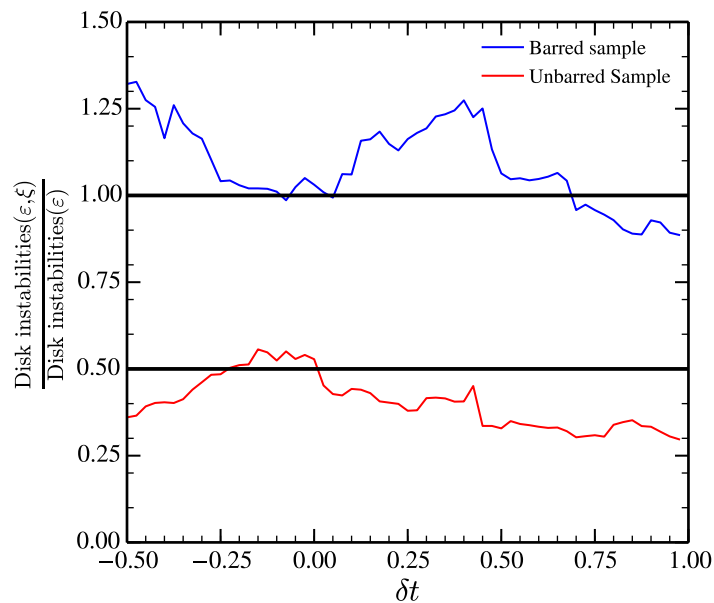


Figure 4.10: Ratio of the number of disk instabilities when we apply a combined criterion of  $\epsilon$  and  $\xi$  and when we only use the condition on  $\epsilon$ . Blue and red lines represent the whole barred and unbarred galaxy sample, respectively.

increases ( $\sim 25\%$ ) while they are considerably reduced in the unbarred galaxy sample (around 50% in the whole unbarred galaxy sample and 75% in the UBUR sample).

Although in this work we have explored a novel extra analytical condition applied on top of the [Efstathiou et al. \(1982\)](#) criterion with promising results, further investigations are needed. The increase in the number of high-resolution hydrodynamical simulations (see for instance TNG50, [Nelson et al., 2019](#); [Pillepich et al., 2019](#)) provides a unique opportunity to test with large statistics the [Efstathiou et al. \(1982\)](#) criterion at lower stellar masses than the one explored in this chapter. Such analysis will help to the understanding of bar formation in low-mass galaxies ( $M_{\text{stellar}} < 10^{10} M_{\odot}$ ) and determine if [Efstathiou et al. \(1982\)](#) criterion still holds in that range of masses.

## CHAPTER 5

### SPINNING BLACK HOLES AND WANDERING BLACK HOLES

“¿Cómo se retoma el hilo de toda una vida?,  
¿cómo seguir adelante cuando en tu corazón empiezas  
a entender que no hay regreso posible, que hay cosas  
que el tiempo no puede enmendar, aquellas que hieren  
muy dentro, que dejan cicatriz?”

El señor de los anillos: El Retorno del Rey.

“How do you pick up the threads of an old life?  
How do you go on, when in your heart you begin  
to understand there is no going back. There are  
some things that time can not mend. Some hurts  
that go too deep, that have taken hold.”

The Lord of the Rings: The Return of the King.

This Chapter is based on the paper: *From galactic nuclei to the halo outskirts: tracing supermassive black holes across cosmic history and environments*. David Izquierdo-Villalba; Silvia Bonoli; Massimo Dotti; Alberto Sesana; Yetli Rosas-Guevara; Daniele Spinoso; *Monthly Notices of the Royal Astronomical Society, Volume 495, Issue 4, pp.4681-4706 (2020)*

## ABSTRACT

In this chapter we study the mass assembly and spin evolution of supermassive black holes (BHs) across cosmic time as well as the impact of gravitational recoil on the population of nuclear and wandering black holes (wBHs) by using the semi-analytical model L-Galaxies run on top of Millennium merger trees. We track spin changes that BHs experience during both coalescence events and gas accretion phases. For the latter, we assume that spin changes are coupled with the bulge assembly. This assumption leads to predictions for the median spin values of  $z = 0$  BHs that depend on whether they are hosted by pseudobulges, classical bulges or ellipticals, being  $\bar{a} \sim 0.9, 0.7$  and  $0.4$ , respectively. The outcomes of the model display a good consistency with  $z \leq 4$  quasar luminosity functions and the  $z = 0$  BH mass function, spin values and black hole-bulge mass correlation. Regarding the wBHs, we assume that they can originate from both the disruption of satellite galaxies (*orphan* wBH) and ejections due to gravitational recoils (*ejected* wBH). The model points to a number density of wBHs that increases with decreasing redshift, although this population is always  $\sim 2$  dex smaller than the one of nuclear black holes. At all redshifts, wBHs are typically hosted in  $M_{\text{halo}} \gtrsim 10^{13} M_{\odot}$  and  $M_{\text{stellar}} \gtrsim 10^{10} M_{\odot}$ , being *orphan* wBHs the dominant type. Besides, independently of redshift and subhalo mass, *ejected* wBHs inhabit the central regions ( $\lesssim 0.3R_{200}$ ) of the host DM subhalo, while *orphan* wBHs linger at larger scales ( $\gtrsim 0.5R_{200}$ ). Finally, we find that gravitational recoils cause a progressive depletion of nuclear BHs with decreasing redshift and stellar mass. Moreover, ejection events lead to changes in the predicted local black hole-bulge relation, in particular for BHs in pseudobulges, for which the relation is flattened at  $M_{\text{bulge}} > 10^{10.2} M_{\odot}$  and the scatter increase up to  $\sim 3$  dex.

## 5.1 Introduction

Since the discovery of the first quasar (Schmidt, 1963) our understanding of supermassive black holes (BHs), their growth and relation with the host galaxies has substantially increased, although a complete and exhaustive picture on their formation, evolution and impact on the environment is still missing. A couple of decades ago, observational results confirmed both the existence of BHs at the center of most massive galaxies and the presence of a correlation between their masses and the properties of their hosts (Soltan, 1982; Haehnelt and Rees, 1993; Faber, 1999; O’Dowd et al., 2002; Häring and Rix, 2004b; Kormendy and Ho, 2013; Savorgnan et al., 2016). Their effect on shaping the star formation of their hosts has also been extensively studied (Silk and Rees, 1998; Bîrzan et al., 2004; Diamond-Stanic and Rieke, 2012; Mullaney et al., 2012b,a; Eisenreich et al., 2017). Observational studies are finally finding direct evidence of AGN-driven winds (Tombesi et al., 2014, 2015; Cresci et al., 2015; Bischetti et al., 2017).

From a theoretical point of view, it is well established that black holes grow via gas accretion and coalescence with other black holes (Marulli et al., 2008; Bonoli et al., 2016; Hirschmann et al., 2012, 2014; Fanidakis et al., 2011; Dubois et al., 2012a). While the former seems to be the main contributor to the total mass-assembly budget (Soltan, 1982), the latter appears to have just a sub-dominant importance (Small and Blandford, 1992; Fanidakis et al., 2011; Dubois et al., 2014b). Concerning gas accretion, several physical processes are believed to be responsible for driving gas towards the black hole surroundings. One of these processes is galaxy mergers, whose gravitational torques can modify the galaxy cold gas structure and trigger gas inflows towards the nuclear region (Hernquist, 1989; Barnes and Hernquist, 1991b; Mihos and Hernquist, 1996a; Di Matteo et al., 2005; Springel, 2005; Li et al., 2007). Secular processes such as the formation of bar structures or the redistribution of gas after supernovae explosions may have similar effects (Shlosman et al., 1989; Hopkins et al., 2009a; Hopkins and Quataert, 2010; Fanali et al., 2015; Dubois et al., 2015; Du et al., 2017). However, no clear observational conclusions about these two latter feeding mechanisms have been reached up to date. After being transported towards the nuclear parts, the gas has to lose a significant amount of its angular momentum to reach closer orbits around the BH to be ultimately accreted by it. Even though this process is not trivial and probably does not have an unique answer, many works have pointed out that both *local viscous stress* and *gravitational torques* (such as bars-within-bars, spiral waves or large-scale magnetic stress) can be very effective in transporting gas close to the BH ( $\lesssim 0.01 - 0.1$  pc) before being transformed into stars (Shlosman and Begelman, 1989; Balbus and Hawley, 1998; Thompson et al., 2005).

As a result of gas accretion onto the BHs, a large amount of energy can be released prompting the birth of a *quasar* or an *Active Galactic Nucleus* (Soltan, 1982; Hopkins et al., 2007; Ueda et al., 2014). The amount of energy released depends on the mass of the black hole, the geometry of the accretion disk and on the spin of the black hole (Shakura and Sunyaev, 1973; Merloni and Heinz, 2008). The dimensionless *spin* parameter,  $a$ , is defined as:  $a = cJ_{\text{BH}}/GM_{\text{BH}}^2 \lesssim 1$  where  $c$  is the speed of light,  $G$  is the gravitation constant and  $J_{\text{BH}}$  is the black hole angular momentum. Its specific value plays an important role in the BH assembly and feedback. While highly-spinning BHs can convert up to  $\sim 40\%$  of the accreted matter into radiation, slowly spinning ones can only reach up to  $\sim 5\%$ . This translates into potentially very bright radiative emission and relatively slow mass-growth of the first ones, as opposed to the generally high growth-rates and low luminosity of the latter ones (Bardeen, 1970; Novikov and Thorne, 1973; Page and Thorne, 1974). Moreover, the production and strength of AGN jets might be related to the value of the BH spin (Blandford and Znajek, 1977). How BHs acquire their spin is not fully understood yet. Up to date, all the proposed theories have assumed that a BH reaches its final spin after repeated gas accretion episodes and BHs coalescence that modify the initial rotation (Fanidakis et al., 2011; Volonteri et al., 2013; Berti and Volonteri, 2008; Barausse, 2012). On the gas accretion side, several theoretical scenarios have been proposed. For instance, King et al. (2005) suggested the *chaotic* scenario where the gas accretion always proceeds via consumption of self-gravitating accretion disks in uncorrelated directions. In this scenario, BHs tend to spin-down towards a typical final value of  $a \lesssim 0.2$  (King et al., 2008). On the other side, Volonteri et al. (2007) showed that a *prolonged* gas accretion in

the form of a constant and coherent gas consumption, efficiently spins-up the BHs up to  $a \sim 1$ . These two can be seen as extreme cases, and intermediate scenarios have been explored (see e.g. [Dotti et al., 2013](#); [Fiacconi et al., 2018](#); [Bustamante and Springel, 2019](#)). Over the last years, some works have attempted to measure BHs spin by using X-ray spectroscopy ([Brenneman and Reynolds, 2006](#); [Reynolds, 2013](#)). However, the challenges and biases in the observations make it difficult to draw solid conclusions. In the near future, with the upcoming experiments such as *Laser Interferometer Space Antenna* (LISA, [Amaro-Seoane et al., 2017b](#)) or *Advanced Telescope for High-ENergy Astrophysics* (ATHENA, [Nandra et al., 2013](#)) it will be possible to reach robust observational conclusions ruling out many theoretical models of BH spin evolution.

Even though BH-BH coalescences seem to play a sub-dominant role in the evolution of both BH mass and spin, they can have an important effect on the co-evolution between black hole and galaxy ([Redmount and Rees, 1989](#)). Because of conservation of linear momentum, the propagation of gravitational waves imparts a recoil (or *kick*) in the remnant BH ([Bekenstein, 1973](#); [Baker et al., 2008](#); [Lousto et al., 2012](#)). Small kicks could simply lead to a small displacement of the remnant BH from the galaxy center whose observational counterpart would be an offset AGN ([Madau and Quataert, 2004](#); [Loeb, 2007](#); [Blecha and Loeb, 2008a](#); [Guedes et al., 2011](#)). At the other extreme, if the recoil velocity is larger than the escape velocity of its host galactic center, the black hole can be *kicked out* of the galaxy becoming a *wandering* black hole. This last case could be more probable at high- $z$ , where the galaxy potential wells are smaller and relatively small recoil kicks can effectively expel the BH from the galaxy and possibly even from the halo potentials. Such BH ejections might have some important consequences to be taken into account when drawing a complete black hole-galaxy co-evolution picture. For instance [Blecha et al. \(2011\)](#), by using hydrodynamical simulations, found that the bulge velocity dispersion and the BH mass relation changes (a shift in the velocity dispersion axis) when the simulation is run with and without the inclusion of recoil velocities. This deviation is due to the fact that the ejection interrupts the BH growth while the galaxy continues its evolution (see similar results of [Blecha and Loeb 2008b](#); [Gerosa and Sesana 2015](#)). In the same work, [Blecha et al. \(2011\)](#) discussed the halting of AGN feedback as a consequence of the BH ejection. The outcome is an extended period of active star formation in the galaxy which yields a dense and massive nuclear stellar cusps. This type of nuclear regions could be a target property which would point out galaxies which underwent a BH ejection. Indeed, from an observational point of view, some galaxies have been tagged as candidates of having undergone a BH recoil (see eg. BCG in A2261 cluster ([Postman et al., 2012](#)), SDSS J1056+5516 ([Kalfountzou et al., 2017](#)), CID-42 ([Civano et al., 2012](#)), NGC 1399, 4261, 4486, IC 429 ([Lena et al., 2014](#)), 3C 186 radio quasar ([Chiaberge et al., 2017](#)) and [Komossa \(2012\)](#) for a review). On top of ejection via gravitational recoil, the complex dynamics of the two BHs before the final coalescence might cause the formation of a wandering black hole. If the two black holes spend enough time orbiting around each other ([Begelman et al., 1980](#); [Quinlan and Hernquist, 1997](#)) a third BH could reach their sphere of influence. As a consequence, the three BHs are likely to undergo a complex 3-body scattering interaction with the final outcome of the ejection of the less massive BH and the shrinking of the separation between the two remnants BHs ([Volonteri et al., 2003](#); [Volonteri and Perna, 2005](#); [Bonetti et al., 2018b](#)). Even though this type of interactions might not have a main role in the population of wandering black holes (see e.g. [Volonteri et al., 2003](#); [Volonteri and Perna, 2005](#)) they seem to play importance in speeding up the final BH-BH coalescence ([Bonetti et al., 2018a](#)).

Wandering black holes can also be a consequence of the disruption of a satellite galaxy during the infall onto a larger system. Environmental processes such as ram pressure or tidal interactions, in fact, can gradually strip away satellites before they merge with the central galaxy ([Moore et al., 1999](#); [Springel et al., 2001](#)). The frequency of satellite galaxy disruptions is still not well constrained. Some recent works have suggested that dwarf galaxies hosted in clusters are the ones which experience these events the most ([Faltenbacher and Mathews, 2005](#); [Martel et al., 2012](#)). Naively, the BHs hosted by the disrupted satellites are expected to be incorporated in the halo of the central galaxy and, thus, contribute to the

population of wandering BHs. Even though such population of BHs is interesting because it would give an idea of the galaxy disruption rate, it has been mainly studied only through hydrodynamical simulations (Bellovary et al., 2010; Miki et al., 2014; Tremmel et al., 2018; Pfister et al., 2019). However, the current limits in the resolution achievable in simulations, make it difficult to well-resolve the fate of the cusp of stars and/or gas around the BH after the disruption and to properly assess the evolution of such “orphan” BHs.

Given the observational limitations in detecting wandering black holes, more theoretical work is needed to constrain where and how these black holes can be found with current and upcoming instruments. Several works have attempted to determine the orbits and time spent by a BH in a wandering orbit. For instance, by using 3D hydrodynamical simulation Blecha et al. (2011) found that at a fixed ratio between recoil and escape velocity, the recoil trajectories have a substantial variation with the galaxy gas fraction. On the other hand, under an analytic perspective, Choksi et al. (2017) explored different parameters and contributions in the orbital damping of wandering BHs finding a longer wandering phase in lighter halo and galaxy systems. These authors found that in many circumstances the wandering phase may be larger than the Hubble time.

In this work we use the L-Galaxies semi-analytical model in the version presented in Chapter 3 to study the statistics and environment of black hole growth and spin evolution and to explore the population of wandering black holes across cosmic time. We include both galaxy mergers and galaxy disk instabilities as physical processes that can lead to BH growth. For tracking spin evolution we follow the approach introduced by Sesana et al. (2014), where spin changes are coupled to the bulge assembly. We also introduce a time-delay between galaxy and BH mergers that depends on the BHs mass ratio and the galaxy gas fraction. Recoil velocities after BH coalescences are calculated on the basis of the progenitors properties while the trajectories of kicked BHs depend on the physical properties of the host halos and galaxies. We also follow the trajectory of *orphan* black holes from stripped satellites to complete the picture of wandering black holes.

The chapter is organised as follows: in section 5.2 we present the semi-analytical model and the merger trees used in this work. In section 5.3 we describe all the physics included in the semi-analytical model to properly follow the BH mass growth, spin evolution and wandering phases. In section 5.4 we presents our main findings regarding nuclear black holes (i.e., black holes in the center of galaxies). In section 5.5 we explore the properties of wandering black holes across cosmic time. In section 5.6 we present the effects of gravitational recoils in both BH occupation fraction and bulge-black hole mass relation. Finally, in section 5.7 we summarize our main findings. A lambda cold dark matter ( $\Lambda$ CDM) cosmology with parameters  $\Omega_m = 0.315$ ,  $\Omega_\Lambda = 0.685$ ,  $\Omega_b = 0.045$ ,  $\sigma_8 = 0.9$  and  $H_0 = 67.3 \text{ km s}^{-1} \text{ Mpc}^{-1}$  is adopted throughout the chapter (Planck Collaboration et al., 2014).

## 5.2 Galaxy formation model

The work of this chapter is based on the L-Galaxies semi-analytical model (Henriques et al., 2015) and the Millennium (MS) dark matter merger trees. The bulk of the model is the one presented in Chapter 2, with the modifications of mergers and disk instabilities presented in Chapter 3 which contribute to a better description of galaxy morphologies and radii at  $10^8 \lesssim M_{\text{stellar}} \lesssim 10^{12} M_\odot$ .

Here, in order to distinguish between bulge morphologies in the SAM, we follow the definition of Chapter 3. In brief, we assume that a galaxy hosts a pseudobulge when the fraction of bulge formed via *secular induced* DI is at least  $2/3$ . Galaxies display a classical bulge or elliptical structure when the fraction of bulge formed via *secular induced* DIs is smaller than  $2/3$  of the total bulge mass and its *bulge-to-total* stellar fraction (B/T) is respectively  $0.01 < B/T < 0.7$  and  $B/T > 0.7$ . Finally, galaxies with  $B/T < 0.01$  are considered bulgeless galaxies.



### Improving the galaxy initialization in Millennium trees

As we discussed in Chapter 2, `L-Galaxies` populates each new resolved subhalo with an amount of hot gas in form of a diffuse atmosphere. From that moment, different analytical recipes are included to deal with the baryonic physical processes that lead to a mature galaxy. The subhalo mass resolution of the Millennium simulation used in this work ( $M_{\text{halo}} \sim 10^{10} M_{\odot}/h$ ) imposes a clear limit on the galaxy and BH evolutionary pathway that can be followed. Nevertheless, new resolved subhalos could already host a mature galaxy and its evolved BH. To improve this aspect we follow the approach of [Bonoli et al. \(2014\)](#) and [Angulo et al. \(2014\)](#) initializing each MS subhalo with random galaxies (hosted in the same redshift and subhalo mass) extracted from a run of `L-Galaxies` on top of the high resolution Millennium II merger trees ( $M_{\text{halo}}^{\text{Res}} \sim 10^8 M_{\odot}/h$ ). The galaxy *grafting* includes all the properties of the galaxy and its respective central black hole (including wandering BHs). We stress that this does not imply for our model to be able to follow subhalos below the resolution limit of MS, as we do not have access to their merger history and cosmological evolution. The aim of this procedure is to better match the DM mass of the newly resolved subhalo to the properties of the newly initialised host galaxy.

## 5.3 A comprehensive model of black hole growth

Astrophysical black holes can be fully determined by two quantities: *mass* and *spin*. In this section we present the implemented physic to track their evolution along the cosmic history.

### 5.3.1 Black hole seeding and spin initialization

Even though the existence of BHs is now well established, their origin is still an open issue. Up to date, several theories have been proposed and explored (see [Volonteri, 2010](#); [Mayer and Bonoli, 2019](#), for a review). The most studied one is the *light seed scenario* where BHs of mass between  $10 - 100 M_{\odot}$  were formed at  $z \gtrsim 20$  as remnants of Population III stars (Pop III, [Madau and Rees, 2001](#); [Heger and Woosley, 2002](#)). Another complementary formation channel is the *heavy seed scenario* where much more massive black holes ( $\sim 10^4 - 10^5 M_{\odot}$ ) are formed after the direct collapse of massive gas clouds, either in pristine primordial subhalos or in gas-rich merging galaxies ([Koushiappas et al., 2004](#); [Volonteri and Stark, 2011](#); [Mayer et al., 2010](#); [Bonoli et al., 2014](#)). In this work we simply assume that each newly resolved subhalo (independently of redshift and subhalo properties) is seeded with an initial BH mass of  $10^4 M_{\odot}$ . This initial seed mass is a reasonable assumption given the minimum mass of new resolved subhalos in MS and MSII ( $\sim 10^{10} M_{\odot}$  and  $\sim 10^8 M_{\odot}$ , respectively). In future works, a proper BH seeding in `L-Galaxies` will be tackled ([Spinoso et al. in prep.](#)).

Besides the initial mass, the BH angular momentum,  $|\vec{J}_{\text{BH}}|$ , has to be set. The exact value of  $|\vec{J}_{\text{BH}}|$  can be expressed as:

$$|\vec{J}_{\text{BH}}| = \frac{1}{\sqrt{2}} M_{\text{BH}} a (GM_{\text{BH}} R_{\text{Sch}})^{1/2} = \frac{a GM_{\text{BH}}^2}{c}, \quad (5.1)$$

where  $R_{\text{Sch}} = 2 GM_{\text{BH}}/c^2$  is the Schwarzschild radius,  $G$  the gravitational constant,  $c$  the light speed, and  $a$  the dimensionless *spin* parameter, whose value can be in the range  $0 < |a| < 0.998$  ([Thorne, 1974](#)). While  $M_{\text{BH}}$  and  $R_{\text{Sch}}$  are fully determined by the seed mass, the value of  $a$  does not have to depend on the initial mass. Indeed, no observational constraints and theoretical predictions about the initial BH spin exist to date (see e.g. [Batta et al., 2017](#); [Fuller and Ma, 2019](#); [Roulet and Zaldarriaga, 2019](#); [Zackay et al., 2019](#)). Here we assume that the initial value of  $a$  is a random number selected between  $0 < |a| < 0.998$ . We have tested that the initial selection of  $a$  does not affect the results presented in this work. In fact, a BH loses any memory of its initial spin when it has accreted in a coherent way a gas mass comparable to its own (see for instance [Fanidakis et al., 2011](#), Figure 1).



### 5.3.2 Black hole gas accretion

In this section we summarize the different mechanisms that feed central black holes with gas: (i) galaxy mergers, (ii) galaxy disk instabilities and, (iii) gas accretion from the hot gas atmosphere.

#### Cold phase accretion

The cold gas accretion is triggered by two different processes: galaxy mergers and disk instabilities.

- i) *Gas accretion after mergers.* Simulations have shown that gravitational torques during galaxy mergers are able to drive cold gas towards the galaxy inner regions, triggering the black hole accretion (Di Matteo et al., 2005; Springel, 2005; Hopkins et al., 2009a). Following Kauffmann and Haehnelt (2000), Croton (2006) and Bonoli et al. (2009) we assume that the fraction of cold gas accreted by the BH after a galaxy merger is:

$$\Delta M_{\text{BH}}^{\text{gas}} = f_{\text{BH}}^{\text{merger}} (1 + z_{\text{merger}})^{3/2} \frac{m_{\text{R}}}{1 + (V_{\text{BH}}/V_{200})^2} M_{\text{gas}}^{\text{Cold}}, \quad (5.2)$$

where  $\Delta M_{\text{BH}}^{\text{gas}}$  includes a dependence on the galaxy baryonic merger ratio,  $m_{\text{R}} < 1$ , the virial velocity of the host DM subhalo,  $V_{200}$ , the redshift of the merger,  $z_{\text{merger}}$ , and two adjustable parameters  $V_{\text{BH}}$  and  $f_{\text{BH}}^{\text{merger}}$  set to 280 km/s and 0.034, respectively.

- ii) *Gas accretion after disk instabilities.* Non-axisymmetric instabilities of galactic disks have a deep impact on the morphology of the nuclear parts. They are able to modify the gas disk structure via gravitational torques (see Shlosman and Begelman, 1989; Hopkins and Quataert, 2010). These processes produce strong gas inflows that lead to nuclear bursts of star formation and can drive part of the gas also in the BH surroundings (Shlosman et al., 1989; Hopkins et al., 2009a; Hopkins and Quataert, 2010; Fanali et al., 2015; Du et al., 2017; Spinoso et al., 2017). Consequently, each time a galaxy undergoes a disk instability episode we allow the central black hole to accrete an amount of gas given by:

$$\Delta M_{\text{BH}}^{\text{gas}} = f_{\text{BH}}^{\text{DI}} (1 + z_{\text{DI}})^{3/2} \frac{\Delta M_{\text{stars}}^{\text{DI}}}{1 + (V_{\text{BH}}/V_{200})^2}, \quad (5.3)$$

where  $V_{\text{BH}}$  and  $V_{200}$  are the same parameters described before,  $z_{\text{DI}}$  the redshift in which the DI takes place and  $\Delta M_{\text{stars}}^{\text{DI}}$  the mass of stars that triggers the stellar disk instability (see Eq. 2.29).  $f_{\text{BH}}^{\text{DI}}$  is a free parameter that takes into account the gas accretion efficiency. As we discussed in Chapter 3, we assume DIs to be the consequence of either the galaxy secular evolution or of galaxy minor mergers. In the former case, we set the efficiency  $f_{\text{BH}}^{\text{DI}} = 0.008$ . Instead, for the case of merger-induced DIs, which are causally connected with the last galaxy minor interaction ( $\lesssim 10t_{\text{dyn}}^*$ , see Section 3.2.2) we assume  $f_{\text{BH}}^{\text{DI}} = f_{\text{BH}}^{\text{merger}}$ , i.e since the system is not relaxed the torque causing the gas inflow during the DI has the same efficiency that the one of the merger (Hopkins and Quataert, 2010). The exact values of  $f_{\text{BH}}$  for both mergers and DI have been chosen to match the observed correlation between the bulge and the BH mass.

In this work, we assume that all the cold gas accreted by the BH after a merger or disk instability is stored in a reservoir,  $M_{\text{Res}}$ . Motivated by numerical simulations, the reservoir is progressively consumed according to a *light curve* composed by two different phases (Hopkins et al., 2005, 2006a). While the first one is characterized by a rapid growth truncated at Eddington limit, the second one is a quiescent regime of low accretion rates which starts when the BH reaches a certain threshold of accreted mass. Previous works have shown that this average AGN light curve is able to match successfully the faint end of the AGN luminosity functions (Marulli et al., 2008; Bonoli et al., 2009; Hirschmann et al., 2012;

Volonteri et al., 2013). Note that if a galaxy undergoes a new merger or DI while the central BH is still accreting mass from a previous event, the new cold gas driven in the BH surroundings is added to the previous remnant gas reservoir and the light curve re-starts under the new initial conditions.

To characterize both phases we use the *Eddington factor*,  $f_{\text{Edd}}$ , defined as:

$$L_{\text{bol}}(t) = f_{\text{Edd}}(t) L_{\text{Edd}}(t), \quad (5.4)$$

where  $L_{\text{bol}}$  and  $L_{\text{Edd}}$  are respectively the black hole bolometric and Eddington luminosity. These quantities can be expressed as:

$$L_{\text{Edd}}(t) = \frac{4\pi G m_p c}{\sigma_T} \dot{M}_{\text{BH}}(t) = \frac{M_{\text{BH}}(t) c^2}{t_{\text{Edd}}}, \quad (5.5)$$

$$L_{\text{bol}}(t) = \frac{\epsilon(t)}{1 - \eta(t)} \dot{M}_{\text{BH}} c^2, \quad (5.6)$$

where  $\sigma_T$  is the Thomson scattering cross-section for the electron,  $m_p$  the proton mass,  $t_{\text{Edd}} = \sigma_T c / (4\pi m_p G) = 0.45$  Gyr and  $\eta$  and  $\epsilon$  the black hole accretion and radiative efficiency, respectively. Notice that, since we want to obtain a general equation that describes the growth of supermassive black holes, in Eq. (5.6) we have distinguished between  $\eta$  and  $\epsilon$ . We refer to other works such as Pacucci and Ferrara (2015) or Volonteri et al. (2015) in which the same distinction is performed.

By definition of Eddington limit, the first phase is characterized by  $f_{\text{Edd}}(t) = 1$ . The BH grows in this phase for the time necessary to reach the mass  $M_{\text{BH,peak}}$  defined by the moment in which the BH consumed a fraction  $\gamma$  (free parameter set to 0.7) of its whole gas mass reservoir (see Marulli et al., 2008; Bonoli et al., 2009; Hirschmann et al., 2012). Once this mass is reached, the black hole enters in a self-regulated or quiescent growth regimen characterized by small  $f_{\text{Edd}}$  values. Following Hopkins et al. (2006b) we assume that  $f_{\text{Edd}}$  in this phase is parametrized as:

$$f_{\text{Edd}}(t) = \frac{1}{\left[1 + (t/t_Q)^{1/2}\right]^{2/\beta}}, \quad (5.7)$$

where  $t_Q = t_0 \xi^\beta / (\beta \ln 10)$ , being  $t_0 = 1.26 \times 10^8$  yr,  $\beta = 0.4$  and  $\xi = 0.3$  (see the discussion of these values in Hopkins et al., 2006b). We highlight that  $t$  is relative to the moment in which the BH finishes the Eddington phase.

As pointed out by Hopkins et al. (2006b) and Merloni and Heinz (2008) we also take into account the fact that the radiative efficiency has a dependence with the accretion efficiency and the nature of the accretion flow:

$$\epsilon(\eta, f_{\text{Edd}}) = \begin{cases} \eta & f_{\text{Edd}} > f_{\text{Edd}}^{\text{crit}} \\ \eta \left( \frac{f_{\text{Edd}}}{f_{\text{Edd}}^{\text{crit}}} \right) & f_{\text{Edd}} \leq f_{\text{Edd}}^{\text{crit}} \end{cases} \quad (5.8)$$

where  $f_{\text{Edd}}^{\text{crit}}$  (Merloni and Heinz, 2008; Volonteri et al., 2013, set to 0.03) is the *Eddington factor* by which below it the accretion disc becomes radiatively inefficient.

Finally, the black hole mass evolution during any accretion event can be obtained from the black hole growth rate,  $\dot{M}_{\text{BH}} = dM_{\text{BH}}/dt$ . By using Eq. (5.4), Eq. (5.5) and Eq. (5.6),  $\dot{M}_{\text{BH}}$  can be computed as:

$$\dot{M}_{\text{BH}} = f_{\text{Edd}}(t) \left( \frac{1 - \eta(t)}{\epsilon(t)} \right) \frac{M_{\text{BH}}(t)}{t_{\text{Edd}}}, \quad (5.9)$$

As we will see in Section 5.3.3,  $\epsilon$  and  $\eta$  experience a time variation given their dependence with the black hole spin,  $a$ , which varies with time as a consequence of BH-BH mergers and gas accretion. In order to ease notation, instead of denoting the accretion and radiative efficiency as  $\eta(a(t))$  and  $\epsilon(a(t))$  we will use just the notation  $\eta$  and  $\epsilon$ .

### Hot phase accretion

This mechanism of black hole growth is triggered by the accretion of the hot gas which surrounds the galaxy. Following [Henriques et al. \(2015\)](#) the BH mass accretion rate during this mode is determined by:

$$\dot{M}_{\text{BH}} = k_{\text{AGN}} \left( \frac{M_{\text{hot}}}{10^{11} M_{\odot}} \right) \left( \frac{M_{\text{BH}}}{10^8 M_{\odot}} \right), \quad (5.10)$$

where  $M_{\text{hot}}$  the total mass of hot gas surrounding the galaxy and  $k_{\text{AGN}}$  is a free parameter set to  $3.5 \times 10^{-3} M_{\odot}/\text{yr}$  to reproduce the turnover at the bright end of the galaxy luminosity function.

As pointed out by [Marulli et al. \(2008\)](#), the accretion rate of Eq. (5.10) is orders of magnitude below the BH Eddington limit. Therefore the contribution of this *radio mode* in the black hole mass growth is minimal. However, the AGN feedback generated during this phase is essential to inject enough energy into the galaxy hot atmosphere to decrease or even stop the gas cooling rate in the galaxy ([Croton, 2006](#); [Bower et al., 2006](#)).

### 5.3.3 Tracing the BH spin evolution

In this section we present the main equations implemented in `L-Galaxies` to properly follow the evolution of BH spin. Note that we have applied the spin model presented here to both modes of gas accretion (hot and cold). However, since the hot gas accretion is characterized by small values of  $f_{\text{Edd}}$ , we do not expect a large variation of the spin during these accretion events.

#### Spin evolution during gas accretion

During an accretion event, the gas settles in a disk which may not lie in the equatorial plane of the black hole. The disk could have a random orientation with an angular momentum  $\vec{J}_d$ , misaligned with respect to the one of the black hole  $\vec{J}_{\text{BH}}$ . When this misalignment happens, the rotating BH induces on the disk the so called *Lense-Thirring precession* ([Bardeen and Petterson, 1975a](#)). For large-viscosity disks<sup>1</sup> this misalignment configuration is unstable making the orbital plane of the inner parts of the disk align (*prograde* orbit) or counter-align (*retrograde* orbit) to the black hole angular momentum. This process is called *Bardeen-Petterson effect* ([Bardeen and Petterson, 1975b](#)). The criterion of counter-alignment was established by [King et al. \(2005\)](#) and it takes into account the ratio between the black hole and disk angular momentum and the angle  $\theta$  formed between them:

$$\cos \theta < - \frac{|\vec{J}_d|}{2|\vec{J}_{\text{BH}}|}. \quad (5.11)$$

Thus, for most of the accretion event, the inner part of the accretion disk is aligned if i)  $|\vec{J}_d| > 2|\vec{J}_{\text{BH}}|$  or ii)  $|\vec{J}_d| < 2|\vec{J}_{\text{BH}}|$  and  $\theta < \pi/2$ . On the contrary, when  $|\vec{J}_d| < 2|\vec{J}_{\text{BH}}|$  and  $\theta > \pi/2$ , the (anti-)alignment depends if the ratio of  $|\vec{J}_d|/2|\vec{J}_{\text{BH}}|$  is small enough with respect to exact value of  $\cos \theta$ .

We model this in our semi-analytical framework following the spin model presented in [Dotti et al. \(2013\)](#) and [Sesana et al. \(2014\)](#). The model assumes that the gas available during an accretion event (given by  $\dot{M}_{\text{BH}}$ , see Section 5.3.2) is accreted in chunks of transient accretion disks limited by self-gravity, instead of being consumed in a single episode ([King et al., 2008](#)). In an  $\alpha$ -disk the self-gravity radius,  $R_{\text{disk}}^{\text{sg}}$ , is determined by the distance to the BH at which the Toomre parameter  $Q$  is less than unity:  $Q \sim c_s \Omega / \pi G \Sigma \lesssim 1$ , where  $\Omega$  is the Keplerian angular velocity,  $c_s$  sound speed and  $\Sigma$  the gas surface density. Thus, the value of  $R_{\text{disk}}^{\text{sg}}$  is:

$$\frac{R_{\text{disk}}^{\text{sg}}}{R_{\text{Sch}}} \approx 10^5 f_{\text{Edd}}^{-22/45} \left( \frac{\alpha}{0.1} \right)^{28/45} \left( \frac{M_{\text{BH}}}{10^6 M_{\odot}} \right)^{-52/45} \left( \frac{\eta}{0.1} \right)^{22/45}, \quad (5.12)$$

<sup>1</sup>This property is met in the  $\alpha$ -disk model which describes the accretion disk around black holes ([Shakura and Sunyaev, 1973](#)).

where  $R_{\text{Sch}}$  is the Schwarzschild radius and  $\alpha$  the radial shear viscosity parameter (set from hereafter to 0.1). Concerning the self-gravity mass,  $M^{\text{sg}}$ , the value is expressed as:

$$M^{\text{sg}} \approx 2 \times 10^4 f_{\text{Edd}}^{4/45} \left( \frac{\alpha}{0.1} \right)^{-1/45} \left( \frac{M_{\text{BH}}}{10^6 M_{\odot}} \right)^{34/45} M_{\odot}, \quad (5.13)$$

which was computed by solving the expression  $M^{\text{sg}} = \int_0^{R_{\text{disk}}^{\text{sg}}} 2\pi\Sigma(R)R^2 dR$  with a surface density:

$$\Sigma(R) = 7 \times 10^7 f_{\text{Edd}}^{7/10} \left( \frac{\alpha}{0.1} \right)^{-4/5} \left( \frac{M_{\text{BH}}}{10^6 M_{\odot}} \right)^{19/20} \left( \frac{\eta}{0.1} \right)^{-7/10} \left( \frac{R}{R_{\text{Sch}}} \right)^{-3/4} \text{ g cm}^{-2}. \quad (5.14)$$

To avoid unrealistic accretion episodes, [Dotti et al. \(2013\)](#) set the maximum mass of the transient accretion disk to the minimum between  $M^{\text{sg}}$  and a fixed molecular cloud mass,  $M^{\text{cld}}$ , set in our case to  $7 \times 10^3 M_{\odot}$ . As pointed out by [Sesana et al. \(2014\)](#), fixing the value of  $M^{\text{cld}}$  is an idealized case, as molecular clouds might be characterized by a broad mass spectrum ( $\lesssim 10^5 M_{\odot}$ ) eventually dependent on the host galaxy properties. However, since the cloud mass function is not trivial, we follow [Dotti et al. \(2013\)](#) keeping  $M^{\text{cld}}$  constant over the whole BH life. The continuous increase of the BH mass during accretion episodes with constant  $M^{\text{cld}}$  implies the formation of accretion disks which carry less angular momentum relative to the BH. In this way, the larger is the BH mass, the larger is the number of retrograde accretions possible given that the condition  $|\vec{J}_d|/2|\vec{J}_{\text{BH}}| < 1$  holds for a significant fraction of the duration of each accretion event. Typically, the number of retrograde accretions exceeds the prograde ones at  $M_{\text{BH}} = 4 \times 10^5 (0.1 f_{\text{Edd}}/\eta)^{-2/27} (M^{\text{cld}}/10^4 M_{\odot})^{45/34} M_{\odot}$ . For a given cloud mass, the radius of the accretion disk is <sup>2</sup>:

$$\frac{R_{\text{disk}}^{\text{cld}}}{R_{\text{Sch}}} \approx 4 \times 10^4 f_{\text{Edd}}^{-14/25} \left( \frac{M_{\text{cloud}}}{10^4 M_{\odot}} \right)^{4/5} \left( \frac{\alpha}{0.1} \right)^{16/25} \left( \frac{M_{\text{BH}}}{10^6 M_{\odot}} \right)^{-44/25} \left( \frac{\eta}{0.1} \right)^{14/25}. \quad (5.15)$$

Each transient accretion disk has associated an angular momentum  $|\vec{J}_d|$  determined by [Perego et al. \(2009\)](#):

$$|\vec{J}_d| = \frac{8}{21} \frac{R_d^{7/4} (GM_{\text{BH}})^{1/2}}{A_v} \dot{M}_{\text{BH}}, \quad (5.16)$$

where

$$A_v = 9.14 \times 10^6 f_{\text{Edd}}^{3/10} \left( \frac{\alpha}{0.1} \right)^{4/5} \left( \frac{M_{\text{BH}}}{10^6 M_{\odot}} \right)^{1/20} \left( \frac{\eta}{0.1} \right)^{-3/10} \text{ cm}^{5/4}/\text{s}, \quad (5.17)$$

and i)  $R_d = R_{\text{disk}}^{\text{cld}}$  if  $M^{\text{cloud}} < M^{\text{sg}}$  or ii)  $R_d = R_{\text{disk}}^{\text{sg}}$  if  $M^{\text{sg}} < M^{\text{cld}}$ .

Therefore, the BH spin evolution during any gas accretion episode is followed by using Eq.(5.12)-(5.16) and checking Eq.(5.11). If  $|\vec{J}_d| > 2|\vec{J}_{\text{BH}}|$ , the fraction of transient disks consumed in a prograd accretion,  $n_{Pa}$ , is always equal to 1. On contrary, when  $|\vec{J}_d| < 2|\vec{J}_{\text{BH}}|$  the scenario is more complex and the exact value of  $\cos\theta$  is needed to check the (anti)alignment. To determine  $\cos\theta$  in the regime of  $|\vec{J}_d| < 2|\vec{J}_{\text{BH}}|$ , previous works have assumed the *chaotic accretion* presented in [King et al. \(2005, 2008\)](#), consisting in choosing randomly the value of  $\cos\theta$  ([Fanidakis et al., 2011; Volonteri et al., 2013](#)). This selection gives the same probability of having an alignment and counter-alignment, i.e  $n_p \approx 0.5$  ([King et al., 2005](#)). Since the gas accretion in a counter-rotating orbit spins down the BH more efficiently than the spin-up due to a co-rotating accretion, the net result of the *chaotic scenario* is a low-spinning BH population

<sup>2</sup>The value of  $R_{\text{disk}}^{\text{cld}}$  is computed by solving  $M^{\text{cld}} = \int_0^{R_{\text{disk}}^{\text{cld}}} 2\pi\Sigma(R)R^2 dR$ .

with a typical  $a$  value oscillating around 0.2 (see King et al., 2008; Berti and Volonteri, 2008). Here, instead, following the approach of Dotti et al. (2013) and Sesana et al. (2014), we assume a much more general scenario, allowing an asymmetry in the  $n_{Pa}$  value. According to Sesana et al. (2014) the fraction of transient disks accreted in a prograde accretion when  $|\vec{J}_d| < 2|\vec{J}_{\text{BH}}|$  is given by:

$$n_{Pa} = F + \frac{|\vec{J}_d|}{2|\vec{J}_{\text{BH}}|}(1 - F), \quad (5.18)$$

where  $F$  is an *isotropy parameter* which takes into account the fraction of accretion events with an initial angular momentum with  $\theta < \pi/2$ <sup>3</sup>.

The particular conditions of the gas inflow at subparsec scales that determine the value of  $F$  are still unknown. Hopkins and Quataert (2010), by analyzing nested hydrodynamical simulations, found out that the gas inflow at  $\sim$  pc scales displays a correlation with the non-axisymmetric disturbances that act on galactic scales such as mergers or dynamical instabilities of self-gravitating disks. As discussed previously, King and Pringle (2007) suggested that a chaotic BH feeding at small scales ( $F = 1/2$ ) would offer a promising explanation of the growth of the most BHs. However, the large level of anisotropy during the chaotic accretion leads to a population of low spinning BHs which makes it difficult to reconcile the model with observations. In this work, to obtain a better agreement with the spin observations, we relaxed the chaotic scenario by following the *assumption* of Sesana et al. (2014) which links the value of  $F$  to the bulge morphology. With this connection we presume that the gas driven to circumnuclear scales retains certain memory of both the event which triggered its nuclear in-inflow and the bulge assembly (see the recent observational work of Smethurst et al. (2019) which would suggest this). Specifically, in Sesana et al. (2014) the exact value of  $F$  is associated to the ratio between the bulk rotation velocity of the bulge,  $v$ , and its velocity dispersion,  $\sigma$ . This ratio gives an idea of the coherence motion of the galactic bulge. If  $v/\sigma > 1$  then  $F = 1$ , if  $v/\sigma = 0$  then  $F = 0.5$  and if  $0 < v/\sigma < 1$  then  $F = (1 + v/\sigma)/2$ . Thus, bulges characterized by a large coherent motion (e.g. bars) feed the BHs with a larger number of transient chunks of co-rotating accretion disks than bulges dominated by velocity dispersion (e.g. ellipticals).

Since the exact value of  $v/\sigma$  is shaped by a complex galaxy dynamics which L-Galaxies does not address, we decide to take the  $v/\sigma$  values from the observed probability distribution function (PDF) of pseudobulges, classical bulges and ellipticals presented in Eq. 14-18 of Sesana et al. (2014). In brief, while elliptical structures have an asymptotic PDF around 0, classical bulges have a PDF centred at  $\sim 0.55$  (see Eq.15 and 16 of Sesana et al. 2014). For pseudobulges, we follow the *hybrid* model of Sesana et al. (2014) assuming a log-normal PDF with 0.34 dex of standard deviation and an average value given by its Eq.14. Following Chapter 3 we assume that in L-Galaxies, DI *secular* events build-up the pseudobulge/bar structure, minor mergers and DIs *merger-induced* assembly the classical bulge component, and major mergers shape an elliptical galaxy. Therefore, each time that a galaxy undergoes one of these events we extract a random number from its  $v/\sigma$  out-coming bulge PDF and we perform a mass-weighted average between that value and the one which characterizes the bulge at that moment. In the case of major mergers, we re-set the value of  $v/\sigma$  with a value randomly selected from the elliptical-bulge PDF. For the special case of *smooth accretion* events which bring gas onto the BH but do not build-up a bulge structure, we assume that the  $v/\sigma$  of the gas brought towards the BH surroundings is linked to the kinematics of the galaxy gaseous disk. For that, as we did with the pseudobulges, we assume a log-normal PDF with 0.34 dex of standard deviation and an average value given by Eq.14 of Sesana et al. (2014).

Following Thorne (1974) we can determine the evolution of the BH spin by:

$$\dot{a} = [L_{\text{ISCO}}(a) - 2aE_{\text{ISCO}}(a)] \left( \frac{\dot{M}_{\text{BH}}}{M_{\text{BH}}} \right), \quad (5.19)$$

<sup>3</sup>Notice that by fixing  $F = 0.5$  the model presented here becomes the standard *chaotic scenario* of King and Pringle (2006).

where  $M_{\text{BH}}$  is the black hole mass,  $\dot{M}_{\text{BH}}$  the accretion rate onto the black hole and  $L_{\text{ISCO}}$ ,  $E_{\text{ISCO}}$  quote respectively the specific angular momentum and energy in the *innermost stable circular orbit* (ISCO). Since an accretion event is composed by a fraction of  $n_{Pa}$  prograde and  $(1 - n_{Pa})$  retrograde orbits, Eq. (5.19) can be rewritten as (Sesana et al., 2014; Barausse, 2012):

$$\begin{aligned} \dot{a} &= \left[ (n_{Pa} L_{\text{ISCO}}^{\text{pro}}(a) + (1-n_{Pa})L_{\text{ISCO}}^{\text{retro}}) \right. \\ &\quad \left. - 2a \left( n_{Pa} E_{\text{ISCO}}^{\text{pro}}(a) + (1-n_{Pa})E_{\text{ISCO}}^{\text{retro}}(a) \right) \right] \frac{\dot{M}_{\text{BH}}}{M_{\text{BH}}}, \end{aligned} \quad (5.20)$$

where  $L_{\text{ISCO}}^{\text{pro}}$  ( $L_{\text{ISCO}}^{\text{retro}}$ ) and  $E_{\text{ISCO}}^{\text{pro}}$  ( $E_{\text{ISCO}}^{\text{retro}}$ ) are, respectively, the specific angular momentum and energy in a prograde (retrograde) ISCO (Bardeen et al., 1972).

Finally, the accretion efficiency,  $\eta$ , it is computed as (Bardeen, 1970):

$$\eta = 1 - E_{\text{ISCO}} = 1 - \sqrt{1 - \frac{2}{3} \frac{1}{r_{\text{ISCO}}}}, \quad (5.21)$$

where  $r_{\text{ISCO}}$  is the radius of the ISCO (in units of  $R_{\text{Sch}}/2$ ) and its exact value depends in the spin value and the (anti)alignment of the transient accretion disk (Bardeen et al., 1972; Barausse et al., 2012):

$$r_{\text{ISCO}} = 3 + Z_2 \mp a \sqrt{(3 - Z_1)(3 + Z_1 + 2Z_2)}, \quad (5.22)$$

where the upper and lower sign refers respectively to a prograde and retrograde orbits and the vales of  $Z_1$  and  $Z_2$  are determined by:

$$\begin{aligned} Z_1 &= 1 + (1 - a^2)^{1/3} \left[ (1 + a)^{1/3} + (1 - a)^{1/3} \right], \\ Z_2 &= \sqrt{3a^2 + Z_1^2}, \end{aligned} \quad (5.23)$$

Therefore, the final value of  $\eta$  after a fraction of prograde  $n_{Pa}$  and  $(1-n_{Pa})$  of retrograde orbits is:

$$\eta(a_{\text{BH}}) = n_{Pa} \eta_{\text{pro}}(a) + (1 - n_{Pa}) \eta_{\text{retro}}(a), \quad (5.24)$$

where  $\eta_{\text{pro}}$  and  $\eta_{\text{retro}}$  are the values of accretion efficiency computed from Eq (5.21) assuming a  $r_{\text{ISCO}}$  radius in a prograde and retrograde orbit, respectively.

### Spin evolution after a BH-BH coalescence

The last stage of a BH binary system is the coalescence. The final spin of the remnant BH is shaped by the initial spin configuration of its progenitors and their initial masses. In this work we follow the results of Barausse and Rezzolla (2009) which found that the spin modulus of the remnant black hole,  $|a_f|$ , is determined by:

$$\begin{aligned} |a_f| &= \frac{1}{(1+q)^2} \left[ |a_1^2| + |a_2^2| q^4 + 2|a_2||a_1|q^2 \cos \alpha \right. \\ &\quad \left. + 2(|a_1|\cos\beta + |a_2|q^2\cos\gamma)|\ell| + |\ell|^2 q^2 \right]^{1/2}, \end{aligned} \quad (5.25)$$

with

$$\begin{aligned} |\ell| &= 2\sqrt{3} + t_2\nu + t_3\nu^2 + \\ &\quad \frac{s_4}{(1+q^2)^2} (|a_1|^2 + |a_2|^2 q^4 + 2|a_1||a_2|q^2 \cos \alpha) \\ &\quad + \left( \frac{s_5\nu + t_0 + 2}{1+q^2} \right) (|a_1|\cos\beta + |a_2|q^2\cos\gamma), \end{aligned} \quad (5.26)$$



where  $q = M_{\text{BH},2}/M_{\text{BH},1} \leq 1$  is the binary mass ratio,  $\nu = q/(1+q)^2$  the symmetric mass ratio,  $|a_1|$  and  $|a_2|$  are the initial spin magnitudes,  $\alpha$  is the angle formed between the two spins and  $\beta$ ,  $\gamma$  the angle formed between the spin (1 and 2) with the orbital angular momentum, respectively. The other parameters are set to the following values:  $s_4 = 0.1229 \pm 0.0075$ ,  $s_5 = 0.4537 \pm 0.1463$ ,  $t_0 = -2.8904 \pm 0.0359$ ,  $t_3 = 2.5763 \pm 0.4833$  and  $t_2 = -3.51714 \pm 0.1208$  (Barausse and Rezzolla, 2009; Barausse, 2012).

Given that in the SAM we only track the evolution of the BH spin modulus we have to establish the direction between the two black hole spins and their directions with respect to the orbital angular momentum, i.e the values of  $\alpha$ ,  $\beta$  and  $\gamma$  of Eq.(5.25) and Eq.(5.26). To do that, we use the standard approach of dividing the BH-BH mergers in two types (Barausse, 2012; Volonteri et al., 2013): *wet* and *dry*. While the former is characterized by  $(M_{\text{Res},1} + M_{\text{Res},2}) > (M_{\text{BH},1} + M_{\text{BH},2})$ , the latter is characterized by  $(M_{\text{Res},1} + M_{\text{Res},2}) < (M_{\text{BH},1} + M_{\text{BH},2})$ . In the case of wet mergers, it has been shown that the dissipative dynamics between black holes and the massive gas disc produces a torque with the effect of aligning both spins to the orbital angular momentum. However, Dotti et al. (2010) showed that this alignment is not perfect and there is a residual offset in the spin direction relative to the orbital angular momentum at the level of  $10^\circ$ . Therefore for the wet BH mergers we assume that  $\cos \alpha$ ,  $\cos \beta$  and  $\cos \gamma$  are random numbers between  $[\cos 0^\circ - \cos 10^\circ]$ . For dry mergers, we assume random values of  $\cos \alpha$ ,  $\cos \beta$  and  $\cos \gamma$ .

### 5.3.4 Black hole coalescence

#### Black hole binaries: merger delay

In the standard *hierarchical* paradigm galaxies grow mainly through mergers with smaller or comparable mass companions (White and Rees, 1978). This fact, together with recent observational results confirming the existence of BHs being hosted in the center of galaxies (Haehnelt and Rees, 1993), suggest that binary BH (BBH) systems have been formed and merged during the whole lifetime of the universe. The evolutionary pathway of BBHs is described by three different stages (Begelman et al., 1980): i) an initial *pairing* phase in which dynamical friction exerted by the galaxy gas and stars drives both BHs individually to the nucleus of the merger remnant eventually forming a binary; ii) a following *hardening* phase in which the BBH orbital separation shrinks due to three-body slingshots and/or interaction with a massive gaseous disk; iii) a final *gravitational wave inspiral* phase which drives the binary to the final coalescence (see Colpi, 2014, and references therein for a review). Building on this scenario, several studies have tackled the evolution of BBHs (see for instance Quinlan and Hernquist, 1997; Sesana, 2013; Kelley et al., 2017a,b; Bonetti et al., 2018a,b). On the semi-analytical modelling side, up to date, most of the studies presented in the literature have assumed an instantaneous coalescence right after a galaxy-galaxy merger (see the few exceptions of Volonteri et al., 2003; Tanaka and Haiman, 2009; Antonini et al., 2015; Bonetti et al., 2018b,a). This might be an acceptable assumption at high- $z$ , where galaxy interactions are gas rich and dynamical friction can efficiently reduce the angular momentum of both BHs and speed up the hardening and final coalescence (Mayer, 2013; del Valle et al., 2015). However, at low- $z$  galaxies are generally poorer in gas and the timescales for merger can become very large.

In this work we relax the assumption of instantaneous BH-BH coalescence by allowing for a time delay between the galaxy merger and the BH binary final coalescence. Therefore, we introduce the possibility for galaxy-merger remnants of hosting a binary BH system for a given time interval  $t_{\text{delay}}^{\text{BH}}$ . Following the results of several dedicated hydrodynamical simulations (Callegari et al., 2011a,b; Fiacconi et al., 2013; Mayer, 2013; del Valle et al., 2015), we implement a simple prescription to determine the lifetime of a BH binary system:

$$t_{\text{delay}}^{\text{BH}} \approx 0.01 \left( \frac{0.1}{q} \right) \left( \frac{0.3}{f_{\text{gas}}} \right) \mathcal{F}(e) \text{ Gyr}, \quad (5.27)$$

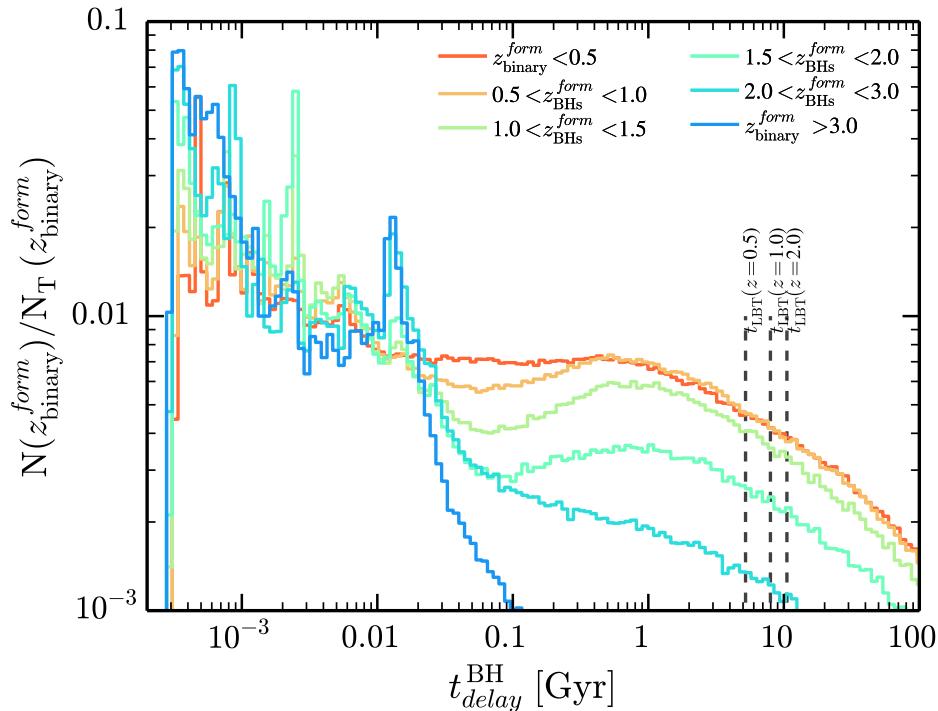


Figure 5.1: Distribution of BBH merger delay timescales,  $t_{\text{delay}}^{\text{BH}}$ , for different formation redshifts ( $z_{\text{BHs}}^{\text{form}}$ , as described in the legend). Vertical lines represents the lookback time ( $t_{\text{LBT}}$ ) at  $z=0.5, 1.0, 2.0$ . Binary systems whose  $z_{\text{BHs}}^{\text{form}}$  is 0.5, 1.0, 2.0 and are beyond these lines will not merge by  $z=0$ . The increase of the binary system lifetime towards low  $z$  is caused principally by the dependence of the gas fraction in Eq. (5.27).

where  $q (< 1)$  is the mass ratio between the two BHs at the moment of the galaxy-galaxy merger,  $f_{\text{gas}}$  is the galaxy gas fraction,  $\mathcal{F}(e)$  is a factor which takes into account the dependence of  $t_{\text{delay}}^{\text{BH}}$  with the binary eccentricity  $e$  (for simplicity, we assume  $\mathcal{F}(e) \approx 1$ ) and the 0.01 Gyr amplitude is based on the hydrodynamical simulations of Dotti et al. (2007), Fiacconi et al. (2013) and del Valle et al. (2015) who found that the BH separation in a binary system decays, typically, at parsecs scales in few Myrs. We clarify that the  $t_{\text{delay}}^{\text{BH}}$  presented in Eq. 5.27 refers only to the time spent by the BBH system in the hardening and gravitational wave inspiral phase. This is counted starting from the galaxy merger time computed by the L-Galaxies, which marks the moment in which the two galactic nuclei merge. We have checked that the black hole mass function, spin distribution and BH-Bulge scaling relation presented in this work do not significantly change if we run the model with a delay  $100 t_{\text{delay}}^{\text{BH}}$ . Even though the hydrodynamical simulations of Escala et al. (2004, 2005), Dotti et al. (2007) and Cuadra et al. (2009) showed that dense gaseous regions are very effective in hardening BBHs, promoting their coalescence in less than  $\lesssim 10^7$  yr, the dependence with the gas fraction might be much more complex. For instance, Tamburello et al. (2017) showed that the final BH-BH coalescence can be speeded-up or delayed depending on the clumpiness of the circumnuclear discs around the BHs. In a future work we plan to explore how different assumptions for the merger delays affect the global BH population.

We allow both BHs to accrete their respective gas reservoir carried before the merger while they are in a binary system. We also assume that any new amount of gas accreted after the galaxy merger (see Section 5.3.2) is added to the reservoir of the most massive BH. Still, the life of a galaxy is rather complicated and it can undergo multiple mergers in short time scales. If a merger happens in a moment in which the galaxy is still hosting a BBH, a third BH (or even another BBH) will perturb the system (Hut and Rees, 1992). The final configuration is not trivial and few studies have addressed this (see e.g.

Bonetti et al., 2018b,a, and references therein). Here we use a simplified approach allowing only the two most massive BHs to remain in the galaxy (see Volonteri et al., 2003; Volonteri and Perna, 2005). The lightest BH suffers a scattering event and it is ejected from the galactic nucleus. We highlight that we do not follow the wandering phase of these scattered BHs since we do not track the binary system separation (as, for instance, Volonteri et al. 2003 do) and therefore we cannot set the initial velocity of the ejection (see Section 5.3.5). We emphasize that our treatment of 3-body scattering is a simplified approach. Recent works of Hoffman and Loeb (2007) and Bonetti et al. (2018a) pointed out that triple interaction can lead to the coalescence of stalled binaries. Even though this effect should be taken into account to have a complete picture of the evolution of BBHs, we do not expect significant modifications to our final results by neglecting it. For instance, Bonetti et al. (2018a) found that triple interactions drive to coalescence *only* the  $\sim 30\%$  of stalled binaries and, for those, the merger timescale is dictated by the dynamical friction timescale of the incoming intruder which is usually few hundreds of Myrs. In Appendix E the number density of both gravitational and 3-body scattering ejections is compared. We show that at any redshift and subhalo mass, the former is  $\gtrsim 2$  dex more frequent. Finally, if the two initial BHs forming the binary system are the most massive ones, we eject the intruder without changing the  $t_{\text{delay}}^{\text{BH}}$  value. Conversely, if there was an exchange of BHs in the system, we reset the value of  $t_{\text{delay}}^{\text{BH}}$  with the new initial conditions. The distribution of BH-BH merger delays,  $t_{\text{delay}}^{\text{BH}}$ , is presented in Fig. 5.1. As shown, the earlier is the redshift of binary formation,  $z_{\text{BHs}}^{\text{form}}$ , the shorter is the time spent by the two BHs in a binary system. While at  $z_{\text{BHs}}^{\text{form}} > 3$  BBHs merge in  $\lesssim 100$  Myr, at  $z_{\text{BHs}}^{\text{form}} < 3$  a considerable fraction of BHs spend more than 1 Gyr orbiting each other before the final coalescence. Besides, at  $z_{\text{BHs}}^{\text{form}} < 3$  a sizeable fraction of BBHs survive for times larger than the lookback time corresponding to their  $z_{\text{BHs}}^{\text{form}}$ , and therefore still inhabit galaxy nuclei today. The increase of the binary system lifetime towards low  $z$  is caused principally by the dependence of the gas fraction in Eq. (5.27). While at high- $z$  galaxy mergers are mainly gas-rich, sinking effectively both BHs until the final coalescence, at low- $z$  galaxies run out of gas stalling the two BHs in a binary system for a long time.

### Final mass after a coalescence

Since gravitational waves carry away part of the energy of the system, the final mass of the remnant black hole,  $M_{\text{BH}}^{\text{f}}$ , is not the sum of the two progenitor black hole masses. According to Tichy and Marronetti (2008), the final mass of a black holes can be computed as:

$$M_{\text{BH}}^{\text{f}} = (M_{\text{BH},1} + M_{\text{BH},2}) \left[ 1 + 4\nu (m_0 - 1) + \frac{16m_1\nu^2 (a_1 \cos\beta + a_2 \cos\gamma)}{M_{\text{BH},1} + M_{\text{BH},2}} \right], \quad (5.28)$$

where  $m_0 = 0.9515 \pm 0.001$ ,  $m_1 = -0.013 \pm 0.007$ .

### 5.3.5 The population of wandering black holes

Black holes outside of a galaxy in bound orbits within the dark matter subhalo are defined as wandering black holes (wBHs). In this section we study two types of events responsible for the formation of the wBH population: (i) *disruption of satellite galaxies* and (ii) *gravitational recoils* after a BH-BH merger.

#### Orphan black holes: a disruption event of its host galaxy

In L-Galaxies, as soon as two dark matter subhalos merge their host galaxies do it as well in a time scale given by the dynamical friction formula of Binney and Tremaine (1987). The smallest galaxy starts to sink towards the inner parts of its new host subhalo. During this process, if the galaxy is not compact enough it can be disrupted before reaching the subhalo center, losing the possibility to merge with the central galaxy. When this happens, the central black hole (or binary system) of the satellite galaxy is deprived of its host and is incorporated in the dark matter subhalo as a wBH. The

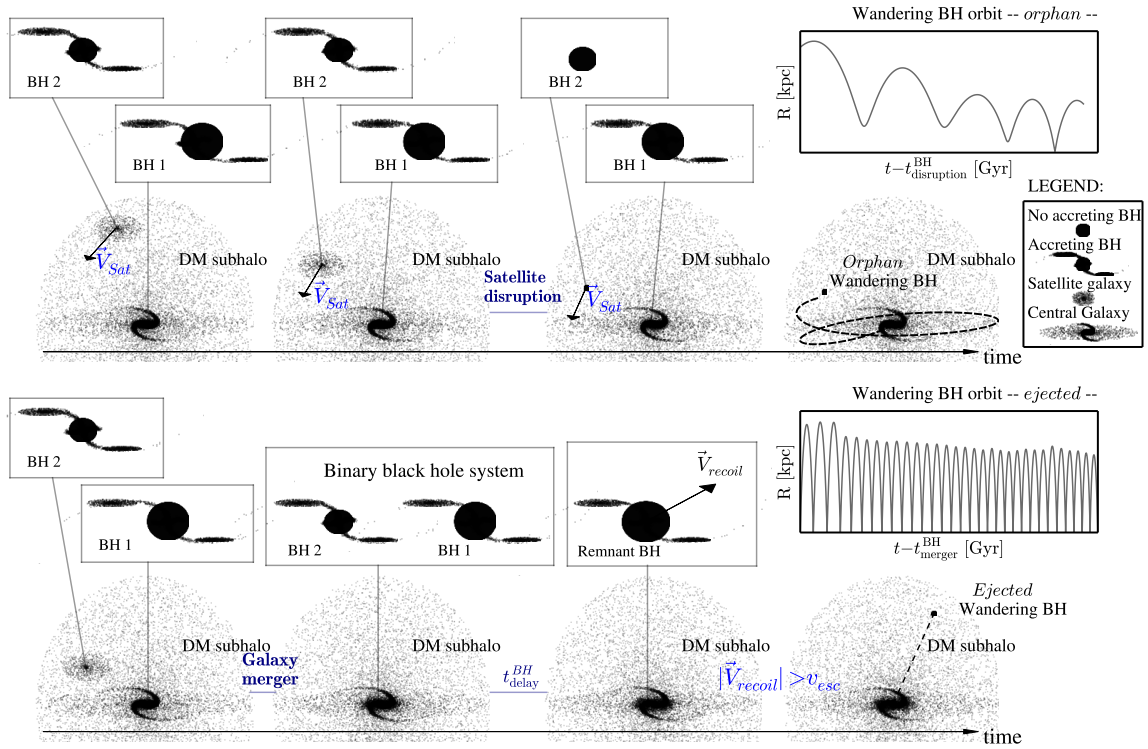


Figure 5.2: A schematic view of the two pathways that lead to wandering BHs. **Upper panel:** *Orphan* wandering black holes originate from the complete disruption of the host galaxy during its infall towards the central galaxy. Once the black hole is deprived of its host galaxy, we assume that its accretion disk (in case it was in an accreting phase), is also removed. The initial orbital speed of the new wandering BH is assumed to be the 3D velocity of the satellite galaxy at the disruption time  $\vec{V}_{Sat}$  (see Section 5.3.5). We highlight that an accreting BH is presented surrounded by a warped accretion disk. This is the result of the Bardeen-Petterson effect which makes the orbital plane of the inner parts of the disk align or counter-align to the black hole angular momentum. **Lower panel:** An *ejected* black hole is the result of the coalescence of a binary system (after a  $t_{delay}^{BH}$  subsequent to the merger of the two host galaxies) and the resulting gravitational recoil. The kick velocity,  $\vec{V}_{recoil}$ , depends on the properties of two progenitors. If the modulus of the recoil velocity is larger than the escape velocity of the galaxy ( $v_{esc}$ ) the kicked BH is ejected from the host galaxy, starting its wandering phase.

disruption process implemented in L-Galaxies is presented in Guo et al. (2011). We follow the 3D orbit of the black hole using the formalism presented in Section 5.3.5. As initial conditions, we consider the position in which the satellite galaxy is disrupted ( $\vec{p}_{Sat} = (x_{Sat}, y_{Sat}, z_{Sat})$ ) and the satellite galaxy velocity ( $\vec{V}_{Sat} = (V_{Sat}^x, V_{Sat}^y, V_{Sat}^z)$ ) evaluated at the same instant. Additionally, we assume that the black hole completely loses its accretion disk. From here onwards, we tag this type of wBHs as *orphan black holes*. In the upper panel of Fig. 5.2 we present a cartoon showing the formation of the orphan black hole population.

### Ejected black holes: Kicks due to gravitational recoils

During a BH merger, the binary system emits gravitational waves able to carry away energy and angular momentum. Due to conservation of linear momentum, in the instant of the merger, the emission of gravitational waves imparts a kick to the remnant black hole. The velocity characterizing this kick is called *recoil velocity*,  $\vec{V}_{recoil}$ . Using numerical simulations of general relativity, it has been shown that recoil velocities can take a wide range of values: from small ones which just displace the remnant BH from the galaxy center, to larger values big enough to exceed the escape velocity of the host galaxy or

even of the host subhalo (Baker et al., 2008; Lousto and Zlochower, 2008; van Meter et al., 2010). Here we use the fitting formula established by Lousto et al. (2012):

$$\begin{aligned}\vec{V}_{\text{recoil}} &= v_m \hat{e}_1 + v_{\perp} (\cos \zeta \hat{e}_1 + \sin \zeta \hat{e}_2) + v_{\parallel} \hat{n}_{\parallel}, \\ v_m &= A_m v^2 \frac{(1-q)}{(1+q)} [1 + B_m v], \\ v_{\perp} &= H \frac{v^2}{(1+q)} (a_2^{\parallel} - q a_1^{\parallel}), \\ v_{\parallel} &= \frac{16v^2}{(1+q)} [V_{1,1} + V_A \tilde{S}_{\parallel} + V_B \tilde{S}_{\parallel}^2 + V_C \tilde{S}_{\parallel}^3] |\vec{a}_2^{\perp} - q \vec{a}_1^{\perp}| \cos(\phi_{\Delta} - \phi_1),\end{aligned}\tag{5.29}$$

where,  $v_m$  is the velocity due to the *mass-asymmetry contribution*<sup>4</sup> and,  $v_{\parallel}$ ,  $v_{\perp}$  are *spin contribution* producing kicks parallel and perpendicular to the orbital angular momentum respectively. As in the previous section,  $q = M_{\text{BH}}^2/M_{\text{BH}}^1 \leq 1$  is the binary mass ratio,  $v = q/(1+q)^2$  the symmetric mass ratio,  $|a_i|$  is the initial spin magnitude of the black hole  $i$ ,  $\parallel$  and  $\perp$  refer respectively to components parallel and perpendicular to the orbital angular momentum.  $\hat{e}_1$  and  $\hat{e}_2$  are orthogonal unit vectors in the orbital plane.  $\zeta = 145^\circ$  is the angle between the unequal mass and spin contribution (González et al., 2007; Lousto and Zlochower, 2008),  $\vec{S} = 2(\vec{a}_2 + q^2 \vec{a}_1)/(1+q)^2$ .  $\phi_{\Delta}$  is the angle between the in-plane component  $\vec{\Delta}^{\perp} = (M_{\text{BH}}^1 + M_{\text{BH}}^2)(\vec{S}_2^{\perp}/M_{\text{BH}}^2 - \vec{S}_1^{\perp}/M_{\text{BH}}^1)$  and the infall direction at merger. The values of the other coefficients are obtained numerically:  $A_m = 1.2 \times 10^4$ ,  $B_m = -0.93$ ,  $H = 6.9 \times 10^3$  (González et al., 2007; Lousto and Zlochower, 2008) and  $V_{1,1} = 3677.76$  km/s,  $V_A = 2481.21$  km/s,  $V_B = 1792.45$  km/s and  $V_C = 1506.52$  km/s (Lousto et al., 2012).

If the modulus of this velocity is larger than the escape velocity of its host galaxy, the black hole is kicked from it and incorporated in the DM subhalo as a wBH. Indeed, if the recoil velocity is large enough, the BH can even escape from the subhalo. This happens more frequently at high- $z$ , where the subhalos are smaller and their potential wells shallower. This scenario is summarized in the lower cartoon displayed in Fig. 5.2. Hereafter, we call this type of wBHs *ejected black holes*. When an *ejected* wBH is kicked out of its host galaxy we assume a *purely* radial motion for the orbital integration (i.e, along the  $\hat{r}$  coordinate without movement in the  $\hat{\theta}$  and  $\hat{\phi}$  ones, see Section 5.3.5). However, when an *ejected* wBH loses its host subhalo and is incorporated to a larger structure, after a galaxy merger, we start treating the *ejected* wBH as an *orphan* wBH, and we start tracking its 3D orbit according to the formalism presented in Section 5.3.5. In what follows, we will call *inborn* the *ejected* wBHs that are still orbiting the galaxy from whose nucleus they were ejected, while we will use the term *acquired* to refer to *ejected* wBHs that have lost their host galaxy and have been incorporated by the subhalo of a larger one.

Finally, we neglect the fact that the ejected BH can retain an accretion disk. It is not clear how massive is the disk that can be retained and subsequently accreted by a BH after a recoil (see Blecha et al., 2011). Loeb (2007) showed that in an  $\alpha$ -disk the maximum amount of the disk material that a recoiled BH can carry out is, at most  $\sim M_{\text{BH}}$  which accounts for a relatively small AGN lifetime ( $\sim 4.5 \times 10^6 f_{\text{Edd}}/\epsilon$  yr, Volonteri and Madau 2008). In this work we neglect the accretion disk of ejected BHs, but we plan to include it in a future work, focused on the observability of AGN pairs.

### Tracking the orbits of wandering black holes

Once in the wandering phase, the BH starts to orbit within the subhalo potential (i.e. around its centre  $r_0$ <sup>5</sup>). The equation of motion can be expressed as:

$$\ddot{\vec{u}} = \left( -\frac{GM(<(r-r_0))}{(r-r_0)^2} + a_{\text{df}}^{\text{cless}} + a_{\text{df}}^{\text{gas}} \right) \hat{u},\tag{5.30}$$

<sup>4</sup>since it does not depend on the spin it disappears in equal binary mass mergers

<sup>5</sup>Here we assume that the galaxy position is always at the center of the host subhalo, i.e  $r_0$



where the first term refers to the gravity acceleration caused by a mass  $M (< (r - r_0))$  of dark matter, stars and gas (in both galaxy and inter-cluster medium) within a radius  $r - r_0$ . The second and third terms are related to the dynamical friction caused by collisionless (stars and dark matter) and gas components, respectively. Since in this work we are interested in the position of wBHs, we track their orbital evolution by solving numerically Eq. (5.30) using a 4<sup>th</sup> order *Runge-Kutta* integrator with time step of 1 Myr<sup>6</sup>. We have also used integration intervals of 0.1 Myr, obtaining nearly identical results.

Assuming a Maxwellian velocity distribution and a black hole velocity  $v_{\text{BH}}$ , the value of  $\vec{a}_{\text{df}}^{\text{class}}$  is determined by (Chandrasekhar, 1943):

$$\vec{a}_{\text{df}}^{\text{class}} = - \frac{4\pi G^2 M_{\text{BH}} \rho(r - r_0) \ln \Lambda}{v_{\text{BH}}^3} \left[ \text{erf}f(\Gamma) - \frac{2\Gamma}{\sqrt{\pi}} e^{-\Gamma^2} \right] \hat{v}, \quad (5.31)$$

with  $\Gamma = |v_{\text{BH}}| / \sqrt{2}\sigma$  where  $\sigma$  is the dark matter velocity dispersion computed as  $\sigma = (GM_{\text{halo}}/2R_{200})^{1/2}$ ,  $\text{erf}f$  is the error function and  $\ln \Lambda$  is the Coulomb logarithm fixed to 3.1 (Escala et al., 2004; Gualandris and Merritt, 2008; Blecha and Loeb, 2008b). Finally,  $\rho(r - r_0)$  is the mass density of the collisionless system enclosed within  $r - r_0$ . In our case  $\rho(r - r_0) = \rho_{\text{DM}}(r - r_0) + \rho_{\text{ICM}}(r - r_0)$ , i.e the mass of dark matter and the mass of stars in the inter-cluster medium (ICM or stellar halo). For the case of dark matter we assume a NFW profile (Navarro et al., 1996)<sup>7</sup> while for ICM an isothermal one.

Since galaxies are surrounded by hot gas which fills their host DM subhalos, we also take into account the dynamical friction caused by that gas. Escala et al. (2004) determined that the damping of the oscillation amplitude for an object moving inside a gas follows the equation:

$$\vec{a}_{\text{df}}^{\text{gas}} = - \frac{4\pi G^2 M_{\text{BH}} \rho_{\text{gas}}(r - r_0)}{v_{\text{BH}}^3} f(\mathcal{M}) \hat{v}, \quad (5.32)$$

where  $\rho_{\text{gas}}(r - r_0)$  is the mass density of the hot gas at position  $r - r_0$ ,  $\ln \Lambda$  is again the Coulomb logarithm fixed to 3.1 and,  $\mathcal{M}$  the *Mach number* equal to  $|v_{\text{BH}}|/c_s$  with  $c_s$  the sound speed computed as in Tanaka and Haiman (2009) and Choksi et al. (2017):  $c_s \approx 1.8(1 + z)^{1/2} (M_{\text{halo}}/10^7 M_{\odot})^{1/3} (\Omega_{\text{M}} h^2 / 0.14) \text{ km/s}$ . The exact value of  $f(\mathcal{M})$  is determined by:

$$f(\mathcal{M}) = \begin{cases} \frac{1}{2} \ln \Lambda \left[ \text{erf}f\left(\frac{\mathcal{M}}{\sqrt{2}}\right) - \sqrt{\frac{2}{\pi}} \mathcal{M} e^{-\mathcal{M}^2/2} \right] & \text{if } \mathcal{M} \leq 0.8 \\ \frac{3}{2} \ln \Lambda \left[ \text{erf}f\left(\frac{\mathcal{M}}{\sqrt{2}}\right) - \sqrt{\frac{2}{\pi}} \mathcal{M} e^{-\mathcal{M}^2/2} \right] & \text{if } 0.8 \leq \mathcal{M} \leq 1.5 \\ \frac{1}{2} \ln(1 - \mathcal{M}^{-2}) + \ln \Lambda & \text{if } \mathcal{M} > 1.5 \end{cases} \quad (5.33)$$

The integration of the wBH orbit stops when i) the black hole is re-incorporated in the galaxy (see Section 5.3.5), ii) the recoil velocity of ejected BHs is larger than the subhalo escape velocity or iii) the black hole position exceed  $3 \times R_{200}$  ( $R_{200}$  is the subhalo virial radius) and it is still moving away from the galaxy.

As an example, in Figure 5.3 we present orbit evolution of an *orphan* wBHs extracted form L-Galaxies run on the MS subhalo merger trees. In particular, the wBH has a mass of  $\sim 10^7 M_{\odot}$  and it was formed at  $z \sim 0.5$  inside of a  $\sim 10^{12} M_{\odot}$  subhalo.

<sup>6</sup>Note that the *sub-steps* that L-Galaxies does between DM *snapshots* are  $\sim 2 - 20$  Myr, depending on redshift

<sup>7</sup>The concentration parameter as a function of redshift and subhalo mass has been computed by using the fits of Dutton and Macciò (2014).



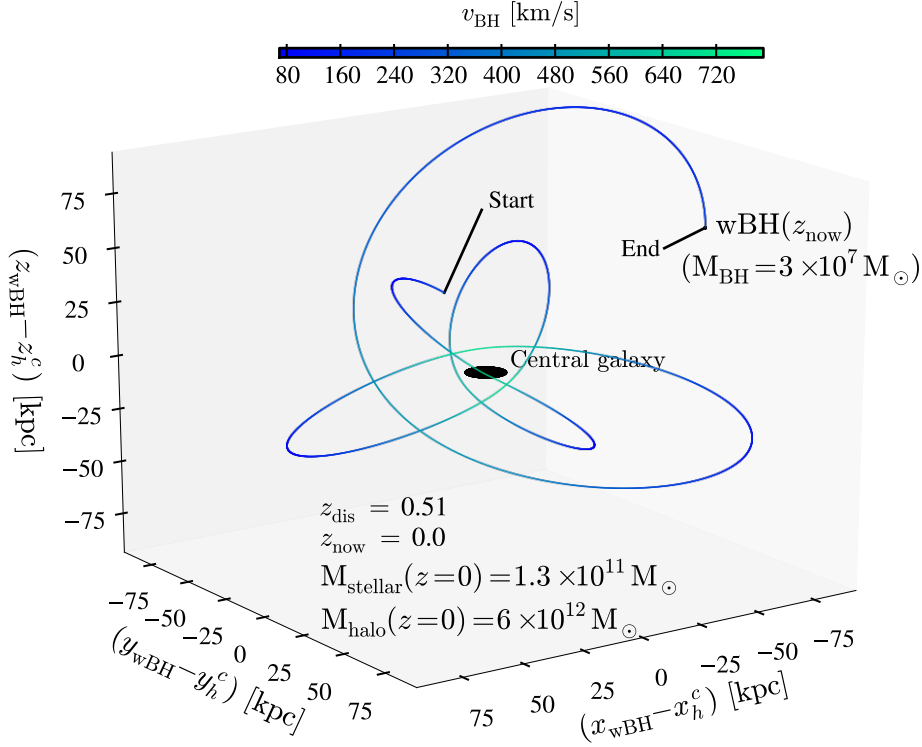


Figure 5.3: *Orphan* wBHs orbit extracted from L-Galaxies run on top of MS subhalo merger trees. The example presents a  $\sim 10^7 M_\odot$  wBH formed at  $z_{\text{dis}} = 0.51$  after the disruption of its host galaxy. The final ( $z_{\text{now}} = 0$ ) subhalo and stellar mass of its central galaxy is  $6 \times 10^{12} M_\odot$  and  $1.3 \times 10^{11} M_\odot$ , respectively. The color of the orbit encodes the modulus of the wBH velocity ( $v_{\text{BH}}$ ).

### Reincorporation of wBHs

We assume that a BH is reincorporated in a galaxy when it passes through the galaxy,  $r < R_{\text{gal}}$ <sup>8</sup>, with a velocity ( $v_{\text{BH}}$ ) smaller than the galaxy escape velocity ( $v_{\text{esc}}$ ), i.e:  $v_{\text{BH}} < v_{\text{esc}}$ . The exact value of  $v_{\text{esc}}$  is computed taking into account both bulge and disk (stellar and cold gas):

$$v_{\text{esc}} = \sqrt{v_{\text{esc,Bulge}}^2 + v_{\text{esc,Stellar disk}}^2 + v_{\text{esc,Cold disk}}^2}, \quad (5.34)$$

In the case of the bulge component we assume a Hernquist profile (Hernquist, 1990) with an escape velocity at  $r_0$ :

$$v_{\text{esc,Bulge}}^2 = 2(1 + \sqrt{2}) \frac{GM_{\text{Bulge}}}{r_{\text{bulge}}}, \quad (5.35)$$

where  $M_{\text{Bulge}}$  is the total bulge mass and  $r_{\text{bulge}}$  the bulge half-mass radius. Although, this profile can approximate classical bulges, it is a rough approximation for pseudobulges.

For stellar and cold gas disk we assume an exponential profile. In this case, the escape velocity at  $r_0$  is determined by:

$$v_{\text{esc,Stellar/Cold disk}}^2 = 3.36 \frac{GM_{\text{Disk}}}{r_{\text{disk}}}, \quad (5.36)$$

where  $M_{\text{Disk}}$  is the total stellar/cold gas disk mass and  $r_{\text{disk}}$  its half-mass radius.

<sup>8</sup> $R_{\text{gal}}$  is the galaxy radius computed as the mass weighted average between the bulge, stellar disk and cold gas disk. In Appendix C we showed that the SAM, after including gas dissipation losses during the bulge size computation, is able to reproduce the galaxy radius of early and late type galaxies.

### Changing reference system during merger events

The scenario described above complicates when galaxies merge. During the interaction, the satellite galaxy is first of all deprived of its host DM subhalo. In the following, we will refer to the “subhalo merger time” as the instant in which the satellite subhalo is no more identified within the underlying merger tree. Any wBHs which was hosted by the satellite galaxy now starts to be influenced by the potential of the larger central galaxy<sup>9</sup>. To track the new orbit, the position and velocity of the recently accreted wBHs, we need to change the reference system, so that the center is given by the new central galaxy position and velocity<sup>10</sup>:

$$\begin{aligned} x_{\text{wBH}}^{\text{new}} &= (x_h^s + x_{\text{wBH}}) - x_h^c ; & v_{\text{wBH}}^{x,\text{new}} &= (v_h^{s,x} + v_{\text{wBH}}^x) - v_h^{c,x}, \\ y_{\text{wBH}}^{\text{new}} &= (y_h^s + y_{\text{wBH}}) - y_h^c ; & v_{\text{wBH}}^{y,\text{new}} &= (v_h^{s,y} + v_{\text{wBH}}^y) - v_h^{c,y}, \\ z_{\text{wBH}}^{\text{new}} &= (z_h^s + z_{\text{wBH}}) - z_h^c ; & v_{\text{wBH}}^{z,\text{new}} &= (v_h^{s,z} + v_{\text{wBH}}^z) - v_h^{c,z}, \end{aligned} \quad (5.37)$$

where  $(x_h^s, y_h^s, z_h^s)$  and  $(v_h^{s,x}, v_h^{s,y}, v_h^{s,z})$  are, respectively, the positions and velocity of the satellite subhalo at the moment of merger.  $[(x_h^c, y_h^c, z_h^c), (v_h^{c,x}, v_h^{c,y}, v_h^{c,z})]$  and  $[(x_{\text{wBH}}, y_{\text{wBH}}, z_{\text{wBH}}), (v_{\text{wBH}}^x, v_{\text{wBH}}^y, v_{\text{wBH}}^z)]$  represent the same as before but for the central subhalo and wandering BH, respectively.

Although obtaining the exact value of  $(x_{\text{wBH}}, y_{\text{wBH}}, z_{\text{wBH}})$  and  $(v_{\text{wBH}}^x, v_{\text{wBH}}^y, v_{\text{wBH}}^z)$  for *orphan* (or *acquired ejected*) wBHs at the moment of the merger is simple because we follow their full 3D orbit, for *inborn ejected* wBHs is not trivial since we only follow their radial coordinate (see Section 5.3.5). In this case, we assume that they start the new orbit from a random location (in  $\theta, \varphi$ ) in a sphere of radius  $r$ . Once  $r, \theta$  and  $\varphi$  are fixed, the Cartesian coordinates and velocities of the *inborn ejected* wBHs are determined by:

$$\begin{aligned} x_{\text{wBH}} &= |r| \sin \theta \cos \varphi ; & v_{\text{wBH}}^x &= |v_{\text{BH}}| \sin \theta \cos \varphi, \\ y_{\text{wBH}} &= |r| \sin \theta \sin \varphi ; & v_{\text{wBH}}^y &= |v_{\text{BH}}| \sin \theta \sin \varphi, \\ z_{\text{wBH}} &= |r| \cos \theta ; & v_{\text{wBH}}^z &= |v_{\text{BH}}| \cos \theta. \end{aligned} \quad (5.38)$$

where  $r$  and  $v_{\text{BH}}$  are respectively the radial position and radial velocity of the *ejected* wBH at the moment of the subhalo merger.

## 5.4 Nuclear black holes

In this section we compare the predictions for nuclear black holes (i.e BHs located at the center of the host galaxy at the analyzed redshift) with a variety of available observational results. By checking the black hole mass function, the bolometric luminosity functions and spin values we prove that our black holes form a reliable population at  $z \leq 4$ . We do not present results beyond  $z = 4$  since the model predictions are very sensitive to the exact seed mass assumed. In a future work, where a more careful seeding in L-Galaxies is modeled, we will analyze the high- $z$  black hole population (Spinoso et al. in prep.). On top of this, we show only the results for BHs whose mass is larger than  $10^6 M_{\odot}$ , as at smaller masses the resolution of Millenium DM simulation does not allow us to draw reliable conclusions.

### 5.4.1 Black hole mass assembly

The evolution of the black hole mass function (BHMF) between  $z = 0$  and  $z = 4$  is shown in the upper panel of Fig.5.4. There is a significant evolution from  $z \sim 4$  up to  $z \sim 2$ , where the BHMF amplitude

<sup>9</sup>The orbits of the wBHs moving around the central subhalo (galaxy) are also affected by the change of the dark matter potential as the differential equation which determines the orbit evolution depends on the subhalo mass at  $r < r_{\text{wBH}}$ , see Eq (5.30).

<sup>10</sup>Notice that we assume that the galaxy position is always at the center of the host subhalo.

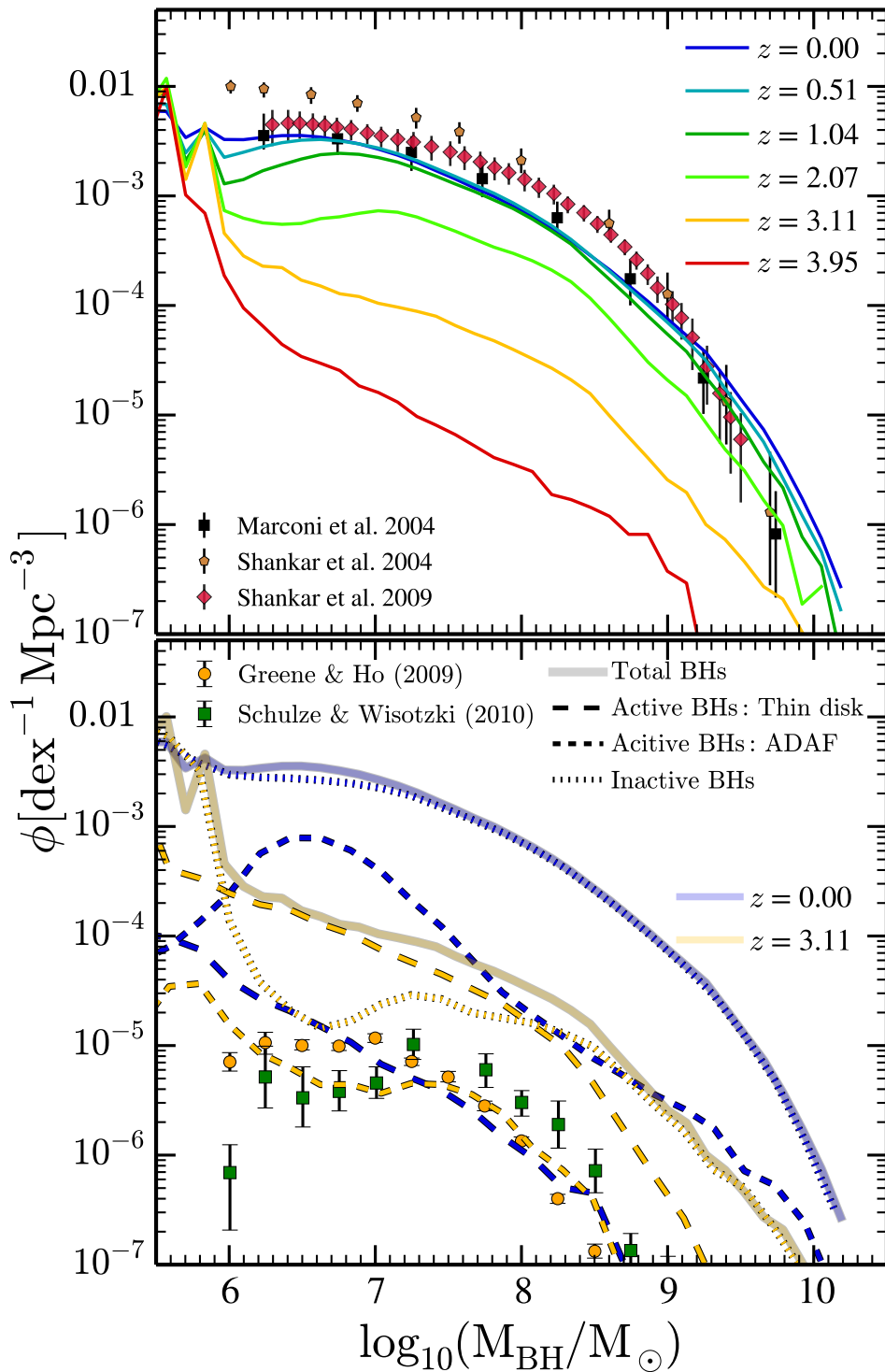


Figure 5.4: **Upper panel:** Redshift evolution of the black hole mass function compared to the observational results of Marconi et al. (2004) and Shankar et al. (2004, 2009). **Lower panel:** Black hole mass function at  $z \sim 0$  and 3 (thick blue and yellow lines, respectively) divided between inactive ( $f_{\text{Edd}} < 10^{-4}$ , dotted lines) and active ( $f_{\text{Edd}} > 10^{-4}$ ) black holes, where the latter are split in BHs accreting in the thin disk ( $f_{\text{Edd}} > f_{\text{Edd}}^{\text{crit}}$ , dashed lines) and ADAF ( $10^{-4} < f_{\text{Edd}} < f_{\text{Edd}}^{\text{crit}}$ , short dashed lines) phase. The black hole mass function of active BHs at  $z \sim 0$  from Greene and Ho (2007) and Schulze and Wisotzki (2010) are added for comparison.

increases up to 2 dex. Conversely, at  $z < 1$  the BHMF does not evolve significantly. Such small evolution at low  $z$  indicates that most of the local BHs were already assembled by  $z \sim 1$ . Similar behavior is found in the theoretical work of Merloni and Heinz (2008) where a very weak evolution in the BHMF is seen below  $z \sim 1$  and, as we find here, most of it happens at small masses ( $< 10^7 M_\odot$ ). On the semi-analytical side, works such as Fanidakis et al. (2011); Griffin et al. (2019) or Marshall et al. (2019a) show a stronger redshift evolution at  $z \lesssim 1$  where the normalization of the BHMF increases relatively fast at  $> 10^8 M_\odot$  and decreases at  $\lesssim 10^8 M_\odot$ . On the other hand, the results of Hirschmann et al. (2012) show a similar weak evolution in the BHMF at  $z \sim 1$ . In the same figure, we have compared the predictions at  $z = 0$  with the observational constraints provided by Marconi et al. (2004) and Shankar et al. (2004, 2009). Even though the BHMF of the model is compatible with the observations, mainly with Marconi et al. (2004), it displays a smaller amplitude when compared with Shankar et al. (2004, 2009). As pointed out by Shankar et al. (2016), this discrepancy might be caused by biases effects affecting the observations. Shankar et al. (2016) showed that, because of selection effects<sup>11</sup>, the normalization of the scaling relations used to link the BH mass with galaxy properties (bulge velocity dispersion, total stellar mass and bulge mass) is increased by a factor  $\gtrsim 3$  (see also Bernardi et al., 2007; Shankar et al., 2019). The lower amplitude in the empirical relations pointed out by Shankar et al. (2019) yields smaller BH masses, lower black hole mass density and higher radiative efficiencies which would support rapidly spinning BHs and lower levels of gravitational wave emission, consistent with the current non-detection of this signal by pulsar timing array experiments (see Sesana et al., 2016).

The lower panel of Fig. 5.4 presents the BHMF of *active* and *inactive* BHs at  $z \sim 0$  and 3. We consider as threshold between active and non-active the Eddington ratio  $f_{\text{Edd}} \sim 10^{-4}$  (Rosas-Guevara et al., 2016b), i.e below this value the emission of the BH is essentially undetectable against the emission of the host galaxy. Even though this threshold is quite arbitrary, we did not find significant differences in the results assuming a threshold between  $10^{-3} - 10^{-5}$ . The inactive population increases from  $z \sim 3$  to  $z \sim 0$ , with the most massive BHs becoming non-active at an earlier epoch: while at  $z \sim 3$  inactive BHs have typical  $M_{\text{BH}} > 10^8 M_\odot$ , at  $z \sim 0$ , black holes with masses  $M_{\text{BH}} > 10^6 M_\odot$  are inactive. This behaviour is usually referred to as *downsizing*, and it has been reported by observational works (Merloni et al., 2004; Heavens et al., 2004; Hasinger et al., 2005), semi-analytical models (Bonoli et al., 2009; Fanidakis et al., 2012; Hirschmann et al., 2012) and cosmological hydro-simulations (Sijacki et al., 2009; Rosas-Guevara et al., 2016b; Thomas et al., 2019). In the same figure we divided the active population by accretion geometry. We assume that the emission of active BHs with  $f_{\text{Edd}} > f_{\text{Edd}}^{\text{crit}}$  can be described by the thin and radiatively-efficient Shakura-Sunyaev disk model (Shakura and Sunyaev, 1973, *thin disk geometry*, hereafter). On the other hand, the emission of active BHs with  $10^{-4} < f_{\text{Edd}} < f_{\text{Edd}}^{\text{crit}}$  are associated to a thick and radiatively-inefficient accretion disk to which we will refer as a *Advection Dominated Accretion Flow* geometry (or just ADAF geometry, Rees et al. 1982; Narayan and Yi 1994). As shown, regardless of the BH mass,  $z \sim 3$  active BHs are characterized by a thin disk geometry fuelled by Eddington limited accretion flows (see Fig. 5.5). This picture changes at  $z \sim 0$ , where ADAF becomes the main accretion geometry for BHs with  $M_{\text{BH}} > 10^6 M_\odot$ . In this case, BHs are powered by the quiescent phase of cold gas accretion and the consumption of hot gas which surrounds its host galaxy (see right panel of Fig. 5.5). We refer the reader to Section 5.3.2, where a detailed description of how  $f_{\text{Edd}}$  values are computed in our BH growth model.

Finally, we have also explored the evolution of the black hole masses in the chaotic scenario proposed by King et al. (2005)<sup>12</sup>. For the sake of the present discussion, we only compare the main predictions of this *chaotic* model to our findings. We have seen that, as a consequence of the different outcomes in the spin distribution, there is a faster BH assembly in the chaotic model than in the one explored in this work. Whereas the former display typically spin values of  $a \lesssim 0.1$ , the latter is characterised by  $a \gtrsim 0.7$ . As shown by Eq.(5.21), the spin has an impact in the mass-to-energy conversion, implying longer timescales in the BH growth at larger spin parameters (see Eq.(5.9)). We have also checked that the fast

<sup>11</sup>For instance, they reported that local galaxies with black hole mass estimate with a dynamical approach are a biased subset of all galaxies, i.e at fixed stellar mass BHs display larger velocity dispersion than the bulk of the population, regardless of the exact morphological type.

<sup>12</sup>Following Sesana et al. (2014), the chaotic scenario presented in King et al. (2005) is obtained fixing  $F = 1/2$  in Eq.(5.18).

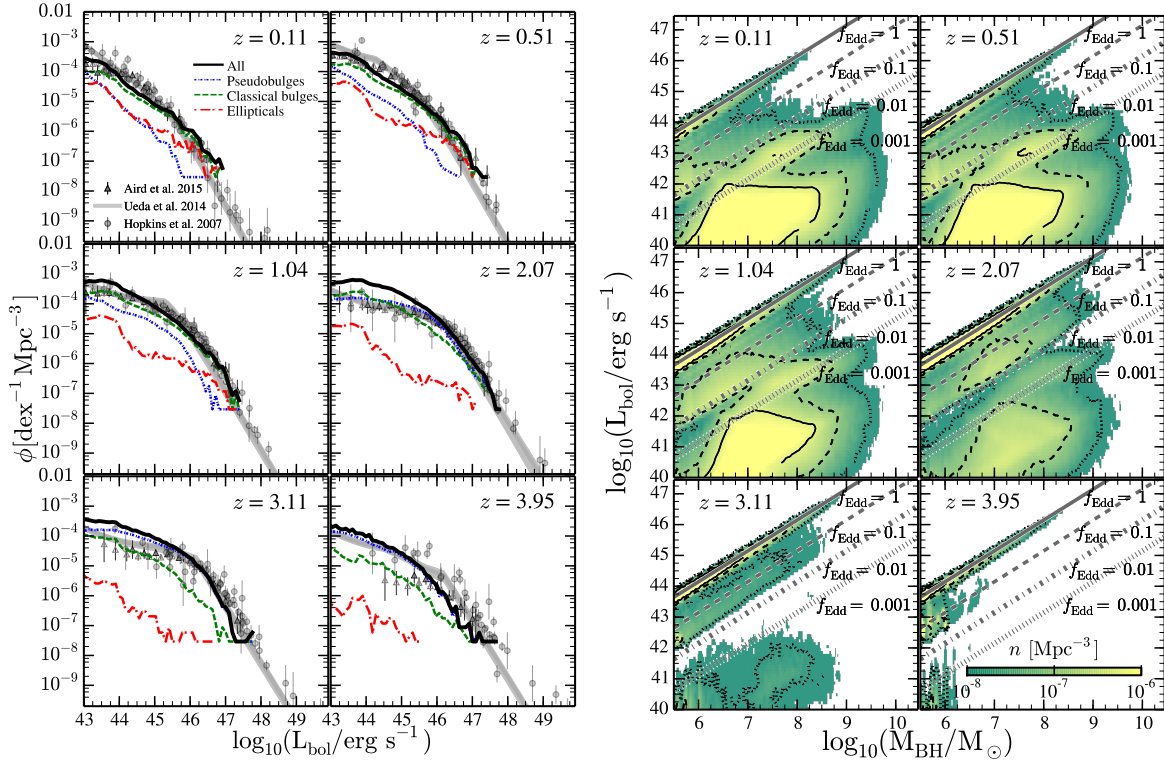


Figure 5.5: **Left panel:** Quasar bolometric luminosity functions ( $L_{\text{bol}}$ ) at  $z \approx 0.1, 0.5, 1.0, 2.0, 3.0, 4.0$ . Solid lines represent the total quasar bolometric luminosity functions. Red dashed-dotted line, green dashed line, and blue dotted lines represent the same but for galaxies hosting respectively elliptical, classical bulge, and pseudobulge bulge structures. Luminosity functions are compared with the data of Hopkins et al. (2007) (circles), Aird et al. (2015) (triangles) and the fit of Ueda et al. (2014) (shaded area). **Right panel:** Bolometric luminosity ( $L_{\text{bol}}$ ) - black hole mass ( $M_{\text{BH}}$ ) plane at  $z \approx 0.1, 0.5, 1.0, 2.0, 3.0$ , and 4.0. The color map encodes the number density ( $n$  [Mpc<sup>-3</sup>]) of objects, with solid, dashed and dotted contours indicating the regions with  $n$  equal to  $5 \times 10^{-7}$  Mpc<sup>-3</sup>,  $10^{-7}$  Mpc<sup>-3</sup>, and  $10^{-8}$  Mpc<sup>-3</sup>, respectively. Diagonal lines represent 1, 0.1, 0.01, and 0.001  $f_{\text{Edd}}$  limits.

growth undergone by the BHs in the chaotic scenario has an imprint in the faint end of  $z \lesssim 1$  bolometric luminosity functions (LFs). Since the BH growth in the chaotic scenario happens on a shorter time-scale than in the model presented here, the BHs tend to consume the gas reservoir faster, hence entering to the quiescent phase earlier. This implies that BHs at low  $z$  do not have enough gas in order to effectively contribute to the faint-end of the bolometric luminosity function, reducing its amplitude. In order to contrast this effect and match the observed faint-end of the AGN bolometric LF, the parameters  $f_{\text{BH}}^{\text{merger}}$  and  $f_{\text{BH}}^{\text{DI}}$  (Eq.(5.2)-(5.3)) controlling the amount of gas accreted during mergers and DI, had to be increased. This resulted in a significant excess on the predicted BHMF at  $M_{\text{BH}} > 10^8 M_{\odot}$ , making difficult its comparison to observations.

#### 5.4.2 The evolution of bolometric luminosity

Since the discovery of the first quasar (Schmidt, 1963), it has been widely accepted that the quasar phase is triggered by the gas accretion onto BHs. The understanding of the quasar luminosity function at different redshifts is a crucial point for inferring the assembly history of BHs. They provide us with information about the BH growth rate, the nature of accretion disks and fundamental quantities such as BH spins and radiative efficiencies. In the left panel of Fig.5.5 we present the evolution of the bolometric luminosity ( $L_{\text{bol}}$ ) function predicted by our model (in Appendix F it is presented the same but for hard



and soft X-rays luminosity). The predictions of our model are compared to the observational work of Hopkins et al. (2007); Aird et al. (2015) and Ueda et al. (2014). A good agreement is achieved at any redshift bin. However, at  $z < 0.5$  our model slightly underestimates the number of objects in the range of  $10^{44} \lesssim L_{\text{bol}} \lesssim 10^{45}$  erg/s. This might be caused by other feeding processes which are not accounted by our model. For instance, Volonteri et al. (2013) discussed that substantial growth of BHs in elliptical galaxies was due to the consumption of recycled gas of the evolving stellar population. In future works, we plan to include this extra growth channel in both elliptical and spiral galaxies. In the same figure, we have divided the luminosity functions in three types of bulge population: galaxies hosting a pseudobulge, classical bulge and elliptical structure. While at high- $z$  ( $z > 2$ ) the bolometric luminosity function is dominated by BHs accreting in pseudobulge structures, at lower redshifts classical bulges and elliptical galaxies are the main structures hosting active BHs. At  $z < 1$ , pseudobulges host only faint AGNs ( $L_{\text{bol}} \lesssim 10^{44}$  erg/s). Since pseudobulges form in galaxies experiencing a quiet merger history (see Figure 3.16 of Chapter 3), our model points out that high- $z$  AGNs ( $z \gtrsim 2$ ) and a fraction ( $\sim 10\text{--}20\%$ ) of intermediate luminous AGNs ( $L_{\text{bol}} \sim 10^{44\text{--}45}$  erg/s) at  $z \lesssim 1$  are mainly triggered by secular processes rather than galaxy encounters. This is in agreement with recent observational and theoretical results. For instance, the observational work of Allevato et al. (2011) pointed out that major or minor mergers alone are not able to reproduce the high bias factors of X-ray AGN selected sample. Similar results were obtained in Marian et al. (2019) for X-ray and optical selected AGNs at  $z \sim 2$ . On the theoretical side, Martin et al. (2018), by using the Horizon-AGN hydrodynamical simulation, found out that only 35% of today's BH mass is directly attributable to merger-driven gas accretion. Similar results were found by Steinborn et al. (2018), which using large-scale cosmological hydrodynamic simulations from the Magneticum Pathfinder set, concluded that mergers could not be the statistically prevalent fueling mechanism for nuclear activity at  $z = 0 - 2$ , except for very luminous AGNs, with  $L_{\text{bol}} > 10^{46}$  erg/s. From the semi-analytical models perspective, recent works of Lagos et al. (2008); Fanidakis et al. (2011); Griffin et al. (2019) and Marshall et al. (2019b) found that, regardless of redshift, DIs are the main drivers of BH growth and AGN activity. Even though all these works use the same analytical prescription to detect instabilities in the galactic disk (see Eq. 2.28), their implementation is slightly different from the one used here. For instance, the model of Fanidakis et al. (2011) (and Griffin et al. 2019) assumes that any disk instability event is able to destroy the galactic disk, transforming the galaxy into a pure spheroidal structure and triggering a burst of star formation. On the other hand, the works of Lagos et al. (2008) and Marshall et al. (2019b) follows the approach presented here transferring to the galaxy spheroidal component only the amount of stellar mass needed to restore the disk stability. However, they do not distinguish between their triggering mechanism, as we do here.

To directly explore the relation between bolometric luminosity and BH mass, in the right panel of Fig.5.5 we show the black hole mass-bolometric luminosity plane at six different redshifts. At  $z \gtrsim 3$  there is a tight correlation between black hole mass and luminosity, as almost all BHs are accreting at  $f_{\text{Edd}} = 1$ . On the contrary, at  $z < 2$  most BHs are far from growing at the Eddington limit, and diverse combinations between BH mass and  $f_{\text{Edd}}$  are present. For instance, whereas at  $z \sim 4$  all the quasars shining at  $L_{\text{bol}} \sim 10^{45}$  erg/s are triggered by BHs of mass  $M_{\text{BH}} \sim 10^7 M_{\odot}$  with  $f_{\text{Edd}} = 1$ , at  $z \lesssim 3$  the same luminosity is triggered by a wide range of BHs ( $M_{\text{BH}} \sim 10^7 - 10^9 M_{\odot}$ ) accreting at  $f_{\text{Edd}} \sim 1 - 0.01$ . Only the highest luminosity ( $L_{\text{bol}} \gtrsim 10^{46}$  erg/s) are reached always by the same type of objects: BHs of mass  $M_{\text{BH}} \gtrsim 10^8 M_{\odot}$  accreting at the Eddington limit. Interestingly, the plane  $L_{\text{bol}} - M_{\text{BH}}$  displays two branches: one at  $f_{\text{Edd}} \gtrsim 10^{-3}$  and the other at  $f_{\text{Edd}} \lesssim 10^{-3}$ . While the former is caused by cold gas accretion, the latter is originated by hot gas consumption. At  $z > 3$  these two regimes are clearly separated, whereas at  $z \sim 2$  the branches start to blend. This is because BHs accreting via the cold gas phase enter in the quiescent (or self-regulated) phase, characterized by low  $f_{\text{Edd}}$ . Eventually, as we discussed in Fig.5.5 left panel, at  $z \sim 0$  the number density of active BHs is dominated by low  $f_{\text{Edd}}$  values (or ADAF geometries) caused by both hot and cold gas accretion.



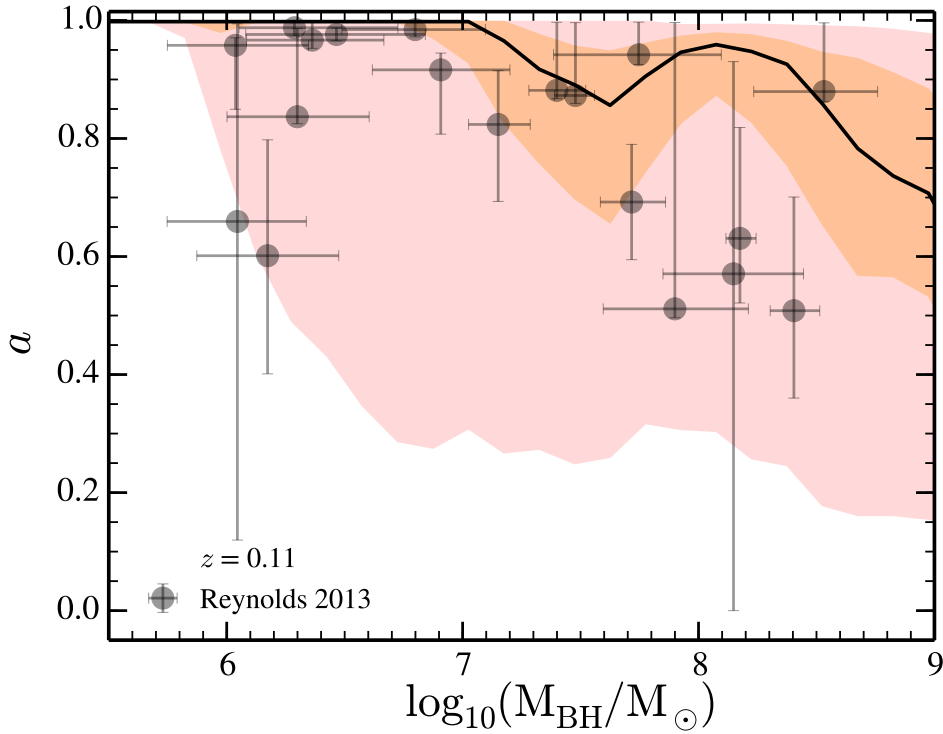


Figure 5.6: Black hole spin,  $a$ , as a function of black hole mass ( $M_{\text{BH}}$ ) at  $z=0$  for black holes with hard X-ray luminosity  $L_{\text{HX}} > 10^{42}$  erg/s. The solid black line represents the median value of the spin, whereas dark and light orange shaded areas display the  $1\sigma$  and  $2\sigma$  of the distribution. Black dots are the observational data of Reynolds (2013).

### 5.4.3 The evolution of black hole spin

Apart from mass, the spin parameter is the other fundamental property of BHs that has to be taken into account to build a complete picture of how black holes assemble their masses across cosmic time, given also the dependence of the radiation efficiency on the spin value. From an observational point of view, spin measurements are still a challenge and the current estimates display large errors. Reynolds (2013) present a compilation of few BHs with reliable measurements of both spin and mass. However, all the spin values have been computed via X-ray spectroscopy of iron  $K\alpha$  line, biasing the results towards AGNs with bright hard X-rays luminosity ( $\gtrsim 10^{42}$  erg/s, see Table 2 in Sesana et al. 2014). As a check of the spin predictions in L-Galaxies, we present in Fig. 5.6 a comparison of the model with Reynolds (2013) data. In order to perform a fair comparison we have only selected in our sample the BHs with hard X-ray luminosity larger than  $10^{42}$  erg/s (see Appendix F for hard and soft X-rays LFs). We see that the model predictions are overall consistent with the observations.

In the left panel of Fig. 5.7 we present the cosmological evolution of BH spin. The model generally predicts a rapidly spinning super-massive black hole population. While at  $M_{\text{BH}} < 10^6 M_{\odot}$  BHs tend to be maximally spinning, at  $M_{\text{BH}} > 10^6 M_{\odot}$  BHs display lower spin values (see also Sesana et al., 2014), with average spin values decreasing with increasing BH mass. Also, the median spin values show a modest decrease with decreasing redshift, but only for BHs with  $M_{\text{BH}} > 10^6 M_{\odot}$ . The different spins of small and high-mass BHs come from the ratio  $|\vec{J}_d|/2|\vec{J}_{\text{BH}}|$  during the gas consumption. At  $M_{\text{BH}} < 10^6 M_{\odot}$ , independently of the redshift and the nature of the accretion episode, the ratio  $|\vec{J}_d|/2|\vec{J}_{\text{BH}}|$  is always larger than one, resulting in a BH feeding characterized by  $n_{Pa} = 1$  (see Section 5.3.3). Conversely, for  $M_{\text{BH}} > 10^6 M_{\odot}$ , the value of  $|\vec{J}_d|/2|\vec{J}_{\text{BH}}|$  is not necessary larger than one and the precise number of  $n_{Pa}$  depends on the galaxy bulge assembly. Indeed, this bulge dependence is seen in Fig. 5.7 when the BH population is divided according to the host bulge type (pseudobulge, classical bulge and elliptical). Re-

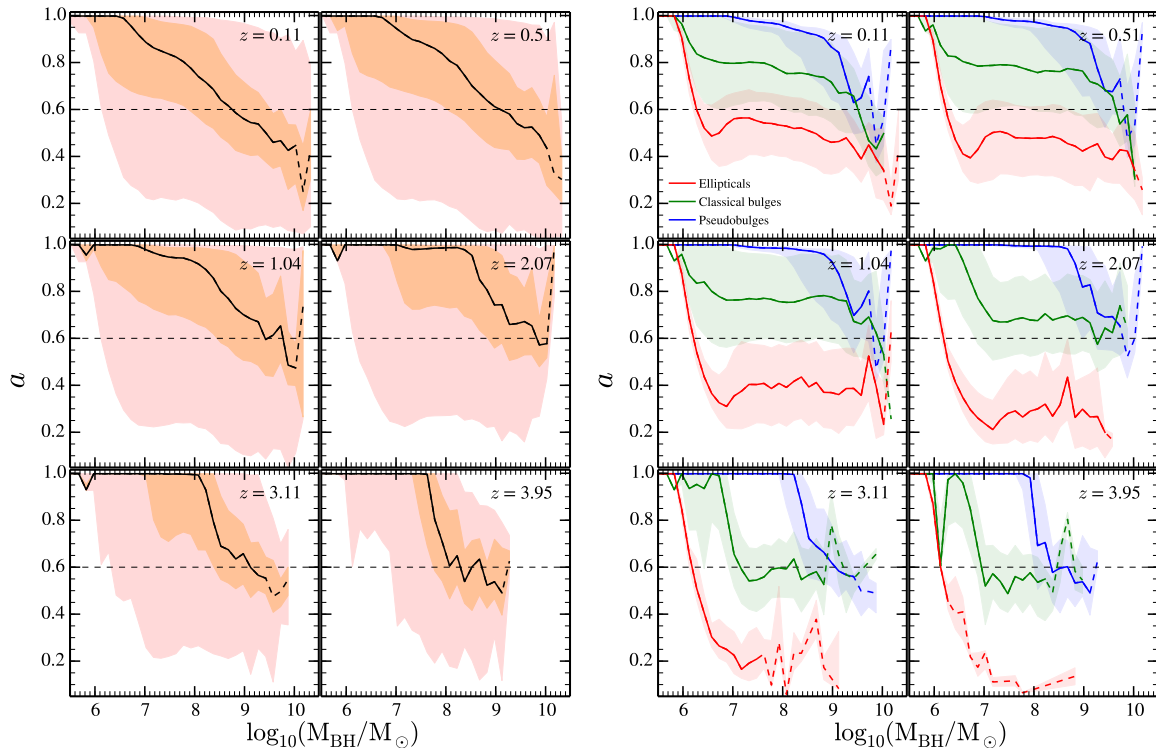


Figure 5.7: **Left panel:** Predicted black hole spins,  $a$ , as a function of black hole mass ( $M_{\text{BH}}$ ) and at different redshifts. Solid black lines represent the median value of the spin per black hole mass. Dark and light orange shaded areas display the  $1\sigma$  and  $2\sigma$  of the distribution. To guide the reader we have highlighted with dashed lines the value of  $a = 0.6$  (corresponding to an accretion efficiency  $\sim 0.1$ ). **Right panel:** The same as in the left panel but dividing the galaxies between classical bulges (green), pseudobulges (blue) and ellipticals (red). Shaded areas display the  $1\sigma$  of the distribution. The large fluctuations at high masses are due to small sample statistics (in both panels dashed lines in the median relation corresponds to the black hole masses where the number of objects is smaller than 5).

regardless of the redshift, at fixed mass, BHs hosted in pseudobulges display larger spin values ( $a \gtrsim 0.9$ ) than the ones in classical bulges ( $a \sim 0.7$ ) and ellipticals structures ( $a \lesssim 0.4$ ). This is in agreement with the work of [Orban de Xivry et al. \(2011\)](#), which concluded, by observing local AGN, that BHs in local Narrow-line Seyfert I galaxies (with masses  $\sim 10^6 M_{\odot}$ ) hosted in pseudobulge structures need to be rapidly spinning in order to explain their duty cycles. Notice that the model predicts a slight spin-up of BHs hosted in elliptical galaxies from  $z \sim 1$  ( $a \sim 0.3$ ) to  $z \sim 0$  ( $a \sim 0.4$ ). This is because after the formation of the elliptical structure the galaxy undergoes successively minor mergers/*smooth accretions* (a median value of 5) which carry gas with large  $v/\sigma$  towards the BH, ultimately causing its spin-up (see [Figure 3.7](#) and [3.16](#) in [Chapter 3](#) where we show the number density of minor/*smooth accretion* events and the typical redshift of the last minor merger). This is along the line of recent observational work, pointing out that minor mergers ( $\sim 8$  with mass ratio 1:10) contribute significantly to the build-up of massive elliptical galaxies at  $z \lesssim 1$  ([Boylan-Kolchin et al., 2006](#); [Trujillo et al., 2011](#)). The dependence on the bulge type is somewhat blurred for BHs with  $> 10^8 M_{\odot}$  inhabiting pseudo- and classical- bulge structures. This is because such massive BHs are hosted in massive galaxies ( $M_{\text{stellar}} > 10^{11} M_{\odot}$ ) whose bulge assembly is complicated, shaped by both mergers and disk instabilities. This intricate bulge assembly results in a complex evolution of the bulge  $v/\sigma$ , significantly deviating from the  $v/\sigma$  values produced by DI or minor mergers alone. For instance, the bulge  $v/\sigma$  in pseudobulges decreases after a minor merger while  $v/\sigma$  in classical bulges increases after a DI. Other mechanisms that blur the spin-bulge dependence at  $\gtrsim 10^8 M_{\odot}$  are the *gas-poor* BH-BH coalescences. In these cases the remnant BHs do not accrete gas and the spin change is driven by the BH coalescence. [Berti and Volonteri \(2008\)](#) showed that the

spin evolution under only BH-BH mergers is driven towards  $a \sim 0.4 - 0.7$  (with some intrinsic dispersion).

During the last years several studies have addressed the evolution of BH spin by using semi-analytical models. For instance, [Fanidakis et al. \(2011\)](#) and [Griffin et al. \(2019\)](#) found out that the *chaotic* scenario suggested by [King et al. \(2005\)](#) applied on GALFORM SAM (run on top of the Millennium and P-Millennium merger trees) yields a population of BHs characterized by low spin values ( $a \lesssim 0.4$ ) at any mass and redshift (see Figure 9 of [Fanidakis et al. 2011](#) and [Griffin et al. 2019](#)). Even though the chaotic scenario was able to reproduce the population of radio-loud AGNs in the local Universe, its outcome spin distribution makes difficult reconciling the model predictions with the recent claims of a rapidly spinning black hole population ([Orban de Xivry et al., 2011](#); [Reynolds, 2013](#); [Trakhtenbrot, 2014](#); [Shankar et al., 2016](#)). In the same work they also explored a *prolonged* accretion scenario. Although in this case the model predicts BHs with  $a > 0.9$ , the observed LFs are systematically above the observed one and its consistency with radio-loud AGNs in the local Universe is worse than in the chaotic scenario (see Figure 10 of [Fanidakis et al. 2011](#) and Figure 16 of [Griffin et al. 2019](#)). Other attempts have been done by [Barausse \(2012\)](#) employing a SAM build on top of Press-Schechter merger trees. By using a more sophisticated approach consisting in feeding the BH respectively in a prograde and chaotic way during gas rich and gas poor mergers, they found a dichotomy in the spin distribution between rapidly ( $a \gtrsim 0.9$ ) and low ( $a \sim 0.2$ ) spinning BHs (see Figure 14 and 15 in [Barausse 2012](#)). [Sesana et al. \(2014\)](#) updated the spin evolution of [Barausse \(2012\)](#) by linking the BH growth with the assembly of the galactic bulge. As in this work, they found different spinning black holes hosted in elliptical and spiral galaxies. Finally, [Volonteri et al. \(2013\)](#) also studied the spin with a SAM based on Press-Schechter merger trees. Similar what we do here, they assumed that the BH quasar phase takes place in two different phases. Whereas the former is described by an Eddington limited growth with a spin evolution characterized by a prograde accretion, the latter displays low Eddington ratios with a chaotic spin evolution (even though they explored a coherent mode as well during this quiescent phase). They found a strong spin redshift evolution whereby  $z > 2$  BHs are characterized by large spin values ( $a > 0.8$ ) whereas  $z < 1$  BHs display small spins ( $a < 0.4$ ). However, the model did not include BH feeding through disk instabilities, a channel which seems to be fundamental in SAMs ([Fanidakis et al., 2012](#); [Menci et al., 2014](#); [Marshall et al., 2019a](#)).

## 5.5 Wandering black holes

In this section we discuss our main results on the wandering black hole population. We first explore the frequency and location of the events at different cosmological times. We then focus on the local universe, investigating the characteristics of wBHs hosted in different kinds of galaxies.

### 5.5.1 Wandering black holes across cosmic time

The left panel of Fig. 5.8 shows the redshift evolution of the wBH number density ( $n$ ). We show only results for BHs whose mass is larger than  $10^6 M_\odot$  since at smaller masses we can not draw solid conclusions given the resolution of the MS simulation, as previously discussed. Regardless of the BH mass, the number density evolves with redshift, reaching a maximum of  $\sim 10^{-3} \text{ Mpc}^{-3}$  at  $z \sim 0$ . The lighter is the mass of the wBH the larger is the number density at high- $z$ . For instance, while at  $z \sim 4$  black holes of  $M_{\text{BH}} > 10^7 M_\odot$  have  $n \lesssim 10^{-6} \text{ Mpc}^{-3}$ , black holes of  $10^6 < M_{\text{BH}} < 10^7 M_\odot$  present 1 dex larger number densities. For comparison, the figure displays the  $n$  values of nuclear black holes. Regardless of mass and redshift, nuclear BHs are 1 – 3 dex more numerous than wandering BHs, especially at  $z \gtrsim 4$ . Concerning the different contribution between *orphan* and *ejected* BHs, we find that at  $M_{\text{BH}} > 10^7 M_\odot$  the former dominate the number density of wBHs. On the other hand, at  $10^6 < M_{\text{BH}} < 10^7 M_\odot$  the relative contribution of the two types of wBHs evolves with redshift; while *ejected* wBHs display larger number density at  $z \gtrsim 1.5$ , *orphan* ones dominate at lower redshifts. This evolution is due to the fact that towards lower  $z$  the number of orphan galaxies increase, and, at the same time, the frequency of the *major/minor* interactions decreases (see, e.g., Figure 3.2 of Chapter 3).

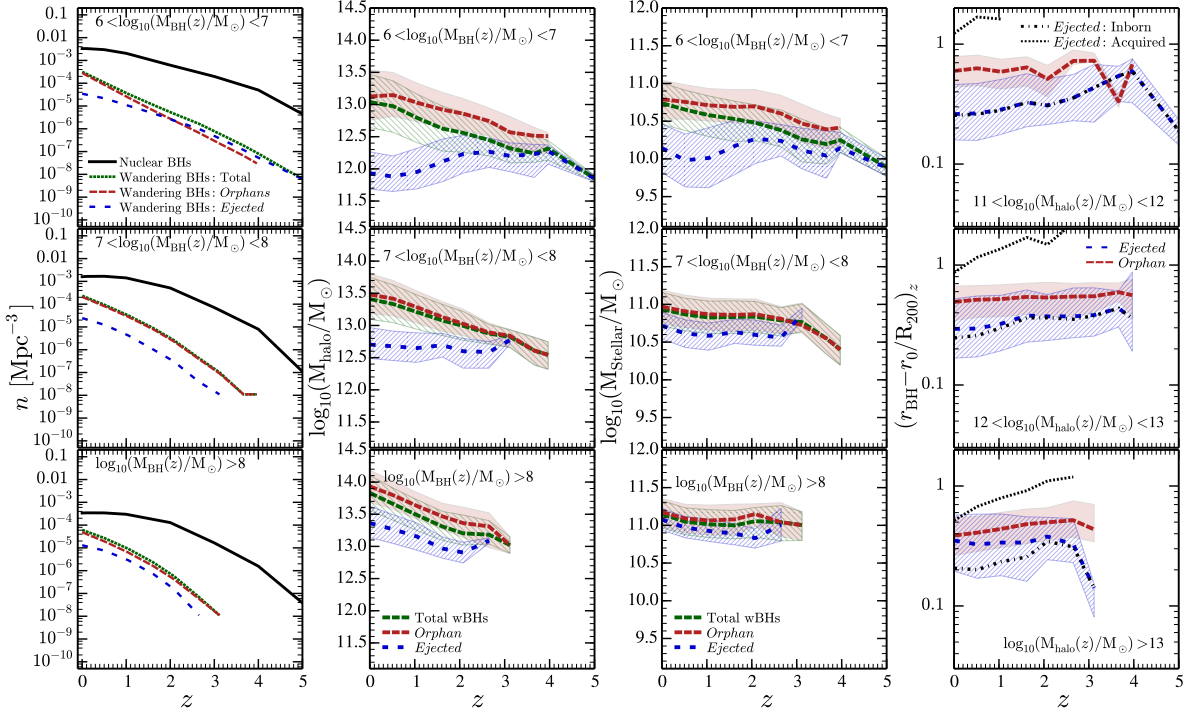


Figure 5.8: **Left panel:** Redshift evolution of the number density ( $n$ ) of nuclear (thick black solid line) and wandering (thick short-dashed dark green line) BHs of in the ranges:  $6 < \log_{10}(M_{\text{BH}}/M_{\odot}) < 7$  (upper panel),  $7 < \log_{10}(M_{\text{BH}}/M_{\odot}) < 8$  (middle panel) and  $\log_{10}(M_{\text{BH}}/M_{\odot}) > 8$  (lower panel). The population of wBHs has been divided into *orphans* (long dashed dark red line) and *ejected* (dotted dark blue line). **Central left panel:** Median subhalo mass in which wandering black holes are hosted at different redshifts. As in the left panel, each figure corresponds to a different BH mass bin. The wBH population has been divided into *orphans* (long dashed dark red line) and *ejected* (dotted dark blue line). The shaded areas indicate the  $1\sigma$  dispersion. **Central right panel:** Same as the central left panel but for stellar masses. **Right panel:** Redshift evolution of the median positions of all wandering black holes with mass  $> 10^6 M_{\odot}$ . The position,  $r_{\text{BH}}$ , is given with respect to the subhalo center,  $r_0$ , and is normalized to the subhalo virial radius,  $R_{200}$ . Each panel corresponds to a different subhalo mass bin. Blue short-dashed and red long-dashed lines represent the median positions of *ejected* and *orphan* wBHs respectively. The shaded areas indicate the  $1\sigma$  dispersion. We further split the ejected population into inborn and acquired, represented by the black short-dashed and blue dotted lines, respectively.

In the two central panels of Fig.5.8 the evolution of the median subhalo and stellar mass in which wandering black holes are hosted is presented. At  $z > 3$  wBHs with  $M_{\text{BH}} > 10^8 M_{\odot}$  inhabit very massive subhalos and galaxies, with typical masses of  $M_{\text{halo}} > 10^{13} M_{\odot}$  and  $M_{\text{stellar}} > 10^{11} M_{\odot}$ . Particularly, the host subhalo mass presents an increasing trend toward low  $z$ , displaying values from  $M_{\text{halo}} \sim 10^{13} M_{\odot}$  at  $z \sim 4$  up to  $M_{\text{halo}} \sim 10^{14} M_{\odot}$  at  $z \sim 0$ . On the contrary, the stellar mass of their central galaxy hardly changes, maintaining a rather constant value of  $\sim 10^{11} M_{\odot}$ . WBHs with  $10^7 < M_{\text{BH}} < 10^8 M_{\odot}$  display a similar behavior but are hosted in slightly less massive subhalos and galaxies. Finally, wBHs with  $10^6 < M_{\text{BH}} < 10^7 M_{\odot}$  are typically placed in  $M_{\text{halo}} \sim 10^{12.2} M_{\odot}$  and  $M_{\text{stellar}} \sim 10^{10.5} M_{\odot}$ . When the population of these wBHs is divided by formation scenario, we see that at  $z < 2$  *ejected* wBHs tend to be hosted in less massive subhalo and galaxies ( $M_{\text{halo}} \sim 10^{11.7} M_{\odot}$  and  $M_{\text{stellar}} \sim 10^{10} M_{\odot}$ , respectively) than at higher redshifts. However, the significance of this trend change is small.

The position of both *ejected* and *orphans* wBHs with  $M_{\text{BH}} > 10^6 M_{\odot}$  as function of redshift is presented in the right panel of Fig.5.8. The population has been divided in 3 different bins of subhalo masses

while the distances (referred to the subhalo center,  $r_0$ ) have been normalized by the subhalo virial radius,  $R_{200}$ . As shown, regardless of subhalo mass, *ejected* and *orphan* wBHs at  $z > 0.8$  are located in different regions inside the subhalo. While the former reside at  $\lesssim 0.3R_{200}$  (with a decreasing trend towards low  $z$ ), the latter orbit at  $\sim 0.6 - 0.8 R_{200}$  radii. On the contrary, at  $z < 0.8$  there are differences from a subhalo mass bin to another. While for  $M_{\text{halo}} < 10^{13} M_{\odot}$  *ejected* and *orphans* wBHs still inhabit different subhalo regions, at  $M_{\text{halo}} > 10^{13} M_{\odot}$  both types of wBHs are at similar distances from the subhalo center,  $\sim 0.3 R_{200}$ . To understand this behavior, in Fig.5.8 we divided the population of *ejected* wBH in two sub-classes: the acquired and inborn ones. While the former have been incorporated from other galaxies after a subhalo merger, the latter were generated in-situ, expelled from the central galaxy of the subhalo after a recoil. A completely different behavior is seen for the two populations, regardless of the redshift. While inborn *ejected* BHs are closer to the subhalo center than orphan BHs, the acquired *ejected* wBHs populate similar regions, further from the subhalo center. Consequently, the change of trend of the ejected population in massive subhalos at low  $z$  it is caused by the acquired *ejected* wBHs, whose number becomes dominant with respect to the inborn ones.

### 5.5.2 The environment of wandering black holes in the local universe

We now focus on the local universe, exploring the typical subhalo and galaxy masses hosting wandering black holes as well as the frequency of wandering BHs for different galaxy type. As discussed before, we assume that wBHs are not accreting, thus not observable as active sources. In future works we will explore how simple assumptions for the growth of wBHs could translate into their observability for different host properties.

The mass function of wBHs at different subhalo and galaxy masses is presented in the the small panels of Fig.5.9. For what concerns the subhalo mass, we note that only the more massive subhalos host a significant population of wBHs, including some with mass larger than  $10^7 M_{\odot}$ . By dividing the wandering BHs by formation scenario we can see that for  $M_{\text{halo}} \lesssim 10^{13} M_{\odot}$  the *ejected* population reaches larger masses than the orphan one, whereas at larger subhalo masses the trend is inverted. Indeed, the amplitude of the *orphan* wBHs mass function increases with subhalo mass due to the increase of the average number of satellite galaxies<sup>13</sup>. Analogously, galaxies with the largest masses are the ones which host the most massive wandering black holes, but already galaxies with  $M_{\text{stellar}} \sim 10^{10} M_{\odot}$  can be surrounded by massive wBHs.

The larger panels of Fig.5.9 present both the probability  $\mathcal{P}$  of finding at least one wBH above a given mass threshold  $M_{\text{BH}}^{\text{th}}$  (upper panel) and the median number of wBHs ( $N_{\text{wBHs}}$ ) at a given subhalo mass (lower panel). Independently of the  $M_{\text{BH}}^{\text{th}}$ , both  $\mathcal{P}$  and  $N_{\text{wBHs}}$  increase with the host subhalo and galaxy mass. However, the exact value of  $M_{\text{BH}}^{\text{th}}$  has an important effect in the values of  $\mathcal{P}$  and  $N_{\text{wBHs}}$ . For instance, at  $M_{\text{BH}}^{\text{th}} = M_{\text{seed}}$  all subhalos above  $10^{13} M_{\odot}$  (galaxies above  $10^{10.75} M_{\odot}$ ) host at least one wBH, with a typical  $N_{\text{wBHs}} > 5$ . However, only subhalos above  $10^{14} M_{\odot}$  (galaxies above  $10^{11.5} M_{\odot}$ ) host a wBH with  $M_{\text{BH}}^{\text{th}} > 10^8 M_{\odot}$ .

## 5.6 The imprint of gravitational recoil on the BH global properties

In this section we investigate the effects of gravitational recoil in the properties of nuclear black holes across cosmic time. As we will show, long wandering phases can have a visible effect in the black hole occupation fraction and in the BH growth, in particular for certain galaxy types.

<sup>13</sup>Typically, the average number of satellite galaxies increases with the subhalo mass in a power-law shape (see e.g. [Berlind et al., 2003](#); [Contreras et al., 2017](#)).



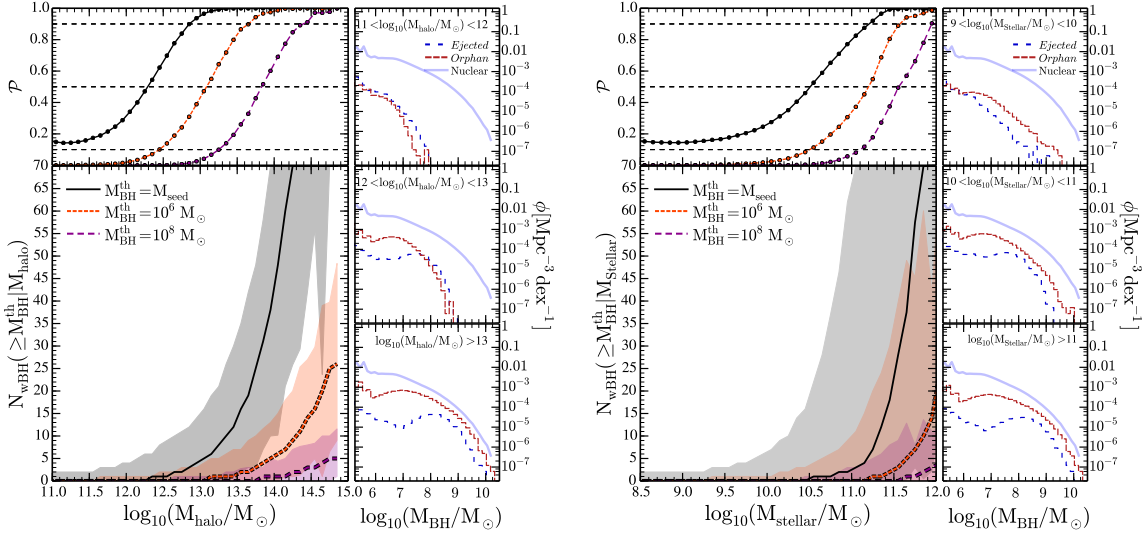


Figure 5.9: **Left panel:** Connection between the wandering black holes and their host subhalos at  $z=0$ . *Left upper panel:* Probability  $\mathcal{P}$  at a given subhalo mass bin of finding at least one wBH above the mass threshold,  $M_{\text{BH}}^{\text{th}}$ . Solid black line, short dashed orange line and long dashed purple line display three different  $M_{\text{BH}}^{\text{th}}$  thresholds:  $M_{\text{seed}} = 10^4 M_{\odot}$ ,  $10^6 M_{\odot}$  and  $10^8 M_{\odot}$ , respectively. Horizontal dashed lines highlight the values  $\mathcal{P} = 0.1, 0.5, 0.9$  the *Left lower panel:* Median number of wandering black holes,  $N_{\text{wBH}}$ , per subhalo mass bin for a given  $M_{\text{BH}}^{\text{th}}$  value. Shaded areas represents the  $3\sigma$  interval of the distributions. *Right panels:* Wandering black hole mass function at three different subhalo mass bins. Solid blue, short red dashed and long blue dashed lines represent, respectively, the mass function for nuclear BHs, *orphan* wBHs and *ejected* wBHs. **Right panel:** Same as in the left panel but for stellar masses.

### 5.6.1 Black hole occupation fraction

The seeding procedure followed in this work (see Section 5.3.1) imply that all galaxies host a BH when they are initialized. But gravitational recoil after BH mergers can leave galaxies without a central BH, at least until the kicked BH loses the acquired energy and settles again in the galaxy center. Therefore, especially at later times, a fraction of galaxies is expected to be deprived of a central BH. In Figure 5.10 we show the nuclear BH occupation fraction as a function of galaxy stellar mass, and for different galaxy morphologies. Regardless of the bulge morphology and redshift,  $f_{\text{BH}}$  decreases towards *low stellar masses*: from  $\sim 80\%$  for  $M_{\text{stellar}} \gtrsim 10^{11} M_{\odot}$  down to  $\sim 60\%$  for galaxies with  $M_{\text{stellar}} \lesssim 10^{8.5} M_{\odot}$ . This mass dependence is related to the potential well of the galaxy: the smaller the galaxy, the lower the escape velocity, thus the higher the ejection probability for the central BH. Moreover, as we will see at the end of this section, for galaxies with  $M_{\text{stellar}} < 10^9 M_{\odot}$ , it is also much more probable the ejection not only from the galaxy, but also from the subhalo. By dividing the galaxy population in different bulge morphological types, we find that, in massive galaxies with  $M_{\text{stellar}} > 10^{10} M_{\odot}$ , pseudobulges and bulgeless galaxies display lower occupation fractions than both classical bulges and ellipticals. This is because pseudobulges and bulgeless galaxies experience very few mergers during their evolution, thus it is more difficult for them to replenish their empty bulge after an ejection. Indeed, as we will see in Section 5.6.2 (Fig. 5.13), the reincorporation of BHs in a pseudobulge galaxy is not very common ( $\lesssim 10\%$  of probability at any stellar mass) making it even more difficult for such structures to increase their nuclear BHs occupation fraction. Besides mass and morphology, Fig. 5.10 shows a trend of decreasing  $f_{\text{BH}}$  towards low  $z$ . This is because BH-BH mergers are characterized by smaller values of  $q$  ( $\sim 0.01, 0.08, 0.1$  for pseudobulges, classical bulges and ellipticals, respectively) and poorer gas environments towards low  $z$ . For instance, at  $z \sim 2$ , 80% of BH-BH mergers in pseudobulges, classical bulges and elliptical galaxies are considered as wet mergers. On contrary, at  $z \sim 1.0$ ,  $\sim 90\%$ ,  $60\%$ ,  $80\%$  of the BH-BH mergers in pseudobulges, classical bulges and elliptical galaxies are classified as gas poor mergers. These conditions increase the modulus



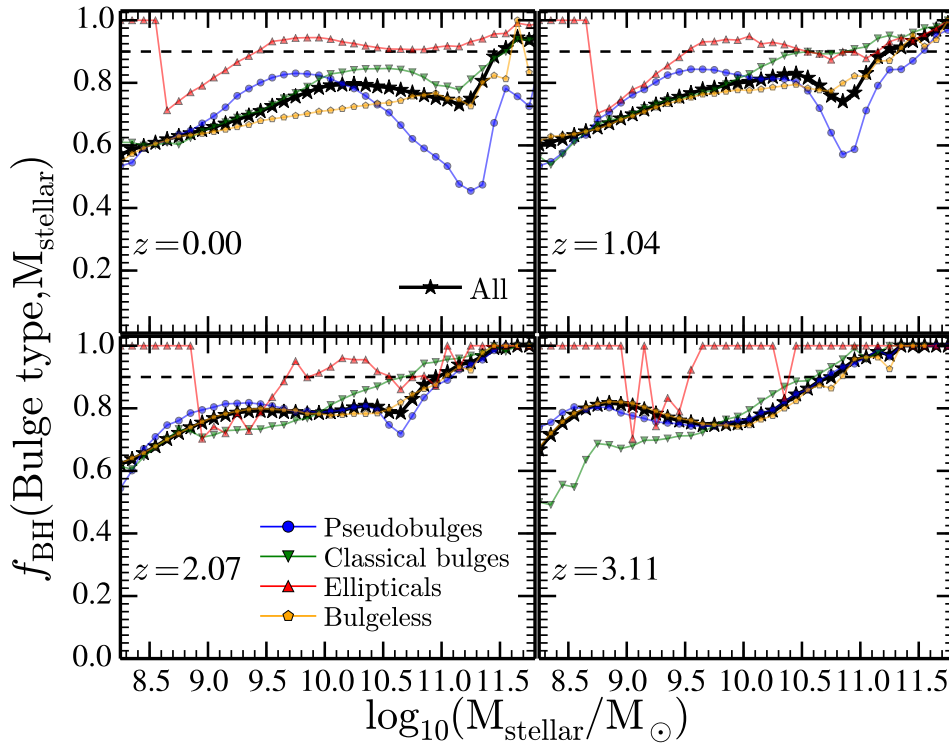


Figure 5.10: Nuclear black hole occupation fraction,  $f_{\text{BH}}$ , as a function of stellar mass and different bulge morphological types at  $z \sim 0, 1, 2, 3$ . Black lines present the  $f_{\text{BH}}$  for all the galaxies. Blue, green, red and, yellow lines display the break-up into pseudobulges, classical bulges, ellipticals and bulgeless galaxies, respectively. Horizontal dashed line highlights  $f_{\text{BH}} = 0.9$ .

of the kick velocity making it easier for a BH to be ejected. In particular, the recoil velocity after a BH-BH coalescence in a gas-rich environment is generally larger than in a gas-poor one since this latter is inefficient in leading the alignment between the two BH spins. On the other hand, small values of  $q$  lead to larger kicks since the recoil value is proportional to the inverse of  $(1 + q)$  (see Eq. (5.29)).

To explore in which moment the BH recoil velocities had major importance in driving ejections, Fig.5.11 shows the comoving number density of BH ejections. Clearly, at  $z \sim 1.5$  the number density reaches a maximum, coinciding with the peak of the galaxy-galaxy merger frequency (see Figure 3.2 of Chapter 3). By dividing the ejections in different bins of BH mass we find that the larger is the BH mass, the lower is the redshift of its ejection. While black holes of  $< 10^6 M_{\odot}$  are typical ejected at  $z \gtrsim 2.5$ , the ones with  $> 10^8 M_{\odot}$  were *kicked out* at  $0.1 < z < 0.6$ . This mass segregation is just a growth matter. At very high- $z$  we do not find massive BHs ( $> 10^8 M_{\odot}$ ) being ejected, since they did not have enough time to accrete gas and grow.

Finally, in Fig.5.11 we also show the number density of reincorporation as compared to the one of ejections. The latter is larger than former by a factor of 2–3 depending on the exact redshift. This is because gravitational recoil would expel more easily a BH from both galaxy and subhalo, rather than only from the galaxy. In other words, gravitational kicks are likely to overcome at once both the subhalo and galaxy escape velocities rather than only the galaxy one. This directly reduces the effective number of BHs that can be reincorporated in the parent galaxy. For instance, regardless of redshift, we have found that galaxies with  $M_{\text{stellar}} < 10^9 M_{\odot}$ ,  $10^9 < M_{\text{stellar}} < 10^{10} M_{\odot}$ ,  $10^{10} < M_{\text{stellar}} < 10^{11} M_{\odot}$  have, respectively, 2.5, 2 and, 1.5 times *more* galaxy+subhalo ejections than only galaxy ejections. On the other hand, in more massive systems ( $M_{\text{stellar}} > 10^{11} M_{\odot}$ ) the trend is inverted and the former is 2 times less common than the latter. A similar behavior is seen with subhalo mass.

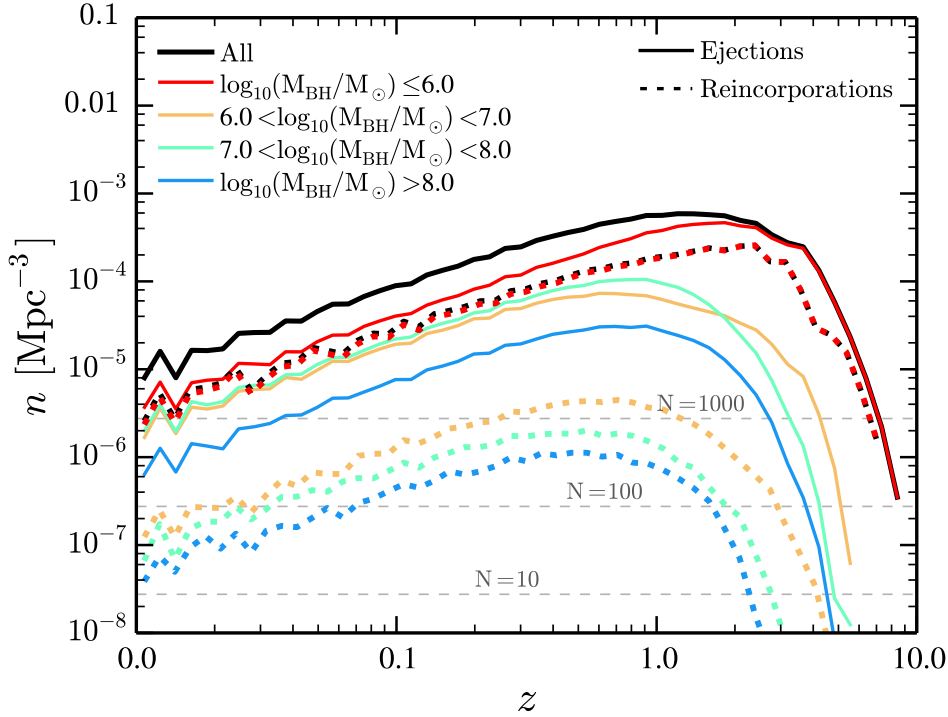


Figure 5.11: Redshift distribution of black hole ejections via gravitational recoils (solid lines) and reincorporation after a wandering phase (dashed lines). While black lines represent the predictions for the whole BH population, different colors are for different black hole mass bins as labeled in figure. Horizontal grey lines display the values of  $n$  in which we have a number of objects ( $N = n(z) \times L_{\text{Box}}^3$ ) equal to 10, 100 and 1000.

### 5.6.2 Effects on the scaling relations

As we have seen in the previous section, the population of nuclear black holes is affected by the physics of gravitational recoil included in the model. In this section we explore how this translates into predictions for the bulge-black hole  $z = 0$  relation.

The left panel of Fig. 5.12 shows the bulge-black hole scaling relation for *all* galaxies when the SAM is run including or not both BH recoil velocities and wandering phase. Clearly, the scatter and the median relation are different in the two runs. The model displays a trend of hosting less massive BHs at fixed bulge mass in the run in which recoil velocities and wandering phase are taken into account. In the other two panels the population is divided by bulge morphological type: classical bulges and ellipticals (middle panel) and pseudobulges (right panel). While we still see some effects in the classical bulge population, the signatures of BH recoil are more pronounced for the pseudobulge population, where the median relation at  $M_{\text{bulge}} \gtrsim 10^{10} M_{\odot}$  changes up to  $\sim 2$  dex and the scatter increases up to 4 dex.

These results clearly show that the inclusion of gravitational recoil physics is important in the predictions for the BH scaling relations, in particular in pseudobulge galaxies. Similar effects were found in the hydro-simulations of Blecha et al. (2011) and the analytical model of Gerosa and Sesana (2015). By running over 200 simulations of gaseous galaxy mergers with 60 different BH-BH merger configurations Blecha et al. (2011) found out that the inclusion of gravitational recoils leaves an imprint in the correlation between bulge velocity dispersion and the mass of the host BH. At fixed BH mass, the run

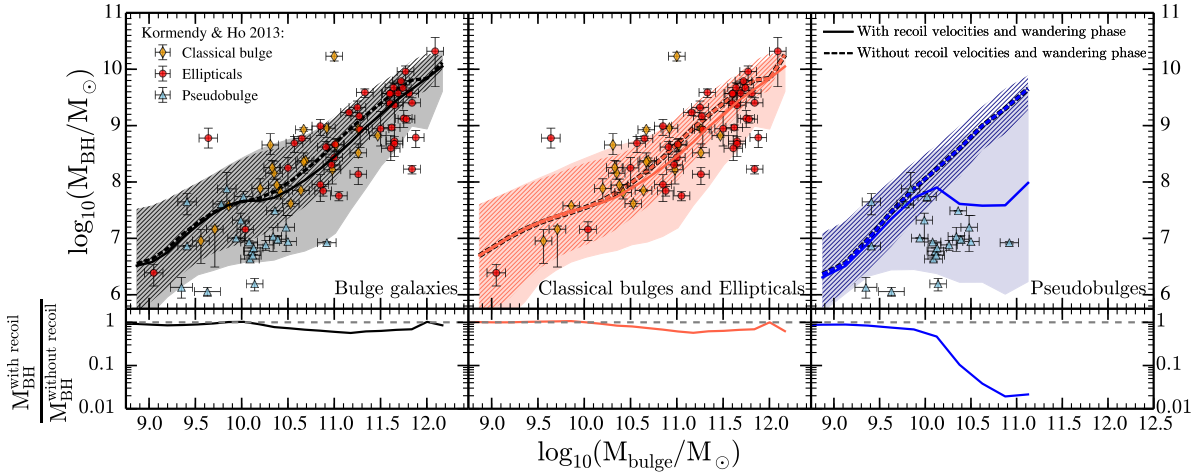


Figure 5.12: **Upper panels:** Black hole mass ( $M_{\text{BH}}$ ) - bulge mass ( $M_{\text{Bulge}}$ ) scaling relation in the local universe ( $z=0$ ). Left panel represents the relation for the entire galaxy population, the central panel is for classical bulges and elliptical galaxies, and the right panel is for pseudobulges. Solid and dashed lines represent, respectively, the median of the relation when the SAM is run with and without including recoil velocities and wandering phase. Plain and dashed shaded area represent, respectively, the  $2\sigma$  of the relation with and without recoil velocities. Dots display the data from [Kormendy and Ho \(2013\)](#). **Lower panels:** Ratio, at a fixed bulge mass, between the black hole mass in the model with recoil velocities and the black hole mass in the model without recoil velocities.

with gravitational recoils displays large bulge velocity dispersion values. This deviation is caused by the ejection interrupting the BH growth while the galaxy continues its evolution. On the other hand, the work of [Gerosa and Sesana \(2015\)](#) explored the repercussion of gravitational recoils in brightest cluster galaxies (BCGs). They pointed out that the ejections and subsequent replenishments of BHs after galaxy mergers increase the scatter of the BCGs black hole - bulge mass relation.

In [Fig.5.13](#) we explore in more details the origin of the deviations of the recoiled population with respect to the median relation. We again present results for classical bulges (left panel) and pseudobulges separately (right panel). The median relation is divided into galaxies whose nuclear BHs never underwent an ejection nor a wandering phase ( $G_0$ ), galaxies whose bulge did not host a central BHs but after a merger<sup>14</sup> it was refilled by one ( $G_{\text{refill}}$ ) and galaxies whose BHs were reincorporated after a wandering phase ( $G_{\text{reincop}}$ ). Regarding pseudobulges, galaxies belonging to  $G_0$  follow a very similar relation as the model without recoil velocities (see [Fig.5.12](#)). A similar trend is visible for the galaxies type  $G_{\text{refill}}$  at  $M_{\text{bulge}} \lesssim 10^{10} M_{\odot}$ . However, their trend breaks at larger bulge masses. Concerning galaxies of type  $G_{\text{reincop}}$ , they show a much more flattened relation compared to the previous ones, regardless of bulge mass. This is because the merger (principally *smooth accretions*) that filled the pseudobulge happened at relatively low  $z$ , typically  $z \lesssim 1.0$ , with a galaxy hosting a BH that is  $\sim 2$  dex ( $q \sim 0.01$ ) lighter than the average BH that would inhabit the empty bulge. As shown in the upper panel of [Fig.5.13](#), the relative contribution of  $G_0$ ,  $G_{\text{refill}}$  and,  $G_{\text{reincop}}$  causes the change on the pseudobulge scaling relation with respect to the one without recoil velocities. Since galaxies  $G_0$  are the dominant ones at  $M_{\text{bulge}} < 10^{10} M_{\odot}$  we do not find any differences between the model with and without BH recoils. However, at  $M_{\text{bulge}} > 10^{10.2} M_{\odot}$  the trend changes since galaxies type  $G_{\text{reincop}}$  take the main importance, causing the flattening in the relation, seen in [Fig.5.12](#).

Concerning classical bulges and ellipticals structures, all the three types  $G_0$ ,  $G_{\text{refill}}$  and,  $G_{\text{reincop}}$  have similar bulge-BH mass relation than the relation without recoil (even though  $G_{\text{reincop}}$  is systematically

<sup>14</sup>major, minor or *smooth accretion*.

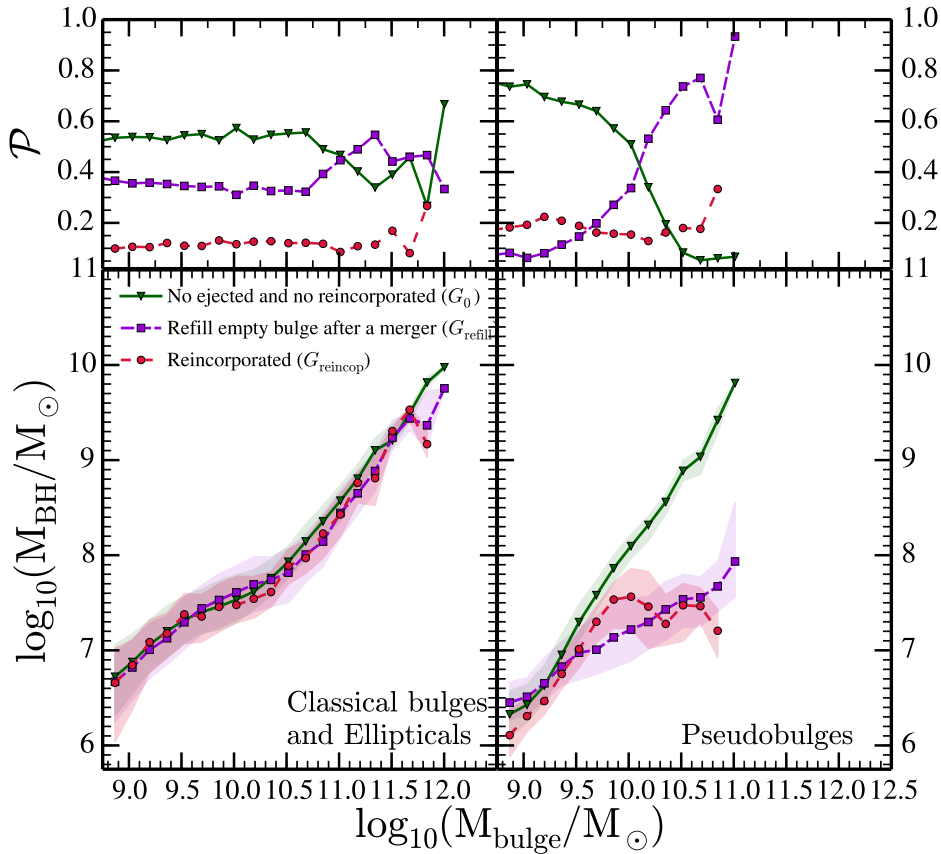


Figure 5.13: **Upper panels:** Probability, for a given bulge mass, of finding a nuclear BH which never underwent an ejection nor a wandering phase ( $G_0$ , green line), a nuclear BH which refilled an empty bulge after a merger (major, minor or *smooth accretion*,  $G_{\text{refill}}$ , violet line) and a BH which was reincorporated after a wandering phase ( $G_{\text{reincop}}$ , red line) **Lower panels:** Scaling relation for classical bulges plus ellipticals (left panel) and pseudobulges (right panel) when the nuclear BH inhabiting that bulge morphology is divided in the three previous types.

below). This is caused by the fact that classical bulges and elliptical galaxies do not spend a lot of time without a BH: the reincorporation time of the BH is relatively low ( $\lesssim 0.01$  Gy) and since their formation is linked with the hierarchical growth of structures, they experience frequent mergers (with  $q \gtrsim 0.2 - 0.3$ ) in short time-scales. As it is shown in the upper panel of Fig. 5.13, galaxies  $G_0$  dominate at any bulge masses. However, at  $M_{\text{bulge}} > 10^{10.5} M_{\odot}$  the probability  $\mathcal{P}$  of finding a galaxy  $G_{\text{refill}}$  increases up to  $\mathcal{P} \sim 0.4$ . This causes the small change seen in the relation with and without recoil velocities in Fig. 5.12. We have also explored the  $G_0$ ,  $G_{\text{refill}}$  and,  $G_{\text{reincop}}$  population at  $z = 2$  for both classical bulges (and ellipticals) and pseudobulges. In this case, at any mass and bulge type the  $G_0$  population dominates. For instance, at  $M_{\text{bulge}} \sim 10^{10.5} M_{\odot}$   $G_0$  counts for more than the 65% and 80% of the population of classical bulges and pseudobulges, respectively. This causes the median value in the runs with and without recoil velocities to be very similar, even though the population  $G_{\text{refill}}$  and  $G_{\text{reincop}}$  helps in increasing the scatter.

In a test run, we have also checked how the bulge-black hole scaling relation behaves when in the model we do not assume any correlation between BH accretion and bulge assembly (see Eq. (5.18)). For that we have run L-Galaxies with the *chaotic* scenario of King et al. (2005) which assumes an isotropic distribution for the angular momentum of the gas clouds<sup>15</sup>. We did not find significant differences, as the

<sup>15</sup>Following Sesana et al. (2014), the chaotic scenario presented in King et al. (2005) is obtained fixing  $F = 1/2$  in Eq. (5.18).

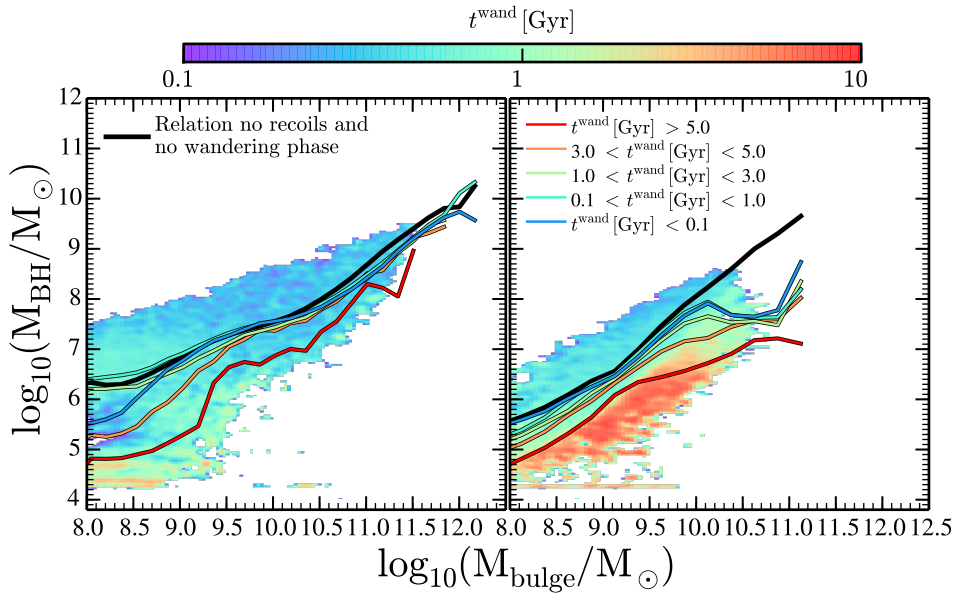


Figure 5.14: Bulge - black hole mass relation for classical bulges plus ellipticals (left panel) and pseudobulges (right panel) when *only* nuclear black holes which underwent a wandering phase are selected. The color map indicates the median value of the time spent in the wandering phase ( $t^{\text{wand}}$ ) per bin of bulge and black hole mass. In each panel, the solid black line represents the scaling relation when no recoil velocities and wandering phase are included, whereas colored lines represent the median relation for nuclear BHs in a given bin of wandering phase, as labelled in figure.

strength of the recoil velocities depends primarily on the capability of the gas surrounding the BBH in aligning the two BH spins at the moment of the merger, rather than on the spin value. BH-BH coalescences at  $z \lesssim 1.5$  are mostly happening in gas poor environments, reducing the number of BH mergers with a spin alignment, independently on the spin model used.

Finally, even though we have showed that reincorporated BHs have small impact in the bulge - black hole mass relation, in Fig.5.14 we have explored the effect of the BH reincorporation after a wandering phase in the scaling relations. In the figure it is shown the scaling relation for only classical bulges (including ellipticals) and pseudobulges whose central black hole was reincorporated after undergoing a wandering phase. Independently of the bulge morphology, there is a segregation by time in the wandering phase ( $t^{\text{wand}}$ ): BHs which underwent longer wandering phase are systematically below the scaling relation, as growth in the model is only allowed when BHs are centrals (see Section 5.3.5). This trend is more clear in the pseudobulge population.

## 5.7 Summary and conclusions

In this chapter we have studied the mass assembly, spin evolution and environment of both nuclear and wandering supermassive black holes. To do that, we have updated with new physical prescriptions the version of L-Galaxies semi-analytical model (SAM) presented in Chapter 3. The new prescriptions have been applied to the merger trees of the Millennium simulation, although galaxies have been initialized using the outputs of the higher-resolution simulation MillenniumII.

The starting point of our BH model is the gas accretion from a *hot* and *cold* phase. While the former is linked with the consumption of part of the hot gas atmosphere which surrounds the galaxy, the latter is triggered by cold gas accretion right after a galaxy disk instability (DI) and/or a galaxy merger. During both phases of gas accretion, we track the evolution of BH spin ( $a$ ) using the approach presented in Dotti



et al. (2013) and Sesana et al. (2014). We linked the number of prograde transient accretion disk (BH spin-up) with the degree of coherent motion in the bulge. In particular, we have assumed that DIs, which lead to the bar/pseudobulge formation in our model, are the processes that increase the coherence of the bulge kinematics. On the other hand, mergers, which lead to the assembly of classical bulges and ellipticals, bring disorder to the bulge dynamics. These assumptions result in a correlation between the predicted BH spin values and the host galaxy morphology. Regardless of redshift and BH or bulge mass, galaxies with a pseudobulge structure host nuclear BHs with larger spin values than both classical and elliptical galaxies. In particular, at  $M_{\text{BH}} > 10^6 M_{\odot}$  pseudobulges, classical bulges and elliptical galaxies host respectively BHs with a typical spin of  $a \sim 0.9, 0.7$  and  $0.4$ . At lower BH masses, as a consequence of the implemented model, all the three bulge morphology host maximum spinning BHs. The model also follows the formation of binary black hole (BBH) systems by assuming that the lifetime of a BBH (from the formation to the coalescence) inversely correlates with the BH merger ratio and the galaxy gas fraction at the moment of the galaxy encounter. This simple assumption will be further improved in future works. After coalescence, the remnant has a spin value fully determined by the Barausse and Rezzolla (2009) analytic expression.

Due to conservation of linear momentum, in the instant of the BH-BH coalescence the propagation of gravitational waves imparts a recoil velocity to the remnant black hole. If the modulus of the recoil velocity, computed according to Lousto et al. (2012) equations, is larger than the escape velocity of the host galaxy, the model assumes that the black hole is kicked from its host and incorporated in the DM subhalo as a *wandering black hole*. Here we tag these BHs as *ejected* wBH. Since it is not clear which is the amount of mass in accretion disk that can be retained or accreted by a BH after the recoil, we have neglected the fact that the ejected BH can retain an accretion disk. The model also tracks the formation of another type of wandering black holes, *orphan* wBH, which are originated after the complete disruption of their host galaxy via tidal forces. Independently of their origin, wBH orbits are tracked by using numerical integration, taking into account the host subhalo and galaxy properties for the computation of gravitational acceleration and dynamical friction. In particular, the integration of the wBH orbit stops when i) the black hole is re-incorporated in the galaxy, i.e., when the BH passes through the galaxy center with a velocity smaller than its escape velocity, ii) the recoil velocity of ejected BHs is larger than the subhalo escape velocity or iii) the black hole position exceed 3 times the hosts subhalo virial radius and it is still moving away from the galaxy.

Turning to the model predictions, we find a good consistency with the observed local black hole mass function (BHMF), spin values, BH-bulge mass relation and quasar (bolometric, soft and hard X-rays) luminosity functions. The model predicts a stalling in the BHMF at  $z \sim 1$ , where no significant change up to  $z = 0$  is shown. This indicates that most of the local BHs were already assembled by  $z \sim 1$ . By dividing the BHs between inactive and active we have found that the former population increases from  $z \sim 3$  to  $z \sim 0$ , with the most massive BHs becoming non-active earlier. The accretion geometry of the active population displays also a redshift evolution. Regardless of BH mass,  $z \sim 3$  active BHs are characterized by a thin disk geometry fuelled by Eddington-limited accretion flows. ADAF, instead, becomes the main accretion geometry at  $z \sim 0$  for BHs with  $M_{\text{BH}} > 10^6 M_{\odot}$ , powering BHs during the quiescent phase of cold and hot gas accretion. On top of this, the luminosity functions of the model indicate that accreting BHs are hosted in different bulge morphologies at different cosmological times. While at  $z > 2$  the high end of the luminosity function is dominated by BHs accreting in pseudobulge structures, at lower redshifts classical bulges and elliptical galaxies are the main structures hosting the most powerful active BHs. Since in the SAM the pseudobulge formation is detached from the merger framework (see Chapter 3) our model points out that  $z \gtrsim 2$  AGNs are mainly triggered by secular processes instead of galaxy encounters, in agreement with recent observational and theoretical results.

One of the main novelties of the present study is a thorough exploration of the population of wandering black holes (wBHs), either *orphan* or *ejected*. When looking at their mass density, we have found



an increasing trend towards low  $z$ , reaching a maximum of  $10^{-4} \text{ Mpc}^{-3}$  at  $z \sim 0$ , which is considerable but still 1–3 dex smaller (depending the BH mass) than that of nuclear black holes. Regarding the spatial distribution, *ejected* and *orphan* wBHs occupy different regions inside the subhalo. While the former reside at  $\lesssim 0.3R_{200}$ , with a decreasing trend towards low  $z$ , the latter inhabit the  $\gtrsim 0.5 R_{200}$  regions. Concerning the environments of wBHs in the local universe, the model predicts that subhalos of  $M_{\text{halo}} < 10^{13} M_{\odot}$  rarely host a wBH with  $> 10^6 M_{\odot}$ . But if they do, the wBH is typically formed after a gravitational recoil, i.e. of the *ejected* type. The picture is inverted at  $M_{\text{halo}} > 10^{13} M_{\odot}$ , where it is relatively more common to find a wBH of  $M_{\text{BH}} > 10^6 M_{\odot}$  (typical  $\sim 5$ ) principally formed after the disruption of satellite galaxies, i.e. of the *orphan* type. We find the same tendency when looking at wBH statistics against the host stellar mass.

Besides being an important channel of wandering black hole formation, we have found that gravitational recoils also affect the co-evolution between the black hole and the host galaxy. In particular, they cause a systematic depletion of nuclear BHs towards low redshift and stellar mass. While the former dependence is because low- $z$  BH-BH coalescences are characterized by poorer gas environments than the ones at higher- $z$ , condition which increase the modulus of the kick velocity, the latter is simply caused by the fact that low-mass galaxies have smaller potential wells than massive ones, making it more difficult for them to retain the BH after a kick. By dividing the galaxy population according to bulge type, we have found that at  $M_{\text{stellar}} \gtrsim 10^{10} M_{\odot}$  both classical bulge and elliptical structures tend to display larger occupancy fractions than pseudobulges and bulgeless galaxies. This behavior is due to the fact that pseudobulges are detached from the merger framework, making more difficult for them to replenish their empty bulge after an ejection. On the other hand, at  $M_{\text{stellar}} \lesssim 10^{10} M_{\odot}$  classical bulges are more affected by the gravitational recoils, having more than the 40% of empty bulges. By running the SAM with and without gravitational recoils and wandering phase we have also explored the imprints of gravitational recoils in the  $z=0$  bulge-BH scaling relation. We have found that both the median of the relation and its scatter are different in the two runs. There is a trend of hosting less massive BHs at fixed bulge mass in the run in which recoil velocities and wandering phase are taken into account. A similar tendency is found when the population is divided into classical bulges, elliptical galaxies and pseudobulges. In particular, the latter structures are the ones which suffer a more pronounced effect, where the median relation at  $M_{\text{bulge}} \gtrsim 10^{10} M_{\odot}$  changes  $\sim 2$  dex and the scatter increases. Finally, we have also explored the effect of BH reincorporation after a wandering phase in the BH-bulge relation. Regardless of bulge morphology, the larger is the time of the BH in the wandering phase before its reincorporation, the larger is its offset from the median BH-bulge relation.

Despite the model presented here represents a considerable step forward in modeling the evolution of the population of black holes across cosmic time, still more effort is needed to construct a full coherent framework that can produce new quantitative predictions that can be tested against current and future observations. For example, including a physical model for the expected activity of wBH will lead to useful predictions about the number of active wBHs that may be observed in the local Universe and their more likely location with respect to their host galaxy/group/cluster. In the near future, new instrumentation will make it possible to constrain several aspects of the cosmic BH formation and evolution. The *Laser Interferometer Space Antenna* (LISA, [eLISA Consortium et al., 2013b](#)) will constrain the nuclear BH merger rate and their spin properties, thus also providing precious information for the theoretical modeling of the *kicked* wBH population; *James Webb Space Telescope* (JWST, [Gardner et al., 2006](#)) and *Advanced Telescope for High-ENergy Astrophysics* (ATHENA, [Nandra et al., 2013](#)) will allow to pierce deeper in the cosmos, probing progressively further and lower mass accreting BHs. Only a concerted interplay of theory and observations will unfold the full history of the cosmic, nuclear and wandering, supermassive black hole population.

## CHAPTER 6

### MOCK LIGHTCONES FOR PHOTOMETRIC SURVEYS

*“¿Se acuerda de La Comarca señor Frodo?  
Será pronto primavera. Los huertos estarán  
todos en flor y en la Avellaneda los pájaros  
tendrán listos sus nidos. Comenzará la fiesta  
estival de la cebada en los Bancales. La degustación  
de las primeras fresas con nata. El sabor de las  
fresas, ¿lo recuerda?”*

El señor de los anillos: El Retorno del Rey.

*“Do you remember the Shire, Mr. Frodo? It'll be  
spring soon. And the orchards will be in blossom.  
And the birds will be nesting in the hazel thicket.  
And they'll be sowing the summer barley in the lower  
fields... and eating the first of the strawberries with  
cream. Do you remember the taste of strawberries?”*

The Lord of the Rings: The Return of the King.

This Chapter is based on the paper: *J-PLUS: Synthetic galaxy catalogues with emission lines for photometric surveys*. David Izquierdo-Villalba; Raul E. Angulo.; Alvaro Orsi; Guillaume Hurier; Gonzalo Vilella-Rojo; Silvia Bonoli; Carlos López-Sanjuan; et al. *Astronomy & Astrophysics, Volume 631, id.A82, 16 pp.*

### ABSTRACT

In this chapter we present a synthetic galaxy lightcone specially designed for narrow-band optical photometric surveys. To reduce time-discreteness effects, unlike previous works, we directly include the lightcone construction in the L-Galaxies semi-analytic model applied to the subhalo merger trees of the Millennium simulation. Additionally, we add a model for the nebular emission in star-forming regions, which is crucial for correctly predicting the narrow/medium-band photometry of galaxies. Explicitly, we consider, individually for each galaxy, the contribution of 9 different lines: Ly $\alpha$  (1216Å), H $\beta$  (4861Å), H $\alpha$  (6563Å), [OII] (3727Å, 3729Å), [OIII] (4959Å, 5007Å), [NeIII] (3870Å), [OI] (6300Å), [NII] (6548Å, 6583Å), and [SII] (6717Å, 6731Å). We validate our lightcone by comparing galaxy number counts, angular clustering, and H $\alpha$ , H $\beta$ , [OII] and [OIII]<sub>5007</sub> luminosity functions to a compilation of observations. As an application of our mock lightcones, we generate catalogues tailored for J-PLUS, a large optical galaxy survey featuring 5 broad and 7 medium band filters. We study the ability of the survey to correctly identify, with a simple *three filter method*, a population of emission-line galaxies at various redshifts. We show that the 4000Å break in the spectral energy distribution of galaxies can be misidentified as line emission. However, all significant excess (larger than 0.4 magnitudes) can be correctly and unambiguously attributed to emission line galaxies. Our catalogues are publicly released to facilitate their use in interpreting narrow-band surveys and for quantifying the impact of line emission in broad band photometry.

## 6.1 Introduction

Optical surveys have been important in establishing our current understanding of how galaxies form and evolve (York et al., 2000; Gunn et al., 2006; Eisenstein et al., 2011; Driver et al., 2009; Grogin et al., 2011; Koekemoer et al., 2011; Sánchez et al., 2012; Dawson et al., 2013; Sobral et al., 2018a). Despite the progress, our picture is still incomplete and ongoing and future surveys, such as *The Extended Baryon Oscillation Spectroscopic Survey* (eBOSS, Dawson et al., 2016), *Dark Energy Spectroscopic Instrument* (DESI, Dark Energy Survey Collaboration et al., 2016), *Euclid* (Laureijs et al., 2011), *Wide Field Infrared Survey Telescope* (WFIRST, Dressler et al., 2012), and *eROSITA* (Merloni et al., 2012), could soon fill the gaps. To optimally exploit the data from these upcoming galaxy surveys, synthetic galaxy catalogues are needed (e.g. Blaizot et al., 2005; Kitzbichler and White, 2007b; Guo et al., 2011; Merson et al., 2013; Lacey et al., 2016; Merson et al., 2018). By using these mock catalogues it is possible to estimate uncertainties in deriving a given galaxy property, study selection effects, or quantify the impact of different sources of errors. In addition, it is possible to modify various assumptions regarding galaxy formation physics, and explore their impact on observable galaxy properties. Thus, realistic and physically motivated mock catalogues are extremely important to interpret observational data in terms of the underlying galaxy-formation physics.

In particular, mock galaxy catalogues are particularly important for interpreting surveys that combine broad-band with narrow-band photometry (Wolf et al., 2003; Moles et al., 2008; Ilbert et al., 2009; Pérez-González et al., 2013; Benitez et al., 2014; Cenarro et al., 2019; Padilla et al., 2019). These surveys attempt to inherit the power of spectroscopy in reliably estimating physical properties of galaxies, and of photometry in measuring the light in a spatially resolved manner while avoiding the pre-selection of targets. Thus, they deliver smaller statistical uncertainties and weaker degeneracies in estimating physical properties of galaxies compared to broad-band surveys. On the other hand, due to the complexity of the data and its acquisition, they might contain more uncertainties related to the measurement of line emission compared to spectroscopic surveys.

There are several requirements for realistic mock catalogues. First, a galaxy formation model is needed that predicts all the relevant observable properties of galaxies, such as position, redshift, metallicity, stellar mass, or star formation rate (Croton, 2006; Somerville et al., 2008; Guo et al., 2011; Lacey et al., 2016; Henriques et al., 2015). Second, it is important to include emission lines from star-forming regions and quasars (Orsi et al., 2014; Molino et al., 2014; Chaves-Montero et al., 2017; Comparat et al., 2019); although lines contribute in a relatively minor way to broad-band magnitudes, they can dominate the total flux in narrow and medium bands (see e.g. Sobral et al., 2009, 2013; Vilella-Rojo et al., 2015; Matthee et al., 2015; Stroe and Sobral, 2015; Stroe et al., 2017; Sobral et al., 2018b). Third, it is necessary to project the light and spatial distribution of mock galaxies onto the observer’s frame of reference. This, the so-called lightcone, is a crucial ingredient since a given narrow band can receive contributions from multiple emission lines at different redshifts.

During recent years various galaxy lightcones using merger trees of dark matter  $N$ -body simulations and galaxy formation models have been developed (Blaizot et al., 2005; Kitzbichler and White, 2007a; Merson et al., 2013; Overzier et al., 2013). These mocks lightcones were designed for broad-band surveys, such as SDSS, where the contribution of emission lines in the final galaxy photometry was neglected. With the advancement of more sophisticated narrow-band photometric surveys such as *Survey for High- $z$  Absorption Red and Dead Sources* (SHARDS, Pérez-González et al., 2013), *Javalambre-Photometric Local Universe Survey*<sup>1</sup> (J-PLUS, Cenarro et al., 2019), *Javalambre Physics of the Accelerating Universe Astrophysical Survey* (J-PAS, Benitez et al., 2014), and *Physics of the Accelerating Universe* (PAU, Padilla et al., 2019) the line contributions from star-forming galaxies need to be taken into account. To date, few works have addressed this. For instance, Merson et al. (2018) by using

---

<sup>1</sup>www.j-plus.es

the CLOUDY photo-ionisation code (Ferland et al., 2013) included the  $H\alpha$  emission in the GALACTICUS galaxy formation model (Benson, 2012). By constructing a 4 square degree catalogue they were able to predict the expected number of  $H\alpha$  emitters as a function of redshift, a critical aspect for *Euclid* and *WFIRST* surveys. On the other hand, Stothert et al. (2018) performed forecasts for PAU employing the GALFORM version of Gonzalez-Perez et al. (2014) where the modelling of  $H\alpha$ , [OII], and [OIII] lines was included.

In this chapter we present a new procedure to generate synthetic galaxy lightcones, specially designed for narrow-band surveys. We employ state-of-the-art theoretical galaxy formation models applied to a large N-body simulation to predict the properties and clustering of galaxies. We improve these results with a model for the nebular emission from star-forming regions considering the contribution of nine different transition lines. The properties of these lines are computed separately for each mock galaxy based on its predicted star formation and metallicity. This is one of the first times that multiple emission lines have been included in mock galaxy lightcones following a self-consistent physical model (Merson et al., 2018; Stothert et al., 2018). Additionally, we embed the lightcone building procedure inside the galaxy formation modelling, allowing us to minimise the time-discreteness effects. As an application of our lightcone construction, we generated catalogues for the photometry of the ongoing J-PLUS photometric survey (Cenarro et al., 2019) by observing thousands of square degrees of the northern sky with a specially designed camera of 2 deg<sup>2</sup> field of view (0.55" pix<sup>-1</sup> scale) and the unique combination of five broad-band ( $u, g, r, i, z$ ) and seven medium- and narrow-band filters (see Table 3 of Cenarro et al., 2019). We employed our mocks to test the capabilities of the survey in identify, with a simple three-filter method (3FM), a population of emission-line galaxies at various redshifts. Specifically, all the emission lines that fall in a narrow-band filter centred at the  $H\alpha$  rest wavelength (*J0660* filter). We showed how the 4000Å break in the galaxy spectral energy distribution can cause an apparent excess, misidentified as line emission. However, we demonstrated that all significant excess (larger than 0.4 magnitudes) can be unambiguously attributed to emission lines<sup>2</sup>.

This chapter is organised as follows. In section 6.2 we describe the methodology we follow to construct the galaxy lightcone, predict galaxy properties, and model the strength of emission lines. In section 6.3 we present various comparisons with observations, which illustrate the accuracy of our predictions. In section 6.4 we employ our synthetic catalogues to study the selection of emission-line galaxies (ELGs) in J-PLUS. Finally, in section 6.5 we summarise our main findings. In this work magnitudes are given in the AB system. A lambda cold dark matter ( $\Lambda$ CDM) cosmology with parameters  $\Omega_m = 0.25$ ,  $\Omega_\Lambda = 0.75$ , and  $H_0 = 73 \text{ km s}^{-1} \text{ Mpc}^{-1}$  is adopted throughout the chapter.

## 6.2 Methodology

In this section we discuss the general procedure used to construct our mock galaxy lightcone. We make use of L-Galaxies semi-analytical model in the version of Guo et al. (2011) applied on top of the Millennium merger trees. We refer the reader to Chapter 2 for a detailed description of Millennium simulation and for the whole baryonic physics included in the SAM.

### 6.2.1 Lightcone construction

In this section we outline our method for constructing a lightcone. We start by defining the location of an observer and specifying the orientation, geometry, and angular extent of the lightcone. Then we define how we identify the moment when a galaxy crosses the observer past lightcone.

The 500 Mpc/ $h$  side-length of the Millennium simulation is not always able to encompass the full volume, or redshift range, of observational surveys. Thus, to cover the relevant regions we take advant-

<sup>2</sup>The mock catalogue is publicly available at [https://www.j-plus.es/ancillarydata/mock\\_galaxy\\_lightcone](https://www.j-plus.es/ancillarydata/mock_galaxy_lightcone)

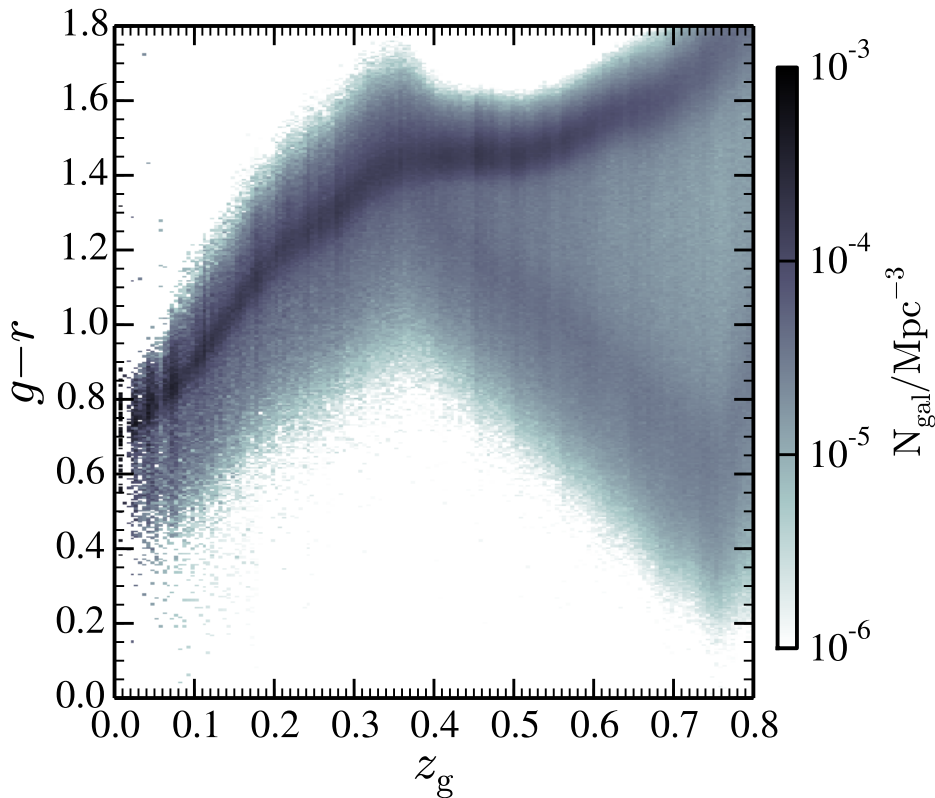


Figure 6.1: For our mock galaxies with  $M_{\text{stellar}} > 10^{10} M_{\odot}/h$ , the observed colour  $g-r$  as a function of redshift ( $z_g$ ). The grey scale represents the number density of galaxies (darker regions corresponds to larger number densities).

age of its periodic boundary conditions and replicate the simulated box eight times in each coordinate direction. This corresponds to a maximum redshift of  $z \sim 3$ , and will also allow us to incorporate high- $z$  ELGs as potential contamination for low- $z$  ELGs.<sup>3</sup> Although the replicated volume underestimates the total number of independent Fourier modes in a survey, it is adequate when different redshift slices are considered separately and the redshift direction is chosen appropriately, as we discuss below.

For convenience, we place the observer at the origin of the first replication, and define the extent of the lightcone as the angular size of  $1000 \text{ Mpc}/h$  at  $z \sim 1$ . This ensures that no more than two repetitions are required to represent the cosmic structure in any redshift shell up to  $z \sim 1$ . This provides a  $22.5^{\circ} \times 22.5^{\circ}$  ( $\sim 309.4 \text{ deg}^2$ ) lightcone. The orientation of the lightcone was chosen following [Kitzbichler and White \(2007a\)](#) to minimise repetition of structure along the line of sight (LOS). According to their methodology, the LOS passes by the first periodic image at the point  $(nL, mL, nmL)$ , where  $m$  and  $n$  are integers with no common factor and  $L$  is the box size. We set the values of  $n = 2$  and  $m = 3$ , resulting in a viewing direction  $(\theta, \varphi) = (58.9^{\circ}, 56.3^{\circ})$ . In [Appendix G](#), we show that this LOS yields a small overlap between box replicas.

The next step is to determine the moment when galaxies cross the observer’s past lightcone. There are several different methods in the literature for this (e.g. [Kitzbichler and White, 2007a](#); [Merson et al., 2013](#)), most of which interpolate galaxy properties across the discrete dark matter simulation snapshots

<sup>3</sup>We apply our lightcone construction in the Millennium merger trees rather than in the Millennium-XXL because of the coarser mass resolution of the latter (with a particle mass of  $\sim 10^9 M_{\odot}/h$ ). The minimum subhalo mass of Millennium-XXL would cause completeness effects in the magnitude range explored in this work and would impose a line luminosity threshold that is too high for us to trust our results (e.g.  $\gtrsim 10^{41} \text{ erg/s}$  at  $z \sim 0$  for  $H\alpha$  line, see [Orsi et al., 2014](#)).



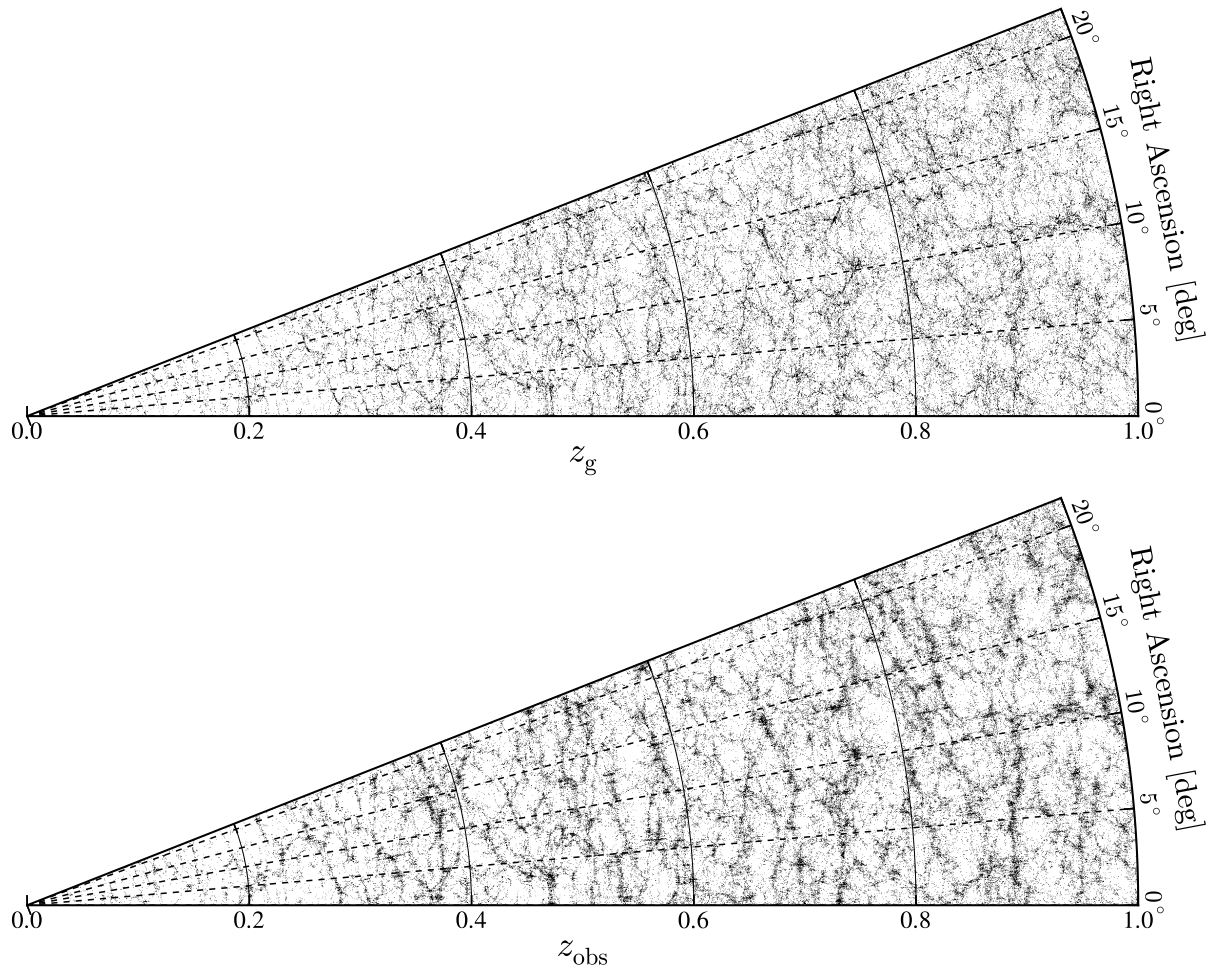


Figure 6.2: **Left panel:** Spatial distribution of galaxies in a thin angular slice (1 deg) inside our mock lightcone. Each galaxy with  $M_{\text{stellar}} > 10^{10} M_{\odot}/h$  is shown as a black dot. The contribution of peculiar velocities is not included. **Right panel:** The same, but including the peculiar velocities in the estimation of the redshift. The clustering is enhanced on large scales due to coherent bulk motions, whereas it is damped on small scales due to random motions inside dark matter haloes.

or by directly storing the DM mass field as the N-body simulation evolves. Here we have decided to follow a different approach. `L-Galaxies` accurately follows in time the evolution of individual galaxies between DM snapshots with a time step resolution  $\lesssim 5 - 19$  Myr. This includes the tracking of central, satellite, and orphan galaxies (i.e. those whose DM host has fallen below the resolution of the simulation), improving along the way the links of the underlying subhalo merger tree (De Lucia and Blaizot, 2007). Here we take advantage of this and use the *galaxy merger trees* as an estimation of the continuous path in space-time of a galaxy. Linearly interpolating between two contiguous galaxy time steps, we search for the lightcone crossing redshift,  $z_g$ , where the comoving radial distance is equal to the distance to the observer. The galaxy properties are then evolved down to that exact moment inside `L-Galaxies`. This approach has the advantage of reducing an artificial discretisation of galaxy properties usually seen in lightcone algorithms (see e.g. Fig. 4 in Merson et al., 2013). To illustrate that discretization effects in our mock galaxy photometry are small, in Fig. 6.1 we show the observed colour  $g-r$  as a function of redshift (which is usually the most affected quantity, see Merson et al., 2013) for galaxies with  $M_{\text{stellar}} > 10^{10} M_{\odot}/h$ . No evident discontinuities are seen along the  $g-r$  axis.



Finally, we add the contribution of peculiar velocities to the observed redshift of a galaxy as

$$z_{\text{obs}} = (1 + z_g) \left( 1 + \frac{v_r}{c} \right) - 1, \quad (6.1)$$

where  $z_g$  is the geometrical redshift at which the galaxy crosses the lightcone and  $v_r$  is the LOS component of its peculiar velocity, and  $c$  is the speed of light.

The spatial distribution of galaxies in our lightcone inside a 1 deg slice is presented in Fig. 6.2. We only display galaxies more massive than  $10^{10} M_{\odot}/h$ . No visible discreteness effects originating from a finite number of simulation snapshots are seen.

### 6.2.2 Line emission modelling

In order to include the contribution of emission lines to the predicted photometry of our mock galaxies, we follow the model described in Orsi et al. (2014). Specifically, we consider the contribution of nine different lines: Ly $\alpha$  (1216Å), H $\beta$  (4861Å), H $\alpha$  (6563Å), [OII] (3727Å, 3729Å), [OIII] (4959Å, 5007Å), [NeIII] (3870Å), [OI] (6300Å), [NII] (6548Å, 6583Å), and [SII] (6717Å, 6731Å), which are those we expect to contribute most significantly to the rest-frame optical wavelength.

In brief, the Orsi et al. (2014) model obtains the lines flux based on a Levesque et al. (2010)<sup>4</sup> model grid of HII region. Four different parameters are needed as an input to the grid: (i) age of the stellar cluster that provides the ionising radiation ( $t_*$ ), (ii) density of the ionised gas ( $n_e$ ), (iii) galaxy gas-phase metallicity ( $Z_{\text{cold}}$ ), and (iv) ionisation parameter ( $q$ ). For the first two parameters we assume constant values:  $t_* = 0$  and  $n_e = 10 \text{ cm}^{-3}$  (see the discussion in Orsi et al., 2014). The last two parameters are directly set by the cold gas metallicity predicted by our galaxy formation model adopting the following relation for the ionisation parameter,

$$q(Z) = q_0 \left( \frac{Z_{\text{cold}}}{Z_0} \right)^{-\gamma} \text{ [cm/s]}, \quad (6.2)$$

where  $q_0$ ,  $Z_0$ , and  $\gamma$  are free parameters set to  $2.8 \times 10^7 \text{ cm/s}$ , 0.012, and 1.3, respectively, to match observational measurements of H $\alpha$ , [OII], and [OIII] luminosity functions (Orsi et al., 2014).

By using the predicted line fluxes, the luminosity of a given line,  $L(\lambda_j)$ , is given by

$$L(\lambda) = 1.37 \times 10^{-12} Q_{\text{H}^0} \frac{F(\lambda_j | q, Z_{\text{cold}})}{F(\text{H}\alpha | q, Z_{\text{cold}})} \text{ [erg/s]}, \quad (6.3)$$

where  $F(\text{H}\alpha | q, Z_{\text{cold}})$  and  $F(\lambda_j | q, Z_{\text{cold}})$  are respectively the flux of H $\alpha$  and  $\lambda_j$  line in a galaxy with ionisation parameter  $q$  and metallicity  $Z_{\text{cold}}$  and  $Q_{\text{H}^0}$  is the ionisation photon rate in units of  $\text{s}^{-1}$  calculated from the galaxy instantaneous star formation rate predicted by our SAM. Here we assume that all the emitted photons contribute to the production of emission lines.

We note that the model predictions for the Baldwin, Phillips & Telervich diagram (BPT diagram, Baldwin et al., 1981)<sup>5</sup> and for the evolution of the emission-line luminosity function are in reasonable agreement with the observations. For more information, we refer the reader to Orsi et al. (2014).

<sup>4</sup>These authors computed the theoretical SEDs for HII regions using the Starburst99 code (Leitherer and Heckman, 1995) in combination with the MAPPINGS-III photo-ionisation code (Dopita and Sutherland, 1995, 1996; Groves et al., 2004).

<sup>5</sup>The BPT diagram of the model can be found in Orsi et al. (2014) Figure 1, with  $\gamma = 1.3$ .

### 6.2.3 Observed magnitudes

Once we had placed galaxies in the lightcone and computed their physical properties (such as stellar mass, star formation rate, and metallicity), we derived their observed photometric properties. The observer-frame apparent magnitudes in the AB system,  $m_{AB}$ , are defined as

$$m_{AB} = -2.5 \log_{10}(f_\nu) - 48.6 = -2.5 \log_{10} \frac{\int T(\lambda) \lambda f_\lambda d\lambda}{c \int \frac{T(\lambda)}{\lambda} d\lambda} - 48.6, \quad (6.4)$$

where  $c$  is the speed of light,  $T(\lambda)$  is the filter transmission curve,  $\lambda$  is the wavelength,  $f_\nu$  is the flux density per frequency interval  $\text{erg s}^{-1} \text{cm}^{-2} \text{Hz}^{-1}$ , and  $f_\lambda$  is the flux density per wavelength interval in  $\text{erg s}^{-1} \text{cm}^{-2} \text{\AA}^{-1}$ .

We assume that our final galaxy photometry is the sum of two contributions. The first is the continuum emission from the mixture of stellar populations hosted by the galaxy ( $f_\lambda^c$ ). The second is the specific flux of all the recombination lines ( $f_\lambda^{l_j}$ ) generated in H II regions. Therefore,

$$f_\lambda \equiv f_\lambda^c + \sum_{j=1}^{n_{\text{lines}}} f_\lambda^{l_j}. \quad (6.5)$$

Including Eq. (6.5) in Eq. (6.4), the magnitude  $m_{AB}$  can be expressed as

$$m_{AB} = 2.5 \log_{10} \left[ 10^{-0.4(m_{AB}^c + 48.6)} + \frac{\int T(\lambda) \lambda \sum_{j=1}^{n_{\text{lines}}} f_\lambda^{l_j} d\lambda}{c \int \frac{T(\lambda)}{\lambda} d\lambda} \right] - 48.6. \quad (6.6)$$

The magnitude  $m_{AB}^c$  is computed by our SAM in a self-consistent way according to the galaxy evolution pathway (Chapter 2, Section 2.3.6). By using the Bruzual and Charlot (2003) synthesis models and a Chabrier initial mass function, L-Galaxies updates the galaxy luminosity in each photometric band every time that the galaxy experiences a star-forming event. Additionally, a model is assumed to account for the light attenuation due to the absorption in the interstellar medium (ISM) and molecular clouds (see De Lucia and Blaizot, 2007; Guo et al., 2011; Henriques et al., 2015). When the galaxy crosses the lightcone, the observed magnitudes in the chosen photometric system are output according to the total luminosity at that moment.

The contribution of emission lines (second term in Eq. 6.6) is taken into account in post processing. Throughout this work we only consider the line emission produced by star formation events, ignoring the contribution of AGNs. The line  $l_j$  is added in its observed wavelength with  $f_\lambda^{l_j}$  determined by a  $\delta$ -Dirac profile of amplitude  $F(\lambda_j|q, Z_{\text{cold}})$ . In our case,  $n_{\text{lines}}$  are the nine lines described in Section 6.2.2. As in the case of the galaxy continuum, all the line fluxes included here are affected by the surrounding dust. A discussion of the impact and modelling of dust is presented in Section 6.3.2.

## 6.3 Validation

In this section we present a set of basic tests for our mock galaxy lightcone. In Section 6.3.1 we compare the predicted galaxy number counts against a compilation of observations in five broad bands ( $u$ ,  $g$ ,  $r$ ,  $i$ ,  $z$ ). In Section 6.3.2, we extend our comparison to the luminosity functions of  $\text{H}\alpha$ ,  $\text{H}\beta$ ,  $[\text{OII}]$ , and  $[\text{OIII}]_{5007}$  lines. We use this comparison to calibrate a dust obscuration model. Finally, in Section 6.3.3 we show the ability of our mock to reproduce the observed clustering of  $g$ -band selected galaxies.

### 6.3.1 Galaxy number counts

In Fig. 6.3 we show the total number of galaxies in our lightcone mock as a function of apparent magnitude. We present our predictions for the five SDSS broad-band magnitudes, and compare them to

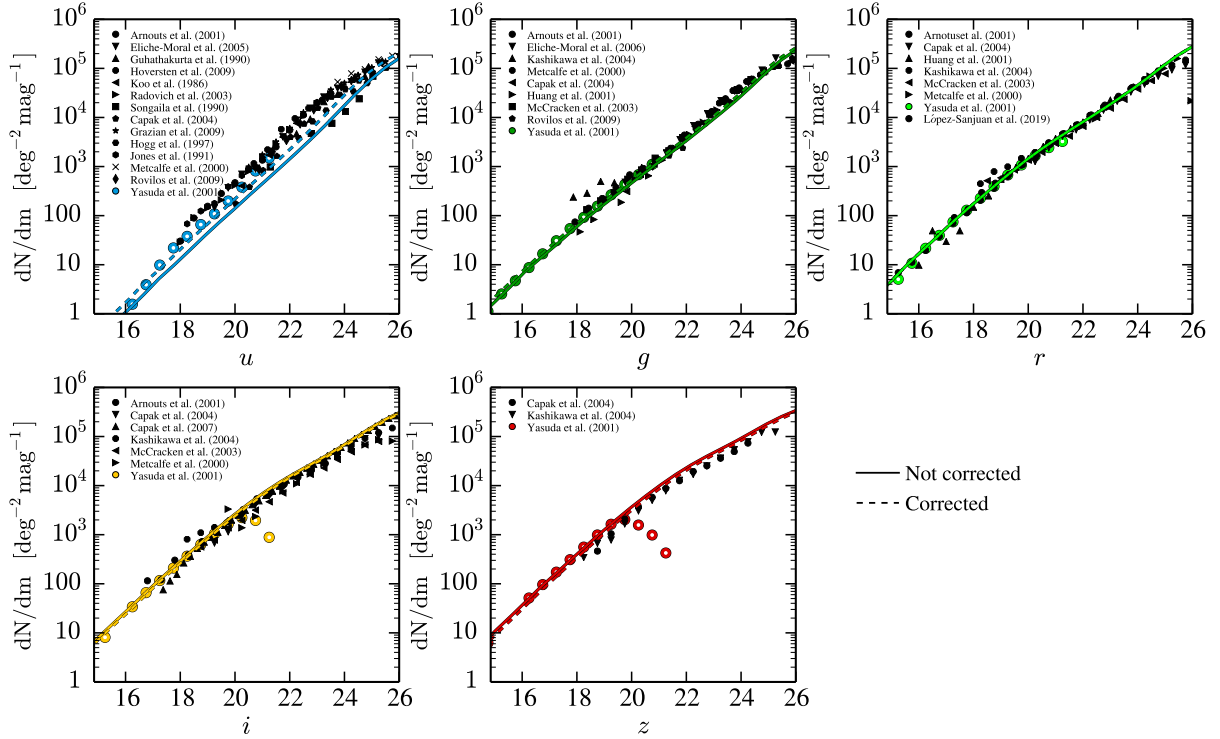


Figure 6.3: Abundance of galaxies as a function of observed magnitude for the different SDSS bands. Symbols show a compilation of observational results from the different datasets, with the measurements from SDSS highlighted as large coloured circles (Yasuda et al., 2001). Shown in each panel are the predictions from our mock galaxy lightcone before and after a correction to apparent magnitudes (solid and dashed lines, respectively) designed to improve the agreement with observations (see Section 6.3.1). The drop in the Yasuda et al. (2001) data in the  $i$  and  $z$  SDSS bands at faint magnitudes is caused by selection effects. The sample used in that work was selected in  $r$  with a magnitude range of  $12 \leq r \leq 21$ .

various observational estimates as indicated by the legend (Koo, 1986; Guhathakurta et al., 1990; Jones et al., 1991; Hogg et al., 1997; Arnouts et al., 2001; Yasuda et al., 2001; Metcalfe et al., 2001; Huang et al., 2001; McCracken et al., 2003; Radovich et al., 2004; Kashikawa et al., 2004; Capak et al., 2004; Eliche-Moral et al., 2005; Capak et al., 2007; Hoversten et al., 2009; Rovilos et al., 2009; Grazian et al., 2009; López-Sanjuan et al., 2019). We note that different observations usually employ slightly different filter transmission curves; however, this introduces only a very minor correction, which we ignore.

Our theoretical predictions and the observations are in good agreement, especially for the  $r$ ,  $i$ , and  $z$  SDSS bands. This represents an important validation of our methodology. Even so, we find a slight systematic disagreement across bands, transiting from well-matched number counts on long wavelengths to an underestimation at short ones ( $u$  and  $g$ ). At such wavelengths the magnitudes are sensitive to the rather crude dust modelling implemented in the SAM. Since our main goal is to create mock galaxy catalogues that are as realistic as possible, we have applied an ad hoc correction to our apparent magnitudes,

$$m_{AB} \rightarrow m_{AB} + \alpha \left( \frac{\lambda_0}{\lambda_{AB}} - 1 \right), \quad (6.7)$$

where  $\lambda_{AB}$  is the effective wavelength of the filter under consideration, and  $\alpha$  and  $\lambda_0$  are free parameters that we set respectively to  $-0.47$  and  $6254 \text{ \AA}$  (the central wavelength of the  $r$  SDSS filter) by requiring an improved agreement with the number counts shown in Fig. 6.3. We apply Eq. (6.7) to all the photometric bands we consider, including narrow and intermediate bands not used in the calibration. Our updated predictions, displayed as dashed lines in Fig. 6.3, are in better agreement with the data for blue bands,

which increases the overall level of realism of our lightcone.

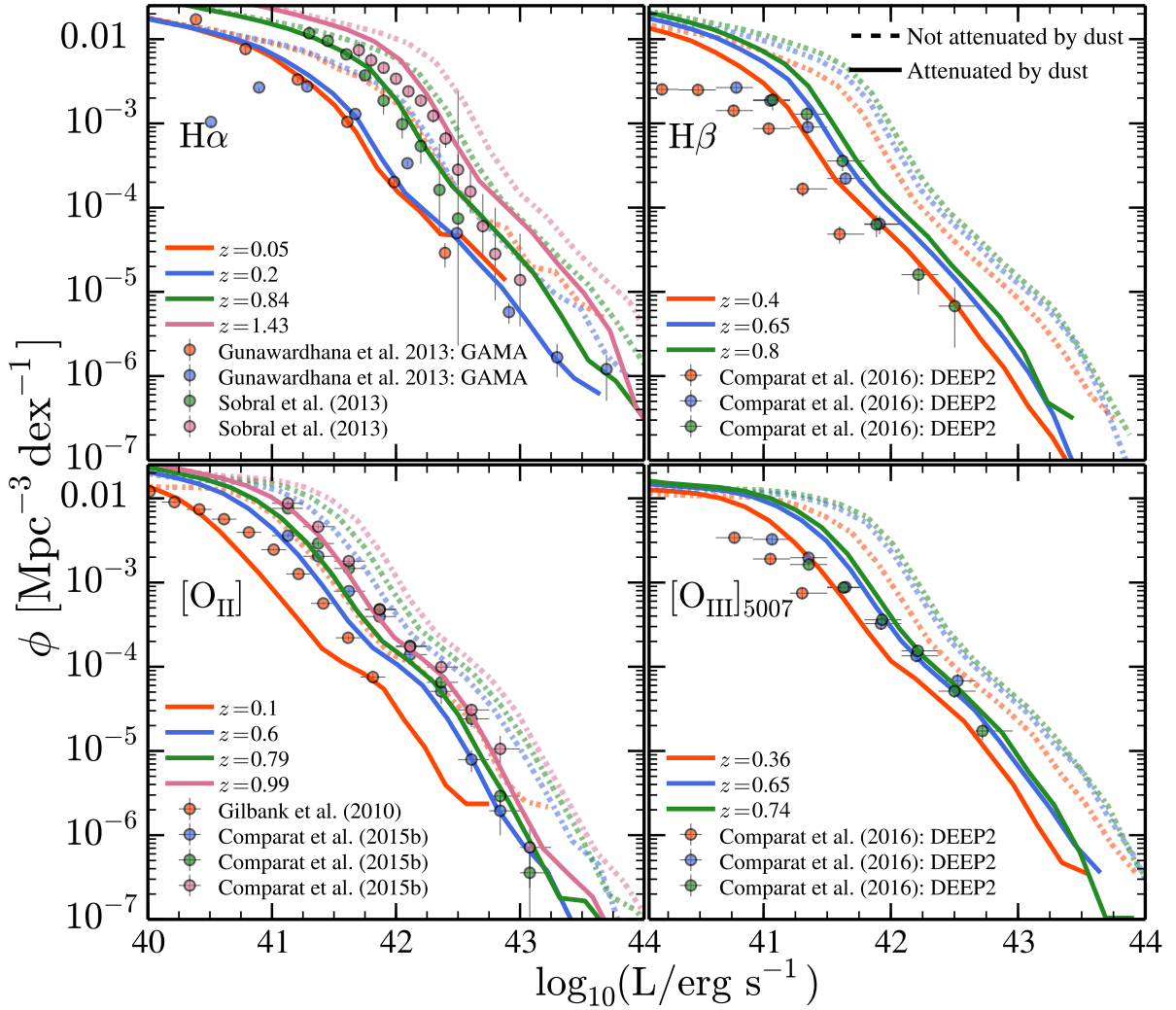


Figure 6.4: Luminosity function of emission lines. Each panel displays the results for a different emission line (from top to bottom and from left to right):  $H\alpha$ ,  $[OII]$ ,  $H\beta$ , and  $[OIII]_{5007}$ . Shown in each panel are the various observational estimates (cf. Section 6.3.2 and Appendix H) at different redshifts, colour-coded as shown in each legend. Dashed and solid lines display the results from our mock galaxy catalogue before and after applying an empirical model for dust attenuated, respectively. This dust model has been calibrated to improve the agreement between the observations and our predictions.

### 6.3.2 Emission-line luminosity functions and line dust attenuation

A distinctive feature of our mock lightcone is the inclusion of emission lines. Our model estimates line luminosities based on the *intrinsic* amount of photons produced during an event of instantaneous star formation. However, star-forming galaxies are expected to also contain a large amount of dust, which can significantly attenuate the luminosity of these emission lines. In the following we detail our dust-attenuation model, which is calibrated by making use of the well-constrained  $H\alpha$ ,  $H\beta$ ,  $[OII]$ , and  $[OIII]_{5007}$  luminosity functions (LFs) provided by previous works<sup>6</sup>. We note that given the much more complex physics involved in  $Ly\alpha$ -photon radiative transfer in star-forming galaxies (Gurung-López et al., 2019; Gurung-Lopez et al., 2019; Weinberger et al., 2019), we do not use  $Ly\alpha$  line luminosities functions

<sup>6</sup>The comparison between observed and predicted LFs includes the small corrections due to the diverse cosmologies assumed by the different works. We checked that the variations in the LF amplitude due to this effect are minimum (< 2%).

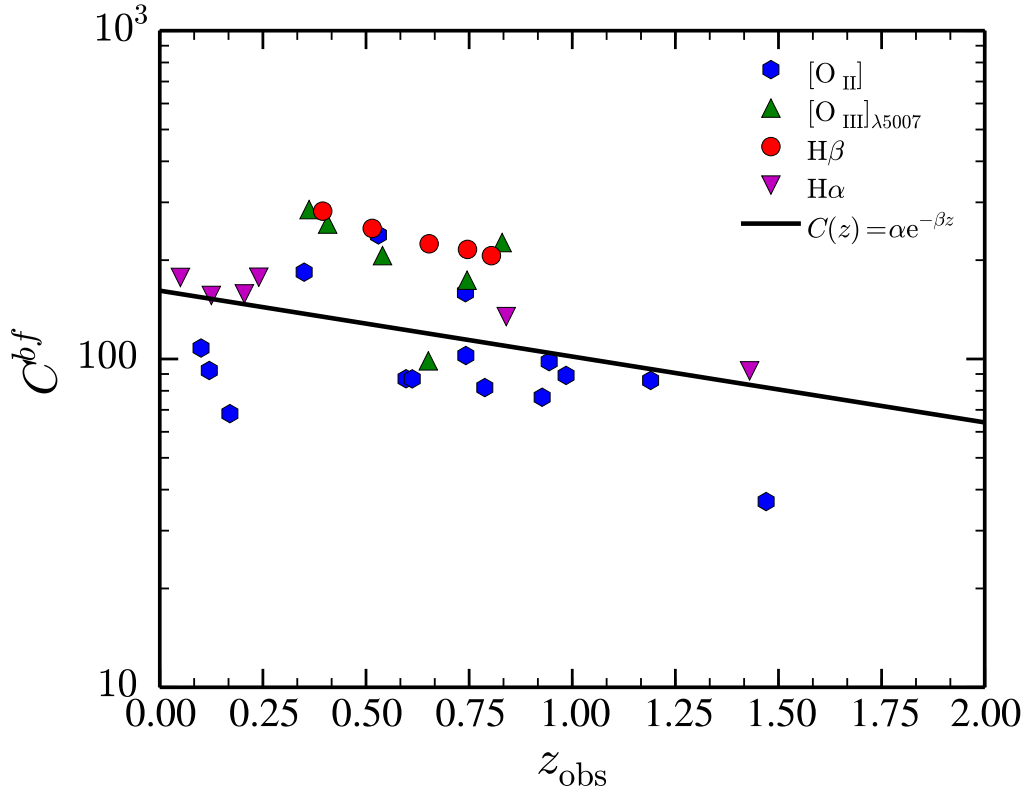


Figure 6.5: Redshift dependence of the dust attenuation coefficient,  $C^{bf}$ , applied to the nebular emission in our mock galaxies. Symbols represent the mean value estimated by requiring agreement between the predicted and observed luminosity function for either  $H\alpha$ ,  $H\beta$ ,  $[OII]$ , or  $[OIII]_{5007}$  (violet, blue, green, and red, respectively). The best fit relation is shown by the solid black line.

for our calibrations.

In Fig. 6.4, we present a comparison of our LF predictions against different observed (not dust corrected) luminosity functions for  $H\alpha$ ,  $H\beta$ ,  $[OII]$ , and  $[OIII]_{5007}$  (Gilbank et al., 2010; Gunawardhana et al., 2013; Sobral et al., 2013; Comparat et al., 2016). For clarity, we only show four different redshifts and defer the comparison with other redshifts to Appendix H. Our *dust-free* predictions are, at all redshifts, above the observed ones. This suggests dust attenuation is required to match the observations.

Given the difficulty in properly simulating dust formation and destruction (e.g. Fontanot and Somerville, 2011), here we resort to a simple empirical dust modelling. The goal is to consistently reproduce the observed luminosity functions across redshifts for different lines. Following De Lucia et al. (2004), for each galaxy we compute a mean absorption coefficient as

$$A_\lambda = -2.5 \log_{10} \left( \frac{1 - e^{-\tau_\lambda \sec \theta}}{\tau_\lambda \sec \theta} \right), \quad (6.8)$$

where  $\theta$  is the inclination angle of the galaxy with respect to the LOS (randomly chosen) and  $\tau_\lambda$  is the optical depth associated with stellar birth clouds. Here, we assume that  $\tau_\lambda$  has the following dependence on the cold gas metallicity of the host galaxy,

$$\tau_\lambda = C(z) Z_{\text{cold}} \frac{A_V}{A_B} \frac{A(\lambda)}{A_V}, \quad (6.9)$$

where the values of  $A_B/A_V$  and  $A(\lambda)/A_V$  are computed based on the extinction curves of Cardelli et al.

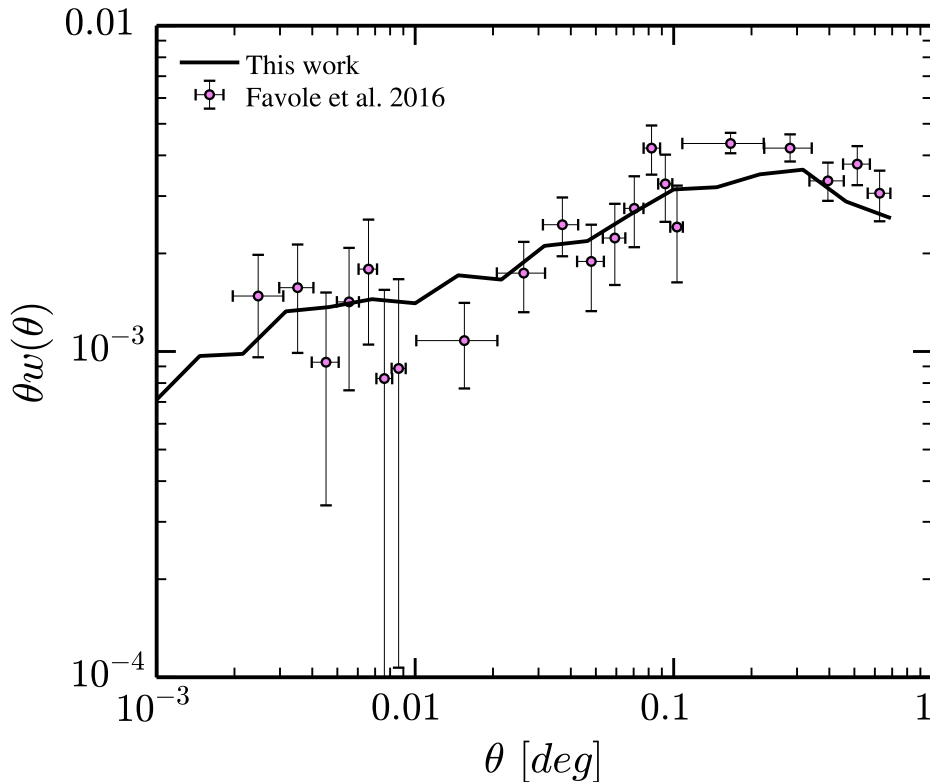


Figure 6.6: Two-point angular correlation function of  $g$ -selected galaxies ( $20 < g < 22.8$ ) in the redshift range  $0.6 < z < 1.0$ . Purple symbols displays the measurements of Favole et al. (2016) whereas solid black line shows the predictions of this work. We display  $\theta \times w(\theta)$  to enhance the dynamic range shown. The clustering has been rescaled from the WMAP cosmology to the PLANCK one following Springel et al. (2018).

(1989) and  $C(z)$  is a free parameter, which we refer to as the *dust attenuation coefficient*, that controls the amplitude and redshift dependence of our dust attenuation model.

To constrain the value of  $C(z)$ , we compute the dust-attenuated luminosity function for a wide set of values for  $C$  (namely  $[0, 1000]$ ). We then find the value of  $C$  that minimises the root mean squared differences with the observed luminosity function. We apply this procedure separately for each line and redshift. The best-fit values for  $C$  ( $C^{bf}$ ) as a function of redshift for the  $H\alpha$ , [OII], [OIII]<sub>5007</sub>, and  $H\beta$  lines is shown in Fig. 6.5, which shows that the corrections for  $H\beta$  and [OIII]<sub>5007</sub> are systematically larger than those for  $H\alpha$  and [OII]. We connect this evidence to the slight overestimation of the galaxy intrinsic  $H\beta$  and [OIII]<sub>5007</sub> luminosity (see Orsi et al., 2014). Because the refinement of  $H\beta$  and [OIII]<sub>5007</sub> modelling is beyond the scope of our work, we absorb these overestimations in our dust correction at the price of using large  $C$  coefficients for these lines.

We find that all three of the lines considered and the whole redshift range display a consistent behaviour, with a smaller attenuation coefficient required at high redshift. Our results are well described by  $C(z) = \alpha e^{-\beta z}$ , with  $\alpha = 161.46 \pm 30.3$  and  $\beta = 0.46 \pm 0.23$ . This relation is shown as a solid black line in Fig. 6.5. We employ it to model dust attenuation for every line we include in our mock, with the exception of  $H\alpha$ . The resulting *dust-attenuated* line luminosity functions in our mock lightcone are displayed in Fig. 6.4. As intended, we find a better agreement with the observational measurements, which supports the validity of our mocks for analysing and predicting emission lines in the Universe. Nevertheless, given the simplicity of our dust correction, the final results have their limitations. For instance, while the [OII] line is slightly over-corrected at low- $z$ ,  $H\beta$  is under-corrected at high- $z$ . In future work we will



address a more sophisticated dust attenuation.

### 6.3.3 Clustering of high redshift $g$ -band selected sources

An important validation of our mock lightcone is the spatial distribution of ELGs. In this subsection we compare our results to the measurements of Favole et al. (2016) who computed the two-point angular correlation function of  $g$ -band and redshift-selected galaxies in SDSS (a selection designed to be a proxy for [OII] emitter selection).

We construct a mock galaxy sample by applying the same selection criteria as in Favole et al. (2016). Specifically, we impose  $20 < g < 22.8$  and  $0.6 < z < 1.0$ . This results in a sample of  $\sim 2 \times 10^5$  galaxies, with a median star formation rate of  $1.70 M_{\odot}/\text{yr}$ . We compute the angular correlation function,  $w(\theta)$ , using the Corfunc package (Sinha, 2016) with the Landy-Szalay estimator (Landy and Szalay, 1993),

$$w(\theta) = \frac{DD(\theta) - 2DR(\theta) + RR(\theta)}{RR(\theta)}, \quad (6.10)$$

where  $DD(\theta)$  is the number of galaxy-galaxy pairs within separation  $\theta$ ,  $RR(\theta)$  is the expected number of such pairs in a random sample generated with the same selection function of our mock data, and  $RD(\theta)$  the data-random pairs.

In Fig. 6.6 we present the comparison. The clustering has been rescaled from the WMAP cosmology of the Millennium to the PLANCK cosmology following Springel et al. (2018). Our predictions display a remarkable agreement with the observations, being statistically consistent within the measurement uncertainties. Additionally, there is a good agreement in the physical properties of the underlying sample: our mock sample has a median host halo mass of  $M_{\text{vir}}^{\text{FOF}} = 1.249 \times 10^{12} M_{\odot}$  with a 27% satellite fraction. These figures are to be compared with a typical host halo mass of  $(1.25 \pm 0.45) \times 10^{12} M_{\odot}$  and a satellite fraction of  $\sim 22.5\%$ , as estimated by Favole et al. (2016). We note that this level of agreement compares favourably with respect to what it is found in other SAMs (e.g. Gonzalez-Perez et al., 2018).

## 6.4 J-PLUS mock galaxy catalogues

In this section, we employ our procedure to build lightcones to mimic the J-PLUS survey. We explore its ability to characterise ELGs in the Universe.

J-PLUS (Cenarro et al., 2019) is an ongoing photometric survey carried out from the Observatorio Astrofísico de Javalambre (OAJ) in Spain. The J-PLUS collaboration plans to observe thousands of square degrees of the northern sky, of which  $\sim 1022 \text{ deg}^2$  have already been completed and publicly released<sup>7</sup> (Cenarro et al., 2019). The survey uses a specially designed camera with a  $2 \text{ deg}^2$  field of view and  $0.55'' \text{ pix}^{-1}$  scale. The unique feature of J-PLUS is its combination of five broad-band and seven medium-band filters (see Table 3 of Cenarro et al., 2019). We show in Fig. 6.7 the J-PLUS filter transmission curves and the observed wavelengths of nine different lines inside the J-PLUS spectral range as a function of redshift. In this way we can visualise the redshifts at which different emission lines could be selected by various narrow bands. We highlight in red the J0660 filter ( $138 \text{ \AA}$  wide and centred at  $6600 \text{ \AA}$ ), which is expected to capture the  $H\alpha$  emission of star-forming regions in the nearby universe ( $z < 0.017$ ),  $H\beta$  and [OIII] at  $z \sim 0.3$ , and [OII] at  $z \sim 0.7$ , but also the  $4000 \text{ \AA}$  break at  $z \sim 0.65$ .

Using the J-PLUS set of transmission curves shown in Fig. 6.7, and the procedure presented in Sections 6.2.3 and 6.3.2, we computed synthetic magnitudes for each galaxy in our mock lightcone. In order

<sup>7</sup>[www.j-plus.es/datareleases/data\\_release\\_dr1](http://www.j-plus.es/datareleases/data_release_dr1)

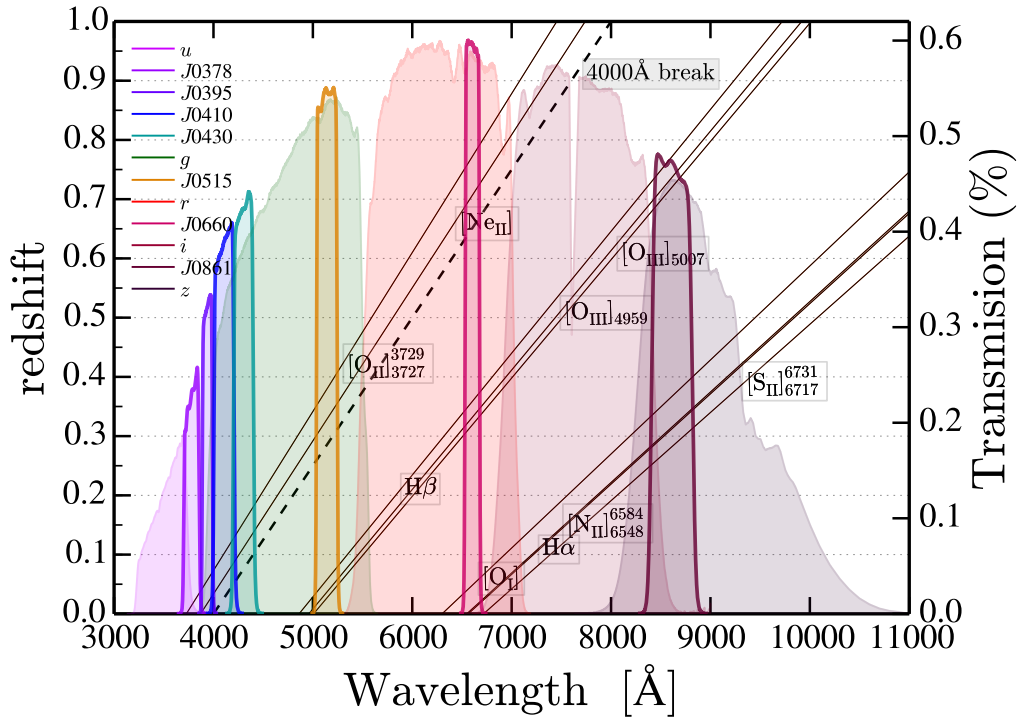


Figure 6.7: **Right y-axis:** Transmission curves of the J-PLUS system obtained by convolving the measured transmission curves for each filter with the quantum efficiency of the CCD and the atmosphere absorption lines. **Left y-axis:** Wavelength at which the nine different lines included in the model fall as a function of redshift. The dashed line represents the same, but for the 4000 break.

to be consistent with the survey, we kept galaxies with an apparent magnitude  $r < 21.3$ , i.e. the  $5\sigma$  detection threshold of galaxies expected in J-PLUS.

The synthetic J-PLUS photo-spectra for four typical ELGs in our mock is shown in Fig. 6.8. For each object, we present its photometry including the contribution of emission lines and excluding it. In the first panel of Fig. 6.8 we display a local galaxy ( $z_{\text{obs}} \sim 0$ ) with a stellar mass of  $3.24 \times 10^{10} M_{\odot}/h$  and an instantaneous star formation rate ( $\text{SFR}^{\text{inst}}$ ) of  $1.64 M_{\odot}/\text{yr}$ . We can see how the measured fluxes in the J-PLUS filters are significantly affected by the line emission. Specifically,  $\text{H}\alpha$ , [OII], and [OIII] increase the flux in the filters J0660, J0378, and J0515, respectively. Emission lines also affect significantly the broad-band fluxes, as is the case for  $r$  which is affected by  $\text{H}\alpha$ , and for  $g$  by [OIII] (doublet). Thus, the line fluxes have to be taken into account even for broad-band-only analyses. This, for instance, will be important for deep photometric surveys such as LSST.

In the second panel of Fig. 6.8, we show a galaxy at  $z \sim 0.31$ , with stellar mass of  $1.57 \times 10^{10} M_{\odot}/h$  and a  $\text{SFR}^{\text{inst}} = 3.2 M_{\odot}/\text{yr}$ . As in the previous example, the emission lines of this galaxy contribute significantly to the flux measured. However, in this particular case the main line contributing to the J0660 filter is [OIII], and [OII] for the J0515 filter. The  $\text{H}\alpha$  emission is outside the narrow bands, falling in the  $z$ -band filter. In the third panel of Fig. 6.8, we show a similar galaxy. In this case the redshift is  $z_{\text{obs}} \sim 0.36$  and the line that falls in the J0660 is  $\text{H}\beta$ . Finally, in the last panel of Fig. 6.8 we present a high star formation rate galaxy ( $\text{SFR}^{\text{inst}} \sim 22 M_{\odot}/\text{yr}$ ) at  $z_{\text{obs}} \sim 0.78$ . The main emission lines that can be observed for this galaxy are [OII] in the narrow-band J0660 filter and the sum of [OIII] and  $\text{H}\beta$  in the J0861 narrow band and  $z$  broad band.

The above examples serve as an illustration of the ability of J-PLUS to detect ELGs, but they also show two potential limitations: (i) disentangling the contribution of continuum and emission line to

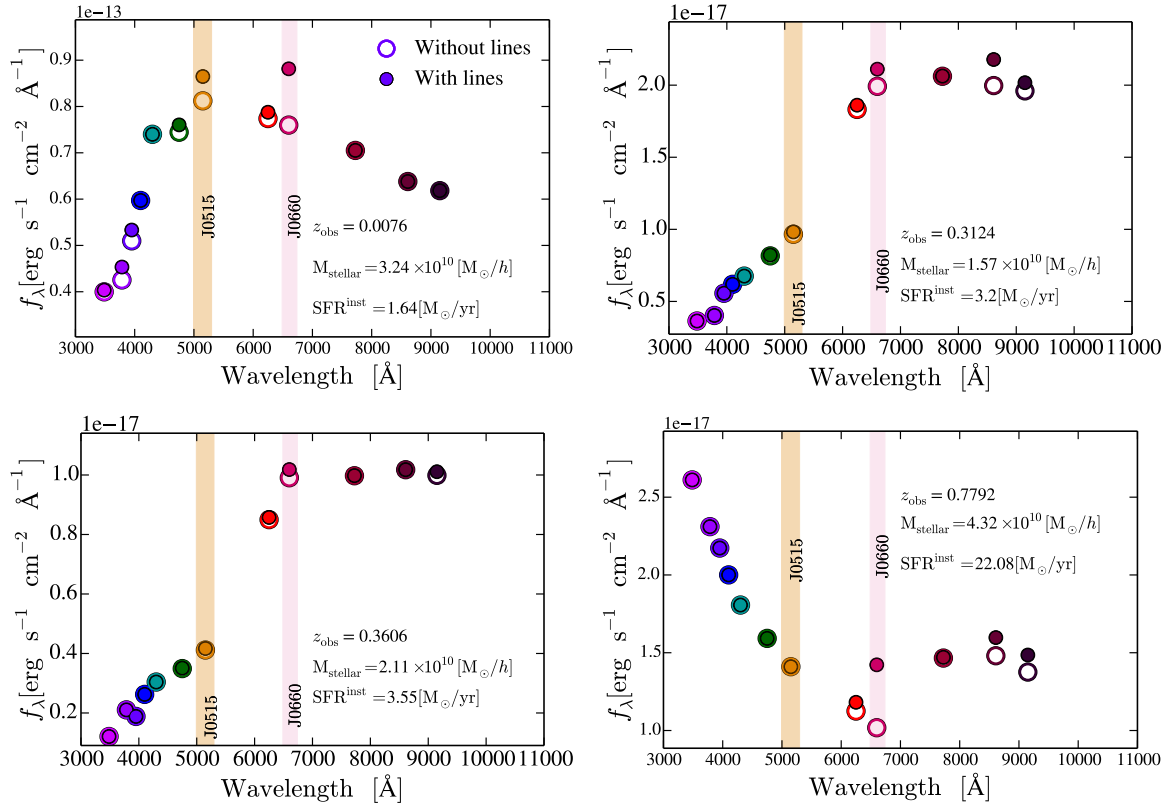


Figure 6.8: Predicted flux in the 12 J-PLUS filters for four mock galaxies in our lightcone. From left to right:  $u$ ,  $J0378$ ,  $J0395$ ,  $J0410$ ,  $J0430$ ,  $g$ ,  $J0515$ ,  $r$ ,  $J0660$ ,  $i$ ,  $J0861$ , and  $z$  filters. The shaded areas indicate the location and extent of the  $J0515$  and  $J0660$  filters. Empty and filled circles represent the galaxy photometry without and with line contributions, respectively. The first and second panels are examples of  $H\alpha$  and  $[OIII]$  emitters at  $z \sim 0$  and  $z \sim 0.3$ , respectively. The third and fourth panels show other examples, but for  $H\beta$  and  $[OII]$  emitters at  $z \sim 0.3$  and  $z \sim 0.78$ , respectively.

the narrow bands, and (ii) distinguishing the fluxes of different emission lines generated by galaxies at different redshift.

#### 6.4.1 Validation of J-PLUS mocks

In this section we further validate our mock by showing the agreement with the currently available data of the survey (Cenarro et al., 2019).

Firstly, the number counts of the 12 J-PLUS bands are presented in Fig. 6.9. Galaxies in the J-PLUS Data Release 1 (DR1) have been selected by imposing the morphological star–galaxy classification parameter of López-Sanjuan et al. (2019) to be less than 0.5. The match between mocks and observations is remarkable. We note that the agreement in the bluest narrow bands starts to fail at magnitude  $\gtrsim 19.5$ . This is principally because our SAM variant underestimates the population of blue counts (see Section 6.3). In the same plot, we added the number counts after removing the line contribution in the galaxy photometry. We do not see significant differences for the global population of galaxies. This is expected since only a small fraction of galaxies would display emission lines falling within one of the J-PLUS narrow bands.

Finally, in Fig. 6.10 we present the predicted and observed  $H\alpha$  luminosity function in the local universe ( $z < 0.017$ ) seen by the J-PLUS survey. The observational results can be found in Vilella-Rojo et al. (in prep.). Again, predictions and observations agree with each other. The fact that our LF is not as

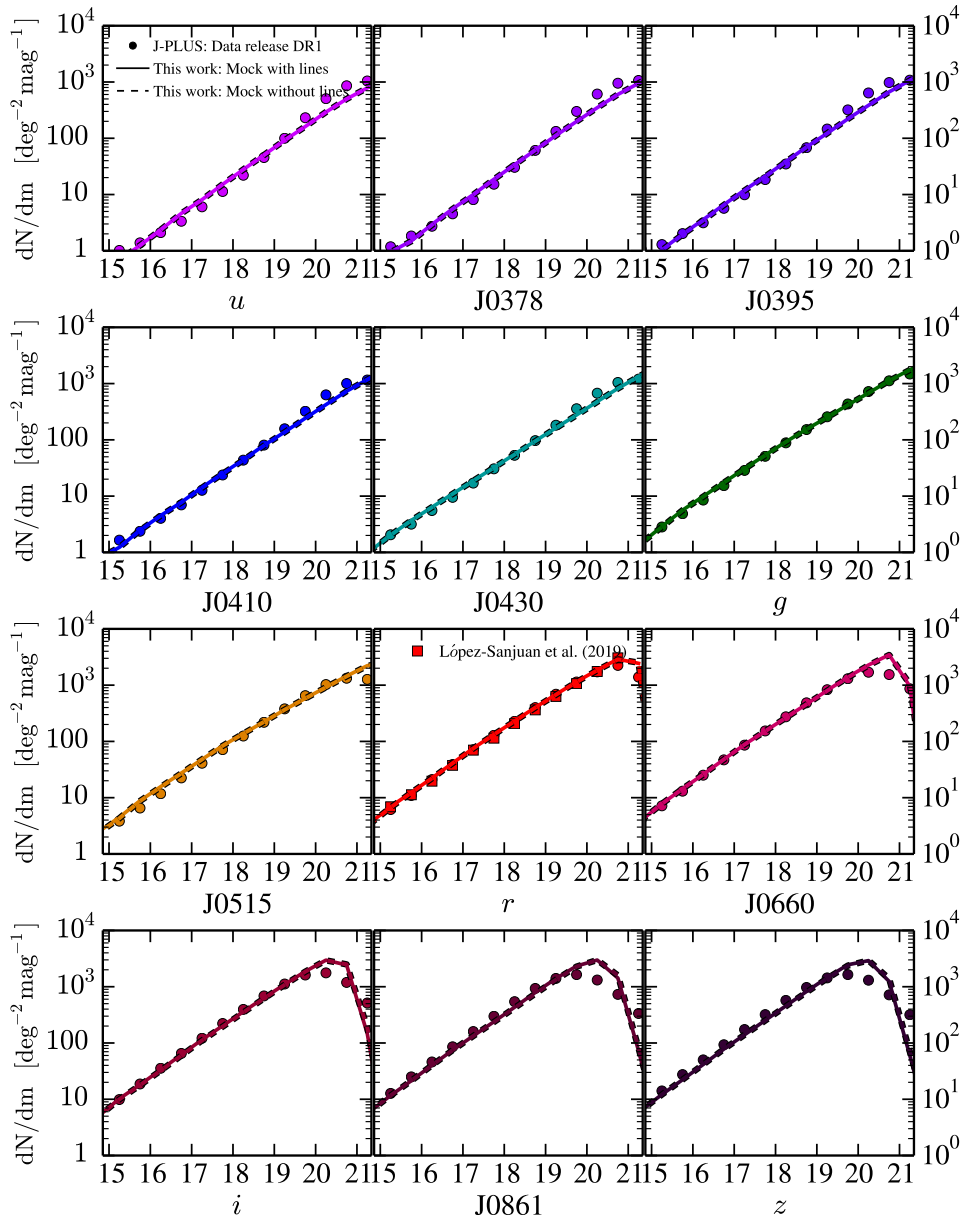


Figure 6.9: Galaxy number counts in each of the 12 J-PLUS filters. Solid and dashed lines respectively show the mock predictions with and without including the line emission in the galaxy photometry. Symbols show their counterpart in actual J-PLUS observations. The data are from the DR1 of J-PLUS after masking for saturated objects and applying quality cuts to separate tiles. In the panel of the  $r$  band are included the number counts presented in López-Sanjuan et al. (2019) computed by using the early data release of J-PLUS.

smooth as the observed one is due to the limitation imposed by the cosmic variance at such low- $z$ . This is the result of the narrow angular aperture that characterises our lightcone.

### 6.4.2 Selecting emission-line galaxies

We now use the 3FM method developed by Vilella-Rojo et al. (2015) to estimate the emission-line flux from a linear combination of broad- and narrow-band filters. In short, this method infers the continuum of galaxy in a narrow band ( $J0660$ ) by linearly interpolating the continuum using two adjacent broad-band filters ( $r$  and  $i$ ). We note that this method takes into account the emission line contribution in the

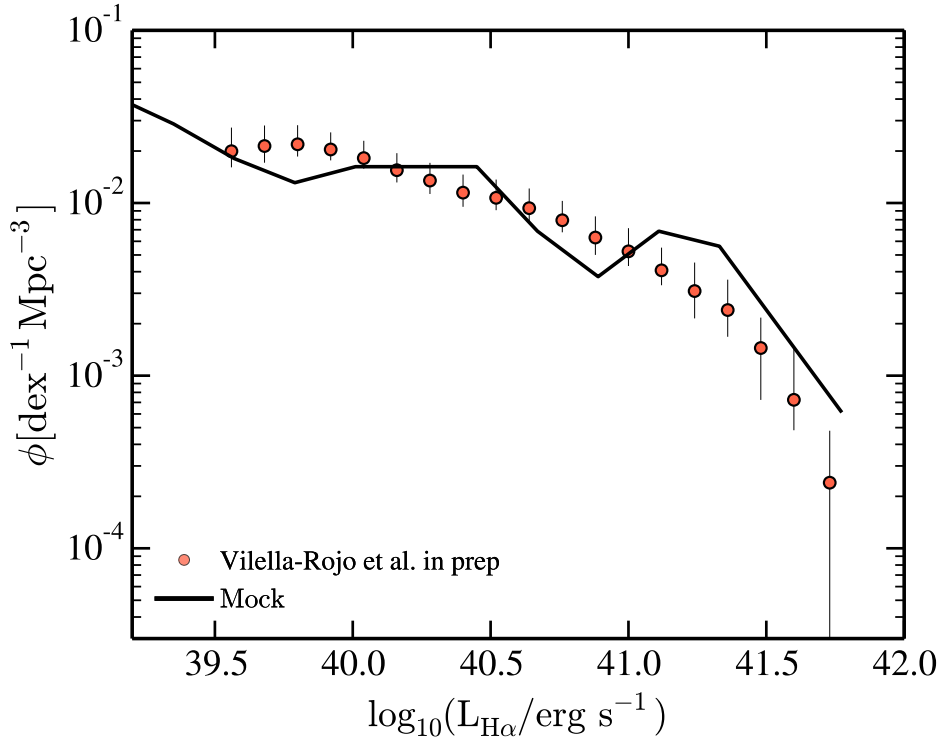


Figure 6.10: Intrinsic  $H\alpha$  luminosity function of the local universe ( $z < 0.017$ ). Red symbols indicate the observational results presented in Vilella-Rojo et al. (2019, in prep.) using J-PLUS. The solid black line displays the predictions from our J-PLUS mock catalogue.

broad band when performing the interpolation. Using synthetic photometry computed from SDSS spectra, Vilella-Rojo et al. (2015) demonstrated that for  $z \sim 0$  galaxies the method is nearly unbiased ( $\lesssim 9\%$ ) in extracting  $H\alpha$  emission.

In the following we explore higher redshifts ( $z > 0.017$ , implying no  $H\alpha$  emission in the  $J0660$  filter) and we assess the performance of the 3FM method to extract line emission of high redshift galaxies. To this end, we applied the 3FM method to every galaxy in our J-PLUS mock using the  $J0660$  narrow band as a line tracer and the  $r$  and  $i$  broad-band filters to estimate the galaxy continuum,  $m_{J0660}^{\text{cont,Est}}$ . We built the magnitude excess,  $\Delta m$ , as follows:

$$\Delta m = m_{J0660}^{\text{cont,Est}} - m_{J0660}. \quad (6.11)$$

Here  $m^{J0660}$  is the observed magnitude in the  $J0660$ . We selected objects with an excess of flux such that  $\Delta m > 0$ . This is close to imposing an equivalent width (EW)<sup>8</sup> cut on the galaxy line emission<sup>9</sup>.

We present the redshift distribution of selected galaxies in Fig. 6.11. From left to right, the red peaks in the distribution correspond to  $H\alpha$ , [OI], [OIII] ( $4959\text{\AA}$ ,  $5007\text{\AA}$ ),  $H\beta$ , [NeII], and the [OII] doublet at redshift 0.01, 0.05, 0.33, 0.36, 0.7, and 0.78, respectively. When using a minimum detection of  $\Delta m > 0.2$ , we see that most of the objects selected correspond to galaxies at  $z \in [0.3, 0.7]$  that do not necessarily present a significant line emission. This implies that a sample selected using this threshold is contaminated by a significant fraction of spurious detections. As we see in Section 6.4.3, these spuri-

<sup>8</sup>The equivalent width is defined as the ratio of the total line flux,  $F(\lambda_j|q, Z_{\text{cold}})$ , to the continuum density flux,  $f_{\lambda}^c$ , at the line position.

<sup>9</sup>By assuming a  $\delta$ -Dirac line profile we can establish the relation  $\Delta m = 2.5 \log_{10} \left[ 1 + \left( \lambda_{\text{Line}}^{\text{obs}} T(\lambda_{\text{Line}}^{\text{obs}}) / \int \lambda T(\lambda) d\lambda \right) \text{EW} \right]$ , where  $\lambda_{\text{Line}}^{\text{obs}}$  is the observed line wavelength,  $T(\lambda)$  is the narrow-band filter transmission curve, and EW is the line equivalent width.

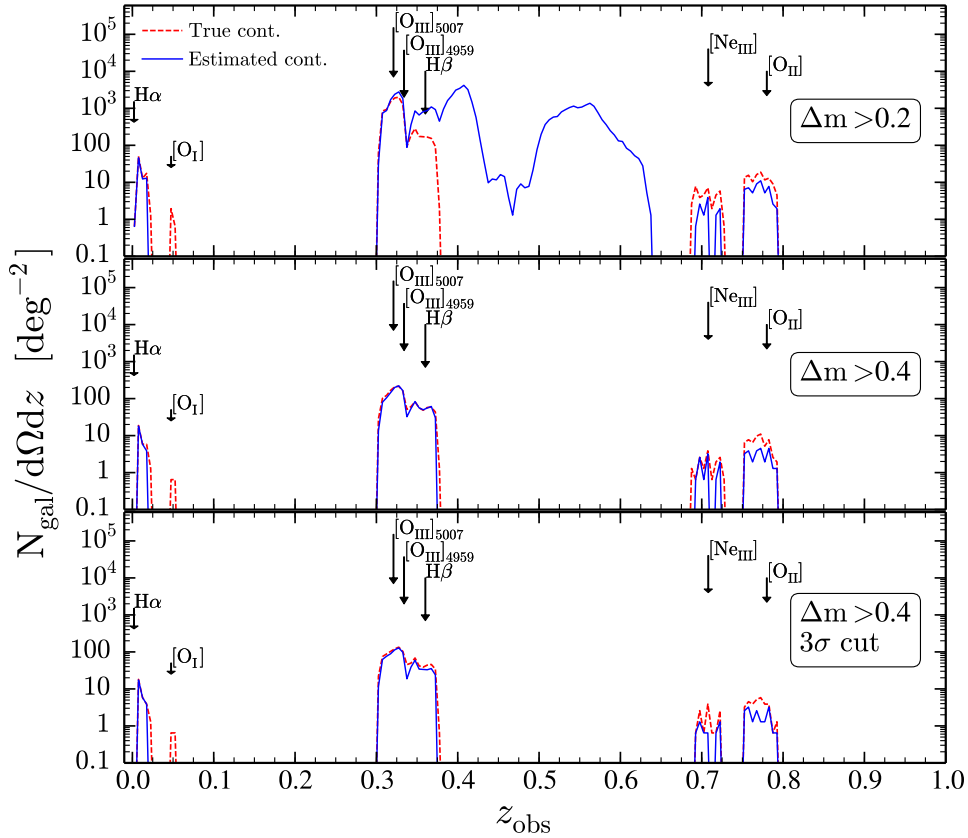


Figure 6.11: Redshift distribution of galaxies selected to have a positive excess in the  $J0660$  filter associated to line emission. The top, middle, and bottom panels display the results employing different magnitude thresholds,  $\Delta m > 0.2$ ,  $\Delta m > 0.4$ , and  $\Delta m > 0.4$ , plus the  $3\sigma$  significance level with respect to the J-PLUS typical uncertainties. The blue histograms show galaxies selected using the 3FM of [Vilella-Rojo et al. \(2015\)](#), whereas the red dashed histograms show galaxies selected using the true magnitude excess associated with a line emission.

ous detections are produced by the non-linear behaviour of the continuum for the concerned range of wavelength, which corresponds to the  $4000\text{\AA}$  break crossing the J-PLUS set of filters  $r$ ,  $J0660$ , and  $i$  in the range  $0.3 \lesssim z \lesssim 0.8$ .

When we apply a higher threshold,  $\Delta m > 0.4$ , the spurious selection is significantly reduced and the detections correspond to galaxies with emission lines, covering the correct range of redshift. For this  $\Delta m$  threshold, 74.7% of the selected emitters are [OIII], 13.1%  $H\beta$ , 10.4%  $H\beta + [\text{OIII}]$ <sup>10</sup>, 0.9%  $H\alpha$ , 0.2% [NeII], and 0.7% [OII]. We note that with the 3FM method we are not able to detect the [OI] emitters due to the weak emission of this line. In addition, independently of the  $\Delta m$  cut, the [NeII] and [OII] emitters have a low completeness; in other words, the true distribution (dashed red line) is above the recovered distribution (solid blue line).

Finally, to mimic a more realistic scenario, in the bottom panel of Fig. 6.11 we also account for the photometric uncertainties of the J-PLUS survey. For this, we applied an extra cut such that the magnitude excess in the narrow-band filter is above a significance of  $3\sigma$  with respect to the J-PLUS typical uncertainties. To estimate the J-PLUS data uncertainty level, we used the median uncertainty reported in the J-PLUS DR1 as a function of  $r$  magnitude. As we can see, the  $3\sigma$  significance cut leaves the distribution almost unchanged when we compare it with the distribution that does not have such cut

<sup>10</sup>The  $H\beta$  and [OIII] overlap inside  $J0660$  in the redshift range  $0.34 \lesssim z \lesssim 0.36$ .



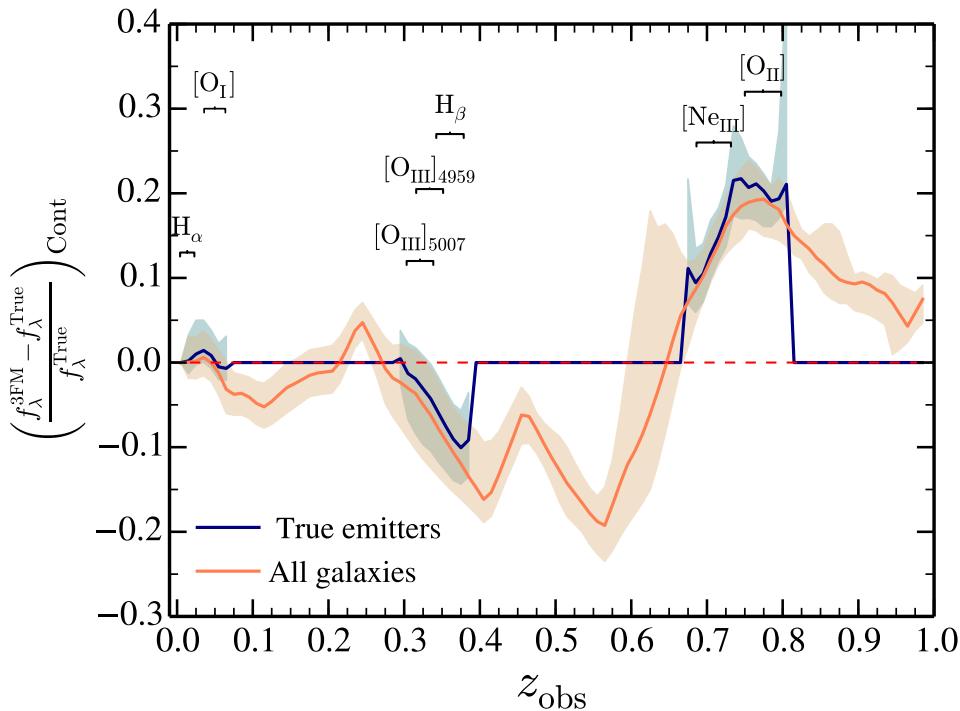


Figure 6.12: Comparison between the true,  $f_{\lambda}^{\text{True}}$ , and inferred,  $f_{\lambda}^{\text{3FM}}$ , values for the continuum density flux. The orange line represents the comparison for all the galaxies (with and without emission lines) in the mock. The blue line are the same, but only for galaxies displaying emission line features in the filter  $J0660$ . In both cases, the shaded areas enclose the 25th and 75th percentiles.

(middle panel). The high- $z$  emitters are the most affected by this extra cut as they are faint sources with typically larger photometric uncertainties.

### 6.4.3 Understanding the population of interlopers

To understand the origin of the *interlopers* and the under-recovered population of [NeII] and [OII] in Fig. 6.12, we compare the true,  $f_{\lambda}^{\text{True}}$ , and inferred,  $f_{\lambda}^{\text{3FM}}$ , values for the continuum density flux. From Fig. 6.12 we confirm the findings of Vilella-Rojo et al. (2015), in that the 3FM provides a nearly unbiased estimate of the continuum at  $z \sim 0$ . However, we find significant biases at higher redshifts, most notably at  $z \sim 0.4$  and  $0.6$  where the continuum is overestimated by  $\sim 20\%$ .

Moreover, there is an underestimation of the continuum at  $z \sim 0.8$  of about  $20\%$ <sup>11</sup>. A similar behaviour can be found for the true emission-line galaxies (blue line in the figure). To investigate the origin of these trends, we applied the 3FM to magnitudes that exclude the contribution of emission lines. We found that the trends are preserved, indicating that the biases are caused by features in the spectral energy distribution (SED) continuum of galaxies. We expect any non-linear feature in a galaxy spectrum to produce biases in the continuum estimation. In particular, the  $4000\text{\AA}$  break crossing our set of filters  $r$ ,  $J0660$  and  $i$  between  $0.40 \lesssim z \lesssim 0.8$  is responsible for the systematic overestimation of the continuum at  $z \sim 0.6$  and the underestimation at  $z \sim 0.8$ . The typical curvature of our mock galaxy photo-spectra moves from positive to negative. A correction of this continuum subtraction bias could be applied by combining photo- $z$  information with a flux correction based on the orange curve of Fig. 6.12. However, this procedure goes beyond the scope of this chapter.

<sup>11</sup>We computed this bias as a function of different  $r$  apparent magnitudes [18,19], [19,20], and [20,21], and found almost identical results.

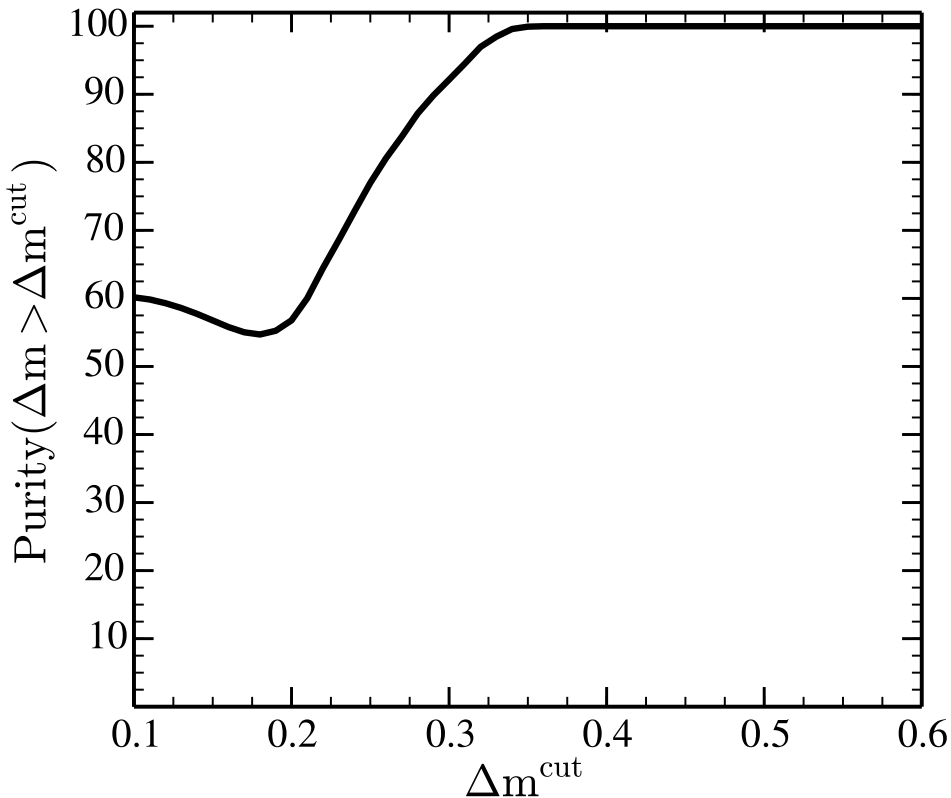


Figure 6.13: Purity in a catalogue of mock J-PLUS galaxies selected to have emission lines, as a function of the threshold used for detection  $\Delta m^{\text{cut}}$ .

The purity of ELGs as a function of magnitude excess cut is presented in Fig. 6.13. The curve displays a decreasing trend between  $0.1 < \Delta m^{\text{cut}} < 0.2$ , a consequence of the fact that these  $\Delta m$  cuts remove low equivalent width ELGs, yet still keep the majority of *interlopers*. As soon as  $\Delta m^{\text{cut}} \gtrsim 0.2$  we start to avoid *interlopers*, recovering the increasing trend. As shown, the 4000 Å break is not capable of generating a fake magnitude excess above  $\Delta m^{\text{cut}} \sim 0.36$ , where we obtain a purity of 100%.

Finally, in Fig. 6.14 we present the typical equivalent width as a function of  $\Delta m$  cuts for the different emission lines that contribute in the J0660 filter i.e.  $H\alpha$  at  $0 < z < 0.02$ ,  $[\text{OIII}]_{5007}$  at  $0.3 < z < 0.35$ ,  $H\beta$  at  $0.33 < z < 0.39$  and  $[\text{OII}]$  at  $0.74 < z < 0.81$ . We find that while  $\Delta m \lesssim 0.2$  imposes  $H\alpha$ ,  $H\beta$ , and  $[\text{OIII}]_{5007}$  EW cuts of  $\sim 10$  Å, it implies a much more strict cut for  $[\text{OII}]$  with an EW  $\sim 50$  Å. When we increase  $\Delta m^{\text{cut}}$ , we can see that a more severe EW requirement is imposed for all the lines. In particular,  $\Delta m > 0.4$  implies  $\text{EW} > 70$  Å.

All this points towards the good capability of J-PLUS to study ELGs in the universe. The forthcoming J-PAS survey (Benitez et al., 2014) will increase the capabilities of detecting line-emission galaxies due to the higher number of narrow bands (56) and the higher depth, with respect to J-PLUS. The methods we developed here can be easily generalised to the J-PAS case, and can thus provide an efficient tool for testing the survey’s data capabilities.

## 6.5 Summary and conclusions

In this chapter we have presented a new procedure to generate synthetic galaxy lightcones specifically designed for narrow-band photometric surveys. Different from previous lightcone construction methods, we embedded its assembly inside the galaxy formation modelling so that each galaxy is evolved up to

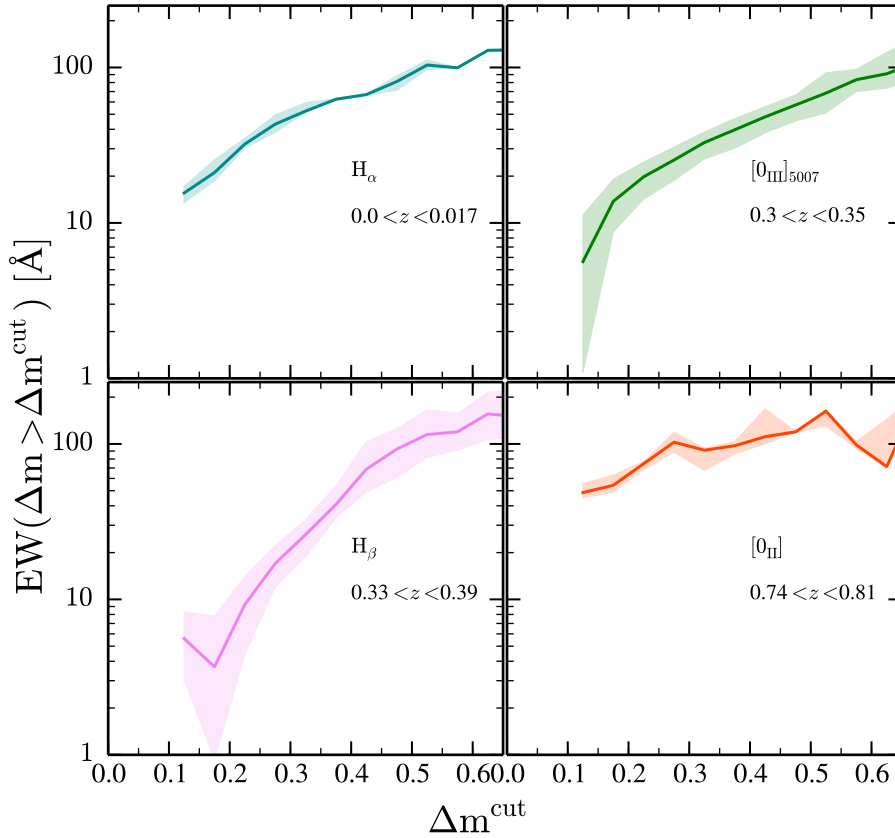


Figure 6.14: Relation between  $\Delta m^{\text{cut}}$  and the equivalent width of the line (EW). From upper left to lower right:  $H\alpha$  at  $0 < z < 0.017$ ,  $[OIII]$  at  $0.3 < z < 0.35$ ,  $H\beta$  at  $0.33 < z < 0.39$ , and  $[OII]$  at  $0.74 < z < 0.81$ . The solid lines represent the median EW for the (emitters) sample with  $\Delta m > \Delta m^{\text{cut}}$ ; the shaded areas represent the  $1\sigma$  value of the distribution.

the exact moment it crosses the past lightcone of a given observer. This produces accurate results across cosmic time, while minimising time-discreteness effects. Specifically, we used L-Galaxies (Guo et al., 2011) implemented on top of the dark matter merger trees of the Millennium  $N$ -body simulation (Springel, 2005). Since the Millennium box size is not able to cover the whole survey volume, we replicated the box eight times in each spatial direction, corresponding to a maximum redshift  $z \sim 3$ , large enough to include high- $z$  ELGs. With the purpose of minimising the repetition of large-scale structures, we placed the observer in the origin of the first replication with a LOS orientation of  $(\theta, \varphi) = (58.9^\circ, 56.3^\circ)$ . The angular extent of the lightcone was chosen to be  $22.5^\circ \times 22.5^\circ$ , i.e. no more than two repetitions of the simulation box would be required to represent the cosmic structure up to  $z \sim 1.0$ .

As a particular feature of our mock, we included the effect of nine different emission lines in the final galaxy photometry. In particular,  $Ly\alpha$  (1216Å),  $H\beta$  (4861Å),  $H\alpha$  (6563Å),  $[OII]$  (3727Å, 3729Å),  $[NeIII]$  (3870Å),  $[OIII]$  (4959Å, 5007Å),  $[OI]$  (6300Å),  $[NII]$  (6548Å, 6583Å), and  $[SII]$  (6717Å, 6731Å). This is one of the first times that multiple emission lines have been included in mock galaxy cones (Merson et al., 2018; Stothert et al., 2018). The properties of these lines were computed using the Orsi et al. (2014) model for nebular emission from star-forming regions. Based on MAPPINGS-III photo-ionisation code the model predicts different line luminosities according to the galaxy gas metallicity, instantaneous star formation rate, and ionisation parameter. For the two former quantities we used the predictions of our mock SAM galaxies.

We presented various tests to validate our lightcone construction. Galaxy photometry has been tested

with the galaxy number counts in the  $u, g, r, i, z$  broad bands. In the case of galaxy spatial distribution we compared the clustering of  $g$  selected galaxies with the work of Favole et al. (2016). In both cases the agreement is good. By comparing our mock line-luminosity functions to observational works we calibrated our dust attenuation. It was based on a dependence with the galaxy redshift and metallicity. In particular, we compared our results with to the well-constrained  $H\alpha$ ,  $H\beta$ , [OII], and [OIII]<sub>5007</sub> luminosity functions to develop a global line attenuation for all the lines included in our mock. Despite its limitations, this simple method produces final luminosity functions in good agreement with observations, even with respect to the observed redshift evolution.

As an application of our lightcone, we have generated catalogues tailored to the photometry of the ongoing J-PLUS survey (Cenarro et al., 2019). With these mocks we have studied the ability of the survey to correctly identify emission-line galaxies at various redshifts. In particular, among all the intermediate- and narrow-band filter available to detect lines, we have focused in the  $J0660$  which is able to capture the  $H\alpha$  emission of star-forming regions in the nearby universe ( $z < 0.017$ ) and other lines at higher redshifts ( $z > 0.3$ ) such as  $H\beta$ , [OIII], and [OII]. To assert the detection of the emission lines in J-PLUS, we used the *three-filters method* developed by Vilella-Rojo et al. (2015). Our mocks proved that the extraction of emission lines is strongly dependent on the continuum shape. In particular, we showed that the  $4000\text{\AA}$  break in the spectral energy distribution of galaxies can be misidentified as line emission, selecting a population of *fake* emission-line galaxies at  $0.3 < z < 0.6$ . However, we showed that all significant excess in the narrow band (larger than 0.4 magnitudes) can be correctly and unambiguously attributed to emission-line galaxies. The mock catalogue is publicly available at [https://www.j-plus.es/ancillarydata/mock\\_galaxy\\_lightcone](https://www.j-plus.es/ancillarydata/mock_galaxy_lightcone).

In summary, in this work we have presented a new approach used to mimic photometric narrow-band survey observations. We have shown that the synergy between galaxy formation models, dark matter  $N$ -body simulations, and photo-ionisation codes is an adequate combination for the creation of realistic mocks for the next generation of narrow-band photometric surveys. In addition, we anticipate that our work will be an important tool for correctly interpreting narrow-band surveys and for quantifying the impact of line emission in broad-band photometry. As a future application the procedure presented here would be extended to the J-PAS survey Benitez et al. (2014) whose unique feature of 56 narrow-band filters would require mock galaxy catalogues to exploit its data capabilities.

# CHAPTER 7

## SUMMARY AND CONCLUSIONS

*“A más ver, mis valientes hobbits. Mi labor ha concluido. Aquí, al fin, a la orilla del mar, llega el adiós a nuestra compañía. No diré no lloréis pues no todas las lágrimas son amargas”*

El señor de los anillos: El Retorno del Rey.

*“Farewell, my brave Hobbits. My work is now finished. Here at last, on the shores of the sea... comes the end of our Fellowship. I will not say do not weep, for not all tears are an evil.”*

The Lord of the Rings: The Return of the King.

In this thesis, we have tackled three different topics: the assembly of galactic bulges, the growth of supermassive black holes and the development of mocks for the new generation of multi-narrow band photometric surveys. We have addressed all these subjects by using the L-Galaxies<sup>1</sup> semi-analytical model (SAM). This SAM is one of the state-of-the-art model whose capability to predict the correct stellar mass function at different redshifts, passive galaxy fraction, galaxy two-point correlation function or star formation rate density (among many other observables) has been proved in the last 15 years (De Lucia et al., 2004; De Lucia and Blaizot, 2007; Croton, 2006; Guo et al., 2011; Henriques et al., 2015). L-Galaxies has the main advantage of being able to be run on top of the dark matter (DM) merger trees of the Millennium suite of simulations whose different DM mass resolution and box size offer to L-Galaxies the possibility of exploring different physical processes undergone by galaxies over a wide range of scales and environments.

In the following sections, we summarize the applied methodology and the main conclusions obtained in each of the topics addressed in this thesis.

### The assembly of pseudobulge structures

The first part of this thesis, which spans from Chapter 3 to Chapter 4, tackles the cosmological build-up of galactic bulges with a special focus on the pseudobulge population. Taking advantage that L-Galaxies can be run on top the merger trees of both the Millennium and the Millennium II N-body simulations, we have been able to study the formation of pseudobulge structures and the properties of their hosts across a wide range of stellar masses ( $10^8 - 10^{11.5} M_{\odot}$ ). Assuming that pseudobulges can only form and grow via secular evolution, we have modified the treatment of galaxy disk instabilities (DI) in L-Galaxies, distinguishing between two kinds of events: DI *secular-induced* and DI *merger-induced*. Although both DI types emerge from stellar disks massive-enough to experience a bar mode instability, the processes leading the disks mass growth are completely different. On one hand, DIs *merger-induced* are produced by galaxy interactions as a consequence of the fast increase of stellar disk mass after the collisional starburst or smooth satellite galaxy accretion. On the other hand, DIs *secular induced* result from the continuous and secular mass growth of the disk with respect to time. This latter DIs are the events which we assume to lead to long-lasting bar structures and the formation/growth of pseudobulges, while *merger-induced*

<sup>1</sup><http://galformod.mpa-garching.mpg.de/public/LGalaxies/>

instabilities contribute, together with mergers, to the growth of classical bulges. The main findings can be summarized in:

- *Merger-induced* instabilities are less numerous than both DI *secular evolution* and galaxy mergers at all cosmic epochs, pointing out that *merger-induced* instabilities are a subdominant process in the bulge growth.
- *Secular-induced* DIs are the most abundant events concerning bulge assembly at any redshift and stellar mass. However, these processes contribute in a very different way depending on the galaxy stellar mass content. While in galaxies with  $M_{\text{stellar}} = 10^9 - 10^{10} M_{\odot}$  these events are able to substantially contribute to the growth of the bulge, in galaxies with  $M_{\text{stellar}} = 10^8 - 10^9 M_{\odot}$  DIs can only lead to a small (sub-percent) transfer of mass from the disk to the pseudobulge.
- Predominant pseudobulge structures at high- $z$  are principally present in galaxies in the range  $10^{9.5} < M_{\text{stellar}} < 10^{10} M_{\odot}$  with a small shift towards larger stellar masses at low- $z$ .
- Pseudobulges at  $z=0$  inhabit Milky Way type galaxies which lie on the main star forming sequence. For more massive galaxies we do not find predominant pseudobulge structures given that they are systematically destroyed by minor and major mergers.

Despite the promising results reached in Chapter 3, we have explored if the disk instability prescription included in L-Galaxies (Efstathiou et al., 1982) is able to capture the whole physics involved in the bar and pseudobulge formation. For such, profuse in Chapter 4 we have studied the performance of the Efstathiou et al. (1982) analytical prescription for bar formation when it is applied on a sample of bar and unbarred galaxy extracted from the TNG100 cosmological hydrodynamical simulation. Despite finding a correlation between the analytical criteria predictions and the actual bar assembly (non-assembly) shown in the TNG100 for the barred (unbarred) galaxies, we have detected cases where the Efstathiou et al. (1982) criterion of bar formation fails, either claiming disk stability for barred galaxies or disk instability for unbarred disks. To better understand the false (un-)stable disks in the Efstathiou et al. (1982) criterion, we have compared the barred and unbarred galaxies in the disk (un-)stable region. The main results are:

- The main differences between barred and unbarred galaxies in the *stable* region of Efstathiou et al. (1982) criterion are present in the maximum circular velocity of the subhalo and in the stellar-to-subhalo ratio within the disk scale length, being these quantities larger for the barred sample.
- Barred and unbarred galaxies in the *unstable* region of Efstathiou et al. (1982) criterion differ in the maximum circular velocity of the subhalo and in the stellar disk spin, being larger for the barred sample.
- Regarding the differences between bar and unbarred galaxies in the (un-)stable region of Efstathiou et al. (1982) we have proposed an extra criterion based on the subhalo circular velocity, stellar disk spin and stellar-to-halo ratio to be applied on top of the Efstathiou et al. (1982) one. We have shown that the combination of the old and new criteria improves the detectability of bar structures and reduces both the contamination of fake barred galaxies and the number of undetected bar formation events.

### Supermassive black holes: Nuclear and wandering

The second part of the thesis is addressed in Chapter 5 which studies the mass assembly, spin evolution and environment of both nuclear and wandering supermassive black holes. To do that, we have updated with new physical prescriptions the version of L-Galaxies presented in Chapter 3. The new prescriptions have been applied to the merger trees of the Millennium simulation, although galaxies have been initialized using the outputs of the higher-resolution simulation MillenniumII. The starting point of our BH model has been the gas accretion from the galaxy *hot* gas atmosphere and the *cold* gas disk



after galaxy mergers or disk instabilities (DIs). During this phase of gas consumption, the evolution of BH spin ( $a$ ) is tracked by using the approach presented in Dotti et al. (2013) and Sesana et al. (2014) which links the number of prograde transient accretion disk (BH spin-up) with the degree of coherent motion in the bulge. In short, we have assumed that DIs increase the coherence of the bulge kinematics while mergers bring disorder to the bulge dynamics. The BH model presented in this thesis leads to the following predictions concerning the BH assembly:

- Most of the BHs in the current universe were already assembled by  $z \sim 1$  becoming non-active at  $z < 3$ .
- The luminosity functions of the model show interesting results regarding the host galaxy of the accreting BHs. At  $z > 2$  the high end of the luminosity function is dominated by BHs accreting in pseudobulge structures, while at lower redshifts classical bulges and elliptical galaxies are the main structures hosting the most powerful active BHs.
- Regarding the spin predictions, black holes with  $M_{\text{BH}} > 10^6 M_{\odot}$  hosted in pseudobulges, classical bulges and elliptical galaxies display respectively spin values of  $a \sim 0.9$ ,  $0.7$  and  $0.4$ , regardless of redshift. At lower BH masses, as a consequence the implemented model, all the three bulge morphologies host maximum spinning BHs.

One of the main novelties of this thesis is the exploration of the formation and evolution of the wandering black hole population, i.e the population of BH outside of galaxies in bound orbits within the dark matter subhalos. If in the instant of the BH-BH coalescence, the recoil velocity experienced by the remnant black hole is larger than the escape velocity of the host galaxy, the model developed in this thesis assumes that the black hole is kicked from its host and incorporated in the DM subhalo as a *wandering black hole*. We tag these BHs as *ejected* wBHs. The model also tracks the formation of another type of wandering black holes, *orphan* wBHs, which are originated after the complete disruption of their host galaxy via tidal forces. Regardless of their origin, the orbits of wBHs are tracked by using the Runge-Kutta numerical integration, taking into account the host subhalo and galaxy properties for the computation of gravitational acceleration and dynamical friction. The main outcomes of the wandering black hole population are:

- When looking at the number density of wandering BHs, the model predicts an increasing trend towards low- $z$  but being 1 – 3 dex smaller (depending on the BH mass) than that of black holes hosted at the center of galaxies.
- Regarding the spatial distribution, *ejected* wBHs reside at  $\lesssim 0.3R_{200}$ , where  $R_{200}$  is the virial radius of the host sunhalo. On contrary, *orphan* wBHs inhabit the  $\gtrsim 0.5 R_{200}$  regions.
- Concerning the environments of wBHs in the local universe, the model predicts that subhalos of  $M_{\text{halo}} < 10^{13} M_{\odot}$  rarely host a wBH with  $> 10^6 M_{\odot}$ . But if they do, the wBH is typically formed after a gravitational recoil. The picture changes at  $M_{\text{halo}} > 10^{13} M_{\odot}$ , where it is more common to find a handful of wBH of  $M_{\text{BH}} > 10^6 M_{\odot}$  principally formed after the disruption of satellite galaxies. The same trend is found when looking at wBH statistics against the host stellar mass.
- Gravitational recoils affect the co-evolution between the black hole and the host galaxy. In particular, they cause a systematic depletion of nuclear BHs towards low redshift and stellar mass, being galaxies with a pseudobulge structure the most affected.
- By running the SAM with and without gravitational recoils and wandering phase we have explored the imprints of gravitational recoils in the  $z = 0$  bulge-BH scaling relation. We have found that both the median of the relation and its scatter are different in the two runs with the trend of hosting less massive BHs at fixed bulge mass in the run in which recoil velocities and wandering phase are taken into account. The same tendency is found when the population is divided into classical bulges, elliptical galaxies and pseudobulges, being the latter structures the ones which suffer a more pronounced effect.

## Mocks for multi-narrow band surveys

The final block of this thesis, presented in Chapter 6, is a technical work whose aim consists in presenting a new procedure to generate synthetic galaxy lightcones specifically designed for narrow-band photometric surveys. Different from previous lightcone construction methods, we have included its assembly inside the `L-Galaxies` code to reduce time-discreteness effects observed in other lightcones (Merson et al., 2013). Regarding the underlying DM merger trees, we have used the Millennium simulation but the procedure can be applied to Millennium II as well. Since the Millennium box size is not large enough to cover the whole volume of current surveys, we have taken advantage of its periodicity replicating the box eight times in each spatial direction, reaching a lightcone depth up to  $z \sim 3$ . With the purpose of minimising the repetition of large-scale structures, we have placed the observer in the origin of the first replication with a line-of-sight direction selected according to Kitzbichler and White (2007a). Since our goal has been producing mocks for multi-narrow band surveys, whose main advantage is the capability of detecting emission lines produced by star forming galaxies, we have included in the final galaxy photometry of `L-Galaxies` the effect of nine different emission lines. In particular,  $\text{Ly}_\alpha$  (1216Å),  $\text{H}\beta$  (4861Å),  $\text{H}\alpha$  (6563Å), [OII] (3727Å, 3729Å), [NeIII] (3870Å), [OIII] (4959Å, 5007Å), [OI] (6300Å), [NII] (6548Å, 6583Å), and [SII] (6717Å, 6731Å). The properties of these lines were computed using the Orsi et al. (2014) model for nebular emission from star-forming regions. Based on MAPPINGS-III photo-ionisation code the model predicts different line luminosities according to the galaxy gas metallicity, instantaneous star formation rate, and ionisation parameter. Given that star forming galaxies are expected to be gas-rich systems, it has been necessary to attenuate line luminosities by dust effects before including them in the galaxy photometry. By comparing our mock line-luminosity functions to observational works (see e.g. Gunawardhana et al., 2013; Sobral et al., 2013; Comparat et al., 2016) we have calibrated our line dust attenuation which displays a dependence with the galaxy redshift and metallicity. Specifically, we compared our results with the well known  $\text{H}\alpha$ ,  $\text{H}\beta$ , [OII], and [OIII]<sub>5007</sub> luminosity functions to develop a global line attenuation for all the lines included in our mock. Despite its limitations, this simple method has been able to produce final luminosity functions which are in good agreement with observations, even with respect to the observed redshift evolution. Finally, to validate our mock we have presented various tests. While galaxy photometry has been tested with the galaxy number counts in the  $u$ ,  $g$ ,  $r$ ,  $i$ ,  $z$  broad bands, galaxy spatial distribution has been checked by comparing the clustering of  $g$  selected galaxies with the work of Favole et al. (2016). In both cases the agreement is good.

As an application of our lightcone, we have generated catalogues specifically designed to mock the ongoing J-PLUS survey (Cenarro et al., 2019). With these mocks, we have studied the ability of the survey to correctly identify emission-line galaxies at various redshifts. In particular, among all the intermediate- and narrow-band filter available to detect lines, we have focused in the  $J0660$  which is able to capture the  $\text{H}\alpha$  emission of star-forming regions in the nearby universe ( $z < 0.017$ ) and other lines at higher redshifts ( $z > 0.3$ ) such as  $\text{H}\beta$ , [OIII], and [OII]. To assert the detection of the emission lines in J-PLUS, we used the *three-filters method* developed by Vilella-Rojo et al. (2015). Our mocks proved that the extraction of emission lines is strongly dependent on the continuum shape. In particular, we showed that the 4000Å break in the spectral energy distribution of galaxies can be misidentified as line emission, selecting a population of *fake* emission-line galaxies at  $0.3 < z < 0.6$ . However, we showed that all significant excess in the narrow band (larger than 0.4 magnitudes) can be correctly and unambiguously attributed to emission-line galaxies.

As a general conclusion, in this thesis we have shown that semi-analytical models are a powerful tool to explore many aspects about galaxy formation and evolution being also capable to generate sophisticated mocks for the next generation of galaxy surveys. Nevertheless, SAMs need to refine even further the physical prescriptions they include to give answers to the new challenges that future surveys will provide. Although in this thesis we have done one a big step on this direction, addressing the mechanism about pseudobulge formation and including a refined model for the black hole growth and spin evolution,

more refinements can be performed. Such refinements can be done by extracting physical information from observations or take advantage of the results of hydrodynamical simulations.

*“Nunca pensé en este final. ¿Final? No, el viaje no concluye aquí. La muerte es sólo otro sendero, que recorreremos todos. El velo gris de este mundo se levanta y todo se convierte en plateado cristal. Es entonces, cuando se ve... ¿Qué, Gandalf? ¿Qué se ve? La blanca orilla. Y mas allá, la inmensa campiña verde, tendida ante un fugaz amanecer. Bueno, eso no está mal. No, no desde luego.”*

El señor de los anillos: El Retorno del Rey.

*“I didn’t think it would end this way. End? No, the journey doesn’t end here. Death is just another path, one that we all must take. The grey rain-curtain of this world rolls back, and all turns to silver glass. And then you see it. What, Gandalf? See what? White shores, and beyond, a far green country under a swift sunrise. Well... that’s isn’t so bad. No.. no, it isn’t.”*

The Lord of the Rings: The Return of the King.

In this chapter we briefly discuss future projects that could expand the work done in this thesis:

i) *New channels of bulge growth*: As extensively discussed in this thesis, elliptical and classical bulge structures are thought to be formed during violent relaxation processes following both major and minor galaxy mergers. On the contrary, pseudobulges are related to the secular evolution of bar structures. Despite these processes seem to depict a complete picture of the formation of different bulge types, the semi-analytical model allows testing alternative scenarios proposed in the literature. For instance, as future work, we intend to include the *clump-origin bulge* scenario presented in [Noguchi \(1998\)](#) for the formation of classical bulges at high- $z$ . Indeed, such a model could be complemented with the high- $z$  bulge assembly presented in [Dubois et al. \(2012b\)](#) where filamentary streams of gas flow towards the centre of the subhalo and produce low angular momentum bulges. An interesting analysis would be to check if these processes can compete with minor mergers in the formation of classical bulges at high- $z$ . Finally, we also plan to include galaxy flybys as processes triggering strong gas inflows towards the nuclear parts of the galaxy leading to the formation of a diffuse bulge component ([Mihos and Hernquist, 1994](#)).

ii) *The usage of TNG100 hydrodynamical simulations to explore the classical bulge formation*: In Chapter 3 we have shown that the  $z=0$  classical bulge population in L-Galaxies displays values of bulge-to-total ratios too small when compared with observations. To understand such discrepancy we plan to compare the formation and evolution of classical bulges in L-Galaxies (when applied on top of the TNG100-Dark merger trees) with the one of the TNG100 hydrodynamical simulation. Such comparison will test whether the assumptions of L-Galaxies for the formation and evolution of classical bulges are compatible with the outcomes of the TNG100 simulation. For instance, with TNG100 we could check if the whole mass of the satellite galaxy during minor mergers is actually transferred to the nuclear parts of the central galaxy (as assumed by L-Galaxies) when both baryonic and large scale effects are taken into account.

iii) *Improving the merger time scale of binary black holes*: During the last years, the study of how binary black holes (BBH) form, evolve and coalesce inside galaxies has been an important topic in the

astrophysical field (see LISA experiment [Amaro-Seoane et al., 2017b](#)). For that reason, in Chapter 5 we included in L-Galaxies the BBH formation by employing a simple assumption for tackling their lifetime. Despite the results showed an interesting trend of increasing the BBH lifetime when we decrease on redshift, we could not draw solid conclusions since the recipe used is an oversimplification which does not capture the whole complexity of the BH coalescence. Hence further improvements are needed. In the future, we plan to explore this topic in more detail using the results of state-of-the-art hydrodynamical simulations. The goal is formulating a rather simple recipe able to capture the dependencies of the binary black hole lifetime on the black hole merger ratio, galaxy gas content or galaxy bulge mass.

iv) *Linking the life of the binary black hole with the bulge morphology*: As discussed in the introduction, many works have used the differential equations presented in [Sesana and Khan \(2015\)](#) to track the separation of a binary black hole (BBH) system during its hardening and gravitational wave inspiral phases. Interestingly, these equations show a dependence on the number of stars inside the BBH orbit, which in turns, correlates with the properties of the host galaxy bulge. The recent work [Biava et al. \(2019\)](#) explored analytically the outcomes of the [Sesana and Khan \(2015\)](#) equations on the lifetime of  $> 10^6 M_{\odot}$  BBHs when several bulge Sérsic profiles of the host galaxy are assumed. The results showed that different stellar profiles lead to very distinct trends with lifetimes ranging between few Gyr to more than 10 Gyr. In the future, we plan to perform a similar analysis but using the galaxy population and the cosmological context provided by L-Galaxies. According to the galaxy bulge type and its bulge-to-total value, different Sérsic profiles will be assumed during the numerical integration of [Sesana and Khan \(2015\)](#) equations. The results will give interesting predictions about the bulge type hosting more binary black holes at different cosmological times.

v) *Generate mocks for the J-PAS survey*: In this thesis we have presented a methodology to generate mocks for any multi-narrow band survey. As an application, we generated catalogues tailored for J-PLUS survey, consisting of a combination of 5 broad-band and 7 medium-band filters. By comparing predicted and measured broad and narrow band number counts and the  $H\alpha$  luminosity function, we proved their successful performance. We plan to push further our methodology and generate simulated catalogues for the spectro-photometric J-PAS survey<sup>1</sup> whose filter system includes 56 narrow-bands. These mocks would help the J-PAS collaboration to test their procedures to detect high- $z$  emission line galaxies and could be used as a training sample in machine learning codes.

vi) *Including in the mock construction emission lines coming from AGNs*: As we described in Chapter 5, we included in L-Galaxies different physical prescriptions to build a model able to tackle the black hole growth and spin evolution across cosmic time. The idea is adding this model inside the mock construction presented in Chapter 6 to have a reliable population of active black holes whose bolometric luminosity can be associated with quasar and AGN SEDs at different cosmological times. The final photometry of a galaxy hosting an accreting BH will be computed by selecting, at a given bolometric luminosity, a random quasar/AGN SED from a library and convolve it with the filter system of the survey that we want to simulate.

---

<sup>1</sup><http://www.j-pas.org/>

## RESUMEN Y CONCLUSIONES

*“Bilbo me contó un día que las grandes historias nunca terminan, que cada uno de nosotros debe coger el relevo de la narración. Su papel en este relato había concluido, no habría más viajes para Bilbo... excepto uno. Dímelo otra vez amigo, ¿a dónde vamos? A los puertos, Bilbo, los elfos te han otorgado un honor especial, una plaza en el último barco que zarpa de la Tierra Media. [...] Vaya, he aquí un horizonte nuevo para mi... Creo que estoy preparado para otra aventura.”*

El señor de los anillos: El Retorno del Rey.

*“Bilbo once told me his part in this tale would end. That each of us must come and go in the telling. Bilbo’s story was now over. There would be no more journeys for him... save one. Tell me again, lad, where are we going? To the harbor, Uncle. The elves have accorded you a special honor. A place on the last ship to leave Middle-Earth. [...] Oh! Well, here is a sight I have never seen before... I think I’m quite ready for another adventure.”*

The Lord of the Rings: The Return of the King.

En esta tesis se han abordado tres temas diferentes: la evolución de bulbos galácticos, el crecimiento de agujeros negros supermasivos y el desarrollo de catálogos simulados para la nueva generación de cartografiados de banda estrecha. Hemos tratado todos estos temas utilizando el modelo semianalítico L-Galaxies<sup>2</sup>. Este modelo es uno de los más avanzados de la literatura cuya capacidad para predecir correctamente la función de masa estelar, la fracción de galaxias pasivas o la densidad de formación estelar a diferentes tiempos cosmológicos ha sido demostrada durante los últimos años (De Lucia and Blaizot, 2007; Guo et al., 2011; Henriques et al., 2015). L-Galaxies tiene la principal ventaja de poder ejecutarse sobre en los árboles de fusiones de materia oscura extraídos de las simulaciones Millennium cuyas diferencias en resolución en masa y tamaños de caja ofrecen la posibilidad de explorar diferentes procesos físicos experimentados por las galaxias en una amplia variedad de escalas y entornos.

En los siguientes apartados resumimos, para cada uno de los temas tratados en esta tesis, la metodología aplicada y las principales conclusiones.

### La formación y crecimiento de pseudobulbos

La primera parte de esta tesis se aborda en el Capítulo 3 y 4. En ella se estudia la formación y evolución cosmológica de bulbos galácticos, con especial énfasis en la población de pseudobulbos. Aprovechando que L-Galaxies puede ser ejecutado en los árboles de fusiones de Millennium y Millennium II, hemos estudiado en un rango muy amplio de masas estelares ( $10^8 - 10^{11.5} M_{\odot}$ ) tanto la formación de pseudobulbos como las propiedades de las galaxias en las que residen. Suponiendo que los pseudobulbos solo pueden formarse y crecer a través de procesos seculares, hemos modificado el tratamiento que L-Galaxies realiza en las inestabilidades de disco, distinguiendo entre dos tipos de eventos: inestabilidad *inducida secularmente e inducida por fusión*. A pesar de que ambos eventos emergen como consecuencia de discos estelares lo suficientemente masivos como para experimentar una inestabilidad de barra, los procesos que condujeron a su formación son completamente diferentes. Por un lado, las in-

<sup>2</sup><http://galformod.mpa-garching.mpg.de/public/LGalaxies/>



estabilidades *inducidas por fusión* son producidas por fusiones de galaxias a causa de un rápido aumento de la masa del disco después de una intensa formación estelar o del accrecimiento de la galaxia satélite. Por otro lado, inestabilidades *inducidas secularmente* se producen en discos cuyo crecimiento en masa ha sido completamente producido por eventos internos y seculares de formación estelar. Este último tipo de inestabilidades son las que consideraremos como las responsables de la formación de barras duraderas que provocan el crecimiento de pseudobulbos. Por otra parte, las inestabilidades *inducidas por fusión* contribuyen, junto con las fusiones de galaxias, al crecimiento de los bulbos clásicos. Los principales hallazgos pueden resumirse en:

- A cualquier tiempo cosmológico, las inestabilidades *inducidas por fusión* son menos numerosas que las *inducidas secularmente*. De hecho, estas primeras son procesos subdominantes en el crecimiento de bulbos clásicos.
- Independientemente del tiempo cosmológico, las inestabilidades de disco *inducidas secularmente* son los eventos más abundantes que conciernen a la formación y evolución de bulbos galácticos. Sin embargo, estas inestabilidades contribuyen de manera muy diferente dependiendo de la masa estelar de la galaxia. Mientras que en galaxias de  $10^9 - 10^{10} M_{\odot}$  estos eventos contribuyen sustancialmente al crecimiento de los bulbos, en galaxias de  $10^8 - 10^9 M_{\odot}$  tienen un efecto marginal.
- A tiempos cosmológicos altos, los pseudobulbos están presentes principalmente en galaxias con masa estelar de  $10^{9.5} - 10^{10} M_{\odot}$ .
- Los pseudobulbos en el universo local residen en galaxias análogas a la Vía Láctea y con una intensa formación estelar. Sin embargo, en galaxias más masivas apenas podemos encontrar este tipo de estructuras dado que son destruidas sistemáticamente por fusiones de galaxias.

A pesar de que los resultados presentados anteriormente son prometedores, hemos explorado la capacidad del criterio de inestabilidades de disco incluido en L-Galaxies (extraído del artículo [Efstathiou et al., 1982](#)) para capturar toda la física involucrada en la formación de barras y pseudobulbos. Con ese fin, hemos estudiado el comportamiento de esta receta cuando es aplicada en una muestra de galaxia con y sin barra extraída de la simulación hidrodinámica TNG100 ([Nelson et al., 2018](#)). Los resultados muestran que a pesar de haber una correlación entre las predicciones del criterio de L-Galaxies y el ensamblaje barras, hay casos en los que el criterio falla ya sea afirmando estabilidad/inestabilidad del disco para galaxias barradas/no barradas. Para comprender mejor estos casos, hemos comparado las galaxias con y sin barra en la región estable/inestable del criterio de [Efstathiou et al. \(1982\)](#). Los resultados encontrados son los siguientes:

- Las principales diferencias entre galaxias barradas y no barradas en la región *estable* del criterio de [Efstathiou et al. \(1982\)](#) están presentes en la máxima velocidad circular del subhalo y el cociente masa estelar-masa de subhalo dentro del disco. Estas cantidades son mayores para la muestra con barra.
- Las galaxias barradas y no barradas en la región *inestable* del criterio [Efstathiou et al. \(1982\)](#) difieren en la velocidad circular máxima del subhalo y en el espín del disco estelar, siendo más grande para la muestra barrada.
- De acuerdo con las diferencias entre galaxias con barra y sin barra en la región estable e inestable del criterio de [Efstathiou et al. \(1982\)](#), hemos propuesto una condición adicional basada en la velocidad circular del subhalo, el espín del disco estelar y el ratio masa estelar-masa del subhalo. Hemos demostrado que la combinación del criterio de L-Galaxies con la nueva condición que proponemos mejora la detectabilidad de las estructuras de barras y reduce la contaminación de falsas galaxias barradas.

### Agujeros negros supermasivos: nucleares y errantes

La segunda parte de la tesis es abordada íntegramente en el Capítulo 5 donde se estudia para agujeros negros nucleares y errantes su ensamblaje en masa, evolución de espín y entorno. Para ello, hemos actualizado con nuevas recetas físicas la versión de L-Galaxies presentada en el Capítulo 3. Éstas se han aplicado cuando L-Galaxies es ejecutado en los árboles de fusiones de materia oscura de Millennium. Hemos asumido que los agujeros negros crecen en masa mediante el consumo de gas procedente de la atmósfera de gas *caliente* que rodea la galaxia y del disco galáctico de gas *frío* tras fusiones de galaxias y/o inestabilidades de disco. Durante esta fase de consumo de gas, se ha seguido la evolución del espín utilizando el enfoque presentado en los artículos de Dotti et al. (2013) y Sesana et al. (2014) que vinculan el número de discos de acreción transitorios prógrados (que aumentan el espín del agujero negro) con el grado de rotación del bulbo. A grandes rasgos, hemos asumido que las inestabilidades de disco aumentan la coherencia cinemática del bulbo, mientras que las fusiones la disminuyen. El modelo presentado en esta tesis muestra las siguientes predicciones en la evolución cosmológica de los agujeros negros:

- Gran parte de los agujeros negros en el universo local adquirieron la mayoría de su masa a tiempos cosmológicos altos.
- Las funciones de luminosidad del modelo muestran resultados interesantes respecto al tipo de galaxias que albergan agujeros negros en crecimiento (es decir, activos). A tiempos cosmológicos altos el extremo débil de la función de luminosidad está dominado por agujeros negros consumiendo gas en pseudobulbos. No obstante, a tiempos cosmológicos más bajos, los bulbos clásicos y galaxias elípticas son las estructuras principales que albergan los agujeros negros activos.
- En cuanto a las predicciones de espín, agujeros negros con masa  $> 10^6 M_{\odot}$  alojados en pseudobulbos, bulbos clásicos y galaxias elípticas tienen un valor de espín de  $\sim 0.9$ ,  $\sim 0.7$  y  $\sim 0.4$ , independientemente del tiempo cosmológico. A masas más bajas, como consecuencia del modelo implementado, los tres tipos de bulbos albergan agujeros negros con el máximo valor de espín ( $\sim 0.998$ ).

Una de las principales novedades de esta tesis ha sido explorar la formación y evolución de agujeros negros errantes, es decir, una población de agujeros negros que se encuentran fuera de las galaxias, en órbitas ligadas dentro de los subhalos de materia oscura. Si en el instante de la fusión de dos agujeros negros, el resultante experimenta una velocidad de retroceso mayor que la velocidad de escape de la galaxia que lo alberga, asumimos que es expulsado de su galaxia e incorporado en el subhalo de materia oscura como un *agujero negro errante*. Nos referiremos a estos tipos de agujeros negros como *eyectados*. El modelo también tiene en cuenta la formación de otro tipo de agujeros negros errantes, los *huérfanos* que son generados después de la completa destrucción de su galaxia a causa de fuerzas de marea. Independientemente de su origen, las órbitas de los agujeros negros errantes son calculadas utilizando la integración numérica de Runge-Kutta, teniendo en cuenta las propiedades de la galaxia y subhalo que los albergan para el cálculo de la aceleración gravitacional y la fricción dinámica. Los principales resultados de la población de agujeros negros errantes son:

- El número de agujeros negros errantes aumenta a bajo tiempo cosmológico. De hecho, el número de este tipo de agujeros negros es de 1–3 dex menor (dependiendo de la masa) que el de los agujeros negros alojados en el centro de las galaxias.
- Respecto a la distribución espacial, los agujeros negros *eyectados* se encuentran a  $\lesssim 0.3R_{200}$ , donde  $R_{200}$  es el radio virial del subhalo que los alberga. Por el contrario, los *huérfanos* residen a  $\gtrsim 0.5 R_{200}$ .
- El modelo predice que los subhalos de masa  $< 10^{13} M_{\odot}$  rara vez albergan un agujero negro errante de masa  $> 10^6 M_{\odot}$ . Sin embargo, en caso de tener, el agujero negro errante es del tipo *eyectado*. Todo esto cambia a masas de subhalo  $> 10^{13} M_{\odot}$  donde es más común encontrar un agujero negro

errante (típicamente  $\sim 5$ ) de masas  $> 10^6 M_{\odot}$  y tipo *huérfano*. Se encuentra la misma tendencia cuando este análisis es realizado con masas estelares.

- La expulsión de agujeros negros afecta la co-evolución entre los agujeros negros y las galaxias. Específicamente, provocan una disminución sistemática del número de agujeros negros albergados en galaxias a tiempos cosmológicos bajos. Las galaxias con pseudobulbos son las que más sufren de esta disminución.
- Al ejecutar L-Galaxies con y sin retrocesos gravitacionales y fase errante, hemos explorado los efectos que estos procesos dejan en la relación masa del bulbo-masa del agujero en el universo local. Hemos encontrado que tanto la mediana de la relación como su dispersión son diferentes cuando se incluyen o no se incluyen los efectos de eyección. La tendencia es albergar agujeros negros menos masivos, a una masa de bulbo fija, en el modelo que incluye los efectos de retroceso. Esta tendencia se encuentra en cualquier tipo de bulbo, sin embargo los pseudobulbos son los que más sufren de este efecto.

### Catálogos simulados para cartografiados de bandas estrechas

El bloque final de esta tesis, presentado en el Capítulo 6, es un trabajo técnico cuyo objetivo consiste en presentar un nuevo procedimiento para generar simulaciones de conos de luz específicamente diseñadas para cartografiados fotométricos de banda estrecha. A diferencia de otros métodos, hemos incluido su construcción dentro de L-Galaxies con el objetivo de reducir los efectos de discreción temporal observados en otros trabajos (Merson et al., 2013). Con respecto a los árboles de fusiones de materia oscura, hemos utilizado los de la simulación Millennium aunque también pueden ser utilizados los de Millennium II. Para conseguir volúmenes similares a los alcanzados por los cartografiados actuales, hemos aprovechado la periodicidad de la simulación Millennium replicándola ocho veces en cada dirección espacial. Para minimizar la repetición de estructuras, hemos colocado al observador del cono de luz en el origen de la primera réplica con una orientación seleccionada de acuerdo con Kitzbichler and White (2007a). Dado que nuestro objetivo ha sido producir catálogos para cartografiados de banda estrecha cuya principal ventaja es detectar líneas de emisión producidas por galaxias con formación estelar, hemos incluido en la fotometría de las galaxias de L-Galaxies el efecto de nueve líneas de emisión diferentes. Específicamente,  $Ly_{\alpha}$  (1216Å),  $H\beta$  (4861Å),  $H\alpha$  (6563Å), [OII] (3727Å, 3729Å), [NeIII] (3870Å), [OIII] (4959Å, 5007Å), [OI] (6300Å), [NII] (6548Å, 6583Å) y [SII] (6717Å, 6731Å). Las propiedades de estas líneas se han calculado utilizando el modelo de Orsi et al. (2014) el cual, basándose en el código de fotoionización MAPPINGS-III, predice diferentes luminosidades de línea de acuerdo con la metalicidad del gas de la galaxia, la tasa instantánea de formación estelar y el parámetro de ionización. Puesto que las galaxias con formación estelar están llenas de gas, ha sido necesario atenuar la luminosidad de las líneas antes de incluirlas en la fotometría de las galaxias. Al comparar las funciones de luminosidad simuladas con trabajos observacionales (ver, por ejemplo, Gunawardhana et al., 2013; Sobral et al., 2013; Comparat et al., 2016), hemos calibrado nuestra atenuación aplicando una dependencia con el tiempo cosmológico y la metalicidad de la galaxia. Concretamente, la calibración se ha realizado mediante el uso de las funciones de luminosidad de  $H\alpha$ ,  $H\beta$ , [OII] y [OIII]<sub>5007</sub>. A pesar de sus limitaciones, nuestra atenuación ha sido capaz de producir funciones de luminosidad en concordancia con las observaciones. Finalmente, para validar nuestros catálogos simulados, hemos realizado varias pruebas, todas ellas satisfactorias.

Como aplicación, hemos generado catálogos específicamente diseñados para el cartografiado J-PLUS (Cenarro et al., 2019). Con la ayuda de éstos hemos estudiado la capacidad de J-PLUS para identificar las galaxias con línea de emisión a varios tiempos cosmológicos. En particular, entre todos los filtros de banda intermedia y estrecha, nos hemos centrado en el J0660 que es capaz de capturar la emisión  $H\alpha$  en el universo cercano y otras líneas a tiempos cosmológicos mayores como  $H\beta$ , [OIII] y [OII]. Utilizando el método de tres filtros (Vilella-Rojo et al., 2015) hemos demostrado que la extracción de líneas de emisión depende en gran medida de la forma del continuo de la galaxia, en particular, de lo que se

conoce como el *salto de 4000Å*. Éste puede identificarse erróneamente como una emisión, haciendo que seleccionemos una población falsa de línea de emisión. Sin embargo, probamos que todo exceso significativo en la banda estrecha (mayor a 0.4 magnitudes) puede atribuirse correcta e inequívocamente a las galaxias con líneas de emisión.

Como conclusión general, en esta tesis hemos demostrado que los modelos semianalíticos son una poderosa herramienta para explorar muchos aspectos sobre la formación y evolución de galaxias además de ser capaces de generar sofisticados catálogos para la próxima generación de cartografiados de galaxias. Sin embargo, para dar respuestas a los nuevos desafíos que brindarán los cartografiados futuros, los semi-analíticos necesitan refinar aún más las prescripciones físicas que incluyen. Aunque en esta tesis hemos dado un gran paso en esta dirección, abordando el mecanismo sobre la formación de pseudobulbos e incluyendo un modelo para el crecimiento de agujeros negros, se pueden realizar más refinamientos. Éstos pueden llevarse a cabo extrayendo información física de las observaciones o aprovechando los resultados de las simulaciones hidrodinámicas.

- Abadi, M. G., Navarro, J. F., Steinmetz, M., and Eke, V. R. (2003). Simulations of Galaxy Formation in a  $\Lambda$  Cold Dark Matter Universe. II. The Fine Structure of Simulated Galactic Disks. *ApJ*, 597:21–34.
- Abel, T., Anninos, P., Zhang, Y., and Norman, M. L. (1997). Modeling primordial gas in numerical cosmology. *New A*, 2(3):181–207.
- Abel, T., Bryan, G. L., and Norman, M. L. (2002). The Formation of the First Star in the Universe. *Science*, 295(5552):93–98.
- Abraham, R. G., van den Bergh, S., Glazebrook, K., Ellis, R. S., Santiago, B. X., Surma, P., and Griffiths, R. E. (1996). The Morphologies of Distant Galaxies. II. Classifications from the Hubble Space Telescope Medium Deep Survey. *ApJS*, 107:1.
- Agarwal, B., Johnson, J. L., Khochfar, S., Pellegrini, E., Rydberg, C.-E., Klessen, R. S., and Oesch, P. (2017). Metallicity evolution of direct collapse black hole hosts: CR7 as a case study. *MNRAS*, 469(1):231–236.
- Agarwal, B., Khochfar, S., Johnson, J. L., Neistein, E., Dalla Vecchia, C., and Livio, M. (2012). Ubiquitous seeding of supermassive black holes by direct collapse. *MNRAS*, 425(4):2854–2871.
- Agertz, O., Teyssier, R., and Moore, B. (2011). The formation of disc galaxies in a  $\Lambda$ CDM universe. *MNRAS*, 410(2):1391–1408.
- Aguerri, J. A. L., Balcells, M., and Peletier, R. F. (2001). Growth of galactic bulges by mergers. I. Dense satellites. *A&A*, 367:428–442.
- Aguerri, J. A. L., Méndez-Abreu, J., and Corsini, E. M. (2009). The population of barred galaxies in the local universe. I. Detection and characterisation of bars. *A&A*, 495(2):491–504.
- Aird, J., Coil, A. L., Georgakakis, A., Nandra, K., Barro, G., and Pérez-González, P. G. (2015). The evolution of the X-ray luminosity functions of unabsorbed and absorbed AGNs out to  $z \sim 5$ . *MNRAS*, 451(2):1892–1927.
- Algorry, D. G., Navarro, J. F., Abadi, M. G., Sales, L. V., Bower, R. G., Crain, R. A., Dalla Vecchia, C., Frenk, C. S., Schaller, M., Schaye, J., and Theuns, T. (2017). Barred galaxies in the EAGLE cosmological hydrodynamical simulation. *MNRAS*, 469(1):1054–1064.
- Allevalo, V., Finoguenov, A., Cappelluti, N., Miyaji, T., Hasinger, G., Salvato, M., Brusa, M., Gilli, R., Zamorani, G., Shankar, F., James, J. B., McCracken, H. J., Bongiorno, A., Merloni, A., Peacock, J. A., Silverman, J., and Comastri, A. (2011). The XMM-Newton Wide Field Survey in the COSMOS Field: Redshift Evolution of AGN Bias and Subdominant Role of Mergers in Triggering Moderate-luminosity AGNs at Redshifts up to 2.2. *ApJ*, 736(2):99.

- Alloin, D., Pelat, D., Phillips, M., and Whittle, M. (1985). Recent spectral variations in the active nucleus of NGC 1566. *ApJ*, 288:205–220.
- Amaro-Seoane, P., Audley, H., Babak, S., Baker, J., Barausse, E., Bender, P., Berti, E., Binetruy, P., Born, M., Bortoluzzi, D., Camp, J., Caprini, C., Cardoso, V., Colpi, M., Conklin, J., Cornish, N., Cutler, C., Danzmann, K., Dolesi, R., Ferraioli, L., Ferroni, V., Fitzsimons, E., Gair, J., Gesa Bote, L., Giardini, D., Gibert, F., Grimani, C., Halloin, H., Heinzl, G., Hertog, T., Hewitson, M., Holley-Bockelmann, K., Hollington, D., Hueller, M., Inchauspe, H., Jetzer, P., Karnesis, N., Killow, C., Klein, A., Klipstein, B., Korsakova, N., Larson, S. L., Livas, J., Lloro, I., Man, N., Mance, D., Martino, J., Mateos, I., McKenzie, K., McWilliams, S. T., Miller, C., Mueller, G., Nardini, G., Nelemans, G., Nofrarias, M., Petiteau, A., Pivato, P., Plagnol, E., Porter, E., Reiche, J., Robertson, D., Robertson, N., Rossi, E., Russano, G., Schutz, B., Sesana, A., Shoemaker, D., Slutsky, J., Sopuerta, C. F., Sumner, T., Tamanini, N., Thorpe, I., Troebs, M., Vallisneri, M., Vecchio, A., Vetrugno, D., Vitale, S., Volonteri, M., Wanner, G., Ward, H., Wass, P., Weber, W., Ziemer, J., and Zweifel, P. (2017a). Laser Interferometer Space Antenna. *arXiv e-prints*, page arXiv:1702.00786.
- Amaro-Seoane, P., Audley, H., Babak, S., Baker, J., Barausse, E., Bender, P., Berti, E., Binetruy, P., Born, M., Bortoluzzi, D., Camp, J., Caprini, C., Cardoso, V., Colpi, M., Conklin, J., Cornish, N., Cutler, C., Danzmann, K., Dolesi, R., Ferraioli, L., Ferroni, V., Fitzsimons, E., Gair, J., Gesa Bote, L., Giardini, D., Gibert, F., Grimani, C., Halloin, H., Heinzl, G., Hertog, T., Hewitson, M., Holley-Bockelmann, K., Hollington, D., Hueller, M., Inchauspe, H., Jetzer, P., Karnesis, N., Killow, C., Klein, A., Klipstein, B., Korsakova, N., Larson, S. L., Livas, J., Lloro, I., Man, N., Mance, D., Martino, J., Mateos, I., McKenzie, K., McWilliams, S. T., Miller, C., Mueller, G., Nardini, G., Nelemans, G., Nofrarias, M., Petiteau, A., Pivato, P., Plagnol, E., Porter, E., Reiche, J., Robertson, D., Robertson, N., Rossi, E., Russano, G., Schutz, B., Sesana, A., Shoemaker, D., Slutsky, J., Sopuerta, C. F., Sumner, T., Tamanini, N., Thorpe, I., Troebs, M., Vallisneri, M., Vecchio, A., Vetrugno, D., Vitale, S., Volonteri, M., Wanner, G., Ward, H., Wass, P., Weber, W., Ziemer, J., and Zweifel, P. (2017b). Laser Interferometer Space Antenna. *arXiv e-prints*.
- Amaro-Seoane, P., Eichhorn, C., Porter, E. K., and Spurzem, R. (2010). Binaries of massive black holes in rotating clusters: dynamics, gravitational waves, detection and the role of eccentricity. *MNRAS*, 401(4):2268–2284.
- Amaro-Seoane, P., Miller, M. C., and Freitag, M. (2009). Gravitational Waves from Eccentric Intermediate-Mass Black Hole Binaries. *ApJ*, 692(1):L50–L53.
- Amaro-Seoane, P. and Santamaría, L. (2010). Detection of IMBHs with Ground-based Gravitational Wave Observatories: A Biography of a Binary of Black Holes, from Birth to Death. *ApJ*, 722(2):1197–1206.
- Angulo, R. E., Springel, V., White, S. D. M., Jenkins, A., Baugh, C. M., and Frenk, C. S. (2012). Scaling relations for galaxy clusters in the Millennium-XXL simulation. *MNRAS*, 426(3):2046–2062.
- Angulo, R. E. and White, S. D. M. (2010). One simulation to fit them all - changing the background parameters of a cosmological N-body simulation. *MNRAS*, 405:143–154.
- Angulo, R. E., White, S. D. M., Springel, V., and Henriques, B. (2014). Galaxy formation on the largest scales: the impact of astrophysics on the baryonic acoustic oscillation peak. *MNRAS*, 442(3):2131–2144.
- Antonini, F., Barausse, E., and Silk, J. (2015). The Coevolution of Nuclear Star Clusters, Massive Black Holes, and Their Host Galaxies. *ApJ*, 812(1):72.
- Antonucci, R. (1993). Unified models for active galactic nuclei and quasars. *ARA&A*, 31:473–521.



- Arimoto, N. and Yoshii, Y. (1987). Chemical and photometric properties of a galactic wind model for elliptical galaxies. *A&A*, 173:23–38.
- Arnouts, S., Vandame, B., Benoist, C., Groenewegen, M. A. T., da Costa, L., Schirmer, M., Mignani, R. P., Slijkhuis, R., Hatziminaoglou, E., Hook, R., Madejsky, R., Rit , C., and Wicenec, A. (2001). ESO imaging survey. Deep public survey: Multi-color optical data for the Chandra Deep Field South. *A&A*, 379:740–754.
- Athanassoula, E. (2003). What determines the strength and the slowdown rate of bars? *MNRAS*, 341(4):1179–1198.
- Athanassoula, E. (2005). On the nature of bulges in general and of box/peanut bulges in particular: input from N-body simulations. *MNRAS*, 358:1477–1488.
- Athanassoula, E. (2008). Disc instabilities and semi-analytic modelling of galaxy formation. *MNRAS*, 390:L69–L72.
- Athanassoula, E. (2012). Towards understanding the dynamics of the bar/bulge region in our Galaxy. In *European Physical Journal Web of Conferences*, volume 19 of *European Physical Journal Web of Conferences*, page 06004.
- Athanassoula, E., Machado, R. E. G., and Rodionov, S. A. (2013). Bar formation and evolution in disc galaxies with gas and a triaxial halo: morphology, bar strength and halo properties. *MNRAS*, 429(3):1949–1969.
- Athanassoula, E. and Misiriotis, A. (2002a). Morphology, photometry and kinematics of N -body bars - I. Three models with different halo central concentrations. *MNRAS*, 330(1):35–52.
- Athanassoula, E. and Misiriotis, A. (2002b). Morphology, photometry and kinematics of N -body bars - I. Three models with different halo central concentrations. *MNRAS*, 330(1):35–52.
- Athanassoula, E. and Sellwood, J. A. (1986). Bi-symmetric instabilities of the Kuz'min/Toomre disc. *MNRAS*, 221:213–232.
- Bahcall, J. N., Kirhakos, S., Saxe, D. H., and Schneider, D. P. (1997). Hubble Space Telescope Images of a Sample of 20 Nearby Luminous Quasars. *ApJ*, 479(2):642–658.
- Baker, J. G., Boggs, W. D., Centrella, J., Kelly, B. J., McWilliams, S. T., Miller, M. C., and van Meter, J. R. (2008). Modeling Kicks from the Merger of Generic Black Hole Binaries. *ApJ*, 682:L29.
- Baker, J. G., Centrella, J., Choi, D.-I., Koppitz, M., and van Meter, J. (2006a). Binary black hole merger dynamics and waveforms. *Phys. Rev. D*, 73(10):104002.
- Baker, J. G., Centrella, J., Choi, D.-I., Koppitz, M., and van Meter, J. (2006b). Gravitational-Wave Extraction from an Inspiring Configuration of Merging Black Holes. *Phys. Rev. Lett.*, 96(11):111102.
- Balbus, S. A. and Hawley, J. F. (1998). Instability, turbulence, and enhanced transport in accretion disks. *Reviews of Modern Physics*, 70(1):1–53.
- Baldwin, J. A., Phillips, M. M., and Terlevich, R. (1981). Classification parameters for the emission-line spectra of extragalactic objects. *PASP*, 93:5–19.
- Barausse, E. (2012). The evolution of massive black holes and their spins in their galactic hosts. *MNRAS*, 423:2533–2557.
- Barausse, E., Morozova, V., and Rezzolla, L. (2012). On the Mass Radiated by Coalescing Black Hole Binaries. *ApJ*, 758:63.

- Barausse, E. and Rezzolla, L. (2009). Predicting the Direction of the Final Spin from the Coalescence of Two Black Holes. *ApJ*, 704:L40–L44.
- Barazza, F. D., Jogee, S., and Marinova, I. (2008a). Bars in Disk-dominated and Bulge-dominated Galaxies at  $z \sim 0$ : New Insights from  $\sim 3600$  SDSS Galaxies. *ApJ*, 675(2):1194–1212.
- Barazza, F. D., Jogee, S., and Marinova, I. (2008b). Bars in Disk-dominated and Bulge-dominated Galaxies at  $z \sim 0$ : New Insights from  $\sim 3600$  SDSS Galaxies. *ApJ*, 675(2):1194–1212.
- Bardeen, J. M. (1970). Kerr Metric Black Holes. *Nature*, 226:64–65.
- Bardeen, J. M. and Petterson, J. A. (1975a). The Lense-Thirring Effect and Accretion Disks around Kerr Black Holes. *ApJ*, 195:L65.
- Bardeen, J. M. and Petterson, J. A. (1975b). The Lense-Thirring Effect and Accretion Disks around Kerr Black Holes. *ApJ*, 195:L65.
- Bardeen, J. M., Press, W. H., and Teukolsky, S. A. (1972). Rotating Black Holes: Locally Nonrotating Frames, Energy Extraction, and Scalar Synchrotron Radiation. *ApJ*, 178:347–370.
- Barger, A. J., Cowie, L. L., Mushotzky, R. F., Yang, Y., Wang, W. H., Steffen, A. T., and Capak, P. (2005). The Cosmic Evolution of Hard X-Ray-selected Active Galactic Nuclei. *AJ*, 129(2):578–609.
- Barnes, D. J., Kay, S. T., Bahé, Y. M., Dalla Vecchia, C., McCarthy, I. G., Schaye, J., Bower, R. G., Jenkins, A., Thomas, P. A., Schaller, M., Crain, R. A., Theuns, T., and White, S. D. M. (2017). The Cluster-EAGLE project: global properties of simulated clusters with resolved galaxies. *MNRAS*, 471(1):1088–1106.
- Barnes, J. E. (1988). Encounters of Disk/Halo Galaxies. *ApJ*, 331:699.
- Barnes, J. E. (1999). Galaxy Transformation by Merging. In Beckman, J. E. and Mahoney, T. J., editors, *The Evolution of Galaxies on Cosmological Timescales*, volume 187 of *Astronomical Society of the Pacific Conference Series*, pages 293–306.
- Barnes, J. E. and Hernquist, L. (1996). Transformations of Galaxies. II. Gasdynamics in Merging Disk Galaxies. *ApJ*, 471:115.
- Barnes, J. E. and Hernquist, L. E. (1991a). Fueling Starburst Galaxies with Gas-rich Mergers. *ApJ*, 370:L65.
- Barnes, J. E. and Hernquist, L. E. (1991b). Fueling Starburst Galaxies with Gas-rich Mergers. *ApJ*, 370:L65.
- Batta, A., Ramirez-Ruiz, E., and Fryer, C. (2017). The Formation of Rapidly Rotating Black Holes in High-mass X-Ray Binaries. *ApJ*, 846(2):L15.
- Baugh, C. M. (2006). A primer on hierarchical galaxy formation: the semi-analytical approach. *Reports on Progress in Physics*, 69:3101–3156.
- Baugh, C. M., Cole, S., and Frenk, C. S. (1996a). Evolution of the Hubble sequence in hierarchical models for galaxy formation. *MNRAS*, 283(4):1361–1378.
- Baugh, C. M., Cole, S., and Frenk, C. S. (1996b). Faint galaxy counts as a function of morphological type in a hierarchical merger model. *MNRAS*, 282:L27–L32.
- Baugh, C. M., Cole, S., Frenk, C. S., Benson, A. J., and Lacey, C. G. (1999). Early-Type Galaxies in the Hierarchical Universe. In Carral, P. and Cepa, J., editors, *Star Formation in Early Type Galaxies*, volume 163 of *Astronomical Society of the Pacific Conference Series*, page 227.

- Begelman, M. C., Blandford, R. D., and Rees, M. J. (1980). Massive black hole binaries in active galactic nuclei. *Nature*, 287:307–309.
- Bekenstein, J. D. (1973). Gravitational-Radiation Recoil and Runaway Black Holes. *ApJ*, 183:657–664.
- Bell, E. F., Wolf, C., Meisenheimer, K., Rix, H.-W., Borch, A., Dye, S., Kleinheinrich, M., Wisotzki, L., and McIntosh, D. H. (2004). Nearly 5000 Distant Early-Type Galaxies in COMBO-17: A Red Sequence and Its Evolution since  $z \sim 1$ . *ApJ*, 608(2):752–767.
- Bellovary, J. M., Governato, F., Quinn, T. R., Wadsley, J., Shen, S., and Volonteri, M. (2010). Wandering Black Holes in Bright Disk Galaxy Halos. *ApJ*, 721(2):L148–L152.
- Bender, R., Ziegler, B., and Bruzual, G. (1996). The Redshift Evolution of the Stellar Populations in Elliptical Galaxies. *ApJ*, 463:L51–L54.
- Benitez, N., Dupke, R., Moles, M., Sodre, L., Cenarro, J., Marin-Franch, A., Taylor, K., Cristobal, D., Fernandez-Soto, A., Mendes de Oliveira, C., Cepa-Nogue, J., Abramo, L. R., Alcaniz, J. S., Overzier, R., Hernandez-Montegudo, C., Alfaro, E. J., Kanaan, A., Carvano, J. M., Reis, R. R. R., Martinez Gonzalez, E., Ascaso, B., Ballesteros, F., Xavier, H. S., Varela, J., Ederoclite, A., Vazquez Ramio, H., Broadhurst, T., Cypriano, E., Angulo, R., Diego, J. M., Zandivarez, A., Diaz, E., Melchior, P., Umetsu, K., Spinelli, P. F., Zitrin, A., Coe, D., Yepes, G., Vielva, P., Sahni, V., Marcos-Caballero, A., Shu Kitaura, F., Maroto, A. L., Masip, M., Tsujikawa, S., Carneiro, S., Gonzalez Nuevo, J., Carvalho, G. C., Reboucas, M. J., Carvalho, J. C., Abdalla, E., Bernui, A., Pigozzo, C., Ferreira, E. G. M., Chandrachani Devi, N., Bengaly, Jr., C. A. P., Campista, M., Amorim, A., Asari, N. V., Bongiovanni, A., Bonoli, S., Bruzual, G., Cardiel, N., Cava, A., Cid Fernandes, R., Coelho, P., Cortesi, A., Delgado, R. G., Diaz Garcia, L., Espinosa, J. M. R., Galliano, E., Gonzalez-Serrano, J. I., Falcon-Barroso, J., Fritz, J., Fernandes, C., Gorgas, J., Hoyos, C., Jimenez-Teja, Y., Lopez-Aguerri, J. A., Lopez-San Juan, C., Mateus, A., Molino, A., Novais, P., OMill, A., Oteo, I., Perez-Gonzalez, P. G., Poggianti, B., Proctor, R., Ricciardelli, E., Sanchez-Blazquez, P., Storchi-Bergmann, T., Telles, E., Schoenell, W., Trujillo, N., Vazdekis, A., Viironen, K., Daflon, S., Aparicio-Villegas, T., Rocha, D., Ribeiro, T., Borges, M., Martins, S. L., Marcolino, W., Martinez-Delgado, D., Perez-Torres, M. A., Siffert, B. B., Calvao, M. O., Sako, M., Kessler, R., Alvarez-Candal, A., De Pra, M., Roig, F., Lazzaro, D., Gorosabel, J., Lopes de Oliveira, R., Lima-Neto, G. B., Irwin, J., Liu, J. F., Alvarez, E., Balmes, I., Chueca, S., Costa-Duarte, M. V., da Costa, A. A., Dantas, M. L. L., Diaz, A. Y., Fabregat, J., Ferrari, F., Gavela, B., Gracia, S. G., Gruel, N., Gutierrez, J. L. L., Guzman, R., Hernandez-Fernandez, J. D., Herranz, D., Hurtado-Gil, L., Jablonsky, F., Laporte, R., Le Tiran, L. L., Licandro, J., Lima, M., Martin, E., Martinez, V., Montero, J. J. C., Penteado, P., Pereira, C. B., Peris, V., Quilis, V., Sanchez-Portal, M., Soja, A. C., Solano, E., Torra, J., and Valdivielso, L. (2014). J-PAS: The Javalambre-Physics of the Accelerated Universe Astrophysical Survey. *ArXiv e-prints*.
- Bennett, C. L., Larson, D., Weiland, J. L., Jarosik, N., Hinshaw, G., Odegard, N., Smith, K. M., Hill, R. S., Gold, B., Halpern, M., Komatsu, E., Nolte, M. R., Page, L., Spergel, D. N., Wollack, E., Dunkley, J., Kogut, A., Limon, M., Meyer, S. S., Tucker, G. S., and Wright, E. L. (2013). Nine-year Wilkinson Microwave Anisotropy Probe (WMAP) Observations: Final Maps and Results. *ApJS*, 208(2):20.
- Benson, A. J. (2012). GALACTICUS: A semi-analytic model of galaxy formation. *New A*, 17:175–197.
- Benson, A. J., Ellis, R. S., and Menanteau, F. (2002). On the continuous formation of field spheroidal galaxies in hierarchical models of structure formation. *MNRAS*, 336:564–576.
- Berlind, A. A., Weinberg, D. H., Benson, A. J., Baugh, C. M., Cole, S., Davé, R., Frenk, C. S., Jenkins, A., Katz, N., and Lacey, C. G. (2003). The Halo Occupation Distribution and the Physics of Galaxy Formation. *ApJ*, 593(1):1–25.

- Bernardi, M., Renzini, A., da Costa, L. N., Wegner, G., Alonso, M. V., Pellegrini, P. S., Rité, C., and Willmer, C. N. A. (1998). Cluster versus Field Elliptical Galaxies and Clues on Their Formation. *ApJ*, 508(2):L143–L146.
- Bernardi, M., Sheth, R. K., Tundo, E., and Hyde, J. B. (2007). Selection Bias in the  $M_{\bullet}$ - $\sigma$  and  $M_{\bullet}$ - $L$  Correlations and Its Consequences. *ApJ*, 660(1):267–275.
- Berti, E., Cardoso, V., Gonzalez, J. A., Sperhake, U., Hannam, M., Husa, S., and Brügmann, B. (2007). Inspiral, merger, and ringdown of unequal mass black hole binaries: A multipolar analysis. *Phys. Rev. D*, 76(6):064034.
- Berti, E. and Volonteri, M. (2008). Cosmological Black Hole Spin Evolution by Mergers and Accretion. *ApJ*, 684:822–828.
- Bertola, F. and Capaccioli, M. (1975). Dynamics of early type galaxies. I. The rotation curve of the elliptical galaxy NGC 4697. *ApJ*, 200:439–445.
- Biava, N., Colpi, M., Capelo, P. R., Bonetti, M., Volonteri, M., Tamfal, T., Mayer, L., and Sesana, A. (2019). The lifetime of binary black holes in Sérsic galaxy models. *MNRAS*, 487(4):4985–4994.
- Binney, J. and Tabor, G. (1995). Evolving cooling flows. *MNRAS*, 276:663–678.
- Binney, J. and Tremaine, S. (1987). *Galactic dynamics*.
- Birnboim, Y. and Dekel, A. (2003). Virial shocks in galactic haloes? *MNRAS*, 345:349–364.
- Bîrzan, L., Rafferty, D. A., McNamara, B. R., Wise, M. W., and Nulsen, P. E. J. (2004). A Systematic Study of Radio-induced X-Ray Cavities in Clusters, Groups, and Galaxies. *ApJ*, 607:800–809.
- Bischetti, M., Piconcelli, E., Vietri, G., Bongiorno, A., Fiore, F., Sani, E., Marconi, A., Duras, F., Zappacosta, L., Brusa, M., Comastri, A., Cresci, G., Feruglio, C., Giallongo, E., La Franca, F., Mainieri, V., Mannucci, F., Martocchia, S., Ricci, F., Schneider, R., Testa, V., and Vignali, C. (2017). The WISSH quasars project. I. Powerful ionised outflows in hyper-luminous quasars. *A&A*, 598:A122.
- Blaña Díaz, M., Gerhard, O., Wegg, C., Portail, M., Opitsch, M., Saglia, R., Fabricius, M., Erwin, P., and Bender, R. (2018). Sculpting Andromeda - made-to-measure models for M31’s bar and composite bulge: dynamics, stellar and dark matter mass. *MNRAS*, 481:3210–3243.
- Blaizot, J., Wadadekar, Y., Guiderdoni, B., Colombi, S. T., Bertin, E., Bouchet, F. R., Devriendt, J. E. G., and Hatton, S. (2005). MoMaF: the Mock Map Facility. *MNRAS*, 360:159–175.
- Blandford, R. D. and Znajek, R. L. (1977). Electromagnetic extraction of energy from Kerr black holes. *MNRAS*, 179:433–456.
- Blázquez-Calero, G., Florido, E., Pérez, I., Zurita, A., Grand, R. J. J., Fragkoudi, F., Gómez, F. A., Marinacci, F., and Pakmor, R. (2020). Structural and photometric properties of barred galaxies from the Auriga cosmological simulations. *MNRAS*, 491(2):1800–1819.
- Blecha, L., Cox, T. J., Loeb, A., and Hernquist, L. (2011). Recoiling black holes in merging galaxies: relationship to active galactic nucleus lifetimes, starbursts and the  $M_{BH}$ - $\sigma_*$  relation. *MNRAS*, 412(4):2154–2182.
- Blecha, L. and Loeb, A. (2008a). Effects of gravitational-wave recoil on the dynamics and growth of supermassive black holes. *MNRAS*, 390(4):1311–1325.
- Blecha, L. and Loeb, A. (2008b). Effects of gravitational-wave recoil on the dynamics and growth of supermassive black holes. *MNRAS*, 390:1311–1325.

- Blumenthal, G. R., Faber, S. M., Primack, J. R., and Rees, M. J. (1984). Formation of galaxies and large-scale structure with cold dark matter. *Nature*, 311:517–525.
- Bode, T., Bogdanović, T., Haas, R., Healy, J., Laguna, P., and Shoemaker, D. (2012). Mergers of Supermassive Black Holes in Astrophysical Environments. *ApJ*, 744(1):45.
- Bogdanović, T., Bode, T., Haas, R., Laguna, P., and Shoemaker, D. (2011). Properties of accretion flows around coalescing supermassive black holes. *Classical and Quantum Gravity*, 28(9):094020.
- Bogdanović, T., Reynolds, C. S., and Miller, M. C. (2007). Alignment of the Spins of Supermassive Black Holes Prior to Coalescence. *ApJ*, 661:L147–L150.
- Bolton, J. G. and Ekers, J. (1966a). Further identifications of radio sources between declinations 0 and 20. *Australian Journal of Physics*, 19:471.
- Bolton, J. G. and Ekers, J. (1966b). Identification of strong extragalactic radio sources in the declination zone 0 to -20. *Australian Journal of Physics*, 19:559.
- Bond, J. R. (1984). *Massive Objects and the First Stars*, volume 109 of *Astrophysics and Space Science Library*, page 297.
- Bond, J. R., Cole, S., Efstathiou, G., and Kaiser, N. (1991). Excursion Set Mass Functions for Hierarchical Gaussian Fluctuations. *ApJ*, 379:440.
- Bonetti, M., Haardt, F., Sesana, A., and Barausse, E. (2018a). Post-Newtonian evolution of massive black hole triplets in galactic nuclei - II. Survey of the parameter space. *MNRAS*, 477:3910–3926.
- Bonetti, M., Sesana, A., Haardt, F., Barausse, E., and Colpi, M. (2018b). Post-Newtonian Evolution of Massive Black Hole Triplets in Galactic Nuclei: IV. Implications for LISA. *arXiv e-prints*.
- Bonoli, S., Marín-Franch, A., Varela, J., Vázquez Ramió, H., Abramo, L. R., Cenarro, A. J., Dupke, R. A., Vílchez, J. M., Cristóbal-Hornillos, D., González Delgado, R. M., Hernández-Monteagudo, C., López-Sanjuan, C., Muniesa, D. J., Civera, T., Ederoclite, A., Hernán-Caballero, A., Marra, V., Baqui, P. O., Cortesi, A., Cypriano, E. S., Daflon, S., de Amorim, A. L., Díaz-García, L. A., Diego, J. M., Martínez-Solaache, G., Pérez, E., Placco, V. M., Prada, F., and Queiroz, C. (2020). The miniJPAS survey: a preview of the Universe in 56 colours. *arXiv e-prints*, page arXiv:2007.01910.
- Bonoli, S., Marulli, F., Springel, V., White, S. D. M., Branchini, E., and Moscardini, L. (2009). Modelling the cosmological co-evolution of supermassive black holes and galaxies - II. The clustering of quasars and their dark environment. *MNRAS*, 396:423–438.
- Bonoli, S., Mayer, L., and Callegari, S. (2014). Massive black hole seeds born via direct gas collapse in galaxy mergers: their properties, statistics and environment. *MNRAS*, 437:1576–1592.
- Bonoli, S., Mayer, L., Kazantzidis, S., Madau, P., Bellovary, J., and Governato, F. (2016). Black hole starvation and bulge evolution in a Milky Way-like galaxy. *MNRAS*, 459:2603–2617.
- Bournaud, F. and Combes, F. (2002). Gas accretion on spiral galaxies: Bar formation and renewal. *A&A*, 392:83–102.
- Bournaud, F., Jog, C. J., and Combes, F. (2005). Galaxy mergers with various mass ratios: Properties of remnants. *A&A*, 437:69–85.
- Bower, R. G. (1991). The evolution of groups of galaxies in the Press-Schechter formalism. *MNRAS*, 248:332–352.
- Bower, R. G., Benson, A. J., Malbon, R., Helly, J. C., Frenk, C. S., Baugh, C. M., Cole, S., and Lacey, C. G. (2006). Breaking the hierarchy of galaxy formation. *MNRAS*, 370:645–655.

- Bowler, R. A. A., McLure, R. J., Dunlop, J. S., McLeod, D. J., Stanway, E. R., Eldridge, J. J., and Jarvis, M. J. (2017). No evidence for Population III stars or a Direct Collapse Black Hole in the  $z = 6.6$  Lyman- $\alpha$  emitter 'CR7'. *MNRAS*, 469(1):448–458.
- Boylan-Kolchin, M., Ma, C.-P., and Quataert, E. (2005). Dissipationless mergers of elliptical galaxies and the evolution of the fundamental plane. *MNRAS*, 362(1):184–196.
- Boylan-Kolchin, M., Ma, C.-P., and Quataert, E. (2006). Red mergers and the assembly of massive elliptical galaxies: the fundamental plane and its projections. *MNRAS*, 369(3):1081–1089.
- Boylan-Kolchin, M., Springel, V., White, S. D. M., Jenkins, A., and Lemson, G. (2009). Resolving cosmic structure formation with the Millennium-II Simulation. *MNRAS*, 398:1150–1164.
- Boyle, B. J., Shanks, T., and Peterson, B. A. (1988). The evolution of optically selected QSOs - II. *MNRAS*, 235:935–948.
- Brenneman, L. (2013). *Measuring the Angular Momentum of Supermassive Black Holes*.
- Brenneman, L. W. and Reynolds, C. S. (2006). Constraining Black Hole Spin via X-Ray Spectroscopy. *ApJ*, 652(2):1028–1043.
- Brenneman, L. W., Reynolds, C. S., Nowak, M. A., Reis, R. C., Trippe, M., Fabian, A. C., Iwasawa, K., Lee, J. C., Miller, J. M., Mushotzky, R. F., Nandra, K., and Volonteri, M. (2011). The Spin of the Supermassive Black Hole in NGC 3783. *ApJ*, 736(2):103.
- Brinchmann, J., Charlot, S., White, S. D. M., Tremonti, C., Kauffmann, G., Heckman, T., and Brinkmann, J. (2004). The physical properties of star-forming galaxies in the low-redshift Universe. *MNRAS*, 351:1151–1179.
- Bromm, V. (2013). Formation of the first stars. *Reports on Progress in Physics*, 76(11):112901.
- Bromm, V. and Larson, R. B. (2004). The First Stars. *ARA&A*, 42(1):79–118.
- Brook, C. B., Kawata, D., Gibson, B. K., and Flynn, C. (2004). Stellar halo constraints on simulated late-type galaxies. *MNRAS*, 349:52–56.
- Brook, C. B., Stinson, G. S., Gibson, B. K., Kawata, D., House, E. L., Miranda, M. S., Macciò, A. V., Pilkington, K., Roškar, R., Wadsley, J., and Quinn, T. R. (2012). Thin disc, thick disc and halo in a simulated galaxy. *MNRAS*, 426:690–700.
- Brooks, A. M., Solomon, A. R., Governato, F., McCleary, J., MacArthur, L. A., Brook, C. B. A., Jonsson, P., Quinn, T. R., and Wadsley, J. (2011). Interpreting the Evolution of the Size-Luminosity Relation for Disk Galaxies from Redshift 1 to the Present. *ApJ*, 728(1):51.
- Brown, M. J. I., Dey, A., Jannuzi, B. T., Brand, K., Benson, A. J., Brodwin, M., Croton, D. J., and Eisenhardt, P. R. (2007). The Evolving Luminosity Function of Red Galaxies. *ApJ*, 654(2):858–877.
- Bruzual, G. and Charlot, S. (2003). Stellar population synthesis at the resolution of 2003. *MNRAS*, 344:1000–1028.
- Bruzual A., G. (1983). Spectral evolution of galaxies. I. Early-type systems. *ApJ*, 273:105–127.
- Buchner, J., Georgakakis, A., Nandra, K., Brightman, M., Menzel, M.-L., Liu, Z., Hsu, L.-T., Salvato, M., Rangel, C., Aird, J., Merloni, A., and Ross, N. (2015). Obscuration-dependent Evolution of Active Galactic Nuclei. *ApJ*, 802(2):89.
- Bullock, J. S., Dekel, A., Kolatt, T. S., Kravtsov, A. V., Klypin, A. A., Porciani, C., and Primack, J. R. (2001). A Universal Angular Momentum Profile for Galactic Halos. *ApJ*, 555(1):240–257.



- Buonanno, A., Chen, Y., and Damour, T. (2006). Transition from inspiral to plunge in precessing binaries of spinning black holes. *Phys. Rev. D*, 74(10):104005.
- Bureau, M. and Athanassoula, E. (2005). Bar Diagnostics in Edge-On Spiral Galaxies. III. N-Body Simulations of Disks. *ApJ*, 626(1):159–173.
- Bureau, M. and Freeman, K. C. (1999). The Nature of Boxy/Peanut-Shaped Bulges in Spiral Galaxies. *AJ*, 118:126–138.
- Bustamante, S. and Springel, V. (2019). Spin evolution and feedback of supermassive black holes in cosmological simulations. *MNRAS*, 490(3):4133–4153.
- Callegari, S., Kazantzidis, S., Mayer, L., Colpi, M., Bellovary, J. M., Quinn, T., and Wadsley, J. (2011a). Growing Massive Black Hole Pairs in Minor Mergers of Disk Galaxies. *ApJ*, 729:85.
- Callegari, S., Kazantzidis, S., Mayer, L., Colpi, M., Bellovary, J. M., Quinn, T., and Wadsley, J. (2011b). Growing Massive Black Hole Pairs in Minor Mergers of Disk Galaxies. *ApJ*, 729:85.
- Campanelli, M. (2005). Understanding the fate of merging supermassive black holes. *Classical and Quantum Gravity*, 22(10):S387–S393.
- Campanelli, M., Lousto, C., Zlochower, Y., and Merritt, D. (2007). Large Merger Recoils and Spin Flips from Generic Black Hole Binaries. *ApJ*, 659(1):L5–L8.
- Campanelli, M., Lousto, C. O., and Zlochower, Y. (2006). Last orbit of binary black holes. *Phys. Rev. D*, 73(6):061501.
- Cano-Díaz, M., Sánchez, S. F., Zibetti, S., Ascasibar, Y., Bland-Hawthorn, J., Ziegler, B., González Delgado, R. M., Walcher, C. J., García-Benito, R., Mast, D., Mendoza-Pérez, M. A., Falcón-Barroso, J., Galbany, L., Husemann, B., Kehrig, C., Marino, R. A., Sánchez-Blázquez, P., López-Cobá, C., López-Sánchez, Á. R., and Vilchez, J. M. (2016). Spatially Resolved Star Formation Main Sequence of Galaxies in the CALIFA Survey. *ApJ*, 821:L26.
- Capak, P., Aussel, H., Ajiki, M., McCracken, H. J., Mobasher, B., Scoville, N., Shopbell, P., Taniguchi, Y., Thompson, D., Tribiano, S., Sasaki, S., Blain, A. W., Brusa, M., Carilli, C., Comastri, A., Carollo, C. M., Cassata, P., Colbert, J., Ellis, R. S., Elvis, M., Giavalisco, M., Green, W., Guzzo, L., Hasinger, G., Ilbert, O., Impey, C., Jahnke, K., Kartaltepe, J., Kneib, J.-P., Koda, J., Koekemoer, A., Komiyama, Y., Leauthaud, A., Le Fevre, O., Lilly, S., Liu, C., Massey, R., Miyazaki, S., Murayama, T., Nagao, T., Peacock, J. A., Pickles, A., Porciani, C., Renzini, A., Rhodes, J., Rich, M., Salvato, M., Sanders, D. B., Scarlata, C., Schiminovich, D., Schinnerer, E., Scodreggio, M., Sheth, K., Shioya, Y., Tasca, L. A. M., Taylor, J. E., Yan, L., and Zamorani, G. (2007). The First Release COSMOS Optical and Near-IR Data and Catalog. *ApJS*, 172:99–116.
- Capak, P., Cowie, L. L., Hu, E. M., Barger, A. J., Dickinson, M., Fernandez, E., Giavalisco, M., Komiyama, Y., Kretchmer, C., McNally, C., Miyazaki, S., Okamura, S., and Stern, D. (2004). A Deep Wide-Field, Optical, and Near-Infrared Catalog of a Large Area around the Hubble Deep Field North. *AJ*, 127:180–198.
- Cappellari, M., Emsellem, E., Bacon, R., Bureau, M., Davies, R. L., de Zeeuw, P. T., Falcón-Barroso, J., Krajnović, D., Kuntschner, H., McDermid, R. M., Peletier, R. F., Sarzi, M., van den Bosch, R. C. E., and van de Ven, G. (2007). The SAURON project - X. The orbital anisotropy of elliptical and lenticular galaxies: revisiting the  $(V/\sigma, \epsilon)$  diagram with integral-field stellar kinematics. *MNRAS*, 379(2):418–444.
- Cappellari, M., Emsellem, E., Krajnović, D., McDermid, R. M., Scott, N., Verdoes Kleijn, G. A., Young, L. M., Alatalo, K., Bacon, R., Blitz, L., Bois, M., Bournaud, F., Bureau, M., Davies, R. L., Davis,

- T. A., de Zeeuw, P. T., Duc, P.-A., Khochfar, S., Kuntschner, H., Lablanche, P.-Y., Morganti, R., Naab, T., Oosterloo, T., Sarzi, M., Serra, P., and Weijmans, A.-M. (2011a). The ATLAS<sup>3D</sup> project - I. A volume-limited sample of 260 nearby early-type galaxies: science goals and selection criteria. *MNRAS*, 413(2):813–836.
- Cappellari, M., Emsellem, E., Krajnović, D., McDermid, R. M., Scott, N., Verdoes Kleijn, G. A., Young, L. M., Alatalo, K., Bacon, R., Blitz, L., Bois, M., Bournaud, F., Bureau, M., Davies, R. L., Davis, T. A., de Zeeuw, P. T., Duc, P.-A., Khochfar, S., Kuntschner, H., Lablanche, P.-Y., Morganti, R., Naab, T., Oosterloo, T., Sarzi, M., Serra, P., and Weijmans, A.-M. (2011b). The ATLAS<sup>3D</sup> project - I. A volume-limited sample of 260 nearby early-type galaxies: science goals and selection criteria. *MNRAS*, 413(2):813–836.
- Cardamone, C. N., van Dokkum, P. G., Urry, C. M., Taniguchi, Y., Gawiser, E., Brammer, G., Taylor, E., Damen, M., Treister, E., Cobb, B. E., Bond, N., Schawinski, K., Lira, P., Murayama, T., Saito, T., and Sumikawa, K. (2010). The Multiwavelength Survey by Yale-Chile (MUSYC): Deep Medium-band Optical Imaging and High-quality 32-band Photometric Redshifts in the ECDF-S. *ApJS*, 189(2):270–285.
- Cardelli, J. A., Clayton, G. C., and Mathis, J. S. (1989). The relationship between infrared, optical, and ultraviolet extinction. *ApJ*, 345:245–256.
- Carollo, C. M., Stiavelli, M., de Zeeuw, P. T., and Mack, J. (1997). Spiral Galaxies with WFPC2.I.Nuclear Morphology, Bulges, Star Clusters, and Surface Brightness Profiles. *AJ*, 114:2366.
- Carpinetti, A., Kaviraj, S., Darg, D., Lintott, C., Schawinski, K., and Shabala, S. (2012). Spheroidal post-mergers in the local Universe. *MNRAS*, 420:2139–2146.
- Cattaneo, A. (2001). Quasars and galaxy formation. *MNRAS*, 324(1):128–140.
- Cenarro, A. J., Moles, M., Cristóbal-Hornillos, D., Marín-Franch, A., Ederoclite, A., Varela, J., López-Sanjuan, C., Hernández-Monteagudo, C., Angulo, R. E., Vázquez Ramió, H., Viironen, K., Bonoli, S., Orsi, A. A., Hurier, G., San Roman, I., Greisel, N., Vilella-Rojo, G., Díaz-García, L. A., Logroño-García, R., Gurung-López, S., Spinoso, D., Izquierdo-Villalba, D., Aguerri, J. A. L., Allende Prieto, C., Bonatto, C., Carvano, J. M., Chies-Santos, A. L., Daflon, S., Dupke, R. A., Falcón-Barroso, J., Gonçalves, D. R., Jiménez-Teja, Y., Molino, A., Placco, V. M., Solano, E., Whitten, D. D., Abril, J., Antón, J. L., Bello, R., Bielsa de Toledo, S., Castillo-Ramírez, J., Chueca, S., Civera, T., Díaz-Martín, M. C., Domínguez-Martínez, M., Garzarán-Calderaro, J., Hernández-Fuertes, J., Iglesias-Marzoa, R., Iñiguez, C., Jiménez Ruiz, J. M., Kruuse, K., Lamadrid, J. L., Lasso-Cabrera, N., López-Alegre, G., López-Sainz, A., Maícas, N., Moreno-Signes, A., Muniesa, D. J., Rodríguez-Llano, S., Rueda-Teruel, F., Rueda-Teruel, S., Soriano-Laguía, I., Tilve, V., Valdivielso, L., Yanes-Díaz, A., Alcaniz, J. S., Mendes de Oliveira, C., Sodr , L., Coelho, P., Lopes de Oliveira, R., Tamm, A., Xavier, H. S., Abramo, L. R., Akras, S., Alfaro, E. J., Alvarez-Candal, A., Ascaso, B., Beasley, M. A., Beers, T. C., Borges Fernandes, M., Bruzual, G. R., Buzzo, M. L., Carrasco, J. M., Cepa, J., Cortesi, A., Costa-Duarte, M. V., De Pr , M., Favole, G., Galarza, A., Galbany, L., Garcia, K., Gonz lez Delgado, R. M., Gonz lez-Serrano, J. I., Guti rrez-Soto, L. A., Hernandez-Jimenez, J. A., Kanaan, A., Kuncarayakti, H., Landim, R. C. G., Laur, J., Licandro, J., Lima Neto, G. B., Lyman, J. D., Ma z Apell niz, J., Miralda-Escud , J., Morate, D., Nogueira-Cavalcante, J. P., Novais, P. M., Oncins, M., Oteo, I., Overzier, R. A., Pereira, C. B., Rebassa-Mansergas, A., Reis, R. R. R., Roig, F., Sako, M., Salvador-Rusi ol, N., Sampedro, L., S nchez-Bl zquez, P., Santos, W. A., Schmidtobreick, L., Siffert, B. B., Telles, E., and Vilchez, J. M. (2019). J-PLUS: The Javalambre Photometric Local Universe Survey. *A&A*, 622:A176.
- Cervantes Sodi, B., Li, C., and Park, C. (2015). Dark Matter Halos of Barred Disk Galaxies. *ApJ*, 807:111.

- Chabrier, G. (2003). Galactic Stellar and Substellar Initial Mass Function. *PASP*, 115(809):763–795.
- Chandrasekhar, S. (1943). Dynamical Friction. I. General Considerations: the Coefficient of Dynamical Friction. *ApJ*, 97:255.
- Chaves-Montero, J., Bonoli, S., Salvato, M., Greisel, N., Díaz-García, L. A., López-Sanjuan, C., Viironen, K., Fernández-Soto, A., Pović, M., Ascaso, B., Arnalte-Mur, P., Masegosa, J., Matute, I., Márquez, I., Cenarro, A. J., Abramo, L. R., Ederoclite, A., Alfaro, E. J., Marin-Franch, A., Varela, J., and Cristobal-Hornillos, D. (2017). ELDAR, a new method to identify AGN in multi-filter surveys: the ALHAMBRA test case. *MNRAS*, 472(2):2085–2106.
- Chiaberge, M., Ely, J. C., Meyer, E. T., Georganopoulos, M., Marinucci, A., Bianchi, S., Tremblay, G. R., Hilbert, B., Kotyla, J. P., Capetti, A., Baum, S. A., Macchetto, F. D., Miley, G., O’Dea, C. P., Perlman, E. S., Sparks, W. B., and Norman, C. (2017). The puzzling case of the radio-loud QSO 3C 186: a gravitational wave recoiling black hole in a young radio source? *A&A*, 600:A57.
- Chiaberge, M., Gilli, R., Lotz, J. M., and Norman, C. (2015). Radio Loud AGNs are Mergers. *ApJ*, 806(2):147.
- Choksi, N., Behroozi, P., Volonteri, M., Schneider, R., Ma, C.-P., Silk, J., and Moster, B. (2017). Recoiling supermassive black hole escape velocities from dark matter haloes. *MNRAS*, 472(2):1526–1537.
- Churazov, E., Sunyaev, R., Forman, W., and Böhringer, H. (2002). Cooling flows as a calorimeter of active galactic nucleus mechanical power. *MNRAS*, 332(3):729–734.
- Ciardullo, R., Gronwall, C., Adams, J. J., Blanc, G. A., Gebhardt, K., Finkelstein, S. L., Jogee, S., Hill, G. J., Drory, N., Hopp, U., Schneider, D. P., Zeimann, G. R., and Dalton, G. B. (2013). The HETDEX Pilot Survey. IV. The Evolution of [O II] Emitting Galaxies from  $z \sim 0.5$  to  $z \sim 0$ . *ApJ*, 769:83.
- Cirasuolo, M., Magliocchetti, M., and Celotti, A. (2005). Faint radio-loud quasars: clues to their evolution. *MNRAS*, 357(4):1267–1280.
- Cisternas, M., Jahnke, K., Inskip, K. J., Kartaltepe, J., Koekemoer, A. M., Lisker, T., Robaina, A. R., Scodreggio, M., Sheth, K., Trump, J. R., Andrae, R., Miyaji, T., Lusso, E., Brusa, M., Capak, P., Cappelluti, N., Civano, F., Ilbert, O., Impey, C. D., Leauthaud, A., Lilly, S. J., Salvato, M., Scoville, N. Z., and Taniguchi, Y. (2011). The Bulk of the Black Hole Growth Since  $z \sim 1$  Occurs in a Secular Universe: No Major Merger-AGN Connection. *ApJ*, 726(2):57.
- Civano, F., Elvis, M., Lanzuisi, G., Aldcroft, T., Trichas, M., Bongiorno, A., Brusa, M., Blecha, L., Comastri, A., Loeb, A., Salvato, M., Fruscione, A., Koekemoer, A., Komossa, S., Gilli, R., Mainieri, V., Piconcelli, E., and Vignali, C. (2012). Chandra High-resolution observations of CID-42, a Candidate Recoiling Supermassive Black Hole. *ApJ*, 752(1):49.
- Cole, S., Lacey, C. G., Baugh, C. M., and Frenk, C. S. (2000). Hierarchical galaxy formation. *MNRAS*, 319(1):168–204.
- Colless, M., Dalton, G., Maddox, S., Sutherland, W., Norberg, P., Cole, S., Bland-Hawthorn, J., Bridges, T., Cannon, R., Collins, C., Couch, W., Cross, N., Deeley, K., De Propriis, R., Driver, S. P., Efstathiou, G., Ellis, R. S., Frenk, C. S., Glazebrook, K., Jackson, C., Lahav, O., Lewis, I., Lumsden, S., Madgwick, D., Peacock, J. A., Peterson, B. A., Price, I., Seaborne, M., and Taylor, K. (2001). The 2dF Galaxy Redshift Survey: spectra and redshifts. *MNRAS*, 328:1039–1063.
- Colpi, M. (2014). Massive Binary Black Holes in Galactic Nuclei and Their Path to Coalescence. *Space Sci. Rev.*, 183:189–221.

- Combes, F. (2009). Secular Evolution and the Assembly of Bulges. In Jogee, S., Marinova, I., Hao, L., and Blanc, G. A., editors, *Galaxy Evolution: Emerging Insights and Future Challenges*, volume 419 of *Astronomical Society of the Pacific Conference Series*, page 31.
- Combes, F., Debbasch, F., Friedli, D., and Pfenniger, D. (1990a). Box and peanut shapes generated by stellar bars. *A&A*, 233:82.
- Combes, F., Debbasch, F., Friedli, D., and Pfenniger, D. (1990b). Box and peanut shapes generated by stellar bars. *A&A*, 233:82–95.
- Combes, F. and Sanders, R. H. (1981a). Formation and properties of persisting stellar bars. *A&A*, 96:164–173.
- Combes, F. and Sanders, R. H. (1981b). Formation and properties of persisting stellar bars. *A&A*, 96:164–173.
- Comparat, J., Merloni, A., Salvato, M., Nandra, K., Boller, T., Georgakakis, A., Finoguenov, A., Dwelly, T., Buchner, J., Del Moro, A., Clerc, N., Wang, Y., Zhao, G., Prada, F., Yepes, G., Brusa, M., and Krumpke, M. (2019). Active Galactic Nuclei and their Large-scale Structure: an eROSITA mock catalogue. *arXiv e-prints*.
- Comparat, J., Zhu, G., Gonzalez-Perez, V., Norberg, P., Newman, J., Tresse, L., Richard, J., Yepes, G., Kneib, J.-P., Raichoor, A., Prada, F., Maraston, C., Yèche, C., Delubac, T., and Jullo, E. (2016). The evolution of the [O II], H  $\beta$  and [O III] emission line luminosity functions over the last nine billions years. *MNRAS*, 461:1076–1087.
- Connors, P. A., Piran, T., and Stark, R. F. (1980). Polarization features of X-ray radiation emitted near black holes. *ApJ*, 235:224–244.
- Conselice, C. J. (2006). The fundamental properties of galaxies and a new galaxy classification system. *MNRAS*, 373:1389–1408.
- Contreras, S., Zehavi, I., Baugh, C. M., Padilla, N., and Norberg, P. (2017). The evolution of the galaxy content of dark matter haloes. *MNRAS*, 465(3):2833–2848.
- Cooper, M. C., Gallazzi, A., Newman, J. A., and Yan, R. (2010). Galaxy assembly bias on the red sequence. *MNRAS*, 402(3):1942–1958.
- Cora, S. A., Vega-Martínez, C. A., Hough, T., Ruiz, A. N., Orsi, Á. A., Muñoz Arancibia, A. M., Gargiulo, I. D., Collacchioni, F., Padilla, N. D., Gottlöber, S., and Yepes, G. (2018). Semi-analytic galaxies - I. Synthesis of environmental and star-forming regulation mechanisms. *MNRAS*, 479(1):2–24.
- Correa, C. A., Schaye, J., and Trayford, J. W. (2019). The origin of the red-sequence galaxy population in the EAGLE simulation. *MNRAS*, 484(4):4401–4412.
- Côté, P., Marzke, R. O., and West, M. J. (1998). The Formation of Giant Elliptical Galaxies and Their Globular Cluster Systems. *ApJ*, 501:554–570.
- Couchman, H. M. P. and Rees, M. J. (1986). Pregalactic evolution in cosmologies with cold dark matter. *MNRAS*, 221:53–62.
- Covington, M., Dekel, A., Cox, T. J., Jonsson, P., and Primack, J. R. (2008). Predicting the properties of the remnants of dissipative galaxy mergers. *MNRAS*, 384(1):94–106.
- Covington, M. D., Primack, J. R., Porter, L. A., Croton, D. J., Somerville, R. S., and Dekel, A. (2011). The role of dissipation in the scaling relations of cosmological merger remnants. *MNRAS*, 415:3135–3152.

- Cowie, L. L. and Binney, J. (1977). Radiative regulation of gas flow within clusters of galaxies: a model for cluster X-ray sources. *ApJ*, 215:723–732.
- Cox, T. J., Dutta, S. N., Di Matteo, T., Hernquist, L., Hopkins, P. F., Robertson, B., and Springel, V. (2006). The Kinematic Structure of Merger Remnants. *ApJ*, 650(2):791–811.
- Cresci, G., Mainieri, V., Brusa, M., Marconi, A., Perna, M., Mannucci, F., Piconcelli, E., Maiolino, R., Feruglio, C., Fiore, F., Bongiorno, A., Lanzuisi, G., Merloni, A., Schramm, M., Silverman, J. D., and Civano, F. (2015). Blowing in the Wind: Both “Negative” and “Positive” Feedback in an Obscured High-z Quasar. *ApJ*, 799(1):82.
- Croton, D. J. (2006). Evolution in the black hole mass-bulge mass relation: a theoretical perspective. *MNRAS*, 369:1808–1812.
- Croton, D. J., Stevens, A. R. H., Tonini, C., Garel, T., Bernyk, M., Bibiano, A., Hodkinson, L., Mutch, S. J., Poole, G. B., and Shattow, G. M. (2016). Semi-Analytic Galaxy Evolution (SAGE): Model Calibration and Basic Results. *ApJS*, 222(2):22.
- Cuadra, J., Armitage, P. J., Alexander, R. D., and Begelman, M. C. (2009). Massive black hole binary mergers within subparsec scale gas discs. *MNRAS*, 393(4):1423–1432.
- Dalgarno, A. and McCray, R. A. (1972). Heating and Ionization of HI Regions. *ARA&A*, 10:375.
- Dark Energy Survey Collaboration, Abbott, T., Abdalla, F. B., Aleksić, J., Allam, S., Amara, A., Bacon, D., Balbinot, E., Banerji, M., Bechtol, K., Benoit-Lévy, A., Bernstein, G. M., Bertin, E., Blazek, J., Bonnett, C., Bridle, S., Brooks, D., Brunner, R. J., Buckley-Geer, E., Burke, D. L., Caminha, G. B., Capozzi, D., Carlsen, J., Carnero-Rosell, A., Carollo, M., Carrasco-Kind, M., Carretero, J., Castander, F. J., Clerkin, L., Collett, T., Conselice, C., Croce, M., Cunha, C. E., D’Andrea, C. B., da Costa, L. N., Davis, T. M., Desai, S., Diehl, H. T., Dietrich, J. P., Dodelson, S., Doel, P., Drlica-Wagner, A., Estrada, J., Etherington, J., Evrard, A. E., Fabbri, J., Finley, D. A., Flaughner, B., Foley, R. J., Fosalba, P., Frieman, J., García-Bellido, J., Gaztanaga, E., Gerdes, D. W., Giannantonio, T., Goldstein, D. A., Gruen, D., Gruendl, R. A., Guarnieri, P., Gutierrez, G., Hartley, W., Honscheid, K., Jain, B., James, D. J., Jeltema, T., Jouvel, S., Kessler, R., King, A., Kirk, D., Kron, R., Kuehn, K., Kuropatkin, N., Lahav, O., Li, T. S., Lima, M., Lin, H., Maia, M. A. G., Makler, M., Manera, M., Maraston, C., Marshall, J. L., Martini, P., McMahon, R. G., Melchior, P., Merson, A., Miller, C. J., Miquel, R., Mohr, J. J., Morice-Atkinson, X., Naidoo, K., Neilsen, E., Nichol, R. C., Nord, B., Ogando, R., Ostrovski, F., Palmese, A., Papadopoulos, A., Peiris, H. V., Peoples, J., Percival, W. J., Plazas, A. A., Reed, S. L., Refregier, A., Romer, A. K., Roodman, A., Ross, A., Roza, E., Rykoff, E. S., Sadeh, I., Sako, M., Sánchez, C., Sanchez, E., Santiago, B., Scarpine, V., Schubnell, M., Sevilla-Noarbe, I., Sheldon, E., Smith, M., Smith, R. C., Soares-Santos, M., Sobreira, F., Soumagnac, M., Suchyta, E., Sullivan, M., Swanson, M., Tarle, G., Thaler, J., Thomas, D., Thomas, R. C., Tucker, D., Vieira, J. D., Vikram, V., Walker, A. R., Wechsler, R. H., Weller, J., Wester, W., Whiteway, L., Wilcox, H., Yanny, B., Zhang, Y., and Zuntz, J. (2016). The Dark Energy Survey: more than dark energy - an overview. *MNRAS*, 460:1270–1299.
- Dasyra, K. M., Tacconi, L. J., Davies, R. I., Genzel, R., Lutz, D., Naab, T., Burkert, A., Veilleux, S., and Sanders, D. B. (2006). Dynamical Properties of Ultraluminous Infrared Galaxies. I. Mass Ratio Conditions for ULIRG Activity in Interacting Pairs. *ApJ*, 638:745–758.
- Dasyra, K. M., Tacconi, L. J., Davies, R. I., Genzel, R., Lutz, D., Peterson, B. M., Veilleux, S., Baker, A. J., Schweitzer, M., and Sturm, E. (2007). Host Dynamics and Origin of Palomar-Green QSOs. *ApJ*, 657:102–115.
- Davé, R., Anglés-Alcázar, D., Narayanan, D., Li, Q., Rafieferantsoa, M. H., and Appleby, S. (2019). SIMBA: Cosmological simulations with black hole growth and feedback. *MNRAS*, 486(2):2827–2849.

- Davidzon, I., Cucciati, O., Bolzonella, M., De Lucia, G., Zamorani, G., Arnouts, S., Moutard, T., Ilbert, O., Garilli, B., Scodeggio, M., Guzzo, L., Abbas, U., Adami, C., Bel, J., Bottini, D., Branchini, E., Cappi, A., Coupon, J., de la Torre, S., Di Porto, C., Fritz, A., Franzetti, P., Fumana, M., Granett, B. R., Guennou, L., Iovino, A., Krywult, J., Le Brun, V., Le Fèvre, O., Maccagni, D., Małek, K., Marulli, F., McCracken, H. J., Mellier, Y., Moscardini, L., Polletta, M., Pollo, A., Tasca, L. A. M., Tojeiro, R., Vergani, D., and Zanichelli, A. (2016). The VIMOS Public Extragalactic Redshift Survey (VIPERS). Environmental effects shaping the galaxy stellar mass function. *A&A*, 586:A23.
- Davies, J. J., Crain, R. A., Oppenheimer, B. D., and Schaye, J. (2020). The quenching and morphological evolution of central galaxies is facilitated by the feedback-driven expulsion of circumgalactic gas. *MNRAS*, 491(3):4462–4480.
- Davies, R. L., Efstathiou, G., Fall, S. M., Illingworth, G., and Schechter, P. L. (1983). The kinematic properties of faint elliptical galaxies. *ApJ*, 266:41–57.
- Davis, M., Efstathiou, G., Frenk, C. S., and White, S. D. M. (1985). The evolution of large-scale structure in a universe dominated by cold dark matter. *ApJ*, 292:371–394.
- Dawson, K. S., Kneib, J.-P., Percival, W. J., Alam, S., Albareti, F. D., Anderson, S. F., Armengaud, E., Aubourg, É., Bailey, S., Bautista, J. E., Berlind, A. A., Bershady, M. A., Beutler, F., Bizyaev, D., Blanton, M. R., Blomqvist, M., Bolton, A. S., Bovy, J., Brandt, W. N., Brinkmann, J., Brownstein, J. R., Burtin, E., Busca, N. G., Cai, Z., Chuang, C.-H., Clerc, N., Comparat, J., Cope, F., Croft, R. A. C., Cruz-Gonzalez, I., da Costa, L. N., Cousinou, M.-C., Darling, J., de la Macorra, A., de la Torre, S., Delubac, T., du Mas des Bourboux, H., Dwelly, T., Ealet, A., Eisenstein, D. J., Eracleous, M., Escoffier, S., Fan, X., Finoguenov, A., Font-Ribera, A., Frinchaboy, P., Gaulme, P., Georgakakis, A., Green, P., Guo, H., Guy, J., Ho, S., Holder, D., Huehnerhoff, J., Hutchinson, T., Jing, Y., Jullo, E., Kamble, V., Kinemuchi, K., Kirkby, D., Kitaura, F.-S., Klaene, M. A., Laher, R. R., Lang, D., Laurent, P., Le Goff, J.-M., Li, C., Liang, Y., Lima, M., Lin, Q., Lin, W., Lin, Y.-T., Long, D. C., Lundgren, B., MacDonald, N., Geimba Maia, M. A., Malanushenko, E., Malanushenko, V., Mariappan, V., McBride, C. K., McGreer, I. D., Ménard, B., Merloni, A., Meza, A., Montero-Dorta, A. D., Muna, D., Myers, A. D., Nandra, K., Naugle, T., Newman, J. A., Noterdaeme, P., Nugent, P., Ogando, R., Olmstead, M. D., Oravetz, A., Oravetz, D. J., Padmanabhan, N., Palanque-Delabrouille, N., Pan, K., Parejko, J. K., Pâris, I., Peacock, J. A., Petitjean, P., Pieri, M. M., Pisani, A., Prada, F., Prakash, A., Raichoor, A., Reid, B., Rich, J., Ridl, J., Rodriguez-Torres, S., Carnero Rosell, A., Ross, A. J., Rossi, G., Ruan, J., Salvato, M., Sayres, C., Schneider, D. P., Schlegel, D. J., Seljak, U., Seo, H.-J., Sesar, B., Shandera, S., Shu, Y., Slosar, A., Sobreira, F., Streblyanska, A., Suzuki, N., Taylor, D., Tao, C., Tinker, J. L., Tojeiro, R., Vargas-Magaña, M., Wang, Y., Weaver, B. A., Weinberg, D. H., White, M., Wood-Vasey, W. M., Yeche, C., Zhai, Z., Zhao, C., Zhao, G.-b., Zheng, Z., Ben Zhu, G., and Zou, H. (2016). The SDSS-IV Extended Baryon Oscillation Spectroscopic Survey: Overview and Early Data. *AJ*, 151:44.
- Dawson, K. S., Schlegel, D. J., Ahn, C. P., Anderson, S. F., Aubourg, É., Bailey, S., Barkhouser, R. H., Bautista, J. E., Beifiori, A., Berlind, A. A., Bhardwaj, V., Bizyaev, D., Blake, C. H., Blanton, M. R., Blomqvist, M., Bolton, A. S., Borde, A., Bovy, J., Brandt, W. N., Brewington, H., Brinkmann, J., Brown, P. J., Brownstein, J. R., Bundy, K., Busca, N. G., Carithers, W., Carnero, A. R., Carr, M. A., Chen, Y., Comparat, J., Connolly, N., Cope, F., Croft, R. A. C., Cuesta, A. J., da Costa, L. N., Davenport, J. R. A., Delubac, T., de Putter, R., Dhital, S., Ealet, A., Ebelke, G. L., Eisenstein, D. J., Escoffier, S., Fan, X., Filiz Ak, N., Finley, H., Font-Ribera, A., Génova-Santos, R., Gunn, J. E., Guo, H., Haggard, D., Hall, P. B., Hamilton, J.-C., Harris, B., Harris, D. W., Ho, S., Hogg, D. W., Holder, D., Honscheid, K., Huehnerhoff, J., Jordan, B., Jordan, W. P., Kauffmann, G., Kazin, E. A., Kirkby, D., Klaene, M. A., Kneib, J.-P., Le Goff, J.-M., Lee, K.-G., Long, D. C., Loomis, C. P., Lundgren, B., Lupton, R. H., Maia, M. A. G., Makler, M., Malanushenko, E., Malanushenko, V., Mandelbaum, R., Manera, M., Maraston, C., Margala, D., Masters, K. L., McBride, C. K., McDonald, P., McGreer, I. D., McMahan, R. G., Mena, O., Miralda-Escudé, J., Montero-Dorta, A. D., Montesano, F., Muna,



- D., Myers, A. D., Naugle, T., Nichol, R. C., Noterdaeme, P., Nuza, S. E., Olmstead, M. D., Oravetz, A., Oravetz, D. J., Owen, R., Padmanabhan, N., Palanque-Delabrouille, N., Pan, K., Parejko, J. K., Pâris, I., Percival, W. J., Pérez-Fournon, I., Pérez-Ràfols, I., Petitjean, P., Pfaffenberger, R., Pforr, J., Pieri, M. M., Prada, F., Price-Whelan, A. M., Raddick, M. J., Rebolo, R., Rich, J., Richards, G. T., Rockosi, C. M., Roe, N. A., Ross, A. J., Ross, N. P., Rossi, G., Rubiño-Martín, J. A., Samushia, L., Sánchez, A. G., Sayres, C., Schmidt, S. J., Schneider, D. P., Scóccola, C. G., Seo, H.-J., Shelden, A., Sheldon, E., Shen, Y., Shu, Y., Slosar, A., Smee, S. A., Snedden, S. A., Stauffer, F., Steele, O., Strauss, M. A., Streblyanska, A., Suzuki, N., Swanson, M. E. C., Tal, T., Tanaka, M., Thomas, D., Tinker, J. L., Tojeiro, R., Tremonti, C. A., Vargas Magaña, M., Verde, L., Viel, M., Wake, D. A., Watson, M., Weaver, B. A., Weinberg, D. H., Weiner, B. J., West, A. A., White, M., Wood-Vasey, W. M., Yeche, C., Zehavi, I., Zhao, G.-B., and Zheng, Z. (2013). The Baryon Oscillation Spectroscopic Survey of SDSS-III. *AJ*, 145:10.
- de La Calle Pérez, I., Longinotti, A. L., Guainazzi, M., Bianchi, S., Dovčiak, M., Cappi, M., Matt, G., Miniutti, G., Petrucci, P. O., Piconcelli, E., Ponti, G., Porquet, D., and Santos-Lleó, M. (2010). FEROS: Finding extreme relativistic objects. I. Statistics of relativistic Fe  $K_{\alpha}$  lines in radio-quiet Type 1 AGN. *A&A*, 524:A50.
- De Lucia, G. and Blaizot, J. (2007). The hierarchical formation of the brightest cluster galaxies. *MNRAS*, 375:2–14.
- De Lucia, G., Kauffmann, G., and White, S. D. M. (2004). Chemical enrichment of the intracluster and intergalactic medium in a hierarchical galaxy formation model. *MNRAS*, 349:1101–1116.
- De Lucia, G., Springel, V., White, S. D. M., Croton, D., and Kauffmann, G. (2006). The formation history of elliptical galaxies. *MNRAS*, 366(2):499–509.
- de Vaucouleurs, G. (1974). Structure, Dynamics and Statistical Properties of Galaxies (invited Paper). In Shakeshaft, J. R., editor, *The Formation and Dynamics of Galaxies*, volume 58 of *IAU Symposium*, page 1.
- Debattista, V. P., Carollo, C. M., Mayer, L., and Moore, B. (2004). Bulges or Bars from Secular Evolution? *ApJ*, 604:L93–L96.
- Debattista, V. P., Carollo, C. M., Mayer, L., and Moore, B. (2005). The Kinematic Signature of Face-On Peanut-shaped Bulges. *ApJ*, 628(2):678–694.
- Debattista, V. P., Mayer, L., Carollo, C. M., Moore, B., Wadsley, J., and Quinn, T. (2006). The Secular Evolution of Disk Structural Parameters. *ApJ*, 645:209–227.
- Debattista, V. P. and Sellwood, J. A. (1998). Dynamical Friction and the Distribution of Dark Matter in Barred Galaxies. *ApJ*, 493(1):L5–L8.
- Debattista, V. P. and Sellwood, J. A. (2000). Constraints from Dynamical Friction on the Dark Matter Content of Barred Galaxies. *ApJ*, 543(2):704–721.
- Dekel, A., Sari, R., and Ceverino, D. (2009). Formation of Massive Galaxies at High Redshift: Cold Streams, Clumpy Disks, and Compact Spheroids. *ApJ*, 703:785–801.
- del Valle, L., Escala, A., Maureira-Fredes, C., Molina, J., Cuadra, J., and Amaro-Seoane, P. (2015). Supermassive Black Holes in a Star-forming Gaseous Circumnuclear Disk. *ApJ*, 811:59.
- Devecchi, B. and Volonteri, M. (2009). Formation of the First Nuclear Clusters and Massive Black Holes at High Redshift. *ApJ*, 694(1):302–313.

- Di Matteo, P., Gómez, A., Haywood, M., Combes, F., Lehnert, M. D., Ness, M., Snaith, O. N., Katz, D., and Semelin, B. (2015). Why the Milky Way's bulge is not only a bar formed from a cold thin disk. *A&A*, 577:A1.
- Di Matteo, T., Khandai, N., DeGraf, C., Feng, Y., Croft, R. A. C., Lopez, J., and Springel, V. (2012). Cold Flows and the First Quasars. *ApJ*, 745(2):L29.
- Di Matteo, T., Springel, V., and Hernquist, L. (2005). Energy input from quasars regulates the growth and activity of black holes and their host galaxies. *Nature*, 433:604–607.
- Diaferio, A., Kauffmann, G., Balogh, M. L., White, S. D. M., Schade, D., and Ellingson, E. (2001). The spatial and kinematic distributions of cluster galaxies in a  $\Lambda$ CDM universe: comparison with observations. *MNRAS*, 323(4):999–1015.
- Diaferio, A., Kauffmann, G., Colberg, J. M., and White, S. D. M. (1999). Clustering of galaxies in a hierarchical universe - III. Mock redshift surveys. *MNRAS*, 307(3):537–552.
- Diamond-Stanic, A. M. and Rieke, G. H. (2012). The Relationship between Black Hole Growth and Star Formation in Seyfert Galaxies. *ApJ*, 746:168.
- Dickinson, H., Fortson, L., Lintott, C., Scarlata, C., Willett, K., Bamford, S., Beck, M., Cardamone, C., Galloway, M., Simmons, B., Keel, W., Kruk, S., Masters, K., Vogelsberger, M., Torrey, P., and Snyder, G. F. (2018). Galaxy Zoo: Morphological Classification of Galaxy Images from the Illustris Simulation. *ApJ*, 853(2):194.
- Diemand, J., Kuhlen, M., Madau, P., Zemp, M., Moore, B., Potter, D., and Stadel, J. (2008). Clumps and streams in the local dark matter distribution. *Nature*, 454(7205):735–738.
- Doeleman, S. S., Weintroub, J., Rogers, A. E. E., Plambeck, R., Freund, R., Tilanus, R. P. J., Friberg, P., Ziurys, L. M., Moran, J. M., Corey, B., Young, K. H., Smythe, D. L., Titus, M., Marrone, D. P., Cappallo, R. J., Bock, D. C. J., Bower, G. C., Chamberlin, R., Davis, G. R., Krichbaum, T. P., Lamb, J., Maness, H., Niell, A. E., Roy, A., Strittmatter, P., Werthimer, D., Whitney, A. R., and Woody, D. (2008). Event-horizon-scale structure in the supermassive black hole candidate at the Galactic Centre. *Nature*, 455(7209):78–80.
- Domínguez-Tenreiro, R., Oñorbe, J., Sáiz, A., Artal, H., and Serna, A. (2006). The Lack of Structural and Dynamical Evolution of Elliptical Galaxies since  $z \sim 1.5$ : Clues from Self-Consistent Hydrodynamic Simulations. *ApJ*, 636(2):L77–L80.
- Domínguez-Tenreiro, R., Sáiz, A., and Serna, A. (2004). Elliptical Galaxies at  $z = 0$  from Self-consistent Hydrodynamic Simulations: Clues on Age Effects in Their Stellar Populations. *ApJ*, 611(1):L5–L8.
- Dopita, M. A., Groves, B. A., Sutherland, R. S., and Kewley, L. J. (2003). Internal Dust Correction Factors for Star Formation Rates Derived for Dusty H II Regions and Starburst Galaxies. *ApJ*, 583(2):727–731.
- Dopita, M. A. and Sutherland, R. S. (1995). Spectral Signatures of Fast Shocks. II. Optical Diagnostic Diagrams. *ApJ*, 455:468.
- Dopita, M. A. and Sutherland, R. S. (1996). Spectral Signatures of Fast Shocks. I. Low-Density Model Grid. *ApJS*, 102:161.
- Doroshkevich, A. G., Zel'dovich, Y. B., and Novikov, I. D. (1967). The Origin of Galaxies in an Expanding Universe. *Soviet Ast.*, 11:233.
- Dotti, M., Colpi, M., Haardt, F., and Mayer, L. (2007). Supermassive black hole binaries in gaseous and stellar circumnuclear discs: orbital dynamics and gas accretion. *MNRAS*, 379:956–962.

- Dotti, M., Colpi, M., Pallini, S., Perego, A., and Volonteri, M. (2013). On the Orientation and Magnitude of the Black Hole Spin in Galactic Nuclei. *ApJ*, 762:68.
- Dotti, M., Volonteri, M., Perego, A., Colpi, M., Ruzszkowski, M., and Haardt, F. (2010). Dual black holes in merger remnants - II. Spin evolution and gravitational recoil. *MNRAS*, 402:682–690.
- Doyon, R., Wells, M., Wright, G. S., Joseph, R. D., Nadeau, D., and James, P. A. (1994). Stellar velocity dispersion in ARP 220 and NGC 6240: Elliptical galaxies in formation. *ApJ*, 437:L23–L26.
- Drake, A. B., Simpson, C., Collins, C. A., James, P. A., Baldry, I. K., Ouchi, M., Jarvis, M. J., Bonfield, D. G., Ono, Y., Best, P. N., Dalton, G. B., Dunlop, J. S., McLure, R. J., and Smith, D. J. B. (2013). Evolution of star formation in the UKIDSS Ultra Deep Survey field - I. Luminosity functions and cosmic star formation rate out to  $z = 1.6$ . *MNRAS*, 433:796–811.
- Dressler, A. (1980). Galaxy morphology in rich clusters: implications for the formation and evolution of galaxies. *ApJ*, 236:351–365.
- Dressler, A. and Richstone, D. O. (1988). Stellar Dynamics in the Nuclei of M31 and M32: Evidence for Massive Black Holes. *ApJ*, 324:701.
- Dressler, A., Spergel, D., Mountain, M., Postman, M., Elliott, E., Bendek, E., Bennett, D., Dalcanton, J., Gaudi, S., Gehrels, N., Guyon, O., Hirata, C., Kalirai, J., Kasdin, N. J., Kruk, J., Macintosh, B., Malhotra, S., Penny, M., Perlmutter, S., Rieke, G., Riess, A., Rhoads, J., Shaklan, S., Somerville, R., Stern, D., Thompson, R., and Weinberg, D. (2012). Exploring the NRO Opportunity for a Hubble-sized Wide-field Near-IR Space Telescope – NEW WFIRST. *arXiv e-prints*.
- Driver, S. P., Norberg, P., Baldry, I. K., Bamford, S. P., Hopkins, A. M., Liske, J., Loveday, J., Peacock, J. A., Hill, D. T., Kelvin, L. S., Robotham, A. S. G., Cross, N. J. G., Parkinson, H. R., Prescott, M., Conselice, C. J., Dunne, L., Brough, S., Jones, H., Sharp, R. G., van Kampen, E., Oliver, S., Roseboom, I. G., Bland-Hawthorn, J., Croom, S. M., Ellis, S., Cameron, E., Cole, S., Frenk, C. S., Couch, W. J., Graham, A. W., Proctor, R., De Propriis, R., Doyle, I. F., Edmondson, E. M., Nichol, R. C., Thomas, D., Eales, S. A., Jarvis, M. J., Kuijken, K., Lahav, O., Madore, B. F., Seibert, M., Meyer, M. J., Staveley-Smith, L., Phillipps, S., Popescu, C. C., Sansom, A. E., Sutherland, W. J., Tuffs, R. J., and Warren, S. J. (2009). GAMA: towards a physical understanding of galaxy formation. *Astronomy and Geophysics*, 50(5):5.12–5.19.
- Drory, N. and Fisher, D. B. (2007). A Connection between Bulge Properties and the Bimodality of Galaxies. *ApJ*, 664:640–649.
- Du, M., Debattista, V. P., Shen, J., Ho, L. C., and Erwin, P. (2017). Black Hole Growth in Disk Galaxies Mediated by the Secular Evolution of Short Bars. *ApJ*, 844(2):L15.
- Du, M., Ho, L. C., Debattista, V. P., Pillepich, A., Nelson, D., Zhao, D., and Hernquist, L. (2020). Kinematic Decomposition of IllustrisTNG Disk Galaxies: Morphology and Relation with Morphological Structures. *ApJ*, 895(2):139.
- Dubinski, J., Berentzen, I., and Shlosman, I. (2009). Anatomy of the Bar Instability in Cuspy Dark Matter Halos. *ApJ*, 697(1):293–310.
- Dubois, Y., Devriendt, J., Slyz, A., and Teyssier, R. (2010). Jet-regulated cooling catastrophe. *MNRAS*, 409(3):985–1001.
- Dubois, Y., Devriendt, J., Slyz, A., and Teyssier, R. (2012a). Self-regulated growth of supermassive black holes by a dual jet-heating active galactic nucleus feedback mechanism: methods, tests and implications for cosmological simulations. *MNRAS*, 420(3):2662–2683.

- Dubois, Y., Gavazzi, R., Peirani, S., and Silk, J. (2013). AGN-driven quenching of star formation: morphological and dynamical implications for early-type galaxies. *MNRAS*, 433(4):3297–3313.
- Dubois, Y., Pichon, C., Haehnelt, M., Kimm, T., Slyz, A., Devriendt, J., and Pogosyan, D. (2012b). Feeding compact bulges and supermassive black holes with low angular momentum cosmic gas at high redshift. *MNRAS*, 423(4):3616–3630.
- Dubois, Y., Pichon, C., Welker, C., Le Borgne, D., Devriendt, J., Laigle, C., Codis, S., Pogosyan, D., Arnouts, S., Benabed, K., Bertin, E., Blaizot, J., Bouchet, F., Cardoso, J. F., Colombi, S., de Lapparent, V., Desjacques, V., Gavazzi, R., Kassin, S., Kimm, T., McCracken, H., Milliard, B., Peirani, S., Prunet, S., Rouberol, S., Silk, J., Slyz, A., Sousbie, T., Teyssier, R., Tresse, L., Treyer, M., Vibert, D., and Volonteri, M. (2014a). Dancing in the dark: galactic properties trace spin swings along the cosmic web. *MNRAS*, 444(2):1453–1468.
- Dubois, Y., Volonteri, M., and Silk, J. (2014b). Black hole evolution - III. Statistical properties of mass growth and spin evolution using large-scale hydrodynamical cosmological simulations. *MNRAS*, 440(2):1590–1606.
- Dubois, Y., Volonteri, M., Silk, J., Devriendt, J., Slyz, A., and Teyssier, R. (2015). Black hole evolution: I. supernova-regulated black hole growth. *Monthly Notices of the Royal Astronomical Society*, 452.
- Dutton, A. A. and Macciò, A. V. (2014). Cold dark matter haloes in the Planck era: evolution of structural parameters for Einasto and NFW profiles. *MNRAS*, 441:3359–3374.
- Efstathiou, G. (1992). Suppressing the formation of dwarf galaxies via photoionization. *MNRAS*, 256(2):43P–47P.
- Efstathiou, G., Lake, G., and Negroponte, J. (1982). The stability and masses of disc galaxies. *MNRAS*, 199:1069–1088.
- Eggen, O. J., Lynden-Bell, D., and Sandage, A. R. (1962). Evidence from the motions of old stars that the Galaxy collapsed. *ApJ*, 136:748.
- Einstein, A. (1916). Die Grundlage der allgemeinen Relativitätstheorie. *Annalen der Physik*, 354(7):769–822.
- Eisenreich, M., Naab, T., Choi, E., Ostriker, J. P., and Emsellem, E. (2017). AGN feedback, quiescence and CGM metal enrichment in early-type galaxies. *ArXiv e-prints*.
- Eisenstein, D. J., Weinberg, D. H., Agol, E., Aihara, H., Allende Prieto, C., Anderson, S. F., Arns, J. A., Aubourg, É., Bailey, S., Balbinot, E., and et al. (2011). SDSS-III: Massive Spectroscopic Surveys of the Distant Universe, the Milky Way, and Extra-Solar Planetary Systems. *AJ*, 142:72.
- Eliche-Moral, C., Balcells, M., Prieto, M., and Cristóbal-Hornillos, D. (2005). GOYA Survey: U and B Number Counts in the Groth-Westphal Strip. In Hidalgo-Gómez, A. M., González, J. J., Rodríguez Espinosa, J. M., and Torres-Peimbert, S., editors, *Revista Mexicana de Astronomía y Astrofísica Conference Series*, volume 24 of *Revista Mexicana de Astronomía y Astrofísica*, vol. 27, pages 237–238.
- Eliche-Moral, M. C., Balcells, M., Aguerri, J. A. L., and González-García, A. C. (2006a). Growth of galactic bulges by mergers. II. Low-density satellites. *A&A*, 457(1):91–108.
- Eliche-Moral, M. C., Balcells, M., Aguerri, J. A. L., and González-García, A. C. (2006b). Growth of galactic bulges by mergers. II. Low-density satellites. *A&A*, 457:91–108.
- eLISA Consortium, Amaro Seoane, P., Aoudia, S., Audley, H., Auger, G., Babak, S., Baker, J., Barausse, E., Barke, S., Bassan, M., Beckmann, V., Benacquista, M., Bender, P. L., Berti, E., Binétruy, P., Bogenstahl, J., Bonvin, C., Bortoluzzi, D., Brause, N. C., Brossard, J., Buchman, S., Bykov, I., Camp,

- J., Caprini, C., Cavalleri, A., Cerdonio, M., Ciani, G., Colpi, M., Congedo, G., Conklin, J., Cornish, N., Danzmann, K., de Vine, G., DeBra, D., Dewi Freitag, M., Di Fiore, L., Diaz Aguilo, M., Diepholz, I., Dolesi, R., Dotti, M., Fernández Barranco, G., Ferraioli, L., Ferroni, V., Finetti, N., Fitzsimons, E., Gair, J., Galeazzi, F., Garcia, A., Gerberding, O., Gesa, L., Giardini, D., Gibert, F., Grimani, C., Groot, P., Guzman Cervantes, F., Haiman, Z., Halloin, H., Heinzl, G., Hewitson, M., Hogan, C., Holz, D., Hornstrup, A., Hoyland, D., Hoyle, C. D., Hueller, M., Hughes, S., Jetzer, P., Kalogera, V., Karnesis, N., Kilic, M., Killow, C., Klipstein, W., Kochkina, E., Korsakova, N., Krolak, A., Larson, S., Lieser, M., Littenberg, T., Livas, J., Lloro, I., Mance, D., Madau, P., Maghami, P., Mahrdt, C., Marsh, T., Mateos, I., Mayer, L., McClelland, D., McKenzie, K., McWilliams, S., Merkowitz, S., Miller, C., Mitryk, S., Moerschell, J., Mohanty, S., Monsky, A., Mueller, G., Müller, V., Nelemans, G., Nicolodi, D., Nissanke, S., Nofrarias, M., Numata, K., Ohme, F., Otto, M., Perreur-Lloyd, M., Petiteau, A., Phinney, E. S., Plagnol, E., Pollack, S., Porter, E., Prat, P., Preston, A., Prince, T., Reiche, J., Richstone, D., Robertson, D., Rossi, E. M., Rosswog, S., Rubbo, L., Rüter, A., Sanjuan, J., Sathyaprakash, B. S., Schlamminger, S., Schutz, B., Schütze, D., Sesana, A., Shaddock, D., Shah, S., Sheard, B., Sopuerta, C. F., Spector, A., Spero, R., Stanga, R., Stebbins, R., Stede, G., Steier, F., Sumner, T., Sun, K. X., Sutton, A., Tanaka, T., Tanner, D., Thorpe, I., Tröbs, M., Tinto, M., Tu, H. B., Vallisneri, M., Vetrugno, D., Vitale, S., Volonteri, M., Wand, V., Wang, Y., Wanner, G., Ward, H., Ware, B., Wass, P., Weber, W. J., Yu, Y., Yunes, N., and Zweifel, P. (2013a). The Gravitational Universe. *arXiv e-prints*, page arXiv:1305.5720.
- eLISA Consortium, Amaro Seoane, P., Aoudia, S., Audley, H., Auger, G., Babak, S., Baker, J., Barausse, E., Barke, S., Bassan, M., Beckmann, V., Benacquista, M., Bender, P. L., Berti, E., Binétruy, P., Bogenstahl, J., Bonvin, C., Bortoluzzi, D., Brause, N. C., Brossard, J., Buchman, S., Bykov, I., Camp, J., Caprini, C., Cavalleri, A., Cerdonio, M., Ciani, G., Colpi, M., Congedo, G., Conklin, J., Cornish, N., Danzmann, K., de Vine, G., DeBra, D., Dewi Freitag, M., Di Fiore, L., Diaz Aguilo, M., Diepholz, I., Dolesi, R., Dotti, M., Fernández Barranco, G., Ferraioli, L., Ferroni, V., Finetti, N., Fitzsimons, E., Gair, J., Galeazzi, F., Garcia, A., Gerberding, O., Gesa, L., Giardini, D., Gibert, F., Grimani, C., Groot, P., Guzman Cervantes, F., Haiman, Z., Halloin, H., Heinzl, G., Hewitson, M., Hogan, C., Holz, D., Hornstrup, A., Hoyland, D., Hoyle, C. D., Hueller, M., Hughes, S., Jetzer, P., Kalogera, V., Karnesis, N., Kilic, M., Killow, C., Klipstein, W., Kochkina, E., Korsakova, N., Krolak, A., Larson, S., Lieser, M., Littenberg, T., Livas, J., Lloro, I., Mance, D., Madau, P., Maghami, P., Mahrdt, C., Marsh, T., Mateos, I., Mayer, L., McClelland, D., McKenzie, K., McWilliams, S., Merkowitz, S., Miller, C., Mitryk, S., Moerschell, J., Mohanty, S., Monsky, A., Mueller, G., Müller, V., Nelemans, G., Nicolodi, D., Nissanke, S., Nofrarias, M., Numata, K., Ohme, F., Otto, M., Perreur-Lloyd, M., Petiteau, A., Phinney, E. S., Plagnol, E., Pollack, S., Porter, E., Prat, P., Preston, A., Prince, T., Reiche, J., Richstone, D., Robertson, D., Rossi, E. M., Rosswog, S., Rubbo, L., Rüter, A., Sanjuan, J., Sathyaprakash, B. S., Schlamminger, S., Schutz, B., Schütze, D., Sesana, A., Shaddock, D., Shah, S., Sheard, B., Sopuerta, C. F., Spector, A., Spero, R., Stanga, R., Stebbins, R., Stede, G., Steier, F., Sumner, T., Sun, K. X., Sutton, A., Tanaka, T., Tanner, D., Thorpe, I., Tröbs, M., Tinto, M., Tu, H. B., Vallisneri, M., Vetrugno, D., Vitale, S., Volonteri, M., Wand, V., Wang, Y., Wanner, G., Ward, H., Ware, B., Wass, P., Weber, W. J., Yu, Y., Yunes, N., and Zweifel, P. (2013b). The Gravitational Universe. *arXiv e-prints*, page arXiv:1305.5720.
- Elmegreen, B. G., Bournaud, F., and Elmegreen, D. M. (2008). Bulge Formation by the Coalescence of Giant Clumps in Primordial Disk Galaxies. *ApJ*, 688(1):67–77.
- Elmegreen, B. G., Elmegreen, D. M., and Hirst, A. C. (2004). A Constant Bar Fraction out to Redshift  $z \sim 1$  in the Advanced Camera for Surveys Field of the Tadpole Galaxy. *ApJ*, 612(1):191–201.
- Erwin, P., Saglia, R. P., Fabricius, M., Thomas, J., Nowak, N., Rusli, S., Bender, R., Vega Beltrán, J. C., and Beckman, J. E. (2015). Composite bulges: the coexistence of classical bulges and discy pseudo-bulges in S0 and spiral galaxies. *MNRAS*, 446:4039–4077.

- Escala, A., Larson, R. B., Coppi, P. S., and Mardones, D. (2004). The Role of Gas in the Merging of Massive Black Holes in Galactic Nuclei. I. Black Hole Merging in a Spherical Gas Cloud. *ApJ*, 607:765–777.
- Escala, A., Larson, R. B., Coppi, P. S., and Mardones, D. (2005). The Role of Gas in the Merging of Massive Black Holes in Galactic Nuclei. II. Black Hole Merging in a Nuclear Gas Disk. *ApJ*, 630(1):152–166.
- Eskridge, P. B., Frogel, J. A., Pogge, R. W., Quillen, A. C., Davies, R. L., DePoy, D. L., Houdashelt, M. L., Kuchinski, L. E., Ramírez, S. V., Sellgren, K., Terndrup, D. M., and Tiede, G. P. (2000). The Frequency of Barred Spiral Galaxies in the Near-Infrared. *AJ*, 119(2):536–544.
- Evans, N. W. and de Zeeuw, P. T. (1994). Observable properties of the power-law galaxies. *MNRAS*, 271:202–222.
- Event Horizon Telescope Collaboration, Akiyama, K., Alberdi, A., Alef, W., Asada, K., Azulay, R., Baczko, A.-K., Ball, D., Baloković, M., Barrett, J., Bintley, D., Blackburn, L., Boland, W., Bouman, K. L., Bower, G. C., Bremer, M., Brinkerink, C. D., Brissenden, R., Britzen, S., Broderick, A. E., Brogiere, D., Bronzwaer, T., Byun, D.-Y., Carlstrom, J. E., Chael, A., Chan, C.-k., Chatterjee, S., Chatterjee, K., Chen, M.-T., Chen, Y., Cho, I., Christian, P., Conway, J. E., Cordes, J. M., Crew, G. B., Cui, Y., Davelaar, J., De Laurentis, M., Deane, R., Dempsey, J., Desvignes, G., Dexter, J., Doeleman, S. S., Eatough, R. P., Falcke, H., Fish, V. L., Fomalont, E., Fraga-Encinas, R., Freeman, W. T., Friberg, P., Fromm, C. M., Gómez, J. L., Galison, P., Gammie, C. F., García, R., Gentaz, O., Georgiev, B., Goddi, C., Gold, R., Gu, M., Gurwell, M., Hada, K., Hecht, M. H., Hesper, R., Ho, L. C., Ho, P., Honma, M., Huang, C.-W. L., Huang, L., Hughes, D. H., Ikeda, S., Inoue, M., Issaoun, S., James, D. J., Jannuzi, B. T., Janssen, M., Jeter, B., Jiang, W., Johnson, M. D., Jorstad, S., Jung, T., Karami, M., Karuppusamy, R., Kawashima, T., Keating, G. K., Kettenis, M., Kim, J.-Y., Kim, J., Kim, J., Kino, M., Koay, J. Y., Koch, P. M., Koyama, S., Kramer, M., Kramer, C., Krichbaum, T. P., Kuo, C.-Y., Lauer, T. R., Lee, S.-S., Li, Y.-R., Li, Z., Lindqvist, M., Liu, K., Liuzzo, E., Lo, W.-P., Lobanov, A. P., Loinard, L., Lonsdale, C., Lu, R.-S., MacDonald, N. R., Mao, J., Markoff, S., Marrone, D. P., Marscher, A. P., Martí-Vidal, I., Matsushita, S., Matthews, L. D., Medeiros, L., Menten, K. M., Mizuno, Y., Mizuno, I., Moran, J. M., Moriyama, K., Moscibrodzka, M., Müller, C., Nagai, H., Nagar, N. M., Nakamura, M., Narayan, R., Narayanan, G., Natarajan, I., Neri, R., Ni, C., Noutsos, A., Okino, H., Olivares, H., Ortiz-León, G. N., Oyama, T., Özel, F., Palumbo, D. C. M., Patel, N., Pen, U.-L., Pesce, D. W., Piétu, V., Plambeck, R., PopStefanija, A., Porth, O., Prather, B., Preciado-López, J. A., Psaltis, D., Pu, H.-Y., Ramakrishnan, V., Rao, R., Rawlings, M. G., Raymond, A. W., Rezzolla, L., Ripperda, B., Roelofs, F., Rogers, A., Ros, E., Rose, M., Roshanineshat, A., Rottmann, H., Roy, A. L., Ruszczyk, C., Ryan, B. R., Rygl, K. L. J., Sánchez, S., Sánchez-Arguelles, D., Sasada, M., Savolainen, T., Schloerb, F. P., Schuster, K.-F., Shao, L., Shen, Z., Small, D., Sohn, B. W., SooHoo, J., Tazaki, F., Tiede, P., Tilanus, R. P. J., Titus, M., Toma, K., Torne, P., Trent, T., Trippe, S., Tsuda, S., van Bemmell, I., van Langevelde, H. J., van Rossum, D. R., Wagner, J., Wardle, J., Weintroub, J., Wex, N., Wharton, R., Wielgus, M., Wong, G. N., Wu, Q., Young, K., Young, A., Younsi, Z., Yuan, F., Yuan, Y.-F., Zensus, J. A., Zhao, G., Zhao, S.-S., Zhu, Z., Algaba, J.-C., Allardi, A., Amestica, R., Anczarski, J., Bach, U., Baganoff, F. K., Beaudoin, C., Benson, B. A., Berthold, R., Blanchard, J. M., Blundell, R., Bustamente, S., Cappallo, R., Castillo-Domínguez, E., Chang, C.-C., Chang, S.-H., Chang, S.-C., Chen, C.-C., Chilson, R., Chuter, T. C., Córdova Rosado, R., Coulson, I. M., Crawford, T. M., Crowley, J., David, J., Derome, M., Dexter, M., Dornbusch, S., Dudevoir, K. A., Dzib, S. A., Eckart, A., Eckert, C., Erickson, N. R., Everett, W. B., Faber, A., Farah, J. R., Fath, V., Folkers, T. W., Forbes, D. C., Freund, R., Gómez-Ruiz, A. I., Gale, D. M., Gao, F., Geertsema, G., Graham, D. A., Greer, C. H., Grosslein, R., Gueth, F., Haggard, D., Halverson, N. W., Han, C.-C., Han, K.-C., Hao, J., Hasegawa, Y., Henning, J. W., Hernández-Gómez, A., Herrero-Illana, R., Heyminck, S., Hirota, A., Hoge, J., Huang, Y.-D., Impellizzeri, C. M. V., Jiang, H., Kamble, A., Keisler, R., Kimura, K., Kono, Y., Kubo, D., Kuroda, J., Lacasse, R., Laing, R. A., Leitch, E. M., Li, C.-T., Lin,



- L. C. C., Liu, C.-T., Liu, K.-Y., Lu, L.-M., Marson, R. G., Martin-Cocher, P. L., Massingill, K. D., Matulonis, C., McColl, M. P., McWhirter, S. R., Messias, H., Meyer-Zhao, Z., Michalik, D., Montaña, A., Montgomerie, W., Mora-Klein, M., Muders, D., Nadolski, A., Navarro, S., Neilsen, J., Nguyen, C. H., Nishioka, H., Norton, T., Nowak, M. A., Nystrom, G., Ogawa, H., Oshiro, P., Oyama, T., Parsons, H., Paine, S. N., Peñalver, J., Phillips, N. M., Poirier, M., Pradel, N., Primiani, R. A., Raffin, P. A., Rahlin, A. S., Reiland, G., Risacher, C., Ruiz, I., Sáez-Madaín, A. F., Sassella, R., Schellart, P., Shaw, P., Silva, K. M., Shiokawa, H., Smith, D. R., Snow, W., Souccar, K., Sousa, D., Sridharan, T. K., Srinivasan, R., Stahm, W., Stark, A. A., Story, K., Timmer, S. T., Vertatschitsch, L., Walther, C., Wei, T.-S., Whitehorn, N., Whitney, A. R., Woody, D. P., Wouterloot, J. G. A., Wright, M., Yamaguchi, P., Yu, C.-Y., Zeballos, M., Zhang, S., and Ziurys, L. (2019). First M87 Event Horizon Telescope Results. I. The Shadow of the Supermassive Black Hole. *ApJ*, 875(1):L1.
- Faber, S. M. (1999). The demography of massive galactic black holes. *Advances in Space Research*, 23(5-6):925–936.
- Faber, S. M., Tremaine, S., Ajhar, E. A., Byun, Y.-I., Dressler, A., Gebhardt, K., Grillmair, C., Kormendy, J., Lauer, T. R., and Richstone, D. (1997). The Centers of Early-Type Galaxies with HST. IV. Central Parameter Relations. *AJ*, 114:1771.
- Fabian, A. C. and Nulsen, P. E. J. (1977). Subsonic accretion of cooling gas in clusters of galaxies. *MNRAS*, 180:479–484.
- Fabian, A. C., Rees, M. J., Stella, L., and White, N. E. (1989). X-ray fluorescence from the inner disc in Cygnus X-1. *MNRAS*, 238:729–736.
- Faltenbacher, A. and Mathews, W. G. (2005). On the dynamics of the satellite galaxies in NGC 5044. *MNRAS*, 362(2):498–504.
- Fan, X., Narayanan, V. K., Lupton, R. H., Strauss, M. A., Knapp, G. R., Becker, R. H., White, R. L., Pentericci, L., Leggett, S. K., Haiman, Z., Gunn, J. E., Ivezić, Ž., Schneider, D. P., Anderson, S. F., Brinkmann, J., Bahcall, N. A., Connolly, A. J., Csabai, I., Doi, M., Fukugita, M., Geballe, T., Grebel, E. K., Harbeck, D., Hennessy, G., Lamb, D. Q., Miknaitis, G., Munn, J. A., Nichol, R., Okamura, S., Pier, J. R., Prada, F., Richards, G. T., Szalay, A., and York, D. G. (2001). A Survey of  $z \gtrsim 5.8$  Quasars in the Sloan Digital Sky Survey. I. Discovery of Three New Quasars and the Spatial Density of Luminous Quasars at  $z \sim 6$ . *AJ*, 122(6):2833–2849.
- Fanali, R., Dotti, M., Fiacconi, D., and Haardt, F. (2015). Bar formation as driver of gas inflows in isolated disc galaxies. *MNRAS*, 454(4):3641–3652.
- Fanidakis, N., Baugh, C. M., Benson, A. J., Bower, R. G., Cole, S., Done, C., and Frenk, C. S. (2011). Grand unification of AGN activity in the  $\Lambda$ CDM cosmology. *MNRAS*, 410:53–74.
- Fanidakis, N., Baugh, C. M., Benson, A. J., Bower, R. G., Cole, S., Done, C., Frenk, C. S., Hickox, R. C., Lacey, C., and Del P. Lagos, C. (2012). The evolution of active galactic nuclei across cosmic time: what is downsizing? *MNRAS*, 419(4):2797–2820.
- Farouki, R. T. and Shapiro, S. L. (1982). Simulations of merging disk galaxies. *ApJ*, 259:103–115.
- Fasano, G., Poggianti, B. M., Couch, W. J., Bettoni, D., Kjærgaard, P., and Moles, M. (2000). The Evolution of the Galactic Morphological Types in Clusters. *ApJ*, 542(2):673–683.
- Favole, G., Comparat, J., Prada, F., Yepes, G., Jullo, E., Niemic, A., Kneib, J.-P., Rodríguez-Torres, S. A., Klypin, A., and Skibba, R. A. (2016). Clustering properties of g-selected galaxies at  $z \sim 0.8$ . *MNRAS*, 461(4):3421–3431.

- Feldmann, R., Carollo, C. M., Mayer, L., Renzini, A., Lake, G., Quinn, T., Stinson, G. S., and Yepes, G. (2010). The Evolution of Central Group Galaxies in Hydrodynamical Simulations. *ApJ*, 709(1):218–240.
- Feng, Y., Di-Matteo, T., Croft, R. A., Bird, S., Battaglia, N., and Wilkins, S. (2016). The BlueTides simulation: first galaxies and reionization. *MNRAS*, 455(3):2778–2791.
- Ferland, G. J., Porter, R. L., van Hoof, P. A. M., Williams, R. J. R., Abel, N. P., Lykins, M. L., Shaw, G., Henney, W. J., and Stancil, P. C. (2013). The 2013 Release of Cloudy. *Rev. Mexicana Astron. Astrofis.*, 49:137–163.
- Ferrarese, L. and Merritt, D. (2000). A Fundamental Relation between Supermassive Black Holes and Their Host Galaxies. *ApJ*, 539(1):L9–L12.
- Fiacconi, D., Mayer, L., Roškar, R., and Colpi, M. (2013). Massive Black Hole Pairs in Clumpy, Self-gravitating Circumnuclear Disks: Stochastic Orbital Decay. *ApJ*, 777:L14.
- Fiacconi, D., Sijacki, D., and Pringle, J. E. (2018). Galactic nuclei evolution with spinning black holes: method and implementation. *MNRAS*, 477(3):3807–3835.
- Fine, S., Croom, S. M., Miller, L., Babic, A., Moore, D., Brewer, B., Sharp, R. G., Boyle, B. J., Shanks, T., Smith, R. J., Outram, P. J., and Loaring, N. S. (2006). The evolution of host mass and black hole mass in quasi-stellar objects from the 2dF QSO Redshift Survey. *MNRAS*, 373(2):613–622.
- Fisher, D. B. and Drory, N. (2008a). The Structure of Classical Bulges and Pseudobulges: the Link Between Pseudobulges and SÉRSIC Index. *AJ*, 136:773–839.
- Fisher, D. B. and Drory, N. (2008b). The Structure of Classical Bulges and Pseudobulges: the Link Between Pseudobulges and SÉRSIC Index. *AJ*, 136:773–839.
- Fisher, D. B. and Drory, N. (2010). Bulges of Nearby Galaxies with Spitzer: Scaling Relations in Pseudobulges and Classical Bulges. *ApJ*, 716:942–969.
- Fisher, D. B., Drory, N., and Fabricius, M. H. (2009). Bulges of Nearby Galaxies with Spitzer: The Growth of Pseudobulges in Disk Galaxies and its Connection to Outer Disks. *ApJ*, 697:630–650.
- Fontanot, F. and Somerville, R. S. (2011). Evaluating and improving semi-analytic modelling of dust in galaxies based on radiative transfer calculations - II. Dust emission in the infrared. *MNRAS*, 416(4):2962–2973.
- Forcada-Miro, M. I. and White, S. D. M. (1997). Radiative shocks in galaxy formation. I: Cooling of a primordial plasma with no sources of heating. *ArXiv Astrophysics e-prints*.
- Foster, R. S. and Backer, D. C. (1990). Constructing a Pulsar Timing Array. *ApJ*, 361:300.
- Fragkoudi, F., Di Matteo, P., Haywood, M., Gómez, A., Combes, F., Katz, D., and Semelin, B. (2017). Bars and boxy/peanut bulges in thin and thick discs. I. Morphology and line-of-sight velocities of a fiducial model. *A&A*, 606:A47.
- Friedli, D. and Benz, W. (1993). Secular evolution of isolated barred galaxies. I. Gravitational coupling between stellar bars and interstellar medium. *A&A*, 268:65–85.
- Friedli, D. and Pfenniger, D. (1991). Destruction of Bars by Dissipative Processes. In Combes, F. and Casoli, F., editors, *Dynamics of Galaxies and Their Molecular Cloud Distributions*, volume 146 of *IAU Symposium*, page 362.

- Fujita, S. S., Ajiki, M., Shioya, Y., Nagao, T., Murayama, T., Taniguchi, Y., Umeda, K., Yamada, S., Yagi, M., Okamura, S., and Komiyama, Y. (2003). The  $H\alpha$  Luminosity Function and Star Formation Rate at  $z \sim 0.24$  Based on Subaru Deep Imaging Data. *ApJ*, 586:L115–L118.
- Fuller, J. and Ma, L. (2019). Most Black Holes Are Born Very Slowly Rotating. *ApJ*, 881(1):L1.
- Gadotti, D. A. (2009). Structural properties of pseudo-bulges, classical bulges and elliptical galaxies: a Sloan Digital Sky Survey perspective. *MNRAS*, 393:1531–1552.
- Gadotti, D. A. and dos Anjos, S. (2001). Homogenization of the Stellar Population along Late-Type Spiral Galaxies. *AJ*, 122(3):1298–1318.
- Gadotti, D. A., Seidel, M. K., Sánchez-Blázquez, P., Falcón-Barroso, J., Husemann, B., Coelho, P., and Pérez, I. (2015). MUSE tells the story of NGC 4371: The dawning of secular evolution. *A&A*, 584:A90.
- Gallego, J., Zamorano, J., Aragon-Salamanca, A., and Rego, M. (1995). The Current Star Formation Rate of the Local Universe. *ApJ*, 455:L1.
- Galli, D. and Palla, F. (1998). The chemistry of the early Universe. *A&A*, 335:403–420.
- Gallo, L. C., Miniutti, G., Miller, J. M., Brenneman, L. W., Fabian, A. C., Guainazzi, M., and Reynolds, C. S. (2011). Multi-epoch X-ray observations of the Seyfert 1.2 galaxy Mrk 79: bulk motion of the illuminating X-ray source. *MNRAS*, 411(1):607–619.
- Gao, L. and White, S. D. M. (2007). Assembly bias in the clustering of dark matter haloes. *MNRAS*, 377(1):L5–L9.
- Gardner, J. P., Mather, J. C., Clampin, M., Doyon, R., Greenhouse, M. A., Hammel, H. B., Hutchings, J. B., Jakobsen, P., Lilly, S. J., Long, K. S., Lunine, J. I., McCaughrean, M. J., Mountain, M., Nella, J., Rieke, G. H., Rieke, M. J., Rix, H.-W., Smith, E. P., Sonneborn, G., Stiavelli, M., Stockman, H. S., Windhorst, R. A., and Wright, G. S. (2006). The James Webb Space Telescope. *Space Science Reviews*, 123(4):485–606.
- Gargiulo, I. D., Cora, S. A., Padilla, N. D., Muñoz Arancibia, A. M., Ruiz, A. N., Orsi, A. A., Tecce, T. E., Weidner, C., and Bruzual, G. (2015). Chemoarchaeological downsizing in a hierarchical universe: impact of a top-heavy IGIMF. *MNRAS*, 446:3820–3841.
- Gargiulo, I. D., Cora, S. A., Vega-Martínez, C. A., Gonzalez, O. A., Zoccali, M., González, R., Ruiz, A. N., and Padilla, N. D. (2017). Stellar Populations in a semi-analytic model I: Bulges of Milky Way-like galaxies. *MNRAS*, 472(4):4133–4143.
- Gargiulo, I. D., Monachesi, A., Gómez, F. A., Grand, R. J. J., Marinacci, F., Pakmor, R., White, S. D. M., Bell, E. F., Fragkoudi, F., and Tissera, P. (2019). The prevalence of pseudo-bulges in the Auriga simulations. *MNRAS*, 489(4):5742–5763.
- Gaspari, M., Brighenti, F., and Temi, P. (2012). Mechanical AGN feedback: controlling the thermodynamical evolution of elliptical galaxies. *MNRAS*, 424(1):190–209.
- Gavazzi, G., Consolandi, G., Viscardi, E., Fossati, M., Savorgnan, G., Fumagalli, M., Gutierrez, L., Hernandez Toledo, H., Boselli, A., Giovanelli, R., and Haynes, M. P. (2015).  $H\alpha 3$ : an  $H\alpha$  imaging survey of HI selected galaxies from ALFALFA . V. The Coma supercluster survey completion. *A&A*, 576:A16.
- Gebhardt, K., Bender, R., Bower, G., Dressler, A., Faber, S. M., Filippenko, A. V., Green, R., Grillmair, C., Ho, L. C., Kormendy, J., Lauer, T. R., Magorrian, J., Pinkney, J., Richstone, D., and Tremaine, S. (2000). A Relationship between Nuclear Black Hole Mass and Galaxy Velocity Dispersion. *ApJ*, 539(1):L13–L16.

- Genel, S., Bouché, N., Naab, T., Sternberg, A., and Genzel, R. (2010). The Growth of Dark Matter Halos: Evidence for Significant Smooth Accretion. *ApJ*, 719(1):229–239.
- Genel, S., Fall, S. M., Hernquist, L., Vogelsberger, M., Snyder, G. F., Rodriguez-Gomez, V., Sijacki, D., and Springel, V. (2015). Galactic Angular Momentum in the Illustris Simulation: Feedback and the Hubble Sequence. *ApJ*, 804(2):L40.
- Genzel, R., Hollenbach, D., and Townes, C. H. (1994). The nucleus of our Galaxy. *Reports on Progress in Physics*, 57(5):417–479.
- Genzel, R. and Townes, C. H. (1987). Physical conditions, dynamics, and mass distribution in the center of the galaxy. *ARA&A*, 25:377–423.
- Georgakakis, A., Coil, A. L., Laird, E. S., Griffith, R. L., Nandra, K., Lotz, J. M., Pierce, C. M., Cooper, M. C., Newman, J. A., and Koekemoer, A. M. (2009). Host galaxy morphologies of X-ray selected AGN: assessing the significance of different black hole fuelling mechanisms to the accretion density of the Universe at  $z \sim 1$ . *MNRAS*, 397(2):623–633.
- Germain, J., Barai, P., and Martel, H. (2009). Anisotropic Active Galactic Nucleus Outflows and Enrichment of the Intergalactic Medium. I. Metal Distribution. *ApJ*, 704(2):1002–1020.
- Gerosa, D. and Sesana, A. (2015). Missing black holes in brightest cluster galaxies as evidence for the occurrence of superkicks in nature. *MNRAS*, 446(1):38–55.
- Ghigna, S., Moore, B., Governato, F., Lake, G., Quinn, T., and Stadel, J. (1998). Dark matter haloes within clusters. *MNRAS*, 300(1):146–162.
- Gierliński, M., Middleton, M., Ward, M., and Done, C. (2008). A periodicity of  $\sim 1$  hour in X-ray emission from the active galaxy RE J1034+396. *Nature*, 455(7211):369–371.
- Gilbank, D. G., Baldry, I. K., Balogh, M. L., Glazebrook, K., and Bower, R. G. (2010). The local star formation rate density: assessing calibrations using [OII], H and UV luminosities. *MNRAS*, 405:2594–2614.
- Gillessen, S., Eisenhauer, F., Perrin, G., Brandner, W., Straubmeier, C., Perraut, K., Amorim, A., Schöller, M., Araujo-Hauck, C., Bartko, H., Baumeister, H., Berger, J. P., Carvas, P., Cassaing, F., Chapron, F., Choquet, E., Clenet, Y., Collin, C., Eckart, A., Fedou, P., Fischer, S., Gendron, E., Genzel, R., Gitton, P., Gonte, F., Gräter, A., Haguenaue, P., Haug, M., Haubois, X., Henning, T., Hippler, S., Hofmann, R., Jocu, L., Kellner, S., Kervella, P., Klein, R., Kudryavtseva, N., Lacour, S., Lapeyrere, V., Laun, W., Lena, P., Lenzen, R., Lima, J., Moratschke, D., Moch, D., Moulin, T., Naranjo, V., Neumann, U., Nolot, A., Paumard, T., Pfuhl, O., Rabien, S., Ramos, J., Rees, J. M., Rohloff, R. R., Rouan, D., Rousset, G., Sevin, A., Thiel, M., Wagner, K., Wiest, M., Yazici, S., and Ziegler, D. (2010). *GRAVITY: a four-telescope beam combiner instrument for the VLTI*, volume 7734 of *Society of Photo-Optical Instrumentation Engineers (SPIE) Conference Series*, page 77340Y.
- Gnedin, N. Y. (2000). Effect of Reionization on Structure Formation in the Universe. *ApJ*, 542(2):535–541.
- González, J. A., Hannam, M., Sperhake, U., Brüggmann, B., and Husa, S. (2007). Supermassive Recoil Velocities for Binary Black-Hole Mergers with Antialigned Spins. *Physical Review Letters*, 98(23):231101.
- Gonzalez-Perez, V., Comparat, J., Norberg, P., Baugh, C. M., Contreras, S., Lacey, C., McCullagh, N., Orsi, A., Helly, J., and Humphries, J. (2018). The host dark matter haloes of [O II] emitters at  $0.5 < z < 1.5$ . *MNRAS*, 474:4024–4038.

- Gonzalez-Perez, V., Lacey, C. G., Baugh, C. M., Lagos, C. D. P., Helly, J., Campbell, D. J. R., and Mitchell, P. D. (2014). How sensitive are predicted galaxy luminosities to the choice of stellar population synthesis model? *MNRAS*, 439:264–283.
- Governato, F., Willman, B., Mayer, L., Brooks, A., Stinson, G., Valenzuela, O., Wadsley, J., and Quinn, T. (2007). Forming disc galaxies in  $\Lambda$ CDM simulations. *MNRAS*, 374(4):1479–1494.
- Graham, A. W., Erwin, P., Caon, N., and Trujillo, I. (2001). A Correlation between Galaxy Light Concentration and Supermassive Black Hole Mass. *ApJ*, 563(1):L11–L14.
- Grand, R. J. J., Gómez, F. A., Marinacci, F., Pakmor, R., Springel, V., Campbell, D. J. R., Frenk, C. S., Jenkins, A., and White, S. D. M. (2017). The Auriga Project: the properties and formation mechanisms of disc galaxies across cosmic time. *MNRAS*, 467(1):179–207.
- Grazian, A., Menci, N., Giallongo, E., Gallozzi, S., Fontanot, F., Fontana, A., Testa, V., Ragazzoni, R., Baruffolo, A., Beccari, G., Diolaiti, E., di Paola, A., Farinato, J., Gasparo, F., Gentile, G., Green, R., Hill, J., Kuhn, O., Pasian, F., Pedichini, F., Radovich, M., Smareglia, R., Speziali, R., Thompson, D., and Wagner, R. M. (2009). Wide and deep near-UV (360 nm) galaxy counts and the extragalactic background light with the Large Binocular Camera. *A&A*, 505:1041–1048.
- Greene, J. E. and Ho, L. C. (2007). The Mass Function of Active Black Holes in the Local Universe. *ApJ*, 667(1):131–148.
- Greene, J. E., Zakamska, N. L., and Smith, P. S. (2012). A Spectacular Outflow in an Obscured Quasar. *ApJ*, 746(1):86.
- Griffin, A. J., Lacey, C. G., Gonzalez-Perez, V., Lagos, C. d. P., Baugh, C. M., and Fanidakis, N. (2019). The evolution of SMBH spin and AGN luminosities for  $z \lesssim 6$  within a semi-analytic model of galaxy formation. *MNRAS*, 487(1):198–227.
- Grogin, N. A., Kocevski, D. D., Faber, S. M., Ferguson, H. C., Koekemoer, A. M., Riess, A. G., Acquaviva, V., Alexander, D. M., Almaini, O., Ashby, M. L. N., Barden, M., Bell, E. F., Bournaud, F., Brown, T. M., Caputi, K. I., Casertano, S., Cassata, P., Castellano, M., Challis, P., Chary, R.-R., Cheung, E., Cirasuolo, M., Conselice, C. J., Roshan Cooray, A., Croton, D. J., Daddi, E., Dahlen, T., Davé, R., de Mello, D. F., Dekel, A., Dickinson, M., Dolch, T., Donley, J. L., Dunlop, J. S., Dutton, A. A., Elbaz, D., Fazio, G. G., Filippenko, A. V., Finkelstein, S. L., Fontana, A., Gardner, J. P., Garnavich, P. M., Gawiser, E., Giavalisco, M., Grazian, A., Guo, Y., Hathi, N. P., Häussler, B., Hopkins, P. F., Huang, J.-S., Huang, K.-H., Jha, S. W., Kartaltepe, J. S., Kirshner, R. P., Koo, D. C., Lai, K., Lee, K.-S., Li, W., Lotz, J. M., Lucas, R. A., Madau, P., McCarthy, P. J., McGrath, E. J., McIntosh, D. H., McLure, R. J., Mobasher, B., Moustakas, L. A., Mozena, M., Nandra, K., Newman, J. A., Niemi, S.-M., Noeske, K. G., Papovich, C. J., Pentericci, L., Pope, A., Primack, J. R., Rajan, A., Ravindranath, S., Reddy, N. A., Renzini, A., Rix, H.-W., Robaina, A. R., Rodney, S. A., Rosario, D. J., Rosati, P., Salimbeni, S., Scarlata, C., Siana, B., Simard, L., Smidt, J., Somerville, R. S., Spinrad, H., Straughn, A. N., Strolger, L.-G., Telford, O., Teplitz, H. I., Trump, J. R., van der Wel, A., Villforth, C., Wechsler, R. H., Weiner, B. J., Wiklind, T., Wild, V., Wilson, G., Wuyts, S., Yan, H.-J., and Yun, M. S. (2011). CANDELS: The Cosmic Assembly Near-infrared Deep Extragalactic Legacy Survey. *ApJS*, 197:35.
- Grogin, N. A., Koekemoer, A. M., Schreier, E. J., Bergeron, J., Giacconi, R., Hasinger, G., Kewley, L., Norman, C., Rosati, P., Tozzi, P., and Zirm, A. (2003). Hubble Space Telescope Imaging in the Chandra Deep Field-South. III. Quantitative Morphology of the 1 Million Second Chandra Counterparts and Comparison with the Field Population. *ApJ*, 595(2):685–697.
- Grosbøl, P., Patsis, P. A., and Pompei, E. (2004). Spiral galaxies observed in the near-infrared K band. I. Data analysis and structural parameters. *A&A*, 423:849–859.

- Groves, B. A., Dopita, M. A., and Sutherland, R. S. (2004). Dusty, Radiation Pressure-Dominated Photoionization. I. Model Description, Structure, and Grids. *ApJS*, 153:9–73.
- Grützbauch, R., Conselice, C. J., Varela, J., Bundy, K., Cooper, M. C., Skibba, R., and Willmer, C. N. A. (2011). How does galaxy environment matter? The relationship between galaxy environments, colour and stellar mass at  $0.4 < z < 1$  in the Palomar/DEEP2 survey. *MNRAS*, 411(2):929–946.
- Gualandris, A. and Merritt, D. (2008). Ejection of Supermassive Black Holes from Galaxy Cores. *ApJ*, 678:780–797.
- Guedes, J., Madau, P., Mayer, L., and Callegari, S. (2011). Recoiling Massive Black Holes in Gas-rich Galaxy Mergers. *ApJ*, 729(2):125.
- Guhathakurta, P., Tyson, J. A., and Majewski, S. R. (1990). Deep CCD imaging of field galaxies in U, BJ, and R - Constraints on galaxy evolution. In Kron, R. G., editor, *Evolution of the Universe of Galaxies*, volume 10 of *Astronomical Society of the Pacific Conference Series*, pages 304–306.
- Guilbert, P. W. and Rees, M. J. (1988a). 'Cold' material in non-thermal sources. *MNRAS*, 233:475–484.
- Guilbert, P. W. and Rees, M. J. (1988b). 'Cold' material in non-thermal sources. *MNRAS*, 233:475–484.
- Gunawardhana, M. L. P., Hopkins, A. M., Bland-Hawthorn, J., Brough, S., Sharp, R., Loveday, J., Taylor, E., Jones, D. H., Lara-López, M. A., Bauer, A. E., Colless, M., Owers, M., Baldry, I. K., López-Sánchez, A. R., Foster, C., Bamford, S., Brown, M. J. I., Driver, S. P., Drinkwater, M. J., Liske, J., Meyer, M., Norberg, P., Robotham, A. S. G., Ching, J. H. Y., Cluver, M. E., Croom, S., Kelvin, L., Prescott, M., Steele, O., Thomas, D., and Wang, L. (2013). Galaxy And Mass Assembly: evolution of the  $H\alpha$  luminosity function and star formation rate density up to  $z < 0.35$ . *MNRAS*, 433:2764–2789.
- Gunn, J. E., Siegmund, W. A., Mannery, E. J., Owen, R. E., Hull, C. L., Leger, R. F., Carey, L. N., Knapp, G. R., York, D. G., Boroski, W. N., Kent, S. M., Lupton, R. H., Rockosi, C. M., Evans, M. L., Waddell, P., Anderson, J. E., Annis, J., Barentine, J. C., Bartoszek, L. M., Bastian, S., Bracker, S. B., Brewington, H. J., Briegel, C. I., Brinkmann, J., Brown, Y. J., Carr, M. A., Czarapata, P. C., Drennan, C. C., Dombeck, T., Federwitz, G. R., Gillespie, B. A., Gonzales, C., Hansen, S. U., Harvanek, M., Hayes, J., Jordan, W., Kinney, E., Klaene, M., Kleinman, S. J., Kron, R. G., Kresinski, J., Lee, G., Limmongkol, S., Lindenmeyer, C. W., Long, D. C., Loomis, C. L., McGehee, P. M., Mantsch, P. M., Neilsen, Jr., E. H., Neswold, R. M., Newman, P. R., Nitta, A., Peoples, Jr., J., Pier, J. R., Prieto, P. S., Prosapio, A., Rivetta, C., Schneider, D. P., Snedden, S., and Wang, S.-i. (2006). The 2.5 m Telescope of the Sloan Digital Sky Survey. *AJ*, 131:2332–2359.
- Guo, Q., White, S., Boylan-Kolchin, M., De Lucia, G., Kauffmann, G., Lemson, G., Li, C., Springel, V., and Weinmann, S. (2011). From dwarf spheroidals to cD galaxies: simulating the galaxy population in a  $\Lambda$ CDM cosmology. *MNRAS*, 413:101–131.
- Gurung-López, S., Orsi, Á. A., Bonoli, S., Baugh, C. M., and Lacey, C. G. (2019). Ly $\alpha$  emitters in a cosmological volume - I. The impact of radiative transfer. *MNRAS*, 486:1882–1906.
- Gurung-Lopez, S., Orsi, A. A., Bonoli, S., Padilla, N., Lacey, C. G., and Baugh, C. M. (2019). Lyman-alpha emitters in a cosmological volume II: the impact of the intergalactic medium. *arXiv e-prints*.
- Habouzit, M., Volonteri, M., Latif, M., Dubois, Y., and Peirani, S. (2016). On the number density of 'direct collapse' black hole seeds. *MNRAS*, 463(1):529–540.
- Haehnelt, M. G. (1994). Low-Frequency Gravitational Waves from Supermassive Black-Holes. *MNRAS*, 269:199.
- Haehnelt, M. G. and Kauffmann, G. (2000). The correlation between black hole mass and bulge velocity dispersion in hierarchical galaxy formation models. *MNRAS*, 318(3):L35–L38.



- Haehnelt, M. G., Natarajan, P., and Rees, M. J. (1998). High-redshift galaxies, their active nuclei and central black holes. *MNRAS*, 300(3):817–827.
- Haehnelt, M. G. and Rees, M. J. (1993). The formation of nuclei in newly formed galaxies and the evolution of the quasar population. *Monthly Notices of the Royal Astronomical Society*, 263(1):168–178.
- Haiman, Z., Rees, M. J., and Loeb, A. (1997). Destruction of Molecular Hydrogen during Cosmological Reionization. *ApJ*, 476(2):458–463.
- Hammer, F., Flores, H., Elbaz, D., Zheng, X. Z., Liang, Y. C., and Cesarsky, C. (2005). Did most present-day spirals form during the last 8 Gyr?. A formation history with violent episodes revealed by panchromatic observations. *A&A*, 430:115–128.
- Häring, N. and Rix, H.-W. (2004a). On the Black Hole Mass-Bulge Mass Relation. *ApJ*, 604:L89–L92.
- Häring, N. and Rix, H.-W. (2004b). On the Black Hole Mass-Bulge Mass Relation. *ApJ*, 604(2):L89–L92.
- Hartwick, F. D. A. and Schade, D. (1990). The space distribution of quasars. *ARA&A*, 28:437–489.
- Hasinger, G., Miyaji, T., and Schmidt, M. (2005). Luminosity-dependent evolution of soft X-ray selected AGN. New Chandra and XMM-Newton surveys. *A&A*, 441(2):417–434.
- Hatfield, P. W., Laigle, C., Jarvis, M. J., Devriendt, J., Davidzon, I., Ilbert, O., Pichon, C., and Dubois, Y. (2019). Comparing galaxy clustering in Horizon-AGN simulated light-cone mocks and VIDEO observations. *MNRAS*, 490(4):5043–5056.
- Hatton, S., Devriendt, J. E. G., Ninin, S., Bouchet, F. R., Guiderdoni, B., and Vibert, D. (2003). GALICS-I. A hybrid N-body/semi-analytic model of hierarchical galaxy formation. *MNRAS*, 343:75–106.
- Hayashi, M., Tanaka, M., Shimakawa, R., Furusawa, H., Momose, R., Koyama, Y., Silverman, J. D., Kodama, T., Komiyama, Y., Leauthaud, A., Lin, Y.-T., Miyazaki, S., Nagao, T., Nishizawa, A. J., Ouchi, M., Shibuya, T., Tadaki, K.-i., and Yabe, K. (2018). A 16 deg<sup>2</sup> survey of emission-line galaxies at  $z < 1.5$  in HSC-SSP Public Data Release 1. *PASJ*, 70:S17.
- Heavens, A., Panter, B., Jimenez, R., and Dunlop, J. (2004). The star-formation history of the Universe from the stellar populations of nearby galaxies. *Nature*, 428(6983):625–627.
- Heckman, T. M., Lehnert, M. D., Strickland, D. K., and Armus, L. (2000). Absorption-Line Probes of Gas and Dust in Galactic Superwinds. *ApJS*, 129(2):493–516.
- Heger, A. and Woosley, S. E. (2002). The Nucleosynthetic Signature of Population III. *ApJ*, 567:532–543.
- Hellwing, W. A., Frenk, C. S., Cautun, M., Bose, S., Helly, J., Jenkins, A., Sawala, T., and Cytowski, M. (2016a). The Copernicus Complexio: a high-resolution view of the small-scale Universe. *MNRAS*, 457(4):3492–3509.
- Hellwing, W. A., Schaller, M., Frenk, C. S., Theuns, T., Schaye, J., Bower, R. G., and Crain, R. A. (2016b). The effect of baryons on redshift space distortions and cosmic density and velocity fields in the EAGLE simulation. *MNRAS*, 461(1):L11–L15.
- Henriques, B. M. B., Thomas, P. A., Oliver, S., and Roseboom, I. (2009). Monte Carlo Markov Chain parameter estimation in semi-analytic models of galaxy formation. *MNRAS*, 396(1):535–547.

- Henriques, B. M. B., White, S. D. M., Thomas, P. A., Angulo, R., Guo, Q., Lemson, G., Springel, V., and Overzier, R. (2015). Galaxy formation in the Planck cosmology - I. Matching the observed evolution of star formation rates, colours and stellar masses. *MNRAS*, 451:2663–2680.
- Henriques, B. M. B., White, S. D. M., Thomas, P. A., Angulo, R. E., Guo, Q., Lemson, G., and Springel, V. (2013). Simulations of the galaxy population constrained by observations from  $z = 3$  to the present day: implications for galactic winds and the fate of their ejecta. *MNRAS*, 431(4):3373–3395.
- Henriques, B. M. B., White, S. D. M., Thomas, P. A., Angulo, R. E., Guo, Q., Lemson, G., and Wang, W. (2017). Galaxy formation in the Planck cosmology - IV. Mass and environmental quenching, conformity and clustering. *MNRAS*, 469:2626–2645.
- Hernquist, L. (1989). Tidal triggering of starbursts and nuclear activity in galaxies. *Nature*, 340(6236):687–691.
- Hernquist, L. (1990). An analytical model for spherical galaxies and bulges. *ApJ*, 356:359–364.
- Hernquist, L. (1992). Structure of Merger Remnants. I. Bulgeless Progenitors. *ApJ*, 400:460.
- Hernquist, L. (1993). Structure of Merger Remnants. II. Progenitors with Rotating Bulges. *ApJ*, 409:548.
- Herrmann, F., Hinder, I., Shoemaker, D., and Laguna, P. (2007a). Unequal mass binary black hole plunges and gravitational recoil. *Classical and Quantum Gravity*, 24(12):S33–S42.
- Herrmann, F., Hinder, I., Shoemaker, D. M., Laguna, P., and Matzner, R. A. (2007b). Binary black holes: Spin dynamics and gravitational recoil. *Phys. Rev. D*, 76(8):084032.
- Hewett, P. C., Foltz, C. B., and Chaffee, F. H. (1993). The Evolution of Bright, Optically Selected QSOs. *ApJ*, 406:L43.
- Hidalgo, S. L., Aparicio, A., Skillman, E., Monelli, M., Gallart, C., Cole, A., Dolphin, A., Weisz, D., Bernard, E. J., Cassisi, S., Mayer, L., Stetson, P., Tolstoy, E., and Ferguson, H. (2011). The ACS LCID Project. V. The Star Formation History of the Dwarf Galaxy LGS-3: Clues to Cosmic Reionization and Feedback. *ApJ*, 730(1):14.
- Hinder, I., Vaishnav, B., Herrmann, F., Shoemaker, D. M., and Laguna, P. (2008). Circularization and final spin in eccentric binary-black-hole inspirals. *Phys. Rev. D*, 77(8):081502.
- Hirschmann, M., Dolag, K., Saro, A., Bachmann, L., Borgani, S., and Burkert, A. (2014). Cosmological simulations of black hole growth: AGN luminosities and downsizing. *MNRAS*, 442(3):2304–2324.
- Hirschmann, M., Somerville, R. S., Naab, T., and Burkert, A. (2012). Origin of the antihierarchical growth of black holes. *MNRAS*, 426:237–257.
- Hoffman, L. and Loeb, A. (2007). Dynamics of triple black hole systems in hierarchically merging massive galaxies. *MNRAS*, 377(3):957–976.
- Hogg, D. W., Blanton, M., Strateva, I., Bahcall, N. A., Brinkmann, J., Csabai, I., Doi, M., Fukugita, M., Hennessy, G., Ivezić, Ž., Knapp, G. R., Lamb, D. Q., Lupton, R., Munn, J. A., Nichol, R., Schlegel, D. J., Schneider, D. P., and York, D. G. (2002). The Luminosity Density of Red Galaxies. *AJ*, 124(2):646–651.
- Hogg, D. W., Pahre, M. A., McCarthy, J. K., Cohen, J. G., Blandford, R., Smail, I., and Soifer, B. T. (1997). Counts and colours of faint galaxies in the U and R bands. *MNRAS*, 288:404–410.
- Holley-Bockelmann, K., Weinberg, M., and Katz, N. (2005). Bar-induced evolution of dark matter cusps. *MNRAS*, 363(3):991–1007.

- Holt, J., Tadhunter, C. N., and Morganti, R. (2008). Fast outflows in compact radio sources: evidence for AGN-induced feedback in the early stages of radio source evolution. *MNRAS*, 387(2):639–659.
- Holt, S. S., Mushotzky, R. F., Becker, R. H., Boldt, E. A., Serlemitsos, P. J., Szymkowiak, A. E., and White, N. E. (1980). X-ray spectral constraints on the broad-line cloud geometry of NGC 4151. *ApJ*, 241:L13–L17.
- Homan, J., Wijnands, R., van der Klis, M., Belloni, T., van Paradijs, J., Klein-Wolt, M., Fender, R., and Méndez, M. (2001). Correlated X-Ray Spectral and Timing Behavior of the Black Hole Candidate XTE J1550-564: A New Interpretation of Black Hole States. *ApJS*, 132(2):377–402.
- Hopkins, P. F., Cox, T. J., Younger, J. D., and Hernquist, L. (2009a). How do Disks Survive Mergers? *ApJ*, 691(2):1168–1201.
- Hopkins, P. F., Cox, T. J., Younger, J. D., and Hernquist, L. (2009b). How do Disks Survive Mergers? *ApJ*, 691:1168–1201.
- Hopkins, P. F., Hernquist, L., Cox, T. J., Robertson, B., Di Matteo, T., and Springel, V. (2006a). The Evolution in the Faint-End Slope of the Quasar Luminosity Function. *ApJ*, 639(2):700–709.
- Hopkins, P. F., Hernquist, L., Martini, P., Cox, T. J., Robertson, B., Di Matteo, T., and Springel, V. (2005). A Physical Model for the Origin of Quasar Lifetimes. *ApJ*, 625:L71–L74.
- Hopkins, P. F., Narayan, R., and Hernquist, L. (2006b). How Much Mass Do Supermassive Black Holes Eat in Their Old Age? *ApJ*, 643:641–651.
- Hopkins, P. F. and Quataert, E. (2010). How do massive black holes get their gas? *MNRAS*, 407(3):1529–1564.
- Hopkins, P. F. and Quataert, E. (2011). An explanation for the slopes of stellar cusps in galaxy spheroids. *MNRAS*, 411(1):L61–L65.
- Hopkins, P. F., Richards, G. T., and Hernquist, L. (2007). An Observational Determination of the Bolometric Quasar Luminosity Function. *ApJ*, 654:731–753.
- Hopkins, P. F., Robertson, B., Krause, E., Hernquist, L., and Cox, T. J. (2006c). An Upper Limit to the Degree of Evolution between Supermassive Black Holes and Their Host Galaxies. *ApJ*, 652(1):107–111.
- Hopkins, P. F., Somerville, R. S., Cox, T. J., Hernquist, L., Jogee, S., Kereš, D., Ma, C.-P., Robertson, B., and Stewart, K. (2009c). The effects of gas on morphological transformation in mergers: implications for bulge and disc demographics. *MNRAS*, 397:802–814.
- Hoversten, E. A., Gronwall, C., Vanden Berk, D. E., Koch, T. S., Breeveld, A. A., Curran, P. A., Hinshaw, D. A., Marshall, F. E., Roming, P. W. A., Siegel, M. H., and Still, M. (2009). Ultraviolet Number Counts of Galaxies from Swift Ultraviolet/Optical Telescope Deep Imaging of the Chandra Deep Field South. *ApJ*, 705:1462–1468.
- Huang, J.-S., Thompson, D., Kümmel, M. W., Meisenheimer, K., Wolf, C., Beckwith, S. V. W., Fockenbrock, R., Fried, J. W., Hippelein, H., von Kuhlmann, B., Phleps, S., Röser, H.-J., and Thommes, E. (2001). The Calar Alto Deep Imaging Survey: K-band Galaxy number counts. *A&A*, 368:787–796.
- Hubble, E. P. (1926). Extragalactic nebulae. *ApJ*, 64:321–369.
- Hunt, M. P., Steidel, C. C., Adelberger, K. L., and Shapley, A. E. (2004). The Faint End of the QSO Luminosity Function at  $z=3$ . *ApJ*, 605(2):625–630.

- Hut, P. and Rees, M. J. (1992). Constraints on massive black holes as dark matter candidates. *MNRAS*, 259:27P–30P.
- Ilbert, O., Capak, P., Salvato, M., Aussel, H., McCracken, H. J., Sanders, D. B., Scoville, N., Kartaltepe, J., Arnouts, S., Le Floch, E., Mobasher, B., Taniguchi, Y., Lamareille, F., Leauthaud, A., Sasaki, S., Thompson, D., Zamojski, M., Zamorani, G., Bardelli, S., Bolzonella, M., Bongiorno, A., Brusa, M., Caputi, K. I., Carollo, C. M., Contini, T., Cook, R., Coppa, G., Cucciati, O., de la Torre, S., de Ravel, L., Franzetti, P., Garilli, B., Hasinger, G., Iovino, A., Kampczyk, P., Kneib, J.-P., Knobel, C., Kovac, K., Le Borgne, J. F., Le Brun, V., Le Fèvre, O., Lilly, S.,Looper, D., Maier, C., Mainieri, V., Mellier, Y., Mignoli, M., Murayama, T., Pellò, R., Peng, Y., Pérez-Montero, E., Renzini, A., Ricciardelli, E., Schiminovich, D., Scodeggio, M., Shioya, Y., Silverman, J., Surace, J., Tanaka, M., Tasca, L., Tresse, L., Vergani, D., and Zucca, E. (2009). Cosmos Photometric Redshifts with 30-Bands for 2-deg<sup>2</sup>. *ApJ*, 690:1236–1249.
- Illingworth, G. (1977). Rotation (?) in 13 elliptical galaxies. *ApJ*, 218:L43–L47.
- Irodoutou, D., Thomas, P. A., Henriques, B. M., and Sargent, M. T. (2018). Morphological evolution and galactic sizes in the L-Galaxies SA model. *ArXiv e-prints*.
- Ishiyama, T., Enoki, M., Kobayashi, M. A. R., Makiya, R., Nagashima, M., and Oogi, T. (2015). The  $\nu^2$ GC simulations: Quantifying the dark side of the universe in the Planck cosmology. *PASJ*, 67(4):61.
- Izquierdo-Villalba, D., Bonoli, S., Dotti, M., Sesana, A., Rosas-Guevara, Y., and Spinoso, D. (2020). From galactic nuclei to the halo outskirts: tracing supermassive black holes across cosmic history and environments. *MNRAS*, 495(4):4681–4706.
- Izquierdo-Villalba, D., Bonoli, S., Spinoso, D., Rosas-Guevara, Y., Henriques, B. M. B., and Hernández-Monteagudo, C. (2019). The build-up of pseudo-bulges in a hierarchical universe. *MNRAS*, 488(1):609–632.
- Izquierdo-Villalba, D., Orsi, Á. A., Bonoli, S., Lacey, C. G., Baugh, C. M., and Griffin, A. J. (2018). The environment of radio galaxies: a signature of AGN feedback at high redshifts. *MNRAS*, 480(1):1340–1352.
- Jaffe, A. H. and Backer, D. C. (2003). Gravitational Waves Probe the Coalescence Rate of Massive Black Hole Binaries. *ApJ*, 583(2):616–631.
- Jefremov, P. I., Tsupko, O. Y., and Bisnovatyi-Kogan, G. S. (2015). Innermost stable circular orbits of spinning test particles in Schwarzschild and Kerr space-times. *Phys. Rev. D*, 91(12):124030.
- Jogee, S., Barazza, F. D., Rix, H.-W., Shlosman, I., Barden, M., Wolf, C., Davies, J., Heyer, I., Beckwith, S. V. W., Bell, E. F., Borch, A., Caldwell, J. A. R., Conselice, C. J., Dahlen, T., Häussler, B., Heymans, C., Jahnke, K., Knapen, J. H., Laine, S., Lubell, G. M., Mobasher, B., McIntosh, D. H., Meisenheimer, K., Peng, C. Y., Ravindranath, S., Sanchez, S. F., Somerville, R. S., and Wisotzki, L. (2004). Bar Evolution over the Last 8 Billion Years: A Constant Fraction of Strong Bars in the GEMS Survey. *ApJ*, 615(2):L105–L108.
- Johnson, J. L., Khochfar, S., Greif, T. H., and Durier, F. (2011). Accretion on to black holes formed by direct collapse. *MNRAS*, 410(2):919–933.
- Jones, L. R., Fong, R., Shanks, T., Ellis, R. S., and Peterson, B. A. (1991). Galaxy number counts. I - Photographic observations to B = 23.5 mag. *MNRAS*, 249:481–497.
- Kalfountzou, E., Santos Lleo, M., and Trichas, M. (2017). SDSS J1056+5516: A Triple AGN or an SMBH Recoil Candidate? *ApJ*, 851(1):L15.

- Kalnajns, A. J. (1972). The Equilibria and Oscillations of a Family of Uniformly Rotating Stellar Disks. *ApJ*, 175:63.
- Kartaltepe, J. S., Dickinson, M., Alexander, D. M., Bell, E. F., Dahlen, T., Elbaz, D., Faber, S. M., Lotz, J., McIntosh, D. H., Wiklind, T., Altieri, B., Aussel, H., Bethermin, M., Bournaud, F., Charmandaris, V., Conselice, C. J., Cooray, A., Dannerbauer, H., Davé, R., Dunlop, J., Dekel, A., Ferguson, H. C., Grogin, N. A., Hwang, H. S., Ivison, R., Kocevski, D., Koekemoer, A., Koo, D. C., Lai, K., Leiton, R., Lucas, R. A., Lutz, D., Magdis, G., Magnelli, B., Morrison, G., Mozena, M., Mullaney, J., Newman, J. A., Pope, A., Popesso, P., van der Wel, A., Weiner, B., and Wuyts, S. (2012). GOODS-Herschel and CANDELS: The Morphologies of Ultraluminous Infrared Galaxies at  $z \sim 2$ . *ApJ*, 757(1):23.
- Kashikawa, N., Shimasaku, K., Yasuda, N., Ajiki, M., Akiyama, M., Ando, H., Aoki, K., Doi, M., Fujita, S. S., Furusawa, H., Hayashino, T., Iwamuro, F., Iye, M., Karoji, H., Kobayashi, N., Kodaira, K., Kodama, T., Komiyama, Y., Matsuda, Y., Miyazaki, S., Mizumoto, Y., Morokuma, T., Motohara, K., Murayama, T., Nagao, T., Nariai, K., Ohta, K., Okamura, S., Ouchi, M., Sasaki, T., Sato, Y., Sekiguchi, K., Shioya, Y., Tamura, H., Taniguchi, Y., Umemura, M., Yamada, T., and Yoshida, M. (2004). The Subaru Deep Field: The Optical Imaging Data. *PASJ*, 56:1011–1023.
- Kataria, S. K. and Das, M. (2018). A study of the effect of bulges on bar formation in disc galaxies. *MNRAS*, 475(2):1653–1664.
- Kataria, S. K., Das, M., and Barway, S. (2020). Testing a theoretical prediction for bar formation in galaxies with bulges. *A&A*, 640:A14.
- Kauffmann, G. (1996a). Disc galaxies at  $z=0$  and at high redshift: an explanation of the observed evolution of damped Ly $\alpha$  absorption systems. *MNRAS*, 281(2):475–486.
- Kauffmann, G. (1996b). The age of elliptical galaxies and bulges in a merger model. *MNRAS*, 281:487–492.
- Kauffmann, G., Colberg, J. M., Diaferio, A., and White, S. D. M. (1999a). Clustering of galaxies in a hierarchical universe - I. Methods and results at  $z=0$ . *MNRAS*, 303(1):188–206.
- Kauffmann, G., Colberg, J. M., Diaferio, A., and White, S. D. M. (1999b). Clustering of galaxies in a hierarchical universe - II. Evolution to high redshift. *MNRAS*, 307(3):529–536.
- Kauffmann, G. and Haehnelt, M. (2000). A unified model for the evolution of galaxies and quasars. *MNRAS*, 311:576–588.
- Kauffmann, G., White, S. D. M., and Guiderdoni, B. (1993a). The formation and evolution of galaxies within merging dark matter haloes. *MNRAS*, 264:201–218.
- Kauffmann, G., White, S. D. M., and Guiderdoni, B. (1993b). The Formation and Evolution of Galaxies Within Merging Dark Matter Haloes. *MNRAS*, 264:201.
- Kazantzidis, S., Bullock, J. S., Zentner, A. R., Kravtsov, A. V., and Moustakas, L. A. (2008). Cold Dark Matter Substructure and Galactic Disks. I. Morphological Signatures of Hierarchical Satellite Accretion. *ApJ*, 688:254–276.
- Keller, B. W., Wadsley, J., and Couchman, H. M. P. (2016). Cosmological galaxy evolution with super-bubble feedback - II. The limits of supernovae. *MNRAS*, 463(2):1431–1445.
- Kelley, L. Z., Blecha, L., and Hernquist, L. (2017a). Massive black hole binary mergers in dynamical galactic environments. *MNRAS*, 464(3):3131–3157.
- Kelley, L. Z., Blecha, L., Hernquist, L., Sesana, A., and Taylor, S. R. (2017b). The gravitational wave background from massive black hole binaries in Illustris: spectral features and time to detection with pulsar timing arrays. *MNRAS*, 471(4):4508–4526.

- Kent, S. M. (1992). Galactic Structure from the Spacelab Infrared Telescope. III. A Dynamical Model for the Milky Way Bulge. *ApJ*, 387:181.
- Kerr, R. P. (1963). Gravitational Field of a Spinning Mass as an Example of Algebraically Special Metrics. *Phys. Rev. Lett.*, 11(5):237–238.
- Kerr, R. P. (1965). Gravitational Collapse and Rotation. In Robinson, I., Schild, A., and Schucking, E. L., editors, *Quasi-Stellar Sources and Gravitational Collapse*, page 99.
- Khandai, N., Di Matteo, T., Croft, R., Wilkins, S., Feng, Y., Tucker, E., DeGraf, C., and Liu, M.-S. (2015). The MassiveBlack-II simulation: the evolution of haloes and galaxies to  $z \sim 0$ . *MNRAS*, 450(2):1349–1374.
- Khochfar, S. and Burkert, A. (2005). On the origin of isophotal shapes in elliptical galaxies. *MNRAS*, 359(4):1379–1385.
- Khostovan, A. A., Sobral, D., Mobasher, B., Best, P. N., Smail, I., Stott, J. P., Hemmati, S., and Nayyeri, H. (2015). Evolution of the  $H\beta + [O III]$  and  $[O II]$  luminosity functions and the  $[O II]$  star formation history of the Universe up to  $z \sim 5$  from HiZELS. *MNRAS*, 452:3948–3968.
- Kim, T., Gadotti, D. A., Athanassoula, E., Bosma, A., Sheth, K., and Lee, M. G. (2016). Evidence of bar-induced secular evolution in the inner regions of stellar discs in galaxies: what shapes disc galaxies? *MNRAS*, 462:3430–3440.
- King, A. R., Lubow, S. H., Ogilvie, G. I., and Pringle, J. E. (2005). Aligning spinning black holes and accretion discs. *MNRAS*, 363:49–56.
- King, A. R. and Pringle, J. E. (2006). Growing supermassive black holes by chaotic accretion. *Monthly Notices of the Royal Astronomical Society: Letters*, 373(1):L90–L92.
- King, A. R. and Pringle, J. E. (2007). Fuelling active galactic nuclei. *MNRAS*, 377:L25–L28.
- King, A. R., Pringle, J. E., and Hofmann, J. A. (2008). The evolution of black hole mass and spin in active galactic nuclei. *MNRAS*, 385:1621–1627.
- Kitzbichler, M. G. and White, S. D. M. (2007a). The high-redshift galaxy population in hierarchical galaxy formation models. *MNRAS*, 376:2–12.
- Kitzbichler, M. G. and White, S. D. M. (2007b). The high-redshift galaxy population in hierarchical galaxy formation models. *MNRAS*, 376:2–12.
- Klypin, A. A., Trujillo-Gomez, S., and Primack, J. (2011). Dark Matter Halos in the Standard Cosmological Model: Results from the Bolshoi Simulation. *ApJ*, 740(2):102.
- Knapen, J. H. (1999). Observations of Barred Galaxies. In Beckman, J. E. and Mahoney, T. J., editors, *The Evolution of Galaxies on Cosmological Timescales*, volume 187 of *Astronomical Society of the Pacific Conference Series*, pages 72–87.
- Kodama, T., Bower, R. G., and Bell, E. F. (1999). The colour-magnitude relation of early-type galaxies in the Hubble Deep Field. *MNRAS*, 306(3):561–566.
- Koekemoer, A. M., Faber, S. M., Ferguson, H. C., Grogin, N. A., Kocevski, D. D., Koo, D. C., Lai, K., Lotz, J. M., Lucas, R. A., McGrath, E. J., Ogaz, S., Rajan, A., Riess, A. G., Rodney, S. A., Strolger, L., Casertano, S., Castellano, M., Dahlen, T., Dickinson, M., Dolch, T., Fontana, A., Giavalisco, M., Grazian, A., Guo, Y., Hathi, N. P., Huang, K.-H., van der Wel, A., Yan, H.-J., Acquaviva, V., Alexander, D. M., Almaini, O., Ashby, M. L. N., Barden, M., Bell, E. F., Bournaud, F., Brown, T. M., Caputi, K. I., Cassata, P., Challis, P. J., Chary, R.-R., Cheung, E., Cirasuolo, M., Conselice,



- C. J., Roshan Cooray, A., Croton, D. J., Daddi, E., Davé, R., de Mello, D. F., de Ravel, L., Dekel, A., Donley, J. L., Dunlop, J. S., Dutton, A. A., Elbaz, D., Fazio, G. G., Filippenko, A. V., Finkelstein, S. L., Frazer, C., Gardner, J. P., Garnavich, P. M., Gawiser, E., Gruetzbauch, R., Hartley, W. G., Häussler, B., Herrington, J., Hopkins, P. F., Huang, J.-S., Jha, S. W., Johnson, A., Kartaltepe, J. S., Khostovan, A. A., Kirshner, R. P., Lani, C., Lee, K.-S., Li, W., Madau, P., McCarthy, P. J., McIntosh, D. H., McLure, R. J., McPartland, C., Mobasher, B., Moreira, H., Mortlock, A., Moustakas, L. A., Mozena, M., Nandra, K., Newman, J. A., Nielsen, J. L., Niemi, S., Noeske, K. G., Papovich, C. J., Pentericci, L., Pope, A., Primack, J. R., Ravindranath, S., Reddy, N. A., Renzini, A., Rix, H.-W., Robaina, A. R., Rosario, D. J., Rosati, P., Salimbeni, S., Scarlata, C., Siana, B., Simard, L., Smidt, J., Snyder, D., Somerville, R. S., Spinrad, H., Straughn, A. N., Telford, O., Teplitz, H. I., Trump, J. R., Vargas, C., Villforth, C., Wagner, C. R., Wand ro, P., Wechsler, R. H., Weiner, B. J., Wiklind, T., Wild, V., Wilson, G., Wuyts, S., and Yun, M. S. (2011). CANDELS: The Cosmic Assembly Near-infrared Deep Extragalactic Legacy Survey—The Hubble Space Telescope Observations, Imaging Data Products, and Mosaics. *ApJS*, 197(2):36.
- Komossa, S. (2012). Recoiling Black Holes: Electromagnetic Signatures, Candidates, and Astrophysical Implications. *Advances in Astronomy*, 2012:364973.
- Koo, D. C. (1986). Multicolor photometry of field galaxies to  $B = 24$ . *ApJ*, 311:651–679.
- Kormendy, J. (1982). Rotation of the bulge components of barred galaxies. *ApJ*, 257:75–88.
- Kormendy, J. (1983). The stellar kinematics and dynamics of barred galaxies. I. NGC 936. *ApJ*, 275:529–548.
- Kormendy, J. (1988a). Evidence for a Central Dark Mass in NGC 4594 (The Sombrero Galaxy). *ApJ*, 335:40.
- Kormendy, J. (1988b). Evidence for a Supermassive Black Hole in the Nucleus of M31. *ApJ*, 325:128.
- Kormendy, J. (1993). Kinematics of extragalactic bulges: evidence that some bulges are really disks. In Dejonghe, H. and Habing, H. J., editors, *Galactic Bulges*, volume 153 of *IAU Symposium*, page 209.
- Kormendy, J. and Bender, R. (1996). A Proposed Revision of the Hubble Sequence for Elliptical Galaxies. *ApJ*, 464:L119.
- Kormendy, J. and Ho, L. C. (2013). Coevolution (Or Not) of Supermassive Black Holes and Host Galaxies. *ARA&A*, 51:511–653.
- Kormendy, J. and Kennicutt, Jr., R. C. (2004a). Secular Evolution and the Formation of Pseudobulges in Disk Galaxies. *ARA&A*, 42:603–683.
- Kormendy, J. and Kennicutt, Jr., R. C. (2004b). Secular Evolution and the Formation of Pseudobulges in Disk Galaxies. *ARA&A*, 42:603–683.
- Kormendy, J. and Richstone, D. (1992). Evidence for a Supermassive Black Hole in NGC 3115. *ApJ*, 393:559.
- Kormendy, J. and Richstone, D. (1995). Inward Bound—The Search For Supermassive Black Holes In Galactic Nuclei. *ARA&A*, 33:581.
- Koushiappas, S. M., Bullock, J. S., and Dekel, A. (2004). Massive black hole seeds from low angular momentum material. *MNRAS*, 354:292–304.
- Kuijken, K. and Merrifield, M. R. (1995). Establishing the Connection between Peanut-shaped Bulges and Galactic Bars. *ApJ*, 443:L13.

- Lacey, C. and Cole, S. (1993). Merger rates in hierarchical models of galaxy formation. *MNRAS*, 262(3):627–649.
- Lacey, C. G., Baugh, C. M., Frenk, C. S., Benson, A. J., Bower, R. G., Cole, S., Gonzalez-Perez, V., Helly, J. C., Lagos, C. D. P., and Mitchell, P. D. (2016). A unified multiwavelength model of galaxy formation. *MNRAS*, 462:3854–3911.
- Lagos, C. D. P., Baugh, C. M., Lacey, C. G., Benson, A. J., Kim, H.-S., and Power, C. (2011). Cosmic evolution of the atomic and molecular gas contents of galaxies. *MNRAS*, 418:1649–1667.
- Lagos, C. D. P., Cora, S. A., and Padilla, N. D. (2008). Effects of AGN feedback on  $\Lambda$ CDM galaxies. *MNRAS*, 388(2):587–602.
- Lagos, C. d. P., Tobar, R. J., Robotham, A. S. G., Obreschkow, D., Mitchell, P. D., Power, C., and Elahi, P. J. (2018). Shark: introducing an open source, free and flexible semi-analytic model of galaxy formation. *ArXiv e-prints*.
- Landy, S. D. and Szalay, A. S. (1993). Bias and variance of angular correlation functions. *ApJ*, 412:64–71.
- Lang, M., Holley-Bockelmann, K., and Sinha, M. (2014). Bar Formation from Galaxy Flybys. *ApJ*, 790(2):L33.
- Lange, R., Driver, S. P., Robotham, A. S. G., Kelvin, L. S., Graham, A. W., Alpaslan, M., Andrews, S. K., Baldry, I. K., Bamford, S., Bland-Hawthorn, J., Brough, S., Cluver, M. E., Conselice, C. J., Davies, L. J. M., Haeussler, B., Konstantopoulos, I. S., Loveday, J., Moffett, A. J., Norberg, P., Phillipps, S., Taylor, E. N., López-Sánchez, Á. R., and Wilkins, S. M. (2015). Galaxy And Mass Assembly (GAMA): mass-size relations of  $z \sim 0.1$  galaxies subdivided by Sérsic index, colour and morphology. *MNRAS*, 447:2603–2630.
- Laor, A., Netzer, H., and Piran, T. (1990). Massive thin accretion discs. II - Polarization. *MNRAS*, 242:560–569.
- Larson, R. B. (1974). Dynamical models for the formation and evolution of spherical galaxies. *MNRAS*, 166:585–616.
- Laureijs, R., Amiaux, J., Arduini, S., Auguères, J. ., Brinchmann, J., Cole, R., Cropper, M., Dabin, C., Duvet, L., Ealet, A., and et al. (2011). Euclid Definition Study Report. *arXiv e-prints*.
- Laurikainen, E. and Salo, H. (2016). Observed Properties of Boxy/Peanut/Barlens Bulges. In Laurikainen, E., Peletier, R., and Gadotti, D., editors, *Galactic Bulges*, volume 418 of *Astrophysics and Space Science Library*, page 77.
- Lawrence, A. (1987). Classification of active galaxies and the prospect of a unified phenomenology. *PASP*, 99:309–334.
- Leitherer, C. and Heckman, T. M. (1995). Synthetic properties of starburst galaxies. *ApJS*, 96:9–38.
- Lena, D., Robinson, A., Marconi, A., Axon, D. J., Capetti, A., Merritt, D., and Batcheldor, D. (2014). Recoiling Supermassive Black Holes: A Search in the Nearby Universe. *ApJ*, 795(2):146.
- Levesque, E. M., Kewley, L. J., and Larson, K. L. (2010). Theoretical Modeling of Star-Forming Galaxies. I. Emission-Line Diagnostic Grids for Local and Low-Metallicity Galaxies. *AJ*, 139:712–727.
- Li, M., Ostriker, J. P., Cen, R., Bryan, G. L., and Naab, T. (2015). Supernova Feedback and the Hot Gas Filling Fraction of the Interstellar Medium. *ApJ*, 814(1):4.

- Li, Y., Hernquist, L., Robertson, B., Cox, T. J., Hopkins, P. F., Springel, V., Gao, L., Di Matteo, T., Zentner, A. R., Jenkins, A., and Yoshida, N. (2007). Formation of  $z \sim 6$  Quasars from Hierarchical Galaxy Mergers. *ApJ*, 665:187–208.
- Lightman, A. P. and White, T. R. (1988). Effects of Cold Matter in Active Galactic Nuclei: A Broad Hump in the X-Ray Spectra. *ApJ*, 335:57.
- Lo, K. Y., Backer, D. C., Ekers, R. D., Kellermann, K. I., Reid, M., and Moran, J. M. (1985). On the size of the galactic centre compact radio source: diameter  $\sim 20$  AU. *Nature*, 315(6015):124–126.
- Lodato, G. and Gerosa, D. (2013). Black hole mergers: do gas discs lead to spin alignment? *MNRAS*, 429:L30–L34.
- Lodato, G. and Natarajan, P. (2006). Supermassive black hole formation during the assembly of pregalactic discs. *MNRAS*, 371(4):1813–1823.
- Loeb, A. (2007). Observable Signatures of a Black Hole Ejected by Gravitational-Radiation Recoil in a Galaxy Merger. *Phys. Rev. Lett.*, 99(4):041103.
- López-Sanjuan, C., Vázquez Ramió, H., Varela, J., Spinoso, D., Angulo, R. E., Muniesa, D., Viironen, K., Cristóbal-Hornillos, D., Cenarro, A. J., and Ederoclite, A. (2019). J-PLUS: Morphological star/galaxy classification by PDF analysis. *A&A*, 622:A177.
- Lousto, C. O. and Zlochower, Y. (2008). Further insight into gravitational recoil. *Phys. Rev. D*, 77(4):044028.
- Lousto, C. O. and Zlochower, Y. (2011). Hangup Kicks: Still Larger Recoils by Partial Spin-Orbit Alignment of Black-Hole Binaries. *Phys. Rev. Lett.*, 107(23):231102.
- Lousto, C. O. and Zlochower, Y. (2013). Nonlinear gravitational recoil from the mergers of precessing black-hole binaries. *Phys. Rev. D*, 87(8):084027.
- Lousto, C. O., Zlochower, Y., Dotti, M., and Volonteri, M. (2012). Gravitational recoil from accretion-aligned black-hole binaries. *Phys. Rev. D*, 85(8):084015.
- Ly, C., Malkan, M. A., Kashikawa, N., Shimasaku, K., Doi, M., Nagao, T., Iye, M., Kodama, T., Morokuma, T., and Motohara, K. (2007). The Luminosity Function and Star Formation Rate between Redshifts of 0.07 and 1.47 for Narrowband Emitters in the Subaru Deep Field. *ApJ*, 657:738–759.
- Lynden-Bell, D. (1969). Galactic Nuclei as Collapsed Old Quasars. *Nature*, 223(5207):690–694.
- Lynden-Bell, D. and Kalnajs, A. J. (1972). On the generating mechanism of spiral structure. *MNRAS*, 157:1.
- MacDonald, D. and Thorne, K. S. (1982). Black-hole electrodynamics - an absolute-space/universal-time formulation. *MNRAS*, 198:345–382.
- Madau, P. and Quataert, E. (2004). The Effect of Gravitational-Wave Recoil on the Demography of Massive Black Holes. *ApJ*, 606(1):L17–L20.
- Madau, P. and Rees, M. J. (2001). Massive Black Holes as Population III Remnants. *ApJ*, 551:L27–L30.
- Magorrian, J., Tremaine, S., Richstone, D., Bender, R., Bower, G., Dressler, A., Faber, S. M., Gebhardt, K., Green, R., Grillmair, C., Kormendy, J., and Lauer, T. (1998). The Demography of Massive Dark Objects in Galaxy Centers. *AJ*, 115(6):2285–2305.
- Maio, U., Borgani, S., Ciardi, B., and Petkova, M. (2019). The seeds of supermassive black holes and the role of local radiation and metal spreading. *PASA*, 36:e020.

- Maraston, C. (2005). Evolutionary population synthesis: models, analysis of the ingredients and application to high- $z$  galaxies. *MNRAS*, 362:799–825.
- Marconi, A. and Hunt, L. K. (2003). The Relation between Black Hole Mass, Bulge Mass, and Near-Infrared Luminosity. *ApJ*, 589(1):L21–L24.
- Marconi, A., Risaliti, G., Gilli, R., Hunt, L. K., Maiolino, R., and Salvati, M. (2004). Local supermassive black holes, relics of active galactic nuclei and the X-ray background. *MNRAS*, 351:169–185.
- Marian, V., Jahnke, K., Mechtley, M., Cohen, S., Husemann, B., Jones, V., Koekemoer, A., Schulze, A., van der Wel, A., Villforth, C., and Windhorst, R. A. (2019). Major Mergers Are Not the Dominant Trigger for High-accretion AGNs at  $z \sim 2$ . *ApJ*, 882(2):141.
- Marinacci, F., Pakmor, R., and Springel, V. (2014). The formation of disc galaxies in high-resolution moving-mesh cosmological simulations. *MNRAS*, 437(2):1750–1775.
- Marinova, I. and Jogee, S. (2007). Characterizing Bars at  $z \sim 0$  in the Optical and NIR: Implications for the Evolution of Barred Disks with Redshift. *ApJ*, 659(2):1176–1197.
- Marshall, M. A., Mutch, S. J., Qin, Y., Poole, G. B., and Wyithe, J. S. B. (2019a). Dark-ages reionization and galaxy formation simulation – XVIII. The high-redshift evolution of black holes and their host galaxies. *arXiv e-prints*, page arXiv:1910.08124.
- Marshall, M. A., Mutch, S. J., Qin, Y., Poole, G. B., and Wyithe, J. S. B. (2019b). Dark-ages reionization and galaxy formation simulation - XVII. Sizes, angular momenta, and morphologies of high-redshift galaxies. *MNRAS*, 488(2):1941–1959.
- Martel, H., Barai, P., and Brito, W. (2012). The Fate of Dwarf Galaxies in Clusters and the Origin of Intracluster Stars. II. Cosmological Simulations. *ApJ*, 757(1):48.
- Martin, C. L. (1999). Properties of Galactic Outflows: Measurements of the Feedback from Star Formation. *ApJ*, 513(1):156–160.
- Martin, C. L., Shapley, A. E., Coil, A. L., Kornei, K. A., Bundy, K., Weiner, B. J., Noeske, K. G., and Schiminovich, D. (2012). Demographics and Physical Properties of Gas Outflows/Inflows at  $0.4 < z < 1.4$ . *ApJ*, 760(2):127.
- Martin, G., Kaviraj, S., Volonteri, M., Simmons, B. D., Devriendt, J. E. G., Lintott, C. J., Smethurst, R. J., Dubois, Y., and Pichon, C. (2018). Normal black holes in bulge-less galaxies: the largely quiescent, merger-free growth of black holes over cosmic time. *MNRAS*, 476(2):2801–2812.
- Martin, R. G., Pringle, J. E., and Tout, C. A. (2007). Alignment and precession of a black hole with a warped accretion disc. *MNRAS*, 381(4):1617–1624.
- Martinez-Valpuesta, I., Shlosman, I., and Heller, C. (2006). Evolution of Stellar Bars in Live Axisymmetric Halos: Recurrent Buckling and Secular Growth. *ApJ*, 637(1):214–226.
- Marulli, F., Bonoli, S., Branchini, E., Moscardini, L., and Springel, V. (2008). Modelling the cosmological co-evolution of supermassive black holes and galaxies - I. BH scaling relations and the AGN luminosity function. *MNRAS*, 385:1846–1858.
- Matt, G., Fabian, A. C., and Reynolds, C. S. (1997). Geometrical and chemical dependence of K-shell X-ray features. *MNRAS*, 289(1):175–184.
- Matt, G., Fabian, A. C., and Ross, R. R. (1993). X-ray photoionized accretion discs : UV and X-ray continuum spectra and polarization. *MNRAS*, 264:839–852.
- Matteucci, F. and Tornambe, A. (1987). Chemical evolution of elliptical galaxies. *A&A*, 185(1-2):51–60.

- Matthee, J., Sobral, D., Santos, S., Röttgering, H., Darvish, B., and Mobasher, B. (2015). Identification of the brightest Ly $\alpha$  emitters at  $z = 6.6$ : implications for the evolution of the luminosity function in the reionization era. *MNRAS*, 451:400–417.
- Matthews, T. A. and Sandage, A. R. (1963). Optical Identification of 3C 48, 3C 196, and 3C 286 with Stellar Objects. *ApJ*, 138:30.
- Mayer, L. (2013). Massive black hole binaries in gas-rich galaxy mergers; multiple regimes of orbital decay and interplay with gas inflows. *Classical and Quantum Gravity*, 30(24):244008.
- Mayer, L. and Bonoli, S. (2019). The route to massive black hole formation via merger-driven direct collapse: a review. *Reports on Progress in Physics*, 82(1):016901.
- Mayer, L., Fiacconi, D., Bonoli, S., Quinn, T., Roškar, R., Shen, S., and Wadsley, J. (2015). Direct Formation of Supermassive Black Holes in Metal-enriched Gas at the Heart of High-redshift Galaxy Mergers. *ApJ*, 810(1):51.
- Mayer, L., Kazantzidis, S., Escala, A., and Callegari, S. (2010). Direct formation of supermassive black holes via multi-scale gas inflows in galaxy mergers. *Nature*, 466:1082–1084.
- Mayer, L., Kazantzidis, S., Madau, P., Colpi, M., Quinn, T., and Wadsley, J. (2007). Rapid Formation of Supermassive Black Hole Binaries in Galaxy Mergers with Gas. *Science*, 316(5833):1874.
- McCarthy, I. G., Schaye, J., Bower, R. G., Ponman, T. J., Booth, C. M., Dalla Vecchia, C., and Springel, V. (2011). Gas expulsion by quasar-driven winds as a solution to the overcooling problem in galaxy groups and clusters. *MNRAS*, 412(3):1965–1984.
- McClintock, J. E., Narayan, R., and Steiner, J. F. (2014). Black Hole Spin via Continuum Fitting and the Role of Spin in Powering Transient Jets. *Space Sci. Rev.*, 183(1-4):295–322.
- McCracken, H. J., Radovich, M., Bertin, E., Mellier, Y., Dantel-Fort, M., Le Fèvre, O., Cuillandre, J. C., Gwyn, S., Foucaud, S., and Zamorani, G. (2003). The VIRMOS deep imaging survey. II: CFH12K BVRI optical data for the 0226-04 deep field. *A&A*, 410:17–32.
- McNamara, B. R. and Nulsen, P. E. J. (2007). Heating Hot Atmospheres with Active Galactic Nuclei. *ARA&A*, 45(1):117–175.
- Menci, N., Cavaliere, A., Fontana, A., Giallongo, E., Poli, F., and Vittorini, V. (2004). Early Hierarchical Formation of Massive Galaxies Triggered by Interactions. *ApJ*, 604:12–17.
- Menci, N., Gatti, M., Fiore, F., and Lamastra, A. (2014). Triggering active galactic nuclei in hierarchical galaxy formation: disk instability vs. interactions. *A&A*, 569:A37.
- Méndez-Abreu, J., de Lorenzo-Cáceres, A., Gadotti, D. A., Fragkoudi, F., van de Ven, G., Falcón-Barroso, J., Leaman, R., Pérez, I., Querejeta, M., Sánchez-Blazquez, P., and Seidel, M. (2019). Inner bars also buckle. The MUSE TIMER view of the double-barred galaxy NGC 1291. *MNRAS*, 482:L118–L122.
- Méndez-Abreu, J., Sánchez-Janssen, R., and Aguerri, J. A. L. (2010). Which Galaxies Host Bars and Disks? A Study of the Coma Cluster. *ApJ*, 711:L61–L65.
- Menéndez-Delmestre, K., Sheth, K., Schinnerer, E., Jarrett, T. H., and Scoville, N. Z. (2007). A Near-Infrared Study of 2MASS Bars in Local Galaxies: An Anchor for High-Redshift Studies. *ApJ*, 657(2):790–804.
- Merloni, A. and Heinz, S. (2008). A synthesis model for AGN evolution: supermassive black holes growth and feedback modes. *MNRAS*, 388:1011–1030.

- Merloni, A., Predehl, P., Becker, W., Böhringer, H., Boller, T., Brunner, H., Brusa, M., Dennerl, K., Freyberg, M., Friedrich, P., Georgakakis, A., Haberl, F., Hasinger, G., Meidinger, N., Mohr, J., Nandra, K., Rau, A., Reiprich, T. H., Robrade, J., Salvato, M., Santangelo, A., Sasaki, M., Schwobe, A., Wilms, J., and German eROSITA Consortium, t. (2012). eROSITA Science Book: Mapping the Structure of the Energetic Universe. *arXiv e-prints*.
- Merloni, A., Rudnick, G., and Di Matteo, T. (2004). Tracing the cosmological assembly of stars and supermassive black holes in galaxies. *MNRAS*, 354(3):L37–L42.
- Merson, A., Wang, Y., Benson, A., Faisst, A., Masters, D., Kiessling, A., and Rhodes, J. (2018). Predicting  $H\alpha$  emission-line galaxy counts for future galaxy redshift surveys. *MNRAS*, 474:177–196.
- Merson, A. I., Baugh, C. M., Helly, J. C., Gonzalez-Perez, V., Cole, S., Bielby, R., Norberg, P., Frenk, C. S., Benson, A. J., Bower, R. G., Lacey, C. G., and Lagos, C. d. P. (2013). Lightcone mock catalogues from semi-analytic models of galaxy formation - I. Construction and application to the BzK colour selection. *MNRAS*, 429:556–578.
- Metcalf, N., Shanks, T., Campos, A., McCracken, H. J., and Fong, R. (2001). Galaxy number counts - V. Ultradeep counts: the Herschel and Hubble Deep Fields. *MNRAS*, 323:795–830.
- Mezcua, M. (2017). Observational evidence for intermediate-mass black holes. *International Journal of Modern Physics D*, 26(11):1730021.
- Mezcua, M. (2019). Dwarf galaxies might not be the birth sites of supermassive black holes. *Nature Astronomy*, 3:6–7.
- Mihos, J. C. and Hernquist, L. (1994). Triggering of Starbursts in Galaxies by Minor Mergers. *ApJ*, 425:L13.
- Mihos, J. C. and Hernquist, L. (1996a). Gasdynamics and Starbursts in Major Mergers. *ApJ*, 464:641.
- Mihos, J. C. and Hernquist, L. (1996b). Gasdynamics and Starbursts in Major Mergers. *ApJ*, 464:641.
- Miki, Y., Mori, M., Kawaguchi, T., and Saito, Y. (2014). Hunting a Wandering Supermassive Black Hole in the M31 Halo Hermitage. *ApJ*, 783(2):87.
- Mo, H., van den Bosch, F. C., and White, S. (2010). *Galaxy Formation and Evolution*.
- Mo, H. J., Mao, S., and White, S. D. M. (1998a). The formation of galactic discs. *MNRAS*, 295:319–336.
- Mo, H. J., Mao, S., and White, S. D. M. (1998b). The formation of galactic discs. *MNRAS*, 295:319–336.
- Mo, H. J. and White, S. D. M. (1996). An analytic model for the spatial clustering of dark matter haloes. *MNRAS*, 282(2):347–361.
- Moetazedian, R., Polyachenko, E. V., Berczik, P., and Just, A. (2017). Effects of galaxy-satellite interactions on bar formation. *A&A*, 604:A75.
- Moles, M., Benítez, N., Aguerri, J. A. L., Alfaro, E. J., Broadhurst, T., Cabrera-Caño, J., Castander, F. J., Cepa, J., Cerviño, M., Cristóbal-Hornillos, D., Fernández-Soto, A., González Delgado, R. M., Infante, L., Márquez, I., Martínez, V. J., Masegosa, J., del Olmo, A., Perea, J., Prada, F., Quintana, J. M., and Sánchez, S. F. (2008). The Alhambra Survey: a Large Area Multimedium-Band Optical and Near-Infrared Photometric Survey. *AJ*, 136:1325–1339.
- Molino, A., Benítez, N., Moles, M., Fernández-Soto, A., Cristóbal-Hornillos, D., Ascaso, B., Jiménez-Teja, Y., Schoenell, W., Arnalte-Mur, P., Pović, M., Coe, D., López-Sanjuan, C., Díaz-García, L. A., Varela, J., Stefanon, M., Cenarro, J., Matute, I., Masegosa, J., Márquez, I., Perea, J., Del Olmo, A., Husillos, C., Alfaro, E., Aparicio-Villegas, T., Cerviño, M., Huertas-Company, M., Aguerri, J. A. L.,



- Broadhurst, T., Cabrera-Caño, J., Cepa, J., González, R. M., Infante, L., Martínez, V. J., Prada, F., and Quintana, J. M. (2014). The ALHAMBRA Survey: Bayesian photometric redshifts with 23 bands for 3 deg. *MNRAS*, 441:2891–2922.
- Moore, B., Ghigna, S., Governato, F., Lake, G., Quinn, T., Stadel, J., and Tozzi, P. (1999). Dark Matter Substructure within Galactic Halos. *ApJ*, 524:L19–L22.
- Moorthy, B. K. and Holtzman, J. A. (2006). Stellar populations in bulges of spiral galaxies. *MNRAS*, 371:583–608.
- Morgan, E. H., Remillard, R. A., and Greiner, J. (1997). RXTE Observations of QPOs in the Black Hole Candidate GRS 1915+105. *ApJ*, 482(2):993–1010.
- Morganti, R., Tadhunter, C. N., and Oosterloo, T. A. (2005). Fast neutral outflows in powerful radio galaxies: a major source of feedback in massive galaxies. *A&A*, 444(1):L9–L13.
- Morrison, P. (1969). Are Quasi-Stellar Radio Sources Giant Pulsars? *ApJ*, 157:L73.
- Mullaney, J. R., Daddi, E., Béthermin, M., Elbaz, D., Juneau, S., Pannella, M., Sargent, M. T., Alexander, D. M., and Hickox, R. C. (2012a). The Hidden “AGN Main Sequence”: Evidence for a Universal Black Hole Accretion to Star Formation Rate Ratio since  $z \sim 2$  Producing an  $M_{BH}$ - $M_*$  Relation. *ApJ*, 753:L30.
- Mullaney, J. R., Pannella, M., Daddi, E., Alexander, D. M., Elbaz, D., Hickox, R. C., Bournaud, F., Altieri, B., Aussel, H., Coia, D., Dannerbauer, H., Dasyra, K., Dickinson, M., Hwang, H. S., Kartaltepe, J., Leiton, R., Magdis, G., Magnelli, B., Popesso, P., Valtchanov, I., Bauer, F. E., Brandt, W. N., Del Moro, A., Hanish, D. J., Ivison, R. J., Juneau, S., Luo, B., Lutz, D., Sargent, M. T., Scott, D., and Xue, Y. Q. (2012b). GOODS-Herschel: the far-infrared view of star formation in active galactic nucleus host galaxies since  $z \approx 3$ . *MNRAS*, 419:95–115.
- Mushotzky, R. F., Fabian, A. C., Iwasawa, K., Kunieda, H., Matsuoka, M., Nandra, K., and Tanaka, Y. (1995). Detection of broad iron K lines in active galaxies. *MNRAS*, 272(2):L9–L12.
- Mutch, S. J., Geil, P. M., Poole, G. B., Angel, P. W., Duffy, A. R., Mesinger, A., and Wyithe, J. S. B. (2016). Dark-ages reionization and galaxy formation simulation - III. Modelling galaxy formation and the epoch of reionization. *MNRAS*, 462(1):250–276.
- Naab, T., Jesseit, R., and Burkert, A. (2006). The influence of gas on the structure of merger remnants. *MNRAS*, 372:839–852.
- Naab, T., Johansson, P. H., and Ostriker, J. P. (2009). Minor Mergers and the Size Evolution of Elliptical Galaxies. *ApJ*, 699(2):L178–L182.
- Naiman, J. P., Pillepich, A., Springel, V., Ramirez-Ruiz, E., Torrey, P., Vogelsberger, M., Pakmor, R., Nelson, D., Marinacci, F., Hernquist, L., Weinberger, R., and Genel, S. (2018). First results from the IllustrisTNG simulations: a tale of two elements - chemical evolution of magnesium and europium. *MNRAS*, 477(1):1206–1224.
- Nandra, K., Barret, D., Barcons, X., Fabian, A., den Herder, J.-W., Piro, L., Watson, M., Adami, C., Aird, J., Afonso, J. M., Alexander, D., Argiroffi, C., Amati, L., Arnaud, M., Atteia, J.-L., Audard, M., Badenes, C., Ballet, J., Ballo, L., Bamba, A., Bhardwaj, A., Stefano Battistelli, E., Becker, W., De Becker, M., Behar, E., Bianchi, S., Biffi, V., Bîrzan, L., Bocchino, F., Bogdanov, S., Boirin, L., Boller, T., Borgani, S., Borm, K., Bouché, N., Bourdin, H., Bower, R., Braitto, V., Branchini, E., Branduardi-Raymont, G., Bregman, J., Brenneman, L., Brightman, M., Brüggén, M., Buchner, J., Bulbul, E., Brusa, M., Bursa, M., Caccianiga, A., Cackett, E., Campana, S., Cappelluti, N., Cappi, M., Carrera, F., Ceballos, M., Christensen, F., Chu, Y.-H., Churazov, E., Clerc, N., Corbel, S., Corral,

- A., Comastri, A., Costantini, E., Croston, J., Dadina, M., D’Ai, A., Decourchelle, A., Della Ceca, R., Dennerl, K., Dolag, K., Done, C., Dovciak, M., Drake, J., Eckert, D., Edge, A., Ettori, S., Ezoe, Y., Feigelson, E., Fender, R., Feruglio, C., Finoguenov, A., Fiore, F., Galeazzi, M., Gallagher, S., Gandhi, P., Gaspari, M., Gastaldello, F., Georgakakis, A., Georgantopoulos, I., Gilfanov, M., Gitti, M., Gladstone, R., Goosmann, R., Gosset, E., Grosso, N., Guedel, M., Guerrero, M., Haberl, F., Hardcastle, M., Heinz, S., Alonso Herrero, A., Hervé, A., Holmstrom, M., Iwasawa, K., Jonker, P., Kaastra, J., Kara, E., Karas, V., Kastner, J., King, A., Kosenko, D., Koutroumpa, D., Kraft, R., Kreykenbohm, I., Lallement, R., Lanzuisi, G., Lee, J., Lemoine-Goumard, M., Lobban, A., Lodato, G., Lovisari, L., Lotti, S., McCharthy, I., McNamara, B., Maggio, A., Maiolino, R., De Marco, B., de Martino, D., Mateos, S., Matt, G., Maughan, B., Mazzotta, P., Mendez, M., Merloni, A., Micela, G., Miceli, M., Mignani, R., Miller, J., Miniutti, G., Molendi, S., Montez, R., Moretti, A., Motch, C., Nazé, Y., Nevalainen, J., Nicastro, F., Nulsen, P., Ohashi, T., O’Brien, P., Osborne, J., Oskinova, L., Pacaud, F., Paerels, F., Page, M., Papadakis, I., Pareschi, G., Petre, R., Petrucci, P.-O., Piconcelli, E., Pillitteri, I., Pinto, C., de Plaa, J., Pointecouteau, E., Ponman, T., Ponti, G., Porquet, D., Pounds, K., Pratt, G., Predehl, P., Proga, D., Psaltis, D., Rafferty, D., Ramos-Ceja, M., Ranalli, P., Rasia, E., Rau, A., Rauw, G., Rea, N., Read, A., Reeves, J., Reiprich, T., Renaud, M., Reynolds, C., Risaliti, G., Rodriguez, J., Rodriguez Hidalgo, P., Roncarelli, M., Rosario, D., Rossetti, M., Rozanska, A., Rovilos, E., Salvaterra, R., Salvato, M., Di Salvo, T., Sanders, J., Sanz-Forcada, J., Schawinski, K., Schaye, J., Schwobe, A., Sciortino, S., Severgnini, P., Shankar, F., Sijacki, D., Sim, S., Schmid, C., Smith, R., Steiner, A., Stelzer, B., Stewart, G., Strohmayer, T., Strüder, L., Sun, M., Takei, Y., Tatischeff, V., Tiengo, A., Tombesi, F., Trinchieri, G., Tsuru, T. G., Ud-Doula, A., Ursino, E., Valencic, L., Vanzella, E., Vaughan, S., Vignali, C., Vink, J., Vito, F., Volonteri, M., Wang, D., Webb, N., Willingale, R., Wilms, J., Wise, M., Worrall, D., Young, A., Zampieri, L., In’t Zand, J., Zane, S., Zezas, A., Zhang, Y., and Zhuravleva, I. (2013). The Hot and Energetic Universe: A White Paper presenting the science theme motivating the Athena+ mission. *arXiv e-prints*, page arXiv:1306.2307.
- Nandra, K., George, I. M., Mushotzky, R. F., Turner, T. J., and Yaqoob, T. (1997). ASCA Observations of Seyfert 1 Galaxies. II. Relativistic Iron  $K\alpha$  Emission. *ApJ*, 477(2):602–622.
- Narayan, R. and Yi, I. (1994). Advection-dominated Accretion: A Self-similar Solution. *ApJ*, 428:L13.
- Natarajan, P. and Pringle, J. E. (1998). The Alignment of Disk and Black Hole Spins in Active Galactic Nuclei. *ApJ*, 506(2):L97–L100.
- Navarro, J. F. and Benz, W. (1991). Dynamics of Cooling Gas in Galactic Dark Halos. *ApJ*, 380:320.
- Navarro, J. F., Frenk, C. S., and White, S. D. M. (1996). The Structure of Cold Dark Matter Halos. *ApJ*, 462:563.
- Navarro, J. F., Hayashi, E., Power, C., Jenkins, A. R., Frenk, C. S., White, S. D. M., Springel, V., Stadel, J., and Quinn, T. R. (2004). The inner structure of  $\Lambda$ CDM haloes - III. Universality and asymptotic slopes. *MNRAS*, 349(3):1039–1051.
- Navarro, J. F. and Steinmetz, M. (2000). Dark Halo and Disk Galaxy Scaling Laws in Hierarchical Universes. *ApJ*, 538(2):477–488.
- Negroponte, J. and White, S. D. M. (1983). Simulations of mergers between disc-halo galaxies. *MNRAS*, 205:1009–1029.
- Nelson, D., Pillepich, A., Springel, V., Pakmor, R., Weinberger, R., Genel, S., Torrey, P., Vogelsberger, M., Marinacci, F., and Hernquist, L. (2019). First results from the TNG50 simulation: galactic outflows driven by supernovae and black hole feedback. *MNRAS*, 490(3):3234–3261.
- Nelson, D., Pillepich, A., Springel, V., Weinberger, R., Hernquist, L., Pakmor, R., Genel, S., Torrey, P., Vogelsberger, M., Kauffmann, G., Marinacci, F., and Naiman, J. (2018). First results from the IllustrisTNG simulations: the galaxy colour bimodality. *MNRAS*, 475(1):624–647.

- Nelson, R. P. and Papaloizou, J. C. B. (2000). Hydrodynamic simulations of the Bardeen-Petterson effect. *MNRAS*, 315(3):570–586.
- Nesvadba, N. P. H., Polletta, M., Lehnert, M. D., Bergeron, J., De Breuck, C., Lagache, G., and Omont, A. (2011). The dynamics of the ionized and molecular interstellar medium in powerful obscured quasars at  $z \geq 3.5$ . *MNRAS*, 415(3):2359–2372.
- Nixon, C. J. and King, A. R. (2012). Broken discs: warp propagation in accretion discs. *MNRAS*, 421(2):1201–1208.
- Noble, S. C., Mundim, B. C., Nakano, H., Krolik, J. H., Campanelli, M., Zlochower, Y., and Yunes, N. (2012). Circumbinary Magnetohydrodynamic Accretion into Inspiral Binary Black Holes. *ApJ*, 755(1):51.
- Noeske, K. G., Weiner, B. J., Faber, S. M., Papovich, C., Koo, D. C., Somerville, R. S., Bundy, K., Conselice, C. J., Newman, J. A., Schiminovich, D., Le Floch, E., Coil, A. L., Rieke, G. H., Lotz, J. M., Primack, J. R., Barmby, P., Cooper, M. C., Davis, M., Ellis, R. S., Fazio, G. G., Guhathakurta, P., Huang, J., Kassin, S. A., Martin, D. C., Phillips, A. C., Rich, R. M., Small, T. A., Willmer, C. N. A., and Wilson, G. (2007). Star Formation in AEGIS Field Galaxies since  $z=1.1$ : The Dominance of Gradually Declining Star Formation, and the Main Sequence of Star-forming Galaxies. *ApJ*, 660:L43–L46.
- Noguchi, M. (1998). Clumpy star-forming regions as the origin of the peculiar morphology of high-redshift galaxies. *Nature*, 392:253.
- Noguchi, M. (1999). Early Evolution of Disk Galaxies: Formation of Bulges in Clumpy Young Galactic Disks. *ApJ*, 514:77–95.
- Norman, C. A., Sellwood, J. A., and Hasan, H. (1996). Bar Dissolution and Bulge Formation: an Example of Secular Dynamical Evolution in Galaxies. *ApJ*, 462:114.
- Novikov, I. D. and Thorne, K. S. (1973). Astrophysics of black holes. In *Black Holes (Les Astres Occlus)*, pages 343–450.
- Obreja, A., Domínguez-Tenreiro, R., Brook, C., Martínez-Serrano, F. J., Doménech-Moral, M., Serna, A., Mollá, M., and Stinson, G. (2013). A Two-phase Scenario for Bulge Assembly in  $\Lambda$ CDM Cosmologies. *ApJ*, 763:26.
- O’Dowd, M., Urry, C. M., and Scarpa, R. (2002). The Host Galaxies of Radio-loud Active Galactic Nuclei: The Black Hole-Galaxy Connection. *ApJ*, 580(1):96–103.
- Okamoto, T., Gao, L., and Theuns, T. (2008). Mass loss of galaxies due to an ultraviolet background. *MNRAS*, 390(3):920–928.
- Oke, J. B. (1966). Photoelectric Spectrophotometry of Quasi-Stellar Sources. *ApJ*, 145:668.
- O’Neill, J. K. and Dubinski, J. (2003). Detailed comparison of the structures and kinematics of simulated and observed barred galaxies. *MNRAS*, 346(1):251–264.
- Oppenheimer, B. D. and Davé, R. (2008). Mass, metal, and energy feedback in cosmological simulations. *MNRAS*, 387(2):577–600.
- Oppenheimer, B. D., Davé, R., Kereš, D., Fardal, M., Katz, N., Kollmeier, J. A., and Weinberg, D. H. (2010). Feedback and recycled wind accretion: assembling the  $z = 0$  galaxy mass function. *MNRAS*, 406(4):2325–2338.

- Orban de Xivry, G., Davies, R., Schartmann, M., Komossa, S., Marconi, A., Hicks, E., Engel, H., and Tacconi, L. (2011). The role of secular evolution in the black hole growth of narrow-line Seyfert 1 galaxies. *MNRAS*, 417(4):2721–2736.
- Orsi, Á., Padilla, N., Groves, B., Cora, S., Tecce, T., Gargiulo, I., and Ruiz, A. (2014). The nebular emission of star-forming galaxies in a hierarchical universe. *MNRAS*, 443:799–814.
- Osterbrock, D. E., Koski, A. T., and Phillips, M. M. (1976). The optical spectra of 3C 227 and other broad-line radio galaxies. *ApJ*, 206:898–909.
- Ostriker, J. P., Choi, E., Ciotti, L., Novak, G. S., and Proga, D. (2010). Momentum Driving: Which Physical Processes Dominate Active Galactic Nucleus Feedback? *ApJ*, 722(1):642–652.
- Ostriker, J. P. and Peebles, P. J. E. (1973). A Numerical Study of the Stability of Flattened Galaxies: or, can Cold Galaxies Survive? *ApJ*, 186:467–480.
- Overzier, R., Lemson, G., Angulo, R. E., Bertin, E., Blaizot, J., Henriques, B. M. B., Marleau, G.-D., and White, S. D. M. (2013). The Millennium Run Observatory: first light. *MNRAS*, 428:778–803.
- Pacucci, F. and Ferrara, A. (2015). Simulating the growth of Intermediate Mass Black Holes. *MNRAS*, 448(1):104–118.
- Padilla, C., Castander, F. J., Alarcon, A., Aleksic, J., Ballester, O., Cabayol, L., Cardiel-Sas, L., Carretero, J., Casas, R., Castilla, J., Crocce, M., Delfino, M., Diaz, C., Eriksen, M., Fernandez, E., Fosalba, P., Garcia-Bellido, J., Gaztanaga, E., Gaweda, J., Granena, F., Illa, J. M., Jimenez, J., Lopez, L., Marti, P., Miquel, R., Neissner, C., Pio, C., Sanchez, E., Serrano, S., Sevilla-Noarbe, I., Tallada, P., Tonello, N., and de Vicente, J. (2019). The Physics of the Accelerating Universe Camera. *arXiv e-prints*.
- Page, D. N. and Thorne, K. S. (1974). Disk-Accretion onto a Black Hole. Time-Averaged Structure of Accretion Disk. *ApJ*, 191:499–506.
- Painleve, P. (1922). Le Mecanique Classique et la Theorie de la Relativite. *L'Astronomie*, 36:6–9.
- Pakmor, R., Bauer, A., and Springel, V. (2011). Magnetohydrodynamics on an unstructured moving grid. *MNRAS*, 418(2):1392–1401.
- Pakmor, R., Marinacci, F., and Springel, V. (2014). Magnetic Fields in Cosmological Simulations of Disk Galaxies. *ApJ*, 783(1):L20.
- Pakmor, R. and Springel, V. (2013). Simulations of magnetic fields in isolated disc galaxies. *MNRAS*, 432(1):176–193.
- Papaloizou, J. C. B. and Pringle, J. E. (1983). The time-dependence of non-planar accretion discs. *MNRAS*, 202:1181–1194.
- Papovich, C., Dickinson, M., Giavalisco, M., Conselice, C. J., and Ferguson, H. C. (2005). The Assembly of Diversity in the Morphologies and Stellar Populations of High-Redshift Galaxies. *ApJ*, 631:101–120.
- Patrick, A. R., Reeves, J. N., Lobban, A. P., Porquet, D., and Markowitz, A. G. (2011a). Assessing black hole spin in deep Suzaku observations of Seyfert 1 AGN. *MNRAS*, 416(4):2725–2747.
- Patrick, A. R., Reeves, J. N., Porquet, D., Markowitz, A. G., Lobban, A. P., and Terashima, Y. (2011b). Iron line profiles in Suzaku spectra of bare Seyfert galaxies. *MNRAS*, 411(4):2353–2370.
- Peñarrubia, J., McConnachie, A., and Babul, A. (2006). On the Formation of Extended Galactic Disks by Tidally Disrupted Dwarf Galaxies. *ApJ*, 650:L33–L36.

- Peacock, J. A. (1999). *Cosmological Physics*.
- Peebles, P. J. E. (2002). When did the Large Elliptical Galaxies Form? In Metcalfe, N. and Shanks, T., editors, *A New Era in Cosmology*, volume 283 of *Astronomical Society of the Pacific Conference Series*, page 351.
- Peimbert, M., Peimbert, A., and Delgado-Inglada, G. (2017). Nebular Spectroscopy: A Guide on Hii Regions and Planetary Nebulae. *PASP*, 129(978):082001.
- Peng, C. Y., Impey, C. D., Rix, H.-W., Kochanek, C. S., Keeton, C. R., Falco, E. E., Lehár, J., and McLeod, B. A. (2006). Probing the Coevolution of Supermassive Black Holes and Galaxies Using Gravitationally Lensed Quasar Hosts. *ApJ*, 649(2):616–634.
- Perego, A., Dotti, M., Colpi, M., and Volonteri, M. (2009). Mass and spin co-evolution during the alignment of a black hole in a warped accretion disc. *MNRAS*, 399:2249–2263.
- Pérez-González, P. G., Cava, A., Barro, G., Villar, V., Cardiel, N., Ferreras, I., Rodríguez-Espinoza, J. M., Alonso-Herrero, A., Balcells, M., Cenarro, J., Cepa, J., Charlot, S., Cimatti, A., Conselice, C. J., Daddi, E., Donley, J., Elbaz, D., Espino, N., Gallego, J., Gobat, R., González-Martín, O., Guzmán, R., Hernán-Caballero, A., Muñoz-Tuñón, C., Renzini, A., Rodríguez-Zaurín, J., Tresse, L., Trujillo, I., and Zamorano, J. (2013). SHARDS: An Optical Spectro-photometric Survey of Distant Galaxies. *ApJ*, 762:46.
- Peters, P. C. and Mathews, J. (1963). Gravitational Radiation from Point Masses in a Keplerian Orbit. *Physical Review*, 131(1):435–440.
- Pfenniger, D. and Norman, C. (1990). Dissipation in barred galaxies - The growth of bulges and central mass concentrations. *ApJ*, 363:391–410.
- Pfister, H., Volonteri, M., Dubois, Y., Dotti, M., and Colpi, M. (2019). The erratic dynamical life of black hole seeds in high-redshift galaxies. *MNRAS*, 486(1):101–111.
- Pillepich, A., Nelson, D., Hernquist, L., Springel, V., Pakmor, R., Torrey, P., Weinberger, R., Genel, S., Naiman, J. P., Marinacci, F., and Vogelsberger, M. (2018a). First results from the IllustrisTNG simulations: the stellar mass content of groups and clusters of galaxies. *MNRAS*, 475(1):648–675.
- Pillepich, A., Nelson, D., Springel, V., Pakmor, R., Torrey, P., Weinberger, R., Vogelsberger, M., Marinacci, F., Genel, S., van der Wel, A., and Hernquist, L. (2019). First results from the TNG50 simulation: the evolution of stellar and gaseous discs across cosmic time. *MNRAS*, 490(3):3196–3233.
- Pillepich, A., Springel, V., Nelson, D., Genel, S., Naiman, J., Pakmor, R., Hernquist, L., Torrey, P., Vogelsberger, M., Weinberger, R., and Marinacci, F. (2018b). Simulating galaxy formation with the IllustrisTNG model. *MNRAS*, 473(3):4077–4106.
- Planck Collaboration, Ade, P. A. R., Aghanim, N., Armitage-Caplan, C., Arnaud, M., Ashdown, M., Atrio-Barandela, F., Aumont, J., Baccigalupi, C., Banday, A. J., and et al. (2014). Planck 2013 results. XVI. Cosmological parameters. *A&A*, 571:A16.
- Planck Collaboration, Ade, P. A. R., Aghanim, N., Arnaud, M., Ashdown, M., Aumont, J., Baccigalupi, C., Banday, A. J., Barreiro, R. B., Bartlett, J. G., Bartolo, N., Battaner, E., Battye, R., Benabed, K., Benoît, A., Benoit-Lévy, A., Bernard, J. P., Bersanelli, M., Bielewicz, P., Bock, J. J., Bonaldi, A., Bonavera, L., Bond, J. R., Borrill, J., Bouchet, F. R., Boulanger, F., Bucher, M., Burigana, C., Butler, R. C., Calabrese, E., Cardoso, J. F., Catalano, A., Challinor, A., Chamballu, A., Chary, R. R., Chiang, H. C., Chluba, J., Christensen, P. R., Church, S., Clements, D. L., Colombi, S., Colombo, L. P. L., Combet, C., Coulais, A., Crill, B. P., Curto, A., Cuttaia, F., Danese, L., Davies, R. D., Davis, R. J., de Bernardis, P., de Rosa, A., de Zotti, G., Delabrouille, J., Désert, F. X., Di Valentino, E.,

- Dickinson, C., Diego, J. M., Dolag, K., Dole, H., Donzelli, S., Doré, O., Douspis, M., Ducout, A., Dunkley, J., Dupac, X., Efstathiou, G., Elsner, F., Enßlin, T. A., Eriksen, H. K., Farhang, M., Fergusson, J., Finelli, F., Forni, O., Frailis, M., Fraisse, A. A., Franceschi, E., Frejsel, A., Galeotta, S., Galli, S., Ganga, K., Gauthier, C., Gerbino, M., Ghosh, T., Giard, M., Giraud-Héraud, Y., Giusarma, E., Gjerløw, E., González-Nuevo, J., Górski, K. M., Gratton, S., Gregorio, A., Gruppuso, A., Gudmundsson, J. E., Hamann, J., Hansen, F. K., Hanson, D., Harrison, D. L., Helou, G., Henrot-Versillé, S., Hernández-Monteaigudo, C., Herranz, D., Hildebrandt, S. R., Hivon, E., Hobson, M., Holmes, W. A., Hornstrup, A., Hovest, W., Huang, Z., Huffenberger, K. M., Hurier, G., Jaffe, A. H., Jaffe, T. R., Jones, W. C., Juvela, M., Keihänen, E., Keskitalo, R., Kisner, T. S., Kneissl, R., Knoch, J., Knox, L., Kunz, M., Kurki-Suonio, H., Lagache, G., Lähteenmäki, A., Lamarre, J. M., Lasenby, A., Lattanzi, M., Lawrence, C. R., Leahy, J. P., Leonardi, R., Lesgourgues, J., Levrier, F., Lewis, A., Liguori, M., Lilje, P. B., Linden-Vørnle, M., López-Cañiego, M., Lubin, P. M., Macías-Pérez, J. F., Maggio, G., Maino, D., Mandolesi, N., Mangilli, A., Marchini, A., Maris, M., Martin, P. G., Martinelli, M., Martínez-González, E., Masi, S., Matarrese, S., McGehee, P., Meinhold, P. R., Melchiorri, A., Melin, J. B., Mendes, L., Mennella, A., Migliaccio, M., Millea, M., Mitra, S., Miville-Deschênes, M. A., Moneti, A., Montier, L., Morgante, G., Mortlock, D., Moss, A., Munshi, D., Murphy, J. A., Naselsky, P., Nati, F., Natoli, P., Netterfield, C. B., Nørgaard-Nielsen, H. U., Novello, F., Novikov, D., Novikov, I., Oxborrow, C. A., Paci, F., Pagano, L., Pajot, F., Paladini, R., Paoletti, D., Partridge, B., Pasian, F., Patanchon, G., Pearson, T. J., Perdureau, O., Perotto, L., Perrotta, F., Pettorino, V., Piacentini, F., Piat, M., Pierpaoli, E., Pietrobon, D., Plaszczynski, S., Pointecouteau, E., Polenta, G., Popa, L., Pratt, G. W., Prézeau, G., Prunet, S., Puget, J. L., Rachen, J. P., Reach, W. T., Rebolo, R., Reinecke, M., Remazeilles, M., Renault, C., Renzi, A., Ristorcelli, I., Rocha, G., Rosset, C., Rossetti, M., Roudier, G., Rouillé d'Orfeuil, B., Rowan-Robinson, M., Rubiño-Martín, J. A., Rusholme, B., Said, N., Salvatelli, V., Salvati, L., Sandri, M., Santos, D., Savelainen, M., Savini, G., Scott, D., Seiffert, M. D., Serra, P., Shellard, E. P. S., Spencer, L. D., Spinelli, M., Stolyarov, V., Stompor, R., Sudiwala, R., Sunyaev, R., Sutton, D., Suur-Uski, A. S., Sygnet, J. F., Tauber, J. A., Terenzi, L., Tofolatti, L., Tomasi, M., Tristram, M., Trombetti, T., Tucci, M., Tuovinen, J., Türlér, M., Umata, G., Valenziano, L., Valiviita, J., Van Tent, F., Vielva, P., Villa, F., Wade, L. A., Wandelt, B. D., Wehus, I. K., White, M., White, S. D. M., Wilkinson, A., Yvon, D., Zacchei, A., and Zonca, A. (2016). Planck 2015 results. XIII. Cosmological parameters. *A&A*, 594:A13.
- Porter, L. A., Somerville, R. S., Primack, J. R., and Johansson, P. H. (2014). Understanding the structural scaling relations of early-type galaxies. *MNRAS*, 444:942–960.
- Postman, M. and Geller, M. J. (1984). The morphology-density relation - The group connection. *ApJ*, 281:95–99.
- Postman, M., Lauer, T. R., Donahue, M., Graves, G., Coe, D., Moustakas, J., Koekemoer, A., Bradley, L., Ford, H. C., and Grillo, C. (2012). A Brightest Cluster Galaxy with an Extremely Large Flat Core. *ApJ*, 756(2):159.
- Potter, D., Stadel, J., and Teyssier, R. (2017). PKDGRAV3: beyond trillion particle cosmological simulations for the next era of galaxy surveys. *Computational Astrophysics and Cosmology*, 4(1):2.
- Prada, F., Klypin, A. A., Cuesta, A. J., Betancort-Rijo, J. E., and Primack, J. (2012). Halo concentrations in the standard  $\Lambda$  cold dark matter cosmology. *MNRAS*, 423(4):3018–3030.
- Press, W. H. and Schechter, P. (1974). Formation of Galaxies and Clusters of Galaxies by Self-Similar Gravitational Condensation. *ApJ*, 187:425–438.
- Pretorius, F. (2005). Evolution of Binary Black-Hole Spacetimes. *Phys. Rev. Lett.*, 95(12):121101.
- Price, D. J. and Monaghan, J. J. (2007). An energy-conserving formalism for adaptive gravitational force softening in smoothed particle hydrodynamics and N-body codes. *MNRAS*, 374(4):1347–1358.



- Quinlan, G. D. (1996). The dynamical evolution of massive black hole binaries I. Hardening in a fixed stellar background. *New A*, 1(1):35–56.
- Quinlan, G. D. and Hernquist, L. (1997). The dynamical evolution of massive black hole binaries — II. Self-consistent N-body integrations. *New A*, 2(6):533–554.
- Radovich, M., Arnaboldi, M., Rippepi, V., Massarotti, M., McCracken, H. J., Mellier, Y., Bertin, E., Zamorani, G., Adami, C., Bardelli, S., Le Fèvre, O., Foucaud, S., Garilli, B., Scaramella, R., Vettolani, G., Zanichelli, A., and Zucca, E. (2004). The VIRMOS deep imaging survey. III. ESO/WFI deep U-band imaging of the 0226-04 deep field. *A&A*, 417:51–60.
- Raha, N., Sellwood, J. A., James, R. A., and Kahn, F. D. (1991). A dynamical instability of bars in disk galaxies. *Nature*, 352(6334):411–412.
- Rahimi, A., Kawata, D., Brook, C. B., and Gibson, B. K. (2010). Chemodynamical analysis of bulge stars for simulated disc galaxies. *MNRAS*, 401:1826–1831.
- Ramos Almeida, C., Bessiere, P. S., Tadhunter, C. N., Pérez-González, P. G., Barro, G., Inskip, K. J., Morganti, R., Holt, J., and Dicken, D. (2012). Are luminous radio-loud active galactic nuclei triggered by galaxy interactions? *MNRAS*, 419(1):687–705.
- Rasio, F. A., Freitag, M., and Gürkan, M. A. (2004). Formation of Massive Black Holes in Dense Star Clusters. In Ho, L. C., editor, *Coevolution of Black Holes and Galaxies*, page 138.
- Ravindranath, S., Ho, L. C., Peng, C. Y., Filippenko, A. V., and Sargent, W. L. W. (2001). Central Structural Parameters of Early-Type Galaxies as Viewed with Nicmos on the Hubble Space Telescope. *AJ*, 122(2):653–678.
- Redmount, I. H. and Rees, M. J. (1989). Gravitational-radiation rocket effects and galactic structure. *Comments on Astrophysics*, 14:165.
- Rees, M. J., Begelman, M. C., Blandford, R. D., and Phinney, E. S. (1982). Ion-supported tori and the origin of radio jets. *Nature*, 295(5844):17–21.
- Reynolds, C. S. (2013). The spin of supermassive black holes. *Classical and Quantum Gravity*, 30(24):244004.
- Reynolds, C. S. and Nowak, M. A. (2003). Fluorescent iron lines as a probe of astrophysical black hole systems. *Phys. Rep.*, 377(6):389–466.
- Rezzolla, L., Barausse, E., Dorband, E. N., Pollney, D., Reisswig, C., Seiler, J., and Husa, S. (2008a). Final spin from the coalescence of two black holes. *Phys. Rev. D*, 78(4):044002.
- Rezzolla, L., Diener, P., Dorband, E. N., Pollney, D., Reisswig, C., Schnetter, E., and Seiler, J. (2008b). The Final Spin from the Coalescence of Aligned-Spin Black Hole Binaries. *ApJ*, 674(1):L29.
- Ribeiro, B., Lobo, C., Antón, S., Gomes, J. M., and Papaderos, P. (2016). Red galaxies with pseudo-bulges in the SDSS: closer to disc galaxies or to classical bulges? *MNRAS*, 456:3899–3914.
- Ricarte, A. and Natarajan, P. (2018). The observational signatures of supermassive black hole seeds. *MNRAS*, 481(3):3278–3292.
- Richards, G. T., Strauss, M. A., Fan, X., Hall, P. B., Jester, S., Schneider, D. P., Vanden Berk, D. E., Stoughton, C., Anderson, S. F., Brunner, R. J., Gray, J., Gunn, J. E., Ivezić, Ž., Kirkland, M. K., Knapp, G. R., Loveday, J., Meiksin, A., Pope, A., Szalay, A. S., Thakar, A. R., Yanny, B., York, D. G., Barentine, J. C., Brewington, H. J., Brinkmann, J., Fukugita, M., Harvanek, M., Kent, S. M., Kleinman, S. J., Krzesiński, J., Long, D. C., Lupton, R. H., Nash, T., Neilsen, Eric H., J., Nitta, A., Schlegel, D. J., and Snedden, S. A. (2006). The Sloan Digital Sky Survey Quasar Survey: Quasar Luminosity Function from Data Release 3. *AJ*, 131(6):2766–2787.

- Rix, H.-W., Carollo, C. M., and Freeman, K. (1999). Large Stellar Disks in Small Elliptical Galaxies. *ApJ*, 513(1):L25–L28.
- Rix, H.-W. and White, S. D. M. (1990). Disks in Elliptical Galaxies. *ApJ*, 362:52.
- Rodriguez-Gomez, V., Genel, S., Vogelsberger, M., Sijacki, D., Pillepich, A., Sales, L. V., Torrey, P., Snyder, G., Nelson, D., Springel, V., Ma, C.-P., and Hernquist, L. (2015). The merger rate of galaxies in the Illustris simulation: a comparison with observations and semi-empirical models. *MNRAS*, 449(1):49–64.
- Romano-Díaz, E., Shlosman, I., Heller, C., and Hoffman, Y. (2008). Disk Evolution and Bar Triggering Driven by Interactions with Dark Matter Substructure. *ApJ*, 687(1):L13.
- Rosas-Guevara, Y., Bonoli, S., Dotti, M., Zana, T., Nelson, D., Pillepich, A., Ho, L. C., Izquierdo-Villalba, D., Hernquist, L., and Pakmor, R. (2020). The buildup of strongly barred galaxies in the TNG100 simulation. *MNRAS*, 491(2):2547–2564.
- Rosas-Guevara, Y., Bower, R. G., Schaye, J., McAlpine, S., Dalla Vecchia, C., Frenk, C. S., Schaller, M., and Theuns, T. (2016a). Supermassive black holes in the EAGLE Universe. Revealing the observables of their growth. *MNRAS*, 462(1):190–205.
- Rosas-Guevara, Y., Bower, R. G., Schaye, J., McAlpine, S., Dalla Vecchia, C., Frenk, C. S., Schaller, M., and Theuns, T. (2016b). Supermassive black holes in the EAGLE Universe. Revealing the observables of their growth. *MNRAS*, 462(1):190–205.
- Roulet, J. and Zaldarriaga, M. (2019). Constraints on binary black hole populations from LIGO-Virgo detections. *MNRAS*, 484(3):4216–4229.
- Rovilos, E., Burwitz, V., Szokoly, G., Hasinger, G., Egami, E., Bouché, N., Berta, S., Salvato, M., Lutz, D., and Genzel, R. (2009). Deep U-B-V imaging of the Lockman Hole with the LBT. Observations and number counts. *A&A*, 507:195–208.
- Rupke, D. S., Veilleux, S., and Sanders, D. B. (2005). Outflows in Infrared-Luminous Starbursts at  $z \sim 0.5$ . II. Analysis and Discussion. *ApJS*, 160(1):115–148.
- Rupke, D. S. N. and Veilleux, S. (2011). Integral Field Spectroscopy of Massive, Kiloparsec-scale Outflows in the Infrared-luminous QSO Mrk 231. *ApJ*, 729(2):L27.
- Ryan, Jr., R. E., Cohen, S. H., Windhorst, R. A., and Silk, J. (2008). Galaxy Mergers at  $z \sim 1$  in the HUDF: Evidence for a Peak in the Major Merger Rate of Massive Galaxies. *ApJ*, 678:751–757.
- Sachdeva, S., Saha, K., and Singh, H. P. (2017). Growth of Bulges in Disk Galaxies Since  $z \sim 1$ . *ApJ*, 840(2):79.
- Saha, K. (2015). Lost in Secular Evolution: The Case of a Low-mass Classical Bulge. *ApJ*, 806:L29.
- Saha, K. and Gerhard, O. (2012). Rotation of classical bulges during secular evolution of barred galaxies. *arXiv e-prints*, page arXiv:1212.4579.
- Saha, K. and Naab, T. (2013). Spinning dark matter haloes promote bar formation. *MNRAS*, 434(2):1287–1299.
- Saha, K., Pfenniger, D., and Taam, R. E. (2013). Meridional Tilt of the Stellar Velocity Ellipsoid during Bar Buckling Instability. *ApJ*, 764(2):123.
- Sakamoto, K., Okumura, S. K., Ishizuki, S., and Scoville, N. Z. (1999). Bar-driven Transport of Molecular Gas to Galactic Centers and Its Consequences. *ApJ*, 525(2):691–701.

- Sales, L. V., Navarro, J. F., Abadi, M. G., and Steinmetz, M. (2007). Satellites of simulated galaxies: survival, merging and their relation to the dark and stellar haloes. *MNRAS*, 379:1464–1474.
- Salpeter, E. E. (1964). Accretion of Interstellar Matter by Massive Objects. *ApJ*, 140:796–800.
- Salvador-Solé, E., Solanes, J. M., and Manrique, A. (1998). Merger versus Accretion and the Structure of Dark Matter Halos. *ApJ*, 499(2):542–547.
- Sánchez, S. F., Kennicutt, R. C., Gil de Paz, A., van de Ven, G., Vílchez, J. M., Wisotzki, L., Walcher, C. J., Mast, D., Aguerri, J. A. L., Albiol-Pérez, S., Alonso-Herrero, A., Alves, J., Bakos, J., Bartáková, T., Bland-Hawthorn, J., Boselli, A., Bomans, D. J., Castillo-Morales, A., Cortijo-Ferrero, C., de Lorenzo-Cáceres, A., Del Olmo, A., Dettmar, R.-J., Díaz, A., Ellis, S., Falcón-Barroso, J., Flores, H., Gallazzi, A., García-Lorenzo, B., González Delgado, R., Gruel, N., Haines, T., Hao, C., Husemann, B., Iglésias-Páramo, J., Jahnke, K., Johnson, B., Jungwiert, B., Kalinova, V., Kehrig, C., Kupko, D., López-Sánchez, Á. R., Lyubenova, M., Marino, R. A., Mármol-Queraltó, E., Márquez, I., Masegosa, J., Meidt, S., Mendez-Abreu, J., Monreal-Ibero, A., Montijo, C., Mourão, A. M., Palacios-Navarro, G., Papaderos, P., Pasquali, A., Peletier, R., Pérez, E., Pérez, I., Quirrenbach, A., Relaño, M., Rosales-Ortega, F. F., Roth, M. M., Ruiz-Lara, T., Sánchez-Blázquez, P., Sengupta, C., Singh, R., Stanishev, V., Trager, S. C., Vazdekis, A., Viironen, K., Wild, V., Zibetti, S., and Ziegler, B. (2012). CALIFA, the Calar Alto Legacy Integral Field Area survey. I. Survey presentation. *A&A*, 538:A8.
- Sanders, D. B. and Mirabel, I. F. (1996). Luminous Infrared Galaxies. *ARA&A*, 34:749.
- Sargent, W. L. W., Young, P. J., Boksenberg, A., Shortridge, K., Lynds, C. R., and Hartwick, F. D. A. (1978). Dynamical evidence for a central mass concentration in the galaxy M87. *ApJ*, 221:731–744.
- Savorgnan, G. A. D., Graham, A. W., Marconi, A. r., and Sani, E. (2016). Supermassive Black Holes and Their Host Spheroids. II. The Red and Blue Sequence in the  $M_{BH}-M_{*,sph}$  Diagram. *ApJ*, 817(1):21.
- Scannapieco, C., Gadotti, D. A., Jonsson, P., and White, S. D. M. (2010). An observer’s view of simulated galaxies: disc-to-total ratios, bars and (pseudo-)bulges. *MNRAS*, 407(1):L41–L45.
- Scannapieco, C., White, S. D. M., Springel, V., and Tissera, P. B. (2011). Formation history, structure and dynamics of discs and spheroids in simulated Milky Way mass galaxies. *MNRAS*, 417(1):154–171.
- Schaye, J., Crain, R. A., Bower, R. G., Furlong, M., Schaller, M., Theuns, T., Dalla Vecchia, C., Frenk, C. S., McCarthy, I. G., Helly, J. C., Jenkins, A., Rosas-Guevara, Y. M., White, S. D. M., Baes, M., Booth, C. M., Camps, P., Navarro, J. F., Qu, Y., Rahmati, A., Sawala, T., Thomas, P. A., and Trayford, J. (2015). The EAGLE project: simulating the evolution and assembly of galaxies and their environments. *MNRAS*, 446(1):521–554.
- Scheuer, P. A. G. and Feiler, R. (1996). The realignment of a black hole misaligned with its accretion disc. *MNRAS*, 282:291.
- Schmidt, M. (1963). 3C 273 : A Star-Like Object with Large Red-Shift. *Nature*, 197(4872):1040.
- Schmidt, M. and Green, R. F. (1983). Quasar evolution derived from the Palomar bright quasar survey and other complete quasar surveys. *ApJ*, 269:352–374.
- Schmidt, M., Schneider, D. P., and Gunn, J. E. (1995). Spectroscopic CCD Surveys for Quasars at Large Redshift. IV. Evolution of the Luminosity Function from Quasars Detected by Their Lyman-Alpha Emission. *AJ*, 110:68.
- Schnittman, J. D. and Krolik, J. H. (2009). X-ray Polarization from Accreting Black Holes: The Thermal State. *ApJ*, 701(2):1175–1187.

- Schulze, A. and Wisotzki, L. (2010). Low redshift AGN in the Hamburg/ESO Survey . II. The active black hole mass function and the distribution function of Eddington ratios. *A&A*, 516:A87.
- Schwarz, M. P. (1981). The response of gas in a galactic disk to bar forcing. *ApJ*, 247:77–88.
- Schwarzschild, K. (1916). Über das Gravitationsfeld eines Massenpunktes nach der Einsteinschen Theorie. *Sitzungsberichte der Königlich Preußischen Akademie der Wissenschaften (Berlin)*, pages 189–196.
- Sellwood, J. A. (2016). Bar Instability in Disk-Halo Systems. *ApJ*, 819:92.
- Sersic, J. L. (1968). *Atlas de Galaxias Australes*.
- Sesana, A. (2013). Systematic investigation of the expected gravitational wave signal from supermassive black hole binaries in the pulsar timing band. *Monthly Notices of the Royal Astronomical Society: Letters*, 433(1):L1–L5.
- Sesana, A., Barausse, E., Dotti, M., and Rossi, E. M. (2014). Linking the Spin Evolution of Massive Black Holes to Galaxy Kinematics. *ApJ*, 794:104.
- Sesana, A., Haardt, F., and Madau, P. (2006). Interaction of Massive Black Hole Binaries with Their Stellar Environment. I. Ejection of Hypervelocity Stars. *ApJ*, 651(1):392–400.
- Sesana, A. and Khan, F. M. (2015). Scattering experiments meet N-body - I. A practical recipe for the evolution of massive black hole binaries in stellar environments. *MNRAS*, 454(1):L66–L70.
- Sesana, A., Shankar, F., Bernardi, M., and Sheth, R. K. (2016). Selection bias in dynamically measured supermassive black hole samples: consequences for pulsar timing arrays. *MNRAS*, 463(1):L6–L11.
- Sesana, A., Vecchio, A., and Colacino, C. N. (2008). The stochastic gravitational-wave background from massive black hole binary systems: implications for observations with Pulsar Timing Arrays. *MNRAS*, 390(1):192–209.
- Seyfert, C. K. (1943). Nuclear Emission in Spiral Nebulae. *ApJ*, 97:28.
- Shakura, N. I. and Sunyaev, R. A. (1973). Black holes in binary systems. Observational appearance. *A&A*, 24:337–355.
- Shankar, F., Bernardi, M., Richardson, K., Marsden, C., Sheth, R. K., Allevato, V., Graziani, L., Mezcua, M., Ricci, F., Penny, S. J., La Franca, F., and Pacucci, F. (2019). Black hole scaling relations of active and quiescent galaxies: Addressing selection effects and constraining virial factors. *MNRAS*, 485(1):1278–1292.
- Shankar, F., Bernardi, M., Sheth, R. K., Ferrarese, L., Graham, A. W., Savorgnan, G., Allevato, V., Marconi, A., Läsker, R., and Lapi, A. (2016). Selection bias in dynamically measured supermassive black hole samples: its consequences and the quest for the most fundamental relation. *MNRAS*, 460(3):3119–3142.
- Shankar, F., Marulli, F., Mathur, S., Bernardi, M., and Bournaud, F. (2012). Black holes in pseudobulges: demography and models. *A&A*, 540:A23.
- Shankar, F., Salucci, P., Granato, G. L., De Zotti, G., and Danese, L. (2004). Supermassive black hole demography: the match between the local and accreted mass functions. *MNRAS*, 354:1020–1030.
- Shankar, F., Weinberg, D. H., and Miralda-Escudé, J. (2009). Self-Consistent Models of the AGN and Black Hole Populations: Duty Cycles, Accretion Rates, and the Mean Radiative Efficiency. *ApJ*, 690(1):20–41.

- Shankar, F., Weinberg, D. H., and Miralda-Escudé, J. (2013). Accretion-driven evolution of black holes: Eddington ratios, duty cycles and active galaxy fractions. *MNRAS*, 428(1):421–446.
- Shapley, A. E., Steidel, C. C., Pettini, M., and Adelberger, K. L. (2003). Rest-Frame Ultraviolet Spectra of  $z \sim 3$  Lyman Break Galaxies. *ApJ*, 588(1):65–89.
- Shen, S., Mo, H. J., White, S. D. M., Blanton, M. R., Kauffmann, G., Voges, W., Brinkmann, J., and Csabai, I. (2003). The size distribution of galaxies in the Sloan Digital Sky Survey. *MNRAS*, 343:978–994.
- Sheth, K., Elmegreen, D. M., Elmegreen, B. G., Capak, P., Abraham, R. G., Athanassoula, E., Ellis, R. S., Mobasher, B., Salvato, M., Schinnerer, E., Scoville, N. Z., Spalsbury, L., Strubbe, L., Carollo, M., Rich, M., and West, A. A. (2008). Evolution of the Bar Fraction in COSMOS: Quantifying the Assembly of the Hubble Sequence. *ApJ*, 675(2):1141–1155.
- Shlosman, I. and Begelman, M. C. (1989). Evolution of Self-Gravitating Accretion Disks in Active Galactic Nuclei. *ApJ*, 341:685.
- Shlosman, I., Frank, J., and Begelman, M. C. (1989). Bars within bars: a mechanism for fuelling active galactic nuclei. *Nature*, 338(6210):45–47.
- Sijacki, D., Springel, V., Di Matteo, T., and Hernquist, L. (2007). A unified model for AGN feedback in cosmological simulations of structure formation. *MNRAS*, 380(3):877–900.
- Sijacki, D., Springel, V., and Haehnelt, M. G. (2009). Growing the first bright quasars in cosmological simulations of structure formation. *MNRAS*, 400(1):100–122.
- Sijacki, D., Vogelsberger, M., Genel, S., Springel, V., Torrey, P., Snyder, G. F., Nelson, D., and Hernquist, L. (2015). The Illustris simulation: the evolving population of black holes across cosmic time. *MNRAS*, 452(1):575–596.
- Silk, J. and Rees, M. J. (1998). Quasars and galaxy formation. *A&A*, 331:L1–L4.
- Simien, F. and de Vaucouleurs, G. (1986). Systematics of bulge-to-disk ratios. *ApJ*, 302:564–578.
- Sinha, M. (2016). Corrfunc: Corrfunc-1.1.0.
- Skibba, R. A. and Sheth, R. K. (2009). A halo model of galaxy colours and clustering in the Sloan Digital Sky Survey. *MNRAS*, 392(3):1080–1091.
- Skillman, S. W., Warren, M. S., Turk, M. J., Wechsler, R. H., Holz, D. E., and Sutter, P. M. (2014). Dark Sky Simulations: Early Data Release. *arXiv e-prints*, page arXiv:1407.2600.
- Small, T. A. and Blandford, R. D. (1992). Quasar evolution and the growth of black holes. *Monthly Notices of the Royal Astronomical Society*, 259(4):725–737.
- Smethurst, R. J., Simmons, B. D., Lintott, C. J., and Shanahan, J. (2019). Secularly powered outflows from AGNs: the dominance of non-merger driven supermassive black hole growth. *MNRAS*, 489(3):4016–4031.
- Smith, B. D., Regan, J. A., Downes, T. P., Norman, M. L., O’Shea, B. W., and Wise, J. H. (2018). The growth of black holes from Population III remnants in the Renaissance simulations. *Monthly Notices of the Royal Astronomical Society*, 480(3):3762–3773.
- Smith, G. P., Treu, T., Ellis, R. S., Moran, S. M., and Dressler, A. (2005). Evolution since  $z = 1$  of the Morphology-Density Relation for Galaxies. *ApJ*, 620(1):78–87.

- Sobral, D., Best, P. N., Geach, J. E., Smail, I., Kurk, J., Cirasuolo, M., Casali, M., Ivison, R. J., Coppin, K., and Dalton, G. B. (2009). Bright Ly $\alpha$  emitters at  $z \sim 9$ : constraints on the LF from HiZELS. *MNRAS*, 398:L68–L72.
- Sobral, D., Matthee, J., Darvish, B., Schaerer, D., Mobasher, B., Röttgering, H. J. A., Santos, S., and Hemmati, S. (2015). Evidence for PopIII-like Stellar Populations in the Most Luminous Lyman- $\alpha$  Emitters at the Epoch of Reionization: Spectroscopic Confirmation. *ApJ*, 808(2):139.
- Sobral, D., Santos, S., Matthee, J., Paulino-Afonso, A., Ribeiro, B., Calhau, J., and Khostovan, A. A. (2018a). Slicing COSMOS with SC4K: the evolution of typical Ly  $\alpha$  emitters and the Ly  $\alpha$  escape fraction from  $\bar{z}$  2 to 6. *MNRAS*, 476:4725–4752.
- Sobral, D., Santos, S., Matthee, J., Paulino-Afonso, A., Ribeiro, B., Calhau, J., and Khostovan, A. A. (2018b). Slicing COSMOS with SC4K: the evolution of typical Ly  $\alpha$  emitters and the Ly  $\alpha$  escape fraction from  $\bar{z}$  2 to 6. *MNRAS*, 476:4725–4752.
- Sobral, D., Smail, I., Best, P. N., Geach, J. E., Matsuda, Y., Stott, J. P., Cirasuolo, M., and Kurk, J. (2013). A large H $\alpha$  survey at  $z = 2.23, 1.47, 0.84$  and  $0.40$ : the 11 Gyr evolution of star-forming galaxies from HiZELS. *MNRAS*, 428:1128–1146.
- Soltan, A. (1982). Masses of quasars. *MNRAS*, 200:115–122.
- Somerville, R. S., Hopkins, P. F., Cox, T. J., Robertson, B. E., and Hernquist, L. (2008). A semi-analytic model for the co-evolution of galaxies, black holes and active galactic nuclei. *MNRAS*, 391:481–506.
- Somerville, R. S. and Primack, J. R. (1999). Semi-analytic modelling of galaxy formation: the local Universe. *MNRAS*, 310(4):1087–1110.
- Somerville, R. S., Primack, J. R., and Faber, S. M. (2001). The nature of high-redshift galaxies. *MNRAS*, 320:504–528.
- Spinoso, D., Bonoli, S., Dotti, M., Mayer, L., Madau, P., and Bellovary, J. (2017). Bar-driven evolution and quenching of spiral galaxies in cosmological simulations. *MNRAS*, 465:3729–3740.
- Spinoso, D., Orsi, A., López-Sanjuan, C., Bonoli, S., Viironen, K., Izquierdo-Villalba, D., Sobral, D., Gurung-López, S., Hernán-Caballero, A., Ederoclite, A., Varela, J., Overzier, R., Miralda-Escudé, J., Muniesa, D. J., Alcaniz, J., Angulo, R. E., Cenarro, A. J., Cristóbal-Hornillos, D., Dupke, R. A., Hernández-Monteagudo, C., Marín-Franch, A., Moles, M., Sodré, Laerte, J., and Vázquez Ramió, H. (2020). J-PLUS: Unveiling the brightest-end of the Ly $\alpha$  luminosity function at  $2.0 < z < 3.3$  over 1000 deg<sup>2</sup>. *arXiv e-prints*, page arXiv:2006.15084.
- Springel, V. (2005). The cosmological simulation code GADGET-2. *MNRAS*, 364:1105–1134.
- Springel, V. (2010). E pur si muove: Galilean-invariant cosmological hydrodynamical simulations on a moving mesh. *MNRAS*, 401(2):791–851.
- Springel, V., Di Matteo, T., and Hernquist, L. (2005). Modelling feedback from stars and black holes in galaxy mergers. *MNRAS*, 361(3):776–794.
- Springel, V. and Hernquist, L. (2003). Cosmological smoothed particle hydrodynamics simulations: a hybrid multiphase model for star formation. *MNRAS*, 339(2):289–311.
- Springel, V., Pakmor, R., Pillepich, A., Weinberger, R., Nelson, D., Hernquist, L., Vogelsberger, M., Genel, S., Torrey, P., Marinacci, F., and Naiman, J. (2018). First results from the IllustrisTNG simulations: matter and galaxy clustering. *MNRAS*, 475:676–698.

- Springel, V., Wang, J., Vogelsberger, M., Ludlow, A., Jenkins, A., Helmi, A., Navarro, J. F., Frenk, C. S., and White, S. D. M. (2008). The Aquarius Project: the subhaloes of galactic haloes. *MNRAS*, 391(4):1685–1711.
- Springel, V. and White, S. D. M. (1999). Tidal tails in cold dark matter cosmologies. *MNRAS*, 307(1):162–178.
- Springel, V., White, S. D. M., Tormen, G., and Kauffmann, G. (2001). Populating a cluster of galaxies - I. Results at  $[formmu2]z=0$ . *MNRAS*, 328:726–750.
- Stark, R. F. and Connors, P. A. (1977). Observational test for the existence of a rotating black hole in Cyg X-1. *Nature*, 266(5601):429–430.
- Steinborn, L. K., Hirschmann, M., Dolag, K., Shankar, F., Juneau, S., Krumpe, M., Remus, R.-S., and Teklu, A. F. (2018). Cosmological simulations of black hole growth II: how (in)significant are merger events for fuelling nuclear activity? *MNRAS*, 481(1):341–360.
- Stewart, K. R., Bullock, J. S., Barton, E. J., and Wechsler, R. H. (2009). Galaxy Mergers and Dark Matter Halo Mergers in  $\Lambda$ CDM: Mass, Redshift, and Mass-Ratio Dependence. *ApJ*, 702(2):1005–1015.
- Stone, N. C., Küpper, A. H. W., and Ostriker, J. P. (2017). Formation of massive black holes in galactic nuclei: runaway tidal encounters. *MNRAS*, 467(4):4180–4199.
- Stothert, L., Norberg, P., Baugh, C. M., Alarcon, A., Amara, A., Carretero, J., Castander, F. J., Eriksen, M., Fernandez, E., Fosalba, P., Garcia-Bellido, J., Gaztanaga, E., Hoekstra, H., Padilla, C., Refregier, A., Sanchez, E., and Tortorelli, L. (2018). The PAU Survey: spectral features and galaxy clustering using simulated narrow-band photometry. *MNRAS*, 481:4221–4235.
- Strateva, I., Ivezić, Ž., Knapp, G. R., Narayanan, V. K., Strauss, M. A., Gunn, J. E., Lupton, R. H., Schlegel, D., Bahcall, N. A., Brinkmann, J., Brunner, R. J., Budavári, T., Csabai, I., Castander, F. J., Doi, M., Fukugita, M., Györy, Z., Hamabe, M., Hennessy, G., Ichikawa, T., Kunszt, P. Z., Lamb, D. Q., McKay, T. A., Okamura, S., Racusin, J., Sekiguchi, M., Schneider, D. P., Shimasaku, K., and York, D. (2001). Color Separation of Galaxy Types in the Sloan Digital Sky Survey Imaging Data. *AJ*, 122(4):1861–1874.
- Stroe, A. and Sobral, D. (2015). A large narrow-band  $H\alpha$  survey at  $z \approx 0.2$ : the bright end of the luminosity function, cosmic variance and clustering across cosmic time. *MNRAS*, 453:242–258.
- Stroe, A., Sobral, D., Matthee, J., Calhau, J., and Oteo, I. (2017). A  $1.4 \text{ deg}^2$  blind survey for C II], C III] and C IV at  $z \approx 0.7\text{--}1.5$  - I. Nature, morphologies and equivalent widths. *MNRAS*, 471:2558–2574.
- Sturm, E., González-Alfonso, E., Veilleux, S., Fischer, J., Graciá-Carpio, J., Hailey-Dunsheath, S., Conrursi, A., Poglitsch, A., Sternberg, A., Davies, R., Genzel, R., Lutz, D., Tacconi, L., Verma, A., Maiolino, R., and de Jong, J. A. (2011). Massive Molecular Outflows and Negative Feedback in ULIRGs Observed by Herschel-PACS. *ApJ*, 733(1):L16.
- Sutherland, R. S. and Dopita, M. A. (1993). Cooling Functions for Low-Density Astrophysical Plasmas. *ApJS*, 88:253.
- Tacconi, L. J., Genzel, R., Lutz, D., Rigopoulou, D., Baker, A. J., Iserlohe, C., and Tecza, M. (2002). Ultraluminous Infrared Galaxies: QSOs in Formation? *ApJ*, 580:73–87.
- Takahashi, M. I., Shioya, Y., Taniguchi, Y., Murayama, T., Ajiki, M., Sasaki, S. S., Koizumi, O., Nagao, T., Scoville, N. Z., Mobasher, B., Aussel, H., Capak, P., Carilli, C., Ellis, R. S., Garilli, B., Giavalisco, M., Guzzo, L., Hasinger, G., Impey, C., Kitzbichler, M. G., Koekemoer, A., Le Fèvre, O., Lilly, S. J., Maccagni, D., Renzini, A., Rich, M., Sanders, D. B., Schinnerer, E., Scodreggio, M., Shopbell, P.,



- Smolčić, V., Tribiano, S., Ideue, Y., and Mihara, S. (2007). The [O II]  $\lambda 3727$  Luminosity Function and Star Formation Rate at  $z \sim 1.2$  in the COSMOS 2 Square Degree Field and the Subaru Deep Field. *ApJS*, 172(1):456–467.
- Tamburello, V., Capelo, P. R., Mayer, L., Bellovary, J. M., and Wadsley, J. W. (2017). Supermassive black hole pairs in clumpy galaxies at high redshift: delayed binary formation and concurrent mass growth. *MNRAS*, 464(3):2952–2962.
- Tamburri, S., Saracco, P., Longhetti, M., Gargiulo, A., Lonoce, I., and Ciocca, F. (2014). The population of early-type galaxies: how it evolves with time and how it differs from passive and late-type galaxies. *A&A*, 570:A102.
- Tanaka, T. and Haiman, Z. (2009). The Assembly of Supermassive Black Holes at High Redshifts. *ApJ*, 696(2):1798–1822.
- Tanaka, Y., Nandra, K., Fabian, A. C., Inoue, H., Otani, C., Dotani, T., Hayashida, K., Iwasawa, K., Kii, T., Kunieda, H., Makino, F., and Matsuoka, M. (1995). Gravitationally redshifted emission implying an accretion disk and massive black hole in the active galaxy MCG-6-30-15. *Nature*, 375(6533):659–661.
- Taylor, E. N., Franx, M., van Dokkum, P. G., Bell, E. F., Brammer, G. B., Rudnick, G., Wuyts, S., Gawiser, E., Lira, P., Urry, C. M., and Rix, H.-W. (2009). The Rise of Massive Red Galaxies: The Color-Magnitude and Color-Stellar Mass Diagrams for  $z_{phot} \lesssim 2$  from the Multiwavelength Survey by Yale-Chile. *ApJ*, 694(2):1171–1199.
- Thomas, N., Davé, R., Anglés-Alcázar, D., and Jarvis, M. (2019). Black hole - Galaxy correlations in SIMBA. *MNRAS*, 487(4):5764–5780.
- Thompson, T. A., Quataert, E., and Murray, N. (2005). Radiation Pressure-supported Starburst Disks and Active Galactic Nucleus Fueling. *ApJ*, 630(1):167–185.
- Thorne, K. S. (1974). Disk-Accretion onto a Black Hole. II. Evolution of the Hole. *ApJ*, 191:507–520.
- Tichy, W. and Marronetti, P. (2008). Final mass and spin of black-hole mergers. *Phys. Rev. D*, 78(8):081501.
- Tombesi, F., Meléndez, M., Veilleux, S., Reeves, J. N., González-Alfonso, E., and Reynolds, C. S. (2015). Wind from the black-hole accretion disk driving a molecular outflow in an active galaxy. *Nature*, 519(7544):436–438.
- Tombesi, F., Tazaki, F., Mushotzky, R. F., Ueda, Y., Cappi, M., Gofford, J., Reeves, J. N., and Guainazzi, M. (2014). Ultrafast outflows in radio-loud active galactic nuclei. *MNRAS*, 443(3):2154–2182.
- Tonini, C., Mutch, S. J., Croton, D. J., and Wyithe, J. S. B. (2016). The growth of discs and bulges during hierarchical galaxy formation - I. Fast evolution versus secular processes. *MNRAS*, 459:4109–4129.
- Tonry, J. L. (1984). Evidence for a central mass concentration in M 32. *ApJ*, 283:L27–L30.
- Tonry, J. L. (1987). A Central Black Hole in M32. *ApJ*, 322:632.
- Toomre, A. (1977). Mergers and Some Consequences. In Tinsley, B. M. and Larson, Richard B. Gehret, D. C., editors, *Evolution of Galaxies and Stellar Populations*, page 401.
- Toomre, A. (1981). What amplifies the spirals. In Fall, S. M. and Lynden-Bell, D., editors, *Structure and Evolution of Normal Galaxies*, pages 111–136.
- Trakhtenbrot, B. (2014). The Most Massive Active Black Holes at  $z \sim 1.5$ -3.5 have High Spins and Radiative Efficiencies. *ApJ*, 789(1):L9.

- Treister, E., Schawinski, K., Urry, C. M., and Simmons, B. D. (2012). Major Galaxy Mergers Only Trigger the Most Luminous Active Galactic Nuclei. *ApJ*, 758(2):L39.
- Tremaine, S. and Weinberg, M. D. (1984). A kinematic method for measuring the pattern speed of barred galaxies. *ApJ*, 282:L5–L7.
- Tremmel, M., Governato, F., Volonteri, M., Pontzen, A., and Quinn, T. R. (2018). Wandering Supermassive Black Holes in Milky-Way-mass Halos. *ApJ*, 857(2):L22.
- Tremmel, M., Quinn, T. R., Ricarte, A., Babul, A., Chadayammuri, U., Natarajan, P., Nagai, D., Pontzen, A., and Volonteri, M. (2019). Introducing ROMULUSC: a cosmological simulation of a galaxy cluster with an unprecedented resolution. *MNRAS*, 483(3):3336–3362.
- Treu, T., Malkan, M. A., and Blandford, R. D. (2004). The Relation Between Black Hole Mass and Velocity Dispersion at  $z \sim 0.37$ . *ApJ*, 615(2):L97–L100.
- Treu, T., Woo, J.-H., Malkan, M. A., and Blandford, R. D. (2007). Cosmic Evolution of Black Holes and Spheroids. II. Scaling Relations at  $z=0.36$ . *ApJ*, 667(1):117–130.
- Trujillo, I., Ferreras, I., and de La Rosa, I. G. (2011). Dissecting the size evolution of elliptical galaxies since  $z \sim 1$ : puffing-up versus minor-merging scenarios. *MNRAS*, 415(4):3903–3913.
- Ueda, Y., Akiyama, M., Hasinger, G., Miyaji, T., and Watson, M. G. (2014). Toward the Standard Population Synthesis Model of the X-Ray Background: Evolution of X-Ray Luminosity and Absorption Functions of Active Galactic Nuclei Including Compton-thick Populations. *ApJ*, 786:104.
- Urry, C. M. and Padovani, P. (1995). Unified Schemes for Radio-Loud Active Galactic Nuclei. *PASP*, 107:803.
- Valencia-Enríquez, D., Puerari, I., and Rodrigues, I. (2019). Assessing Disk Galaxy Stability through Time. *AJ*, 157(5):175.
- Valenzuela, O. and Klypin, A. (2003). Secular bar formation in galaxies with a significant amount of dark matter. *MNRAS*, 345(2):406–422.
- Valiante, R., Schneider, R., Volonteri, M., and Omukai, K. (2016). From the first stars to the first black holes. *MNRAS*, 457(3):3356–3371.
- van Albada, G. D. and Roberts, W. W., J. (1981). A high-resolution study of the gas flow in barred spirals. *ApJ*, 246:740–750.
- van Albada, T. S. (1982). Dissipationless galaxy formation and the R to the 1/4-power law. *MNRAS*, 201:939–955.
- van den Bergh, S. (1976). A new classification system for galaxies. *ApJ*, 206:883–887.
- van der Wel, A., Franx, M., van Dokkum, P. G., Skelton, R. E., Momcheva, I. G., Whitaker, K. E., Brammer, G. B., Bell, E. F., Rix, H.-W., Wuyts, S., Ferguson, H. C., Holden, B. P., Barro, G., Koeke-moer, A. M., Chang, Y.-Y., McGrath, E. J., Häussler, B., Dekel, A., Behroozi, P., Fumagalli, M., Leja, J., Lundgren, B. F., Maseda, M. V., Nelson, E. J., Wake, D. A., Patel, S. G., Labbé, I., Faber, S. M., Grogin, N. A., and Kocevski, D. D. (2014). 3D-HST+CANDELS: The Evolution of the Galaxy Size-Mass Distribution since  $z = 3$ . *ApJ*, 788:28.
- van Dokkum, P. G. (2005). The Recent and Continuing Assembly of Field Elliptical Galaxies by Red Mergers. *AJ*, 130:2647–2665.
- van Meter, J. R., Miller, M. C., Baker, J. G., Boggs, W. D., and Kelly, B. J. (2010). Test of a General Formula for Black Hole Gravitational Wave Kicks. *ApJ*, 719:1427–1432.

- van Wassenhove, S., Volonteri, M., Walker, M. G., and Gair, J. R. (2010). Massive black holes lurking in Milky Way satellites. *MNRAS*, 408(2):1139–1146.
- Vazza, F., Brügggen, M., and Gheller, C. (2013). Thermal and non-thermal traces of AGN feedback: results from cosmological AMR simulations. *MNRAS*, 428(3):2366–2388.
- Veilleux, S., Cecil, G., and Bland-Hawthorn, J. (2005). Galactic Winds. *ARA&A*, 43(1):769–826.
- Veilleux, S., Kim, D. C., Peng, C. Y., Ho, L. C., Tacconi, L. J., Dasyra, K. M., Genzel, R., Lutz, D., and Sanders, D. B. (2006). A Deep Hubble Space Telescope H-Band Imaging Survey of Massive Gas-rich Mergers. *ApJ*, 643(2):707–723.
- Veilleux, S., Kim, D. C., Rupke, D. S. N., Peng, C. Y., Tacconi, L. J., Genzel, R., Lutz, D., Sturm, E., Contursi, A., Schweitzer, M., Dasyra, K. M., Ho, L. C., Sanders, D. B., and Burkert, A. (2009). A Deep Hubble Space Telescope H-Band Imaging Survey of Massive Gas-Rich Mergers. II. The QUEST QSOs. *ApJ*, 701(1):587–606.
- Vilella-Rojo, G., Viironen, K., López-Sanjuan, C., Cenarro, A. J., Varela, J., Díaz-García, L. A., Cristóbal-Hornillos, D., Ederoclite, A., Marín-Franch, A., and Moles, M. (2015). Extracting  $H\alpha$  flux from photometric data in the J-PLUS survey. *A&A*, 580:A47.
- Villforth, C., Hamann, F., Rosario, D. J., Santini, P., McGrath, E. J., van der Wel, A., Chang, Y. Y., Guo, Y., Dahlen, T., Bell, E. F., Conselice, C. J., Croton, D., Dekel, A., Faber, S. M., Grogin, N., Hamilton, T., Hopkins, P. F., Juneau, S., Kartaltepe, J., Kocevski, D., Koekemoer, A., Koo, D. C., Lotz, J., McIntosh, D., Mozena, M., Somerville, R., and Wild, V. (2014). Morphologies of  $z \sim 0.7$  AGN host galaxies in CANDELS: no trend of merger incidence with AGN luminosity. *MNRAS*, 439(4):3342–3356.
- Vogelsberger, M., Genel, S., Sijacki, D., Torrey, P., Springel, V., and Hernquist, L. (2013). A model for cosmological simulations of galaxy formation physics. *MNRAS*, 436(4):3031–3067.
- Vogelsberger, M., Genel, S., Springel, V., Torrey, P., Sijacki, D., Xu, D., Snyder, G., Bird, S., Nelson, D., and Hernquist, L. (2014a). Properties of galaxies reproduced by a hydrodynamic simulation. *Nature*, 509(7499):177–182.
- Vogelsberger, M., Genel, S., Springel, V., Torrey, P., Sijacki, D., Xu, D., Snyder, G., Nelson, D., and Hernquist, L. (2014b). Introducing the Illustris Project: simulating the coevolution of dark and visible matter in the Universe. *MNRAS*, 444(2):1518–1547.
- Vogelsberger, M., Marinacci, F., Torrey, P., and Puchwein, E. (2020). Cosmological simulations of galaxy formation. *Nature Reviews Physics*, 2(1):42–66.
- Volonteri, M. (2010). Formation of supermassive black holes. *A&A Rev.*, 18:279–315.
- Volonteri, M., Haardt, F., and Madau, P. (2003). The Assembly and Merging History of Supermassive Black Holes in Hierarchical Models of Galaxy Formation. *ApJ*, 582:559–573.
- Volonteri, M. and Madau, P. (2008). Off-Nuclear AGNs as a Signature of Recoiling Massive Black Holes. *The Astrophysical Journal*, 687(2):L57.
- Volonteri, M., Madau, P., Quataert, E., and Rees, M. J. (2005). The Distribution and Cosmic Evolution of Massive Black Hole Spins. *ApJ*, 620(1):69–77.
- Volonteri, M. and Perna, R. (2005). Dynamical evolution of intermediate-mass black holes and their observable signatures in the nearby Universe. *MNRAS*, 358:913–922.
- Volonteri, M., Sikora, M., and Lasota, J.-P. (2007). Black Hole Spin and Galactic Morphology. *ApJ*, 667(2):704–713.

- Volonteri, M., Sikora, M., Lasota, J.-P., and Merloni, A. (2013). The Evolution of Active Galactic Nuclei and their Spins. *ApJ*, 775:94.
- Volonteri, M., Silk, J., and Dubus, G. (2015). The Case for Supercritical Accretion onto Massive Black Holes at High Redshift. *ApJ*, 804(2):148.
- Volonteri, M. and Stark, D. P. (2011). Assessing the redshift evolution of massive black holes and their hosts. *MNRAS*, 417:2085–2093.
- Walker, I. R., Mihos, J. C., and Hernquist, L. (1996). Quantifying the Fragility of Galactic Disks in Minor Mergers. *ApJ*, 460:121.
- Wang, L., Dutton, A. A., Stinson, G. S., Macciò, A. V., Penzo, C., Kang, X., Keller, B. W., and Wadsley, J. (2015). NIHAO project - I. Reproducing the inefficiency of galaxy formation across cosmic time with a large sample of cosmological hydrodynamical simulations. *MNRAS*, 454(1):83–94.
- Weinberg, M. D. (1985). Evolution of barred galaxies by dynamical friction. *MNRAS*, 213:451–471.
- Weinberg, M. D. and Katz, N. (2007a). The bar-halo interaction - I. From fundamental dynamics to revised N-body requirements. *MNRAS*, 375(2):425–459.
- Weinberg, M. D. and Katz, N. (2007b). The bar-halo interaction - II. Secular evolution and the religion of N-body simulations. *MNRAS*, 375(2):460–476.
- Weinberger, L. H., Haehnelt, M. G., and Kulkarni, G. (2019). Modelling the observed luminosity function and clustering evolution of Ly  $\alpha$  emitters: growing evidence for late reionization. *MNRAS*, 485:1350–1366.
- Weinberger, R., Springel, V., Hernquist, L., Pillepich, A., Marinacci, F., Pakmor, R., Nelson, D., Genel, S., Vogelsberger, M., Naiman, J., and Torrey, P. (2017). Simulating galaxy formation with black hole driven thermal and kinetic feedback. *MNRAS*, 465(3):3291–3308.
- Weinberger, R., Springel, V., Pakmor, R., Nelson, D., Genel, S., Pillepich, A., Vogelsberger, M., Marinacci, F., Naiman, J., Torrey, P., and Hernquist, L. (2018). Supermassive black holes and their feedback effects in the IllustrisTNG simulation. *MNRAS*, 479(3):4056–4072.
- Whalen, D. J., Johnson, J. L., Smidt, J., Meiksin, A., Heger, A., Even, W., and Fryer, C. L. (2013). The Supernova that Destroyed a Protogalaxy: Prompt Chemical Enrichment and Supermassive Black Hole Growth. *ApJ*, 774(1):64.
- White, S. D. M. and Frenk, C. S. (1991). Galaxy formation through hierarchical clustering. *ApJ*, 379:52–79.
- White, S. D. M. and Rees, M. J. (1978). Core condensation in heavy halos - A two-stage theory for galaxy formation and clustering. *MNRAS*, 183:341–358.
- Wilkins, D. C. (1972). Bound Geodesics in the Kerr Metric. *Phys. Rev. D*, 5(4):814–822.
- Wilkins, S. M., Feng, Y., Di Matteo, T., Croft, R., Lovell, C. C., and Waters, D. (2017). The properties of the first galaxies in the BlueTides simulation. *MNRAS*, 469(3):2517–2530.
- Wilson, A. S. and Willis, A. G. (1980). Radio structures of Seyfert galaxies. I. *ApJ*, 240:429–441.
- Wise, J. H., Turk, M. J., and Abel, T. (2008). Resolving the Formation of Protogalaxies. II. Central Gravitational Collapse. *ApJ*, 682(2):745–757.
- Wolf, C., Meisenheimer, K., Rix, H.-W., Borch, A., Dye, S., and Kleinheinrich, M. (2003). The COMBO-17 survey: Evolution of the galaxy luminosity function from 25 000 galaxies with  $0.2 < z < 1.2$ . *A&A*, 401:73–98.

- Wyndham, J. D. (1965). A search for optical objects associated with 50 radio sources. *AJ*, 70:384–392.
- Yasuda, N., Fukugita, M., Narayanan, V. K., Lupton, R. H., Strateva, I., Strauss, M. A., Ivezić, Ž., Kim, R. S. J., Hogg, D. W., Weinberg, D. H., Shimasaku, K., Loveday, J., Annis, J., Bahcall, N. A., Blanton, M., Brinkmann, J., Brunner, R. J., Connolly, A. J., Csabai, I., Doi, M., Hamabe, M., Ichikawa, S.-I., Ichikawa, T., Johnston, D. E., Knapp, G. R., Kunszt, P. Z., Lamb, D. Q., McKay, T. A., Munn, J. A., Nichol, R. C., Okamura, S., Schneider, D. P., Szokoly, G. P., Vogeley, M. S., Watanabe, M., and York, D. G. (2001). Galaxy Number Counts from the Sloan Digital Sky Survey Commissioning Data. *AJ*, 122:1104–1124.
- York, D. G., Adelman, J., Anderson, Jr., J. E., Anderson, S. F., Annis, J., Bahcall, N. A., Bakken, J. A., Barkhouser, R., Bastian, S., Berman, E., Boroski, W. N., Bracker, S., Briegel, C., Briggs, J. W., Brinkmann, J., Brunner, R., Burles, S., Carey, L., Carr, M. A., Castander, F. J., Chen, B., Colestock, P. L., Connolly, A. J., Crocker, J. H., Csabai, I., Czarapata, P. C., Davis, J. E., Doi, M., Dombeck, T., Eisenstein, D., Ellman, N., Elms, B. R., Evans, M. L., Fan, X., Federwitz, G. R., Fiscelli, L., Friedman, S., Frieman, J. A., Fukugita, M., Gillespie, B., Gunn, J. E., Gurbani, V. K., de Haas, E., Haldeman, M., Harris, F. H., Hayes, J., Heckman, T. M., Hennessy, G. S., Hindsley, R. B., Holm, S., Holmgren, D. J., Huang, C.-h., Hull, C., Husby, D., Ichikawa, S.-I., Ichikawa, T., Ivezić, Ž., Kent, S., Kim, R. S. J., Kinney, E., Klaene, M., Kleinman, A. N., Kleinman, S., Knapp, G. R., Korienek, J., Kron, R. G., Kunszt, P. Z., Lamb, D. Q., Lee, B., Leger, R. F., Limmongkol, S., Lindenmeyer, C., Long, D. C., Loomis, C., Loveday, J., Lucinio, R., Lupton, R. H., MacKinnon, B., Mannery, E. J., Mantsch, P. M., Margon, B., McGehee, P., McKay, T. A., Meiksin, A., Merelli, A., Monet, D. G., Munn, J. A., Narayanan, V. K., Nash, T., Neilsen, E., Neswold, R., Newberg, H. J., Nichol, R. C., Nicinski, T., Nonino, M., Okada, N., Okamura, S., Ostriker, J. P., Owen, R., Pauls, A. G., Peoples, J., Peterson, R. L., Petravick, D., Pier, J. R., Pope, A., Pordes, R., Prosapio, A., Rechenmacher, R., Quinn, T. R., Richards, G. T., Richmond, M. W., Rivetta, C. H., Rockosi, C. M., Ruthmansdorfer, K., Sandford, D., Schlegel, D. J., Schneider, D. P., Sekiguchi, M., Sergey, G., Shimasaku, K., Siegmund, W. A., Smeed, S., Smith, J. A., Snedden, S., Stone, R., Stoughton, C., Strauss, M. A., Stubbs, C., SubbaRao, M., Szalay, A. S., Szapudi, I., Szokoly, G. P., Thakar, A. R., Tremonti, C., Tucker, D. L., Uomoto, A., Vanden Berk, D., Vogeley, M. S., Waddell, P., Wang, S.-i., Watanabe, M., Weinberg, D. H., Yanny, B., Yasuda, N., and SDSS Collaboration (2000). The Sloan Digital Sky Survey: Technical Summary. *AJ*, 120:1579–1587.
- Yoshida, N., Omukai, K., and Hernquist, L. (2008). Protostar Formation in the Early Universe. *Science*, 321(5889):669.
- Yun, K., Pillepich, A., Zinger, E., Nelson, D., Donnari, M., Joshi, G., Rodriguez-Gomez, V., Genel, S., Weinberger, R., Vogelsberger, M., and Hernquist, L. (2019). Jellyfish galaxies with the IllustrisTNG simulations - I. Gas-stripping phenomena in the full cosmological context. *MNRAS*, 483(1):1042–1066.
- Zackay, B., Venumadhav, T., Dai, L., Roulet, J., and Zaldarriaga, M. (2019). Highly spinning and aligned binary black hole merger in the Advanced LIGO first observing run. *Phys. Rev. D*, 100(2):023007.
- Zana, T., Dotti, M., Capelo, P. R., Bonoli, S., Haardt, F., Mayer, L., and Spinoso, D. (2018a). External versus internal triggers of bar formation in cosmological zoom-in simulations. *MNRAS*, 473:2608–2621.
- Zana, T., Dotti, M., Capelo, P. R., Mayer, L., Haardt, F., Shen, S., and Bonoli, S. (2018b). Bar resilience to flybys in a cosmological framework. *MNRAS*, 479:5214–5219.
- Zel'dovich, Y. B. (1964). The Fate of a Star and the Evolution of Gravitational Energy Upon Accretion. *Soviet Physics Doklady*, 9:195.

- Zhai, Z., Benson, A., Wang, Y., Yepes, G., and Chuang, C.-H. (2019). Prediction of H  $\alpha$  and [O III] emission line galaxy number counts for future galaxy redshift surveys. *MNRAS*, 490(3):3667–3678.
- Zhang, S. N., Cui, W., and Chen, W. (1997). Black Hole Spin in X-Ray Binaries: Observational Consequences. *ApJ*, 482(2):L155–L158.
- Zhou, Z.-B., Zhu, W., Wang, Y., and Feng, L.-L. (2020). Barred galaxies in the Illustris-1 and TNG100 simulations. *arXiv e-prints*, page arXiv:2004.11620.
- Zoldan, A., De Lucia, G., Xie, L., Fontanot, F., and Hirschmann, M. (2018). Structural and dynamical properties of galaxies in a hierarchical Universe: sizes and specific angular momenta. *MNRAS*, 481:1376–1400.

## APPENDIX A

### THE MOTION OF A SPINLESS TEST BODY AROUND A BLACK HOLE: INNERMOST STABLE CIRCULAR ORBIT

In this appendix we describe the motion of a test particle around a black hole to derive the position, energy and angular momentum of the *innermost stable circular orbit* (ISCO)<sup>1</sup>, i.e the smallest circular orbit which a particle can establish around a black hole before being accreted into it. All the information presented in this section can be found in [Jefremov et al. \(2015\)](#). In case the reader is interested, the same paper performs similar computations but for a spinning test particle.

\* **Schwarzschild black hole**: The radial motion of a particle in General relativity under the Schwarzschild metric (see Eq. (1.12), in units of  $c = G = 1$ ) can be expressed as:

$$\left(\frac{dr}{d\tau}\right)^2 = E^2 - \left(1 - \frac{2M}{r}\right)\left(1 + \frac{L^2}{r^2}\right) \quad (\text{A.1})$$

where  $E$  is the total energy per unit particle rest mass at the infinity,  $L$  is the angular momentum per unit of particle rest mass parallel to the symmetry axis and  $\tau$  the proper time, being the relation between  $dt$  and  $d\tau$ :

$$\left(\frac{dt}{d\tau}\right)^2 = \frac{E}{1 - 2M/r} \quad (\text{A.2})$$

Transforming Eq. (A.1) to:

$$\left(\frac{dr}{d\tau}\right)^2 = E^2 - U_{\text{eff}}^{\text{Sch},2} \quad (\text{A.3})$$

we can express the *effective potential* (E.P) experienced by the particle as:

$$U_{\text{eff}}^{\text{Sch}} = \sqrt{\left(1 - \frac{2M}{r}\right)\left(1 + \frac{L^2}{r^2}\right)} \quad (\text{A.4})$$

To establish a circular motion around the BH, the test particle must satisfy two different conditions:

i) The radial motion must to be zero:

$$\frac{dr}{d\tau} = 0 \quad (\text{A.5})$$

which yields to:

$$E = U_{\text{eff}}^{\text{Sch}} \quad (\text{A.6})$$

<sup>1</sup>The ISCO orbit is particularly interesting in the accretion disk theory given that it is assumed that the accretion disk is truncated at that distance.



ii) The radial acceleration must be zero:

$$\frac{d^2 r}{d\tau^2} = 0 \quad (\text{A.7})$$

which implies:

$$\frac{dU_{\text{eff}}^{\text{Sch},2}}{dr} = 0, \quad U_{\text{eff}}^{\text{Sch}} > 0 \quad (\text{A.8})$$

Solving the system of equations created by Eq.(A.6) and Eq.(A.8) we find that both radius,  $r$ , and energy,  $E$ , for a circular motion can be expressed as:

$$r = \frac{L}{2M} \left[ 1 \pm \sqrt{1 - \frac{12M^2}{L^2}} \right] \quad (\text{A.9})$$

$$E = L \sqrt{\frac{1}{Mr} \left( 1 - \frac{2M}{r} \right)} \quad (\text{A.10})$$

To find the ISCO position it is needed to determine the last value of  $L$  at which the effective potential still has extremum. This corresponds to finding the inflection point of the effective potential:

$$\frac{d^2 U_{\text{eff}}^{\text{Sch},2}}{dr^2} = 0 \quad (\text{A.11})$$

From Eq. (A.6) it is evident that the maximum and minimum of  $U_{\text{eff}}^{\text{Sch}}$  happens at  $L = 2\sqrt{3}M$ . Therefore:

$$r_{\text{ISCO}} = 6M, \quad L_{\text{ISCO}} = 2\sqrt{3}M, \quad E_{\text{ISCO}} = \sqrt{\frac{8}{9}} \quad (\text{A.12})$$

\* **Kerr black hole:** In the Kerr metric we can perform a similar analysis as before. According to Eq. (1.13) and in units of  $c = G = 1$  the motion of a particle can be written as:

$$\left( \frac{dr}{d\tau} \right)^2 = E^2 - \left( 1 - \frac{2M}{r} - \frac{a^2(E^2 - 1) - L^2}{r^2} - \frac{2M(L - aE)^2}{r^3} \right) \quad (\text{A.13})$$

with the relation between  $dt$  and  $d\tau$ :

$$\frac{dt}{d\tau} = -\frac{2Ma}{r\Delta}L + \frac{E}{\Delta} \left( r^2 + a^2 + \frac{2Ma^2}{r} \right) \quad (\text{A.14})$$

where  $E$  is the total energy per unit particle rest mass at the infinity and  $L$  corresponds to the angular momentum per particle rest mass parallel to the symmetry axis. Usually, to make a more compact expression, Eq. (A.13) is rewritten as:

$$\left( \frac{dr}{d\tau} \right)^2 = \frac{1}{r^4} (\alpha E^2 - 2\beta E + \gamma) \quad (\text{A.15})$$

where

$$\begin{aligned} \alpha &= (r^2 + a^2)^2 - \Delta a^2 \\ \beta &= [a(r^2 + a^2) - \Delta a] = 2MraL \\ \gamma &= a^2 L^2 - \Delta(r^2 + L^2) \end{aligned} \quad (\text{A.16})$$

As we did with the Schwarzschild metric, to establish a circular motion the orbit of the particle has to satisfy both the velocity and acceleration conditions presented in Eq. (A.5) and Eq. (A.7). This yields to:

$$\begin{aligned} \frac{1}{r^4} (\alpha E^2 - 2\beta E + \gamma) &= 0 \\ \frac{d}{dr} \left[ \frac{1}{r^4} (\alpha E^2 - 2\beta E + \gamma) \right] &= 0 \end{aligned} \quad (\text{A.17})$$

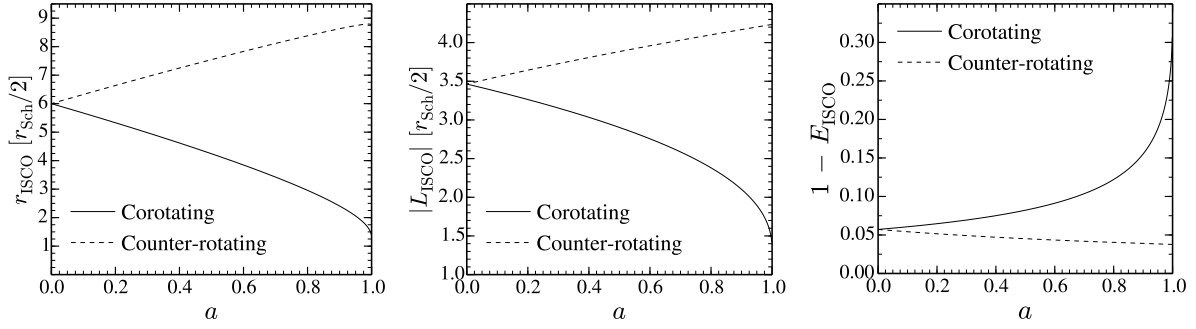


Figure A.1: **Left panel:** Position of the innermost stable circular orbit,  $r_{\text{ISCO}}$ , as a function of the spin parameter,  $a$ , for a co- and counter- rotating orbit (solid and dashed lines, respectively). **Middle panel:** The same as the left panel but for the angular momentum of the innermost stable circular orbit,  $L_{\text{ISCO}}$ . **Right panel:** The same as the left panel but for the energy of the innermost stable circular orbit,  $E_{\text{ISCO}}$ .

By solving Eq.(A.17), the energy,  $E$ , and angular momentum,  $L$ , of an orbit given by a radius  $r$  can be expressed as:

$$E = \frac{r^{3/2} - 2Mr^{1/2} \pm aM^{1/2}}{r^{3/4} (r^{3/2} - 3Mr^{1/2} \pm 2aM^{1/2})^{1/2}} \quad (\text{A.18})$$

$$L = \frac{\pm M^{1/2} (r^2 \mp 2aM^{1/2}r^{1/2} + a^2)}{r^{3/4} (r^{3/2} - 3Mr^{1/2} \pm 2aM^{1/2})^{1/2}} \quad (\text{A.19})$$

where the upper sign refers to direct orbits (i.e co-rotating orientation between particle angular momentum  $L$  and BH spin  $a$ ) and lower sign refers to retrograde orbits (i.e counter-rotating orientation between particle angular momentum  $L$  and BH spin  $a$ ).

Finally, to find the ISCO radius it is needed to add to Eq. (A.5) and Eq. (A.7) the extra condition of:

$$\frac{d^2}{dr^2} \left[ \frac{1}{r^4} (\alpha E^2 - 2\beta E + \gamma) \right] = 0 \quad (\text{A.20})$$

By solving the system created by Eq. (A.5), Eq. (A.7) and Eq. (A.20) we obtain the expression:

$$r^2 - 6Mr - 3a^2 \mp 8aM^{1/2}r^{1/2} \quad (\text{A.21})$$

The solution of this equation is presented in Bardeen et al. (1972):

$$r_{\text{ISCO}} = M \left[ 3 + Z_2 \mp \sqrt{(3 - Z_1)(3 + Z_1 + 2Z_2)} \right] \quad (\text{A.22})$$

where the upper (lower) sign refers to co-rotating (counter-rotating) orbits and  $Z_1$  and  $Z_2$  are two functions that depend on  $a$ :

$$\begin{aligned} Z_1 &\equiv 1 + (1 - a^2)^{1/3} \left[ (1 + a)^{1/3} + (1 - a)^{1/3} \right] \\ Z_2 &\equiv (3a^2 + Z_1^2)^{1/2} \end{aligned} \quad (\text{A.23})$$

To guide the reader, in the extreme case in which  $a = M$ :

i) For a co-rotating orbit:

$$r_{\text{ISCO}} = M, \quad L_{\text{ISCO}} = \frac{2}{\sqrt{3}}, \quad E_{\text{ISCO}} = \frac{1}{\sqrt{3}} \quad (\text{A.24})$$

ii) For a counter-rotating orbit:

$$r_{\text{ISCO}} = 9M, \quad L_{\text{ISCO}} = -\frac{22}{3\sqrt{3}}, \quad E_{\text{ISCO}} = \frac{5}{3\sqrt{3}} \quad (\text{A.25})$$

Fig. A.1 presents the position, angular momentum and energy of the innermost stable circular orbit as a function of the spin parameter for a co- and counter- rotating orbit. Note that for the case of  $a = 0$ , the parameters of the ISCO correspond to the Schwarzschild metric.

## APPENDIX B

### FEEDING CONSTRAINTS ON SUPERMASSIVE BLACK HOLE: THE EDDINGTON LIMIT

Let assume that a particle in the infinity is settled in the accretion disk around a BH. The particle kinetic energy,  $E_K$ , can be expressed as:

$$E_K = \frac{m M_{\text{BH}} G}{r} \quad (\text{B.1})$$

where  $m$  is the mass of the particle,  $M_{\text{BH}}$  is the BH mass,  $G$  is the gravitational constant and  $r$  is the distance between the particle and the BH. The change of kinetic energy corresponds to a luminosity,  $L$ , given by the expression:

$$L = f \frac{dE_K}{dt} = \frac{dm}{dt} \frac{M_{\text{BH}} G}{r} \quad (\text{B.2})$$

where  $f$  is the fraction of kinetic energy which is converted to luminosity. Note that  $M_{\text{BH}}$  is assumed to be constant given that the BH is so massive that the change of mass given by the mass accreted can be just neglected. From Eq. (B.2) we could conclude that the luminosity of the accretion disk would increase as long as  $dm/dt$  increases. However, this is not the case since the radiation emitted by the accretion process would cause a pressure force in the incoming particle which could delay or even stop  $dm/dt$ .

To characterize which is the maximum luminosity emitted by a BH during an accretion event, it is necessary to understand the balance of forces involved in the accretion. For simplicity, it is going to be considered a spherical model in which the central BH is surrounded by gas with density  $\rho(r)$ , the accreting material is ionized hydrogen (protons of mass,  $m_p$ ) and the emitted radiation can be characterized by a luminosity  $L$ . The pressure force experienced by a particle can be defined as:

$$\vec{F}_{\text{rad}} = -\sigma_T P_{\text{rad}}(r) n_e(r) \hat{r} \quad (\text{B.3})$$

where  $\sigma_T$  is the Thomson scattering cross-section,  $n_e(r)$  is the density of electrons at a radius  $r$  from the black hole, the negative sign corresponds to an outward force and  $P_{\text{rad}}$  is the radiation pressure at a radius  $r$  expressed as:

$$P_{\text{rad}}(r) = \frac{L}{4\pi r^2 c} \quad (\text{B.4})$$

In order to the gas not being blown away and being accreted by the BH it is needed that:

$$|\vec{F}_{\text{rad}}| \leq |\vec{F}_{\text{grav}}| = \frac{GM_{\text{BH}}\rho(r)}{r^2} \quad (\text{B.5})$$

Therefore, the maximum luminosity (usually called Eddington luminosity,  $L_{\text{Edd}}$ ) is reached when both pressure and gravity forces balance:

$$|\vec{F}_{\text{rad}}| = |\vec{F}_{\text{grav}}| \quad (\text{B.6})$$

corresponding to:

$$L_{\text{Edd}} = \frac{4\pi GcM_{\text{BH}}m_{\text{p}}}{\sigma_{\text{T}}} \approx 1.3 \times 10^{46} \left( \frac{M_{\text{BH}}}{10^8 M_{\odot}} \right) \text{ erg/s} \quad (\text{B.7})$$

## APPENDIX C

### IMPROVEMENTS IN THE BULGE SIZE

In this appendix we present the main changes in the bulge size computation during mergers. After this, we compare at different redshifts the predicted galaxy effective radius of early and late type galaxies with some recent observational works.

As we have described in Section 2.3.3, L-Galaxies assumes energy conservation to compute the final bulge size of the remnant galaxy after a major/minor interaction. Even though this procedure leads to a reasonable agreement between SAM and observations (see Figure 5 of Guo et al., 2011) it has been shown that SAMs generate too large bulge sizes at low stellar masses if the dissipation of energy during gas rich mergers is not taken into account (Naab et al., 2006; Shankar et al., 2013; Zoldan et al., 2018). As part of this thesis we address this issue, *modifying* the procedure presented in Section 2.3.3 assuming that the initial energy of Eq. 2.32 can be rewritten as (see also Shankar et al., 2013):

$$E_{\text{ini}} = C \sum_{i=1}^{i=2} E_0^i + E_{\text{orbital}} + E_{\text{dissipation}} \quad (\text{C.1})$$

where  $E_0^i$  is the gravitational self-binding energy of the galaxy  $i$ ,  $E_{\text{orbital}}$  is the orbital energy at merger (see Section 2.3.3 for more details) and  $E_{\text{dissipation}}$  is the term that takes into account the energy losses due to gas dissipation. As in Section 2.3.3, the first term of Eq. C.1 is expressed as

$$C \sum_{i=1}^{i=2} E_0^i = C \sum_{i=1}^{i=2} \frac{GM_{P_i}^2}{R_{P_i}}, \quad (\text{C.2})$$

where  $C$  is a structural parameter set to 0.5, and  $M_{P_i}$  and  $R_{P_i}$  the mass and the half mass radius of the  $i = 1, 2$  progenitor involved in the bulge formation. In the standard approach of L-Galaxies, during *major* merger the values of  $M_{P_1}$  and  $M_{P_2}$  are the sum of stars and cold gas converted into stars during the burst of SF (see Eq 2.27) of the two merging galaxies.  $R_{P_1}$  and  $R_{P_2}$  correspond to their respective half mass radii. However, Covington et al. (2008) showed that during this type of galaxy mergers the central part of the dark matter subhalo is expected to behave with similar stellar dynamic, increasing the effective mass involved in the bulge formation. In this thesis we have taken into account these results, changing  $M_{P_1}$  by  $M_{P_1} + \alpha M_{\text{halo}}(r < R_{P_1})$  (see Shankar et al., 2013; Lagos et al., 2018). Following Lagos et al. (2018) we set  $\alpha = 2$ . The value of  $M_{\text{halo}}(r < R)$  is computed assuming a Navarro-Frenk-White profile (Navarro et al., 1996) with a concentration parameter computed using the fit presented in Dutton and Macciò (2014) for the Planck cosmology. Finally, minor mergers are treated as in Section 2.3.3.

Regarding the orbital energy at merger:

$$E_{\text{orbital}} = f_{\text{orb}} \frac{GM_{P_1}M_{P_2}}{R_{P_1} + R_{P_2}}, \quad (\text{C.3})$$

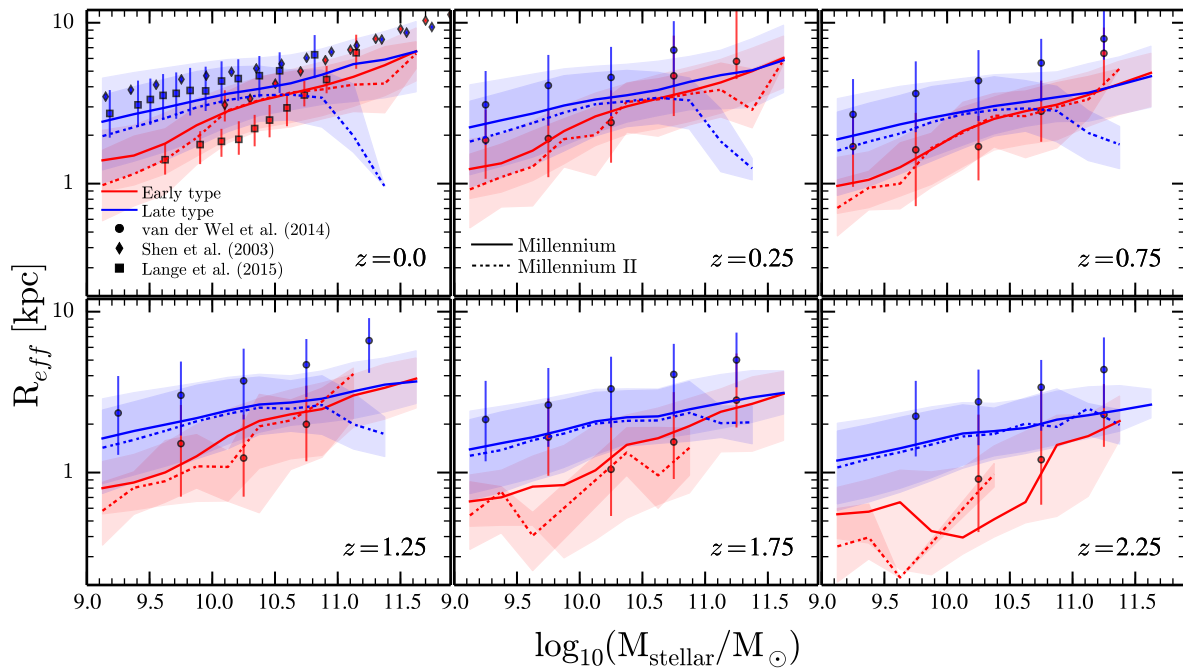


Figure C.1: Effective radius of early and late type galaxies in the Millennium (solid lines) and Millennium II (dashed lines). Blue lines corresponds to late-type galaxies (*disk-to-total* ratio  $D/T > 0.8$ ) and red ones with early-type (*bulge-to-total* ratio  $B/T > 0.7$ ). Shaded areas corresponds to  $1\sigma$  dispersion. We compare the predictions with the data available from Shen et al. (2003); van der Wel et al. (2014) and Lange et al. (2015).

where  $f_{\text{orb}}$  is a coefficient which quantify the interaction energy deposited in the bulge. We have followed the works of Covington et al. (2011), Porter et al. (2014) and Tonini et al. (2016) setting  $f_{\text{orb}} = 0$ . As pointed out by Covington et al. (2011) the effects of the orbital energy in the bulge computation are minimum and the values of  $f_{\text{orb}}$  are biased towards major mergers of disk-dominated galaxies. Finally, the value of  $E_{\text{dissipation}}$  has been expressed as (Covington et al., 2011):

$$E_{\text{dissipation}} = C_{\text{rad}} f_{\text{gas}} \left( \sum_{i=1}^{i=2} E_0^i \right) \quad (\text{C.4})$$

where  $C_{\text{rad}}$  is an efficiency parameter set to 2.75 (Covington et al., 2011) and  $f_{\text{gas}}$  the total merger gas fraction, defined as:

$$f_{\text{gas}} = \frac{\sum_{i=1}^{i=2} M_{\text{cold}}^i}{(\sum_{i=1}^{i=2} M_{\text{cold}}^i + M_{\text{stellar}}^i)} \quad (\text{C.5})$$

where  $M_{\text{cold}}$  and  $M_{\text{stellar}}$  are, respectively, the cold gas and total stellar content of the galaxy. The subscript  $i$  refers to the central ( $i = 1$ ) and satellite ( $i = 2$ ) galaxies involved in the interaction. Since during minor mergers the gas does not reach the bulge region, we assume no dissipation losses, i.e  $E_{\text{dissipation}} = 0$  (see more details in Shankar et al., 2013). On the other hand, during *major* mergers we do allow dissipation effects as a consequence of the violent interaction.

In Fig C.1 we present the redshift evolution of galaxy sizes for MS and MSII (solid and dashed lines, respectively). The 3D galaxy effective radius ( $R_{\text{eff}}^{3D}$ ) has been computed as the mass weighted average of the bulge ( $R_{\text{bulge}}$ ) and stellar disc ( $1.68R_{\star}^{\text{d}}$ ) half-mass radii. To compare with data, we have converted the 3D into 2D projected half-mass radii ( $R_{\text{eff}}$ ) by using the conversion factor 0.68 presented in Shankar et al. (2013). Blue and red lines represents respectively the population of late-type (*disk-to-total* ratio  $D/T > 0.8$ ) and early-type ( $B/T > 0.7$ ) galaxies. We have presented the predictions at 6 different redshift



$z = 0, 0.25, 0.75, 1.25, 1.75$  and  $2.25$ , comparing them with the data available in [Shen et al. \(2003\)](#); [van der Wel et al. \(2014\)](#) and [Lange et al. \(2015\)](#). As shown, low massive galaxies in both early and late type population follow the observational trend. Nevertheless, for the most massive galaxies we predict slightly smaller radius. Probably, this is the consequence of the fact that we under-predict (overpredict) the elliptical (spiral) population in the most massive stellar mass bins (see Fig 3.3). In spite of that, the improvements included in the model allow us to reproduce the redshift evolution of the stellar-size relation with a remarkable agreement with the observations.

## APPENDIX D

### THE MORPHOLOGY FOR MILLENNIUM AND MILLENNIUM II: A MATTER OF MAJOR, MINOR MERGERS AND SMOOTH ACCRETION

In this appendix we explore the convergence of the  $z=0$  galaxy morphology at intermediate and low stellar masses between Millennium and Millennium II. By studying the mergers characteristics we find out that the responsible of the morphological disagreement between MS and MSII is a combination of major mergers and extreme minor mergers lead by small *dwarf galaxies* ( $M_{\text{stellar}} \lesssim 10^6 M_{\odot}$ ).

In order to investigate the  $z=0$  morphology discrepancy between Millennium simulations, we started to explore the major mergers predictions. In Fig D.1 upper panel it is presented the redshift evolution of MS and MSII major mergers number density  $n_{\text{Mm}}$  at various  $m_{\text{R}}^{\text{th}}$  values. Each panel correspond to different central galaxy stellar mass at the moment of the merger,  $M_{\text{stellar}}^{\text{Central}}(z)$ . While galaxies with  $M_{\text{stellar}}^{\text{Central}}(z) > 10^9 M_{\odot}$  display similar  $n_{\text{Mm}}$  values in MS and MSII at any  $m_{\text{R}}^{\text{th}}$  threshold<sup>1</sup>, the  $n_{\text{Mm}}$  predictions for galaxies with  $M_{\text{stellar}}^{\text{Central}}(z) < 10^9 M_{\odot}$  diverge. At small thresholds ( $m_{\text{R}}^{\text{th}} < 0.2$ ) the deviation between MSII and MS is almost one order of magnitude regardless of redshift. Increasing the  $m_{\text{R}}^{\text{th}}$  value ( $m_{\text{R}}^{\text{th}} > 0.2$ ) the difference is reduced to a factor 3. Such disagreement can be easily understood by the fact that MSII is able to resolve smaller subhalos around central galaxies. Hence, small galaxies hosted in the *friend-of-friend* central subhalo experience more frequently mergers with satellites galaxies of comparable *baryonic* mass. As can be seen in Fig D.4 first row the change of  $m_{\text{R}}^{\text{th}}$  has also an impact in the  $z=0$  galaxy morphology. The high N-body resolution of MSII combined with low values of  $m_{\text{R}}^{\text{th}}$  (set to 0.1 in the *standard model*) favors an increase of the elliptical galaxies at small stellar masses and overestimate the spiral population at  $M_{\text{stellar}} \sim 10^{8-9.5} M_{\odot}$ . Our analysis suggest that an improvement in the convergence of MS and MSII galaxy morphology and in the MSII disk-dominated galaxy population is achieved by imposing large  $m_{\text{R}}^{\text{th}}$  values. From hereafter we decide to use  $m_{\text{R}}^{\text{th}} = 0.2$  (closer to other thresholds imposed in others SAMs, see Somerville et al. (2001); Hatton et al. (2003); Lacey et al. (2016); Lagos et al. (2018)), based on the  $n_{\text{Mm}}$  number densities presented in Fig D.1.

Nevertheless, as can be seen in Fig D.4 first row the difference in  $n_{\text{Mm}}$  is not the unique cause of the MS and MSII morphology deviation. It is needed to explore the effect of the other type of galaxy mergers, i.e *minor mergers*. In Fig D.1 lower panel we present, as we did with before, the number density of minor mergers  $n_{\text{mm}}$  as a function of redshift split in different central galaxy stellar mass. As we can see, the figure shows something expected: L-Galaxies run on top of MSII mergers trees predicts higher  $n_{\text{mm}}$  than run on the MS ones (see black lines). In particular the differences increases when we decrease the central stellar mass: from 1 dex at masses  $M_{\text{stellar}}^{\text{Central}}(z) > 10^{11} M_{\odot}$  up to 2 dex at masses  $M_{\text{stellar}}^{\text{Central}}(z) \sim 10^{8-9} M_{\odot}$ . To explore the characteristics of the merging satellite galaxies, in Fig D.2 it is presented at different redshifts

<sup>1</sup>The small disagreement is just due to MSII box size: massive galaxies are rare in a  $\sim 100$  [Mpc/h] box side, especially at high- $z$ .

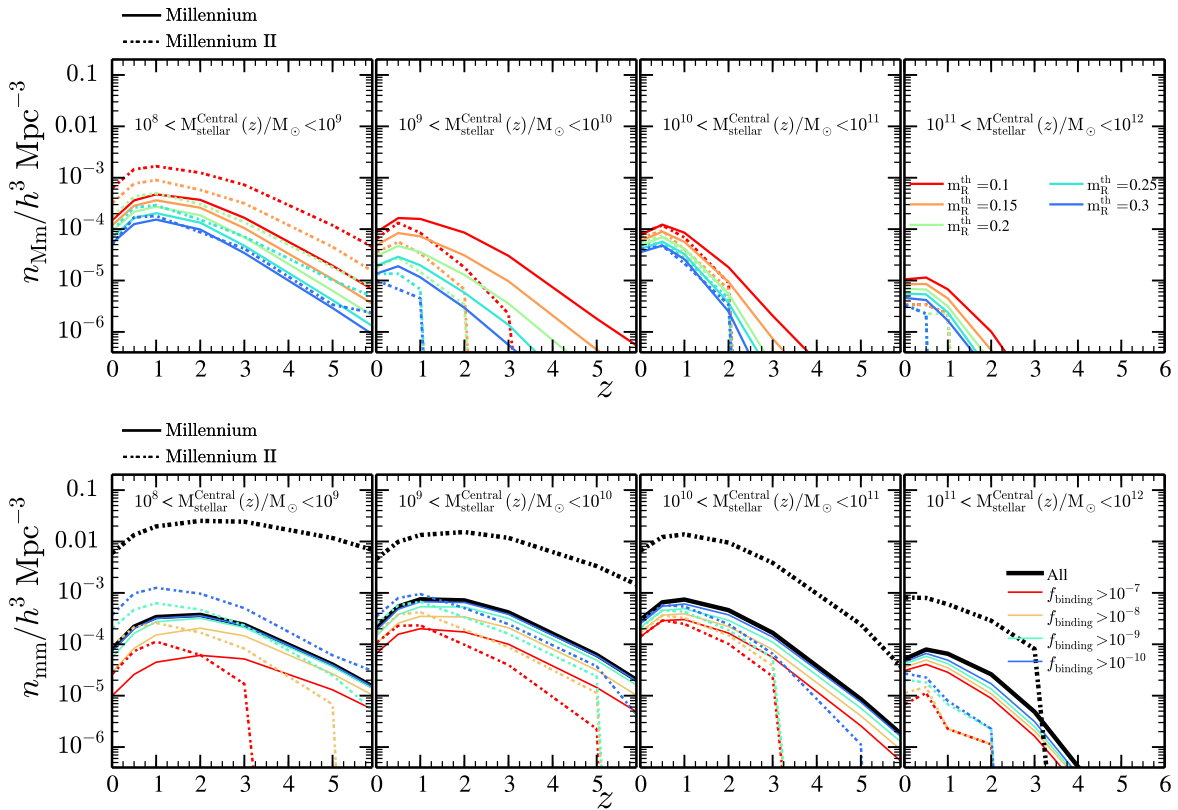


Figure D.1: **Upper row:** Number density of major mergers  $n_{Mm}$ . Different colors corresponds to different major/minor merger threshold ( $m_R^{\text{th}}$ ). Solid and dashed lines represent respectively the predictions for MS and MSII merger trees. Each panel corresponds to different stellar masses of central galaxies at the moment of the merger. **Upper row:** Number density of minor mergers  $n_{mm}$ . Each panel corresponds to different stellar masses of central galaxies at the moment of the merger. Here we have established  $m_R^{\text{th}} = 0.2$ . Different colors corresponds to different  $f_{\text{binding}}$  thresholds. Solid and dashed lines represent respectively the predictions for MS and MSII merger trees.

( $z < 3$ ) their typical stellar mass. MS predicts a median merging satellite mass  $\sim 10^{7.5}M_{\odot}$  with a small redshift evolution. Besides, more massive galaxies experience minor merger with slightly more massive galaxies. On contrary, MSII predicts smaller merging satellites  $\sim 10^5M_{\odot}$  (*dwarf galaxies*) with not redshift evolution and dependence with the central galaxy stellar mass. In particular, we have found that these small mergers are the ones that lead the morphological change in galaxies with  $M_{\text{stellar}} < 10^{9.5}M_{\odot}$ . Such extreme interactions enlarge the bulges of the small central galaxies by incorporating the whole stellar mass of the satellites while their stellar disks are unable to increase in mass as the cold-gas content is no large enough to overpass the critical mass imposed by the SAM to trigger an important episode of star formation ( $M_{\text{crit}}^0 = 2.4 \times 10^9 M_{\odot}$ , see Eq.S14 of [Henriques et al. 2015](#))<sup>2</sup>. Besides, merger induced bursts are not efficient either in this task. According to the merger ratios and the SAM efficiency parameters, less than the 0.2% of the total cold gas component is transformed in stars, i.e.  $\lesssim 10^5 M_{\odot}$  of new stars is added in the disk. Hence, the combination of the high number density of small interactions, the inefficient star formation and the simple minor merger recipe of L-Galaxies produces the unrealistic bust in the *bulge-to-total* ratio in the low mass population of MSII, as can be seen in Fig D.4. All this points to the needed to update the minor mergers prescription implemented in L-Galaxies, as this appears to be not fully valid for treating interactions with extreme mass-ratios, particularly common in the MSII merger trees. We thus introduced a new set of prescriptions to include *smooth accretion* as an additional

<sup>2</sup>Note that a more accurate description of star formation might come by linking this process with the molecular gas component instead of the total cold gas (see [Lagos et al., 2011](#)), as also discussed in [Henriques et al. \(2015\)](#).

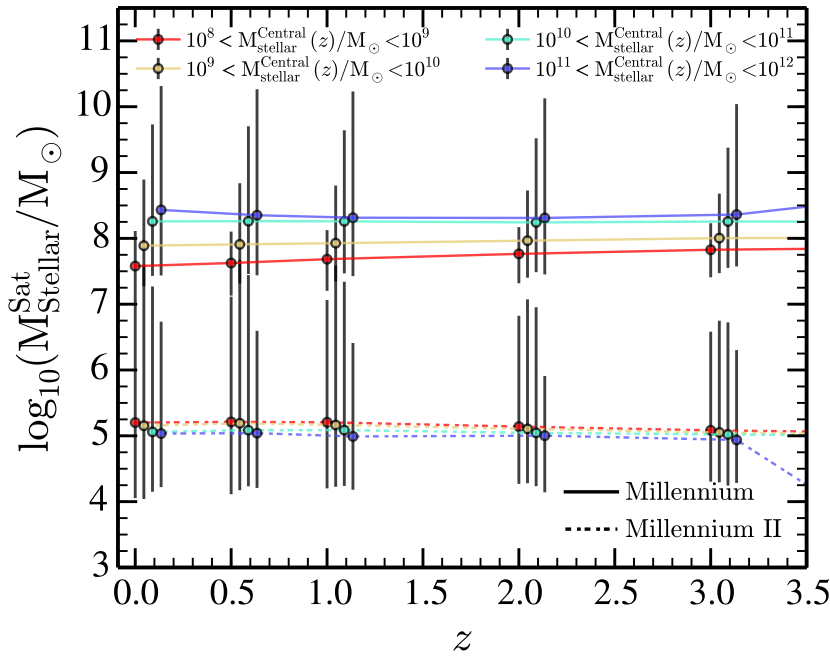


Figure D.2: Median stellar mass of the merging satellite galaxy ( $M_{\text{Stellar}}^{\text{Sat}}$ ). We have established a value of major/minor merger separation of  $m_{\text{R}}^{\text{th}} = 0.2$ . Bars represents the  $2\sigma$  value and colors different stellar mass bins of central galaxies at the moment of the merger ( $M_{\text{Stellar}}^{\text{Central}}(z)$ ).

channel for galaxy interactions (see e.g. [Abadi et al., 2003](#); [Peñarrubia et al., 2006](#); [Sales et al., 2007](#); [Kazantzidis et al., 2008](#)).

As we said, probably the crude minor merger recipe implemented in L-Galaxies is not completely valid in MSII. Its merger trees allow us to resolve the mergers of *dwarf galaxies* whose merger interaction may not be completely address with the L-Galaxies standard recipe. In order to improve this scenario, we are going to allow another different minor interaction: *smooth accretion* ([Abadi et al., 2003](#); [Peñarrubia et al., 2006](#); [Sales et al., 2007](#); [Kazantzidis et al., 2008](#)). While in minor mergers we follow the standard procedure presented L-Galaxies assuming that the whole stellar mass of the satellite galaxy is able to keep bound during the merger episode and reaches the central galaxy bulge, *smooth accretions* are characterized by a deposit of the whole satellite stellar mass onto the central galaxy stellar disk. This scenario takes place when the stellar system (bulge and disk) of the satellite galaxy does not have the enough energy to keep it together and it is progressively diluted in the central galaxy stellar disk without the possibility of reaching the central galaxy center. We want to emphasize that *smooth accretion* concept introduced here is not related with the already implemented tidal stripping events before the merger. *Smooth accretion* goes beyond it and takes into account the redistribution of the satellite stellar mass that would happen during its interaction with the central galaxy disk throughout the galaxy-galaxy collision.

In order to establish in which systems the minor mergers or *smooth accretions* take place, we are going to study the ratio of the two merging galaxies binding energies,  $f_{\text{binding}}$ . For the binding energy definition we only consider the interacting systems: for the satellite binding energy,  $E_{\text{binding}}^{\text{Satellite}}$ , we only consider its stellar mass while for the central one,  $E_{\text{binding}}^{\text{Central}}$ , we use the total mass in the disk (gas + stars). Therefore:

$$f_{\text{binding}} = \frac{E_{\text{binding}}^{\text{Satellite}}}{E_{\text{binding}}^{\text{Central}}} = \frac{M_{\text{Sat,Stellar}}^2 R_{\text{disk}}^{\text{Central}}}{M_{\text{Cent,disk}}^2 R_{\text{Stellar}}^{\text{Sat}}} \quad (\text{D.1})$$

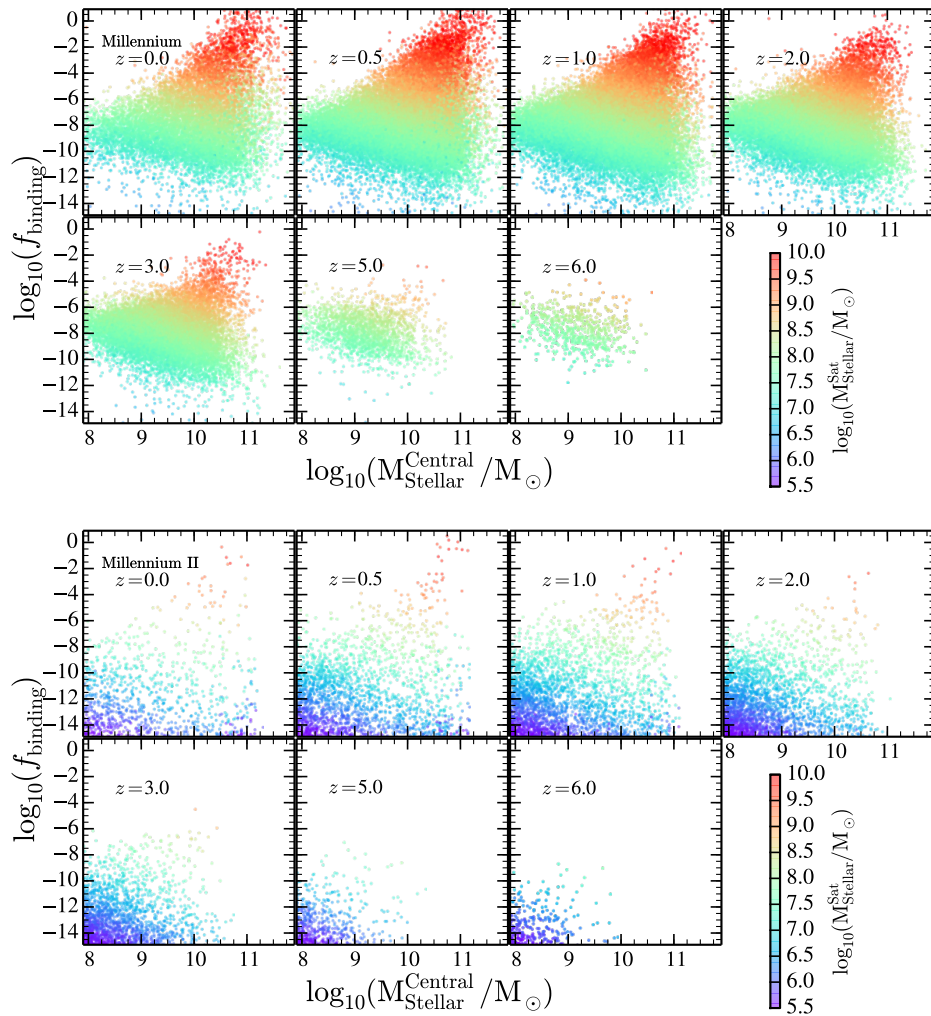


Figure D.3: Plane  $f_{\text{binding}} - M_{\text{stellar}}^{\text{Central}}$  for MS (top) and MSII (bottom) at different redshifts. The color codes the stellar mass of the merging satellite galaxy.

where  $R_{\text{Stellar}}^{\text{Sat}}$  is the mass-weighted average of the half-mass radii of the satellite bulge and the disc components and  $R_{\text{disk}}^{\text{Central}}$  the same but using the cold and stellar disk of the central galaxy. Large values of  $f_{\text{binding}}$  means that the two interacting systems have similar binding energy so the satellite galaxy might survive the interaction inside of the central disk and reach the centre of its massive companion. On the contrary, low values of  $f_{\text{binding}}$  imply the the central galaxy can easily unbound the satellite stellar system inside its disk. In Fig D.3 we present the plane  $f_{\text{binding}} - M_{\text{stellar}}^{\text{Central}}$  at different redshifts for MS and MSII. The color encodes the satellite stellar mass. The figure shows that  $f_{\text{binding}}$  is span in a wide range of values with a clear stellar mass trend and independence with redshift. On one hand, large  $f_{\text{binding}}$  are concentrated in the more massive galaxies ( $\gtrsim 10^{10} M_{\odot}$ ) as a natural consequence of the fact that they can experience minor interactions with massive galaxies harder to unbound. On the other hand, small central galaxies ( $\lesssim 10^{10} M_{\odot}$ ) display smaller  $f_{\text{binding}}$  values during their minor interactions. This ones happen with satellites of low stellar mass compared with the central galaxy stellar and gas disk mass (as we will see in the stellar merger ratio of Fig D.5).

In Fig D.1 lower panel it is presented the evolution of  $n_{\text{mm}}$  when we impose different  $f_{\text{binding}}$  values to set apart minor mergers from *smooth accretion*. Different colors correspond to different thresholds in  $f_{\text{binding}}$ . As we can see, smalls thresholds ( $f_{\text{binding}} > 10^{-10}$ ) have almost a null effect in MS but with dramatic consequences for MSII as they are able to reduce  $\sim 2$  dex the value of MSII  $n_{\text{mm}}$ . Among all

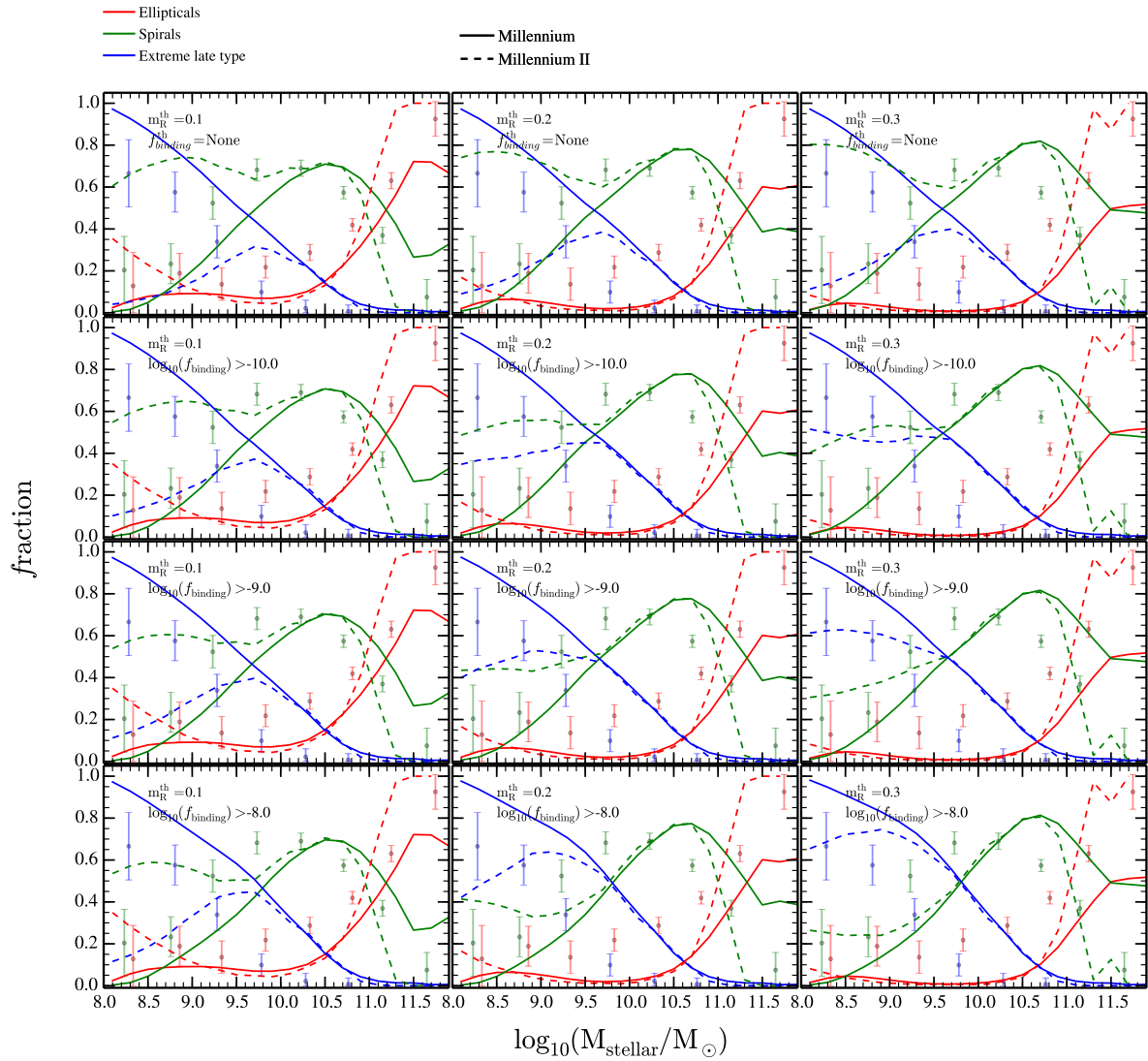


Figure D.4: Evolution of morphology with different combinations of  $f_{\text{binding}}^{\text{th}}$  and major/minor merger threshold  $m_R^{\text{th}}$ . Each row and column correspond to a fix value of  $f_{\text{binding}}^{\text{th}}$  and  $m_R^{\text{th}}$ . Here we have presented the values  $f_{\text{binding}}^{\text{th}} = 10^{-10}, 10^{-9}, 10^{-8}$  and  $m_R^{\text{th}} = 0.1, 0.2, 0.3$

the possible values of  $f_{\text{binding}}$  we find a reasonable  $n_{\text{mm}}$  convergence at  $f_{\text{binding}} \lesssim 10^8 - 10^9$ . Naturally, different  $f_{\text{binding}}$  cuts have also a different repercussion in the  $z=0$  galaxy morphology. In order to study this, in Fig D.4 second column we present the morphology at different  $f_{\text{binding}}$  thresholds, fixing  $m_R^{\text{th}} = 0.2$ . Other columns display the same but varying  $m_R^{\text{th}}$  too. As we can see, despite  $f_{\text{binding}}^{\text{th}} < 10^{-10}$  values have an improvement in the low mass galaxies it is not enough to make MS and MSII converge. When we impose  $f_{\text{binding}}^{\text{th}} > 10^{-9}$ , the improvement in MSII is remarkable. Notice that different  $f_{\text{binding}}$  thresholds have a minimum effect in MS. We have found that the best threshold is  $f_{\text{binding}}^{\text{th}} = 10^{-8.5}$  in binding energy ratios to differentiate between *smooth accretion* ( $f_{\text{binding}} < f_{\text{binding}}^{\text{th}}$ ) and minor merger ( $f_{\text{binding}} > f_{\text{binding}}^{\text{th}}$ ). Notice, that even though this procedure is a way to make converge the two simulations and make the MSII follow the observational data, one could try to implement others prescriptions like an smooth transition between major-minor merger like Hatton et al. (2003) and Somerville et al. (2008) do or try to implement the fact that during major mergers part of the galactic disc could survive (see Hopkins et al. (2009b) and Hopkins et al. (2009c)). Nevertheless, given that our approx works and is the simplest thing we do not implement any of the previous cases but in futures works this topic should be



address and take into account.

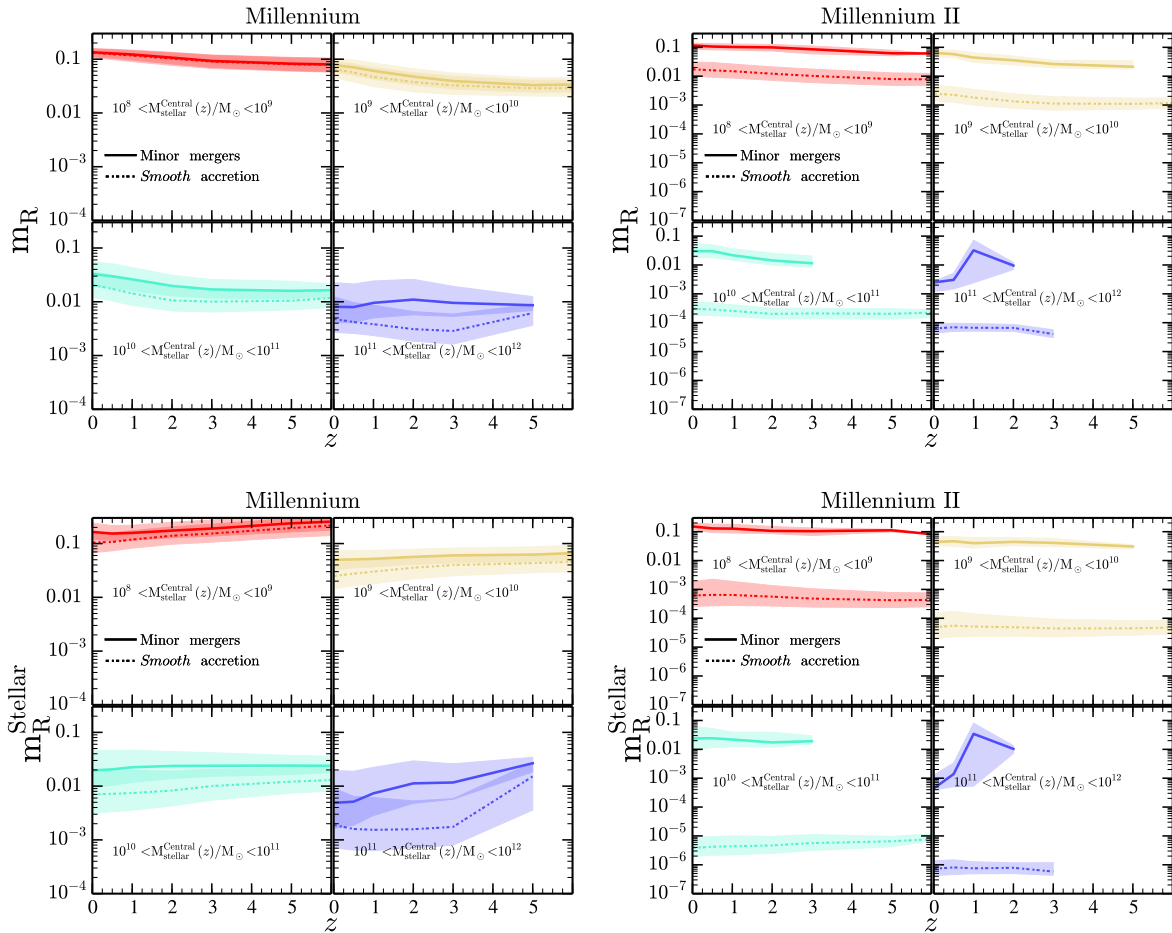


Figure D.5: **Upper panels:** Typical baryonic merger ratios,  $m_R$ , for mergers with  $m_R < m_R^{\text{th}}$  ( $m_R^{\text{th}} = 0.2$ ) in the MS (left) and MSII (right) simulation. The episodes have been divided between minor mergers (solid lines) and *smooth accretion* (dotted dashed lines). Each panel corresponds to a different bin of central galaxy stellar mass at the moment of the merger,  $M_{\text{Stellar}}^{\text{Central}}(z)$ . The shaded area represents the  $1\sigma$  value. **Lower panels:** The same but for the stellar merger ratios.

Finally, we have explore for minor mergers and *smooth accretion* the typical baryonic and stellar merger ratio,  $m_R$  and  $m_R^{\text{Stellar}}$  respectively. Fig D.5 presents the results as a function of redshift and central galaxy stellar mass at the moment of the merger,  $M_{\text{Stellar}}^{\text{Central}}(z)$ . Regarding the baryonic merger ratio, we can see that both MS and MSII display the increasing trend of  $m_R$  value towards lower stellar masses. Interestingly, independently of redshift and central galaxy stellar mass both MS and MSII show that *smooth accretion* display smaller merger ratios than minor merger, fact that is more evident in the MSII than in the MS (consequence of resolution effects). Concerning  $m_R^{\text{Stellar}}$ , we see a similar behavior to the  $m_R$  one. However, in this case the difference between minor mergers and *smooth accretion* is more extreme. While minor mergers  $m_R^{\text{Stellar}}$  values are between 0.1 - 0.01, *smooth accretion* ones display values of  $10^{-3} - 10^{-7}$ .



## APPENDIX E

### EJECTIONS VIA GRAVITATIONAL RECOIL AND THREE BODY SCATTERING

As we have discussed in Section 5.3.4 nuclear BHs can be expelled from the galaxy nuclear region through both gravitational recoils and recoils after 3-body scattering. While the former is led by the final BH-BH coalescence, the latter is the consequence of a complex interaction between a binary BH system and an intruder BH which causes the ejection of the less massive BH. In this appendix, we show that the ejections after a gravitational recoil are more common than the ejections via 3-body scattering. Thus, the population of *ejected* wBHs is fully dominated by gravitationally recoiled BHs. To prove so, in Figure E.1 we present the evolution of the number density ( $n$ ) of ejections through gravitational ejection and 3-body scattering. As shown, at  $M_{\text{halo}} > 10^{11} M_{\odot}$  ejections after gravitational recoils dominate the ejected population, being 1 – 2 dex more frequent at any redshift. As we can see, the ejection after 3-body scattering is dominated by low mass BHs ( $M_{\text{BH}} < 10^6 M_{\odot}$ ) at any redshift and subhalo mass. On the other hand, the ejection of BHs of  $M_{\text{BH}} > 10^8 M_{\odot}$  after a 3-body scattering is relatively rare, with less than 300 events at  $z < 2$ . These events happen mainly in  $M_{\text{halo}} > 10^{13} M_{\odot}$ , which are the ones hosting the galaxies with the most massive BHs in the SAM.

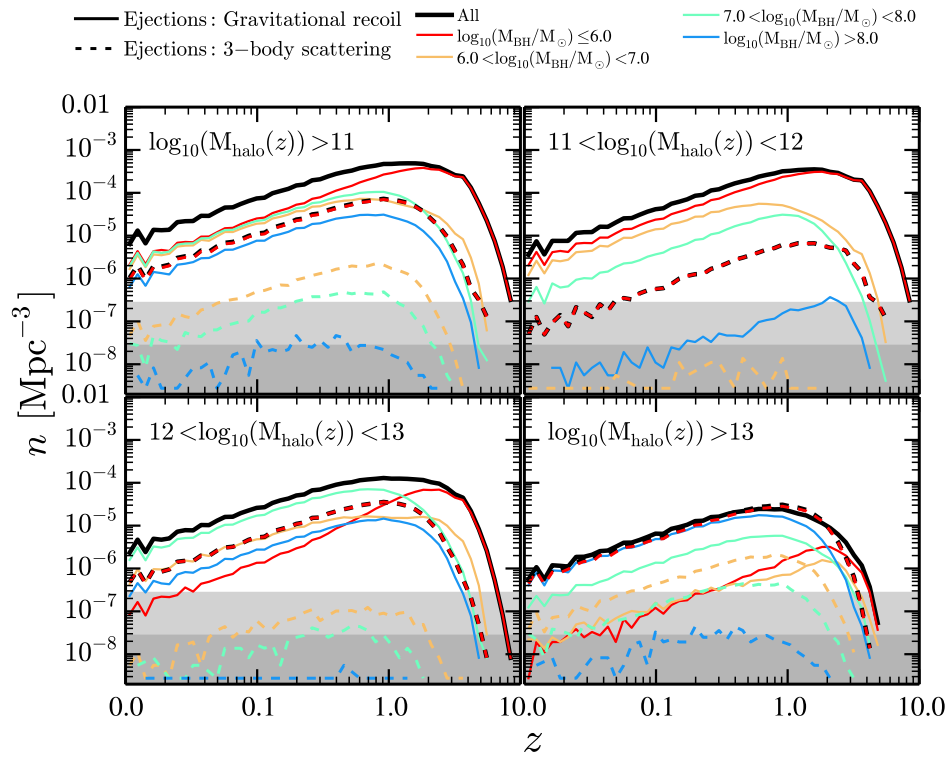


Figure E.1: Number density ( $n$ ) of nuclear black holes that are ejected from the nuclear part of the galaxy. Each panel represents a bin of subhalo mass ( $M_{\text{halo}}$ ). While solid lines display the ejections caused by gravitational recoils, dashed ones display the same but for BHs that were ejected via 3-body scattering. Colors represents different bins of BH mass. With shaded areas it is highlighted the value of  $n$  in which we have less than 100 (faint grey) and 10 (dark grey) events.

## APPENDIX F

### X-RAY LUMINOSITY FUNCTIONS

The redshift evolution of X-ray luminosity functions is presented in Fig.F.1 and Fig.F.2. Soft (0.5 – 2 keV) and hard (2 – 10 keV) X-ray luminosity have been computed by using the bolometric corrections derived in Marconi et al. (2004):

$$\log_{10}(L_{\text{Hx}}/L_{\text{bol}}) = -1.54 - 0.24\mathcal{L} - 0.012\mathcal{L}^2 + 0.0015\mathcal{L}^3 \quad (\text{F.1})$$

$$\log_{10}(L_{\text{Sx}}/L_{\text{bol}}) = -1.64 - 0.22\mathcal{L} - 0.012\mathcal{L}^2 + 0.0015\mathcal{L}^3 \quad (\text{F.2})$$

where  $\mathcal{L} = \log_{10}(L_{\text{bol}}/L_{\odot}) - 12$ ,  $L_{\text{Hx}}$  is the hard X-ray luminosity and  $L_{\text{Sx}}$  soft X-ray luminosity. Predictions are compared to the observational works of Ueda et al. (2014) Aird et al. (2015) and Buchner et al. (2015). Given the uncertainty in modelling the fraction of obscured AGNs, we prefer to compare the simulations to Aird et al. (2015) observed soft X-ray luminosity functions for which the obscured fraction has already been taken into account. The fraction of obscured objects in the hard X-ray band is thought to be relatively small, so for this work we consider that there is no obscuration at hard X-ray wavelengths. As we can see, good agreement between observations and model is reached. In the same figures we have divided the population between elliptical, classical bulges and pseudobulges. As we found with the bolometric luminosity, at  $z \gtrsim 2$  the luminosity functions are dominated by BHs accreting in pseudobulges structures. On contrary, at  $z \lesssim 1$  classical bulges and elliptical galaxies are the structures that preferentially host AGNs and quasars.

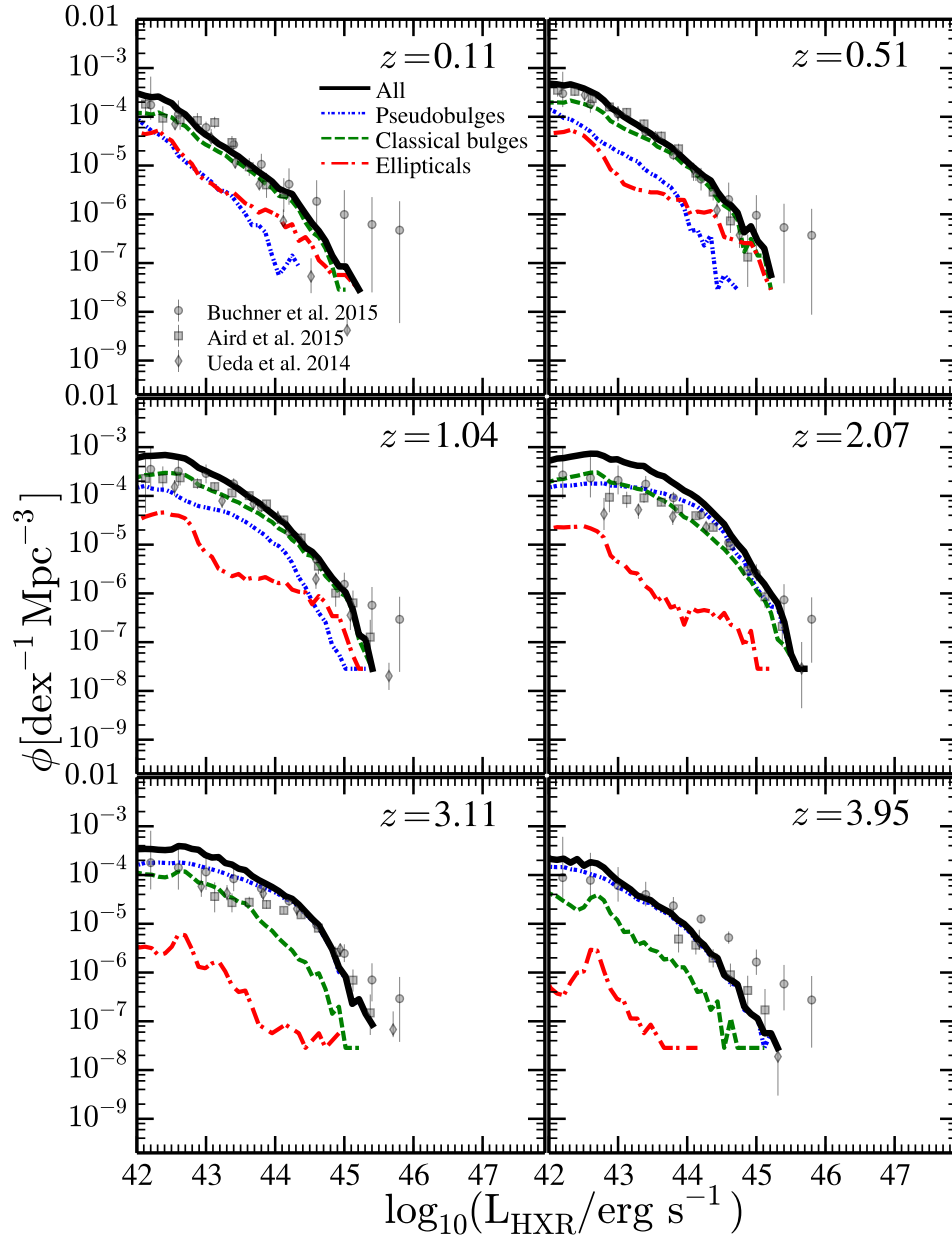


Figure F.1: X-ray luminosity functions at  $z \approx 0.1, 0.5, 1.0, 2.0, 3.0, 4.0$ . In solid black line we present the predicted *hard* X-ray (2-10 keV) luminosity functions. Red dashed-dotted line, green dashed line, and blue dotted line represents the luminosity functions for galaxies hosting, respectively, elliptical, classical bulge, and pseudobulge bulge structure. Each luminosity function is compared with the compilation of Buchner et al. (2015); Aird et al. (2015); Ueda et al. (2014) (circle, square and, diamond points, respectively).

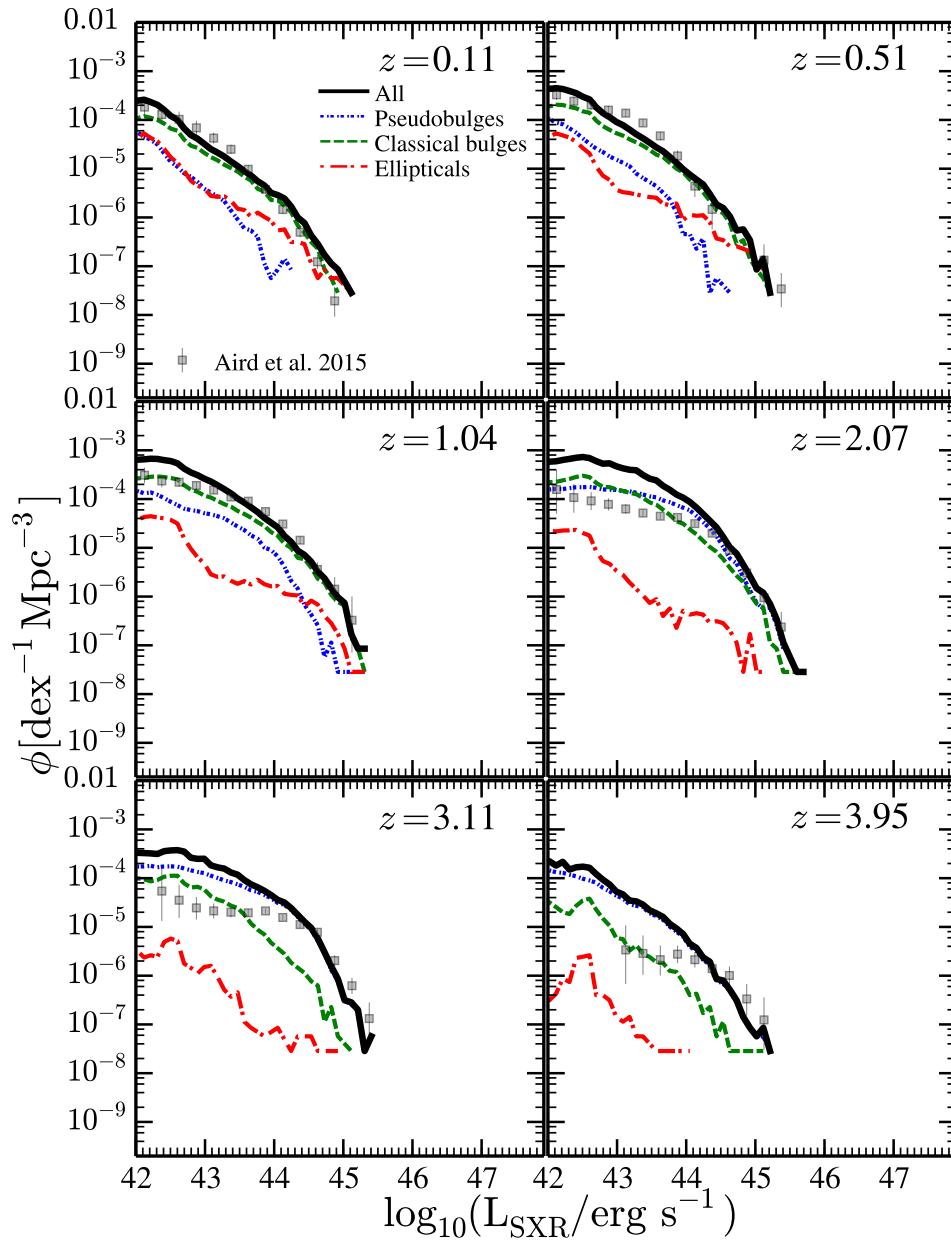


Figure F.2: X-ray luminosity functions at  $z \approx 0.1, 0.5, 1.0, 2.0, 3.0, 4.0$ . In solid black line we present the predicted *soft* X-ray (0.5-2 keV) luminosity functions. Each luminosity functions is compared with the compilation of [Buchner et al. \(2015\)](#); [Aird et al. \(2015\)](#); [Ueda et al. \(2014\)](#) (circle, square and, diamond points, respectively).

## APPENDIX G

### MINIMUM STRUCTURE REPETITION IN THE LIGHTCONE CONSTRUCTION

In this appendix we show that the chosen orientation of the lightcone yields a small overlap between box replicas. In Fig. G.1 we present, for different  $z$ -axis slabs, the original  $(x,y)$  coordinates (i.e. without replication) for galaxies in the redshift range  $0.75 < z < 0.77$ . Each colour represents a different box replication. As we can see, the overlap between the same structures belonging to different replication boxes is minimum. The bigger the redshift range, the larger the overlapping will be.

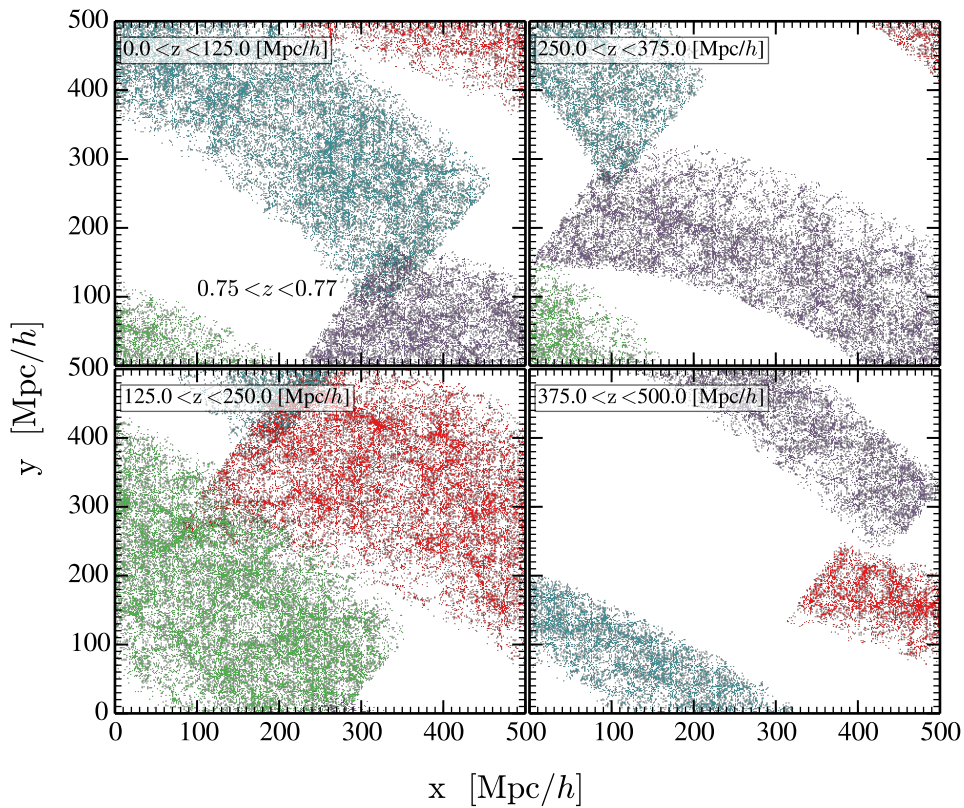


Figure G.1: Example of the minimum repetition between Millennium box replications. For four different  $z$ -axis thicknesses the plane  $x$ - $y$  is shown for galaxies in the redshift bin  $0.75 < z < 0.77$ . To check the structure repetition the modulus 500  $\text{Mpc}/h$  (box size) of the  $x$  and  $y$  position was used. Each colour represents a different box replication. A minimum overlap is present.

# APPENDIX H

## COMPARISON BETWEEN OBSERVED AND PREDICTED LUMINOSITY FUNCTION

In this appendix we extend Section 6.3.2 presenting all the  $H\alpha$ ,  $H\beta$ ,  $[OII]$ , and  $[OIII]_{5007}$  luminosity functions (LF) predicted by our mocks at different redshifts. In Fig. H.1, Fig. H.2, Fig. H.3, Fig. H.4 are presented the LF of the  $H\alpha$ ,  $H\beta$ ,  $[OIII]_{5007}$ , and  $[OII]$  lines, respectively. In all of them black dots represent the observational data, while the solid orange lines and grey dashed lines the predictions of our mock LFs with and without dust attenuation.

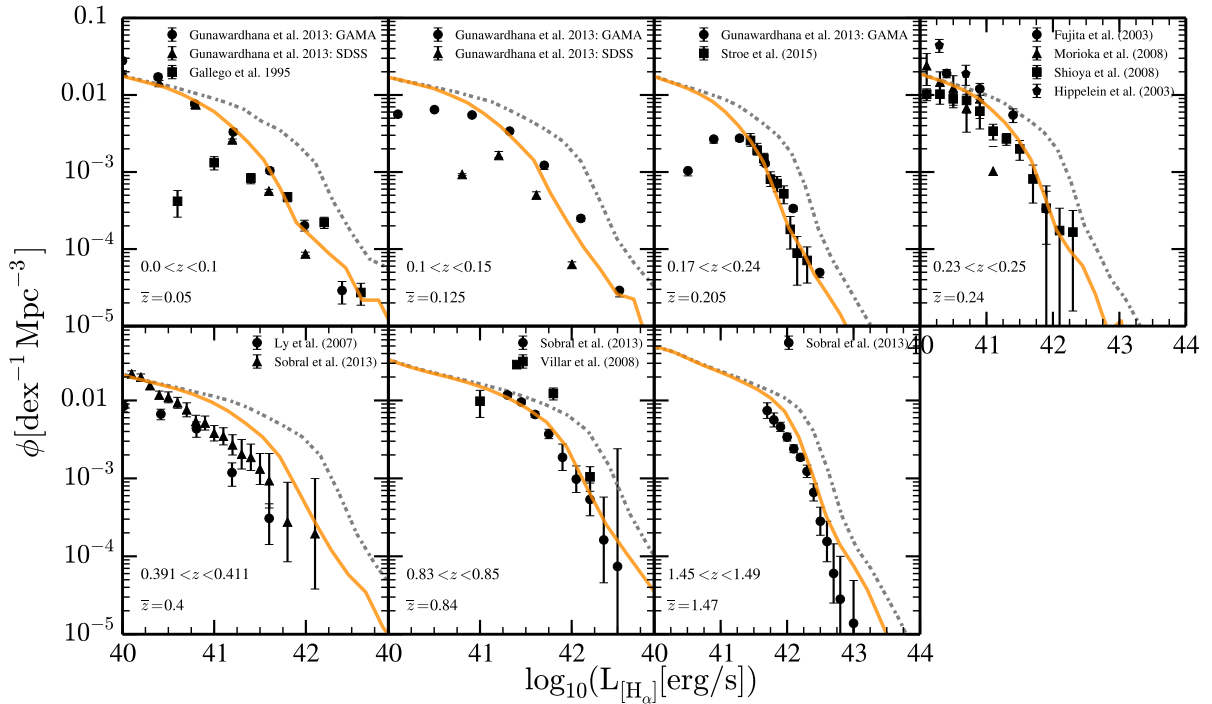


Figure H.1: Luminosity function of  $H\alpha$  line at seven different redshifts. Shown are the comparisons with the Gallego et al. (1995), Fujita et al. (2003), Gunawardhana et al. (2013), Sobral et al. (2013) and Stroe and Sobral (2015) observational data.



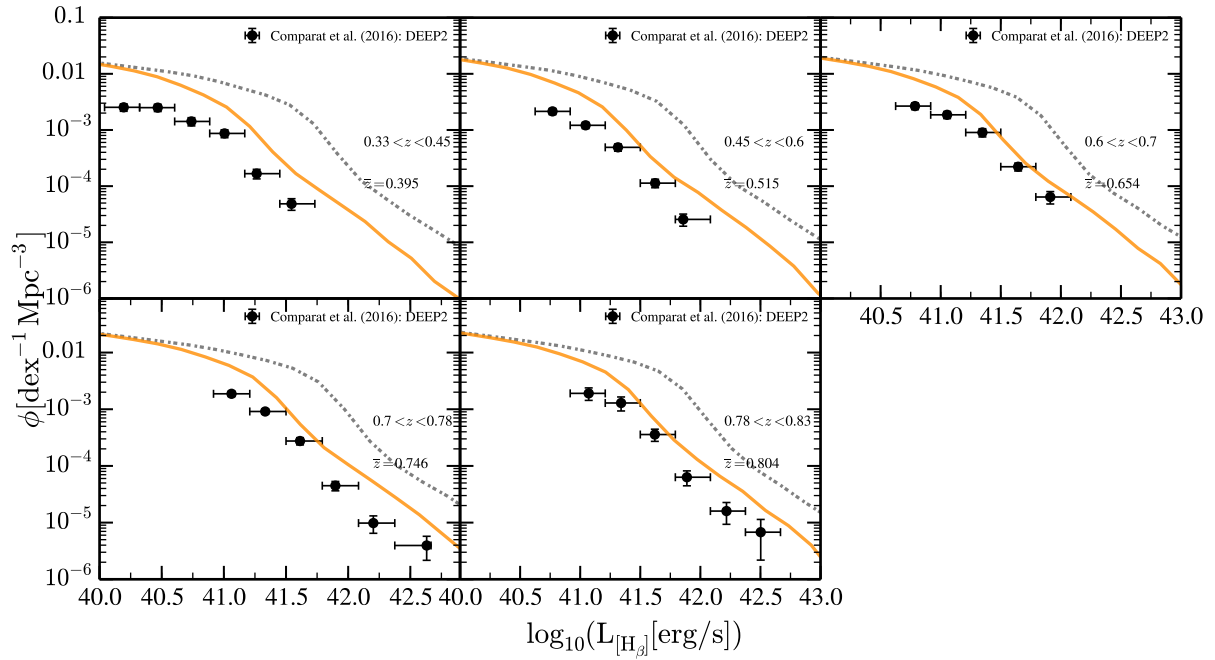


Figure H.2: Luminosity function of H $\beta$  line at five different redshifts. Shown is the comparison with the recent observational work of Comparat et al. (2016). The black dots represent the observational data, while the solid orange line and grey dashed line the predictions of our mocks LF with and without dust attenuation.

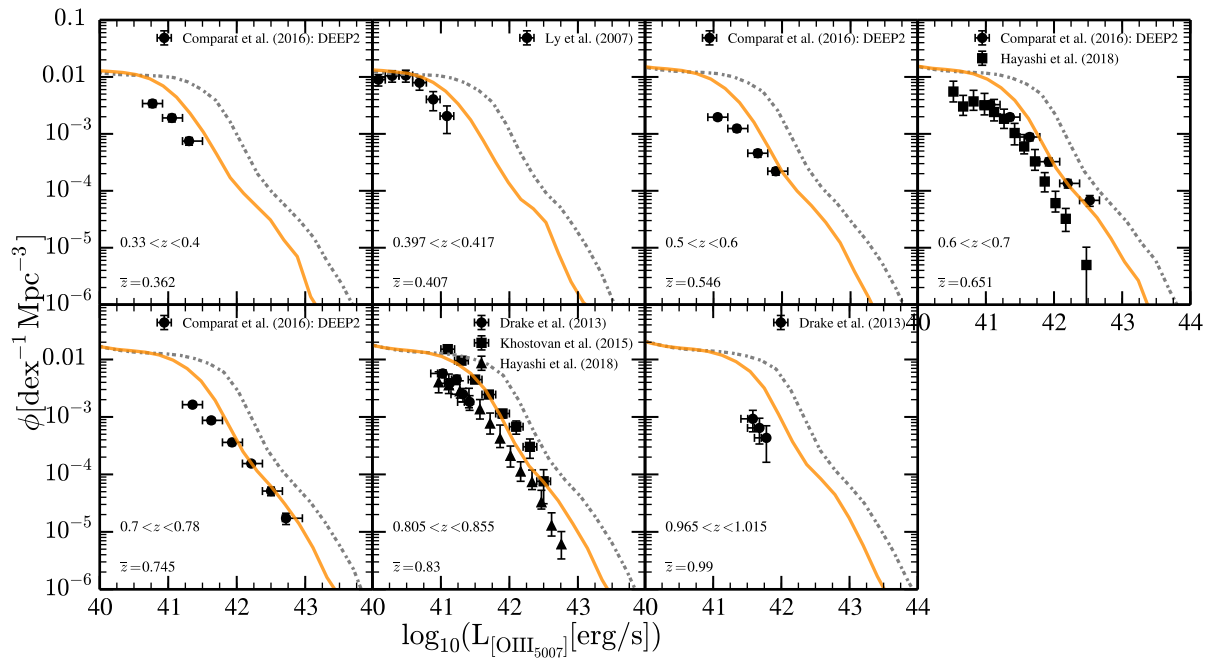


Figure H.3: Luminosity function of [OIII] $_{5007}$  line at seven different redshifts. Shown are the comparisons with the recent observational work of Comparat et al. (2016), Ly et al. (2007), Drake et al. (2013), Khostovan et al. (2015) and Hayashi et al. (2018). The black dots represent the observational data, while the solid orange line and grey dashed line the predictions of our mocks LF with and without dust attenuation.

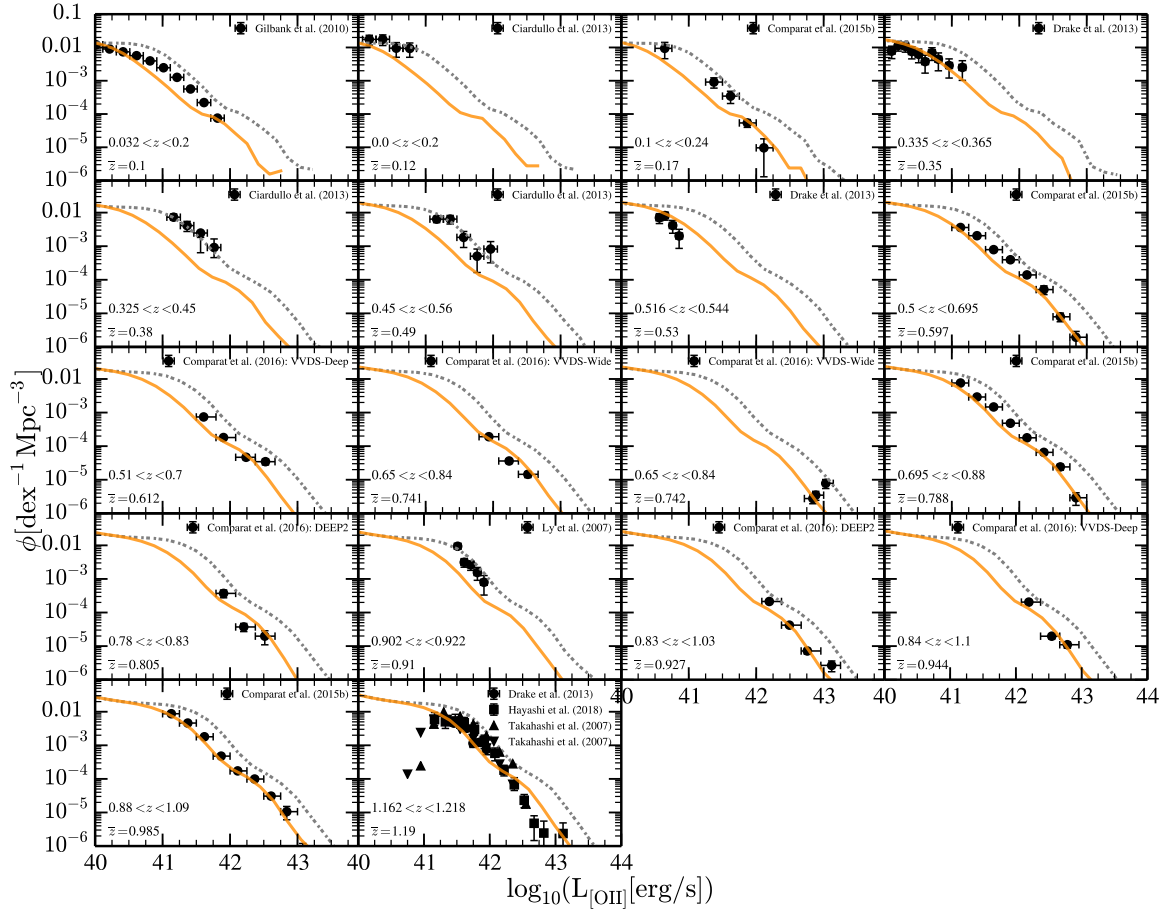


Figure H.4: Luminosity function of [OII] line at 18 different redshifts. Shown are the comparisons with the observational works of Ly et al. (2007), Takahashi et al. (2007), Gilbank et al. (2010), Drake et al. (2013), Ciardullo et al. (2013), Comparat et al. (2016) and Hayashi et al. (2018). The black dots represent the observational data, while the solid orange line and grey dashed line the predictions of our mocks LF with and without dust attenuation.

# David IZQUIERDO-VILLALBA

## *Curriculum vitae*

### Personal Data

INSTITUTION: Centro de Estudios de Física del Cosmos de Aragón (CEFCA)  
ADDRESS: Plaza San Juan 1, Planta-2, Teruel E-44001, Spain  
E-MAIL: [dizquierdo@cefca.es](mailto:dizquierdo@cefca.es)  
E-MAIL 2: [david7y93@gmail.com](mailto:david7y93@gmail.com)

### Education

- 2016 - 2020 **PhD in ASTROPHYSICS**,  
Centro de estudios de Física del Cosmos de Aragón (CEFCA), Teruel, Spain  
Thesis: “*Galactic bulges, spinning black holes and star forming galaxies in their cosmological context: Insights from a semi-analytical perspective*”  
| Supervisor: Dr. Silvia BONOLI and Dr. Carlos HERNÁNDEZ-MONTEAGUDO
- 2015 - 2016 **Master in ASTROPHYSICS**,  
Universidad Complutense de Madrid, Madrid, Spain  
Thesis: “*The environments of radio galaxies in  $\Lambda$ CDM universe: A signature of AGN feedback at high redshifts*”  
| Supervisor: Dr. Alvaro ORSI and Dr. Silvia BONOLI
- 2011 - 2015 **Undergraduate Degree in PHYSICS**,  
Universidad de Zaragoza, Zaragoza, Spain  
Thesis: “*Cosmic rays on the earth surface: Gas detectors*”  
| Supervisor: Dr. Gloaria LUZÓN MARCO

### Grants and fellowships

- 2017 PhD grant – Programa Operativo Fondo Social Europeo de Aragón 2014-2020.  
2020 Erasmus grant – Zaragoza University – Not used because the COVID-19 pandemic.

## Research interest

During my academic career I have been working with semi-analytical models of galaxy formation. In particular, I have focused on the build-up of galaxy bulges, growth of supermassive black holes and creating mock lightcones for the new generation of multi-narrow band photometric surveys. Despite my interest in semi-analytical models, I started working with the outputs of hydrodynamical simulations. Particularly, with the ones of TNG100.

*Theoretical galaxy formation (galaxy formation models). Black hole growth. Black hole spin. Black hole binaries. Galaxy morphology. Galaxy bulges. Mock galaxy lightcones. Emission line galaxies. Photometric surveys: narrow-band and broad-band.*

## Publication list

- i) *The miniJPAS survey: a preview of the Universe in 56 colours*  
Bonoli, S.; Marín-Franch, A.; Varela, J.; Vázquez Ramió, H.; Abramo, L. R.; Cenarro, A. J.; Dupke, R. A.; Vílchez, J. M.; Cristóbal-Hornillos, D.; González Delgado, R. M.; Hernández-Monteagudo, C.; ...; **Izquierdo-Villalba, David**; et al. 2020, arXiv200701910B (Submitted to A&A)
- ii) *J-PLUS: Unveiling the brightest-end of the Ly $\alpha$  luminosity function at  $2 < z < 3.3$  over  $1000 \text{ deg}^2$*   
Spinoso, Daniele; Orsi, Alvaro; López-Sanjuan, Carlos; Bonoli, Silvia; Viironen, Kerttu; **Izquierdo-Villalba, David**; Sobral, David; Gurung-López, Siddhartha; et al. 2020, arXiv200615084S (Accepted to publication in A&A)
- iii) *From galactic nuclei to the halo outskirts: tracing supermassive black holes across cosmic history and environments*  
**Izquierdo-Villalba, David**; Bonoli, Silvia; Dotti, Massimo; Sesana, Alberto; Rosas-Guevara, Yetli; Spinoso, Daniele; 2020, MNRAS 495 4681
- iv) *J-PLUS: Synthetic galaxy catalogues with emission lines for photometric surveys*  
**Izquierdo-Villalba, David**; Angulo, Raul E.; Orsi, Alvaro; Hurier, Guillaume; Vilella-Rojo, Gonzalo; Bonoli, Silvia; López-Sanjuan, Carlos; et al. 2019, A&A, 631, A82
- v) *The buildup of strongly-barred galaxies in the TNG100 simulation*  
Rosas-Guevara, Yetli; Bonoli, Silvia; Dotti, Massimo; Zana, Tommaso; Nelson, Dylan; Pillepich, Annalisa; Ho, Luis C.; **Izquierdo-Villalba, David**; Hernquist, Lars; Pakmor, Ruediger 2019 MNRAS 491 2547
- vi) *The build-up of pseudo-bulges in a hierarchical universe*  
**Izquierdo-Villalba, David**; Bonoli, Silvia; Spinoso, Daniele; Rosas-Guevara, Yetli; Henriques, Bruno M. B.; Hernández-Monteagudo, Carlos 2019, MNRAS 488 609
- vii) *J-PLUS: The Javalambre Photometric Local Universe Survey* Cenarro, A. J.; Moles, M.; Cristóbal-Hornillos, D.; Marín-Franch, A.; Ederoclite, A.; Varela, J.; López-Sanjuan, C.; Hernández-Monteagudo, C.; Angulo, R. E.; Vázquez Ramió, H.; Viironen, K.; Bonoli, S.; Orsi, A. A.; Hurier, G.; San Roman, I.; Greisel, N.; Vilella-Rojo, G.; Díaz-García, L. A.; Logroño-García, R.; Gurung-López, S. Spinoso, D.; **Izquierdo-Villalba, D.**; et al. 2018, A&A 622, A176
- viii) *The environment of radio galaxies: a signature of AGN feedback at high redshifts*  
**Izquierdo-Villalba, David**; Orsi, Álvaro A.; Bonoli, Silvia; Lacey, Cedric G.; Baugh, Carlton M.; Griffin, Andrew J. 2018, MNRAS, 480, 1340

## Talks and conferences

- SEPT. 2019 *Young Astronomers on Galactic Nuclei*, Instituto de Astrofísica de Canarias, Spain  
| Talk: "The cosmological context of wandering black holes"
- JULY 2019 *Seminar of cosmology*, Max-Planck-Institut für Astrophysik (MPA), Germany  
| Talk: "The effect of gravitational recoil on black hole growth and scaling relation"
- JUNE 2019 *Ph.D conferences*, Zaragoza, Spain  
| Talk: "Can the black holes live outside of the galaxies?"
- MAY 2019 *XVII J-PAS meeting*, Madrid, Spain  
| Talk: "Mock galaxy lightcones for photometric surveys"
- OCT. 2018 *Young Astronomers on Galactic Nuclei*, Budapest, Hungary  
| Talk: "Supermassive black hole growth: gas accretion and spin evolution"
- SEPT. 2018 *Probing the dark universe: OAJ-LSC synergies*, Zaragoza, Spain  
| Only attendance
- SEPT. 2018 *Understanding emission line galaxies for the next generation of cosmological surveys*, Teruel, Spain  
| Talk: "Mock galaxy lightcone with emission line for narrow band photometric surveys"
- JULY 2018 *The early growth of supermassive black holes*, Sexten, Italy  
| Talk: "Supermassive black hole growth in galaxy formation models"
- APRIL 2018 *Simulated skies for new-generation spectroscopic surveys*, Madrid, Spain  
| Talk: "Mock galaxy lightcone with emission line for narrow band photometric surveys"
- OCT. 2017 *Young Astronomers on Galactic Nuclei*, Teruel, Spain  
| Talk: "Supermassive black hole growth in galaxy formation models"
- OCT. 2017 *Early data release and scientific Exploitation of J-PLUS survey*, Teruel, Spain  
| Talk: "Mock galaxy lightcones for narrow-band photometric surveys"
- SEPT. 2017 *Fundamental cosmology meeting*, Teruel, Spain  
| Only attendance
- SEPT. 2017 *Ph.D conference*, Zaragoza, Spain  
| Talk: "Living in a semi-analytical universe: Black holes and mocks catalogues"
- OCT. 2016 *Aragón-Valencia meeting: Astro and Cosmo with LSS*, Canfranc, Spain  
| Talk: "The environments of radio galaxies in  $\Lambda$ CDM universe"
- SEPT. 2016 *13th J-PAS meeting*, Teruel, Spain  
| Only attendance

## Posters

- JULY 2018 *Sociedad Española de astronomía: XIII Reunión Científica*, Salamanca, Spain  
| Poster: "Supermassive black hole growth in galaxy formation models"  
| Poster: "Mock galaxy lightcone with emission line for narrow band photometric surveys"
- JAN. 2018 *48th Saas-Fee Advance course: Black hole formation and growth*, Saas-Fee, Switzerland  
| Poster: "Supermassive black hole growth in galaxy formation models"

## Schools

- JAN. 2018 *48th Saas-Fee Advance course: Black hole formation and growth*, Saas-Fee, Switzerland

## Projects involved

- Javalambre Photometric Local Universe Survey (J-PLUS)  
Javalambre Physics of the Accelerating Universe Astrophysical Survey (J-PAS)

## Experience as referee

- 2020 Referee for the journal *Monthly Notices of the Royal Astronomical Society* (MNRAS)  
2019 Referee for the journal *Monthly Notices of the Royal Astronomical Society* (MNRAS)

## Experience as a local organizing committee (LOC)

- 2019 *J-PAS RIA Workshop: The Universe in 56 colours: science with the first J-PAS data*  
2018 *Understanding Emission-line galaxies for the next generation of cosmological surveys*  
2017 *Early Data Release and Scientific Exploitation of the J-PLUS Survey*  
2017 *Meeting on Fundamental cosmology*

## Visits to other institutes

- JANUARY 2020 DONOSTIA INTERNATIONAL PHYSICS CENTER (DIPC), SAN SEBASTIÁN, SPAIN  
| Dr. Silvia BONOLI (2 weeks)  
OCTOBER 2019 DONOSTIA INTERNATIONAL PHYSICS CENTER (DIPC), SAN SEBASTIÁN, SPAIN  
| Dr. Silvia BONOLI (2 weeks)  
JULY 2019 MAX-PLANCK-INSTITUT FÜR ASTROPHYSIK (MPA), GARCHING, GERMANY  
| Dr. Volker SPRINGEL (1 month)  
MARCH 2019 DONOSTIA INTERNATIONAL PHYSICS CENTER (DIPC), SAN SEBASTIÁN, SPAIN  
| Dr. Silvia BONOLI (2 weeks)  
OCTOBER 2018 DONOSTIA INTERNATIONAL PHYSICS CENTER (DIPC), SAN SEBASTIÁN, SPAIN  
| Dr. Silvia BONOLI (2 weeks)

## Languages and Skills

SPANISH (Mother tongue), ENGLISH (B2 level)  
C, C++, PYTHON, LINUX, BASH, HDF5 FILES, L<sup>A</sup>T<sub>E</sub>X

## References

Dr. Silvia BONOLI  
| DONOSTIA INTERNATIONAL PHYSICS CENTER (DIPC), SAN SEBASTIÁN, SPAIN  
| [sb.bonoli@gmail.com](mailto:sb.bonoli@gmail.com)

Dr. Raúl ANGULO  
| DONOSTIA INTERNATIONAL PHYSICS CENTER (DIPC), SAN SEBASTIÁN, SPAIN  
| [reangulo@gmail.com](mailto:reangulo@gmail.com)

Dr. Álvaro ORSI  
| CENTRO DE ESTUDIOS DE FISICA DEL COSMOS DE ARAGÓN (CEFCA), TERUEL, SPAIN  
| [aaorsi@gmail.com](mailto:aaorsi@gmail.com)

Dr. Carlos HERNÁNDEZ-MONTEAGUDO  
| CENTRO DE ESTUDIOS DE FISICA DEL COSMOS DE ARAGÓN (CEFCA), TERUEL, SPAIN  
| [chm@cefca.es](mailto:chm@cefca.es)





